Methods in Molecular Biology 1745

Springer Protocols

Natasha S. Barteneva
Ivan A. Vorobjev *Editors*

Cellular Heterogeneity

Methods and Protocols

Humana Press

METHODS IN MOLECULAR BIOLOGY

Series Editor
John M. Walker
School of Life and Medical Sciences
University of Hertfordshire
Hatfield, Hertfordshire, AL10 9AB, UK

For further volumes:
http://www.springer.com/series/7651

Cellular Heterogeneity

Methods and Protocols

Edited by

Natasha S. Barteneva

PCMM-Harvard Medical School,
Boston Children's Hospital, Boston, MA, USA;
Department of Biology, School of Sciences and Technology,
Nazarbayev University, Astana, Kazakhstan

Ivan A. Vorobjev

Department of Biology, School of Sciences and Technology,
Nazarbayev University, Astana, Kazakhstan

Humana Press

Editors
Natasha S. Barteneva
PCMM-Harvard Medical School
Boston Children's Hospital
Boston, MA, USA

Department of Biology
School of Sciences and Technology
Nazarbayev University
Astana, Kazakhstan

Ivan A. Vorobjev
Department of Biology
School of Sciences and Technology
Nazarbayev University
Astana, Kazakhstan

ISSN 1064-3745 ISSN 1940-6029 (electronic)
Methods in Molecular Biology
ISBN 978-1-4939-7679-9 ISBN 978-1-4939-7680-5 (eBook)
https://doi.org/10.1007/978-1-4939-7680-5

Library of Congress Control Number: 2018930254

Printed on acid-free paper

This Humana Press imprint is published by Springer Nature
The registered company is Springer Science+Business Media, LLC
The registered company address is: 233 Spring Street, New York, NY 10013, U.S.A.

Dedication

To the memory of Anatoly Shatkin (1928–1994), colleague and mentor, and to all my mentors: Thank you.

Natasha S. Barteneva

To the memory of my grandmothers and to my dad whose outstanding and dramatic fates I have always drawn upon as the source of inspiration to work.

Ivan A. Vorobjev

Preface

"The more specific idea of Evolution now reached is—a change from an indefinite, incoherent homogeneity to a definite, coherent heterogeneity, accompanying the dissipation of motion and integration of matter."

–Herbert Spencer

Cellular heterogeneity results from distinct intrinsic features like a stage in the cell cycle, developmental stage, mutational status or epigenetic inheritance, or external parameters such as growth conditions, the available sources of energy, stress conditions, etc. Efforts of many researchers who concentrated on single-cell individual characteristics and related analytical techniques made possible the emergence of highly powerful and sophisticated methods of research. Cellular heterogeneity is a universal property of cellular systems in nature and was disregarded for years with major attention paid to averaging methods such as Western blotting, Southern blotting, etc. In recent years, however, an urgent need for new approaches and technologies suitable for the determination of group structure and analysis of heterogeneity of larger cellular populations with precision and sensitivity applied for analysis of single cells had appeared. These methods are high dimensional by nature and include such high-throughput technologies as mass cytometry and imaging flow cytometry. Integrating diverse sources of data not only increases a statistical power of cellular analysis but also provides deeper biological understanding and systemic biological insights into cell states and mechanisms of cell functioning.

The *Cellular Heterogeneity: Methods and Protocols* volume strives to fill this gap by covering the need for a manual that goes beyond single-cell analysis toward new detection methods to reveal cell population heterogeneity and its mechanisms of development. It would not be possible to provide perspective on all available techniques to study cellular heterogeneity; therefore, the primary accent of the book is on cytometric, live cell imaging and spectroscopic approaches that reflect the experience and opinions of editors and authors. The eclectic combination of topics reveals intrinsic heterogeneity as a fast-developing research area. It is becoming increasingly evident that a snapshot of heterogeneity on the subcellular or cellular level of prokaryotic or metazoan populations of cells is not sufficient to understand underlying mechanisms of its development. Acquisition of significant amounts of quantitative data and further description using cluster analysis or other sophisticated statistical algorithms are required. All chapters are written by internationally recognized experts and pioneering researchers in the field of cellular heterogeneity, who have particular interest and expertise in techniques covered in their chapters. Based on the author's personal experience, it provides insights in a workflow of techniques and challenges. We hope that this volume will assist researchers from different scientific areas.

The volume is organized into five parts. *The first general part* provides an introduction to the analysis of cell heterogeneity in different systems (Chapter 1) and a detailed description of integrating the analysis of cell heterogeneity in assay development using Kolmogorov-

Smirnov statistics (Gough et al., Chapter 2). Patsch et al. (Chapter 3) describe dynamic phenotype measurements of heterogeneous cell populations using the novel Tracking Aberration Measure (TrAM) algorithm. *The next part* focuses on the use of cytometry in cell heterogeneity research. Brodie and Tosevski (Chapter 4) describe the innovative mass-cytometry analysis of T helper cells and its activation status using the 33-parameter panel and cluster analysis, whereas Dashkova et al. (Chapter 5) apply imaging and spectral flow cytometry toward taxonomic and phenotypic analysis of microalgae heterogeneity based on spectral and imaging cytometry approaches. Moreover, Crawford and Penner-Hahn (Chapter 6) describe a technique to characterize cell-to-cell elemental variability (cellular metallome) by X-ray fluorescence and provide an excellent overview of the experimental setup and key methodological applications using mammalian cells and *Saccharomyces cerevisiae*. The next four chapters describe imaging and flow cytometry methods for the characterization of cellular heterogeneity in different populations, such as myeloid cells (Mathie et al., Chapter 7; Trifonova and Barteneva, Chapter 8), neurons (Kopeikina et al., Chapter 9) and glial cells (Dukhinova et al., Chapter 10).

The third part is devoted to high-throughput fluorescent microscopy and microscopy-based spectroscopy methods in heterogeneity studies. Detailed microscopic analysis of microtubule dynamics in cell culture (Serikbayeva et al., Chapter 11) shows the large degree of heterogeneity of microtubule behavior in the cell population and response to the treatment with anti-tubulin drugs. Substantial heterogeneity in the dynamics of formation of focal adhesions and focal contacts in motile fibroblasts (Gladkikh et al., Chapter 12) might represent differences in the behavior of individual cells on the substrate. Maria Navas-Moreno and James W. Chan (Chapter 13) describe Raman spectroscopy of single cells isolated using optical tweezers that allow obtaining strong spectrum from a single cell or its part (nucleus). This label-free approach provides an opportunity to monitor dynamic chemical alterations at a single-cell level.

The fourth part describes metabolic and molecular biological methods in bacterial and protozoan cell heterogeneity tracking. Bhat and coauthors (Chapter 14) describe the creation of reporter strains of mycobacteria making it possible to measure heterogeneity of cellular levels of NADH/NAD^+ among these bacteria and show high variance in the NADH/NAD^+ levels among individual mycobacteria residing in macrophages. Seco-Hidalgo and others (Chapter 15) analyze heterogeneity in protozoan parasites using PCR fingerprinting of multigene surface proteins. Pablo Nickel and Víctor de Lorenzo (Chapter 16) propose a procedure to examine integral bacterial culture growth along with monitoring the metabolic activity of individual cells and show that gradual change in the whole population results from a stochastic switch in the individual bacteria.

The last part deals with heterogeneity in the chromatin structure and cell cycle progression of mammalian cells. Elizaveta Fasler-Kan et al. (Chapter 17) describe methods for single-cell cloning, karyotype analysis, and fluorescence in situ hybridization (FISH) and discuss different chromosomal aberrations stably expressed in tumor and nearly normal cell lines. Potashnikova et al. (Chapter 18) demonstrate the possibility of FACS isolation and subsequent NGS analysis of cells in different stages of the cell cycle and discuss heterogeneity of gene expression during cell cycle progression. Gladstein et al. (Chapter 19) describe in detail instrumentation and measurements made by partial wave spectroscopic microscopy. Authors discuss heterogeneity of chromatin structure at the nanoscale level determined by this technique and its possible role in carcinogenesis.

The methodology of the volume applies to a variety of fields and benefit from collaborative, innovative efforts.

We wish to thank authors for their great contributions. Also, we are grateful to Harvard Medical School and Boston Children's Hospital scientific administration that our international collaborative team did not cease to exist and still supported in our endeavors. Finally, we would like to thank the production team at Springer for their excellent support as well as Professor John Walker, the founder and father of MiMB (*Methods in Molecular Biology* series), for his outstanding editorial help.

We will be very pleased if this volume will become a useful resource for researchers in academia and industry.

Boston, MA, USA ***Natasha S. Barteneva***
Astana, Kazakhstan ***Ivan A. Vorobjev***

Contents

Contributors

Nijas Aliu • *Department of Human Genetics, University Children's Hospital, Inselspital, Bern, Switzerland*

Luay M. Almassalha • *Department of Biomedical Engineering, Northwestern University, Evanston, IL, USA*

Vadim Backman • *Department of Biomedical Engineering, Northwestern University, Evanston, IL, USA*

Natasha S. Barteneva • *PCMM-Harvard Medical School, Boston Children's Hospital, Harvard Medical School, Boston, MA, USA; Department of Biology, School of Sciences and Technology, Nazarbayev University, Astana, Kazakhstan*

Steffen Berger • *Department of Pediatric Surgery, Inselspital, University Hospital Bern and Department of Biomedical Research, University of Bern, Bern, Switzerland*

Shabir Ahmad Bhat • *Council of Scientific and Industrial Research, Institute of Microbial Technology, Chandigarh, India*

Tess Melinda Brodie • *Mass Cytometry Facility, University of Zurich, Zurich, Switzerland*

James W. Chan • *Center for Biophotonics, University of California, Davis, Sacramento, CA, USA; Department of Pathology and Laboratory Medicine, Center for Biophotonics, University of California, Davis, Sacramento, CA, USA*

John E. Chandler • *Department of Biomedical Engineering, Northwestern University, Evanston, IL, USA*

Lusik Cherkezyan • *Department of Biomedical Engineering, Northwestern University, Evanston, IL, USA*

Jeff Clapper • *Sony Biotechnology Inc., San Jose, CA, USA*

Alastair L. Corbin • *Kennedy Institute of Rheumatology, Oxford University, Oxford, UK*

Andrew M. Crawford • *Department of Geology, University of Saskatchewan, Saskatoon, SK, Canada*

Veronika Dashkova • *National Laboratory Astana, Department of Biology, School of Science and Technology, Nazarbayev University, Astana, Kazakhstan*

Víctor de Lorenzo • *Systems and Synthetic Biology Program, Centro Nacional de Biotecnología (CNB-CSIC), Madrid, Spain*

Luis Miguel de Pablos • *Departamento de Parasitología, Grupo de Bioquímica y Parasitología Molecular CTS-183, Universidad de Granada, Granada, Spain*

Marina Dukhinova • *School of Biomedical Sciences, Faculty of Medicine, The Chinese University of Hong Kong, Hong Kong, SAR, China*

Hayley L. Eames • *Kennedy Institute of Rheumatology, Oxford University, Oxford, UK*

Elizaveta Fasler-Kan • *Department of Biomedicine, University of Basel and University Hospital Basel, Basel, Switzerland; Department of Pediatric Surgery, Inselspital, University Hospital Bern and Department of Biomedical Research, University of Bern, Bern, Switzerland*

Aleena Gladkikh • *Department of Cell Biology and Histology, School of Biology, M.V. Lomonosov Moscow State University, Moscow, Russia*
Scott Gladstein • *Department of Biomedical Engineering, Northwestern University, Evanston, IL, USA*
Sergey A. Golyshev • *A.N. Belozersky Institute of Physico-Chemical Biology, M.V. Lomonosov Moscow State University, Moscow, Russia*
Albert Gough • *Drug Discovery Institute, University of Pittsburgh, Pittsburgh, PA, USA; Department of Computational and Systems Biology, University of Pittsburgh, Pittsburgh, PA, USA*
Iram Khan Iqbal • *Council of Scientific and Industrial Research, Institute of Microbial Technology, Chandigarh, India*
Sholpan Kauanova • *School of Engineering, Nazarbayev University, Astana, Kazakhstan; National Laboratory Astana, Nazarbayev University, Astana, Kazakhstan*
Sylvia Ketterer • *Department of Biomedicine, University of Basel and University Hospital Basel, Basel, Switzerland*
Anna V. Klepikova • *A.N. Belozersky Institute of Physico-Chemical Biology, M.V. Lomonosov Moscow State University, Moscow, Russia; Institute for Information Transmission Problems, Russian Academy of Sciences, Moscow, Russia; School of Bioengineering and Bioinformatics, M.V. Lomonosov Moscow State University, Moscow, Russia*
Ekaterina Kopeikina • *School of Biomedical Sciences, Faculty of Medicine, The Chinese University of Hong Kong, Hong Kong, SAR, China*
Anastasia Kovaleva • *Department of Cell Biology and Histology, School of Biology, M.V. Lomonosov Moscow State University, Moscow, Russia*
Ashwani Kumar • *Council of Scientific and Industrial Research, Institute of Microbial Technology, Chandigarh, India*
Maria D. Logacheva • *A.N. Belozersky Institute of Physico-Chemical Biology, M.V. Lomonosov Moscow State University, Moscow, Russia; Institute for Information Transmission Problems, Russian Academy of Sciences, Moscow, Russia*
Sara A. Mathie • *Kennedy Institute of Rheumatology, Oxford University, Oxford, UK*
Peter Meyer • *Department of Ophthalmology, University of Basel, Basel, Switzerland*
Andrey A. Mironov • *Institute for Information Transmission Problems, Russian Academy of Sciences, Moscow, Russia; School of Bioengineering and Bioinformatics, M.V. Lomonosov Moscow State University, Moscow, Russia*
Shannon M. Mumenthaler • *Lawrence J. Ellison Institute for Transformative Medicine, University of Southern California, Los Angeles, CA, USA*
Maria Navas-Moreno • *Center for Biophotonics, University of California, Davis, Sacramento, CA, USA; Department of Pathology and Laboratory Medicine, Center for Biophotonics, University of California, Davis, Sacramento, CA, USA*
Pablo I. Nikel • *The Novo Nordisk Foundation Center for Biosustainability, Technical University of Denmark, Lyngby, Denmark*
Antonio Osuna • *Departamento de Parasitología, Grupo de Bioquímica y Parasitología Molecular CTS-183, Universidad de Granada, Granada, Spain*
Katherin Patsch • *Lawrence J. Ellison Institute for Transformative Medicine, University of Southern California, Los Angeles, CA, USA*

Alexey A. Penin • *A.N. Belozersky Institute of Physico-Chemical Biology, M.V. Lomonosov Moscow State University, Moscow, Russia; Department of Genetics, School of Biology, M.V. Lomonosov Moscow State University, Moscow, Russia; Institute for Information Transmission Problems, Russian Academy of Sciences, Moscow, Russia*

James E. Penner-Hahn • *Department of Chemistry and Biophysics, University of Michigan, Ann Arbor, MI, USA*

Eugene D. Ponomarev • *School of Biomedical Sciences, Faculty of Medicine, The Chinese University of Hong Kong, Hong Kong, SAR, China*

Daria M. Potashnikova • *Department of Cell Biology and Histology, School of Biology, M.V. Lomonosov Moscow State University, Moscow, Russia*

Daniel Ruderman • *Lawrence J. Ellison Institute for Transformative Medicine, University of Southern California, Los Angeles, CA, USA*

Sabrina Ruggiero • *Department of Pediatric Surgery, Inselspital, University Hospital Bern and Department of Biomedical Research, University of Bern, Bern, Switzerland*

Mark Schurdak • *Drug Discovery Institute, University of Pittsburgh, Pittsburgh, PA, USA; Department of Computational and Systems Biology, University of Pittsburgh, Pittsburgh, PA, USA; Pittsburgh Cancer Institute, University of Pittsburgh, Pittsburgh, PA, USA*

Víctor Seco-Hidalgo • *Escuela de Medicina, Universidad Internacional de Ecuador, Quito, Ecuador*

Anara Serikbaeva • *Department of Biology, School of Science and Technology, Nazarbayev University, Astana, Kazakhstan; Department of Biology, School of Science and Technology, Nazarbayev University, Astana, Kazakhstan*

Eugene V. Sheval • *A.N. Belozersky Institute of Physico-Chemical Biology, M.V. Lomonosov Moscow State University, Moscow, Russia*

Tong Ying Shun • *Drug Discovery Institute, University of Pittsburgh, Pittsburgh, PA, USA*

Andrew Stawarz • *Department of Biomedical Engineering, Northwestern University, Evanston, IL, USA*

Hariharan Subramanian • *Department of Biomedical Engineering, Northwestern University, Evanston, IL, USA*

D. Lansing Taylor • *Drug Discovery Institute, University of Pittsburgh, Pittsburgh, PA, USA; Department of Computational and Systems Biology, University of Pittsburgh, Pittsburgh, PA, USA; Pittsburgh Cancer Institute, University of Pittsburgh, Pittsburgh, PA, USA*

Vinko Tosevski • *Mass Cytometry Facility, University of Zurich, Zurich, Switzerland*

Radiana T. Trifonova • *Program in Cellular and Molecular Medicine, Boston Children's Hospital, Harvard Medical School, Boston, MA, USA; Department of Pediatrics, Harvard Medical School, Boston, MA, USA; Ragon Institute of MGH, MIT and Harvard, Cambridge, MA, USA*

Anna Tvorogova • *A.N. Belozersky Institute of Physico-Chemical Biology, M.V. Lomonosov Moscow State University, Moscow, Russia*

Irina A. Udalova • *Kennedy Institute of Rheumatology, Oxford University, Oxford, UK*

Ivan A. Vorobjev • *Department of Biology, School of Sciences and Technology, Nazarbayev University, Astana, Kazakhstan*
Kerstin Wunderlich • *Department of Biomedicine, University of Basel and University Hospital Basel, Basel, Switzerland; Department of Ophthalmology, University of Basel, Basel, Switzerland*
Anastasia A. Zharikova • *School of Bioengineering and Bioinformatics, M.V. Lomonosov Moscow State University, Moscow, Russia*
Xiang Zhou • *Department of Biomedical Engineering, Northwestern University, Evanston, IL, USA*

Part I

General

Chapter 1

Heterogeneity of Metazoan Cells and Beyond: To Integrative Analysis of Cellular Populations at Single-Cell Level

Natasha S. Barteneva and Ivan A. Vorobjev

Abstract

In this paper, we review some of the recent advances in cellular heterogeneity and single-cell analysis methods. In modern research of cellular heterogeneity, there are four major approaches: analysis of pooled samples, single-cell analysis, high-throughput single-cell analysis, and lately integrated analysis of cellular population at a single-cell level. Recently developed high-throughput single-cell genetic analysis methods such as RNA-Seq require purification step and destruction of an analyzed cell often are providing a snapshot of the investigated cell without spatiotemporal context. Correlative analysis of multiparameter morphological, functional, and molecular information is important for differentiation of more uniform groups in the spectrum of different cell types. Simplified distributions (histograms and 2D plots) can underrepresent biologically significant subpopulations. Future directions may include the development of nondestructive methods for dissecting molecular events in intact cells, simultaneous correlative cellular analysis of phenotypic and molecular features by hybrid technologies such as imaging flow cytometry, and further progress in supervised and non-supervised statistical analysis algorithms.

Key words Cellular heterogeneity, Phenotypic heterogeneity, Cellular profiling, Single-cell analysis, Imaging flow cytometry, RNA-sequencing, Mass cytometry, Cluster analysis

1 Introduction

Heterogeneity is a fundamental characteristic of biological systems, and cell heterogeneity has been widely described in metazoan and protozoan cellular systems [1–3]. In fact, heterogeneity has been observed practically in every aspect of cellular physiology, where it has been investigated. For a long time, cellular clones were considered as homogenous cell populations. However, even if cells are part of a clonal population and are genetically identical, they exhibit heterogeneity of phenotypes and cell-to-cell variations in response to uniform perturbations [4, 5]. Heterogeneity is a cell population property and implies the presence of cell-to-cell variability with respect to one (or many) measurable morphological or functional

Natasha S. Barteneva and Ivan A. Vorobjev (eds.), *Cellular Heterogeneity: Methods and Protocols*, Methods in Molecular Biology, vol. 1745, https://doi.org/10.1007/978-1-4939-7680-5_1,

parameters [6, 7]. The challenge is not to identify a presence of heterogeneity, since differences between cells are always present with increase size of an analyzed cell population, but to determine which cellular heterogeneity components are biologically meaningful and related to biological function. Measuring cell population-level averaged characteristics is masking how these characteristics are distributed and can mask certain effects (cell fate decisions, gene-regulatory mechanisms) and can hide the presence of small size cellular populations (rare cell populations). In microbial communities, the coexistence of different phenotypes in genetically identical cells can be a result of stochastic gene expression [8, 9] that is considered to be beneficial for their existence.

Cell classifications are usually phenotype-based and not genetically-based since a significant percentage of mutations do not result in a distinct phenotype associated with these gene changes. Thus, in *S. cerevisiae* app 66% of deletion mutants do not reveal the detectable effect on growth in the rich medium [10, 11] or genome-wide expression phenotype, which was essentially the same in approximately 55% gene deletions [12]. Similar results are observed with a number of different organisms: *Caenorhabditis elegans* [13] and *Bacillus subtilis* [14]). Lack of phenotype can be attributed to redundancy mechanisms: (1) homology-based functional redundancy due to the presence of closely-related duplicate (paralogous) genes against deleterious yeast and human mutations [15–18], but this may be not a major compensatory mechanism in mouse [19, 20]; (2) pathway-based redundancy achieved through existence of parallel metabolic pathways, which can help to facilitate same biological process [15, 21]. It might be also condition-dependent since some genes are only transcribed under certain growth conditions [22]. The advancement in the integrative correlative analysis of phenotype, biological function, and genotype is crucial for our understanding of biological systems functionality. Paradoxically, in the wealth of acquired information, there are a small number of studies that are comparing molecular expression with cellular function or morphology. To facilitate further progress, we need to adapt new integrative techniques of cellular analysis. In this review, we discuss advances and limitations of current methods to study and analyze cell heterogeneity.

2 Genetic vs. Phenotypic Heterogeneity and Its Sources

Cells are part of a cellular ecosystem. The nongenetic heterogeneity is a response to fluctuating environment and environmental stressors and therefore may reflect different cell cycle states, differences in nutritional state, the effect of drug treatments, etc. (Fig. 1). However, each cell behaves uniquely because of unique genetic information and fluctuating environmental factors such as (1) tem-

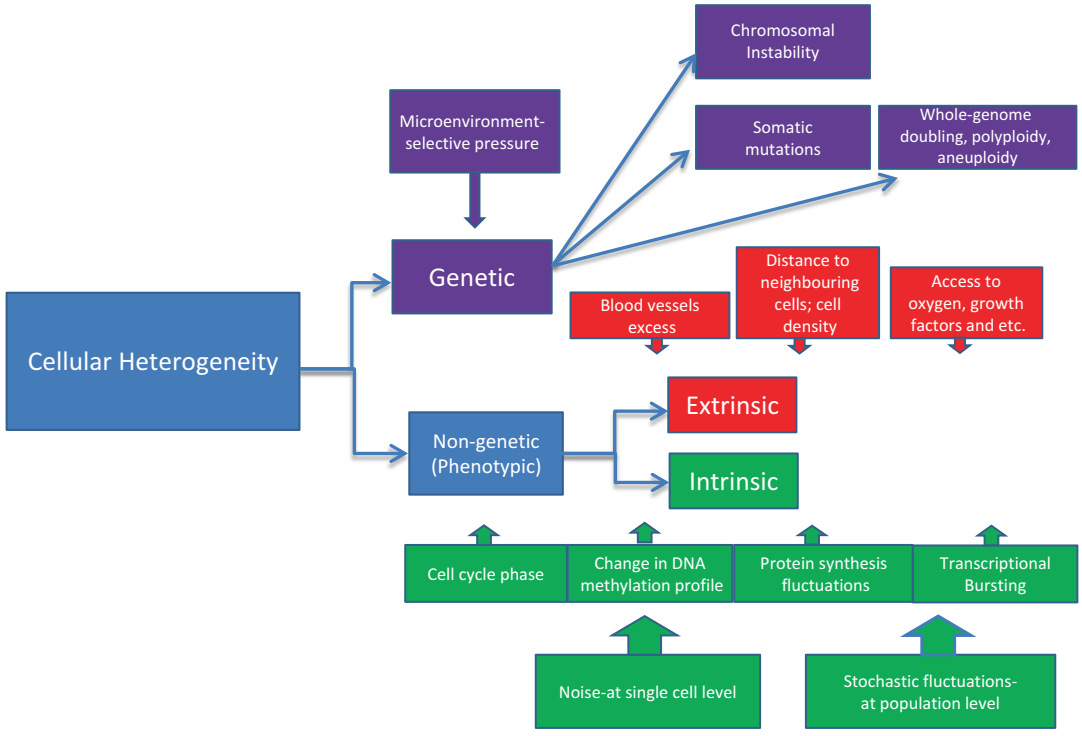

Fig. 1 A cell population heterogeneity. A schematic representation of concepts used in the study of cellular heterogeneity

perature [23], (2) presence of extracellular signals, (3) drug treatment [24], (4) age [25], (5) proximity to other cells, (6) presence different and distinct cells-regulators, and very importantly (7) genotypes [26]. Mitochondrial content and energy level in the cell are other important sources of phenotypic variability [27]. Due to small cellular size and limited volume, biochemical reactions in cells are also a subject to stochastic fluctuations. Tracking fluorescent protein reporters in single *E.coli* cells, it was possible to demonstrate that phenotypic heterogeneity in bacterial populations is often associated with gene expression stochasticity and differences in gene products abundance [28]. However, a biochemical noise can also be responsible for functional differences such as for competence decision in *B. subtilis* (rev [29]). The prevailing view is that gene expression in individual cells of bacterial, yeast, or mammalian origin has bursts of transcriptional activity that contribute to a level of cellular noise (Fig. 1). Temporal cellular noise includes fluctuations in a property X (e.g., level of protein X) in the individual cell over time [6]. In metazoan cells, a substantial part of heterogeneity in expression of developmental markers may be explained by different stages of developmental maturity rather than stochasticity in expression levels of cellular markers. Scattered differentiation will occur, if cells have different differentiation threshold [30].

2.1 Heterogeneity of Cell Differentiation

Cellular differentiation or capability of cells to transform from one specialized cell type to another is crucial in the development of multicellular organisms. Cellular heterogeneity of differentiated cells has been revealed and studied in normal metazoan cells such as human stem cells (HSCs) [31, 32] and murine stem cells models using transcriptional analysis by a combination of index sorting, fluidigm, and RNA-seq [33]. Heterogeneity of phenotype and functional states may reflect a presence of multiple stages in cell development like it was recently demonstrated for T follicular helper cells by Trüb and coauthors [34]. Even subtle differences between developmental stages time may lead to significant intro-genotype diversity as demonstrated by Francesconi and Lehner [35].

2.2 Heterogeneity of Cellular Subtypes in Population

The phenotypic classification of cells into distinct types in first was relied on morphology observables, origin, and functional behavior but gradually starts to include molecular characteristics such as quantitative expression of proteins or mRNA. Some of the human cells could be segregated into major categories based on their surface markers identified by fluorescent-tagged antibodies and flow cytometry analysis. Thus, initially, human T-cells were divided into four major categories based on their ability to produce different cytokines, cytotoxic, and proliferative potential: naïve T-cells ($CCR7^{+}CD45RA^{+}$), central memory ($CCR7^{+}CD45RA^{-}$), effector memory ($CCR7^{-}CD45RA^{-}$), and terminal effector T-cells ($CCR7^{-}CD45RA^{+}$) [36]. However, adding more surface markers, such as CD27, CD28, CD62L, CD95, and others, and transcription factors profiles, functional activities allows for further segregation of T-cells into different categories. This approach can be applied to several human tissues as well as tissues of human primates, mice, and rats (mostly studied models of human diseases). However, it is limited by a number of pre-known surface and transcriptional markers and may require the introduction of additional parameters not available in standard flow cytometry but available through the development of other technologies (mass cytometry).

Recent advances in gene profiling studies together with FACS-based cell sorting provide definitive proof that some tissues or cell types considered before uniform such as different classes of glia and neurons are in fact highly heterogeneous [37–39]. Determining whether a cellular subpopulation has a functional significance is based on assumption that cells that belong to a same subtype should behave similarly and a mixture of different subtypes have different functional features [29]. Molecular heterogeneity of cellular types opens a possibility that each subtype responds differently to environmental challenges such as injury, which is related to their specialized function such as remyelination for oligodendrocytes [40]. Recently, several groups of investigators tried to use single-

cell RNA sequencing (scRNA-seq) to classify cells into cell types based on gene expression signatures [39, 41–45]. In many instances, these findings uncovered previously overlooked heterogeneities in considered "uniform" cell populations and altered existing classifications by introducing new cell categories and redefining relationships between different cell categories [46, 47]. However, these studies have not been able to answer the question what is a full cohort of analyzed cell subtypes and are cellular subtypes represented by genuine and stable subtypes. Multiple analytical methods (HC and principal component analysis) require confirmation that classification of cellular subtypes based on molecular features is robust and correlates with phenotypic morphological features.

2.3 Disease-Related Heterogeneity

2.3.1 Heterogeneity in Tumors

Vast heterogeneity during tumor development leads to the formation of subpopulations of distinct cells inside the tumor. The distribution of mutations in these subpopulations (or subclones) is usually not revealed by averaged pooled sample analysis [48]. Tumor heterogeneity and evolution of resistant tumor clones from rare cells are challenges for the development of effective therapeutic strategy [49]. Intra-tumoral heterogeneity present at different levels (DNA, RNA, epigenetics, protein, lipids) forms the basis for the evolution of resistance, tumor treatment response, and metastasis [50]. The biological significance of nongenetic heterogeneity is to provide additional diversity for further selection in spontaneously evolving or drug-treated tumors [51–53]. Characterization of rare cell subpopulations is one of the most intriguing questions in tumor heterogeneity and limited by detection limits of circulating tumor cells (CTC) studies. Transcriptional profiling of CTCs revealed extreme differences in different gene expression [54]; moreover, CTCs also exhibit exceptional phenotypic variability [55]. However, the question what is a specific rare cell subtype (s) and how to define it stays open. Examples of recognized rare cell types include CTC, cancer stem cells, stem cells, and progenitor cells. Recently developed single-cell genomics and proteomics analytical methods led to the discovery of new cell types in a variety of tissues such as brain tissue, immune and digestion systems, and tumor cells. However, systemic identification of rare cell types from SCA gene expression data remains challenging [56]. What is appearing as rare cell subpopulation could be related to either technical artifacts or disease- and infection-related factors.

2.3.2 Heterogeneity of Infection

Metazoans are home for different viruses, prokaryotes, and other metazoans which coexist as symbionts, commensals, or parasites, in extreme cases leading to the development of acute or chronic infection in the hosts. Due to heterogeneity of existing in cellular and pathogen (bacterial, viral, or parasite) populations, the differences in the outcomes of infection on single-cell level and on the level of a multicellular organism can be observed.

3 Methods to Study Heterogeneity in Cellular Systems

Till the recent time, the leading assumption was that population average is a good representation of overall behavior in the cellular population. However, population-averaging-based analytical techniques are applied not to single cells but averaged components of pooled lysed cells (Western blotting, PCR, microarrays). Anything in the range of statistical deviation will be masked since pooled samples can (1) mask important small subpopulations and (2) generate false data due to contaminating components (a comparison of pool-averaging Western blotting analysis and flow cytometry approach provided at Fig. 2).

Thus, a method based on the analysis of averaged population can miss small or rare subpopulation with an important biological function such as dormant stem cells in tumor or tissue and "persister cells" in bacterial populations which are responsible for survival after drug treatment [3]. Currently, "persister" populations are identified practically in each examined bacterial strain with frequency varying between 0.001% and 1% [rev. 57]. Moreover, "persisting" populations have been described in human cancer cell lines [58, 59] and recently in cultured patient-derived melanoma cells [60] and are responsible for drug resistance and therapy failure. Shaffer and coauthors [60] documented mechanism of nongenetic rare cell variability describing rare transient cell state that involves infrequent semi-coordinated transcription of high levels of resistance markers in a tiny percentage of cells.

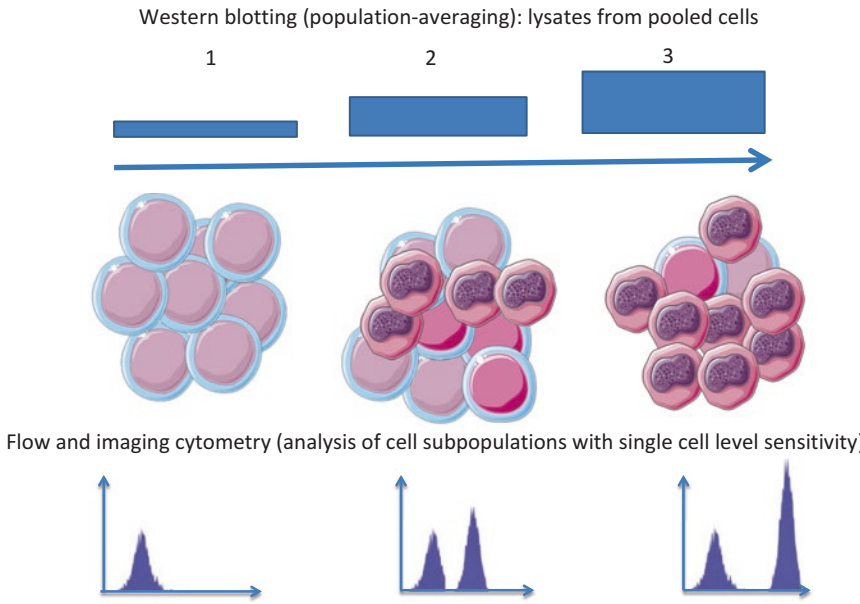

Fig. 2 A comparison of Western blotting and cytometric analysis of homogenous and heterogeneous populations

Cellular heterogeneity is potentially confounding factor for population-averaging methods and traditional gene expression analysis. The recent development of single-cell genomics at the resolution of single cells, in particular, single-cell RNA sequencing, improved cellular resolution and provided unprecedented details of compartmentalization in cellular systems. Though initial studies analyzed up to 100 cells, a further development of technology and the use of microfluidics, hydrogel droplets, and robotics increased the throughput to thousands and hundreds of thousands of cells. The growth in a number of independent measures that can be combined in one single assay led to the development of profiling technologies that allow measuring hundreds and thousands of distinct properties in the cellular sample [61]. However, single-cell RNA-based and DNA-based methods are lacking spatial-temporal context and similar with pool-averaged methods in what they require a destruction of the cell being investigated. During pre-processing stage, cell population goes through the next steps: cell isolation and purification, library preparation, sequencing, and statistical data analysis. This approach leads to a loss of critical spatial information about cell as well as its position in the developmental trajectory [62]. Current methods to study cell population at the single-cell level can be divided into the next two major categories:

(A) Methods that are requiring purification stage. They include the next steps: (a) dissociation for solid tissue; (b) identification of cell s (selection criteria: cell size, combination of fluorescent signals, amperometry); (c) sorting or isolation of single cells (droplet-based sorting and analysis, FACS, microfluidics, magnetic sorting; cell-trapping techniques (acoustic, optical, dielectrophoretic trapping, etc.); (d) purification of cell components (DNA, RNA, proteins, lipids, etc.); (e) high-throughput analysis (DNA and RNA single-cell sequencing, transcriptomics, mass-spectrometry); and (f) bioinformatics and statistical analysis. The purification of cells from primary cultures is a critical step for analysis of cellular heterogeneity, and lack of available procedures has been a central limitation for our understanding of structure and functionality of some human tissues such as glia and neurons [37].

(B) Methods that do not require purification stage. They include different types of cytometry, such as flow cytometry (FCM), imaging flow cytometry (IFC), and mass cytometry, as well as high-content imaging study of the entire cell population with single-cell resolution.

There are new developments in SCA sequencing strategies that can capture and amplify RNA in association with the specifically labeled cell using in situ hybridization approach (FISH) that detects

transcripts utilizing fluorescently labeled probes. Alternatively, emerging in situ methods sequence RNA directly inside unlysed cells by ligation in situ using the SOLiD platform [63, 64].

3.1 Cell Purification and Isolation Methods in Combination with Molecular Analysis

The first step of individual cell isolation from tissue includes enzymatic and mechanical dissociation that may impact viability and affect the further cellular analysis. Alternatively, the method that utilizes single-cell nuclei for SCA transcriptional RNA-seq does not require harsh protease sequencing [65]. Cell pre-enrichment can be performed using physical features (size, deformability, electrical, magnetic properties), surface markers stained with fluorescent antibodies (antibody conjugated with fluorochrome), or biochemical marker (aptamer-mediated, immunomagnetic) [66]. Although laser dissection techniques are capable of isolating cells from a specific location within a cell population, these methods are labor-intensive and provide a limited number of cells for further manipulations. Fluorescence-activated cell sorting (FACS) utilizes surface or biochemical markers and is offering the a priori selection of limited marker sets and sorting panels. Moreover, many biological systems are lacking markers that can be identified by antibodies conjugated with fluorochromes and used to determine the cell types. In FACS approach utilizing for sorting fluorescent intensity of fluorescent protein from genetically modified cells, variations in cellular protein level measured by FACS typically cover a range from 10- to 1000-fold. In the same time, the measurement error (for FCM) determined with fluorescent beads cover a tenfold range of variability [67] and can mask variations in the samples. Sorting out "tail fractions" demonstrated that they have distinct gene expression patterns [67, 68]. Alternatively, for cell purification, microfluidics technology can be used, which provides advantages of precious fluidics control, multiplexing capabilities, automated controlled mode of chemicals delivery (see Fig. 3). Microfluidics platforms based on microchambers have so far limited throughput capability compared to the droplet microfluidics though allowing more than a thousand single-cell events per experiment in some cases [69]. Valve-based devices can benefit biological assays by increasing control and reducing background, for example, by allowing researcher to work with individual chromosomes in whole-genome sequencing. The droplet microfluidics systems utilize encapsulation cells inside microdroplets created by injecting aqueous samples into a stream of hydrophobic carrier and can be operated a long time to analyze millions of droplets and cellular events [70]. Initial strategies for performing amplifications within droplets were expanded by introducing strategies for droplet-based detection. Thus, Zhu and coauthors [71] developed a method to perform PCR in droplets with fluorescent-labeled primers and subsequential FACS analysis [71].

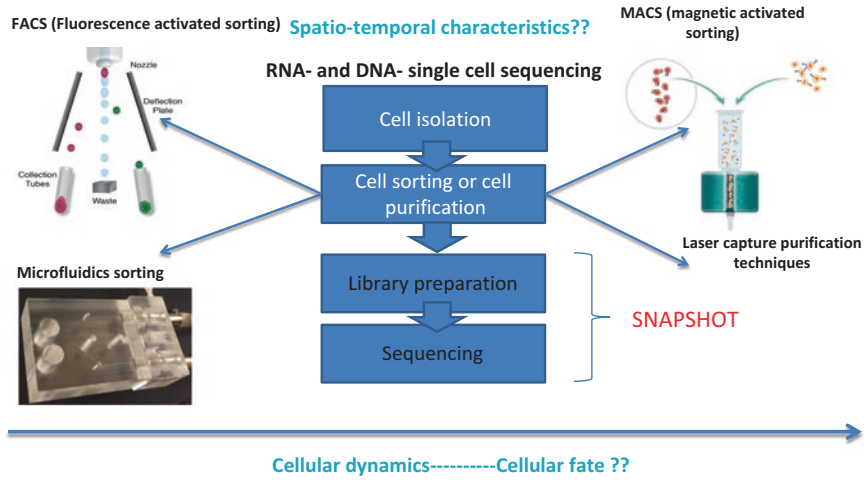

Fig. 3 Comparison of standard approaches with purification stage in genetic analysis methods of cellular heterogeneous populations

3.2 Cellular Screening

FACS-based sorting and analysis and cell imaging are considered the major techniques to study in biomedical and cell biology research [72] and do not require purification step before actual analysis. Flow cytometry (FC) is lacking spatiotemporal information due to the absence of imaging capabilities. Recent progress in high-content microscopy led to read out of large screens. However, one or two parameters of interest are usually measured with low magnification (20×, in some cases 40×) and quantitated from images for cell scoring. The major advantage of these technologies is that there are methods of cell heterogeneity analysis without cell destruction or purification step and associated artifacts.

3.2.1 Time-Lapse Imaging and Videomicroscopy

Long-term time-lapse microscopy allows observation and quantitative analysis of individual cells and their progeny from hours up to the weeks [73, 74]. Modern automated microscopes are usually equipped with epifluorescent optics, cell incubation unit connected to CO_2 supply, automated stage, and autofocusing. These instruments allow one to acquire hundreds of images of multiple fields of view in a time-lapse manner. Analysis of the cell populations with low frequencies of cells of interest (rare cell subpopulations), long divisional rates, and high heterogeneity, such as in a hematopoietic system with rare stem cell subsets, requires long periods of observation.

Several types of staining could be utilized in microscopy—specific labeling of some cells with fluorescent proteins (GFP, RFP, etc.), highly specific labeling like in flow cytometry (e.g., using antibodies against CDs) and nonspecific labeling (Hoechst 33342 for chromatin staining, TMRE(M) for staining mitochondria, etc.). In the last case, the information on the heterogeneity of a cell

population is obtained not only by the measuring of the intensity of a signal but also from the analysis of the spatial distribution of a dye.

However, limitations of software required for handling of gigabytes of images, challenges of the cell and organelle tracking, and lack of automated image processing hamper the extensive usage of this technology. There are some pioneering efforts to address the challenges of high-throughput microscopy including automated analysis of images, the sharing, and integration of image formats and analysis of large image datasets [75].

Time-lapse microscopy also allows one to analyze changes of some of the cell features over time on a single-cell level. Thus, cell-to-cell variability described by Gaussian distribution in the MOMP onset in cell lines responding to apoptotic stimuli, whereas in the duration of MOMP to caspase activation stages, it is following the γ-distribution model [76]. It is worthwhile to mention that in some cases cells in the population are significantly heterogeneous compared to each other yet stable over time by themselves [77] (this volume).

3.2.2 Imaging Flow Cytometry (IFC)

Development of IFC technology, which unites microscopy and cytometry in hybrid in-flow microscope, allowed a correlative high-speed analysis (up to 5000 cellular events/s) of fluorescence and morphology features in tenths and hundreds of thousands of cellular images [7, 78]. In microscopy, a supervised approach strategy uses expert-selected features such as fluorescent intensity or localization of marker, shape, and area of the cell. In more complex, machine-based algorithms computers are trained to identify cellular subpopulations based on examples provided by the researcher [79–84]. The recent software development in IFC for ImageStream family of instruments ("Feature Finder" algorithm in IDEAS software) allows unbiased analysis of statistically significant image features based on a comparison of image panels manually picked by the researcher [85]. IFC analyzes cell and cell clusters in suspension and does not require image segmentation.

3.2.3 Flow Cytometry and Mass Cytometry

Flow cytometry (FC) is an indispensable classical tool to study different cell subsets with single-cell precision and high speed (up to 10,000 single-cell events/s) in heterogeneous cell subpopulations [86], recently expanded the number of possible simultaneous analysis parameters to dozens and more. The fluorescent dyes and tags for antibodies as well as fluorescent proteins used for cellular tagging may have wide and overlapping emission spectra that require a sophisticated spectral compensation for cellular analysis by FC and IFC. Initial strategy to analyze FC data is manual gating, which is labor-intensive and subjective. A single-parameter histogram of fluorescent intensity which continues to be used for flow cytometry data analysis can mask important cellular

subpopulations by not taking in the account autofluorescence of cells. The increase in dimensionality motivated the development of cluster analysis methods (Table 1 and Subheading 3.2). FC and mass cytometry also apply fluorescent cellular bar coding to increase the number of simultaneously analyzed samples. The introduction of mass cytometry and CyTOF instrument allowed to distinguish many more parameters (currently app 40 limited by commercially available lanthanide and other metals tags and dozens more in the future) [107] but with lower speed (currently at 500 cells/s). Due to a relatively lower speed (in comparison with flow cytometry) pre-enrichment strategies are required for detection and studies of rare cell subsets. Both methods heavily rely on the availability of specific antibodies to cellular markers. Thus, mass cytometry is optimized for single-cell suspension analysis; however, recent expansion of this technology led to the development of imaging mass cytometry (IMC) which uses laser ablation to scan histological sections (rev by [108]) albeit limited by the low rate of acquisition (1.5 mm^2 in 2 h).

3.3 Cellular Profiling

Multidimensional multiplexed single-cell profiling enables measuring hundreds to thousands of distinct cellular features and is a robust approach to distinguish true single-cell heterogeneity from biological noise. SCA methods are critical for analysis of heterogeneous multicomponent cellular populations which include rare cell populations and differ regarding what type of information they provide on the nature of heterogeneity [6]. With the development of high-throughput microscopy, image profiling started to generate massive amounts of data available for drug discovery and systems biology use. However, molecular profiling of human tissues is often problematic due to limited access to intact cells and biopsy availability, poor RNA quality, and low yield from autopsy materials. Therefore immunohistochemistry- and image-based cell profiling prevails in biopsies analysis require the development of low-input RNA sequencing in the future [109]. Recent technological developments enabled more and more precise differentiation and characterization of lymphocyte subsets defined not only by presence but also by the intensity of markers. It created new opportunities to analyze cellular heterogeneity at OMICS level. However, a few studies investigated a diagnostic significance of disturbed subsets, mostly limited to analysis of peripheral blood cells (<5% of the total mononuclear pool) and produced data are scarce and insufficient to be used as classification criteria [110]. Thus, a multi-OMIC approach using multi-parametric flow cytometry analysis on 2500 patients with systemic autoimmune diseases will be performed in 11 centers in Europe (http://www.precisesads.eu/) to get unbiased lymphocyte profiles for different patient groups with autoimmune diseases [111].

Table 1
Statistical algorithms for analyzing single cells and cell heterogeneity

Category	Type of information	Algorithm name	Advantages/features	Limitations	References
Clustering-based	Identification of subpopulation/ phenotype	Manual gating	Easy implementation to identify target populations Using prior knowledge	Subjective; sequential gating at FCM may require prior knowledge Dissimilation of small-sized populations by large populations Unexpected populations can be missed	Herzenberg et al. [87]
	Cell populations Hierarchies Cluster-abundance matrix (cell #) Cluster-phenotype matrix (marker median)	Spade SPADEVizR SPADE and t-SNE combo	Density-based clustering; tree structure for subpopulations visualization; can compare clusters and markers over cell subsets of different samples; suited for identifying rare cell types	Reproducibility problems Limited by the choice of experimental markers used for building the tree (FCM)	Qiu et al. [88–90], Gautreau et al. [91], Diggins et al. [92], Aghaeepour et al. [93]
	Correlation between sample and clinical outcome	Citrus	Identification of correlation between sample and clinical outcome		Bruggner et al. [94]
	Correlation between sample and disease	Cell CNN	Detection rare cell subsets associated with disease (<0.01%); associates a multicell input with phenotype by means of a convolutional neural network		Arvaniti and Claassen [95]

Dimensionality reduction	Global data structure and SCA	Principal component analysis (PCA)	Provides visualization in 3D space; data representation restricted to linear combinations of original parameters	Loss of nonlinear relationships between parameters; may miss subtle variations between parameters	Hotteling [96], Newell et al. [97], Deininger et al. [98]
	Cell subset heterogeneity	viSNE t-SNE	Nonlinear dimensionality reduction; Cytobank viSNE can analyze millions of cells	Rare cell subpopulations can be missed	Van der Maaten [99], Makosco et al. [100], Inglese et al. [101]
Clustering and dimensionality reduction algorithm	Data structuring with subdividing to subpopulations	ACCENSE	Nonlinear dimensionality reduction combined with density-based subdividing	Loss of SCA resolution	Shekhar et al. [102]
Seriation-based analysis	Progression (pseudo-temporal) through cell states	Wanderlust	Most likely linear path	Not works with bifurcating trajectory	Bendall et al. [103]
		Cycler—New version of wanderlust	A continuous trajectory of cell cycle progression	Not directly applicable to time set of images	Gut et al. [104]
		Wishbone	Create bifurcating trajectories	Not directly applicable to time set of images	Paul et al. [105], Setty et al. [106]

3D three-dimensional, *ACCENSE* automatic classification of cellular expression by nonlinear stochastic embedding, *CITRUS* cluster identification, characterization, and regression, *PCA* principal component analysis, *SPADE* spanning-tree progression analysis of density-normalized events, *t-SNE* t-distributed stochastic neighbor embedding

3.4 Statistical Analysis

The prevailing assumption of traditional pooling methods for fitting models to signaling pathways has been a mechanistic approach to fit only the population average as the best representation of the cellular population. Statistical analysis of cell heterogeneity requires a collection of data from a statistically significant number of cells under variable growth conditions in the systematic fashion. The ability to determine subtle differences between different cellular phenotypes is directly correlated with the size of dataset [112]. The escalation of data dimensionality and datasets size points out limitations of manual analysis as being labor-intensive, subjective, slow, and incapable of identifying and showing detailed parameters of each single cell within a cell population. The challenge is to create computational algorithms that will use the single-cell resolution and to identify the branch points that will lead to a whole spectrum of functionally distinct cells. Some current approaches to represent obtained information such as histogram-snapshot of distribution of trait X in cellular population, in many cases not enough to detect a noise and evaluate a source of noise (temporal or population noise).

To integrate morphological and molecular analysis and to decrease dimensionality, principal component analysis (PCA) and its variants are widely used. PCA creates composite parameters. These parameters incorporate morphological and fluorescent information (IFC) or phenotypic and functional information, etc. and provide information how different cell subsets and markers related to each other could be separated. In contrast with PCA, clustering analysis techniques allow analyzing common patterns inside datasets such as the most prevalent cell populations based on cellular surface markers [113]. The selected algorithms for analyzing of single cells and cell heterogeneity are provided in Table 1. We anticipate that PCA and different variants of cluster algorithms such as K-means and other distance-based and density-based clustering, such as hierarchical clustering that is used for various cellular heterogeneity analysis applications, will further develop to provide high-dimensional analysis of heterogeneous cellular subsets.

3.5 Challenges

The experimental challenges in cellular heterogeneity analysis are numerous, and we are discussing just a few. For example, the primary limitation is related to a cell size and limited quantity of cellular components. Nucleic acid analysis of single cells is challenging due to the available amount of DNA (app 7 pg from the human cell), total RNA (app 20 pg), and less than total 1 pg of mRNA and requires significant amplification of initial material, which may lead to stochastic effects [114, 115]. Moreover, limitations can be specific for different steps of SCA technologies. Thus, limitations of

purification stage are related to a preexisting set of canonical cell surface markers that are used to discriminate cell populations [116]. Using cell sorting technologies may lead to changes in viability during sorting for fragile and adhesive cells (increasing percentage of apoptotic and dead cell populations). Approaches based on cell studies expressing fluorescent proteins prone to limitations related to variability in the level of fluorescent protein expression and toxicity of some plasmid constructs.

It is technically impossible to eliminate noise in SCA due to the low quantity of samples. To differentiate noise from low prevalence signals, it may require additional steps of identification (FISH—fluorescence in situ hybridization) or unique identifiers on a molecular level [117, 118]. Limitations of scRNA sequencing include problems in the computational management of dropout events, the understanding of biological pathways, and the isolation of populations of cell targets [119]. If SCA method involves amplification step, it is imperative to distinguish amplification errors from preexisting genetic mutations. The methods reviewed in the paper will undoubtedly improve, and adding spatial-temporal information to the analysis of single cell as well as increasing speed and size of analyzed cellular populations will increase our understanding of cellular heterogeneity mechanisms.

4 Future Perspectives

The past few years have seen exponential progress in methods of single-cell analysis (SCA), but it barely was applied to characterize cell heterogeneity on a population level. We are moving from revealing heterogeneity in general or revealing different levels of heterogeneity (taking a snapshot of the cellular population on single-cell level) to understanding dynamics and quantitative analysis of cellular heterogeneity. Several technological limitations of SCA should be addressed to facilitate further progress. The analysis of highly heterogeneous cellular populations is currently driven by changes in experimental techniques: (1) increasing number of analyzed cells (throughput), (2) increasing the number of different molecules that can be analyzed from each cell, (3) improving robustness in the samples of different qualities and increasing ratio signal-to-noise, and (4) combining molecular SCA technologies with fluorescent probes in situ in order to visualize individual nucleic acid molecules inside cells (smFISH) [120]. The ongoing efforts to join molecular analysis with imaging methodology will enable the description of spatial structure and dynamics of biological systems and correlative quantitative analysis of morphological and functional parameters.

Acknowledgments

Authors are grateful for grant support from Swiss IBD Cohort to N.S.B., Ministry of Science, Kazakhstan to N.S.B. and I.A.V., and RFBR to I.A.V.

References

1. Spudich JL, Koshland DE Jr (1976) Non-genetic individuality: chance in the single cell. Nature 262:467–471
2. Shackney SE, Shankey TV (1995) Genetic and phenotypic heterogeneity of human malignancies: finding order in chaos. Cytometry 21:2–5
3. Balaban NQ, Merrin J, Chait R, Kowalik L, Leibler S (2004) Bacterial persistence as a phenotypic switch. Science 305:1622–1625
4. Niepel M, Spencer SL, Sorger PK (2009) Non-genetic cell-to-cell variability and the consequences for pharmacology. Curr Opin Chem Biol 13(56):556–561. https://doi.org/10.1016/j.cbpa.2009.09.015
5. Cotari JW, Voisinne G, Dar OE, Karabacak V, Altan-Bonnet G (2013) Cell-to-cell variability analysis dissects the plasticity of signaling of common gamma chain cytokines in T cells. Sci Signal 6(266):ra17. https://doi.org/10.1126/scisignal.2003240
6. Huang S (2009) Non-genetic heterogeneity of cells in development: more than just noise. Development 136:3853–3862. https://doi.org/10.1242/dev.035139
7. Vorobjev IA, Barteneva NS (2016) Quantitative functional morphology by imaging flow cytometry. Methods Mol Biol 1389:3–11. https://doi.org/10.1007/978-1-4939-3302-0_1
8. Becskei A, Seraphin B, Serrano L (2001) Positive feedback in eukaryotic gene networks: cell differentiation by graded to binary response conversion. EMBO J 20:2528–2535
9. Dubnau D, Losick R (2006) Bistability in bacteria. Mol Microbiol 61:564–572
10. Winzeler EA, Shoemaker DD, Astromoff A, Liang H, Anderson K, Andre B et al (1999) Functional characterization of the *S. cerevisiae* genome by gene deletion and parallel analysis. Science 285:901–906
11. Giaever G, Chu AM, Ni L, Connelly C, Riles L, Veronneau S et al (2002) Functional profiling of the *Saccharomyces cerevisiae* genome. Nature 418:387–391. https://doi.org/10.1038/nature00935
12. Kemmeren P, Sameith K, van de Pasch LA, Benschop JJ, Lenstra TL, Margaritis T et al (2014) Large-scale genetic perturbations reveal regulatory networks and an abundance of gene-specific repressors. Cell 157:740–752. https://doi.org/10.1016/j.cell.2014.02.054
13. Kamath RS, Fraser AG, Dong Y, Poulin G, Durbin R, Gotta M et al (2003) Systematic functional analysis of the *Caenorhabditis elegans* genome using RNAi. Nature 421:231–237. https://doi.org/10.1038/nature01278
14. Kobayashi T, Mizuno H, Imayoshi I, Furusawa C, Shirahige K, Kageyama R (2009) The cyclic gene Hes1 contributes to diverse differentiation responses of embryonic stem cells. Genes Dev 23:1870–1875. https://doi.org/10.1101/gad.1823109
15. Wagner A (2000) Robustness against mutations in genetic networks of yeast. Nat Genet 24:355–361. https://doi.org/10.1038/74174.
16. Ihmels J, Collins SR, Schuldiner M, Krogan NJ, Weissman JS (2007) Backup without redundancy: genetic interactions reveal the cost of duplicate gene loss. Mol Syst Biol 3:86. https://doi.org/10.1038/msb4100127
17. Hsiao TL, Vitkup D (2008) Role of duplicate genes in robustness against deleterious human mutations. PLoS Genet 4:e1000014. https://doi.org/10.1371/journal.pgen.1000014
18. Plata G, Vitkup D (2014) Genetic robustness and functional evolution of gene duplicates. Nucleic Acids Res 42:2405–2414. https://doi.org/10.1093/nar/gkt1200
19. Liao BY, Zhang J (2007) Mouse duplicate genes are as essential as singletons. Trends Genet 23(8):378–381
20. Su Z, Wang J, Gu X (2014) Effect of duplicate genes on mouse genetic robustness: an update. Biomed Res Int 2014:758672

21. Papp B, Pal C, Hurst LD (2004) Metabolic network analysis of the causes and evolution of enzyme dispensability in yeast. Nature 429:661–664. https://doi.org/10.1038/nature02636
22. Amini S, Holstege FC, Kemmeren P (2017) Growth condition dependency is the major cause of non-responsiveness upon genetic perturbation. PLoS One 12(3):e0173432. https://doi.org/10.1371/journal.pone.0173432
23. Jo J, Kang H, Choi MY, Koh DS (2005) How noise and coupling induce bursting action potentials in pancreatic beta-cells. Biophys J 89(3):1534–1542
24. Dar RD, Hosmane NN, Arkin MR, Siliciano RF, Weinberger LS (2014) Screening for noise in gene expression identifies drug synergies. Science 344:1392–1396. https://doi.org/10.1126/science.125022.
25. Bahar R, Hartmann CH, Rodriguez KA, Denny AD, Busuttil RA, Dollé ME et al (2006) Increased cell-to-cell variation in gene expression in ageing mouse heart. Nature 441:1011–1014. https://doi.org/10.1038/nature04844
26. Raser JM, O'Shea EK (2004) Control of stochasticity in eukaryotic gene expression. Science 304:1811–1814. https://doi.org/10.1126/science.1098641
27. Guantes R, Diaz-Colunga J, Iborra FJ (2015) Mitochondria and the non-genetic origins of cell-to-cell variability: more is different. BioEssays 38:64–76. https://doi.org/10.1002/bies.201500082
28. Elowitz MB, Levine AJ, Siggia ED, Swain PS (2002) Stochastic gene expression in a single cell. Science 297:1183–1186. https://doi.org/10.1126/science.1070919
29. Altschuler SJ, Wu LF (2010) Cellular heterogeneity: do differences make a difference? Cell 141:559–563. https://doi.org/10.1016/j.cell.2010.04.033
30. Chattwood A, Thompson CRL (2011) Non-genetic heterogeneity and cell fate choice in *Dictostelium discoideum*. Dev Growth Diff 53:558–566
31. Sieburg HB, Cho RH, Dykstra B, Uchida N, Eaves CJ, Muller-Sieburg CE (2006) The hematopoietic stem compartment consists of a limited number of discrete stem cell subsets. Blood 107:2311–2316. https://doi.org/10.1182/blood-2005-07-2970
32. Miller PH, Knapp DJ, Eaves CJ (2013) Heterogeneity in hematopoietic stem cell populations: implications for transplantation. Curr Opin Hematol 20:257–264. https://doi.org/10.1097/MOH.0b013e328360aaf6
33. Wilson NK, Kent DG, Buettner F, Shehata M, Macaulay IC, Calero-Nieto FJ et al (2015) Combined single-cell functional and gene expression analysis resolves heterogeneity within stem cell populations. Cell Stem Cell 16:712–724. https://doi.org/10.1016/j.stem.2015.04.004
34. Trŭb M, Barr TA, Morrison VL, Brown S, Caserta S, Rixon J, Ivans A, Gray D (2017) Heterogeneity of phenotype and function reflects the multistage development of T follicular helper cells. Front Immunol 8:489. https://doi.org/10.3389/fimmu.2017.00489
35. Francesconi M, Lehner B (2014) The effects of genetic variation on gene expression dynamics during development. Nature 505:208–211. https://doi.org/10.1038/nature1277.
36. Sallusto F, Lenig D, Forster R, Lipp M, Lanzavecchia A (1999) Two subsets of memory T lymphocytes with distinct homing potentials and effector functions. Nature 401:708–712
37. Cahoi JD, Emery B, Kaushal A, Foo LC, Zamanian JL, Chrisopherson KS, Xing Y, Lubischer JL, Krieg PA, Krupenko SA, Thompson WJ, Barres BA (2008) A transcriptome database for astrocytes, neurons, and oligodendrocytes: a new resource for understanding brain development and function. J Neurosci 28:264–278. https://doi.org/10.1523/JNEUROSCI.4178-07.2008
38. Zeisel A, Munoz-Manchado AB, Codeluppi S, Lonnerberg P, Le Manno G, Jureus A, Marques S, Munguba H, He L, Betsholtz C, Rolny C, Castelo-Branco G, Hierling-Leffler J, Linnarsson S (2015) Brain structure. Cell types in the mouse cortex and hippocampus revealed by single-cell RNA-seq. Science 347:1138–1142. https://doi.org/10.1126/science.aaa1934.
39. Barteneva NS, Ketman K, Fasler-Kan E, Potashnikova D, Vorobjev IA (2013) Cell sorting in cancer research-diminishing degree of cell heterogeneity. Biochem Biophys Acta 1836:105–122. https://doi.org/10.1016/j.bbcan.2013.02.004
40. Masgrau R, Guaza C, Ransohoff RM, Galea E (2017) Should we stop saying 'glia' and 'neuroinflammation'. Trends Mol Med 23(6):486–500. https://doi.org/10.1016/j.molmed.2017.04.005

41. Darmanis S, Sloan SA, Zhang Y, Enge M, Caneda C, Shuer LM, Hayden Gephart MG, Barres BA, Quake SR (2015) A survey of human brain transcriptome diversity at the single cell level. Proc Natl Acad Sci U S A 112:7285–7290. https://doi.org/10.1073/pnas.1507125112
42. Darmanis S, Gallant CJ, Marinescu VD, Niklasson M, Segerman A, Flamourakis G, Fredriksson S, Assarsson E, Lundberg M, Nelander S, Westermark B, Landegren U (2016) Simultaneous multiplexed measurement of RNA and proteins in single cells. Cell Rep 14:380–389. https://doi.org/10.1016/j.celrep.2015.12.021
43. See K, Tan WLW, Lim EH, Tiang Z, Lee LT et al (2017) Single cardiomyocyte nuclear transcriptomes reveal a lincRNA-regulated de-differentiation and cell cycle stress-response in vivo. Nat Commun 8:225. https://doi.org/10.1038/s41467-017-00319-8
44. Macosco EZ, Basu A, Satija R, Nemesh J, Shekhar K et al (2015) Highly parallel genome-wide expression profiling of individual cells using nanoliter droplets. Cell 161:1202–1214. https://doi.org/10.1016/j.cell.2015.05.002
45. Tasic B, Menon V, Nguen TN, Kim TK, Jarsky T, Yao Z et al (2016) Adult mouse cortical cell taxonomy revealed by single cell transcriptomics. Nat Neurosci 19:335–346. https://doi.org/10.1038/nn.4216
46. Shalek AK, Satija R, Adiconis X, Gertner RS, Gaublomme JT et al (2013) Single-cell transcriptomics reveals bimodality in expression and splicing in immune cells. Nature 498:236–240. https://doi.org/10.1038/nature12172
47. Bjorklund AK, Forkel M, Picelli S, Konya V, Theorell J, Friberg D et al (2016) The heterogeneity of human CD127+ innate lymphoid cells revealed by single-cell RNA sequencing. Nat Immunol 17:451–460. https://doi.org/10.1038/ni.3368
48. Ding L, Ellis MJ, Li S, Larson DE, Chen K, Wallis JW et al (2010) Genome re-modelling in a basal-like breast cancer metastasis and xenograft. Nature 464:999–1005. https://doi.org/10.1038/nature08989
49. Polyak K (2014) Tumor heterogeneity confounds and illuminates: a case for Darwinian tumor evolution. Nat Med 20:344–346. https://doi.org/10.1038/nm.3518
50. Burrell RA, McGranahan N, Bartek J, Swanton C (2013) The causes and consequences of genetic heterogeneity in cancer evolution. Nature 501:338–345. https://doi.org/10.1038/nature12625
51. Brock A, Chang H, Huang S (2009) Non-genetic heterogeneity-a mutation-independent driving force for the somatic evolution of tumours. Nat Rev Genet 10:336–342. https://doi.org/10.1038/nrg2556
52. Cohen AA, Geva-Zatorsky N, Eden E, Frenkel-Morgenstern M, Issaeva I, Sigal A, Milo R, Cohen-Saidon C, Liron Y, Kam Z et al (2008) Dynamic proteomics of individual cancer cells in response to a drug. Science 322:1511–1516. https://doi.org/10.1126/science.1160165
53. Spencer SL, Gaudet S, Albeck JG, Burke JM, Sorger PK (2009) Non-genetic origins of cell-to-cell variability in TRAIL-induced apoptosis. Nature 459:428–432. https://doi.org/10.1038/nature08012
54. Schiro PG, Zhao M, Kuo JS, Koehler KM, Sabath DE, Chiu DT (2012) Sensitive and high-throughput isolation of rare cells from peripheral blood with ensemble-decision aliquot ranking. Angew Chem Int Ed Engl 51:4618–4622. https://doi.org/10.1002/anie.201108695
55. Marrinucci D, Bethel K, Lazar D, Fischer J, Huynh E, Clark P, Bruce R, Nieva J, Kuhn P (2010) Cytomorphology of circulating colorectal tumor cells: a small case series. J Oncol 2010:861341. https://doi.org/10.1155/2010/861341
56. Jiang L, Chen H, Pinello L, Yuan G-C (2016) GiniClust: detecting rare cell types from single-cell expression data with Gini index. Genome Biol 17:144. https://doi.org/10.1186/s13059-016-1010-4.
57. Van den Bergh B, Fauvart M, Michiels J (2017) Formation, physiology, ecology, evolution and clinical importance of bacterial persisters. FEMS Microbiol Rev 41:219–251. https://doi.org/10.1093/femsre/fux001
58. Chen J, Li Y, T-S Y, McKay RM, Burns DK, Kernie SG, Parada LF (2012) A restricted cell population propagates glioblastoma growth after chemotherapy. Nature 488:522–526
59. Ramirez M, Rajaram S, Steininger RJ et al (2016) Diverse drug-resistance mechanisms can emerge from drug-tolerant cancer persister cells. Nat Commun 7:10690
60. Shaffer SM, Dunagin MC, Torborg SR, Torre EA, Emert B et al (2017) Rare cell variability and drug-induced reprogramming as a mode of cancer drug resistance. Nature 546:431–435. https://doi.org/10.1038/nature22794
61. Caicedo JC, Singh S, Carpenter AE (2016) Applications in image-based profiling of perturbations. Curr Opin Biotechnol 39:134–142. https://doi.org/10.1016/j.copbio.2016.04.003

62. Skylaki S, Hilsenbeck O, Schroeder T (2016) Challenges in long-term imaging and quantification of single-cell dynamics. Nat Biotechnol 34:1137–1144. https://doi.org/10.1038/nbt.3713
63. Lee JH, Daugharthy ER, Scheiman J, Kalhor R, Yang JL, Ferrante TC et al (2014) Highly multiplexed subcellular RNA sequencing in situ. Science 343(6177):1360–1363. https://doi.org/10.1126/science.1250212
64. Lee JH, Daugharthy ER, Scheiman J, Kalhor R, Ferrante TC, Terry R et al (2015) Fluorescent in situ sequencing (FISSEQ) of RNA for gene expression profiling in intact cells and tissues. Nat Protoc 10(3):442–458. https://doi.org/10.1038/nprot.2014.191
65. Grindberg RV, Yee-Greenbaum JL, McConnell MJ, Novotny M, O'Shaughnessy AL, Lambert GM et al (2013) RNA-sequencing from single nuclei. Proc Natl Acad Sci U S A 110(49):19802–19807. https://doi.org/10.1073/pnas.1319700110
66. Alix-Panabieres C, Pantel K (2014) Technologies for detection of circulating tumor cells: facts and vision. Lab Chip 14:57–62. https://doi.org/10.1039/c3lc50644d
67. Chang HH, Hemberg M, Barahona M, Ingber DE, Huang S (2008) Transcriptome-wide noise controls lineage choice in mammalian progenitor cells. Nature 453:544–547. https://doi.org/10.1038/nature06965
68. Kobayashi K, Ehrlich SD, Albertini A, Amati G, Andersen KK, Arnaud M et al (2003) Essential Bacillus subtilis genes. Proc Natl Acad Sci U S A 100:4678–4683. https://doi.org/10.1073/pnas.0730515100
69. Hümmer D, Kurth F, Naredi-Rainer N, Dittrich PS (2016) Single cells in confined volumes: microchambers and microdroplets. Lab Chip 16:447–458. https://doi.org/10.1039/c5lc01314c
70. Zinchenko A, Devenish SRA, Kintses B, Colin P-Y, Fischlechner M, Hollfelder F (2014) One in a million: flow cytometric sorting of single cell-lysate assays in monodisperse picolitre double emulsion droplets for directed evolution. Anal Chem 86:2526–2533. https://doi.org/10.1021/ac403585p
71. Zhu Z, Zhang W, Leng X, Zhang M, Guan Z, Lu J, Yang CJ (2012) Highly sensitive and quantitative detection of rare pathogens through agarose droplet microfluidic emulsion PCR at the single-cell level. Lab Chip 12:3907–3913
72. Lang P, Yeow K, Nichols A, Scheer A (2006) Cellular imaging in drug discovery. Nat Rev Drug Discov 5:343–356
73. Shroeder T (2008) Imaging stem-cell-driven regeneration in mammals. Nature 453:345–351. https://doi.org/10.1038/nature07043
74. Shroeder T (2011) Long-term single-cell imaging of mammalian stem cells. Nat Methods 8(4 Suppl):S30–S35. https://doi.org/10.1038/nmeth.1577
75. Horwitz R (2016) Integrated, multi-scale, spatial-temporal cell biology—a next step in the post genomic era. Methods 96:3–5. https://doi.org/10.1016/j.ymeth.2015.09.007
76. Vorobjev I, Barteneva NS (2015) Temporal heterogeneity metrics in apoptosis induced by anticancer drugs. J Histochem Cytochem 63:494–510. https://doi.org/10.1369/0022155415583534
77. Serikbayeva A, Tvorogova A, Kauanova S, Vorobjev IA (2017) Analysis of microtubule dynamics heterogeneity in cell culture. In: Barteneva NS, Vorobjev IA (eds) Cellular heterogeneity: methods and protocols, Methods Mol Biol. Humana, New York
78. Basiji DA (2016) Principles of Amnis imaging flow cytometry. Methods Mol Biol 1389:13–21. https://doi.org/10.1007/978-1-4939-3302-0_2
79. Boland MV, Murphy RF (2001) A neural network classifier capable of recognizing the patterns of all major subcellular structures in fluorescence microscope images of HeLa cells. Bioinformatics 17:1213–1223
80. Shamir L, Orlov N, Eckley DM, Macura T, Johnston J, Goldberg IG (2008) Wndchrm—an open source utility for biological image analysis. Source Code Biol Med 3:13. https://doi.org/10.1186/1751-0473-3-13
81. Yin Z, Zhou X, Bakal C, Li F, Sun Y, Perrimon N, Wong ST (2008) Using iterative cluster merging with improved gap statistics to perform online phenotype discovery in the context of high-throughput RNAi screens. BMC Bioinformatics 9:264
82. Jones TR, Carpenter AE, Lamprecht MR, Moffat J, Silver SJ, Grenier JK, Castoreno AB, Eggert US, Root DE, Golland P et al (2009) Scoring diverse cellular morphologies in image-based screens with iterative feedback and machine learning. Proc Natl Acad Sci U S A 106:1826–1831
83. Laksameethanasan D, Tan RZ, Wei-Ling Toh G, Loo L-H (2013) cellXpress: a fast and user-friendly software platform for profiling cellular phenotypes. BMC Bioinformatics 14(Suppl 16):S4. https://doi.org/10.1186/1471-2105-14-S16-S4

84. Pärnamaa T, Parts L (2017) Accurate classification of protein subcellular localization from high-throughput microscopy images using deep learning. G3 (Bethesda) 7:1385–1392. https://doi.org/10.1534/g3.116.033654.
85. Haridas V, Ranjbar S, Vorobjev IA, Goldfeld AE, Barteneva NS (2017) Imaging flow cytometry analysis of intracellular pathogens. Methods 112:91–104. https://doi.org/10.1016/j.ymeth.2016.09.007
86. Krutzik PO, Irish JM, Nolan JP, Perez OD (2004) Analysis of protein phosphorylation and cellular signaling events by flow cytometry: techniques and clinical applications. Clin Immunol 110:206–221
87. Herzenberg LA, Tung J, Moore WA, Herzenberg LA, Parks DR (2006) Interpreting flow cytometry data: a guide for the perplexed. Nat Immunol 7(7):681–685
88. Qiu P, Gentles AJ, Plevritis SK (2011a) Discovering biological progression underlying microarray samples. PLoS Comput Biol 7:e1001123
89. Qiu P, Simonds EF, Bendall SC, Gibbs KD, Bruggner RV, Linderman MD, Sachs K, Nolan GP, Plevritis SK (2011b) Extracting a cellular hierarchy from high-dimensional cytometry data with SPADE. Nat Biotechnol 29:886–891. https://doi.org/10.1038/nbt.1991
90. Qiu P (2017) Toward deterministic and semi-automated SPADE analysis. Cytometry A 91(3):281–289. https://doi.org/10.1002/cyto.a.23068
91. Gautreau G, Pejoski D, Le Grand R, Cosma A, Beignon AS, Tchitchek N (2017) SPADEVizR: an R package for visualization, analysis and integration of SPADE results. Bioinformatics 33(5):779–781. https://doi.org/10.1093/bioinformatics/btw708
92. Diggins KE, Ferrell PB, Irish JM (2015) Methods for discovery and characterization of cell subsets in high dimensional mass cytometry data. Methods 82:55–63. https://doi.org/10.1016/j.ymeth.2015.05.008
93. Aghaeepour N, Chattopadhyay P, Chikina M et al (2016) A benchmark for evaluation of algorithms for identification of cellular correlates of clinical outcomes. Cytometry A 89(1):16–21
94. Bruggner RV, Bodenmiller B, Dill DL, Tibshirani RJ, Nolan GP (2014) Automated identification of stratifying signatures in cellular subpopulations. Proc Natl Acad Sci U S A 111(26):E2770–E2777. https://doi.org/10.1073/pnas.1408792111
95. Arvaniti E, Claassen M (2017) Sensitive detection of rare disease-associated cell subsets via representation learning. Nat Commun 8:14825. https://doi.org/10.1038/ncomms14825
96. Hotteling H (1933) Analysis of a complex of statistical variables in principal components. J Educ Psychol 24:417
97. Newell EW, Sigal N, Bendall SC, Nolan GP, Davis MM (2012) Cytometry by time-of-flight shows combinatorial cytokine expression and virus-specific cell niches within a continuum of CD8+ T cell phenotypes. Immunity 36(1):142–152. https://doi.org/10.1016/j.immuni.2012.01.002
98. Deininger SR-O, Ebert MP, Fütterer A, Gerhard M, Röcken C (2008) MALDI imaging combined with hierarchical clustering as a new tool for the interpretation of complex human cancers. J Proteome Res 7:5230–5236
99. van der Maaten LJP, Hinton GE (2008) Visualizing high-dimensional data using t-SNE. J Mach Learn Res 9:2579–2605
100. Macosko EZ, Basu A, Satija S et al (2015) Highly-parallel genome-wide expression profiling of individual cells using nanolietr droplets. Cell 161:1202–1214
101. Inglese P, McKenzie JS, Mroz A, Kinross J, Veselkov K, Holmes E, Takats Z, Nicholson JK, Glen RC (2017) 2017. Deep learning and 3D-DESI imaging reveal the hidden metabolic heterogeneity of cancer. Chem Sci 8(5):3500–3511. https://doi.org/10.1039/c6sc03738k
102. Shekhar K, Brodin P, Davis MM, Chakraborty AK (2014) 2014. Automatic classification of cellular expression by nonlinear stochastic embedding (ACCENSE). Proc Natl Acad Sci U S A 111(1):202–207. https://doi.org/10.1073/pnas.1321405111
103. Bendall SC, Davis KL, Amir ED, Tadmor MD, Simonds EF, Chen TJ, Shenfeld DK, Nolan GP (2014) Pe'er D. 2014. Single-cell trajectory detection uncovers progression and regulatory coordination in human B cell development. Cell 157(3):714–725. https://doi.org/10.1016/j.cell.2014.04.005.
104. Gut G, Tadmor MD, Pe'er D, Pelkmans L, Liberali P (2015) Trajectories of cell-cycle progression from fixed cell populations. Nat Methods 12:951–954. https://doi.org/10.1038/nmeth.3545
105. Paul F et al (2015) Transcriptional heterogeneity and lineage commitment in myeloid progenitors. Cell 163(7):1663–1677

106. Setty M, Tadmor MD, Reich-Zeiliger S, Angel O, Salame TM, Kathail P, Choi K, Bendall S, Friedman N, Pe'er D (2016) Wishbone identifies bifurcating developmental trajectories from single-cell data. Nat Biotechnol 34(6):637–645. https://doi.org/10.1038/nbt.3569.

107. Ornatsky O, Bandura D, Baranov V, Nitz M, Winnik MA, Tanner S (2010) Highly multiparametric analysis by mass cytometry. J Immunol Methods 361:1–20. https://doi.org/10.1016/j.jim.2010.07.002

108. Chang Q, Ornatsky OI, Siddiqui I, Loboda A, Barabov VI, Hedley DW (2017) Imaging mass cytometry. Cytometry 91:160–169. https://doi.org/10.1002/cyto.a.23053

109. Combs PA, Eisen MB (2015) Low-cost, low-input RNA-seq protocols perform nearly as well as high protocols. PeerJ 3:e869. https://doi.org/10.7717/peerj.869

110. Carvajal-Alegria G, Gazeau P, Hillion S, Daien CI (2017) Could lymphocyte profiling be useful to diagnose systemic autoimmune diseases? Clin Rev Allerg Immunol Epub May 4. doi: https://doi.org/10.1007/s12016-017-8608-5

111. Jamin C, Le Lann L, Alvarez-Errico D, Barbarroja N, Cantaert T, Ducreux J, Dufour AM, Gerl V, Kniesch K, Neves E, Trombetta E, Alarcon-Riquelme M, Maranon C, Pers J-O (2016) Multi-center harmonization of flow cytometers in the context of the European "PRECISESADS" project. Autoimmun Rev 15(11):1038–1045. https://doi.org/10.1016/j.autrev.2016.07.034

112. Krzywinski M, Altman N (2013) Points of significance: power and sample size. Nat Methods 10:1139–1140

113. Levine JH, Simonds EF, Bendall SC, Davis KL, Amir e-AD et al (2015) Data-driven phenotypic dissection of AML reveals progenitor-like cells that correlate with prognosis. Cell 162:184–197. https://doi.org/10.1016/j.cell.2015.05.047

114. Macaulay IC, Voet T (2014) Single cell genomics: advances and future perspectives. PLoS Genet 10:e1004126. https://doi.org/10.1371/journal.pgen.1004126

115. Kawasaki ES (2004) Microarrays and the gene expression profile of a single cell. Ann N Y Acad Sci 1020:92–100

116. Lutsik P, Slawski M, Gasparoni G, Vedeneev N, Hein M, Walter J (2017) MeDeCon: discovery and quantification of latent components of heterogeneous methylomes. Genome Biol 18:55. https://doi.org/10.1186/s13059-017-1182-6.

117. Shiroguchi K, Jia TZ, Sims PA, Xie XS (2012) Digital RNA sequencing minimizes sequence-dependent bias and amplification noise with optimized single-molecule barcodes. Proc Natl Acad Sci U S A 109:1347–1352. https://doi.org/10.1073/pnas.1118018109

118. Grun D, Kester L, van Oudenaarden A (2014) Validation of noise models for single-cell transcriptomics. Nat Methods 11:637–644. https://doi.org/10.1038/nmeth.2930

119. Gong W, Rasmussen TL, Singh BN, Koyano-Nakagawa N, Pan W, Garry DJ (2017) Dpath software reveals hierarchical haemato-endothelial lineages of Etv2 progenitors based on single-cell transcriptome analysis. Nat Commun 8:14362. https://doi.org/10.1038/ncomms14362

120. Raj A, van den Bogaard P, Rifkin SA, van Oudenaarden A, Tyagi S (2008) Imaging individual mRNA molecules using multiple singly labeled probes. Nat Methods 5:877–879

Chapter 2

Integrating Analysis of Cellular Heterogeneity in High-Content Dose-Response Studies

Albert Gough, Tong Ying Shun, D. Lansing Taylor, and Mark Schurdak

Abstract

Heterogeneity is a complex property of cellular systems and therefore presents challenges to the reliable identification and characterization. Large-scale biology projects may span many months, requiring a systematic approach to quality control to track reproducibility and correct for instrumental variation and assay drift that could mask biological heterogeneity and preclude comparisons of heterogeneity between runs or even between plates. However, presently there is no standard approach to the tracking and analysis of heterogeneity. Previously, we demonstrated the use of the Kolmogorov-Smirnov statistic as a metric for monitoring the reproducibility of heterogeneity in a screen and described the use of three heterogeneity indices as a means to characterize, filter, and browse cellular heterogeneity in big data sets (Gough et al., Methods 96:12–26, 2016). In this chapter, we present a detailed method for integrating the analysis of cellular heterogeneity in assay development, validation, screening, and post screen. Importantly, we provide a detailed method for quality control, to normalize cellular data, track heterogeneity over time, and analyze heterogeneity in big data sets, along with software tools to assist in that process. The example screen for this method is from an HCS project, but the approach applies equally to other experimental methods that measure populations of cells.

Key words Cellular heterogeneity, High-content screening, Systems biology, Drug discovery, Phenotypic profiling

1 Introduction

Heterogeneity is a fundamental property of cellular systems, even when composed of isogenic cells, which contributes to biological adaptability [1] and impacts biomedical research, the development of therapeutics, and diagnostics [2]. For example, the association between cellular heterogeneity and adaptation suggests that ignoring heterogeneity may lead to the selection of compounds to which cells will rapidly adapt. Cell-to-cell variability is not simply the result of intrinsic noise in molecular

Electronic supplementary materials: The online version of this chapter (https://doi.org/10.1007/978-1-4939-7680-5_2) contains supplementary material, which is available to authorized users.

Natasha S. Barteneva and Ivan A. Vorobjev (eds.), *Cellular Heterogeneity: Methods and Protocols*, Methods in Molecular Biology, vol. 1745, https://doi.org/10.1007/978-1-4939-7680-5_2,

networks; rather it is often the result of deterministic regulatory molecular mechanisms that remain largely uncharacterized [3–5]. Studies have shown that patterns of signaling heterogeneity can distinguish cellular populations with different drug sensitivities [6, 7]. Analysis of heterogeneity can provide insights into the pathways and networks involved in the cellular response to perturbagens [8, 9] and insights into the adaptation and development of resistance in tumors [9] and can inform the development of combination therapies [10–12]. Thus, it is important to incorporate heterogeneity analysis in large-scale screens in drug discovery and phenotypic profiles in basic biomedical research.

1.1 Why This Method Was Developed

Methods such as high-content screening (HCS), high-throughput microscopy, flow cytometry, mass spec imaging, and digital pathology capture cell-level data for populations of cells that can be used to identify and analyze heterogeneity. However, in these methods, compound activity is typically characterized by the well average value, and the cell-level data is only occasionally reviewed. Metrics to quantify well-to-well and plate-to-plate reproducibility in large-scale screens/profiles, including signal-to-background (S/B) and Z′-factor, have been widely adopted [13]. However, these metrics do not address the reproducibility of the biological heterogeneity present in the individual cell populations [7]. A variety of methods to analyze and compare biological heterogeneity has been described [7, 14–21]. While these methods are useful, they do not address the routine quality control of heterogeneity and do not all address the application to large-scale projects. Recently, we proposed a new metric for well-to-well and plate-to-plate characterization of the reproducibility of heterogeneity based on the Kolmogorov-Smirnov (KS) statistic, the QC-KS [22]. In this chapter, we present a procedure that integrates the use of this metric, in combination with established screening quality control metrics, for routine characterization of reproducibility of assay readouts and the cellular heterogeneity of those readouts.

1.2 Overview of the Method

This chapter presents detailed procedures and tools for processing and analyzing heterogeneity in the cell-level data acquired by HCS systems, but the procedures and tools should be easily adapted to other single cell measurements on populations of cells. Although the example used here is from an HCS screen, the methods used to make the plates, scan the plates, and analyze the images are not presented, as they have been previously published [7], and there are many other examples of procedures for HCS assay development. The focus of the procedures in this chapter is on the analysis of the cellular data generated by most HCS systems, but not often analyzed. There are many possible reasons for this, but there are two that seem likely. First, HCS analysis software rapidly reduces the measurements of hundreds to thousands of cells to a simple

average of the population. Many HCS assays have been validated and are quite robust with respect to the population average and therefore are screened in that mode. Second, the informatics tools and procedures needed to process and analyze the distributions of cellular responses are not commonly available. To address this gap, we have developed a systematic approach to the analysis of heterogeneity in moderate- to large-scale HCS projects. These tools were developed and tested on dose-response data from over 200 compounds screened at ten concentrations in triplicate for the inhibition of the IL-6 activation of STAT3. The screen consisted of over 100 plates (384 well) and generated multiple features for over 40 million cells.

Table 1 is an overview of the procedure detailed in this chapter. The procedure is divided into four sections corresponding to four

Table 1
Overview of procedures

General procedure
• Generate assay plates and assay data • Evaluate screening QC metrics (e.g., S/B, Z′, etc.) • Extract cell-level data from the HCS database • Merge cell-level data with experiment metadata • Calculate and review QC-KS values • Calculate heterogeneity indices • Review results
Assay development-specific tasks
• Evaluate cellular heterogeneity and select reference distribution(s) • Select optimal assay parameter, "intensity," or "%responders," for validation and screening
Assay validation-specific tasks
• Establish the reference assay distribution for QC and median for normalization • Review results and make screening decision
Screening-specific tasks
• Normalize cell-level data • QC plates using the QC-KS value • Review batch results using the PHIs to filter, group, or browse distributions
Analysis of results
• Combine all screening data and the PHIs into a single file • Use the heterogeneity indices to filter, group, or arrange data to compare compounds

phases of developing and running a screen: assay development, assay validation, screening, and analysis of results. The general procedure (top of Table 1) is similar in each phase, but each phase also has some key specific tasks. A key component of this procedure is the establishment of reference distributions for normalization and quality control. During assay development, the final design of the assay and the nature of the heterogeneity will determine the selection of the reference distribution (Table 1). For example, in the inhibition of IL-6, the negative control exhibited maximum signal and heterogeneity and therefore was the most important reference distribution. During assay validation, two reference distributions, one each for the positive and negative controls, are established from the validation plates to measure the reproducibility of the cellular heterogeneity (Table 1). During screening, each plate is normalized to the median of the reference distribution, QC'ed., and the results are reviewed (Table 1). At the end of the screen, the data are accumulated into a single file for global analysis of the results.

1.3 Importance of Data Normalization

High-content assays based on the measurement of the average fluorescent intensity of a labeled biomarker, such as pSTAT3 in the example used here, often exhibit drift in the measured average intensity. Drift can be due to variation in assay preparation, such as the efficiency of anti-pSTAT3 labeling, variation in acquisition parameters that may be adjusted to one or two plates in batch, or variation in the image analysis due to variation in background or other factors. As a result, the average intensities in the control wells may vary from plate to plate. Usually this is corrected by normalizing the readout to the on-plate control wells. For the same reason, the cellular data requires normalization. In the example screen for inhibitors of STAT3, the negative control (maximum IL-6) exhibits maximum heterogeneity (Fig. 1), and the positive control (no IL-6) has an average intensity near zero. Because the distribution of the negative control is not normal and, in general, cellular distributions should not be assumed to be normal, we normalize the cellular data to the median of the negative control, in order to maintain an intensity range that was nominally consistent with the data range acquired on the HCS system.

1.4 Establishing Quality Control of the Reproducibility of Heterogeneity

In addition to the assay drift discussed above, the distribution of cellular responses may vary over time for other reasons. During validation, it is important to assess the reproducibility of the heterogeneity (Fig. 2). To identify changes in the distribution, we establish a reference distribution using the validation plates (Fig. 3a) and use the KS statistic (which we call the QC-KS) to quantitate the difference between the negative control wells on each plate and the reference distribution. The KS statistic measures the maximum difference between the cumulative distributions for

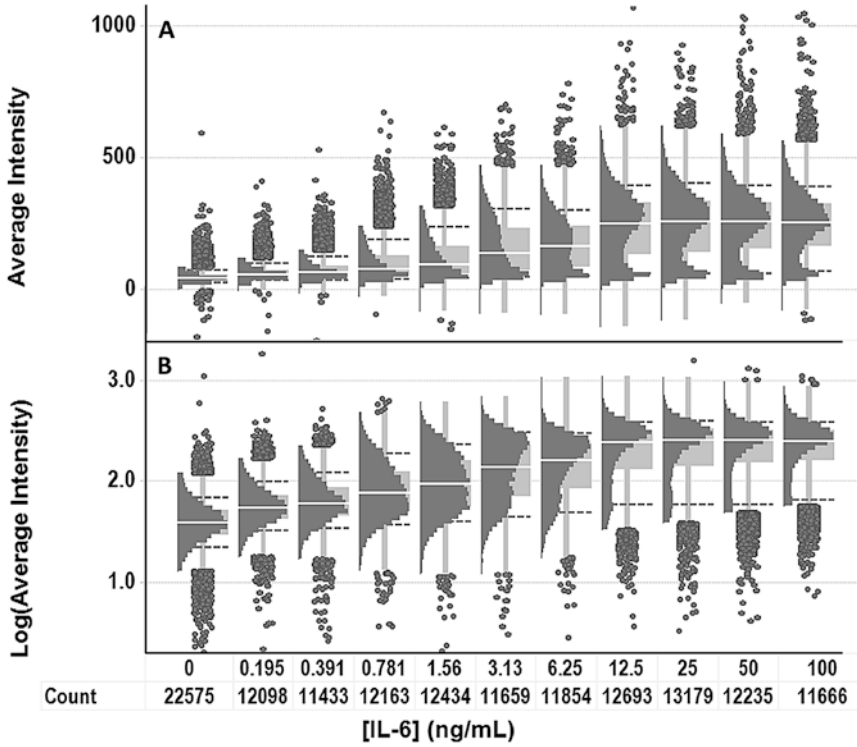

Fig. 1 Histobox plots for the dose-response analysis of the activation of STAT3 by IL-6. An assay development plate was prepared with a ten-dose series of twofold dilutions of IL-6 and no IL-6 as the positive control for inhibition, to evaluate the heterogeneity in the activation of STAT3, indicated as the Mean Inner Intensity (nuclear intensity) of the pSTAT3 antibody label. Histobox plots are box plots (light gray) with a histogram (dark gray) overlaid. The count indicates the total number of cells in each histogram. (**a**) Plots of linear-scaled intensities. (**b**) Plots of log-scaled intensities

two distributions [23], providing a quantitative measure of the difference between distributions. During assay validation, we establish a threshold value for the QC-KS metric which is used to flag wells and plates on which the negative controls vary significantly from the reference distribution (Fig. 3b). For example, in this screen, there was a batch of plates that were flagged for increased QC-KS values, indicating different distributions in the negative control wells [22]. We believe the variation was a result of using an older aliquot of IL-6 with lower potency.

1.5 Analysis of Heterogeneity in Large Data Sets

In a large-scale analysis of biological activity, taking the average of a population is a quick way to reduce the dimension of the data to a size that can be easily managed, filtered, and interpreted but neglects the information contained in the distribution of cellular responses. The lack of an established analytical approach to the analysis of heterogeneity suggested the need for metrics to characterize heterogeneity in order to extract insights into the underlying cellular functions [24, 25]. To address this need, we adopted a set

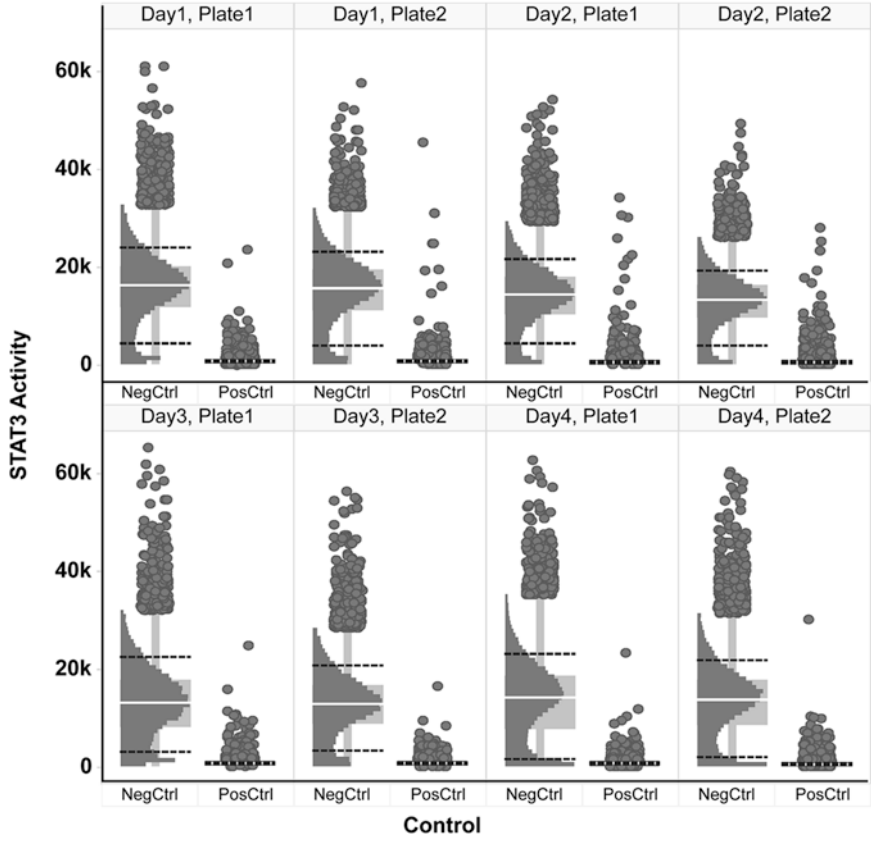

Fig. 2 Histobox plots of the distributions of STAT3 activity in the negative and positive control wells on the validation plates. White lines indicate the median of the distribution; dashed lines indicate the 10th and 90th percentiles of the distribution

of three heterogeneity indices (HI): quadratic entropy (QE), a measure of diversity; KS-norm, a measure of the extent of deviation from a normal distribution; and %Outliers, a measure of the fraction of the distribution that is based on the standard box plot definition of an outlier [7]. Collectively we refer to these specific heterogeneity indices as the Pittsburgh Heterogeneity Indices (PHI), to distinguish them from other measures of heterogeneity. In addition to providing a quantitative measure of heterogeneity in a population (Fig. 4), the PHI have proven to be useful for sorting, filtering, and clustering large collections of distributions for interactive analysis.

Analyzing all the cellular data in a compound screen, RNA_i screen, or other large biology project is a "big data" problem. For a screen of 100,000 compounds and 1000 cells/well, there will be 100 million data points for each feature (potentially 4–20 or many more) measured on the screen. Data that is well organized, such as in an HCS database, may be easily extracted by a query, but efficient analysis of 30–500 million or more data points acquired over

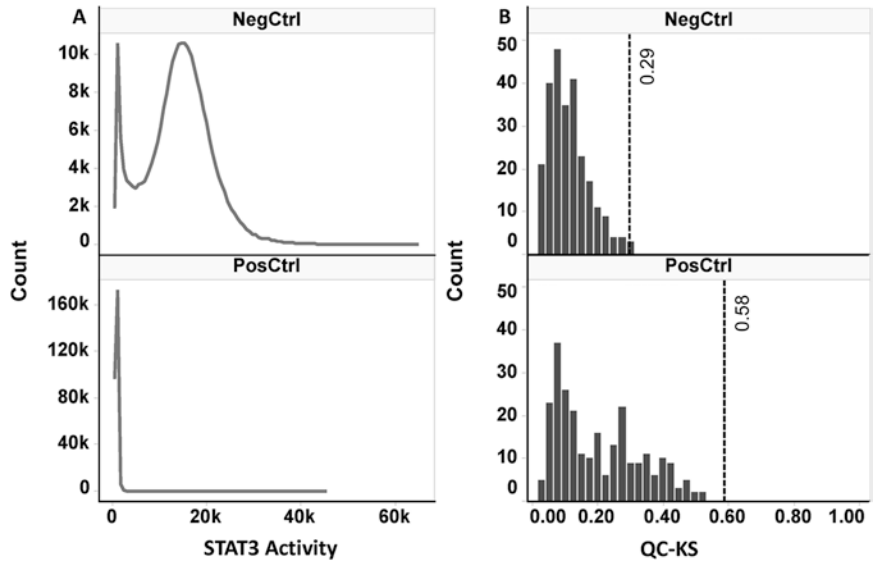

Fig. 3 Establishing the reference distributions and evaluating the reproducibility of the heterogeneity on the validations plates. (**a**) The distributions of STAT3 activity in all the negative control and positive control wells on the validation plates. (**b**) The distributions of the QC-KS values calculated with respect to the reference distributions (**a**) for all the negative control and positive control wells on the validation plates. The dashed lines indicate the Mean + 3 * Stdev, 0.29 for the negative control wells and 0.58 for the positive control wells. We will round to 0.3 and 0.6 to use as thresholds to flag wells with a distribution that is different than the reference (**a**)

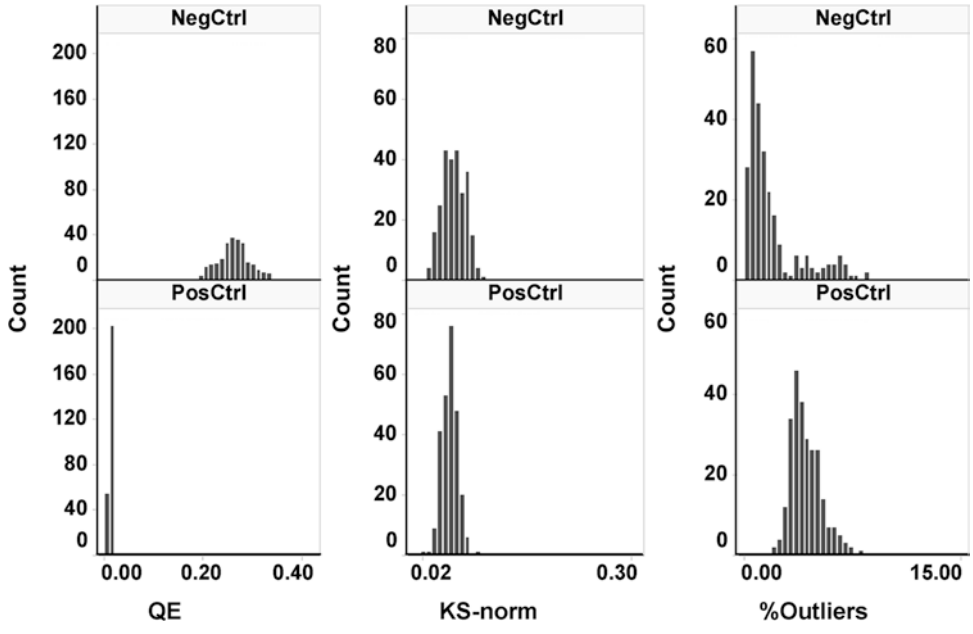

Fig. 4 Histograms of the distributions of the PHIs for the validation plates. The PHIs were calculated in Spotfire using the accompanying R-script, and histograms were created to assess the sensitivity of each to the heterogeneity in the activation of STAT3

several months for patterns in response at least requires some thought, planning, and tools for manipulating and comparing the distributions. In Subheading 3.4, we present an approach to this problem. We take advantage of the complexity in the distributions by using the PHI to characterize the complexity and then to cluster and filter the distributions to identify normal and novel distributions. We present an interactive software tool to summarize the shapes of the distributions across all the wells in the screen, provide a means to identify compounds by the distribution (Fig. 5), as well as compare distributions between compounds (Fig. 6). The cell-level data generated by HCS and other single cell profiling methods can be a rich source of information provided it was collected and processed with attention to quality control and information tools are available to sift, sort, and analyze the data. Hopefully, the procedures in this chapter provide a starting point for mining current HCS databases and extracting deeper insights from future screening projects.

2 Materials

2.1 R Statistical Computing Environment

The R software environment for statistical computing and graphics can be downloaded from one of the mirror websites listed at the Comprehensive R Archive Network (https://cran.r-project.org/mirrors.html) (*see* **Note 1**).

2.2 Spotfire Desktop for Graphical Analysis

Spotfire is used for visualization, some data analysis and accumulation of data for analysis of results. Personal subscription available from PerkinElmer (http://www.cambridgesoft.com/ensemble/spotfire/) (*see* **Note 2**).

2.3 SQL-Query to Extract Cell-Level Data from the HCS Database

An example SQL-Query File, **HCS_extract.sql**, is provided in the Supplemental Material (https://www.updi.pitt.edu/uploads/Articles/MIMB-Supplemental-Material.zip) (*see* **Note 3**).

2.4 Experiment Metadata Excel File

An Excel file for recording the experimental data and importing into Spotfire is provided in the Supplemental Materials (https://www.updi.pitt.edu/uploads/Articles/MIMB-Supplemental-Material.zip).

2.5 PHI-R-Scripts to Calculate the Heterogeneity Indices

An R-script to calculate the PHI is provided in the Supplemental Materials (https://www.updi.pitt.edu/uploads/Articles/MIMB-Supplemental-Material.zip). The script is intended to be loaded and run within Spotfire (*see* **Note 4**).

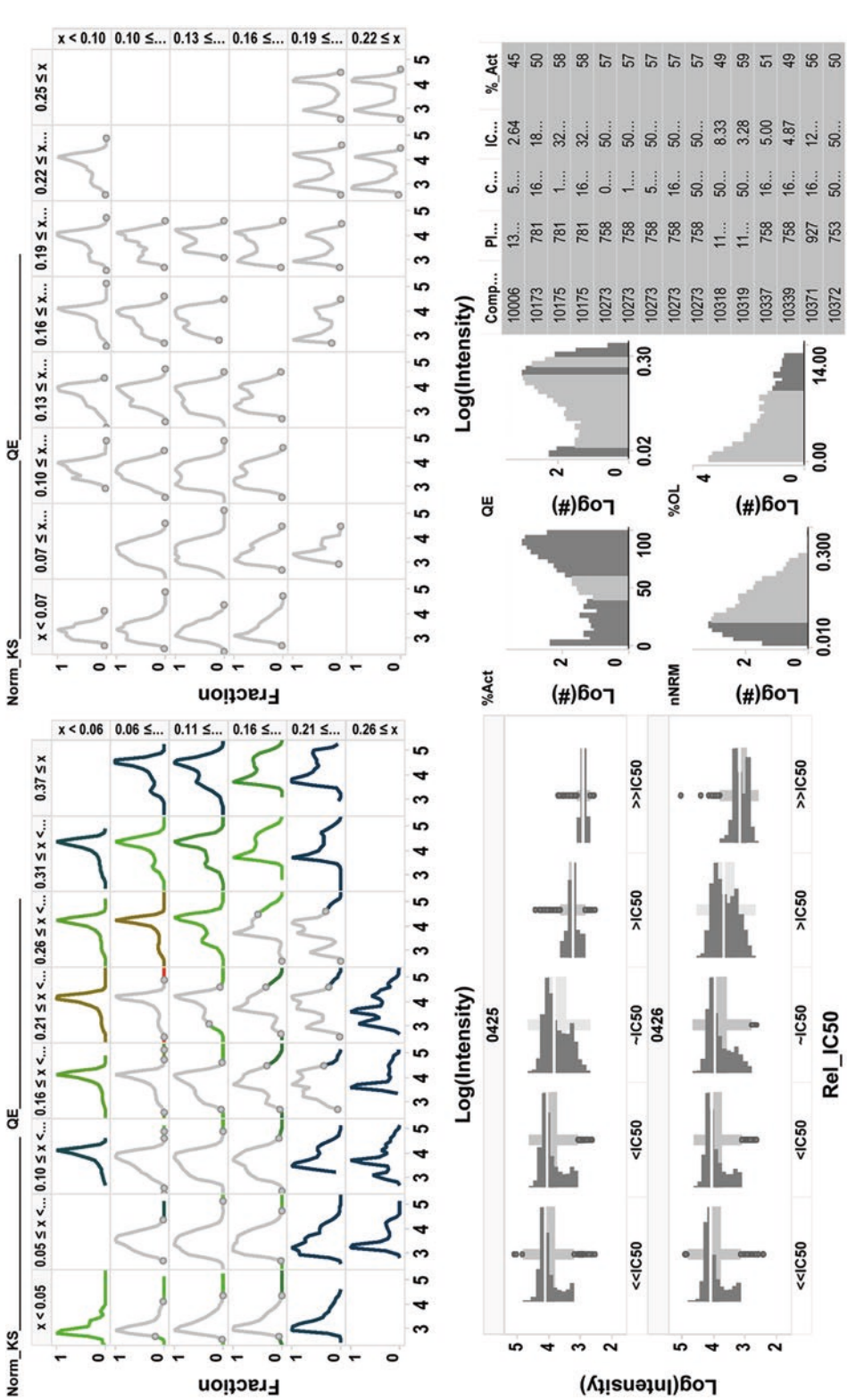

Fig. 5 Comparing the distributions around the IC_{50}. In this visualization, distributions with 50% activity were selected in the %Act histogram and are highlighted in light gray. In the upper left, the full range of over 30,000 distributions is summarized, with the selection shown in gray. In the upper right, only the selected curves are shown, highlighting the range of distributions near the IC_{50}, including clearly bimodal distributions as well as near-normal distributions. The cells in the bimodal distributions have different IC_{50}s, while the near-normal distributions indicate a more uniform response by all cells. The plates, wells, compounds, and concentrations associated with each curve are easily accessed as a tooltip or in tabular form

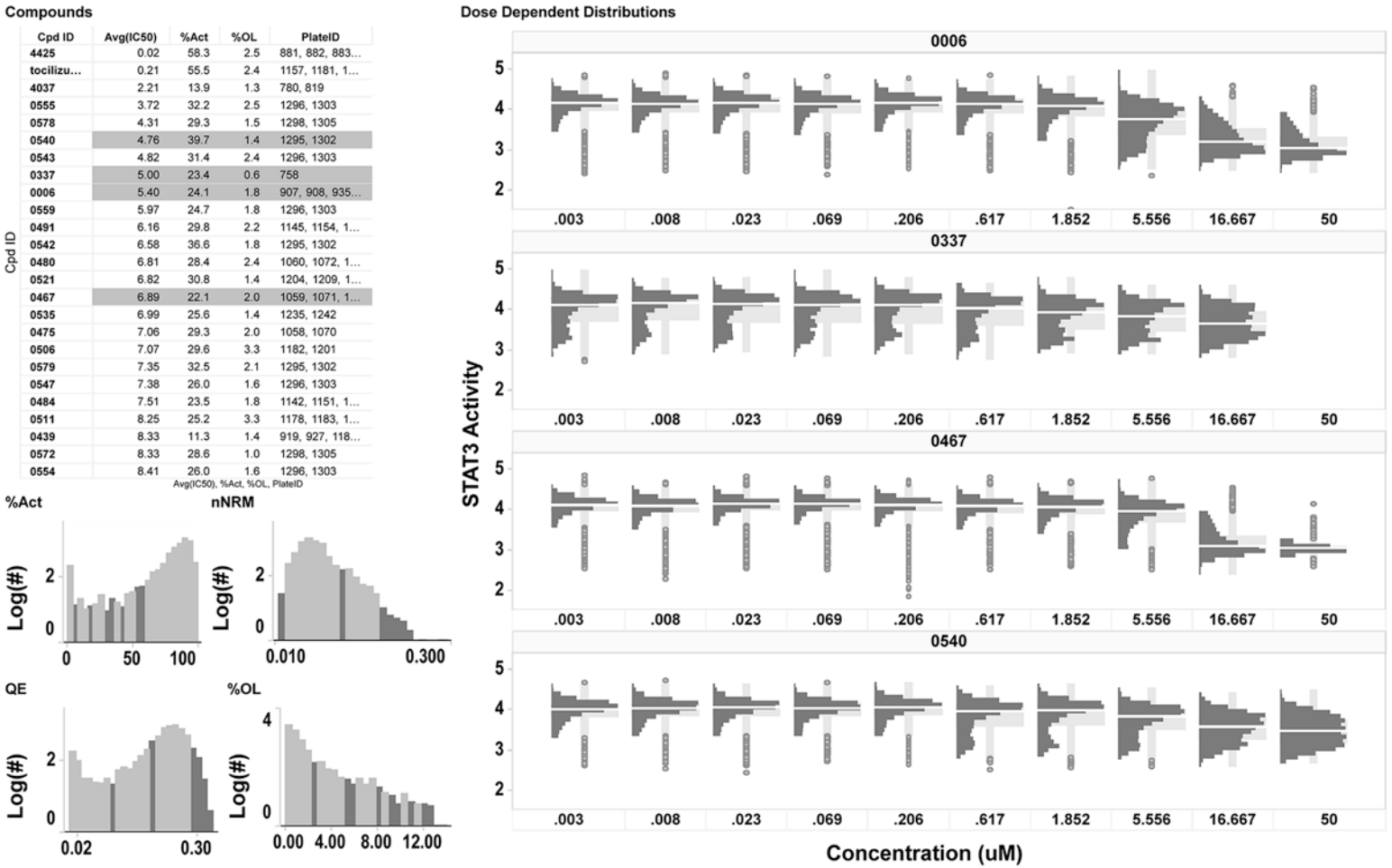

Fig. 6 Comparison of dose-dependence of heterogeneity in selected compounds. This Spotfire visualization allows selection of compounds by compound ID, IC_{50}, %Activation, or any of the PHIs for comparison of the dose effect on heterogeneity. For example, in this view, compounds 0006 and 0337 have essentially the same IC_{50}, but 0006 has a complete inhibition, while 0337 has a low level of inhibition even at low concentration. Compound 0467 has a very sharp dose-response, while 0540 has a shallower slope

3 Methods

3.1 Assay Development: Evaluate Heterogeneity and Reproducibility and Identify Reference Distributions

Early in the development of a new HCS assay, it is important to evaluate the heterogeneity of the response to a control compound or an agonist or antagonist (*see* **Note 5**).

1. Generate a dose-response plate with positive and negative controls, and image the plate on an HCS system, collecting at least 1000 cells/well (*see* **Note 6**).
2. Evaluate standard assay QC factors including evaluation of S/B, V-factor, and Z′-factor to determine whether assay has a sufficient window and reproducibility for screening at the well level (*see* **Note 7**).
3. Extract the cell-level data from the HCS database into Spotfire using the database interface. In the Spotfire menu select ***File***: ***Add Data Tables…***, and then select ***Add▼:Other:Database***. Select ***ODBC Data Provider***, and then select the ***HCS database*** from the list of ODBC connections (*see* **Note 8**). In the resulting **Specify Tables and Columns** window, choose ***Load SQL…***, and then browse to and select the file **HCS_extract.sql** to load the query (*see* **Note 9**). In the **SQL query** pane, add the ScanID(s) for the plate(s) containing the data to be extracted. Provide a **Data source name** such as "HCS_Cell_Data" to identify the new Spotfire table, and click OK to initiate the data download.
4. The data for this assay contains a column named "Mean Inner Intensity" which represents the average intensity of the pSTAT3 antibody in the nucleus of each cell, which is the primary feature of interest. Change the column name in Spotfire by selecting ***Edit:Column Properties***, then scroll down to "Mean Inner Intensity," and replace the **Name** with "STAT3_Activity" (*see* **Note 10**).
5. Edit the Experiment Metadata file in Excel to create the plate maps for the compounds and concentrations used on the dose-response plate, and save the file with a name like "Assay-Heterogeneity_Development_170525" (*see* **Note 11**).
6. Import the Experiment Metadata into Spotfire to associate the compounds and concentrations with the assay data by selecting ***Insert:Columns…***, and then ***Select▼*:File…**. Browse to the Experiment Metadata file and open it, switch to the "Table" worksheet, and click OK and Next. In the "Insert Columns – Match Columns" dialog, select the **plate ID** and **well_name** from the "current data" and the **plate ID** and **well_name** from the "new data" to match the Compounds and Concentrations to the appropriate wells. Select Next, select the columns to add, and then select Finish.

7. Create "histobox plots" (Fig. 1) as follows. Choose ***Insert:Visualization:Box Plot***. On the *X*-axis select "Concentration," and on the *Y*-axis, select "STAT3_Activity". To add the distributions to the resulting box plot, select ***Edit:Visualization Properties:Appearance***, and check the box next to **Show distribution**. Upon closing the dialog, you will see a plot similar to Fig. 1a.
8. Create histobox plots of the log10(STAT3_Activity) (*see* **Note 12**). To create log-scaled plots, simply duplicate the current visualization, right-click on the *Y*-axis label, and select ***Custom Expression…***. Enter the expression "log10([STAT3_Activity])," and assign a **Display name** like "log(STAT3_Activity)."
9. Review the linear and log-scaled histobox plots for insights into the heterogeneity of the populations and its dependence on concentration (*see* Fig. 1).
10. Run the PHI-R-Script to generate a set of heterogeneity indices for the wells on the validation plates including the QC-KS, QE, KS-norm, and %Outliers. To run the script, go to ***Tools:Register Data Functions***, double-click ***Import***, browse to the PHI-R-Script, and ***Open*** it. Click ***Run*** and follow the instructions (*see* **Note 13**).
11. Review the PHI for each concentration to evaluate whether there is significant heterogeneity (i.e., QE > 0.03, KS > 0.05, or %OL > 4.5). If there is significant heterogeneity, consider setting a threshold between responders and nonresponders, and use the percent of responding cells as the assay readout instead of the mean (*see* **Note 14**).
12. Save the Spotfire file with an appropriate name, such as "STAT3-Heterogeneity_Development_160525.dxp."

3.2 Assay Validation: Evaluate Reproducibility and Establish Reference Distributions for Quality Control

The primary goals during this phase are to evaluate plate-to-plate and day-to-day reproducibility, establish the assay reference distribution of the negative controls, record the median of that distribution, and evaluate the QC-KS measures of the similarity of the distribution in each negative control well to the assay reference distribution.

1. Prepare a series of plates for assay reproducibility analysis. There are variations on this, but in this project, we prepared pairs of plates on four different days, with both positive and negative control wells on each plate.
2. Image the plate(s) on an HCS system, collecting at least 1000 cells/well.
3. Evaluate the standard assay QC factors including evaluation of S/B, V-factor, and/or Z′-factor to determine whether assay

has a sufficient window and reproducibility for screening at the well level (*see* **Note 7**).

4. Extract the cell-level data from the HCS database into Spotfire. In Spotfire, in the menu select ***File:Add Data Tables…***, and then select ***Add▼:Other:Database***. Select ***ODBC Data Provider***, and then select the ***HCS database*** from the list of ODBC connections. In the resulting **Specify Tables and Columns** window, choose ***Load SQL…***, then browse to and select the file **HCS_extract.sql** to load the query. In the SQL query, add the ScanID(s) for the plate(s) containing the data to be extracted. Provide a **Data source name** to identify the new Spotfire table such as "HCS_Cell_Data," and click OK to initiate the data download.
5. Edit the Experiment Metadata file in Excel to create the plate maps for the compounds and concentrations used on the validation plate(s), and save the file with a name like "STAT3-Heterogeneity_Validation_170526.xlsx."
6. Import the Experiment Metadata into Spotfire to associate the compounds and concentrations with the assay data by selecting ***Insert:Columns…***, and then ***Select▼:File…***. Browse to the Experiment Metadata file and open it, switch to the "Table" worksheet, and click OK and Next. In the "Insert Columns – Match Columns" dialog, select the **plate ID** and **well_name** from the "current data" and the **plate ID** and **well_name** from the "new data" to match the Compounds and Concentrations to the appropriate wells. Select Next, select the columns to add, and then select Finish.
7. Create "histobox plots" (Fig. 2) as follows. Choose ***Insert:Visualization:Box Plot***. On the X-axis, select "Concentration," and on the Y-axis, select "STAT3_Activity." Right click on the graph to select ***Properties:Trellis:Panels***, and choose ***Split by*** **Plate_ID** (or barcode) to create the array of plots for all of the validation plates. To add the distributions to the resulting box plot, select ***Edit:Visualization Properties:Appearance***, and check the box next to **Show distribution**. Select OK to create graphs similar to Fig. 2.
8. Review the distributions in Fig. 2 for plate-to-plate consistency. If the distributions are not similar, identify the outlier plate(s) and run additional plates or omit the outliers. If the distributions pass qualitative review, make a single histogram of all the cells in all the negative control wells (Fig. 3a). It is important to have consistent distributions at this point, as this combined distribution will be used as the reference distribution for QC throughout the screen. Copy the reference values (the cell data from the negative control wells) to a new Spotfire table by selecting **File:Add Data Tables** and then **Add:From**

current analysis:HCS_Cell_Data and giving it the name "Reference_Data."

9. Calculate the median of the reference distribution, and save the value in Spotfire. From the menu select ***Edit:Document Properties*** and then select the ***Properties*** tab. Click **New** and enter **Property name** "MedianReference," **Data type** "Integer," **Description** "The median of the Assay Reference distribution for normalization," and **Value** "14,278", for this example. Save the Median in Spotfire for future use. Click **OK** and **OK** to exit the dialog (*see* **Note 15**).
10. Run the PHI-R-Script (*see* Supplemental Material) to generate a baseline set of heterogeneity indices for the wells on the validation plates including the QC-KS, QE, KS-norm, and %Outliers. To run the script, go to ***Tools:Register Data Functions***, double-click ***Import***, browse to the PHI-R-Script, and ***Open*** it. Click ***Run*** and follow the instructions (*see* **Note 16**).
11. Plot histograms of the QC-KS values for the validation wells on the plates (Fig. 3b) (*see* **Note 17**). Establish the QC criteria to flag wells and plates with inconsistent distributions. The Mean + 3 * Stdev, 0.29 for the negative control wells and 0.58 for the positive control wells, is a common statistical criterion. We rounded to 0.3 and 0.6 to use as thresholds to flag wells with a distribution that was different than the reference. Add a dashed vertical line to the histograms (as in Fig. 3b) to indicate the QC cutoff, in this case 0.3 for the negative control and 0.6 for the positive control. In Spotfire, that can be done by right-clicking the graph and selecting ***Properties:Lines & Curves:Add:Vertical Line:Straight Line:Fixed Value*** and entering the cutoff value.
12. Plot and review histograms of the HI's, QE, KS-norm, and %Outliers for the negative and positive control wells (Fig. 4). The distributions of the PHIs indicate that the most significant difference between the negative and positive controls is the much greater diversity of the cells (QE) in the negative control.
13. This Spotfire file will be used throughout the screen to accumulate data for global analysis of heterogeneity. Save the Spotfire file with an appropriate name such as "STAT3-Heterogeneity_Validation_170525.dxp".

3.3 Screening: Routine Processing of Screening Data for Heterogeneity Analysis

The major goals of this procedure are to normalize the cell-level data to the median of the assay reference distribution, QC the negative control wells, and evaluate the heterogeneity resulting from the compound exposure.

1. For each batch of screening plates, evaluate the standard assay QC factors including S/B, V-factor, and/or Z′-factor to determine whether the plates are consistent with the validation plate at the well level.
2. Extract the cell-level data from the HCS database into Spotfire. Open the file saved in **step 9** in Subheading 3.2, "STAT3-Heterogeneity_Dose-Response-Analysis_170525.dxp." Select ***File:Save As:File*** and name the file for the batch, such as "STAT3-Heterogeneity_Batch 1_170527.dxp." Select ***File:Replace Data Table…***, and then select ***Add▼:Other:Database***. Select ***ODBC Data Provider***, and choose the ***HCS database*** from the list of ODBC connections (*see* **Note 2**). In the resulting **Specify Tables and Columns** window, choose ***Load SQL…***, and then browse to and select the file **HCS_extract.sql** to load the query. In the SQL query add the ScanID(s) for the plate(s) containing the data. Provide a **Data source name** such as the batch number, and click OK to initiate the data download.
3. Edit the Experiment Metadata file in Excel to create the plate maps for the compounds and concentrations used on the dose-response plate and save the file (*see* **Note 11**).
4. Normalize all the plate data to the median of the Reference distribution. This step has very little impact on the HI's but is a critical step for later visualization of data collected over many months. Normalize the cellular data according to the following formula:

$$\mathrm{Norm}\left(\mathrm{MII}\left(\mathrm{Cell}_i\right)\right) = \frac{\mathrm{Median}\left(\mathrm{MII}\left(\text{Reference cells}\right)\right)}{\mathrm{Median}\left(\mathrm{MII}\left(\mathrm{Cell}_{1\,\mathrm{to}\,n}\right)\right.} * \mathrm{MII}\left(\mathrm{Cell}_i\right).$$

   To normalize the Mean Inner Intensity in Spotfire, from the menu select ***Insert:Calculated Column.*** In the **Expression field** insert "${MedianReference}/Median(If([Compound ID] = "NegControl", [Mean Inner Intensity], NULL)) OVER ([PLATE_ID]) * [Mean Inner Intensity]" without the closing quotes. In the **Column name** field, insert a name like "Norm(MII)." Click **OK,** and Spotfire will create a new column with the data normalized plate by plate (*see* **Note 18**).
5. Run the PHI-R-Script (*see* Supplemental Material) to generate a set of heterogeneity indices, QC-KS, QE, KS-norm, and %Outliers, for all the wells on the batch of plates. To run the script, go to ***Tools:Register Data Functions***, double-click ***Import***, browse to the PHI-R-Script, and ***Open*** it. Click ***Run*** and follow the instructions (*see* **Note 4**).

6. Plot histograms of the QC-KS values for the plates (as in Fig. 3b). Identify flagged wells that exceed the dashed lines at 0.3 for negative control wells and 0.6 for positive control wells. If there are too many flagged wells, it may be necessary to fail and rerun the plate. We failed plates with more than 25% failed wells (>4 out of 16 negative control wells). Tooltips can be used to identify the plate and well in the graph, or a table can be inserted and sorted on the QC-KS values. If necessary, filter out the flagged wells by left-clicking and dragging a rectangle around the points then selecting ***Edit:Marked Rows:Filter Out***.
7. Create histobox plots for the compounds on the plates (as in Fig. 1) as follows. Choose ***Insert:Visualization:Box Plot***. On the *X*-axis select "Concentration," and on the *Y*-axis select, "STAT3_Activity." Right click on the graph to select ***Properties:Trellis:Rows and Columns:Rows:*** and select ***Compound_ID*** to create an array of plots for all the compounds. To add the distributions to the resulting box plot, select ***Edit:Visualization Properties:Appearance***, and check the box next to **Show distribution**. Select OK to create graphs similar to Fig. 1a (*see* **Note 19**).
8. Save the Spotfire file (it was renamed in **step 2** as "STAT3-Heterogeneity_Batch 1_170527.dxp"). This file will be reused as a template for each new batch of plates throughout the screen.

3.4 Analysis of Heterogeneity Across an HCS Campaign

The major goals of this procedure are to accumulate the data into a single analysis file to evaluate and compare differences in the cellular heterogeneity in the responses to compound exposure, identify compounds with more uniform cellular effects, identify compounds with novel cellular heterogeneity, and evaluate the dose-response variation in cellular heterogeneity.

1. Create a master Spotfire file to accumulate results as batches of plates are processed. Open the first batch file "STAT3-Heterogeneity_Batch 1_160527.dxp," and select ***File:Save As:File…***, and give it a name like "STAT3-Heterogeneity_Screen_Results_160527.dxp."
2. For each new batch file, open the file and select ***File:Export:Data to File…:Export data from:Data Table***, and choose the table you imported the data to. Export all rows and ***Save as type: TIBCO Spotfire Binary Data Format (*.sbdf)*** with a name like "STAT3-Heterogeneity_Batch 1_160527.sbdf." Again, select ***File:Export:Data to File…:Export data from:Data Table***, and choose the "Heterogeneity Indices" table. Export all rows and ***Save as type: TIBCO Spotfire Binary Data Format (*.sbdf)*** with a name like "STAT3-PHIs_Batch 1_160527.sbdf" (*see* **Note 20**).

3. Add new data to the master file, "STAT3-Heterogeneity_Screen_Results_160527.dxp," by selecting ***Insert:Rows…***, then choose the HCS_cell_data table, ***Select:File***, and browse to and open a "STAT3-Heterogeneity_Batch #_160527.sbdf" file. Similarly, select ***Insert:Rows…***, then choose the Heterogeneity Indices table, ***Select:File***, and browse to and open a "STAT3-PHIs_Batch #_160527.sbdf" file.
4. Open the master file to review and analyze the results of the screen (*see* **Note 21**).
5. Example 1: compare the distributions near the IC_{50} for all compounds. Figure 5 shows a view of an interactive tool for comparing heterogeneity in large data sets (in this example, there were >30,000 distributions).
6. Example 2: select compounds to compare the distributions as a function of concentration. Figure 6 shows a view from another interactive tool for comparing the dose effects on heterogeneity.

Clearly, with the data QC'ed and organized in this way, there are many potentially interesting analyses that can be readily implemented to extract insights and make better decisions.

4 Notes

1. The R statistical software must be installed along with Spotfire (PerkinElmer) to use the R-script for calculating the heterogeneity indices.
2. Most of the Spotfire visualizations used in this procedure could be created in other data analysis and visualization tools, including R. However, the Spotfire environment provides a much more interactive and dynamic interface for data analysis, along with an easy to use GUI. An example Spotfire file with the validation data and the figures from this chapter is provided in the Supplemental Materials.
3. The provided SQL query was developed at the University of Pittsburgh Drug Discovery Institute for use with the in-house MDC Store database (Molecular Devices) to load the assay data into Spotfire. The features extracted by the query are somewhat specific to the example STAT3 screen. Each project will likely require customization of the query used to extract data.
4. The PHI-R-Script was developed in the R environment and could be run in R, but it is left up to the reader to work out the procedure for running the PHI-R-Script in R.
5. In this example screen, STAT3 was activated by IL-6, and the screen was for inhibitors of IL-6 induction of STAT3 activity.

Because heterogeneity varies with dose, it is important to evaluate heterogeneity at each dose in the series.

6. In the STAT3 screen, assay plates consisted of ten concentrations in a threefold dilution with three replicate wells for each concentration. In order to identify potentially small subpopulations of cells, a reasonably large number of cells are needed. During assay development, more is better. When the assay moves to validation, the cell number can be optimized. However, keep in mind that it takes something like 50 cells to establish a consistent response and therefore at least 1000 cells to identify a subpopulation consisting of about 5% of the population.
7. Whether or not the assay window is sufficient during development, analysis of the cell-level data may provide insights into the distribution of cellular responses that can be used to improve assay performance. For example, if only a portion of the cells respond, it may be more effective to set a threshold between subpopulations and report "%Responders" or "%Inhibited" rather than "Avg Intensity."
8. To simplify routine connections to the HCS database, we use ODBC. Note that Spotfire also has a *Replace Data Table…* option. Once a Spotfire file has been created with graphs and new column names, it can be used as a template for the next plates by replacing the data table rather than creating a new one.
9. Our HCS databases, Thermo Fisher Store (Thermo Fisher) and MDC Store (Molecular Devices) were implemented in MS-SQL Server. A query that works for the MDC Store database is provided. The same approach should be compatible with other databases. If you are not able to retrieve data directly from the database, most HCS systems provide a means to extract cell-level data. Contact your HCS system representative for more information.
10. Changing the column name is not essential; however, if there are multiple readouts for an assay, it will be easier to keep them straight in Spotfire and when making graphs. Spotfire will remember the external name, "Mean Inner Intensity," and will substitute the new name, STAT3_Activity, when a new data set is imported.
11. Included with the Supplemental Materials is an Excel file that is used to create the plate layouts in plate "matrix" format to capture the compound name, concentration, and other necessary factors as they appear on the plate and converts them to a single table with well names that can be imported into Spotfire to associate the compounds and the results.

12. The linear- and log-scaled plots expose different details in the data. For example, in Fig. 1a, the linear histograms make it is easier to see the nonresponding subpopulation at high concentrations, while in Fig. 1b, the log-scaled plots better show the heterogeneity at low concentrations.
13. The PHI-R-Script calculates the three heterogeneity metrics and the QC-KS. The calculation of the QC-KS requires a reference distribution, which has not yet been established. On this development plate, the best reference would be the Max IL-6, as it appears to have maximal heterogeneity. However, it is also OK at this point to simply choose the Mean Inner Intensity of the whole plate, in which case the QC-KS will indicate the deviation of each well from the overall distribution.
14. Assays with significant heterogeneity are likely to perform better by setting a response threshold and counting the percentage of responding cells, rather than the population average. In the STAT3 assay, despite the small subpopulation (about 7–10%) of nonresponding cells (*see* Fig. 1), the population average of the "Mean Inner Intensity" was selected as the primary assay readout.
15. By saving this value as a property in Spotfire, it can be used later in the normalization of data sets.
16. When the PHI-R-Script is loaded, the instructions appear at the beginning of the file. To use the PHI-R-Script, the Spotfire file requires at least two data tables, one containing the assay data which is used to calculate the heterogeneity indices and the other containing the assay reference distribution which is used to calculate the QC-KS. At the end of this procedure, we will save this file including the Reference_Data table, and the median reference to be reused throughout the screen to process new data, avoiding the need to reload the reference distribution.
17. Note that the distributions of QC-KS values are not normal distributions, but they are close. If the distributions was very different from normal, we might have chosen different statistical criteria. In addition, note that the distribution of the QC-KS values for the positive control is broader than the negative control. However, the distribution of the positive control cells is extremely steep, narrow, and near 0, so larger proportional variation can be tolerated. Here, 0.6 is a good threshold.
18. We normalize the cellular intensities because the intensity in the high-content images may vary from day to day or over many months as a result of variation in labeling reagents, image acquisition parameters such as integration time, laser

power, detector gain, or image algorithm settings such as background subtraction. This changes the scaling of the distributions and can interfere with comparison of heterogeneity from batch to batch. In this screen, the median of the negative control, which is fully activated STAT3, exhibits the maximum heterogeneity and is used for normalization. For some assays, it may be necessary to perform normalization to both the positive and negative controls. When this file is saved, Spotfire will retain the formula and column and automatically calculate the normalized intensities when new data is imported. Normalization can also be done in R, Excel, or any standard statistical software package.

19. All the plots in the Spotfire file are saved and reapplied when a new data table is imported. Therefore, the configuration of this plot only has to be completed once.
20. To transfer data from one Spotfire file to another requires exporting and importing. The *.sbdf format is a binary file format that provides smaller files that are faster to export and import than text files. However, the files could just as well be transferred as Tab separated text or Excel format files for portability. Within the Spotfire file, there can be multiple data tables. In this case there should be three, the HCS_cell_data table that was imported, the Heterogeneity Indices table that was created by the PHI-R-Script, and the Reference table that was created during validation. Only the first two need to be transferred as the Reference table does not change and is carried along as files are cloned.
21. Included with the Supplementary Materials is a Spotfire file that contains the figures from this paper as visualizations that can be incorporated into your data analysis.

Acknowledgments

This work was funded by a Pennsylvania Department of Health CURE research Grant (SAP# 4100054875) and used the University of Pittsburgh Cancer Institute (UPCI) Chemical Biology Facility that is supported in part by award P30CA047904, the NIH-National Cancer Institute, Cancer Center Support Grant, to the UPCI. The data analyzed in this project was generated under the NExT-CBC agreement number 29XS131-TO6 funded by the National Cancer Institute to D.L. Taylor. The funders had no role in study design, data collection and analysis, decision to publish, or preparation of the manuscript.

References

1. Tawfik DS (2010) Messy biology and the origins of evolutionary innovations. Nat Chem Biol 6(10):692–696. https://doi.org/10.1038/nchembio.441
2. Gough A, Stern AM, Maier J, Lezon T, Shun T-Y, Chennubhotla C, Schurdak ME, Haney SA, Taylor DL (2017) Biologically relevant heterogeneity: metrics and practical insights. SLAS Discov 22(3):213–237. https://doi.org/10.1177/2472555216682725
3. Huang S (2009) Non-genetic heterogeneity of cells in development: more than just noise. Development 136(23):3853–3862. https://doi.org/10.1242/dev.035139
4. Snijder B, Pelkmans L (2011) Origins of regulated cell-to-cell variability. Nat Rev Mol Cell Biol 12(2):119–125. https://doi.org/10.1038/nrm3044
5. Altschuler SJ, Wu LF (2010) Cellular heterogeneity: when do differences make a difference? Cell 141(4):559–563
6. Singh DK, Ku CJ, Wichaidit C, Steininger RJ 3rd, Wu LF, Altschuler SJ (2010) Patterns of basal signaling heterogeneity can distinguish cellular populations with different drug sensitivities. Mol Syst Biol 6:369
7. Gough AH, Chen N, Shun TY, Lezon TR, Boltz RC, Reese CE, Wagner J, Vernetti LA, Grandis JR, Lee AV, Stern AM, Schurdak ME, Taylor DL (2014) Identifying and quantifying heterogeneity in high content analysis: application of heterogeneity indices to drug discovery. PLoS One 9(7):e102678. https://doi.org/10.1371/journal.pone.0102678
8. Gascoigne KE, Taylor SS (2008) Cancer cells display profound intra- and interline variation following prolonged exposure to antimitotic drugs. Cancer Cell 14(2):111–122. https://doi.org/10.1016/j.ccr.2008.07.002
9. Janiszewska M, Liu L, Almendro V, Kuang Y, Paweletz C, Sakr RA, Weigelt B, Hanker AB, Chandarlapaty S, King TA, Reis-Filho JS, Arteaga CL, Park SY, Michor F, Polyak K (2015) In situ single-cell analysis identifies heterogeneity for PIK3CA mutation and HER2 amplification in HER2-positive breast cancer. Nat Genet 47(10):1212–1219. https://doi.org/10.1038/ng.3391
10. Niepel M, Spencer SL, Sorger PK (2009) Non-genetic cell-to-cell variability and the consequences for pharmacology. Curr Opin Chem Biol 13(5–6):556–561. https://doi.org/10.1016/j.cbpa.2009.09.015
11. Zhao B, Pritchard JR, Lauffenburger DA, Hemann MT (2014) Addressing genetic tumor heterogeneity through computationally predictive combination therapy. Cancer Discov 4(2):166–174. https://doi.org/10.1158/2159-8290.CD-13-0465
12. Pritchard JR, Bruno PM, Gilbert LA, Capron KL, Lauffenburger DA, Hemann MT (2013) Defining principles of combination drug mechanisms of action. Proc Natl Acad Sci USA 110(2):E170–E179. https://doi.org/10.1073/pnas.1210419110
13. Zhang J-H, Chung TDY, Oldenburg KR (1999) A simple statistical parameter for use in evaluation and validation of high throughput screening assays. J Biomol Screen 4(2):67–73. https://doi.org/10.1177/108705719900400206
14. Steininger RJ, Rajaram S, Girard L, Minna JD, Wu LF, Altschuler SJ (2015) On comparing heterogeneity across biomarkers. Cytometry A 87(6):558–567. https://doi.org/10.1002/cyto.a.22599.
15. Ruiz C, Li J, Luttgen MS, Kolatkar A, Kendall JT, Flores E, Topp Z, Samlowski WE, McClay E, Bethel K, Ferrone S, Hicks J, Kuhn P (2015) Limited genomic heterogeneity of circulating melanoma cells in advanced stage patients. Phys Biol 12(1):016008. https://doi.org/10.1088/1478-3975/12/1/016008
16. Balluff B, Frese CK, Maier SK, Schone C, Kuster B, Schmitt M, Aubele M, Hofler H, Deelder AM, Heck A Jr, Hogendoorn PC, Morreau J, Maarten Altelaar AF, Walch A, McDonnell LA (2015) De novo discovery of phenotypic intratumour heterogeneity using imaging mass spectrometry. J Pathol 235(1):3–13. https://doi.org/10.1002/path.4436
17. Schwarz RF, Trinh A, Sipos B, Brenton JD, Goldman N, Markowetz F (2014) Phylogenetic quantification of intra-tumour heterogeneity. PLoS Comput Biol 10(4):e1003535. https://doi.org/10.1371/journal.pcbi.1003535
18. Haney SA (2014) Rapid assessment and visualization of normality in high-content and other cell-level data and its impact on the interpretation of experimental results. J Biomol Screen. https://doi.org/10.1177/1087057114526432
19. Loo LH, Lin HJ, Steininger RJ 3rd, Wang Y, Wu LF, Altschuler SJ (2009) An approach for extensibly profiling the molecular states of cellular subpopulations. Nat Methods 6(10):759–765

20. Gingold JA, Coakley ES, Su J, Lee DF, Lau Z, Zhou H, Felsenfeld DP, Schaniel C, Lemischka IR (2015) Distribution Analyzer, a methodology for identifying and clustering outlier conditions from single-cell distributions, and its application to a Nanog reporter RNAi screen. BMC Bioinformatics 16:225. https://doi.org/10.1186/s12859-015-0636-7
21. Bhang HE, Ruddy DA, Krishnamurthy Radhakrishna V, Caushi JX, Zhao R, Hims MM, Singh AP, Kao I, Rakiec D, Shaw P, Balak M, Raza A, Ackley E, Keen N, Schlabach MR, Palmer M, Leary RJ, Chiang DY, Sellers WR, Michor F, Cooke VG, Korn JM, Stegmeier F (2015) Studying clonal dynamics in response to cancer therapy using high-complexity barcoding. Nat Med 21(5):440–448. https://doi.org/10.1038/nm.3841
22. Gough A, Shun TY, Lansing Taylor D, Schurdak M (2016) A metric and workflow for quality control in the analysis of heterogeneity in phenotypic profiles and screens. Methods 96:12–26. https://doi.org/10.1016/j.ymeth.2015.10.007
23. Young IT (1977) Proof without prejudice: use of the Kolmogorov-Smirnov test for the analysis of histograms from flow systems and other sources. J Histochem Cytochem 25(7):935–941
24. Polyak K (2014) Tumor heterogeneity confounds and illuminates: a case for Darwinian tumor evolution. Nat Med 20(4):344–346. https://doi.org/10.1038/nm.3518
25. Kleppe M, Levine RL (2014) Tumor heterogeneity confounds and illuminates: assessing the implications. Nat Med 20(4):342–344. https://doi.org/10.1038/nm.3522

Chapter 3

Image-Based Tracking of Heterogeneous Single-Cell Phenotypes

Katherin Patsch, Shannon M. Mumenthaler, and Daniel Ruderman

Abstract

Cells display broad heterogeneity across multiple phenotypic features, including motility, morphology, and cell signaling. Live-cell imaging techniques are beginning to capture the importance and interdependence of these phenomena. However, existing image analysis pipelines often fail to capture the intricate changes that occur in small subpopulations, either due to poor segmentation protocols or cell tracking errors. Here we report a pipeline designed to image and track single-cell dynamic phenotypes in heterogeneous cell populations. We provide step-by-step instructions for three phenotypically different cell lines across two time scales as well as recommendations for adaptation to custom data sets. Our protocols include steps for quality control that can be used to filter out erroneous tracks and improve assessment of heterogeneity. We demonstrate possible phenotypic readouts including motility, nuclear receptor translocation, and mitosis.

Key words Live-cell imaging, Tracking, Heterogeneity, Phenotypes, Motility, Receptor translocation, Mitosis

1 Introduction

Time-lapse microscopy has revealed extensive heterogeneity in the dynamic behavior of living cells [1–4]. Variations in gene expression [5, 6], motility [7, 8], morphology [9–12], and responsiveness to drug treatment [13] are well documented and have been shown to correlate with the dynamics of critical signaling molecules. To deepen our understanding of the spatiotemporal dynamics of cell behavior, an array of both proprietary and open-source computational tools has been developed to track cells while collecting phenotypic information [14–25]. However, generating image analysis pipelines that are broadly available and easily adaptable to phenotypically diverse cell types has proven to be challenging.

Another persisting problem in time-lapse microscopy is the difficulty in determining whether outliers are technical artifacts (e.g., errors due to poor segmentation or tracking) or instead

Natasha S. Barteneva and Ivan A. Vorobjev (eds.), *Cellular Heterogeneity: Methods and Protocols*, Methods in Molecular Biology, vol. 1745, https://doi.org/10.1007/978-1-4939-7680-5_3,

credible observations of a heterogeneous population. This problem has recently been addressed in a couple of ways: (1) by data filtering [4, 26] and (2) by correcting errors [25] based on a selected phenotypic readout.

To capture the complex changes occurring in single cells over time, there remains a need for a set of robust guidelines to rapidly fine-tune tracking tools to individual data sets. In this chapter, we provide detailed protocols to prepare, image, track, and analyze the dynamic phenotypes of individual cells. For image analysis, we used the open-source image analysis software CellProfiler. Our pipeline incorporates the quality control metric *Tracking Aberration Measure* (TrAM) to identify tracks with unrealistic jumps in multiple phenotypic features [4]. Our protocol can be adapted to a broad range of data sets. Here we demonstrate the flexibility of our pipeline by tracking three different cell lines across two time scales.

2 Materials

2.1 Cell Preparation

1. Tissue culture medium: RPMI 1640 (supplemented with L-glutamine, 10% fetal bovine serum, 1% penicillin/streptomycin) (*see* **Note 1**).
2. Imaging medium 1 (for motility and mitosis experiments): phenol red-free RPMI 1640 (supplemented with L-glutamine, 10% fetal bovine serum, and 1% penicillin/streptomycin) (*see* **Note 2**).
3. Imaging medium 2 (for AR translocation experiments): phenol red-free RPMI 1640 (supplemented with L-glutamine, 10% charcoal/dextran stripped fetal bovine serum, and 1% penicillin/streptomycin).
4. 1× Phosphate buffered saline (PBS).
5. Trypsin 0.05%.
6. 96-Well tissue culture-treated microplates with black walls and clear bottom (*see* **Note 3**).
7. Automated cell counter (*see* **Note 4**).
8. Nuclear markers: nuclear dyes for short-term time-lapse experiments and nuclear localization constructs for long-term time-lapse experiments (*see* **Note 5**).
9. *If applicable:* transfection reagent for transient expression of fluorescent proteins of interest (*see* **Note 6**).
10. *If applicable:* reagent for positive selection of cells stably expressing fluorescent proteins (*see* **Note 7**).
11. Androgen receptor ligand methyltrienolone (R1881) (*see* **Note 8**).

2.2 Image Acquisition

1. Imaging system with automated stage and multi-well mounting frame, environmental control, and ability to perform time-lapse imaging sequences (*see* **Note 9**).
2. Acquisition filters to collect fluorescent signals: DRAQ5 (620–640 nm excitation, 650–760 nm emission), dsRed (520–550 nm excitation, 560–630 nm emission), EGFP (460–490 nm excitation, 500–550 nm emission), and BF (transmission, 650–760 nm emission) (*see* **Note 10**).

2.3 Cell Tracking

1. Image analysis software with cell segmentation and tracking capabilities. Available readouts should include cell positions (XY), morphology features (nuclear area, nuclear roundness), and fluorescence intensity. Specific readouts required to apply data filtering steps and analyze dynamics are listed in the respective assay and in Table 1. To exemplify our workflow using an open-source application, we used CellProfiler (*see* **Note 11**).
2. TrAM functionality for CellProfiler: https://github.com/RudermanLab/TrAM_CellProfiler (*see* **Note 11**).
3. Open-source image processing program ImageJ to compile movies (avi files) using images exported from CellProfiler (tiff files).

3 Methods

3.1 Preparation of Cells

1. Prepare tissue culture and imaging media as described in the materials section. Preheat all reagents in a 37 °C water bath.
2. Culture cells in a 10 cm dish, and maintain at 37 °C in a humidified incubator with 5% carbon dioxide. Passage at least twice before performing experiments.
3. To seed cells, aspirate tissue culture media and wash monolayer twice with 5 ml 1× PBS.
4. Aspirate PBS, add 3 ml trypsin, and incubate for 5 min at 37 °C or until cells have detached from the plate.
5. Add 7 ml imaging medium and transfer cell suspension to 15 ml canonical tube.
6. Centrifuge cells at 200 × *g* for 5 min at room temperature.
7. Aspirate supernatant and resuspend cell pellet in 2 ml imaging medium 1 or 2.
8. Count cells: mix 10 μl cell solution with 10 μl trypan blue, pipet mixture onto both sides of cell counting slide, and count cells.

Table 1
Summary of time-lapse assays to measure cellular dynamics

Steps of the workflow	Variable	Short-term dynamics: motility and protein translocation			Long-term dynamics: mitosis
1. Cell preparation	Cell line	HeLa	PC3	Panc-1	HeLa
	Cell number/well	5000	10,000	12,000	3000
	Nuclear marker	DNA stain DRAQ5			nuclear protein Nucleus-RFP
	Other proteins of interest	GFP-tagged nuclear receptor AR			
2. Image acquisition	Channels	DRAQ5 (620–640 nm excitation, 650–760 nm emission), EGFP (460–490 nm excitation, 500–550 nm emission), BF (transmission, 650–760 nm emission)			dsRed (520–550 nm excitation, 560–630 nm emission), BF (transmission, 650–760 nm emission)
	# Conditions (wells), # technical replicates (fields)	2, 4			2, 35
	Imaging increment, total time, number of time points	1 min, 24 min, 25			30 min, 20 h, 41
3. Cell tracking	Border objects	discard			discard
	Threshold	1.0	1.1	1.0	1.0
	Nuclear diameter (px)	23–44	17–53	16–36	13–63
	Nuclear area (px)	400–3000	300–3000	200–3000	300–3000
	Incomplete tracks	Minimum lifetime filter 24			Minimum lifetime filter 40
4. Dynamic phenotype	TrAM filtering criteria	Motility: Nuclear area, nuclear roundness Nuclear translocation: XY positions			Mitosis: XY positions, nuclear roundness
	Population stratification	Responders vs. non-responders: Total Math_NtoCRatio increase >0.147			Mitotic cells: Step nuclear area increase (30 min) > 18.2%

9. Plate 3000–12,000 cells in 100 µl/well. For short-term time-lapse experiments, plate cells at 70% confluency. For long-term time-lapse experiments, where cell proliferation is expected, plate cells at 40% confluency to avoid overgrowth (*see* **Note 12**).

10. *If applicable:* if needed for protein translocation assay or long-term nuclear tracking in mitosis assay, perform transient transfection of fluorescently labeled proteins following manufacturer's recommendations (*see* **Note 13**).
11. Incubate cells for 24 h at 37 °C.
12. *If applicable:* if nuclear dyes are used, replace overnight medium with 100 µl imaging medium 1 or 2, supplemented with nuclear dye at desired end concentration (*see* **Note 14**).
13. Transfer plate to microscope and begin time-lapse after 30 min incubation in the live-cell chamber (*see* **Note 15**).

3.2 Image Acquisition

Here it is key to balance temporal resolution (imaging increment) with total imaging time to avoid phototoxic imaging conditions. Below, we provide two protocols to exemplify different adjustments based on applications and needs.

1. Choose image acquisition filter combinations to detect nuclear stain and proteins of interest (e.g., fluorescently nuclear receptors) and collect bright-field images (*see* Table 1).
2. Select wells (conditions) and imaging fields (technical replicates) to be imaged (*see* **Note 16**).
3. Select imaging increment and number of time points to achieve desired total imaging time. Details for two assays are listed below and can be found in Table 1.
4. *Applicable to short-term time-lapse imaging to measure cell motility and nuclear translocation:* generate sequence to image every minute for 24 min, resulting in 25 time points (*see* **Note 17**).
5. *Applicable to long-term time-lapse imaging to track cell division:* generate sequence to image cells every 30 min for 20 h, resulting in 41 time points.
6. Start time-lapse experiment.

3.3 Cell Tracking

The following section provides step-by-step instructions to build a CellProfiler pipeline to track cells. We list specific parameters for three different cell lines across two time scales and provide guidelines to customize the pipeline as needed. Detailed information on each step and alternative settings can be found by clicking on the respective question marks in CellProfiler.

3.3.1 Data Import

1. Download and install the open-source software CellProfiler [20]. Accept default options and add-ons.
2. Download and install TrAM for CellProfiler at https://github.com/RudermanLab/TrAM_CellProfiler.
3. Import data into CellProfiler using the four default import modules (Images, Metadata, NamesAndTypes, and Groups).

The included CellProfiler pipelines contain a regular expression in the Metadata module that parses out information from the image file names (row, column, field, channel, time point). These metadata are used to group the images by well and organize into time series (*see* **Note 18**).

4. To analyze images from different imaging channels, assign names to each channel. This can be done under NamesAndTypes. We assigned images acquired in channel 2 Nuclear_Marker and images acquired in channel 4 Nuclear_Receptor. Adjust these names accordingly.
5. For batch analysis of multiple image sequences, group images by the desired metadata item, e.g., well or field. Verify under grouping list that the resulting image count represents the total number of imaging time points.

3.3.2 Identify Cells

Detect and segment nuclei using images of nuclear fluorescence marker by selecting the corresponding channel.

1. Select IdentifyPrimaryObjects module.
2. Select Nuclear_Marker (name that identifies images acquired in nuclear marker channel from NamesAndTypes), and name the primary objects to be identified: Nuclei.
3. Set min/max to define object diameter range in pixel units: to include cells of all sizes, start with broad range of 10–60 pixels (8–30 μm) and adjust once you reach point 13 of the protocol (*see* **Note 19**).
4. Discard objects outside the diameter range and discard objects touching the border of the image.
5. Apply adaptive two-class thresholding strategy using the Otsu method [27], and keep the threshold smoothing scale at the default value 1.3488.
6. Set threshold correction factor to 1.0 with lower and upper bounds set to 0.0 to 1.0.
7. Size adaptive window to 50.
8. Use Shape to distinguish clumped objects and draw dividing lines between clumped objects.
9. Automatically calculate size of smoothing filter for declumping and minimum allowed distance between local maxima.
10. Speed up by using lower-resolution image to find local maxima.
11. Fill holes in identified objects after both thresholding and declumping.
12. Handling of objects if excessive number of objects is identified: Continue.

13. Select MeasureObjectSizeShape module to measure features of the Nuclei.
14. Within the FilterObjects module, select to filter Nuclei and name the output objects FilteredNuclei. Filter Measurements by setting limits to AreaShape, using the measurement Area. Set a min/max for nuclear area to 300–3000 pixels to exclude objects that are too small (debris) and too large (e.g., clusters not well segmented) (*see* **Note 19**).

3.3.3 Fine-Tune Nuclear Segmentation

We recommend incorporating the following steps to fine-tune nuclear segmentation to custom data sets.

1. *Fine-tune threshold:* start Test Mode and click Step. Inspect output image NucleiOutlines to verify preliminary cell segmentation. The threshold correction factor can be empirically determined based on the identified objects, e.g., if objects are missed, reduce the threshold correction factor. If areas of the background are erroneously identified as objects, increase this number (Fig. 1a). Test thresholds on images from various time points (click Next Image Set and Step within Test Mode), to account for any photobleaching.
2. *Fine-tune nuclear area:* within the Test Mode, inspect output image NucleiOutlines to verify preliminary cell segmentation. Click Step twice to obtain image of FilteredNuclei. If needed, go back to FilterObjects module, and fine-tune nuclear area thresholds (Fig. 1b).
3. *Fine-tune nuclear diameter:* within Test Mode, click Step to obtain output table from the next module MeasureObjectSizeShape of FilteredNuclei. Calculate adjusted values: median MinFeretDiameter—STD rounded down and median MaxFeretDiameter + STD rounded up. Repeat for two to three time points throughout the time course and use the broadest obtained range to adjust nuclear diameter range. For long time-lapse experiments, broaden the adjusted range further by a factor of 1.5 to ensure tracking of nuclei during all stages of mitosis: multiply the maximum calculated value, and divide minimum calculated value by 1.5. Finally, inspect new output image NucleiOutlines, and compare with the previous version to verify optimized segmentation (Fig. 1c). Exit Test Mode and return to protocol overview. For short time-lapse experiments, we used values 23–44 for HeLa cells, 17–53 for PC3 cells, and 16–36 for small Panc-1 cells. To track mitotic events in long time-lapse experiments, we used 13–63 for HeLa cells (*see* **Note 19**).

3.3.4 Track Cells

The following steps connect sequential cell measurements to track cells over time.

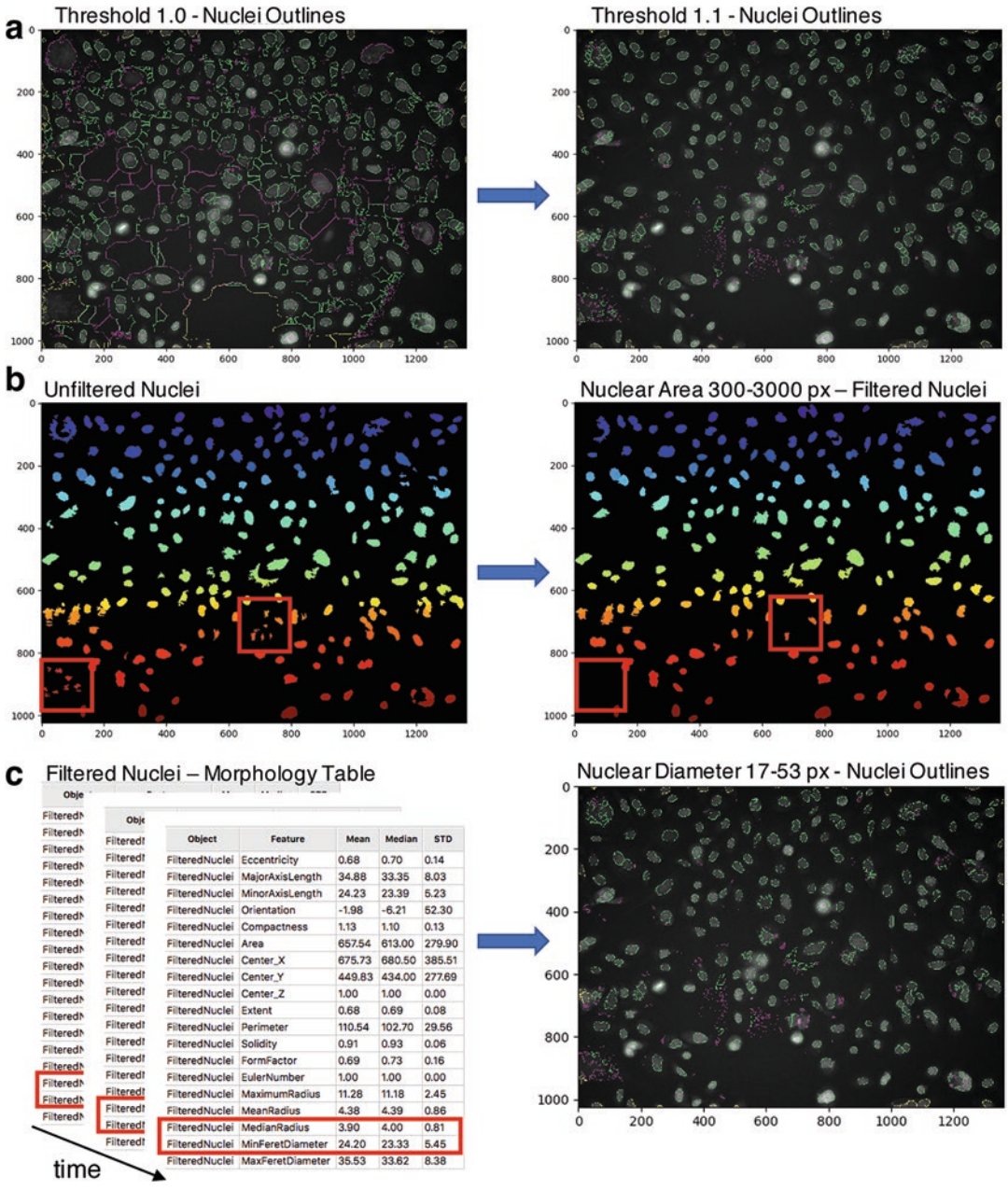

Object	Feature	Mean	Median	STD
FilteredNuclei	Eccentricity	0.68	0.70	0.14
FilteredNuclei	MajorAxisLength	34.88	33.35	8.03
FilteredNuclei	MinorAxisLength	24.23	23.39	5.23
FilteredNuclei	Orientation	-1.98	-6.21	52.30
FilteredNuclei	Compactness	1.13	1.10	0.13
FilteredNuclei	Area	657.54	613.00	279.90
FilteredNuclei	Center_X	675.73	680.50	385.51
FilteredNuclei	Center_Y	449.83	434.00	277.69
FilteredNuclei	Center_Z	1.00	1.00	0.00
FilteredNuclei	Extent	0.68	0.69	0.08
FilteredNuclei	Perimeter	110.54	102.70	29.56
FilteredNuclei	Solidity	0.91	0.93	0.06
FilteredNuclei	FormFactor	0.69	0.73	0.16
FilteredNuclei	EulerNumber	1.00	1.00	0.00
FilteredNuclei	MaximumRadius	11.28	11.18	2.45
FilteredNuclei	MeanRadius	4.38	4.39	0.86
FilteredNuclei	MedianRadius	3.90	4.00	0.81
FilteredNuclei	MinFeretDiameter	24.20	23.33	5.45
FilteredNuclei	MaxFeretDiameter	35.53	33.62	8.38

Fig. 1 Step-by-step fine-tuning of nuclear segmentation. Example Test Mode images of PC3 cells to adjust (**a**) threshold, (**b**) nuclear area, and (**c**) nuclear diameter to custom data sets. (**a**) Outlines in yellow represent border objects; outlines in magenta represent objects outside of nuclear diameter range. Green outlines are retained nuclei. (**b**) Boxes demonstrate objects rejected due to below threshold nuclear area. (**c**) Morphology table contains feature values to adjust nuclear diameter. Outlines in magenta represent objects outside of diameter range. Green outlines are retained nuclei

1. Select TrackObjects module and choose the Overlap tracking method.
2. Select the objects to track: FilteredNuclei.
3. Set maximum pixel distance to consider matches to 10 (*see* **Note 20**).
4. Filter incomplete tracks, i.e., cells without tracking data at every time point. Within the TrackObjects module, filter objects by lifetime and set the minimum lifetime filter to the total number of acquired time points − 1: set to 24 for short and 40 for long time-lapse experiments.
5. Select display option: Color and Number and save color-coded image.
6. Name the output image: TrackedCells.

3.3.5 Additional Modules to Measure Nuclear Translocation of Receptor Proteins

First, complete the steps listed above to obtain tracked cells, and then, before running the pipeline, include the additional steps listed below.

1. Select IdentifySecondaryObjects module.
2. Select input image Nuclear_Marker and input objects FilteredNuclei. Name the primary objects to be identified: Cells.
3. Select the Distance N method to expand primary objects by 10 pixels and generate cell masks that extend beyond the nuclear membrane.
4. Select IdentifyTertiaryObjects module. Select Cells as larger identified objects and FilteredNuclei as smaller identified objects.
5. Name the tertiary objects PerinuclearCytoplasm.
6. Shrink smaller object prior to subtraction.
7. Retain outlines of the tertiary objects.
8. Name the outline image PerinulcearCytoplasmOutlines (*see* **Note 21**).
9. Select MeasureObjectIntensity module to use Nuclear_Receptor images to measure objects FilteredNuclei and PerinuclearCytoplasm.
10. Measure nuclear to cytoplasmic fluorescence intensity ratio: within the CalculateMath module, select the Divide operation and name the output measurement NtoCRatio.
11. To define the numerator measurement, select Object, FilteredNuclei, category Intensity, measurement MeanIntensity, and image Nuclear_Receptor.

12. To define the denominator measurement, select Object, PerinuclearCytoplasm, category Intensity, measurement MeanIntensity, and image Nuclear_Receptor.

3.3.6 Additional Steps to Measure Track Quality

This section consists of steps to compute the Tracking Aberration Measure (TrAM) for each cell to determine the credibility of its tracking. A detailed description of the TrAM method, benchmarking, and validation including examples of the effect on single-cell and population-based data can be found in our paper [4].

1. Select the MeasureTrackQuality module (Fig. 2).
2. Select the tracked FilteredNuclei. Press button to select measurements and compute TrAM, as listed in Table 1: for motility, use nuclear area (Area) and roundness (FormFactor); to measure receptor translocation, use X and Y coordinates (Center X, Y); and for long-term tracking across multiple generations, use X and Y coordinates (Center X, Y) and nuclear roundness (FormFactor) (*see* **Note 22**).
3. Select number of spline knots: 5 for 25 time point and 8 for 41 time point experiments.
4. TrAM values are computed and reported as MeasureTrackQuality_TrAM in the data spreadsheets that are exported for downstream processing (*see* steps below).

3.3.7 Export Data, Images, and Movies

The following steps are incorporated in the pipeline to specify movies that are useful for data quality control, pipeline verification and to export data for downstream analysis.

1. Export data: within the ExportToSpreadsheet module, select the comma delimiter to separate columns and select output file location and a prefix to generated file names. Export all measurement types.
2. Generate overlay images: select RescaleIntensity module and apply to Nuclear_Marker images. Choose specific values to be reset to the full intensity range using min/max for each image and save out ScaledNuclei. Select OverlayOutlines module and name the output image NucOverlay. Overlay ScaledNuclei images with segmentation outlines of FilteredNuclei or, if present, PerinuclearCytoplasm.
3. Export cell segmentation images and compile movie: select SaveImages module to export images of NucOverlay. Use sequential numbers and the prefix TrackedSegmentation to save tiff image at every cycle. Compile movie from tiff files, e.g., in ImageJ.
4. Export tracking images and compile movie: select SaveImages module to export images of TrackedCells. Use sequential numbers and the prefix TrackedCells to save tiff file at every cycle. Compile movie from tiff files, e.g., in ImageJ.

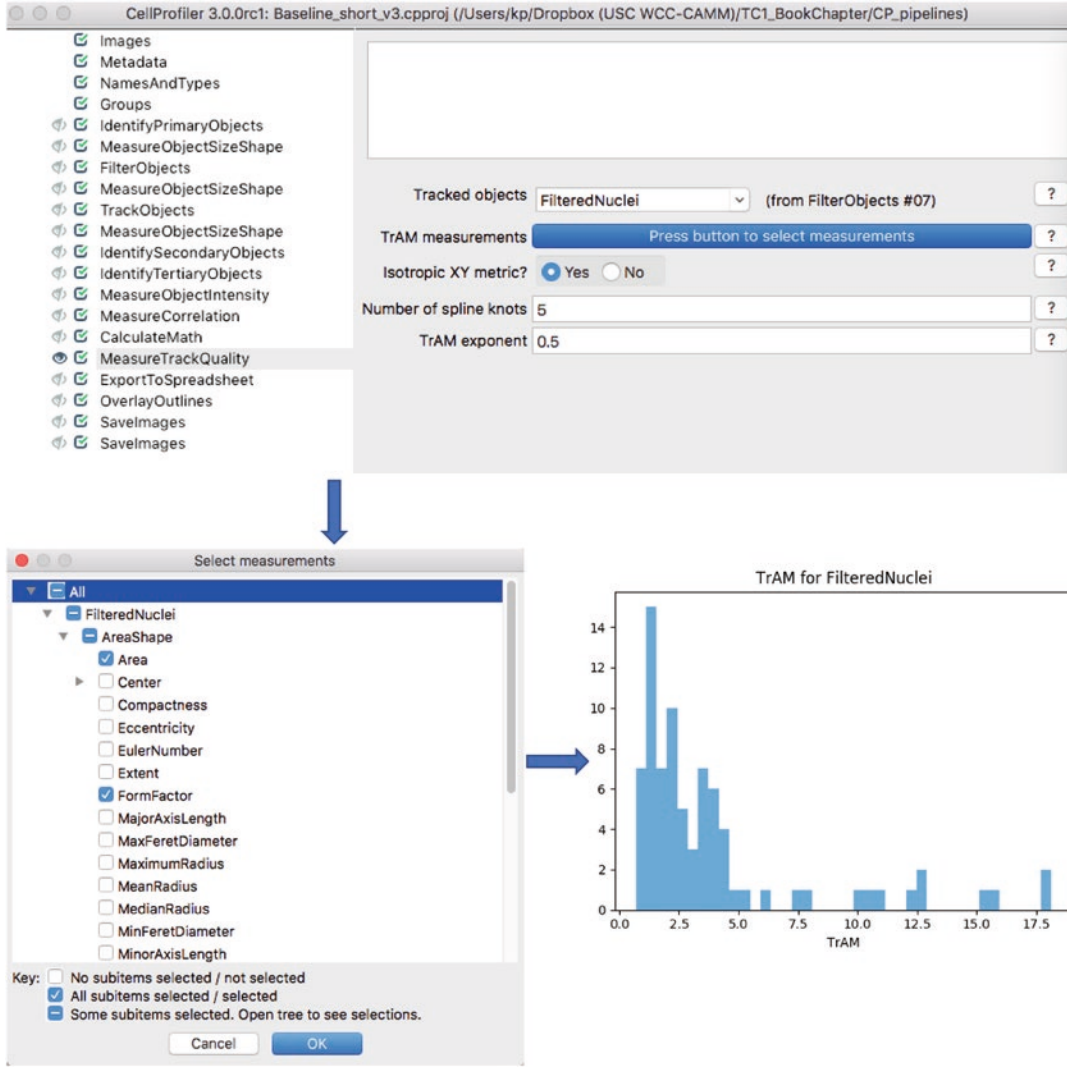

Fig. 2 Computation of the track quality metric TrAM. Top: snapshot of TrackQC module and associated settings. Middle: press button to select measurements opens a new window with check boxes to select features for computation of TrAM. Bottom: TrAM histogram visualizes distribution across filtered nuclei. Low TrAM values represent higher-quality tracks

5. Once the protocol is set up, data sets are ready to be analyzed. To reduce run time, keep the eye in the MeasureTrackQuality modules open while closing all others and click Analyze Images (*see* **Note 23**).

3.4 Analysis of Dynamic Phenotypes

The following section describes steps downstream of CellProfiler to validate the data and analyze various phenotypic readouts.

1. Verify data quality by evaluating generated output movies of tracking and segmentation.

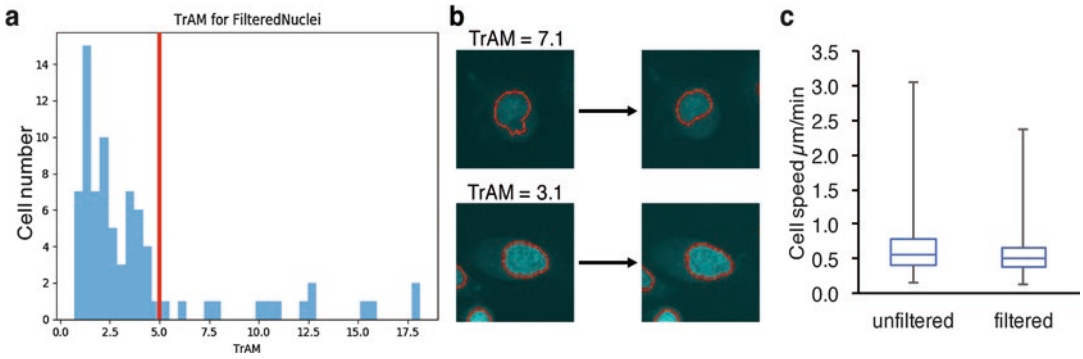

Fig. 3 Overview of TrAM filtering to measure heterogeneity. (**a**) TrAM histogram to determine cutoff (red line). (**b**) Verification of TrAM cutoff. Cell not rejected due to low TrAM value (TrAM = 3.1) vs. cell filtered out due to high TrAM value (TrAM = 7.1). Nuclear segmentation images are shown after 3 min and 6 min imaging. (**c**) Speed distribution of PC3 cells before and after TrAM filtering

2. Evaluate tracking using TrAM histogram: for high-quality data, expect most cells to have low TrAM values (<5) and a steep slope. Broader peaks including higher TrAM values indicate lower tracking quality (Fig. 2).
3. *Optional filtering step based on TrAM* (*see* **Note 24**). To filter out tracks with a high probability of poor segmentation, set a TrAM threshold (x-axis) where the cell number (y-axis) slope flattens out (Fig. 3). In our experience, poor segmentation tracks always had TrAM values above 5 and therefore can be used as a low-stringency cutoff (*see* **Note 25**).
4. *Optional step to verify TrAM cutoff:* the spreadsheet FilteredNuclei contains a TrackObjects_Label and a MeasureTrackQuality_TrAM value for each cell. Compare tracking and segmentation movies to verify that errors have TrAM values above the chosen threshold, and good tracks are retained in the data set (Fig. 3).
5. Analysis of motility (μm/min) (*see* **Note 26**) (Fig. 3):

$$\frac{\text{Total TrackObjects\_IntegratedDistance\_10}\,(\text{px})}{\text{Total imaging time}\,(24\ \text{min})} \times \text{Pixel size}\,(0.5\ \mu\text{m})$$

6. Analysis of dynamic nuclear translocation: plot Math_NtoCRatio across time to see changes in subcellular distribution. *Optional step to stratify responders* vs. *non-responders in nuclear translocation assay:* set threshold to total Math_NtoCRatio >0.147 (Fig. 3) (*see* **Note 27**).
7. Analysis of mitosis: MeasureTrackQuality_Is_Parent: marks cells that divide (1) vs. cells that don't divide (0) during the time-lapse experiment. MeasureTrackQuality_Labels: TrAM value that is assigned to a trajectory. Parent cells can have multiple values, determined by the respective track of their

daughter cells. MeasureTrackQuality_Split_Trajectory: marks daughter cells (1) that are born during the time-lapse experiment. Calculate hourly proliferation rate:

$$\frac{\text{MeasureTrackQuality\_Split\_Trajectory}}{25} \times 60$$

Optional step to stratify mitotic vs. *non-mitotic cells:* set threshold to step nuclear area increase (30 min) >18.2%.

4 Notes

1. Media and supplements can be replaced as needed to culture other cell types.
2. Media and supplements can be replaced as needed to image other cell types. To increase signal-to-noise ratios, we suggest using phenol red-free medium with reduced levels of riboflavin (0.05 mg/l vs. 0.2 mg/l).
3. Other multi-well formats, e.g., 384-well plates, can be used to save on reagents, although the smaller wells are more difficult if system perturbations are conducted manually, i.e., without a liquid handler. To increase the signal-to-noise ratio, we chose specialized imaging plates with a thin plastic bottom. Other plates can be used as well, including glass-bottom multi-well plates, if they are tissue culture treated and black.
4. Other methods of cell counting, i.e., hemocytometer, may be used.
5. We used 2.5 μM DRAQ5 nuclear dye for short-term time-lapse experiments. Other nuclear stains can be used, e.g., siR-DNA or Hoechst. Be aware of possible drug interactions when using Hoechst. We used Nucleus-RFP nuclear localization constructs for long-term time-lapse experiments; other constructs can be used as well, e.g., H2B-RFP. The advantage of nuclear constructs is the avoidance of cytotoxic effects caused by nuclear dyes. However, transfection rates and levels of expression can vary widely, making cell detection and segmentation less efficient.
6. Transfection reagent and optimal conditions for your cell line should be determined empirically. We used Promega FuGENE to express GFP-tagged androgen receptors (AR) in all three cell lines. Similarly, we used 80 PPC (particles per cell) of Nucleus-RFP Bac-Mem to track nuclei over several hours.
7. We used 200 ng/ml G418 sulfate solution to select for cells stably expressing GFP-AR construct containing the neomycin resistance gene. Care should be taken that the appropriate reagent is chosen for the respective construct.

8. If working with R1881 or any other ligands or drugs, it is important to be aware of potential light sensitivity. R1881 is rapidly destroyed upon exposure to UV light. In these cases, we suggest either avoiding dyes/proteins that emit light in the blue spectrum or using compounds that are light stable, e.g., Cl-4AS-1.
9. For all our assays, we used the PerkinElmer Operetta high-content imaging system.
10. Not all channels are needed for each assay; necessary are filter combinations that image nuclear stain and, if applicable to the assay, protein of interest. We suggest acquiring bright-field images in parallel, as they can provide useful information for quality control, e.g., detection of cell debris and assessment of cell health.
11. Previously, we used proprietary software applications Harmony 3.5.2 (PerkinElmer) and Imaris version 8.3.1 (Bitplane). Protocols for these applications including access to TrAM outside of CellProfiler (Github, https://github.com/RudermanLab/tram) can be found in our previously published paper [4].
12. Exact cell numbers to be plated to achieve the desired confluency depends on cell area in monolayer. For short experiments, we plated 10,000 PC3 cells, 5000 HeLa cells (cells are larger and flatter), and 12,000 Panc-1 cells (smaller cells). For long experiments, we plated 3000 HeLa cells to avoid confluency. Confluency makes tracking very difficult and alters proliferation and migration properties. Ideally, cells should be within exponential phase of growth throughout the experiment.
13. In both cases, we performed reverse transfections while plating cells for experiments the next day. Alternatively, traditional transfections can be performed 1 day after cell seeding. In this case, one must consider the extra day cells are plated until the experiment is performed when determining optimal cell seeding number.
14. We used 2.5 μM DRAQ5 to stain the nuclei.
15. A 30 min incubation step in the microscope ensures efficient nuclear staining and increased stabilization of environmental settings in the live-cell chamber. Thermal instability can lead to a plate shift and biased results.
16. A number of wells and fields that can be read within desired increment time will vary depending on the assay. Examples are listed in Table 1.
17. Adjustment of total assay time may be necessary to adapt to slower kinetics of other nuclear receptors.

18. We imported images generated by the PerkinElmer Operetta. These files use a naming convention to denote where and when an image was collected from a plate. An example filename might be "r05c09f03p01-ch3sk26fk1fl1.tiff" where the letters r, c, f, p, ch, and sk denote row, column, field, plane, channel, and time point, respectively. Our CellProfiler pipelines use a regular expression to parse these values out of the filename. In this case, a regular expression defines a pattern that is used to extract values into variables. From the example above, the correct parsing would be row = 5, column = 9, field = 3, plane = 1, channel = 3, and time point = 26. Since the metadata extraction relies on naming convention, data collected on different imaging systems will not just "plug and play" with our analysis routines.
19. These values are based on 0.5 μm/px images. Adjust pixel values according to the magnification.
20. When working with 0.5 μm/px images and imaging every min, this protocol assumes cells migrate at a maximum speed of 5 μm/min. If needed, adjust pixel values to image size and imaging increment.
21. Appropriate segmentation of nuclei and surrounding perinuclear cytoplasm can be verified in Test Mode.
22. To compute TrAM, we suggest choosing measurements that are nonessential for the respective assay to minimize bias, e.g., we specifically avoided using Center X, Y for motility or nuclear area for mitosis.
23. Closing the eyes in image analysis modules will prevent pop-ups and reduce run time. The open eye in the MeasureTrackQuality module is necessary to obtain TrAM histogram.
24. TrAM filtering is especially useful if the goal of the assay is to capture the full range of cellular behavior, e.g., to detect small subpopulations of cells within a much larger population. These steps can also affect averages across populations and thus increase overall data accuracy. A full description of the method can be found in our methods paper [4].
25. Here we establish thresholds based on a by-eye estimation of the TrAM distribution curve. Alternatively, one can establish a data-specific ground truth to statistically determine thresholds that maximize balanced accuracy, i.e., sum of sensitivity and specificity. Details and protocols for this approach can be found in our paper [4].
26. Formula assumes 0.5 μm/px images. Adjust pixel values to different image size.
27. The value was determined using ROC approach. *See* publication for details [4].

Acknowledgments

We thank Beth Cimini and Anne Carpenter for their support in building the CellProfiler pipeline. We thank Thomas Do and Dane Lemons for help plating cells and generating cell tracking movies. We thank Naim Matasci, Torin Gerhart, and Colleen Garvey for technical discussions throughout the project. We would like to express our deepest gratitude to our philanthropic supporters: the Stephenson family, Emmet, Toni, and Tessa, for their donation of the Operetta HCS platform.

References

1. Purvis JE, Lahav G (2013) Encoding and decoding cellular information through signaling dynamics. Cell 152:945–956. https://doi.org/10.1016/j.cell.2013.02.005
2. Altschuler SJ, LF W (2010) Cellular heterogeneity: do differences make a difference? Cell 141:559–563. https://doi.org/10.1016/j.cell.2010.04.033
3. Snijder B, Pelkmans L (2011) Origins of regulated cell-to-cell variability. Nat Rev Mol Cell Biol 12:119–125. https://doi.org/10.1038/nrm3044
4. Patsch K, Chiu C-L, Engeln M et al (2016) Single cell dynamic phenotyping. Sci Rep 6:34785. https://doi.org/10.1038/srep34785
5. Aw Yong KM, Zeng Y, Vindivich D et al (2014) Morphological effects on expression of growth differentiation factor 15 (GDF15), a marker of metastasis. J Cell Physiol 229:362–373. https://doi.org/10.1002/jcp.24458
6. Purvis JE, Karhohs KW, Mock C et al (2012) p53 dynamics control cell fate. Science 336:1440–1444. https://doi.org/10.1126/science.1218351
7. Palmieri B, Bresler Y, Wirtz D, Grant M (2015) Multiple scale model for cell migration in monolayers: elastic mismatch between cells enhances motility. Sci Rep 5:11745. https://doi.org/10.1038/srep11745
8. Lee M-H, P-H W, Staunton JR et al (2012) Mismatch in mechanical and adhesive properties induces pulsating cancer cell migration in epithelial monolayer. Biophys J 102:2731–2741. https://doi.org/10.1016/j.bpj.2012.05.005
9. Chen CS, Mrksich M, Huang S et al (1997) Geometric control of cell life and death. Science 276:1425–1428. https://doi.org/10.1126/science.276.5317.1425
10. Rangamani P, Lipshtat A, Azeloglu EU et al (2013) Decoding information in cell shape. Cell 154:1356–1369. https://doi.org/10.1016/j.cell.2013.08.026
11. Bakal C, Aach J, Church G, Perrimon N (2007) Quantitative morphological signatures define local signaling networks regulating cell morphology. Science 316:1753–1756
12. Sero JE, Sailem HZ, Ardy RC et al (2015) Cell shape and the microenvironment regulate nuclear translocation of NF-κB in breast epithelial and tumor cells. Mol Syst Biol 11:790
13. Slack MD, Martinez ED, LF W, Altschuler SJ (2008) Characterizing heterogeneous cellular responses to perturbations. Proc Natl Acad Sci U S A 105:19306–19311. https://doi.org/10.1073/pnas.0807038105
14. Held M, Schmitz MHA, Fischer B et al (2010) CellCognition: time-resolved phenotype annotation in high-throughput live cell imaging. Nat Methods 7:747–754. https://doi.org/10.1038/nmeth.1486
15. Georgescu W, Wikswo JP, Quaranta V (2012) CellAnimation: an open source MATLAB framework for microscopy assays. Bioinformatics 28:138–139. https://doi.org/10.1093/bioinformatics/btr633
16. Huth J, Buchholz M, Kraus JM et al (2011) TimeLapseAnalyzer: multi-target analysis for live-cell imaging and time-lapse microscopy. Comput Methods Prog Biomed 104:227–234. https://doi.org/10.1016/j.cmpb.2011.06.002
17. Huth J, Buchholz M, Kraus JM et al (2010) Significantly improved precision of cell migration analysis in time-lapse video microscopy through use of a fully automated tracking system. BMC Cell Biol 11:24. https://doi.org/10.1186/1471-2121-11-24
18. Zhong Q, Busetto AG, Fededa JP et al (2012) Unsupervised modeling of cell morphology dynamics for time-lapse microscopy.

Nat Methods 9:711–713. https://doi.org/10.1038/nmeth.2046

19. Gonzalez G, Fusco L, Benmansour F, et al. (2013) Automated quantification of morphodynamics for high-throughput live cell time-lapse datasets. In: 2013 IEEE 10th Int. Symp biomed imaging. IEEE, pp 664–667.
20. Carpenter AE, Jones TR, Lamprecht MR et al (2006) CellProfiler: image analysis software for identifying and quantifying cell phenotypes. Genome Biol 7:R100. https://doi.org/10.1186/gb-2006-7-10-r100
21. Tyson DR, Garbett SP, Frick PL, Quaranta V (2012) Fractional proliferation: a method to deconvolve cell population dynamics from single-cell data. Nat Methods 9:923–928. https://doi.org/10.1038/nmeth.2138
22. Dzyubachyk O, van Cappellen WA, Essers J et al (2010) Advanced level-set-based cell tracking in time-lapse fluorescence microscopy. IEEE Trans Med Imaging 29:852–867. https://doi.org/10.1109/TMI.2009.2038693
23. Dzyubachyk O, Essers J, van Cappellen WA et al (2010) Automated analysis of time-lapse fluorescence microscopy images: from live cell images to intracellular foci. Bioinforma 26:2424–2430
24. Harder N, Mora-Bermudez F, Godinez WJ et al (2009) Automatic analysis of dividing cells in live cell movies to detect mitotic delays and correlate phenotypes in time. Genome Res 19:2113–2124. https://doi.org/10.1101/gr.092494.109
25. Sadanandan SK, Baltekin O, Magnusson KEG et al (2016) Segmentation and track-analysis in time-lapse imaging of bacteria. IEEE J Select Topics Signal Process 10:174–184. https://doi.org/10.1109/JSTSP.2015.2491304
26. Masuzzo P, Huyck L, Simiczyjew A et al (2017) An end-to-end software solution for the analysis of high-throughput single-cell migration data. Sci Rep 7:42383. https://doi.org/10.1038/srep42383
27. Sezgin M, Sankur B (2004) Survey over image thresholding techniques and quantitative performance evaluation. J Electron Imaging 13:146–168

Part II

Cytometry in Cellular Heterogeneity Research

Chapter 4

Broad Immune Monitoring and Profiling of T Cell Subsets with Mass Cytometry

Tess Melinda Brodie and Vinko Tosevski

Abstract

Mass cytometry (*cy*tometry by *t*ime-*o*f-*f*light, CyTOF) is a high-dimensional single-cell analytical technology that allows for highly multiplexed measurements of protein or nucleic acid abundances by bringing together the detection capacity of atomic mass spectroscopy and the sample preparation workflow typical of regular flow cytometry. In 2014 the mass cytometer was adapted for the acquisition of samples from microscopy slides (termed imaging mass cytometry), greatly increasing the applicability of this technology with the inclusion of spatial information. By using antibodies (or other probes) labeled with purified metal isotopes, mass cytometers are currently able to detect more than 50 different parameters at a single-cell level, exceeding the dimensionality of any other flow cytometry methodology currently on the market. This capability licenses unprecedented possibilities in many areas dealing with complex cellular mixtures (immunology, cell biology, and beyond), improving biomarker discovery and moving us closer to affordable personalized medicine than before.

Key words Mass cytometry, CyTOF, Helios, High-dimensional single-cell analysis, T cells, Immunophenotyping

1 Introduction

Mass cytometry represents a thorough rethinking of the usual concept of flow cytometry, replacing the fluorescence measurement with measuring the abundance of probes labeled with purified metal isotopes (mostly lanthanides, but also a selection of other elements can be used; *see* **Note 1**). Since the inception of flow cytometry, the number of fluorescent probes that could be simultaneously detected has grown steadily [1]. However, the range of wavelengths that prevalent PMTs can measure is finite, and increasing the number of fluorochromes leads to the increased probability of their emission spectra overlapping, resulting in reduced sensitivity and dynamic range. An obvious, albeit radical, solution to this problem is to eliminate fluorescence as a primary readout and to measure the abundance of metal isotopes instead. The probes (most often antibodies) could remain the same, but instead of

Natasha S. Barteneva and Ivan A. Vorobjev (eds.), *Cellular Heterogeneity: Methods and Protocols*, Methods in Molecular Biology, vol. 1745, https://doi.org/10.1007/978-1-4939-7680-5_4,

carrying a fluorescent tag, in mass cytometry they now carry a metal tag [2, 3]. Practically free of the excessive signal overlap and with a range of isotopes amenable to probe labeling, this allowed for the measurement of a greater number of probes simultaneously. The increased multiplexing capacity came at a price, as the inclusion of the atomic mass spectrometer as a detector meant more complex hardware design, imposing limitations due to novel engineering requisites. Mass cytometers have a lower transmission efficiency (around 50% at the moment) and sensitivity per channel when compared to traditional flow cytometers [1]. This can be accounted for during experiment planning and has been shown not to be prohibitive to using mass cytometry as a cutting-edge single-cell analysis methodology, as exemplified by the number of high-impact publications surfacing since 2011.

Briefly, a sample is obtained and the single-cell suspension is prepared in largely the same way it would be for a regular flow cytometry experiment [4, 5]. The cells are then stained with a panel of antibodies and are delivered to the instrument via a capillary system ending in a glass nebulizer that disperses the liquid into little droplets, each carrying mostly none or one cell. The droplets are captured by a stream of flowing argon gas and passed through a heated spray chamber (200 °C) where their volume is reduced as the liquid evaporates. The spray chamber connects to the sample injector which delivers the cells to the torch, an element where the argon plasma is maintained and cells are atomized and ionized. This process creates spatially separated ion clouds in place of cells with each cloud moving through the three-cone interface where a vacuum is gradually initiated. A portion of the cloud will pass through the three-cone interface and continue toward the time-of-flight (TOF) chamber. A sequence of electromagnetic lenses to eliminate non-ionized particles (turn block) and ionized low-mass biological elements (quadrupole ion guide) filter the ion cloud so that only probe-derived heavy metals reach the TOF chamber.

The measured isotope abundances are interpreted as probe amounts, and acquired intensities are converted into the standard FCS file (*F*low *C*ytometry *S*tandard, the data file standard for reading and writing of data from flow cytometry experiments [6]).

Since the nature of the signal differs from flow cytometry, mass cytometry FCS files have novel parameters that are not present in flow cytometry data (and vice versa), yet the data analysis pipeline is comparable for data derived from both platforms.

Most notably, the mass cytometry datasets will not have parameters like forward and side scatter. Instead, they will have a few unique parameters, like event length and Gaussian discrimination parameters (available with the Helios platform). In author's experience, a number of flow cytometry data analysis software packages can directly be used to also analyze mass cytometry data.

2 Materials

Materials and working solutions should be free of metal contamination, and usage of dedicated, metal-free reagents and buffers is highly recommended:

1. Ficoll-Paque PLUS.
2. SepMate™ 50 ml tubes (STEMCELL Technologies).
3. Phosphate-buffered saline.
4. Recombinant human IL-2 (PeproTech), store at −20 °C.
5. Anti-human CD3 (clone OKT3, BioXcell), store at −20 °C.
6. Cell-ID cisplatin (Fluidigm), store at −20 °C.
7. Maxpar Cell Staining Buffer (Fluidigm), store at 4 °C.
8. Paraformaldehyde aqueous solution, 16% (Electron Microscopy Sciences).
9. Maxpar metal-conjugated and validated antibodies, store at 4 °C.
10. Maxpar Fix and Perm Buffer (Fluidigm), store at 4 °C.
11. Cell-ID Intercalator-Ir (Cat# 201192A [125 μM] or 201192B [500 μM]), store at −20 °C.
12. Maxpar water (Fluidigm).
13. EQ Four Element Calibration Beads (Fluidigm), store at 4 °C.
14. 5 ml Round-bottom polystyrene test tube with cell strainer snap cap.
15. Freezing medium: 10% DMSO in FBS.
16. Wash medium: 10% FBS in RPMI 1640.
17. Culture medium: RPMI 1640 complemented with 10% FBS, 1× GlutaMAX, 1× penicillin/streptomycin, 1 nM sodium pyruvate, 1× NEAA.
18. Cell-ID cisplatin solution: 5000× dilution of the stock solution in PBS.
19. Cell-ID iridium solution: the 100 nM solution prepared by diluting stock solution (**item 11**) in Maxpar Fix and Perm Buffer (**item 10**).

3 Methods

The protocol outlined below (Table 1) contains a 33-parameter mass cytometry panel (30 antibodies and 2 Cell-ID reagents, where Cell-ID Intercalator-Ir is measured in 2 distinct channels.) composed of human cell surface targets. The staining procedure is quite straightforward, with the greatest time investment spent in antibody validation and determination of optimal conditions for

Table 1
Thirty three parameter human immunophenotyping panel with antibody clone information and general biological context of the targets

Target	Clone	Element	Biological context
Lineage markers			
CD45	HI30	154Sm	Pan-leukocyte marker
CD3	UCHT1	170Er	T cells
CD56	NCAM16.2	176Yb	Natural killer T cells
CD14	RMO52	148Nd	Monocytes
CD11b	ICRF44	144Nd	Natural killer cells, monocytes, macrophages
CD4	RPA-T4	145Nd	T helper cells
CD8a	RPA-T8	146Nd	Cytotoxic T cells
CD19	HIB19	142Nd	B cells
T cells, naive and memory subsets			
CD197 (CCR7)	G043H7	159Tb	Central memory T cells
CD45RA	HI100	169Tm	T cell naïve and memory
CD27	O323	167Er	T cell memory subsets
CD127	A019D5	143Nd	Memory and effector T cells
T helper subsets			
CD196 (CCR6)	G034E3	141Pr	Th17
CD195 (CCR5)	NP-6G4	156Gd	Th1 cells
CD194 (CCR4)	205,410	158Gd	Th2 cells
CXCR5	RF8B2	171Yb	T follicular helper cells
CD294 (CRTH2)	BM16	163Dy	Th2 cells
CCR10	314,305	164Dy	Th22 cells
CD25 (IL-2R)	2A3	149Sm	T regulatory cells
Maxpar human T cell Immuno-oncology EX panel kit			
CD95 (FAS)	DX2	152Sm	Apoptosis-inducing receptor
CD366 (Tim-3)	F38-2E2	153Sm	Transmembrane receptor
CD279 (PD-1)	EH12.2H7	155Gd	Inhibitory receptor
CD137 (4-1BB)	4B4-1	173Yb	Stimulatory receptor
CD223 (LAG3)	11C3C65	175Lu	Inhibitory receptor
CD278 (ICOS)	C398.4A	168Er	Stimulatory receptor
CD152 (CTLA-4)	14D3	161Dy	Inhibitory receptor

(continued)

Table 1
(continued)

Target	Clone	Element	Biological context
Cell activation			
CD69	FN50	162Dy	T cell early activation
CD28	CD28.2	160Gd	T cell costimulation
CD38	HIT2	172Yb	Cell activation
HLA-DR	L243	174Yb	Antigen presentation
Identification of cells			
DNA2		191Ir and 193Ir	Cell identification
Live/dead		198Pt	Dead cell identification

sample preparation and staining (*see* **Note 2**). The selected targets allow for identification of the major cell subsets in human blood (T cells, B cells, plasma cells, NK cells, and monocytes) with an emphasis on T cell memory and helper subsets. They have been chosen based on existing publications and author's previous experiences. The antibody panel also incorporates the Maxpar Human T Cell Immuno-Oncology EX Panel Kit (Cat# 201321).

All antibodies are stained together in one staining cocktail for a quick, robust, and easy-to-follow protocol that works well on fresh or frozen cells. In order to observe transient changes in the expression level of certain surface molecules, PBMC are cultured for 5 days in the presence of IL-2 and plate-bound anti-human CD3 antibody. After the stimulation, cells are stained with cisplatin in order to exclude dead cells from further analysis.

3.1 Cell Isolation and Culture

1. To acquire PBMCs from fresh blood, perform Ficoll separation with SepMate 50 ml tubes, count cells and freeze in *freezing media*. For short-term storage, keep at −80 °C; for longer-term storage, place in liquid nitrogen.
2. On the day before cell stimulation, pre-coat wells in 96-well flat-bottom plate with 2 μg/ml anti-human CD3 antibody.
3. Add 100 μl of antibody plus PBS per well and incubate overnight at 4 °C.
4. Next day, discard the supernatant and wash the wells twice with *culture media*.
5. Thaw the cells in 15 ml *wash medium*.
6. Spin the cells down at 400 × *g* for 10 min. Discard the supernatant, and resuspend the pellet in *culture medium*. Repeat the wash.

7. Count the cells and plate 1×10^6 cells per 1 ml (250 µl of cells per well in 4 wells of the 96-well flat-bottom plate).
8. Culture the cells for 5 days in *culture medium* supplemented with 2 µg/ml of human IL-2 in the presence of plate-bound anti-human CD3.
9. On day 5, collect the cells and spin them down at 400 × *g* for 5 min. Discard the supernatant and resuspend in PBS (*see* **Note 3**).
10. Spin the cells down at 400 × *g* for 5 min; aspirate the supernatant.
11. Count 1×10^6 cells and transfer them to a fresh staining tube in preparation for the live/dead staining.
12. Prepare unstimulated control cells by thawing a fresh aliquot of human PBMCs following steps 5 and 6 and place 1×10^6 cells into a new staining tube labeled 'Unstimulated'.
13. Spin the unstimulated cells down at 400×*g* for 5 min and discard supernatant.

3.2 Staining

1. To assess cell viability, add 200 µl of freshly prepared *cell-ID cisplatin solution* to cell pellets, and mix well (*see* **Note 1**).
2. Incubate 10 min at RT.
3. Wash the cells by adding 2 ml cell staining buffer (CSB) per tube, and mix well by resuspending with the pipette or vortexing. Centrifuge at 400 × *g* for 5 min and aspirate supernatant (*see* **Note 2**).
4. Fix the cells by adding 200 µl of freshly prepared 1.6% paraformaldehyde to the cell pellet; mix well. Incubate the cells for 10 min (or longer) at RT.
5. Spin the cells down for 5 min at 800 × *g* (*see* **Note 4**).
6. Wash the cells by adding 2 ml of cell staining buffer (CSB) per tube, mix well, and centrifuge at 800 × *g* for 5 min.
7. Prepare for each tube 100 µl total volume of antibody cocktail in CSB following the titration amounts outlined in Table 1.
8. Add antibody cocktail to pelleted cells, mix well, and incubate 20 min at RT.
9. Wash the cells by adding 2 ml of CSB per tube, mix well, and centrifuge at 800 × *g* for 5 min; discard the supernatant.
10. To discriminate single-nucleated cells from the doublets and non-cells, prepare fresh *iridium intercalator solution* and add 300 µl to each tube of pelleted cells, vortex, or pipette mix and incubate 1 hour (h) at RT or overnight at 4 °C. Cells are stable in *iridium intercalator solution* for up to 1 week at 4 °C with no effect on sample quality before processing on the CyTOF.

3.3 Sample Acquisition

1. Pellet the cells by centrifuging at 800 × *g* for 5 min and remove the supernatant.
2. Wash cells once in 1 ml CSB per tube, centrifuge for 5 min at 800 × *g*, and discard supernatant.
3. Aspirate and repeat washing step two more times, but instead of CSB, wash the cells with Maxpar water.
4. Resuspend cells at a concentration of 1×10^6 cells per ml in water spiked with 10% EQ Four Element Beads, and filter sample through cell strainer cap tubes. Four Element Beads should be vortexed vigorously before adding to your cells (*see* **Note 5**).
5. Acquire samples on the mass cytometer.

3.4 Data Analysis

The advancement in multiplexing capacity of mass cytometers compared to their conventional flow cytometry brethren has given a major impetus to the further development and adoption of computational methods for data analysis. The conceptual approach to evaluating data may have remained the same for a number of experimental layouts, but the methodology had to adapt to the increased information content of mass cytometry datasets. There is still a need to visualize the dataset in its entirety and to summarize features of discrete subsets, most notably their abundance and expression level of a particular epitope. A common approach was to visualize the dataset by drawing a series of bivariate plots, an approach very impractical and cumbersome for the mass cytometry data. Partitioning of the dataset into subsets of biological relevance is commonly done through gating, manually drawing regions of interest on aforementioned bivariate plots. While technically possible, the approach falls short of effectively capturing the diversity of the information and is virtually incompatible with exploratory data analysis in high-dimensional space. Instead, mass cytometry data is often represented by projections of the high-dimensional data (point cloud) into two dimensions where the distance between any two points reflects their proximity (phenotypic similarity) in original, high-dimensional space [7, 8]. This approach allows for a one-plot representation of the entire phenotypic diversity contained in the dataset.

Instead of gating, partitioning of the dataset is better performed using one of the many available clustering algorithms [9]. As a general primer in algorithm-based analysis of high-dimensional mass cytometry datasets, consider reading Saeyes et al. or Mair et al. [10, 11].

For our experiment, we have used t-distributed stochastic neighbor embedding algorithm (tSNE) [12] and performed a dimensionality reduction of the initial dataset (high-dimensional point cloud) (Figs. 1, 2 and 3), projecting it into two-dimensional space for a clear representation of the entire phenotypic complexity

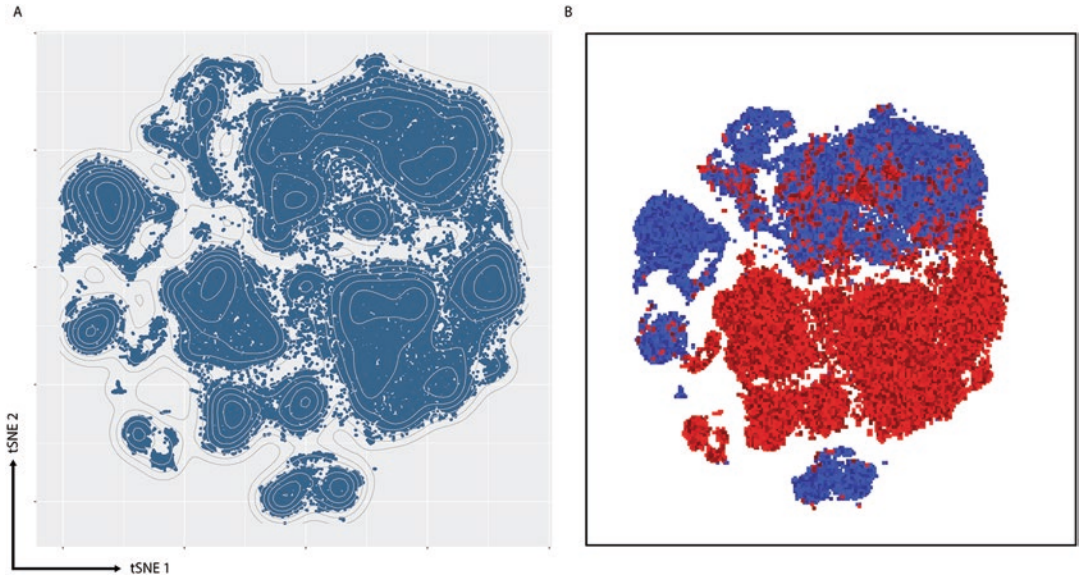

Fig. 1 Stimulated and unstimulated human PBMC subsets displayed with tSNE maps. Human peripheral blood mononuclear cells were stained with the panel of antibodies either directly after thawing or after 5 day stimulation with plate-bound anti-CD3 antibody in the presence of IL-2. For the analysis workflow, samples were processed together for enhanced visualization of the entire phenotypic diversity captured by the panel. (**a**) Two-dimensional representations of the 27-dimensional point cloud computed by the tSNE algorithm outline the phenotypical landscape of the samples (tSNE map). The map represents phenotypical similarity in the context of 27 differentially expressed parameters (of the 30 antibodies in the panel, CD45, CD69, and CD27 were not included in the computation as they did not show differential expression). A complex density distribution suggests diverse phenotypes present in the sample. (**b**) Individual sample contributions are depicted in blue for the unstimulated human PBMCs and in red for the stimulated ones

in a single plot [7]. Further clustering analysis was performed with the FlowSOM algorithm [13] and the five main cell lineages in the data were identified (CD4 and CD8 T cells, B cells, NK cells, and monocytes) and shown as an overlay on the tSNE map (Fig. 4). To more precisely capture and describe the phenotypic landscape of the acquired sample, the dataset was further partitioned/clustered using the FlowSOM algorithm, resulting in 20 clusters whose phenotype has been depicted as a heatmap of median signal intensities for each cluster, with the most similar clusters arranged close to one another (Fig. 5). Similarity of clusters depicted in the heatmaps was evaluated by agglomerative hierarchical clustering using Euclidean distance metric and Ward's linkage criterion.

3.5 Metal Probes

Most antibodies are conjugated to purified isotopes of lanthanide metals (non-radioactive) from lanthanum to lutetium, but some transition metal elements are also used. Elements can directly stain cells through binding of functional groups or be conjugated to antibodies. DNA-binding agents like iridium and rhodium stain

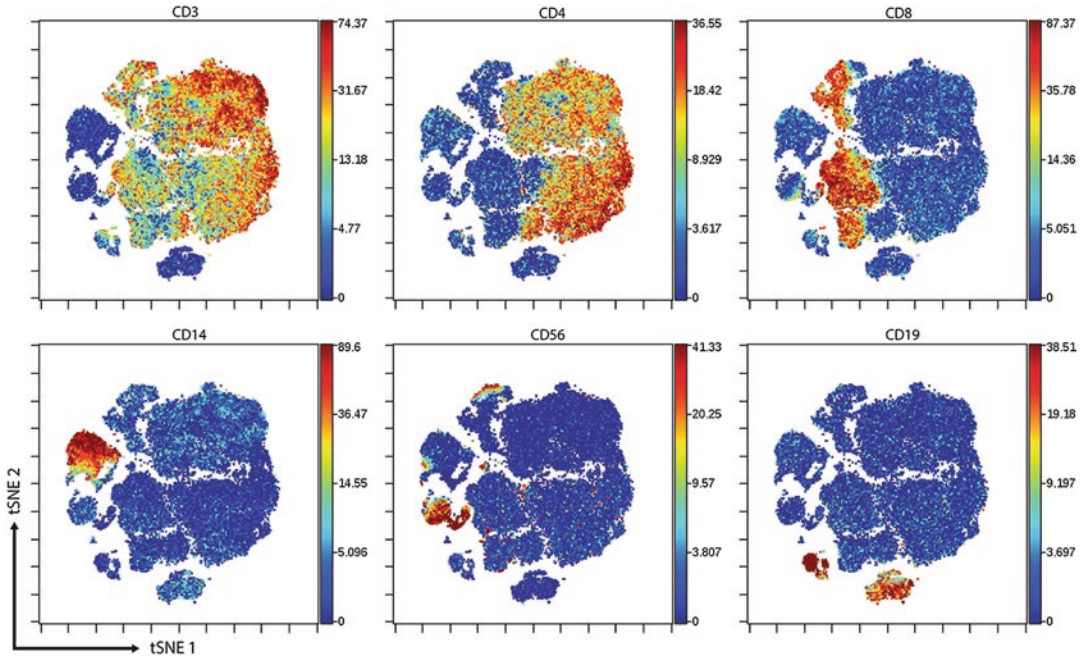

Fig. 2 Expression of 6 major lineage markers on the tSNE map from Fig. 1. Overlaying expression profiles of six broad lineage markers onto the tSNE map clearly outlines five major cell lineages (cytotoxic T cells, T helper cells, B cells, monocytes, and NK cells) and confirms monocytes are absent from the stimulated sample (loss likely due to adherence to the plate plastic)

cells directly and identify ion clouds originating from nucleated cells, while platinum is employed for exclusion of dead cells and, more recently, for labeling antibodies [14]. Palladium is also dual-use and can be used as a barcoding reagent, as well as labeled to antibody. Ruthenium and osmium can be used in single-cell barcoding [15]. Indium is a newer metal that has been shown to work conjugated to antibodies [16] and Qdot nanocrystals have cadmium cores in the detectable range for the CyTOF [17]. New metal tags such as silver-loaded nanoparticles have recently been published for reporting cell surface antigens [18]. There are also limited pre-conjugated antibodies to bismuth and yttrium now available from Fluidigm, and iodine (iodine-deoxyuridine) was shown to efficiently label proliferating cells [19]. All these additional metals provide further evidence that novel elements are being continuously developed for this technology.

3.6 Mass Calibration

The TOF chamber generates time-resolved signals that are interpreted in terms of isotope mass based on the previously performed mass calibration. In short, a calibration solution containing known amounts of five elements (Tuning solution, Fluidigm Cat# 201072) is acquired, and reference peaks of cesium and iridium are sought in an approximate expected range (in nanoseconds). After identified, other mass channels are calculated accordingly.

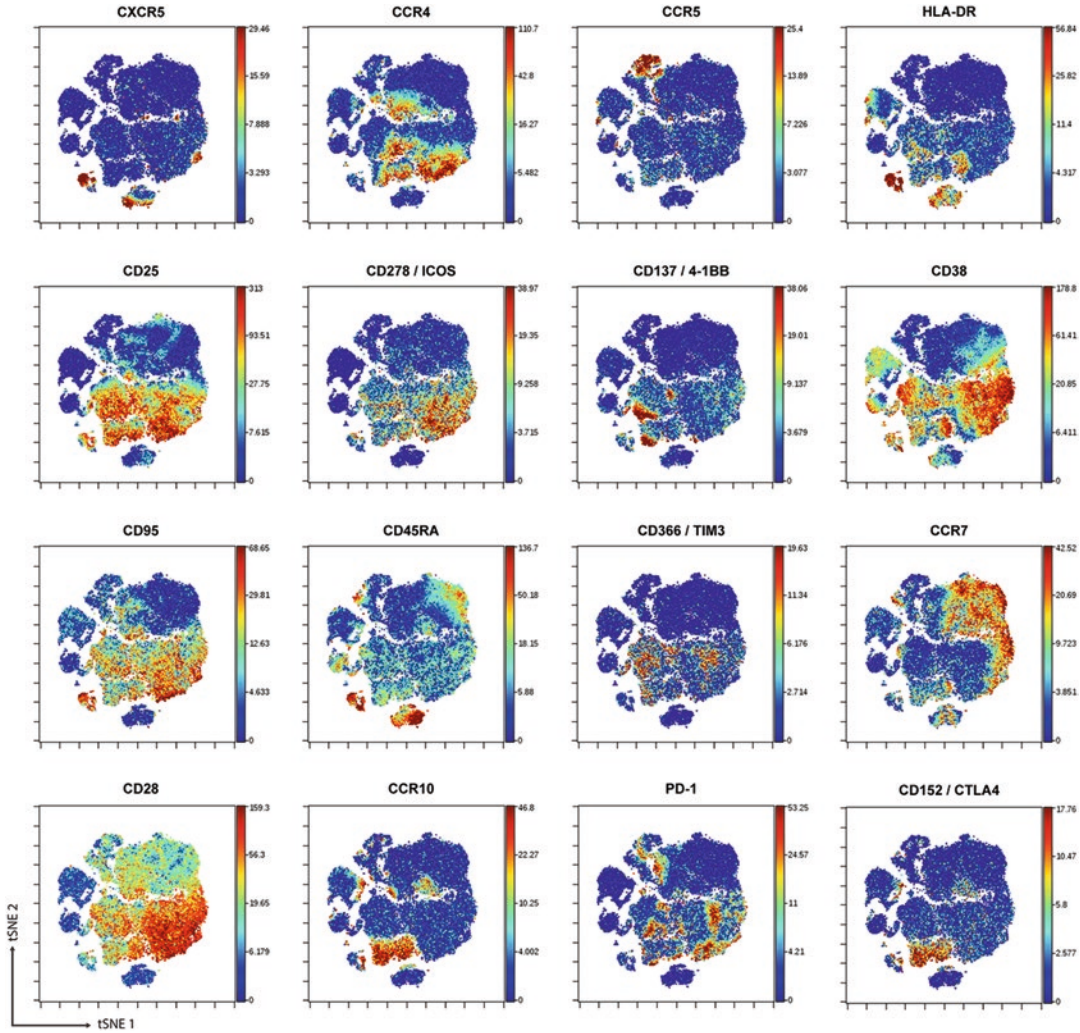

Fig. 3 Overlay of expression profiles for 16 lineage-specific surface molecules and activation markers onto the tSNE map. This method of visualization highlights the sample diversity. Overlaying expression profiles of 16 lineage-specific surface molecules and activation markers onto the tSNE map further outlines the phenotypic diversity present in the sample. CD25 and CD95 are almost exclusively found on stimulated cells and represent the most robust predictor of sample origin in our case

3.7 Guidelines for Panel Development

Panel development for mass cytometry streamlines with that of flow cytometry in that the primary aim for both technologies is to maximize specific signal intensity and minimize non-specific signal or noise.

Specific signal intensity is affected by factors like antigen abundance, instrument mass response, and conjugated antibody properties like epitope affinity and the number of metal atoms bound per antibody. The ion transmission efficiency (mass response) is not the same for all metals; elements between 155 and 165 atomic mass units (AMU) are the most sensitive, and elements on either

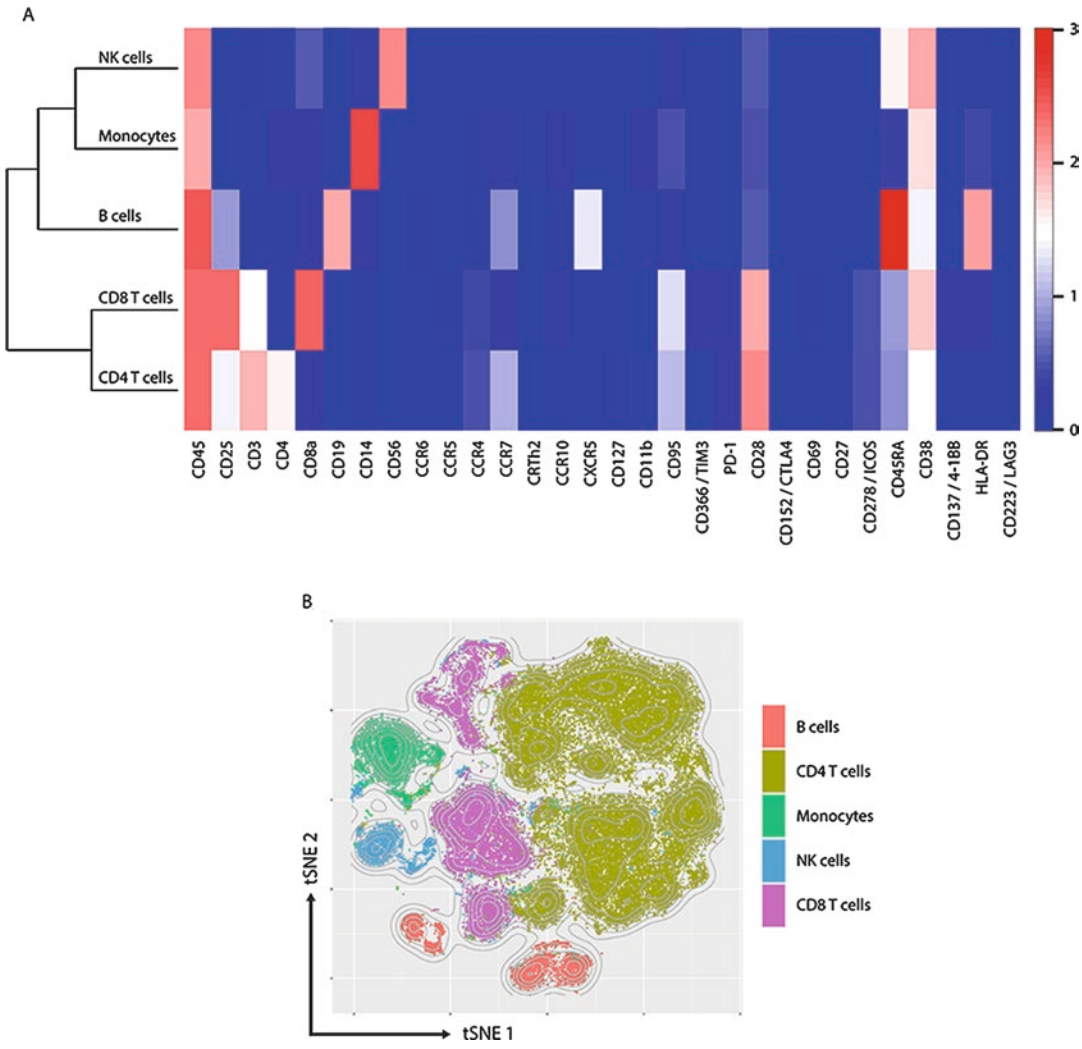

Fig. 4 Heatmap of median signal intensities for each of the 5 major lineages identified with flowSOM clustering algorithm. Dataset needs to be partitioned in order to express summary statistics describing the sample in terms of abundance of subsets or expression levels for a particular epitope. Most often, flow cytometry datasets are partitioned through gating. For mass cytometry datasets, purpose is better served through cluster analysis. The flowSOM clustering algorithm defines five clusters matching the major cell lineages recognized in Fig. 2. (**a**) Heatmap shows the expression pattern in terms of median signal intensity of the 30 epitopes examined on designated clusters. This is just a methodological representation as median expression level on broadly defined lineages fails to capture the expression of less abundant and more subset-specific epitopes. (**b**) Designated clusters overlaid onto the tSNE map, closely matching the the expression profiles from Fig. 2

end of these masses gradually decline in sensitivity. The difference between the most and the least sensitive masses is between three- and four-fold, so authors recommend placing the less abundant targets on metals in the most sensitive mass range. Non-specific signals arise from factors covered in more detail below and include environmental contaminants, metal impurities, element oxides, and abundance sensitivity.

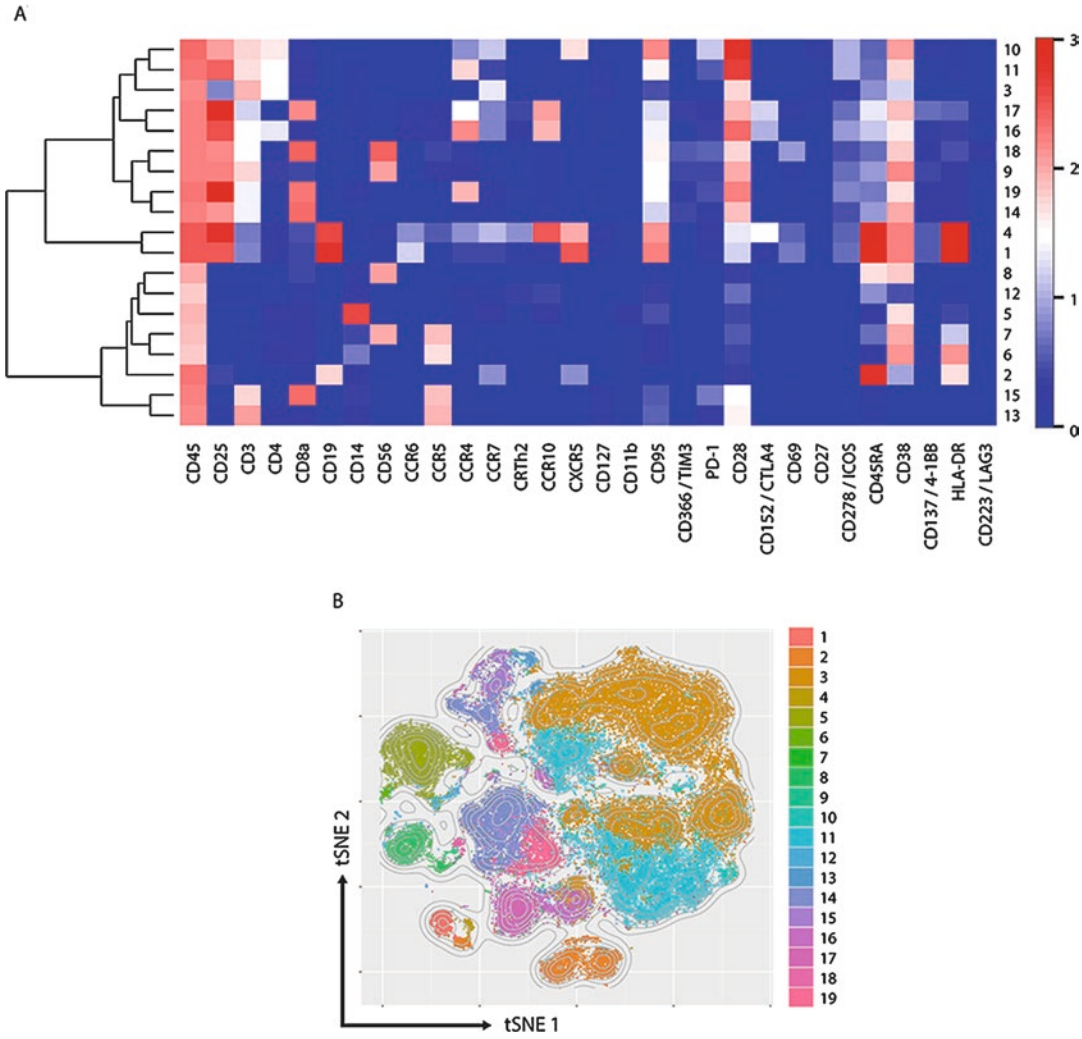

Fig. 5 Detailed phenotypic profiling with deeper cluster analysis and tSNE visualization. For cluster analysis to be most useful and the group statistic revealing, dataset needs to be partitioned beyond the major cell lineages. (**a**) Here we show 19 clusters defined by the FlowSOM algorithm. Heatmap shows the expression pattern in terms of median signal intensity of 30 epitopes examined on designated clusters. The more extensive partitioning compared to Fig. 4 provides far more informative group statistics. (**b**) Designated clusters overlaid onto the tSNE map for visualization and presentation purposes

The process of labeling antibodies with metal atoms is a harsh procedure involving a reduction step to reveal thiol groups to which maleimide-functionalized metal-loaded chelating polymer is conjugated. Unfortunately, there is currently no quality control procedure in place for identifying and separating labeled from unlabeled antibody, so the end product likely contains diverse conjugation products. This variability means that each antibody conjugation should be followed by a standardized validation procedure.

There are varying sources of environmental elemental contamination within the detection range of the CyTOF, with the primary

sources being dust or soap (barium), water (iodine), reagent containers (lead), and some stock buffers (samarium, mercury). Authors recommend having a dedicated set of pipettes for mass cytometry, using barrier tips, and containers made of polymer or Pyrex glass. A dedicated lab space that is away from known sources of contamination (like osmium tetroxide for electron and optical microscopy) is also advised.

Another source of noise in mass cytometry comes from metal impurities that are often the result of the presence of minor isotopes (or other elements with similar properties) from incomplete elemental purification. Fluidigm offers purified metals for antibody labeling that are documented to be more than 98% pure. This varies by metal and should be experimentally confirmed during antibody validation.

Non-specific signal is also the result of metal oxidation in the argon plasma. This is a property of all metals used, but to varying extents depending on the metal. Lanthanum (^{139}La) is the most oxide-forming element, and this signal is detected in the +16 mass channel (155 atomic mass units (AMU)). As a result, lanthanum is exploited in the Tuning solution to quantify as a worst-case scenario the amount of oxide formation during instrument calibration.

The last notable source of noise in mass cytometry is the abundance sensitivity. This is a TOF phenomenon in which highly abundant isotopes are detected in the neighboring mass channel due to spreading of the signal as they reach the detector. The TOF output is a time-resolved signal in which detected peaks are assigned a specific mass channel that is determined from the mass calibration during daily machine tuning. A typical mass channel has a width of 20–25 ns, and very abundant isotopes can be detected in the neighboring mass channels (M + 1 and M − 1). This signal is minor (less than 1%), so signal intensities below or around 1000 dual counts do not typically see issues. Overall, metal impurities, oxide formation, and abundance sensitivity only account for 1–5% of the primary signal, making it possible to handle this "noise" by careful panel validation.

3.8 Signal Normalization Over Time

The mass cytometer is very sensitive to the buildup of cellular material inside of the instrument and also to environmental conditions (temperature changes), both of which will manifest themselves as a reduction in sensitivity (albeit for different reasons and to a different extent). The loss in sensitivity can take place over the course of hours, and to correct for this, samples are spiked with EQ Four Element Calibration Beads. These are synthetic beads containing natural abundance cerium, europium, holmium, and lutetium, spanning a large portion of the measurement range. Using a computer algorithm (Normalizer), correction coefficients are calculated from the bead signals and applied to every element in the

staining panel so that the signal shows stable intensity over the entire acquisition time.

3.9 FCS File Generation and Manual Data Analysis

The mass cytometer's primary output data format is the so-called IMD file (integrated mass data). Standard FCS files are created through conversion of IMD files according to user-specified criteria. The most important criteria affecting the composition of the FCS file are event duration boundaries and lower convolution threshold, briefly described below.

The CyTOF instrument measures the relevant atomic spectrum (from 76 to 209 AMU) 76′800 times per second, resulting in an approximate time of measurement of 13 μs for each spectrum. One full spectrum measurement is also known as a "push" since a portion of the ion cloud quite literally gets "pushed" into the TOF chamber by the pulsing electromagnetic field oscillating at 76.8 kHz.

The detector output during one full spectrum measurement is integrated and the threshold applied (lower convolution threshold, LCT). If the entire signal is below the LCT, it is not further processed and does not get stored. Usually, the ion cloud originating from a cell will be measured across multiple pushes. Therefore, this fact can be used to discriminate between sporadic signals rising above the LCT and signals originating from cells, as the latter will be presented as uninterrupted measurement across multiple pushes in at least one mass channel, therefore giving rise to the parameter called "event length" (in pushes). The user specifies the lower and higher length limit (minimum and maximum event duration), and only uninterrupted signals having the length (in pushes) between the two values are converted to an "event" of the FCS file. With this in mind, manual inspection of the CyTOF-generated FCS files usually starts by plotting the DNA intercalator signal vs. event length (in pushes) or, even better, DNA intercalator vs. dead cell reagent (often cisplatin). This allows for fairly robust recognition of cells over non-cells and somewhat less robust recognition of singlets over doublets (multiplets). The subsequent gating steps (if any) are usually carried out according to the dictate of the experimental hypothesis and in the same fashion as they would be in a regular flow cytometry experiment.

4 Notes

1. Cisplatin binds covalently to cellular proteins and labels the cells with compromised cell membranes to a much greater extent than live cells.
2. Cells are washed in PBS before the cisplatin staining since any additional protein content in staining solution would also bind cisplatin, thus reducing the staining intensity on cells [20].

3. After the cisplatin staining, cells are washed with CSB (contains soluble protein) to quench the staining reaction.
4. Fixed cells should be centrifuged at 600–800 × *g* to pellet them well (higher buoyancy after fixing), while fresh cells are efficiently centrifuged at 300–400 × *g*.
5. Cell strainer cap tubes are essential for any cellular sample run through the CyTOF because the machine tubing is readily clogged and even partial clogs will impact data quality.

Acknowledgments

Authors thank Paulina Kulig for assistance in manuscript preparation and Annette Audigé-Schmitz for assistance in validating the panel reagents.

References

1. Bendall SC, Nolan GP, Roederer M, Chattopadhyay PK (2012) A deep profiler's guide to cytometry. Trends Immunol 33(7): 323–332. https://doi.org/10.1016/j.it.2012.02.010
2. Lou X, Zhang G, Herrera I, Kinach R et al (2007) Polymer-based elemental tags for sensitive bioassays. Angew Chem Int Ed Engl 46(32):6111–6114. https://doi.org/10.1002/anie.200700796
3. Majonis D, Herrera I, Ornatsky O et al (2010) Synthesis of a functional metal-chelating polymer and steps toward quantitative mass Cytometry bioassays. Anal Chem 82(21):8961–8969. https://doi.org/10.1021/ac101901x
4. Bandura DR, Baranov VI, Ornatsky OI et al (2009) Mass cytometry: technique for real time single cell multitarget immunoassay based on inductively coupled plasma time-of-flight mass spectrometry. Anal Chem 81(16):6813–6822. https://doi.org/10.1021/ac901049w
5. Tanner SD, Baranov VI, Ornatsky OI, Bandura DR, George TC (2013) An introduction to mass cytometry: fundamentals and applications. Cancer Immunol Immunother 62(5):955–965. https://doi.org/10.1007/s00262-013-1416-8
6. Spidlen J, Moore W, Parks D et al (2010) Data file standard for flow cytometry, version FCS 3.1. Cytometry A 77(1):97–100. https://doi.org/10.1002/cyto.a.20825
7. Amir ED, Davis K, Tadmor MD et al (2013) viSNE enables visualization of high dimensional single-cell data and reveals phenotypic heterogeneity of leukemia. Nat Biotech 31(6):545–552. https://doi.org/10.1038/nbt.2594
8. Newell EW, Sigal N, Bendall SC, Nolan GP, Davis MM (2012) Cytometry by time-of-flight shows combinatorial cytokine expression and virus-specific cell niches within a continuum of CD8+ T cell phenotypes. Immunity 36(1):142–152. https://doi.org/10.1016/j.immuni.2012.01.002
9. Weber LM, Robinson MD (2016) Comparison of clustering methods for high-dimensional single-cell flow and mass cytometry data. Cytometry A 89(12):1084–1096. https://doi.org/10.1002/cyto.a.23030
10. Saeys Y, Gassen SV, Lambrecht BN (2016) Computational flow cytometry: helping to make sense of high-dimensional immunology data. Nat Rev Immunol 16(7):449–462. https://doi.org/10.1038/nri.2016.56
11. Mair F, Hartmann FJ, Mrdjen Det al. (2015) The end of gating? An introduction to automated analysis of high dimensional cytometry data. Eur J Immunol 46(1):34–43. https://doi.org/10.1002/eji.201545774
12. Van der Maaten L, Hinton G (2008) Visualizing data using t-SNE. J Machine Learn Res 9:2579–2605
13. Van Gassen S, Callebaut B, Van Helden MJ et al (2015) FlowSOM: using self-organizing maps for visualization and interpretation of cytometry data. Cytometry A 87(7):636–645. https://doi.org/10.1002/cyto.a.22625
14. Mei HE, Leipold MD, Maecker HT (2016) Platinum-conjugated antibodies for application

in mass cytometry. Cytometry A 89(3):292–300. https://doi.org/10.1002/cyto.a.22778

15. Catena R, Özcan A, Zivanovic N, Bodenmiller B (2016) Enhanced multiplexing in mass cytometry using osmium and ruthenium tetroxide species. Cytometry A 89(5):491–497. https://doi.org/10.1002/cyto.a.22848
16. Mei HE, Leipold MD, Schulz AR, Chester C, Maecker HT (2015) Barcoding of live human peripheral blood mononuclear cells for multiplexed mass cytometry. J Immunol 194(4): 2022–2031. https://doi.org/10.4049/jimmunol.1402661
17. Bendall SC, Simonds EF, Qiu P et al (2011) Single-cell mass cytometry of differential immune and drug responses across a human hematopoietic continuum. Science 332(6030): 687–696. https://doi.org/10.1126/science.1198704
18. Schulz AR, Stanislawiak S, Baumgart S, Grützkau A, Mei HE (2017) Silver nanoparticles for the detection of cell surface antigens in mass cytometry. Cytometry A 91(1):25–33. https://doi.org/10.1002/cyto.a.22904
19. Behbehani GK, Bendall SC, Clutter MR et al (2012) Single cell mass cytometry adapted to measurements of the cell cycle. Cytometry A 81((7):552–566. https://doi.org/10.1002/cyto.a.22075
20. Fienberg H, Simonds EF, Fantl WJ, Nolan GP, Bodenmiller B (2012) A platinum-based covalent viability reagent for single cell mass cytometry. Cytometry A 81(6):467–475. https://doi.org/10.1002/cyto.a.22067

Chapter 5

Spectral and Imaging Flow Cytometry in Phytoplankton Research

Veronika Dashkova, Jeff Clapper, Ivan A. Vorobjev, and Natasha S. Barteneva

Abstract

Spectral and imaging flow cytometry are emerging technologies that allow quantifying spectral, fluorescent, and/or morphological parameters of heterogeneous cellular populations. The protocol describes a detailed step-by-step analysis of microalgae using these techniques and examples from our laboratory (*Aphanizomenon* sp., *Cryptomonas pyrenoidifera*, and *Chlorella* sp.). Moreover, the chapter will be helpful to scientists who want to perform spectral flow cytometry and apply principal component analysis.

Key words Spectral flow cytometry, Imaging flow cytometry, Microalgae, Programmed cell death, Population heterogeneity

1 Introduction

Besides the stunning (overwhelming) diversity of the phytoplankton in respect to taxonomy [1–3], morphology, concentration, and size, phytoplankton organisms can also be characterized by a high degree of intraspecific cell heterogeneity. The sources of cell heterogeneity in microbial populations may be of genotypic origin arising via mutations and/or phenotypic origin resulting from the differential cell cycle progression or changes in the surrounding environment [4] leading to phenotypic heterogeneity. Various studies showed the presence of numerous cell subpopulations within one focal phytoplankton population differing (varying) in size and morphology [5], pigment composition and autofluorescence signal [6], DNA content [7], and physiological proxies such as viability and metabolic activity [8–13].

Veronika Dashkova, Ivan A. Vorobjev, and Natasha S. Barteneva contributed equally to this work.

Natasha S. Barteneva and Ivan A. Vorobjev (eds.), *Cellular Heterogeneity: Methods and Protocols*, Methods in Molecular Biology, vol. 1745, https://doi.org/10.1007/978-1-4939-7680-5_5,

The concept of programmed cell death (PCD), well developed for animal cells, has been recently introduced to explain mechanisms of cyanobacteria and phytoplankton cell death [14–16]. PCD has been analyzed in microalgae using as a proxy (1) caspase-like activity [17, 18], (2) DNA fragmentation assays such as TUNEL method [14, 18], and (3) recently by staining with annexin-V [11, 19].

Despite the widespread occurrence of intraspecific cell heterogeneity in algal monocultures and natural phytoplankton populations, the statistical evaluation of the cell-to-cell phenotypic variability using traditional methods (e.g., microscopy, spectrofluorimetry) remains a challenge. Thus, techniques that provide the combination of single-cell analysis and high-throughput capacity for measuring properties of single cells in large numbers may offer significant advantages for analysis of heterogeneous microbial populations [4]. High-throughput multiparameter techniques, including flow cytometry (FCM), imaging flow cytometry (imaging FCM), and spectral flow cytometry (spectral FCM), are particularly useful for capturing and characterizing cell heterogeneity in diverse phytoplankton populations [20–24].

FCM was first introduced in algal research by oceanographers [25–28] and rapidly developed in recent decades become a state-of-the art tool for phytoplankton analysis and microalgae biotechnology as summarized in many reviews [29–32]. In the last years, imaging FCM or "inflow microscopy," a hybrid technology combining capabilities of fluorescent microscopy with a statistical power of flow cytometry, contributed to the advancement of microalgae analysis in situ and in the laboratory. Various commercially available imaging flow cytometers such as dynamic imaging particle analyzer FlowCam (Fluid Imaging Technologies, USA) [19], Imaging FlowCytobot (IFCB) (McLane Research Laboratories, USA) [33], and Imagestream family of imaging flow cytometers (Amnis-Merck, USA) [20, 23] are now widely used for phytoplankton applications. A spectral FCM allows combined measurement of cell scattering and complete spectra from tenths to thousandths of single cells, using prisms or gratings to disperse light and CCD cameras and detector arrays as collection devices [34–38]. The earliest instruments implementing spectral analysis capability for flow cytometry utilized vidicon image sensors coupled with dispersive optical elements [39, 40]. Recently, spectral flow cytometer that uses 32-channel photomultiplier (PMT) for spectral signal detection and 3-laser combination as a source of excitation (405, 488, and 638 nm laser sources) became commercially available (SP6800, SONY Biotechnology Inc.). We applied imaging and spectral FCM for microalgae analysis [20].

New methods combining high statistical power and high spectral resolution based on detailed single-cell analysis will allow performing in-depth analysis of intraspecific phytoplankton cell

heterogeneity. In this chapter we are providing a detailed step-by-step description of spectral and imaging FCM approach for assessing microalgae heterogeneity based on spectral and phenotypic characteristics and viability and PCD markers.

2 Materials

2.1 Phytoplankton Cell Viability and Programmed Cell Death Assessment Using Imaging FCM

1. Phytoplankton cell culture (e.g., *Aphanizomenon* sp. CCMP2764).
2. Sterile 0.5 M $CaCl_2$. Store at 4 °C.
3. 0.5 ml annexin-V FITC stock solution. Store at 4 °C.
4. 1 mM Sytox Blue stock solution (Life Technologies). Store in the dark at −20 °C.
5. 1.5 ml polypropylene tubes.
6. Imagestream X Mark II imaging flow cytometer (Amnis-Merck, USA) equipped with Amnis INSPIRE and Amnis IDEAS software and lasers with adjustable power: 405 nm violet laser (max. 120 mW), 488 nm blue laser (max. 200 mW), 642 nm red laser (max. 150 mW), and 785 nm infrared laser (max. 8.75 mW) source.
7. Phosphate-buffered saline (PBS) 1×.
8. Speed beads (Amnis). Store at 4 °C.

2.2 Spectral Analysis of Phytoplankton Cell Culture Mixture Using Spectral FCM

1. Two or more phytoplankton cell cultures (e.g., *Cryptomonas pyrenoidifera* CCMP1177 and *Chlorella* sp. CCMP251).
2. The spectral flow cytometer (spectral FCM) analyzer SP6800 (Sony Biotechnology Inc., San Jose, USA) equipped with 40 mW blue 488, 60 mW violet 405, and 60 mW red 638 lasers, 10 consecutive transparent optical prisms, and a 32-channel linear array photomultiplier (500–800 nm range for 488 nm excitation and 420–800 nm range for 405/638 lasers combination) and equipped with Sony software (Sony Biotechnology Inc., San Jose, USA).
3. Ultra Rainbow calibration beads (Spherotech, USA).
4. 12 × 75 mm round-bottom Falcon polystyrene tubes.

2.3 Principal Component Analysis (PCA) of Spectral Data

1. Unscrambler X v10.4 software (CAMO Software).

3 Methods

3.1 Annexin-V and SB Staining for Imaging FCM Analysis

Cell cultures were stained directly without preceding centrifugation or washing steps. A sample volume of 100 µl with intermediate cell density was sufficient to record required 10,000 events.

1. Pipette 100 µl of cell culture into a 1.5 ml polypropylene tube.
2. Add 5 µl of annexin-V FITC stock solution (in Ca^{++}-containing solution) immediately to the sample, and incubate in the dark at room temperature for 20 min.
3. Add 0.5 µl of SB stock solution, making up 5 µM SB concentration, and incubate in the dark for 10–15 min (concentration of DNA dye can be adjusted for different microalgae).

3.2 Imaging FCM Analysis

1. In the INSPIRE software, set the appropriate parameters in the menu to the right. Under the Illumination tab, set the following laser powers:

405 nm laser	10 mW
488 nm laser	100 mW
642 nm laser	0.5 mW (*see* **Note 1**)
785 nm laser	0.5 mW
561 nm	0 mW

2. In the Magnification and EDF tab, set 60× magnification or other appropriate magnification (*see* **Note 2**).
3. Before loading the sample, vortex it for 2–5 s to allow for homogeneous cell distribution in the sample.
4. Click on "Load" and place the open polypropylene tube with the sample into the released sample port. Click on "OK" when the tube is placed.
5. Once the run starts, wait until the images appear to be in focus and centered (about 30–60 s), and apply additional live gating, if necessary (*see* **Note 3**).
6. Click on "New Histogram" and click on the "All" population to select it. Choose "Raw Max Pixel_MC_Ch01" as the x-axis feature.
7. Thresholding on the size and/or fluorescence: Click on "Create Line Region," and draw a line that gates all events excluding small particles and debris ("R1").
8. In the left upper bar, select R1 population to view cells from that region only. Observe fluorescence signal of annexin-V in channel 2 (e.g., by blue 488 nm laser; collecting filter 528/65), SB in channel 7 (e.g., by violet 405 nm laser; collecting filter

457/45), and chlorophyll autofluorescence in channel 11 (e.g., by red 658 nm laser; collecting filter 702/85).

9. If required, adjust the laser power accordingly to increase the dye signal over the background and/or diminish saturating autofluorescence.
10. Create a folder to which images should be saved and name the file. Set the desired number of events to be acquired. The events to be acquired should come from "R1" – gate excluding debris.
11. Start acquisition of sample by click on "Acquire."
12. After instrument acquire defined by researcher # of events, it will stop automatically. Alternatively, you can stop it when speed becomes slow (usually, after 45 min of acquisition). You can collect several files with high speed and merge them later.
13. Imagestream instruments have a cleaning cycle after cell acquisition. However, microalgal cultures are water-resistant and may require additional manual cleaning cycles (*see* **Note 4**).
14. Software keeps track of remaining volume of sample. Click on "Load" to start a new sample tube without returning the remainder of the sample. Alternatively, click on "Return" button to return the tube with remainder of cell suspension. Click on "Load" to run the next sample.
15. Go to the IDEAS software for analysis and open the experiment file.
16. Click on "Image Properties" icon in the upper command panel to create an image viewing mode with channels of interest only.
17. In the appeared window, under the "Views" tab, click on "New" button to create an image view, and enter a name of the view. Click on "Add Column," and specify the channel of the image to be displayed, e.g., Ch01, and press OK. Add additional columns for Ch02 corresponding to annexin-V, Ch07 corresponding to SB, and Ch11 associated with chlorophyll fluorescence.
18. Go to the "Composites" tab and create a composite view of Ch01 or Ch09, Ch02, Ch07, and Ch11 channels by clicking on "Add image," specifying the channel and the relative proportion of fluorescent channel.
19. Go back to the "Views" tab and add the created composite parameter as an additional column to the previously created image view. Close the "Views" window to return to the main analysis view.
20. Select the created image view in the "View" command in the upper bar. Only specified channels are now displayed.

21. To gate single "focused" events, use scattergram area/aspect ratio (single events) and histogram Gradient Rmax (focused events) features for bright field channels.
22. To quantify cell size distribution, create histogram or two-dimensional scattergram, and use area and/or perimeter parameters.
23. For further analysis in the lower panel, create a new scatterplot, and select gated "single focused cell" population. Specify "Intensity_MC_Ch02" as the x-axis feature and "Intensity_MC_Ch07" as the y-axis feature and press OK.
24. In the generated scatterplot, locate differentiated populations, and click on "Create Polygon region" to enclose them in gates.
25. Click on "Show/Hide Statistics" to view to statistical information on each population.
26. In the upper panel menu, the region-associated populations can be then selected and displayed (examples of acquired with Imagestream X Mark II cyanobacteria images and scattergrams displayed at Fig. 1).
27. In many cases IDEAS software (Amnis-Merck, USA) is sufficient for quantitative analysis of samples. Furthermore, data

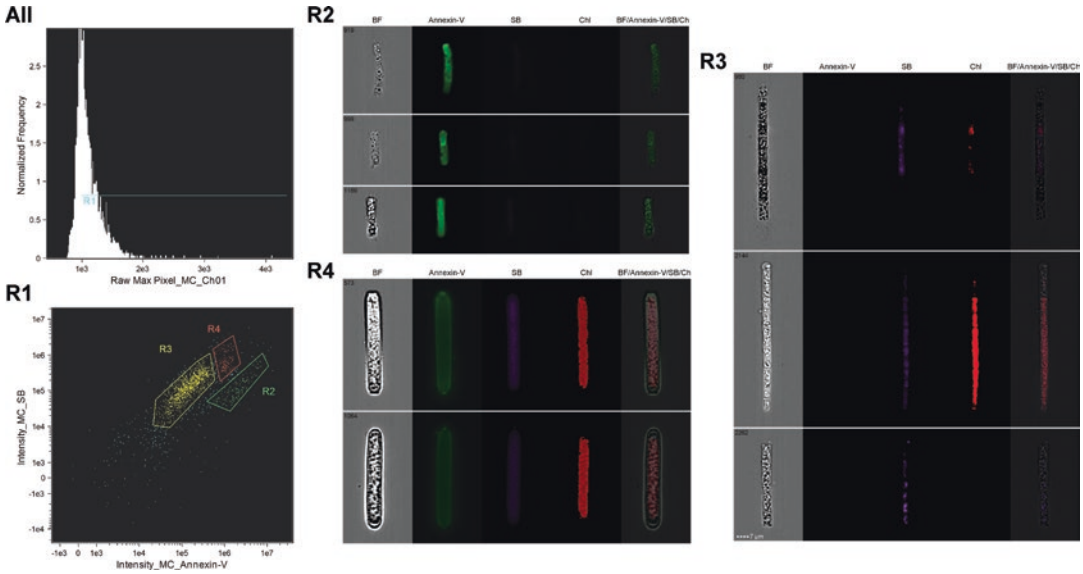

Fig. 1 Analysis of *Aphanizomenon* sp. cells stained with annexin-V and Sytox Blue (SB) using Imagestream X Mark II imaging cytometer (Amnis). R1 population was gated on the histogram displaying all cells and was visualized on dot plot SB intensity vs. annexin-V intensity. Three distinct populations R2, R3, and R4 were gated and examined using corresponding images. Representative images of each cell population are shown in bright field (BF), annexin-V corresponding (Ch2; e.g., by blue 488 nm laser/collecting filter 528/65), SB corresponding (Ch7; e.g., by 405 nm/collecting filter 457/45), and chlorophyll corresponding (Ch11; e.g., 658 nm laser/collecting filter 702/85) and merged BF, annexin-V, SB, and chlorophyll channels

can be exported and analyzed with statistical programs. Created FCS files can be analyzed with off-line flow cytometry software. A last version of FCS Express software (De Novo Inc., USA) capable to analyze images acquired with Imagestream instruments as well as spectral information acquired with Sony SP6800 (Sony Biotechnology Inc., USA) spectral flow cytometer (see below).

3.3 Spectral FCM Analysis of Phytoplankton Cell Culture Mixture Based on Virtual Filtering

1. Mix *C. pyrenoidifera* and *Chlorella* sp. cultures with relatively equal cell densities in 1:1 volume ratio making up to 1 ml sample.
2. Open Acquisition window in the SP6800 software.
3. Check 405 nm and 488 nm lasers leaving the 638 nm laser inactive under the "Laser" tab to avoid the missing part of the spectra around 638 (617-650) nm resulting from the emission of the 638 red laser.
4. Set FSC gain to 17, SSC gain to 17, the threshold value to 1.7%, and fluorescence PMT voltage from 50 to 60% under the "Detector & Threshold" tab.
5. Press the icon in upper right corner of the "Detector & Threshold" tab, and set the gain of 24–30 PMT channels to 2 to decrease a strong chlorophyll-associated signal, and leave the rest of the channels with a max gain of 8 (*see* **Note 5**).
6. Set the sample flow rate to 60 under the "Flow Control" tab to keep the intermediate flow velocity.
7. Set the stopping condition to 50,000 or 100,000 events depending on the sample concentration.
8. Create FSC_A vs. SSC_A dot plot and spectrum plots for 488 nm and 405 nm excitation.
9. Place the round-bottom tube with the sample in the sample port and click "Preview."
10. Once the sample is being processed, observe if any parameters from the "Detector & Threshold," e.g., fluorescence PMT voltage and/or FSC/SSC gain, need to be tuned.
11. Click "Acquire" to record the sample.
12. Once the acquisition is completed, go to the Analysis window and open the recorded experiment.
13. Select the tube corresponding to the mixture of cultures, and refer to the spectrum 488 nm and 405 nm spectrum plots for the most variable and elongated (in height) regions of the spectra.
14. Create a matrix of virtual filters by clicking on "Add" button under the "Color Palette" tab and specifying the channel range and name of the filter to be created.

15. To achieve a better separation of the two populations, the spectral regions of the virtual filter combination to be used for the discrimination based on a dot plot should not be closely located.
16. After creating a set of several variants of virtual filters capturing the spectra variability, create a dot plot to select the combination of filters that provides the best separation of the two cell populations (e.g., CH 12–14 and CH 32 (488 nm excitation) for *C. pyrenoidifera* and *Chlorella* sp. mixture) (*see* **Note 6**).
17. It may be also useful to go to the one of the filters on the dot plot under the "Color palette" and play around with the channel range covered, increasing or decreasing the channel range of the filter. See how the selected channel range affects the separation of the populations on the dot plot.
18. Create spectrum plots for the discriminated populations (Fig. 2) to observe if they are different and validate with the spectra of the corresponding single phytoplankton culture controls.

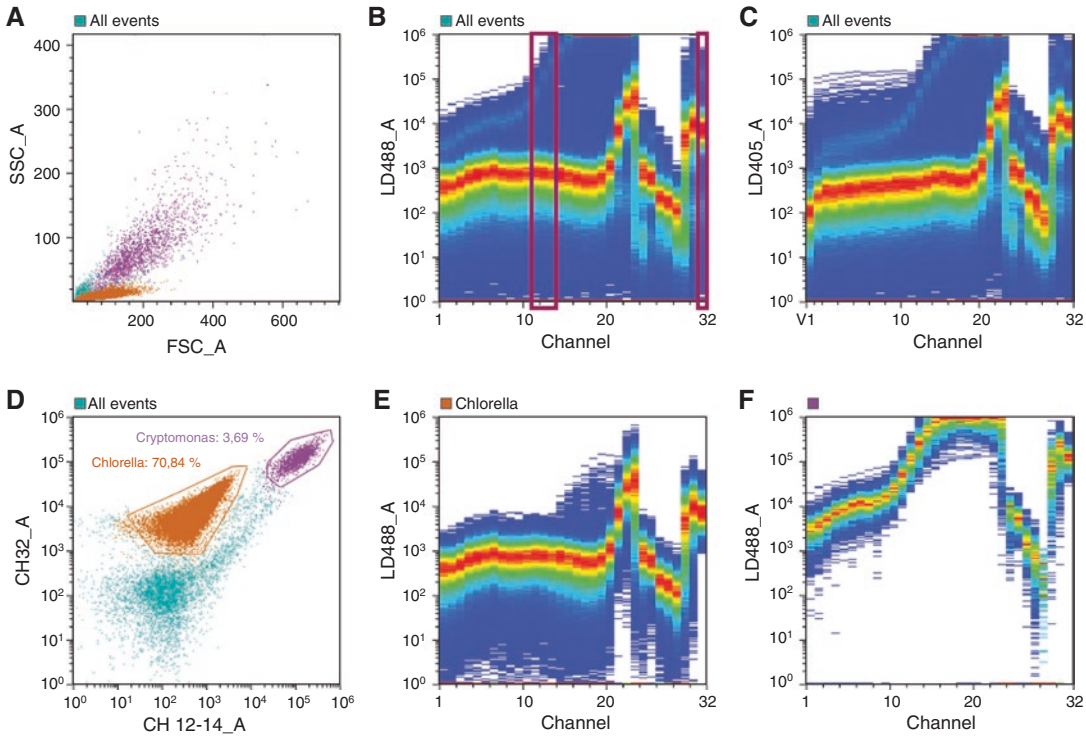

Fig. 2 Spectral analysis of *C. pyrenoidifera* and *Chlorella* sp. algal culture mixtures using spectral FCM analyzer SP6800. Spectral data of all cells (**a**) in the mixture were visualized in 488 nm laser excitation (**b**) and 405 nm laser excitation (**c**) spectrum charts. Based on the most variable spectral regions, combination of virtual filters corresponding to spectrum regions in channels 12–14 (488 nm excitation) and channel 32 (488 nm excitation) (**d**) were selected to achieve the best discrimination of the two cell populations. Spectra of populations gated in **d** were then plotted to confirm the identity of discriminated populations (**e** and **f**)

3.4 Preparation of Spectral Data for PCA

1. Open Analysis window in the SP6800 software.
2. Send the experiment containing recorded data of the single cultures and mixtures of the cultures into the "Public" access folder by selecting the experiment folder and clicking "Send to public" button in the upper Analysis tab.
3. Go to the Experiment folder in the Public database.
4. Export cells to be analyzed (100–500 cells) from a gated region of interest into a separate file in the format compatible with the Unscrambler X software.

3.5 PCA of Phytoplankton Spectral Data

1. In the Unscrambler X software, import data in the Excel format under the "File" tab.
2. In the Excel preview window, select Excel sheet to be analyzed, check that the dataset is correctly highlighted, and press OK.
3. In the appeared data table, create an additional column before the B1 channel column.
4. Select the column and change data type to text by right-clicking. Select range of cells corresponding to one population and press Fill by right-clicking to enter the name of the population (e.g., *Cryptomonas*). Repeat the same for the other population (s).
5. Select the whole column and change the data type to Category.
6. Right-click on the selected column and press Create Colum range and enter the title of the data in the appeared box in the left panel (e.g., Species).
7. Select columns with channel values and right-click to create a column range under a title (e.g., Spectra).
8. When the column ranges are created, proceed to Analyze—principal component analysis command under the "Tasks" tab.
9. Choose the column range to be analyzed in the "Cols" tab (e.g., spectra) in the Setup window and set preferences in Weights, Validation, and Algorithm tabs.
10. Click "Finish," and PCA is conducted with display of associated plots (Fig. 3).

4 Notes

1. For acquisition of highly autofluorescent microalgae cultures with Imagestream X to prevent a saturation of images, the absolute requirement is minimizing the power of the laser and/or using notch filter for red laser (Chroma Tech 642 notch filter) [23].

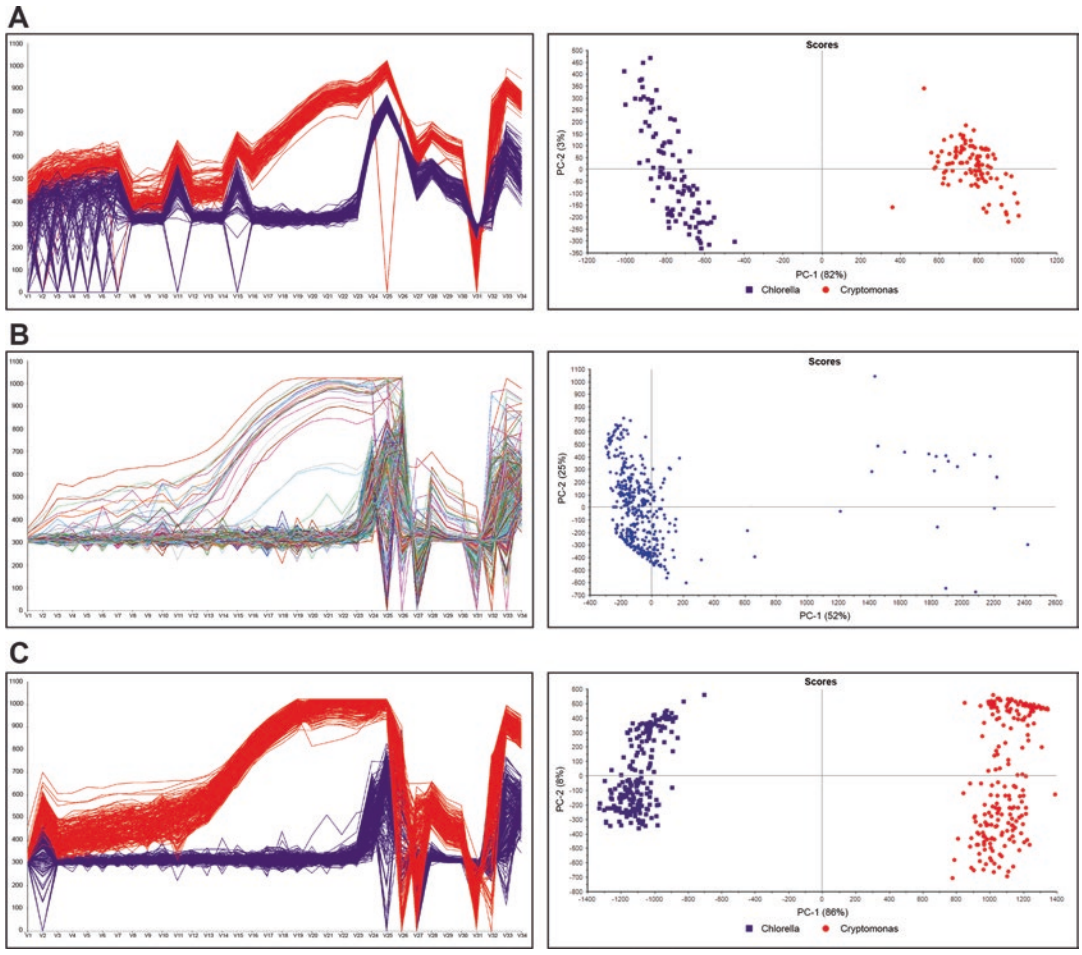

Fig. 3 Principal component analysis (PCA) performed for spectral data of *C. pyrenoidifera* and *Chlorella* sp. algal cultures. **a**—Projection of spectra of individual cells (left) of artificially mixed algal cultures onto the plane of the first two principal components (PC) (right). **b**—Projection of spectra of individual cells (left) of physical mixture of algal cultures onto the plane of the first two PCs (right). **c**—Projection of spectra of individual cells (left) of FCM gated populations based on virtual filtering from the mixture of algal cultures onto the plane of the PC1 and PC2 (right)

2. Some applications may require a maximal magnification on Imagestream instrument (60×); however, it would have a reverse effect on speed of acquisition (a max speed of acquisition corresponds to a min magnification (20×)). You can increase a speed of sample acquisition by using higher sample concentration such as 20–30 × 10^6 cells/ml. Though there is no effect on imaging quality data from higher sample concentrations (CCD camera has no dead time), there is a danger to clog the instrument.
3. When acquire algal sample with INSPIRE software and Imagestream X Mark II, use a live gating on scattergram with

parameters "Area" vs. "Aspect ratio" to exclude speed beads, debris, and aggregates. The instrument may not be suitable for some bulky diatoms due to limitations of flow cell size. Minimize magnification, if you need to image microalgae of large size. However, we successfully acquired filamentous cyanobacteria up to 500 μM length even with 60× magnification.

4. Additional cleaning of the instrument following sample acquisition is advisable for microalgal cultures. Consider to wash instrument with water, then diluted 10% bleach, and then again water between algal samples. If you clog flow cell, it is necessary to run a sample vial with diluted Contrad or heated bleach solution.
5. For spectral FCM analysis of phytoplankton mixtures, it is important to decrease the gain of 24–30 PMT channels to 2 and leave the rest of the channels with a max gain of 8 to enhance the non-chlorophyll-associated spectral differences between the strains/species.
6. Extracted spectral data of some phytoplankton populations may have a remarkably high number of cells with 0 values in channels 24–27 which may be associated with low chlorophyll signal due to dying of the cells. To reduce the cell heterogeneity within the sample, cells with no chlorophyll signal can be removed from the population before the further statistical analysis.

Acknowledgments

Support for this work was provided by grants from MES of Republic of Kazakhstan #4350/ГФ4 and PI NURIS 055 project #100/14 to N.S.B. We are grateful to Steve Conway and Greg Veltri, Sony Biotechnology Inc., and John Daley, Dana-Farber Cancer Institute, for access to spectral flow cytometer and to Brian Hall and Richard De Marco (Amnis-Merck) for their advice. Veronika Dashkova, Ivan A. Vorobjev, and Natasha S. Barteneva contributed equally to this work.

References

1. Moon-van der Staay SY, De Wachter R, Vaulot D (2001) Oceanic 18S rDNA sequences from picoplankton reveal unsuspected eukaryotic diversity. Nature 409:607–610
2. Béjà O, Suzuki M, Heidelberg J, Nelson W, Preston C, Hamada T et al (2002) Unsuspected diversity among marine aerobic anoxygenic phototrophs. Nature 415:630–633
3. Irigoien X, Huisman J, Harris R (2004) Global biodiversity patterns of marine phytoplankton and zooplankton. Nature 429: 863–867
4. Davey HM, Kell DB (1996) Flow cytometry and cell sorting of heterogeneous microbial populations: the importance of single-cell analyses. Microbiol Rev 60:641–696

5. Sukenik A, Hadas O, Stojkovic S, Malinsky-Rushansky N, Viner-Motzini Y, Beardall J (2009) Fluorescence microscopy reveals variations in cellular composition during formation of akinetes in the cyanobacterium *Aphanizomenon ovalisporum*. Eur J Phycol 44:309–317
6. Stolte W, Kraay GW, Noordeloos AA, Riegman R (2000) Genetic and physiological variation in pigment composition of *Emiliania huxleyi* (*Prymnesiophyceae*) and the potential use of its pigment ratios as a quantitative physiological marker. J Phycol 36:529–539
7. Dapena C, Bravo I, Cuadrado A, Figueroa RI (2015) Nuclear and cell morphological changes during the cell cycle and growth of the toxic dinoflagellate *Alexandrium minutum*. Protist 166:146–160
8. Brussaard CP, Marie D, Thyrhaug R, Bratbak G (2001) Flow cytometric analysis of phytoplankton viability following viral infection. Aquat Microb Ecol 26:157–166
9. Veldhuis MJ, Cucci TL, Sieracki ME (1997) Cellular DNA content of marine phytoplankton using two new fluorochromes: taxonomic and ecological implications. J Phycol 33:527–541
10. Franklin DJ, Airs RL, Fernandes M, Bell TG, Bongaerts RJ, Berges JA, Malin G (2012) Identification of senescence and death in *Emiliania huxleyi* and *Thalassiosira pseudonana:* cell staining, chlorophyll alterations, and dimethylsulfoniopropionate (DMSP) metabolism. Limnol Oceanogr 57:305–317
11. Zheng W, Rasmussen U, Zheng S, Bao X, Chen B, Gao Y, Guan X, Larsson J, Bergman B (2013) Multiple modes of cell death discovered in a prokaryotic (cyanobacterial) endosymbiont. PLoS One 8:e66147
12. Lee DH, Bae CY, Han JI, Park JK (2013) In situ analysis of heterogeneity in the lipid content of single green microalgae in alginate hydrogel microcapsules. Anal Chem 85:8749–8756
13. Traller JC, Hildebrand M (2013) High throughput imaging to the diatom *Cyclotella cryptica* demonstrates substantial cell-to-cell variability in the rate and extent of triacylglycerol accumulation. Algal Res 2:244–252
14. Ning SB, Guo HL, Wang L, Song YC (2002) Salt stress induces programmed cell death in prokaryotic organism Anabaena. J Appl Microbiol 93:15–28
15. Franklin DJ (2014) Explaining the causes of cell death in cyanobacteria: what role for asymmetric division? J Plankton Res 36:11–17
16. Bidle KD (2016) Programmed cell death in unicellular phytoplankton. Curr Biol 26:R594–R607
17. Ross C, Santiago-Vázquez L, Paul V (2006) Toxin release in response to oxidative stress and programmed cell death in the cyanobacterium Microcystis aeruginosa. Aquat Toxicol 78: 66–73
18. Ding Y, Gan N, Li J, Sedmak B, Song L (2012) Hydrogen peroxide induces apoptotic-like cell death in *Microcystis aeruginosa* (*Chroococcales, Cyanobacteria*) in a dose-dependent manner. Phycologia 51:567–575
19. Sieracki CK, Sieracki ME, Yentsch CS (1998) An imaging-in-flow system for automated analysis of marine microplankton. Mar Ecol Prog Ser 168:285–296
20. Dashkova V, Malashenkov D, Poulton N, Vorobjev I, Barteneva NS (2017) Imaging flow cytometry for phytoplankton analysis. Methods 112:188–200
21. George TC, Basiji DA, Hall BE, Lynch DH, Ortyn WE, Perry DJ, Seo MJ, Zimmerman CA, Morrissey PJ (2004) Distinguishing modes of cell death using the ImageStream® multispectral imaging flow cytometer. Cytometry A 59:237–245
22. Zmerli Triki H, Laabir M, Daly-Yahia OK (2015) Life history, excystment features, and growth characteristics of the Mediterranean harmful dinoflagellate *Alexandrium pseudogonyaulax*. J Phycol 51:980–989
23. Hildebrand M, Davis A, Abbriano R, Pugsley HR, Traller JC, Smith SR, Shrestha RP, Cook O, Sánchez-Alvarez EL, Manandhar-Shrestha K, Alderete B (2016) Applications of imaging flow cytometry for microalgae. In: Barteneva NS, Vorobjev IA (eds) Imaging flow cytometry: methods and protocols. Humana Press, New York, pp 47–67
24. Dashkova V, Segev E, Malashenkov D, Kolter R, Vorobjev I, Barteneva NS (2016) Microalgal cytometric analysis in the presence of endogenous autofluorescent pigments. Algal Res 19: 370–380
25. Paau AS, Oro J, Cowles JR (1978) Application of flow microflorometry to the study of algal cells and isolated chloroplasts. J Exp Bot 29:1011–1020
26. Trask BJ, Van den Engh GJ, Elgershuizen JH (1982) Analysis of phytoplankton by flow cytometry. Cytometry 2:258–264
27. Yentsch CM, Horan PK, Muirhead K, Dortch Q, Haugen E, Legendre L, Murphy LS, Perry MJ, Phinney DA, Pomponi SA, Spinrad RW (1983) Flow cytometry and cell sorting: a technique for analysis and sorting of aquatic particles. Limnol Oceanogr 28:1275–1280
28. Olson RJ, Frankel SL, Chisholm SW, Shapiro HM (1983) An inexpensive flow cytometer for

the analysis of fluorescence signals in phytoplankton: chlorophyll and DNA distributions. J Exp Mar Biol Ecol 68:129–144

29. Yentsch CM, Horan PK (1989) Cytometry in the aquatic sciences. Cytometry 10:497–499
30. Olson RJ, Zettler ER, Chisholm SW, Dusenberry JA (1991) Advances in oceanography through flow cytometry. In: Demers S (ed) Particle analysis in oceanography, vol 27 of the NATO ASI series. Springer, Berlin Heidelberg, pp 351–399
31. Vives-Rego J, Lebaron P, Nebe-von Caron G (2000) Current and future applications of flow cytometry in aquatic microbiology. FEMS Microbiol Rev 24:429–448
32. Hyka P, Lickova S, Přibyl P, Melzoch K, Kovar K (2013) Flow cytometry for the development of biotechnological processes with microalgae. Biotechnol Adv 31:2–16
33. Olson RJ, Sosik HM (2007) A submersible imaging-in-flow instrument to analyze nano- and microplankton: imaging FlowCytobot. Limnol Oceanogr Methods 5:195–203
34. Robinson JP (2004) Multispectral cytometry: the next generation. Biophotonics Int 11: 36–40
35. Goddard G, Martin JC, Naivar M, Goodwin PM, Graves SW, Habbersett R, Nolan JP, Jett JH (2006) Single particle high resolution spectral analysis flow cytometry. Cytometry A 69:842–851
36. Futamura K, Sekino M, Hata A, Ikebuchi R, Nakanishi Y, Egawa G, Kabashima K, Watanabe T, Furuki M, Tomura M (2015) Novel full spectral flow cytometry with multiple spectrally adjacent fluorescent proteins and fluorochromes and visualization of in vivo cellular movement. Cytometry A 87:830–842
37. Sanders CK, Mourant JR (2013) Advantages of full spectrum flow cytometry. J Biomed Opt 18:037004
38. Nolan JP, Condello D, Duggan E, Naivar M, Novo D (2013) Visible and near infrared fluorescence spectral flow cytometry. Cytometry A 83:253–264
39. Talmi Y (1975) Applicability of TV-type multichannel detectors to spectroscopy. Anal Chem 47:A658
40. Wade CG, Rhyne RH, Woodruff WH, Bloch DP, Bartolomew JC (1979) Spectra of cells in flow cytometry using a vidicon detector. J Histochem Cytochem 27:1049–1052

Chapter 6

X-Ray Fluorescence-Detected Flow Cytometry

Andrew M. Crawford and James E. Penner-Hahn

Abstract

X-ray fluorescence-detected flow cytometry can enable the detection and characterization of ultra-trace, trace, and bulk elemental content at the cellular level using synchrotron-induced x-ray emission from fully aquated actively respiring cells. Although very much still a technique in development, this technique has been used to characterize cell-to-cell elemental variability in bovine red blood cells, *Saccharomyces cerevisiae*, and NIH3T3 mouse fibroblasts. Herein we describe the experimental setup and the key methodological aspects of data collection and processing.

Key words Cytometer, Cells, Flow cytometer, X-ray fluorescence, Metallome

1 Introduction

Several techniques are capable of trace element detection on single cells, including mass spectrometry, metal-specific organic fluorophores, and intrinsic x-ray fluorescence (XRF) [1–4]. Mass spectrometry has a wide dynamic range and excellent detection limits [5]. Unfortunately, mass spectrometry can suffer from matrix effects, with ionization efficiency depending both on the metal oxidation state and the local environment (e.g., matrix) such that it can be challenging to identify suitable calibration standards for an unknown system [6]. Metal-specific organic fluorophores are suitable to study living organisms allowing time resolved in vivo investigations [7] and, due to the penetration depth of visible light, allowing for three-dimensional fluorescence measurements [8]. However, the fluorescence depends not only on metal concentration but also on local fluorophore concentration and the fraction of metal that is available for fluorophore binding, making it difficult to determine total cellular metal content.

In XRF spectroscopy, one detects the intrinsic x-ray fluorescence that results from excitation of a core electron, and thus no fluorophore is required. Any ionizing radiation can be used to excite XRF; in this work, we make use of x-ray excitation from

Natasha S. Barteneva and Ivan A. Vorobjev (eds.), *Cellular Heterogeneity: Methods and Protocols*, Methods in Molecular Biology, vol. 1745, https://doi.org/10.1007/978-1-4939-7680-5_6,

intense synchrotron sources. Each element has characteristic x-ray emission lines, thus allowing simultaneous multielement detection. Because the x-ray absorption cross section and the x-ray fluorescence yield are essentially independent of chemical environment, it is straightforward to measure a universal calibration curve, allowing accurate quantitation. With the intense x-rays available at modern synchrotron x-ray sources, XRF can be used to determine the metal composition of individual cells with micromolar detection limits for elements from ~P through Zn. Although XRF can also be used for heavier elements, such as Mo, this requires higher energy x-ray excitation, resulting in decreased sensitivity for the lighter elements. These properties make XRF an ideal tool for interrogating the cellular metallome.

Most of the applications of XRF to biological samples have focused on XRF imaging, and this is one of the most sensitive techniques for trace element detection in biological samples [1, 9–12]. In the present, we have constructed an instrument which emphasizes high throughput rather than high spatial resolution. We use a microfluidic flow cytometer to pass fully aquated cells through an x-ray beam to allow determination of the metal composition of cells at rates close to 1 Hz. This relatively low sampling rate in comparison with conventional flow cytometry is determined by the time required to obtain an adequate signal/noise ratio and could in principle be increased in studies of bulk elements or by improvements in x-ray detection efficiency.

2 Materials

Prepare and store all solutions and reagents using MilliQ® ddH_2O (unless indicated otherwise).

2.1 Sample Preparation

Cell cultures should be diluted using an appropriate buffering media. The cell density should be low enough that it is rare for two cells to overlap in the x-ray beam but high enough that cells pass the x-ray beam as often as possible (*see* **Note 1**). The optimal concentration will depend on the capillary size; if the capillary diameter is much larger than the cell diameter, a high cell concentration means that there will frequently be two cells that cross the x-ray beam at the same time, complicating analysis. If the capillary and cell diameter are similar, the concentration can be as high as 10–20% of the total volume.

Example: Experiments using trypsinized bovine red blood cells (bRBCs, 0.1 hematocrit, obtained from Lampire) were performed in [13, 14] with a 50 μm i.d. capillary, samples diluted 1:30 using phosphate-buffered saline (PBS).

2.2 Standard Reference Solutions

Prepare standard reference solutions of the appropriate elements from the corresponding nitrate salts using the appropriate concentration of Na_2EDTA to ensure 99.9% chelation of all elements in solution. Ion chelation with EDTA prevents hydroxide formation and subsequent precipitation of some of the metal ions. For the first transition series, the Kβ emission for an element with atomic number Z overlaps the Kα emission of the element with atomic number $Z + 1$. For this reason, it is best to choose standard elements that are separated by 2 (or more) in atomic number. Ideally, the atomic numbers of the elements in the standard should span the range of elements that are of interest.

Example: In refs. 13, 14, three different concentrations of $Cr(NO_3)_3$, $Fe(NO_3)_3$, $Ni(NO_3)_2$, and $Zn(NO_3)_2$ were prepared in water (pH = 10.0; [EDTA] = 1 mM) . Metal concentrations (0.1–0.5 mM) were chosen to span the expected concentrations in biological samples. The metal concentrations of the standards were verified by ICP-OES pre- and post-experiment.

2.3 Capillary Material

Capillaries can be either hydrophilic or hydrophobic. Hydrophilic capillaries are easier to work with since samples can be loaded using capillary action. However, hydrophilic capillaries are generally found to contain higher levels of contaminant transition metal ions. Hydrophobic capillaries have lower metal ion contaminants and therefore give lower detection limits but must be loaded using negative pressure.

2.4 Visible-Light Microscope (Three of Each; See Note 2)

1. 2×—InfiniTube Mounting C-Clamp with ¼–20.
2. ¼″ × 48″, flexible fiber-optic light guide.
3. 2×—¼″ light guide adapters.
4. Fiber-optic illuminator.
5. Fiber-optic focusing lens.
6. 2×—fiber-optic focusing lens clamps.
7. 1×—Mitutoyo, M Plan Apo 5×/10× objective.
8. 1×—Infinitube Standard with iris diaphragm.
9. 1×—Edmund Optics 5012C, Color GigE Camera.
10. IDS Camera Manager and μEye Cockpit software (*see* **Note 3**).

3 Methods

3.1 Instrument Alignment and Calibration

This section describes the process of characterizing the incident x-ray beam, determining the conversion factor from measured counts to sample mass, and physically preparing and aligning the instrument at the synchrotron. The cytometer consists of three independent units: the twin vertical cameras in the hutch, the

sample holder, and a loading station with a single vertical microscope stationed in the wet lab. The sample holder is designed to be able to dock with the kinematic mount in the hutch or the loading station (*see* **Note 4**).

3.1.1 Measuring and Calculating the Beam Profile

For correct signal quantitation, the x-ray beam profile must be measured:

1. Measure the profile of the incident x-ray beam along the horizontal and vertical directions using a knife-edge scan by moving a sample of uniform thickness with a very straight and clean edge (analogous to a knife's edge) into the beam keeping its edge perpendicular to the direction of travel.
2. As the sample moves through the beam, record the intensity of detected fluorescence of the knife-edge material or absorbance (calculated as the $\log(I_0/I_1)$, where I_0 and I_1 are the upstream and downstream ion chambers, respectively). The measured signal, S, when the edge is at $x = b$ is $S(b) = \int_{b}^{-\infty} I(x)\,dx$, where I is the intensity ratio (normalized fluorescence or absorbance of the x-ray beam).
3. Calculate the beam profile by taking the numerical first derivative of the knife-edge scan and normalizing it to a maximum value of 1.

3.1.2 Mass Calibration and Sensitivity Calibration Slopes

The measured signal, fluorescence counts normalized by the upstream ion chamber reading, is converted to concentration using a calibration curve:

1. The total mass of a given element that is illuminated by the x-ray beam depends both on the concentration of the element in the standard and on the volume that is irradiated. This can be calculated as:

$$mass(fg) = h \times \pi r^2 \times c \times 10^9$$

   where h is the height (cm) of the vertical beam profile (±95%), r is the inner radius (cm) of the capillary, and c is the solution concentration (mg/L) for the given element reported from ICP-OES.
2. The sensitivity is the slope of the straight line fit of XRF intensity normalized by I_0 vs mass and is in units of counts I_0^{-1} fg^{-1}.
3. To estimate the sensitivity for elements where there isn't a calibration standard, interpolate the measured sensitivity for those elements (*see* **Note 5**).

3.2 Mounting and Loading the Capillary

Since movement in the hutch is limited and this step can be time-consuming, mounting and loading the capillary are performed in the wet lab using a sample loading dock.

3.2.1 Mounting the Capillary

The capillary material should be mounted between the two extended arms of the sample holder (Fig. 1):

1. Cut about 20 cm of a capillary and place the piece of capillary material on a smooth, clean surface (*see* **Note 6**).

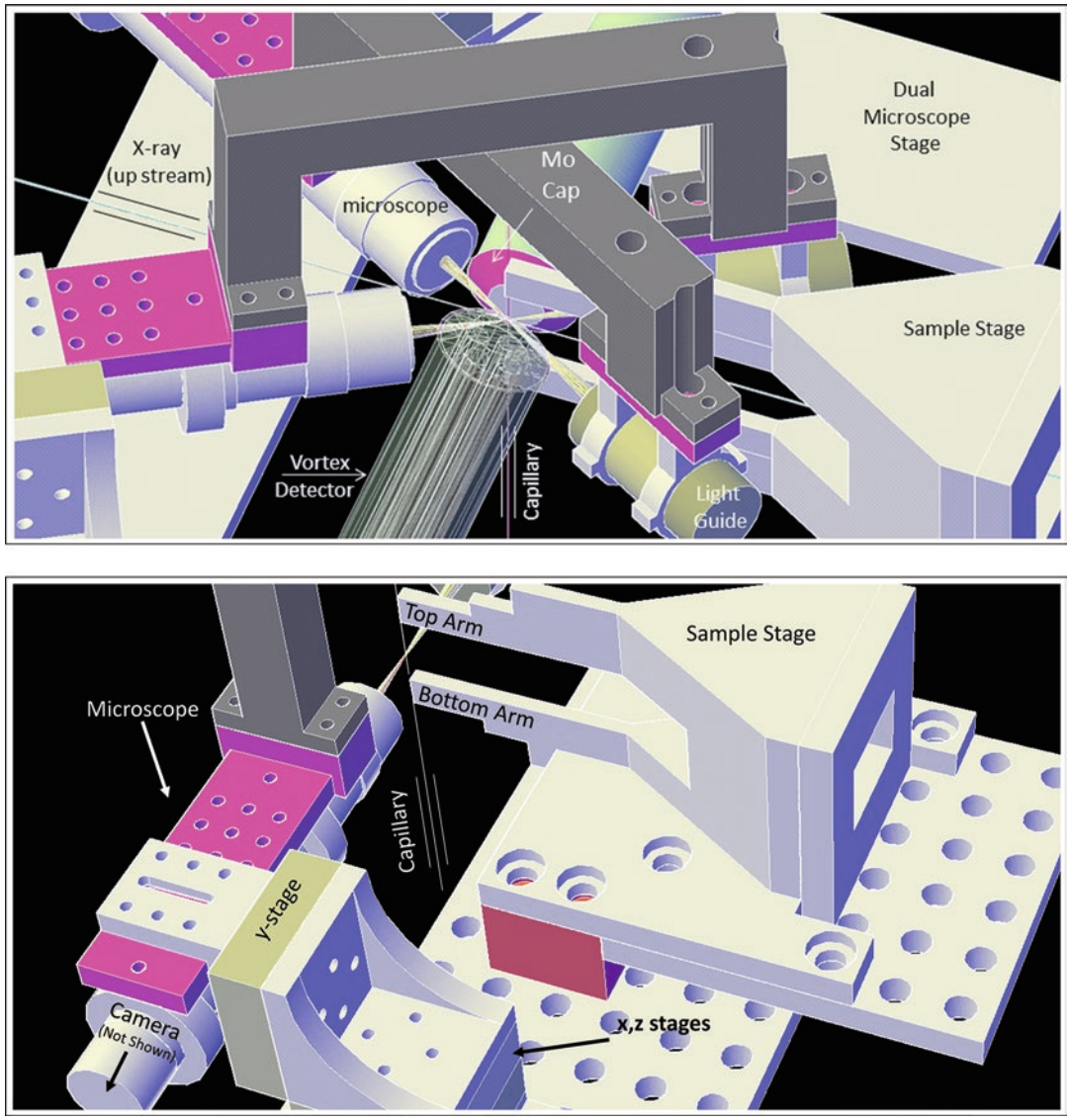

Fig. 1 Schematic illustration of the instrument. (Top) The two horizontal microscopes, the sample holder, and the XRF detectors (Reproduced with permission of the International Union of Crystallography (http://journals.iucr.org/) [14]). (Bottom) The loading station, the sample holder indicating the top and bottom arms, the microscope, and the associated *x*, *y*, *z* stages. Design schematics for construction are available on request

2. With the capillary material stretched out in a straight line, place a piece of tape (~4 cm × 0.5 cm), and press the center of it down on the capillary (~3 cm above the center of the capillary length), such that the capillary traverses the tape in a straight line and is not crinkled.
3. Lift up the piece of tape with the capillary adhered to the back (*see* **Note 7**).
4. With the tape stretched out and the capillary straight up and down, line up the capillary with the top arm of the sample holder, and gently press the tape and capillary onto the sample holder arm.
5. Wrap the tape around the side of the sample holder arm to secure it in place (*see* **Note 8**).
6. With the capillary hanging down from the top sample holder arm, gently position the capillary in front of the lower sample arm and gently push a piece of tape (~4 cm × 0.5 cm) onto the capillary.
7. Gently pull the capillary taut between the upper and lower sample holder arms.
8. Keeping the capillary taut, press the capillary and tape gently onto the lower sample holder arm positioning the capillary so that it is vertical.
9. Repeat **step 5**.

3.2.2 Capillary Loading (Hydrophobic Capillaries)

This section introduces how to load hydrophobic capillaries. A syringe is used to initially fill the capillary and to establish a syphon pump to move the cells past the x-ray beam (*see* **Note 9**):

1. Fill 1000 μL pipette tips with a PDMS mixture using a 10% cross-linking agent and allow to cure for 24 h. In order to prevent the PDMS from leaking out before it is cured, the bottom of the pipette tip is packed with a small piece of tissue (e.g., Kimwipes®).
2. Use a razor blade to cut off the end of the pipette tip that was packed with the tissue leaving a column of cured PDMS surrounded by the remaining pipette tip.
3. Insert an 18-gauge hypodermic needle through the PDMS.
4. Attach a 50 mL syringe to the needle and force air through the needle to remove any PDMS that is lodged in the needle.
5. Insert the capillary into the tip of the needle.
6. In order to seal the capillary to the needle, carefully slide the PDMS/pipette tip relative to the needle/capillary until the PDMS covers the needle/capillary junction. This is the receiving end of the capillary. If one is not careful when sliding

the PDMS, the needle can slice the capillary such that there is no suction (**step 8**).

7. Submerge the other end of the capillary (the loading end) into a cuvette containing the sample solution.
8. Using the syringe, apply negative pressure to pull the sample through the capillary until the entire length of the capillary is filled.
9. Once the capillary is loaded, bring the receiving end of the capillary to a relative height lower than the sample cuvette at the loading end of the capillary.
10. Keeping the receiving end at a relative height lower than both the loading end and the sample cuvette, cut the capillary free from the syringe using a fresh 0.09 mm razor blade (*see* **Note 10**). If the loading was successful, cells should be flowing in the capillary which can be seen by the microscope video.
11. With the receiving end still maintained at relative height lower than both the loading end and the sample cuvette (*see* **Note 11**), insert the freshly cut end of the capillary into a second sample holder for receiving. This forms a syphon pump. Cell velocity can be adjusted by changing the relative heights of the two sample holders. It is important to make sure that the receiving end of the capillary is always at a lower relative height than the loading end until the syphon has been established to make sure no air enters into the capillary.
12. In principle, once the capillary is aligned and the flow of cells is initiated, measurements could be continued until sufficient cells have been measured. In practice, radiation damage leads to capillary discoloration, interfering with cell tracking. For this reason, scans are limited to 5–10 min.

3.2.3 Capillary Loading (Hydrophilic Capillaries)

Hydrophilic (acrylic) capillaries can be loaded using simple capillary action. To achieve adequate cell flow, perform the following steps:

1. With the sample holder at the bottom and the capillary rising straight up from the sample holder, submerge the loading end of the capillary into a freshly agitated sample culture solution.
2. Capillary action results in measured cell velocities on the order of ~1 mm/s (with 50 μm i.d.). This velocity is far too fast for sufficient XRF detection.
3. Wait until the sample solution passes the view of the camera frame (at 1 mm/s and a distance of ~10 cm between the loading end and the camera view, this will take ~5 min).
4. To slow the cell solution, curve the end of the capillary and place a droplet of water over the terminal end of the capillary, sealing it and trapping a pocket of air (*see* **Note 12**). This

results in a 1000× decrease in cellular velocity (final velocity on the order of ~5 μm/s). As the droplet slowly evaporates, the air pocket rises resulting in an upward flow of cells.

3.3 Positioning the Capillary

The cameras are independently mounted on their *x*, *y*, *z* translation stages. In the following, *z* is defined as vertical, *y* is defined as the camera-capillary vector (i.e., the focus of the camera), and *x* is a motion perpendicular to the capillary-camera vector:

1. With the capillary mounted on the sample holder, use the *x* and *z* microstages to adjust either the position of the sample holder (in the hutch) or the microscope (in the wet lab when using the loading station) (*see* **Note 13**).
2. Adjust lighting (*see* **Note 14**) and camera sensitivity to maximize the contrast between the capillary and the background (*see* **Note 15**).

3.4 Locating the X-Ray Beam with the Twin Microscopes

The sample holder and capillary are positioned in the focal spot of the x-ray beam, using the sample holder's *x*, *y*, *z* stage. The twin microscopes are then brought to focus on the capillary and translated vertically to the beam spot on the capillary. For this section the *y*-axis is vertical, the *z*-axis is the vector along the x-ray beam direction, and the *x*-axis runs between the detector and the capillary. It is assumed that prior to beginning this process, the x-ray fluorescence detectors have been aligned such that they are centered on the focus of the x-ray beam:

1. The location of the x-ray beam is determined using a third x-ray positioning camera, fixed relative to the x-ray experimental table, such that the camera does not move when the cytometer is adjusted (*see* **Note 16**). Using an x-ray fluorescent screen, the location of the x-ray beam is determined, and this location is marked on a video output from the x-ray positioning camera.
2. The x-ray fluorescent screen is removed and replaced with the cytometer. The approximate positioning of the capillary in the x-ray beam can be accomplished visually using the x-ray positioning camera and optimized by scanning *x* while measuring either the transmitted x-ray intensity or, with greater sensitivity, the fluorescence of the calibration standard as the cytometer is scanned along *x* and *z*.
3. Once the capillary position has been optimized, the x-ray beam is left on the capillary for several minutes. This is sufficient to cause noticeable discoloration of the capillary. This, in turn, is used to vertically adjust the microscope positions so that the center of the microscope is aligned with the x-ray beam.
4. Once adjusted, the 3D position of the twin microscopes should not need to be changed (*see* **Note 17**).

4 Data Analysis

To deconvolve the measured signal, which may include XRF from multiple cells, one needs to know the path of each cell through the beam at every point in time. Since there is very little contrast in either x-ray absorption or scattering between cell and solution, cell detection relies on visible-light microscopy. Video data is collected synchronously with XRF using a visible-light microscope. The experimental apparatus is shown schematically in Fig. 1. It incorporates two horizontal visible-light microscopes (Mitutoyo, M Plan Apo 5×/10× objective; Infinitube Standard with iris diaphragm; Edmund Optics 5012C, Color GigE Camera). By using two microscopes arranged as close to perpendicular as possible, one can determine the three-dimensional position of each cell. This section describes the process for aligning the video data with the XRF signal and for using this alignment to convert the measured fluorescence into the cellular composition.

4.1 Post Collection Processing of Video Data

Quantitative analysis requires knowing when and for how long each cell overlaps with which portion of the x-ray beam, since these, together with the metal composition of the cell, determine the time dependence of the XRF. The key to determining this correlation rests in determining a cell-area-in-beam-trace (CAIBT). The steps in processing the video data are to use the microscope images to identify cells, determine the path followed by each cell, use this path to determine the time points at which each cell was in the beam and the area of the cell that was illuminated during those times, and estimate the fluorescence signal as a function of time for each cell.

4.1.1 Video Data: Separation of Cell and Non-cell

Each cell is fitted as an ellipse, giving the cell's center (x, y), the ellipse size (r_{minor}, r_{major}), and angle (φ), all in the coordinates of the video frame:

1. Several frames are selected as "seeds" for manual video parameter optimization (*see* **Note 18**).
2. For each frame, a blank (*see* **Note 19**) is subtracted, and an intensity threshold is set (which best suits all selected seeds) to generate a binary mask of the cell (1) and non-cell (0) that corresponds to the visual image. Once a binary mask is generated, a size threshold is set to minimize the false identification of noise as a cell. The intensity and size thresholds are then held constant and used for all remaining frames.
3. For each frame, every group of 8-connected (*see* **Note 20**) cell pixels from the resulting binary masks is fit with an ellipse.

4.1.2 Connecting the Centroids to Create Tracks

To determine the path of each cell through the beam, the centroids from each video frame need to be assigned to specific cells. For the most part, discriminating cells and determining their tracks can be done automatically by considering three points. (1) Based on average cell velocity (mean frame to frame displacement), there is a maximum allowable frame-to-frame displacement, D_1, between the centroids for a single cell. (2) To discriminate against video noise, which can occasionally mimic a cell, it is helpful to set a minimum number of frames, F_1, in which centroids must be present. (3) Similarly, video noise and x-ray-induced capillary discoloration can occasionally cause a cell to be missed in one or more frames. To account for frames where a cell may be "lost" and then later "found," it is useful to set a maximum number of frames, F_2, from which a cell can be missing. The automatically assigned cell tracks should be compared visually with the video and manually adjusted when necessary. With properly chosen thresholds (typically, $D_1 = 3$, $F_1 = 300$, $F_2 = 15$; though these might vary slightly depending on cell velocity and video quality), we found a manual intervention to be required less than 5% of the time.

4.1.3 Initial Video Rotation and Placement of the Vertical Beam Profile

1. The measured beam profile is first interpolated onto the x, y grid of the video image.
2. An initial alignment of the beam relative to the capillary is made based on the visual discoloration of the capillary due to radiation damage as visualized using the last video frame. Although both the capillary and the video camera are nominally vertical, we find in practice that alignment of the beam profile with the beam image requires both a vertical adjustment and a small rotation (*see* **Note 21**).

4.1.4 Cell-Area-in-Beam-Trace

1. The track information for each cell is combined with the beam profile to give an output array containing the convolution of each cell's vertical profile (the summation of its ellipse's area along each row of pixels) with the vertical profile of the beam. This is the cell-area-in-beam-trace or CAIBT.
2. The CAIBT is an $M \times N$ array, where M is video frame index and N is cell index. The columns of this array are each normalized to a maximum of one (*see* **Note 22**).
3. The CAIBT represents the fluorescence counts that would be detected for each cell if all cells had the same elemental mass, regardless of cell size, homogenously distributed throughout the cell. Summation along a row of the CAIBT gives a number that is proportional to the XRF signal that is expected at that time point. Summation down a column of the CAIBT gives the integrated counts for that cell.

4. The calculated CAIBT depends on the vertical positioning of the beam profile and the rotation of the video image. These values are refined iteratively (see next section).

4.1.5 Aligning Video Data with XRF DFC Data

1. Although the frame rate of the XRF (~4 Hz) and the video data (~20 Hz; *see* **Note 23**) are in principle well defined, they are not experimentally synchronized. For that reason, the nominal ratio is set initially and then treated as an adjustable parameter. Similarly, the relative start time of the video and the XRF traces is not precisely defined; this too is treated as an adjustable parameter (*see* **Note 24**).
2. Using the fitted fluorescence signal from the element with the greatest signal intensity, the preliminary CAIBT matrix is used to calculate the expected fluorescence signal from each cell (*see* **Note 25**). For bRBCs, we used Fe. This expected fluorescence signal is fitted to the measured fluorescence signal, with the relative frame rates, relative start times, and the fraction of counts from each cell at each time point as variable parameters. If the initial placement of the beam profile relative to the video was perfect, this would give the fitted counts for that element for each cell.
3. A grid search of vertical profile position and rotation is performed and the fitting repeated to refine the placement of the beam profile (*see* **Note 26**).

4.2 Determination of the Elemental Composition of each Cell

Once the beam alignment and time-base alignment have been optimized, the CAIBT can be used in conjunction with the measured XRF to give the metal quantitation for each cell:

1. If each cell moved at a constant velocity, Eq. 1 could be used to calculate the total mass of each element in each cell:

$$\text{Mass}\left(\text{fg}\right) = \frac{\text{XRF} \times \text{Integration Time} \times \text{Cell Velocity}}{\text{Mass Calibration} \times \text{Beam Height}} \qquad (1)$$

   where XRF is the integrated signal from the cell (i.e., the sum of the measured counts for each data point) normalized to incident intensity (I_0) and is in units of counts I_0^{-1}, integration time is the measurement time for each data point in units of s, cell velocity is in units of μm s^{-1}, mass calibration is in units of counts × fg^{-1} × I_0^{-1}, and beam height is in units of μm.
2. In practice, cells follow non-ideal paths through the beam, due to the relatively slow flow rate, the possibility of cell interactions with the wall, and convection currents caused by heating from the beam. As a consequence, cells may spend longer or shorter than expected time in the beam, giving higher or lower total counts. As long as a cell equally samples all positions vertically along the path through the beam, the variation in total

counts will not matter. Unfortunately, in practice, this is never the case.

3. It is very simple to correct for non-ideal paths through the beam. The aligned and fitted data are converted from the time domain (counts, time) to the space domain (counts, *y*-position) (*see* **Note 27**), such that the fitted XRF counts are associated with the vertical position of the cell (or cells). It is now straightforward to integrate the XRF signal over position to give the total metal content of the cell, like the integrations used in XRF imaging.

4.3 Horizontal Correction

Since the beam intensity is not completely uniform horizontally, the measured fluorescence will vary slightly depending on the *x*-coordinate of a cell as it passes through the beam. Using the video data from both microscopes, the horizontal positions of each cell through the beam can be calculated from their apparent *x*- and *y*-coordinates from the fitted ellipses used to calculate the CAIBT. After correcting for the true horizontal position of the cells, if all of the cells contained the same amount of a given element, the measured elemental content would reproduce the measured horizontal beam profile. Cells don't contain identical quantities; however, given enough cells, the beam profile can be scaled vertically to align with the data. The scaled profile is then used to correct for the relative signal seen for variable horizontal cell positions. In work presented by Crawford et al. [14], cells at the peak of the profile had an intensity that was 1.4-fold larger than the average for the capillary, while cells at the edge had an intensity that was approximately two-thirds as large as the average.

5 Notes

1. Although ideal, in practice, at times, this may be difficult due to low velocity. More often than not, one cell will exit the beam as another cell enters the beam. What is important is that no cells have identical paths across the vertical profile of the x-ray beam at the exact same time, i.e., for cells with coordinates (x, y, t) through the beam, two cells cannot have identical y and t. Such a situation is identical to (and mathematically indistinguishable from) a single cell with the combined masses of the two cells. Said differently, the solution set for these two cells will exist along the mathematical plane containing all possible linear combinations of the cells' masses.
2. The best practice with the cytometer includes three cameras and two sample mounts. It was found that it was best to position the capillaries and load them in the wet lab and then move the mounted capillary and sample holder into the hutch.

The twin vertical microscopes in the hutch are used for recording video data, whereas the third camera is used in the wet lab.

3. Camera software came with the Edmund Optics 5012C, Color GigE Camera.
4. To minimize down time between sample changes, you should have two identical sample holders. This allows for one sample holder to be actively running experiments in the hutch, while the other sample holder is being prepared in the wet lab for the next experiment.
5. We found it best to interpolate the elements by dividing each standard element's mass calibration value (units of counts I_0^{-1} fg^{-1}) by the associated absorption cross section and fluorescence yields. The resulting values are then plotted as a function of the associated absorption edge energy and fit to a first-order polynomial such that

$$f(E_i) = \frac{g(E_i)}{C_{Si} F_{Yi}} \tag{2}$$

where $f(E_i)$ is the mass calibration, $g(E_i)$, as a function of absorption edge energy, E_i, normalized by the absorption cross section, $C_{S,i}$ and the fluorescence yield, and $F_{Y,i}$, for element i. Using the associated E_i, the output from Eq. 2 is multiplied by the associated $C_{S,i}$ and $F_{Y,i}$ to interpolate the mass calibration for element i.

6. Laminated desktops work great.
7. Be careful not to have any other part of the capillary touch the tape (you most likely won't be able to "unstick" it). Electrostatic interactions of the capillary can make this difficult.
8. Folding over a small piece of each end of the tape will make it much easier to change out the capillary for a new one later.
9. The purpose of the PDMS in this step is to act as a seal between the capillary and the hypodermic needle.
10. A fresh razor blade is necessary for a clean cut; otherwise the capillary may collapse and seal.
11. If the receiving end was raised to a relative height higher than either the loading end or the sample cuvette, air will enter the capillary at the receiving end and compromise the syphon pump. If this happens, take the receiving end to the lowest possible elevation relative to both the loading end and the sample cuvette, and wait 30 s. This should result in rapid capillary flow from the loading end to the receiving end and should force the air out.
12. If the air pocket is not trapped in the capillary, the droplet at the terminal end will enter the capillary and reverse the flow direction, but it will not slow the flow rate. As such, the curve and the trapped air pocket are essential to obtaining an adequate flow rate.

13. When positioning the capillary in the wet lab, the microscope is moved to focus on the capillary and visualize the process. In the hutch, after the microscopes have been focused at the detector-x-ray beam intersection, they are not moved. Rather, the mounted loaded capillary is translated using the microstages of the sample holder until the capillary is in focus with both microscopes. This is the initial position for scanning and is optimized via raster scans of the capillary.
14. The fiber-optic focusing lenses can be equipped with polarization filters which can be used to reduce glare.
15. Subtle changes to the angle of the fiber-optic focusing lenses can be instrumental in reducing glare and improving resolution. This can be done at any time with the microscope at the loading station. However, for the twin microscopes of the cytometer, these should only be adjusted when locating the x-ray beam with the twin microscopes (Subheading 3.4). Otherwise, the fiber-optic focusing lenses should be left alone as modifying these puts a strain on the entire microscope assembly and can (most likely will) change the focus of the microscopes resulting in the user needing to relocate the x-ray beam with the twin microscopes.
16. Later the twin microscopes assume this role, and the third camera is used in conjunction with the twin microscopes to give three angles of view for positioning the capillary.
17. The complete cytometer (capillary + microscopes) consists of two independent units: the microscope and the sample holder. Vertical adjustment of the sample holder and thus repositioning of the capillary relative to the x-ray beam to illuminate new sections of the capillary will not affect the twin vertical microscopes.
18. Seed frames should contain cells in different parts of the frame, providing a good subset for parameter generation (i.e., threshold, approximate cell size in pixels, etc.). Usually, 5–6 seeds provide a decent set of robust parameters.
19. A blank is best calculated as a moving average by taking the mean frame calculated from 1000 frames preceding the current frame through 1000 frames following the current frame.
20. In order to be part of a group of "8-connected pixels," a pixel must touch either an edge or a corner of one of the other pixels in the group.
21. This rotation should be constant across the dataset assuming the cameras were not dismounted and then remounted to the microscope during an experimental run.
22. Alternatively, the columns of the CAIBT can be normalized to a unit area of one. This has the advantage that when the CAIBT is later used to fit the data using linear least squares matrix

inversion, the solved matrix of coefficients will be the total fitted counts for each cell, and no further calculations will be necessary.

23. Video data should always be collected at a higher frequency than XRF data.
24. Since the limiting piece of information is the frame rate of XRF collection, the video data is down-sampled to the XRF frame rate to save on computational resources.
25. If a cell gets stuck in the beam, the apparent fluorescence decreases in a manner consistent with first-order loss of metal.
26. The fitting is performed using a linear least squares matrix inversion at each alignment of the search grid to adjust the amplitudes of the expected fluorescence counts for each cell and then calculate the rmsd from the total fit. Subsequent minimization of the rmsd is the determining factor for the optimal grid location.
27. At each centroid position (x, y), the cell will give a specific number of integrated counts. The y-points are sorted in increasing order, and the corresponding integrated photon counts are reorganized to match the resorting of the y-points. These points are then used to interpolate integrated photon counts that would be associated with every y-position through the beam. Numerical integration is used to calculate the total counts corresponding to the convolution of the beam with a point separation equivalent to the pixel resolution of the camera (e.g., 2.2 μm/pixel) divided by the objective magnification (e.g., 5×). This convolution is now equivalent to the convolution seen for a cell traveling at a velocity of one pixel (distance) per integration (time). For an integration time of 0.25 s with an objective magnification of 5× and a camera pixel resolution of 2.2 μm, this gives a pixel separation of 0.44 μm/pixel and hard-sets the velocity (or the apparent velocity associated with the integration) to 1.76 μm/s. The resulting values for integrated counts and velocity are inserted into Eq. 1 (*see* Section 4.2) to yield the total mass in fg for each element detected for each cell.

Acknowledgment

This research was funded in part by the National Science Foundation under (NSF-IDBR-0852802 to J.E.P.H.) and used resources of the Advanced Photon Source, a US Department of Energy (DOE) Office of Science User Facility operated for the DOE Office of Science by Argonne National Laboratory under Contract No. DE-AC02-06CH11357.

References

1. McRae R, Lai B, Fahrni CJ (2013) Subcellular redistribution and mitotic inheritance of transition metals in proliferating mouse fibroblast cells. Metallomics 5(1):52–61. https://doi.org/10.1039/c2mt20176c
2. Penner-Hahn JE (2014) Technologies for detecting metals in single cells. In: Banci L (ed) Metallomics and the cell, vol 12. Springer, Dordrecht. https://doi.org/10.1007/978-94-007-5561-1_2
3. Zhao FJ, Moore KL, Lombi E, Zhu YG (2014) Imaging element distribution and speciation in plant cells. Trends Plant Sci 19(3):183–192. https://doi.org/10.1016/j.tplants.2013.12.001
4. Kaufmann R, Hagen C, Grunewald K (2014) Fluorescence cryo-microscopy: current challenges and prospects. Curr Opin Chem Biol 20:86–91. https://doi.org/10.1016/j:cbpa.2014.05.007.
5. Nemes P, Vertes A (2012) Ambient mass spectrometry for in vivo local analysis and in situ molecular tissue imaging. TrAC Trends Anal Chem 34:22–34. https://doi.org/10.1016/j.trac.2011.11.006.
6. Becker JS, Matusch A, Becker JS, Wu B, Palm C, Becker AJ, Salber D (2011) Mass spectrometric imaging (MSI) of metals using advanced BrainMet techniques for biomedical research. Int J Mass Spectrom 307(1-3):3–15. https://doi.org/10.1016/j.ijms.2011.01.015
7. Wang D, Hosteen O, Fierke CA (2012) ZntR-mediated transcription of zntA responds to nanomolar intracellular free zinc. J Inorg Biochem 111:173–181. https://doi.org/10.1016/j.jinorgbio.2012.02.008
8. O'Malley D (2008) Imaging in depth: controversies and opportunities. In: Correia JJ, Detrich HW (eds) Biophysical tools for biologists, vol 2: In vivo techniques, vol 89. Methods in cell biology. pp 95. doi:https://doi.org/10.1016/s0091-679x(08)00605-5
9. Fahrni CJ (2007) Biological applications of X-ray fluorescence microscopy: exploring the subcellular topography and speciation of transition metals. Curr Opin Chem Biol 11:121–127
10. Paunesku T, Vogt S, Maser J, Lai B, Woloschak G (2006) X-ray fluorescence microprobe imaging in biology and medicine. J Cell Biochem 99(6):1489–1502. https://doi.org/10.1002/jcb.21047
11. Paunesku T, Wanzer MB, Kirillova EN, Muksinova KN, Revina VS, Lyubchansky ER, Grosche B, Birschwilks M, Vogt S, Finney L, Woloschak GE (2012) X-ray fluorescence microscopy for investigation of archival tissues. Health Phys 103(2):181–186. https://doi.org/10.1097/HP.0b013e31824e7023
12. Vogt S, Lai B, Finney L, Palmer B, LE W, Harris H, Paunesku T, de Jonge M, Legnini D, Maser J, Glesne D, Lay P, Woloschak G (2007) Imaging trace elements in cells with x-ray fluorescence microscopy. Microsc Microanal 13:40–41. https://doi.org/10.1017/s1431927607076283
13. Crawford AM (2015) Methodologies in XRF Cytometry. PhD thesis, University of Michigan
14. Crawford AM, Kurecka P, Yim TK, Kozemchak C, Deb A, Dostal L, Sun CJ, Brewe DL, Barrea R, Penner-Hahn JE (2016) Development of a single-cell X-ray fluorescence flow cytometer. J Synchrotron Radiat 23:901–908. https://doi.org/10.1107/s1600577516008006

Chapter 7

Multiparametric Analysis of Myeloid Populations by Flow Cytometry

Sara A. Mathie, Alastair L. Corbin, Hayley L. Eames, and Irina A. Udalova

Abstract

Flow cytometry is extensively used for the immune-profiling of leukocytes in tissue during homeostasis and inflammation. The multiparametric power of using fluorescently conjugated antibodies for specific surface and activation markers provides a comprehensive profile of immune cells. This chapter describes the identification and characterization of myeloid populations using flow cytometric analysis in an acute model of resolving inflammation. This model allows the examination of heterogenic populations across different systemic and tissue locations. We describe tissue processing, antibody staining, and analysis, which include a newly described viSNE tool to generate two-dimensional clustering within myeloid populations. We also reference the use of transgenic reporter mice on specific myeloid cells that provides enhanced specificity and profiling when defining myeloid heterogeneity.

Key words Cellular heterogeneity, Myeloid, Monocytes, Macrophages, Neutrophils, Flow cytometry, Transgenic reporter mice, viSNE

1 Introduction

Myeloid cell populations consisting of neutrophils, macrophages, and monocytes predominate many chronic inflammatory conditions. The prevalence of these cells in a range of chronic disease is well described. Macrophages are distributed throughout the body in various organs, tissue, and fluids and provide an effective first-line defense [1–3]. Upon invasion with pathogen or injury, they can send signals for the recruitment of other immunologic cells. Macrophages display heterogeneity of phenotype and can adapt to their local environment [4, 5]. Different subsets of monocytes exist and can mature into macrophages in tissue [6]. Inflammatory monocytes and patrolling monocytes are distinct in their Ly6C expression, hi and lo, respectively. However, other cells express Ly6C; therefore, defining monocyte subsets requires further discrimination. Permutations in the expression of the markers, CD11b, Ly6C, F4/80, CD64, CX3CR1, and MHCII, can sepa-

Natasha S. Barteneva and Ivan A. Vorobjev (eds.), *Cellular Heterogeneity: Methods and Protocols*, Methods in Molecular Biology, vol. 1745, https://doi.org/10.1007/978-1-4939-7680-5_7,

rate monocyte subsets and tissue macrophages. CX3CR1 is a marker of tissue monocytes and macrophages and negatively correlates with Ly6C.

Of recent, it has been established that at homeostasis, tissue macrophage populations are often represented by a mix of embryonically derived macrophages seeded during embryonic development and capable of maintaining themselves through self-renewal [7, 8] and monocyte-derived macrophages entering the tissue in the adult animals from the blood. The proportion of embryonically derived and monocyte-derived macrophages varies between the tissues, with microglia macrophages being exclusively embryonically derived and colon macrophages being exclusively monocyte-derived after weaning [7, 9, 10]. In the tissue, monocyte adaptation to the tissue environment and transition into macrophages add further complexity to the cell populations. This has large implications on how we study and interpret monocytes and macrophages function and phenotype, during both homeostasis and disease.

It is now emerging that this heterogeneity observed in monocytes and macrophages may be mirrored in neutrophil populations. Neutrophils display distinct phenotypes depending on location and may demonstrate heterogeneity between organs [11].

We have developed a basic flow cytometric panel to identify phenotype myeloid subsets in blood and tissue. This panel assesses myeloid populations through recruitment from the blood, to migration and activation in the tissue. We can examine and characterize the myeloid populations consisting of monocytes, macrophages, and neutrophils which predominate this response [12, 13]. In this chapter, we utilize a 6-day air pouch inflammatory model. This acute resolving inflammatory system mimics the synovium environment of the knee joint [12]. The same panel is applicable and forms the basis, for the analysis of more complex models of disease in our laboratory, such as rheumatoid arthritis, obesity, and colitis [14, 15]. We can examine heterogeneity among myeloid subsets across different systemic and tissue compartments. This chapter describes methods for tissue processing, antibody staining, and flow cytometry analysis, including viSNE, a tool that permits the mapping of high-dimensional cytometry data onto two dimensions, to examine and characterize myeloid populations in air pouch model of inflammation [16]. We also reference studies with transgenic reporter mice for myeloid markers that and can be incorporated into our flow panel and demonstrate improved cellular specificity.

2 Materials

2.1 General

All RPMI-1640 used supplemented with L-glutamate.

Dulbecco's cell culture phosphate-buffered saline (PBS) buffer used is free from magnesium and calcium.

FACS buffer: Dulbecco's cell culture PBS with 1% FCS and 0.01% NaN_3.

ACK (ammonium-chloride-potassium) lysing buffer used for red blood cell lysis.

Falcon tubes used with conical bottom.

2.2 Blood Preparation

1. Ethylenediaminetetraacetic acid (EDTA) 0.5 mM.
2. 1 mL Luer slip syringe with 27 gauge needle.
3. 1.5 mL Eppendorf tube.
4. ACK red blood cell lysis buffer.
5. FACS buffer.

2.3 Air Pouch Lavage and Dissection of Air Pouch Membrane (See Note 1)

1. Curved forceps.
2. Fine scissors.
3. Sterile cold PBS.
4. 5 mL Luer slip syringes.
5. 15 mL Falcon tube.
6. 70 μM cell strainer.
7. DNAse 1 grade II, from bovine pancreas.
8. Liberase™ TL Research Grade, low thermolysin concentration.
9. RPMI-1640 complete medium.
10. FACS buffer.

2.4 Flow Cytometric Analysis

1. FACS buffer.
2. 15 mL Falcon tube.
3. 96-well clear round bottom TC-treated microplate.
4. 5 mL FACS round bottom polystyrene test tube.
5. Purified rat anti-mouse CD16/CD32 (Mouse BD Fc-Block™) (*see* **Note 2).**
6. Anti-mouse fluorescently labeled antibodies: CD45, CD11b, Ly6G, SiglecF, Ly6C, F4/80, MHCII, CD11c, CD206, CD62L, live/dead stain (*see* **Note 3**).
7. LIVE/DEAD™ Fixable Far-Red Dead Cell Stain Kit, Thermo Fisher Scientific.
8. Anti-rat/hamster calibration bead set (*see* **Note 4**).
9. Brilliant violet stain buffer.
10. Cytofix™ fixation buffer.
11. Flow cytometer with four lasers: blue 488 nm, yellow-green 561 nm, red 633 nm, and violet 405 nm.

3 Methods

3.1 Blood Preparation

1. Coat syringe and needle for blood collection with EDTA. Insert syringe into 200 μL 0.5 M EDTA and push up and down. Dispense EDTA into Eppendorf tube.
2. Collect blood, remove the needle, and dispense into Eppendorf tube containing 0.5 M EDTA. Invert and keep on ice or at 4 °C (*see* **Note 5**).
3. Pipette 10 mL ACK buffer to 15 mL Falcon tube, then with 1 mL pipette transfer blood + EDTA mix from Eppendorf slowly into ACK buffer, and leave for 10 min.
4. Spin cells 500 × *g* for 5 min with the brake on.
5. To wash tip off supernatant, add 10 mL PBS and spin as in **step 4**. Check if cell pellet is free from red blood cells (RBC) (*see* **Note 6**).
6. Discard supernatant and resuspend cell pellet in 1 mL FACS buffer.
7. Count cell suspension and adjust the concentration to 3–5 × 10^6 cells/mL.

3.2 Air Pouch Lavage and Dissection of Air Pouch Membrane

1. Inject 3 mL cold PBS into the dorsal air pouch ensuring the needle passes through the skin and into the pouch space (*see* **Note 7**).

3.2.1 Air Pouch Lavage

2. Place the mouse on the side, and gently massage the pouch.
3. Carefully hold the skin around the pouch and snip a small incision into the epidermis to create a "window" and reveal intact membrane.
4. Gently snip into the membrane.
5. Carefully pinching the membrane, use 5 mL syringe (without needle) to lavage out injected PBS (*see* **Note 8**).
6. Dispense into chilled 15 mL Falcon tube (*see* **Note 9**).
7. Spin Falcon tube at 500 × *g*, 5 min, 4 °C at cell centrifuge with the brake on (*see* **Note 10**).
8. Resuspend cell pellet in 1 mL FACS buffer.
9. Count cell suspension and adjust concentration to 3–5 × 10^6 cells/mL.

3.2.2 Dissection and Digestion of Air Pouch Membrane

1. To collect the membrane, hold the visible membrane near incision with forceps and snip carefully under the epidermis to separate the membrane from overlying soft tissue. Collect in pre-weighed 15 mL Falcon tube containing 1 mL of serum-free RPMI-1640 (*see* **Note 11**).
2. Add 1 mL of RPMI containing 10 μg DNAse and 2.5 μg Liberase and place in water bath or shaker for 1 h at 37°C.

3. After 1 h of incubation, pour membrane digest mix through a 70 μM sieve into a 50 mL Falcon tube (*see* **Note 12**).
4. With the flat end of a 1 mL syringe plunger, gently massage the membrane to release any leukocytes through sieve. Wash through with RPMI.
5. Transfer into 15 mL Falcon tube and spin at 500 × *g*, 5 min, 4 °C.
6. Discard supernatant and check if there is no RBC contamination. Add 10 mL PBS and spin as in **step 5**.
7. Resuspend cell pellet in FACS buffer.
8. Count cell suspension and adjust concentration to 3–5 × 10^6 cells/mL.

3.3 Flow Antibody Staining

1. Plate 100 μL cell suspension prepared from the blood, membrane, and lavage and diluted in FACS buffer in well of the round bottom 96-well plate.
2. Add 100 μL cold FACS buffer to each well and centrifuge for 4 min at 500 × *g*, 4 °C with the brake on. Discard supernatant.
3. Dilute Fc-block in FACS buffer 1:100 and add 30 μL per well. Incubate for 15 min at 4 °C.
4. Without washing, add 30 μL antibodies diluted in FACS buffer. Vortex plate gently and incubate for 20 min at 4 °C in the dark (*see* **Note 13**).
5. To wash, add 150 μL FACS buffer and spin as in **step 3**. Discard supernatant and repeat **step 5**.
6. After the second wash, discard supernatant and fix with 50 μL Cytofix™ for 20 min and resuspend cells gently.
7. Wash ×2 in FACS buffer as in **step 5** and resuspend in 150 μL FACS buffer.
8. Create a single-color compensation tube for each fluorochrome: In a 5 mL FACS tube, add 300 μL FACS buffer +10 μL negative bead and 10 μL anti-rat/hamster Ig bead +4 μL of single fluorochrome antibody. Vortex and incubate in the dark for at least 15 min (*see* **Note 14**).

3.4 Flow Cytometric Analysis: Spectral Compensation and Gating

1. Using unstained samples, set forward and side scatter so that myeloid populations are clearly identifiable, central on the plot (Fig. 1b).
2. Use unstained sample to set voltage values to define the negative gate. Using a spare stained sample, verify positive events which are distinguished from negative gate for each fluorochrome. Adjust voltage values so that the maximal fluorescent intensity is not off the scale.

A

PerCP/Cy5.5	Ly6G
PeCy7	Ly6C
BV785	CD11c
PE Dazzle	F4/80
BV650	CD45
v500	CD11b
AF700	MHCII
APC/Cy7	Live/ Dead
AF488	CD206
BV421	SiglecF
PE	CD62L

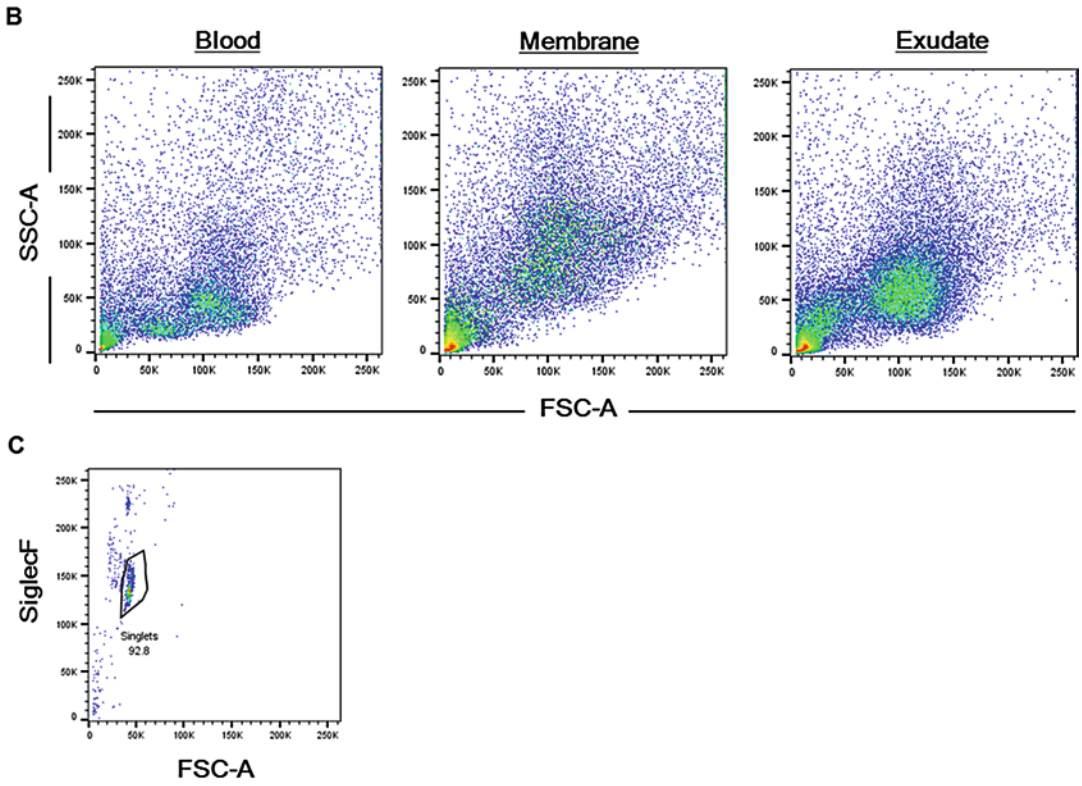

Fig. 1 Compensation and analysis setup. (**a**) List of fluorescently labeled antibodies for the FACS panel described in this chapter. (**b**) Forward (FSC-A) and side scatter (SSC-A) for blood, membrane, and exudate samples. (**c**) Singlet selection for compensation bead set

3. Run each tube containing compensation beads separately on the flow cytometer. Gate on singlet population based on forward and side scatter (Fig. 1c). Collect and save 5000 events. Follow BD FACSDiva software instructions to calculate spectral compensation.
4. Start running samples. Collect around 50,000 events from sample wells. The gating strategy for selecting CD11b$^+$ leukocytes is depicted in Fig. 2 (*see* **Note 15**).

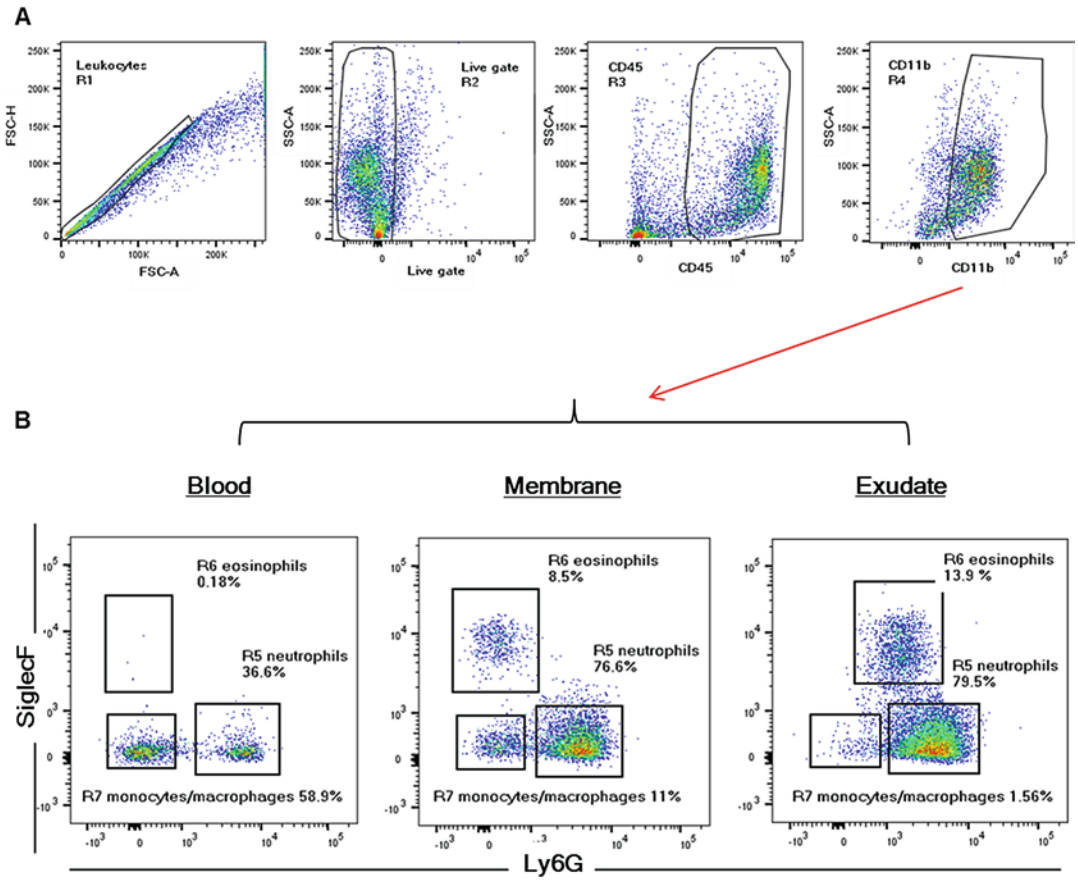

Fig. 2 Flow cytometric analysis of the air pouch model. (**a**) Gating strategy for CD11b + leukocytes in the blood, tissue, and exudate. (**b**) Gating of major myeloid populations in the blood, membrane tissue, and exudate: neutrophils, eosinophils, and monocyte/macrophage populations

5. We have also analyzed cells taken from the air pouch model carried out in transgenic reporter mice with Ly6G^{tdTom} and Cx3CR1^{GFP}, incorporated into this basic panel (*see* **Note 16**).
6. Analysis is carried out using FlowJo (Treestar) software program. FSC files can be run through viSNE (Cytobank) software (*see* **Note 17**).

4 Notes

1. Mice are given a subcutaneous injection of 3 mL air on day 0, and on day 3, the pouch is topped up with injection of 3 mL of air. On day 6, the pouch was injected with 1 mg zymosan. The blood, membrane, and exudate are taken at 4 h after challenge.

2. This antibody reacts specifically with extracellular domains of the mouse Fc γ III and Fc γ II receptor to block non-specific binding of antigens. We find this antibody gives clean and consistent blocking compared to whole serum alternatives.
3. Our panel consists of antibodies conjugated with fluorochromes selected for optimal detection of each antigen: We matched bright fluorochromes with low-density antigen and vice versa. To minimize spillover, we spread multiple markers on the same cell type over different laser lines. Fixable live/dead marker far-red dye in APC-Cy7 channel allows for intracellular detection of cytokines and transcription factors. Table of antibody panel, Fig. 1a. For gating strategies, we also create fluorescence-minus-one (FMO) controls which we use to confirm gating of these myeloid cell types. This is the full panel of antibodies except one. FMO controls are used to determine data spread effects induced by high spectral compensation values and prevent overestimation of populations.
4. In our protocol, we use BD™ CompBead calibration beads for compensation. This saves on precious samples, especially for the membrane where we have a low cell yield.
5. Blood is ready to be processed after a minimum of 30 min.
6. If red blood cell lysis is required a second time, repeat from **step 3** and incubate for 5 min in ACK buffer.
7. Mice are terminated following CO_2 asphyxiation and exsanguination.
8. Using round-ended forceps, hold the skin and soft tissue to prevent any loss of PBS wash. Carefully insert the 5 mL syringe into incision in the membrane and lavage.
9. Take a note of the volume retrieved; this can vary between mice and can be used to normalize cells/mL.
10. The supernatant can be kept at −80°C for analysis of cellular mediators, such as cytokines, chemokines, and lipids.
11. Following lavage, the pouch will be deflated, grab exposed membrane, and with scissors snip around. As it becomes detached from the epidermis, more membrane should be made available, and gently continue snipping until collected. Record weight using pre-weighed tubes, between 50 and 75 μg is expected membrane retrieved. The amount of membrane tissue retrieved may vary. Membrane weight used to normalize cells count reported as cells/mg tissue.
12. Tip contents of membrane into sieve, gently push membrane with end 1 mL syringe, rinse through with RPMI media, and transfer into 15 mL Falcon tube to spin. Approximately 5×10^5 cells are expected back from the membrane, 15 mL Falcon tube allows more compact pellet for a small number of cells.

13. When using more than one BD horizon bright violet dye in a panel, there may be fluorescent interference. Using BD Horizon™ Brilliant Stain Buffer 1:10 in FACS buffer will prevent any staining artifacts when using these antibodies conjugated with brilliant violet dyes.
14. For each single control to set spectral compensation, use the conjugated antibody used for the panel. To preserve antibody volume is effective at 1 μL.
15. Singlets (R1) are selected based on the linear correlation between FSC-A and FSC-H. From this population, events negative for live/dead marker are selected (R2). These live leukocytes are then gated for $CD45^+$ (R3) and $CD11b^+$ (R4) expression. FMO control samples are a useful reference at this stage. Gating $CD11b^+$ selected events against Ly6G and SiglecF separate leukocytes into three broad populations: neutrophils (R5), eosinophils (R6), and monocytes and macrophage containing gate (R7) (Fig. 2b). From gate R5, we calculate the mean fluorescent intensity expression of CD62L to determine activation status of neutrophils. CD62L selectin is highly expressed on blood neutrophils. Levels are downregulated upon activation, and expression of CD62L is decreased on neutrophil populations found in the membrane and exudate. Drilling down from R7 mono-/macrophage gate to Ly6C vs. MHCII, there are three distinct populations: inflammatory monocytes, $Ly6C^{hi}$ $MHCII^-$, macrophages $Ly6C^-$ $MHCII^+$, and a gate containing $Ly6C^-$ patrolling lymphocytes (Fig. 3b). From the R7 gate, the $Ly6C^-$ $MHCII^+$ population predominantly expresses F4/80 in tissue and exudate compartments (Fig. 3c). More in-depth analysis of monocyte and macrophage populations can be determined using CD64, CD206, and CD11c depending on the tissue or disease of interest: CD64 is expressed on $F4/80^+$ macrophage populations from R7. However, in more complex tissue settings, particularly in the gut, CD64 antigen is very useful at delineating resident from recently replenished and differentiated macrophages. CD206 is considered a classic marker of M2 macrophages; however, it is expressed on most tissue macrophages and may be best used for expression rather than for specifically identifying M2 macrophage population. CD11c may be used to define dendritic cell subsets from R7 gate (gating not shown) [15].
16. The development of transgenic reporter mice expressing fluorescent protein on a range of myeloid-specific markers is providing a popular approach to analyzing and sorting cells from tissue by Fluorescence-Activated Cell Sorting (FACS) [5, 7]. Transgenic (tg) fluorescent Ly6G reporter gene mice

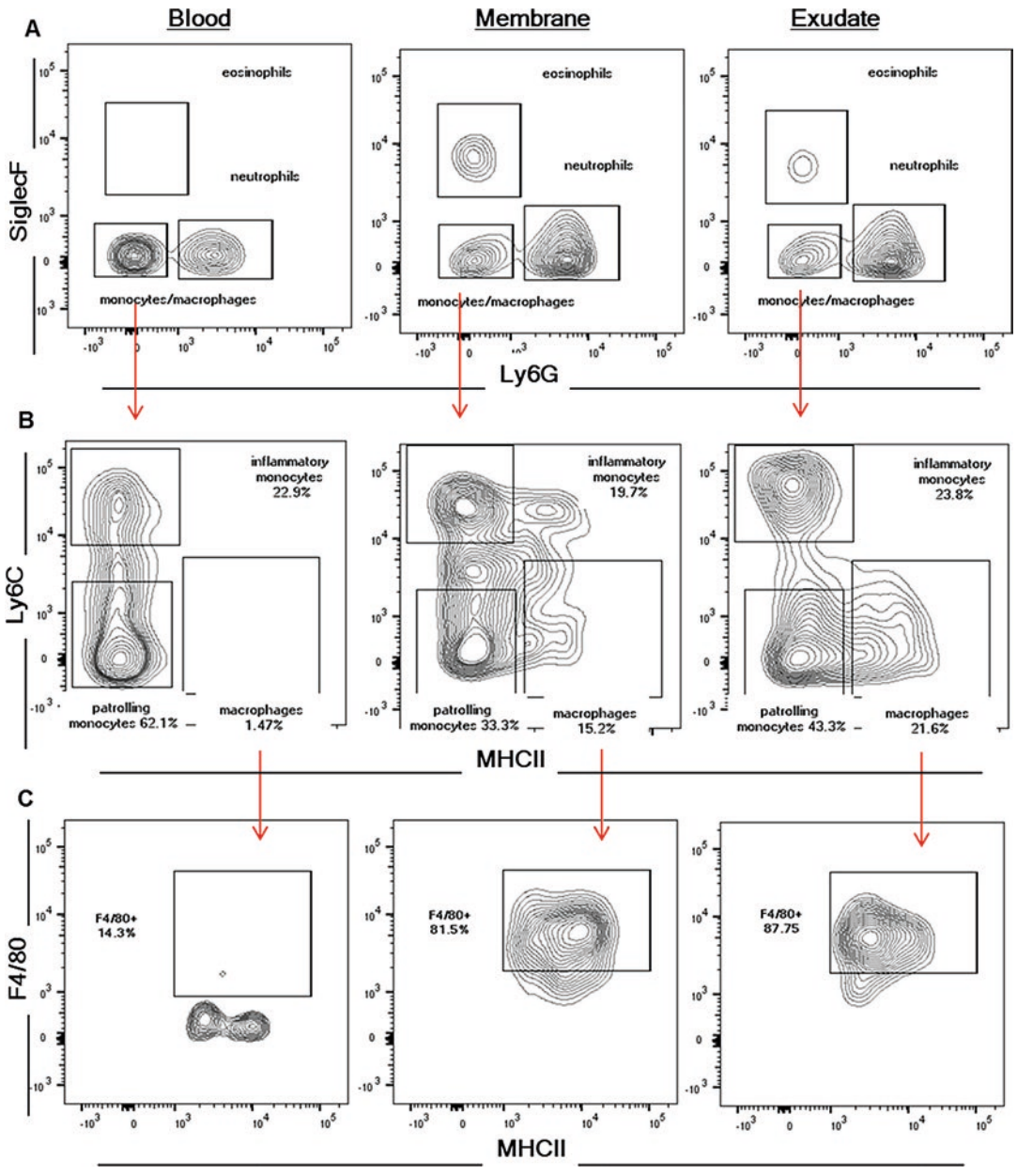

Fig. 3 Monocyte and macrophage subpopulations (**a**) Gating strategy for major myeloid cells. (**b**) CD11b^{+} Ly6G^{-} SiglecF^{-} monocyte/macrophage populations gated for Ly6C and MHCII: Inflammatory monocytes depicted Ly6C^{hi} and MHCII^{-}; patrolling lymphocytes containing gate Ly6C^{-} MHCII^{-}; Ly6C^{-} MHCII^{+} macrophages. (**c**) F4/80 expression on Ly6C^{-}MHCII^{+} populations

give a clear strategy for identifying and isolating neutrophils with minimum handling and activation from antibodies [11]. Transgenic fluorescent CX3CR1 reporter gene mice allow for immune-phenotyping of monocytes and macrophages. CX3CR1 is highly expressed on macrophages and expression is low inflammatory monocytes [7]. This panel can be applied to cells that express Ly6G*tdTom* and CX3CR1*gfp* by swapping CD62L and CD206 to APC.

17. FSC files saved from FACS can be run through viSNE to give a two-dimensional picture and depict cellular clustering of markers. By using all markers simultaneously, viSNE achieves a more accurate grouping of myeloid subsets. We show example files of murine colon taken from flow cytometry studies in our laboratory. Heatmaps depict levels of expression of MHC II, Ly6C, CD11c, and F4/80 and display cell clusters and changes in marker expression levels between healthy and disease monocytes/macrophages (Fig. 4). viSNE is available for download at http://www.c2b2.columbia.edu/danapeerlab/html/index.html.

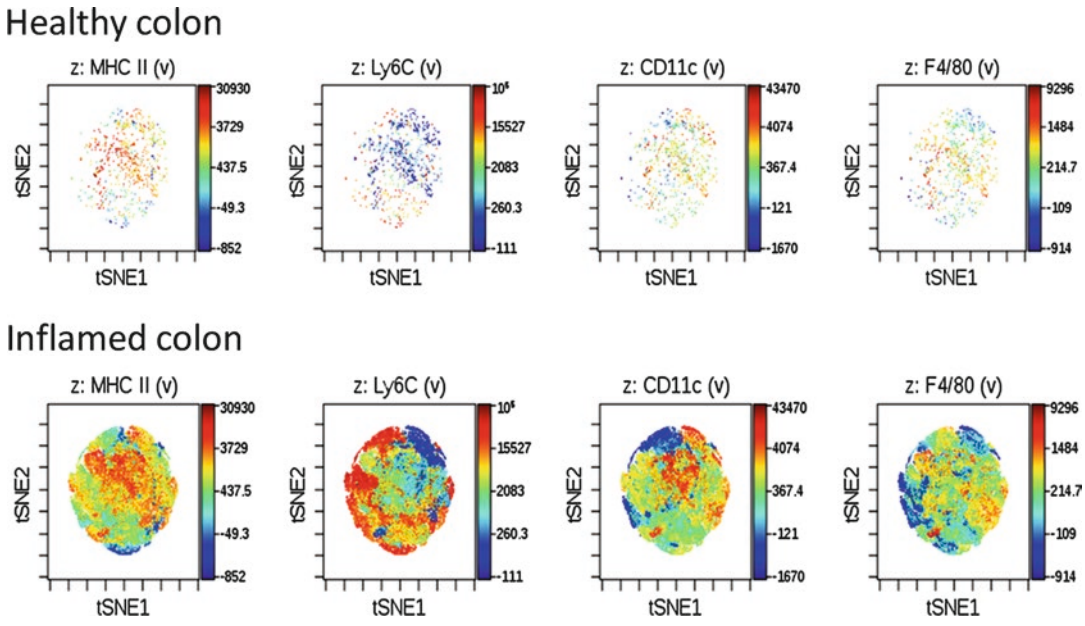

Fig. 4 viSNE heatmaps of monocyte/macrophage populations. Heatmap depicting the level of expression and clustering within gate R7, $CD45^{+}CD11b^{+}Ly6G^{-}SiglecF^{-}$ population in the normal and inflamed murine colon

Acknowledgments

This work is supported by the Arthritis Research United Kingdom and Novo Nordisk Foundation.

References

1. Wynn TA, Chawla A, Pollard JW (2013) Macrophage biology in development, homeostasis and disease. Nature 496(7446):445–455
2. Franken L, Schiwon M, Kurts C (2016) Macrophages: sentinels and regulators of the immune system. Cell Microbiol 18(4):475–487
3. Byrne AJ, Mathie SA, Gregory LG, Lloyd CM (2015) Pulmonary macrophages: key players in the innate defence of the airways. Thorax 70(12):1189–1196
4. Udalova IA, Mantovani A, Feldmann M (2016) Macrophage heterogeneity in the context of rheumatoid arthritis. Nat Rev Rheumatol 12(8):472–485
5. Kierdorf K, Prinz M, Geissmann F, Gomez Perdiguero E (2015) Development and function of tissue resident macrophages in mice. Semin Immunol 27(6):369–378. https://doi.org/10.1016/j.smim.2016.03.017
6. Geissmann F, Jung S, Littman DR (2003) Blood monocytes consist of two principal subsets with distinct migratory properties. Immunity 19(1):71–82
7. Yona S, Kim KW, Wolf Y, Mildner A, Varol D, Breker M et al (2013) Fate mapping reveals origins and dynamics of monocytes and tissue macrophages under homeostasis. Immunity 38(1):79–91. https://doi.org/10.1016/j.immuni.2012.12.001
8. Hashimoto D, Chow A, Noizat C, Teo P, Beasley MP, Leboeuf M et al (2013) Tissue-resident macrophages self-maintain locally throughout adult life with minimal contribution from circulating monocytes. Immunity 38(4):792–804. https://doi.org/10.1016/j.immuni.2013.04.004
9. Bain CC, Bravo-Blas A, Scott CL, Perdiguero EG, Geissmann F, Henri S et al (2014) Constant replenishment from circulating monocytes maintains the macrophage pool in the intestine of adult mice. Nat Immunol 15(10):929–937. https://doi.org/10.1038/ni.2967
10. Sieweke MH, Allen JE (2013) Beyond stem cells: self-renewal of differentiated macrophages. Science 342(6161):1242974
11. Kolaczkowska E, Kubes P (2013) Neutrophil recruitment and function in health and inflammation. Nat Rev Immunol 13(3):159–175
12. Edwards JCW, Sedgwick AD, Willoughby DA (1981) The formation of a structure with the features of synovial lining by subcutaneous injection of air: an in vivo tissue culture system. J Pathol 134(2):147–156
13. Pessler F, Mayer CT, Jung SM, Behrens EM, Dai L, Menetski JP, Schumacher HR (2008) Identification of novel monosodium urate crystal regulated mRNAs by transcript profiling of dissected murine air pouch membranes. Arthritis Res Ther 10(3):R64. https://doi.org/10.1186/ar2435
14. Dalmas E, Toubal A, Alzaid E, Blazek K, Eames HL, Lebozec K et al (2015) Irf5 deficiency in macrophages promotes beneficial adipose tissue expansion and insulin sensitivity during obesity. Nat Med 21(6):610–618. https://doi.org/10.1038/nm.3829
15. Weiss M, Byrne AJ, Blazek K, Saliba DG, Pease JE, Perocheau D et al (2015) IRF5 controls both acute and chronic inflammation. Proc Natl Acad Sci U S A 112(35):11001–11006. https://doi.org/10.1073/pnas.1506254112
16. Amir e-AD, Davis KL, Tadmor MD, Simonds EF, Levine JH, Bendall SC et al (2013) viSNE enables visualization of high dimensional single-cell data and reveals phenotypic heterogeneity of leukemia. Nat Biotechnol 31(6):545–552. https://doi.org/10.1038/nbt.2594

Chapter 8

Quantitation of IRF3 Nuclear Translocation in Heterogeneous Cellular Populations from Cervical Tissue Using Imaging Flow Cytometry

Radiana T. Trifonova and Natasha S. Barteneva

Abstract

Imaging flow cytometry (IFC) has become a powerful tool for studying the activation of transcriptional factors in heterogeneous cell populations in high-content imaging mode. With considerable interest to the clinical development of IFC, the question becomes how we can accelerate its application to solid tissues. We developed the first IFC-based procedure to quantify the nuclear translocation of interferon regulatory factor (IRF) 3, an important measure of induction of type I interferon antiviral response, in primary human immune cells including in solid tissues. After tissue digestion and protocol optimization by spectral flow cytometry, cell suspension is stained for intracellular IRF3 and acquired by IFC. Image analysis is performed using an optimized nuclear mask and similarity score parameter to correlate the location of IRF3 staining and a nuclear dye. The technique measures IRF3 activation at a single cell level and can detect small changes in the percent of activated cells providing objective quantitative data for statistical analysis.

Key words Solid tissue, Imaging flow cytometry, Nucleocytoplasmic translocation, IRF3, Signal transduction, Cellular heterogeneity

1 Introduction

The physical separation of genomic DNA in the nucleus is a hallmark of the eukaryotic cell creating a requirement for highly coordinated transport of macromolecules through the nuclear envelope. Shuttling of cellular proteins such as transcription factors, receptors, kinases, and scaffolding proteins in and out of the nucleus is a key step in intracellular signaling and essential for the response to external stimuli, regulation of proliferation, programmed cell death, and/or experimental interference by small molecules [1–3]. The analysis of nucleocytoplasmic transport in human primary samples relies mainly on quantitation of averaged cellular populations in Western blotting and statistically limited fluorescent microscopy [4]. However, the application of such strategy to heterogeneous cell populations such as solid tumor and tissue samples is complicated due to transcriptomic

Natasha S. Barteneva and Ivan A. Vorobjev (eds.), *Cellular Heterogeneity: Methods and Protocols*, Methods in Molecular Biology, vol. 1745, https://doi.org/10.1007/978-1-4939-7680-5_8,

and genetic differences. Imaging flow cytometry (IFC) or "inflow" microscopy is a recently emerging technology that allows successful imaging analysis of heterogeneous cell populations [5, 6]. IFC helps analyze a broader pool of potential target antigens in primary cells [5], eliminating the need for cell lines expressing cell-specific fluorescent reporters. We have recently applied IFC to analyze the transcription factor interferon regulatory factor (IRF) 3 in response to human immunodeficiency virus (HIV) [7]. Herein, we describe a detailed protocol for the evaluation of IRF3 nucleocytoplasmic shuttling in primary human immune cells by IFC, illustrating the use of this method to monitor intracellular signaling in primary human tissue sample cells (*see* **Experimental Design** for details). This method takes advantage of the IFC high-content analysis approach allowing rapid acquisition (up to 5000 cellular events/s) of a statistically reasonably sized sample (average file size 10–20,000 events) [8]. We have adapted the protocol for use with human cervical tissue samples, and it can be applied to other human solid tissues such as tumor samples. The protocol is highly sensitive and allows for detection of small changes in the percent of activated cells even for cell types with low abundance in tissue samples. We hope that this protocol and its modifications will accelerate research in the intracellular signaling field. More comprehensive characterization of nuclear import and export pathways for proteins participating in the regulation of immune response and cancer-related proteins might reveal new therapeutic targets [9].

1.1 Development of the Protocol

IRF3 is a transcription factor which is a major regulator of the type I interferon (IFN) antiviral response after recognition of viral DNA or RNA by intracellular foreign nucleic acid sensors, such as Toll-like receptors (TLRs), retinoic acid-inducible gene I (RIG-I), and cyclic GMP-AMP synthase (cGAS) (reviewed in [10]). IRF3 activation triggers phosphorylation by the TANK-binding kinase 1 (TBK-1) followed by homodimerization and nuclear translocation leading to binding to the promoter and enhancer regions of type I IFN genes. Type I IFN response is critical for the control of viral infections by direct antiviral effects and by enhancing antiviral immunity [11]. The activation of IRF3 is an important measure of type I IFN induction, and cellular localization of this factor is regulated by nuclear export signals (NES), nuclear localization sequence (NLS), non-IRF proteins, and inducible phosphorylation [12]. In this protocol, we describe a novel technique to quantify the nuclear translocation of IRF3 at a single cell level using IFC. IFC is an emerging hybrid technology that combines flow cytometry with microscopy imaging and allows determining intracellular localization of proteins. A high number of cells (up to 100,000 per file) can be imaged in a short amount of time to provide quantitative data of the percent of cells with nuclear translocation of IRF3. We have used this protocol in a recent publication to measure type I IFN response induced by HIV after the knockdown of the exonuclease TREX-1 in

human primary monocyte-derived macrophages (MDMs) and CD4+ T cells [7]. IFC has been also used previously to measure the nuclear translocation of NFkB in cell lines [13], but no protocol available to characterize transcriptional factors shuttling in heterogenous cell populations is derived from human solid tissues. Phosphorylated IRF3 has been visualized in mouse tumor-derived antigen-presenting cells by IFC [14]; however, the nuclear-cytoplasmic translocation of IRF3 is a more specific and accurate measure of IRF3 activation. The nuclear translocation of IRF3 is difficult to detect compared to NFkB because IRF3 is activated only in a small fraction of the cells in a cell population and the event is transient [15, 16]. Also, IRF3 signal in the cytoplasm remains very high in cells with nuclear translocation, so the nuclear-to-cytosolic ratio of the IRF3 signal is not sensitive enough. It is therefore better to measure the signal for IRF3 in the nucleus and to compare the percent of cells positive for nuclear IRF3 between untreated control and activated samples.

We have developed IFC technique to analyze nucleocytoplasmic translocation of IRF3 in myeloid cells recovered from primary human solid tissue after tissue mechanical and enzymatic digestion [17], and we have optimized the fixation/permeabilization and IRF3 intracellular staining steps for these samples (*see* **Experimental Design**). The principle of this method is illustrated in Fig. 1. Although the IFC approach has been tested on the number of cell

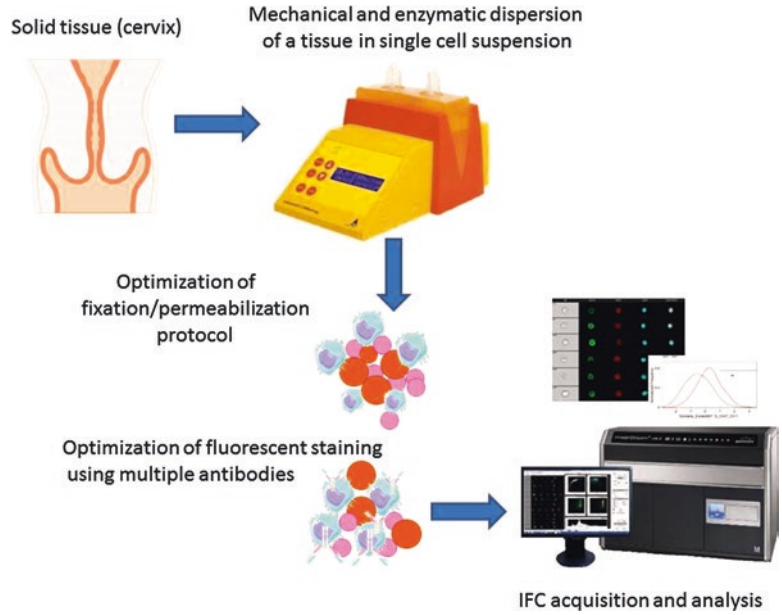

Fig. 1 Flow chart of procedure steps for sample preparation of single-cell suspension from solid tissue and nucleocytoplasmic translocation analysis by imaging flow cytometry

Table 1
Comparison of common techniques used to measure nuclear translocation of transcription factors

Protein	Function	Detection method	Type of sample	Reference
IRF3	Transcription factor	Western blot after cellular fractionation (nuclear/cytoplasmic fractions)	Murine bone marrow-derived macrophages	[19]
		SDS polyacrylamide gel electrophoresis (PAGE), western blot (phosphorylated protein)	Murine T cells	[20]
		Native PAGE western blot (dimer formation)	Human MDMs	[21]
			SV80 cells	[22]
			HeLa cells	[23]
		Immunohistochemistry (nuclear translocation)	Huh7 cells	[16]
			LLC-MK-2 cells	[15]
		Immunofluorescence (IRF3-green fluorescent protein (GFP) expression)	HEK293 cells	[24]
		Luciferase dimerization reporter system	HEK293 cells	[25]
		Imaging flow cytometry (phosphorylated protein)	Mouse tumor antigen-presenting cells	[14]
IRF5	Transcription factor	Immunohistochemistry (nuclear translocation)	MDAH041 cells	[26]
IRF7	Transcription factor	Immunohistochemistry (nuclear translocation)	MDAH041 cells	[26]
		Western blot after cellular fractionation (nuclear/cytoplasmic fractions)	293T cells	[27]
		IFC (nuclear translocation)	Human pDC	[13]
NFkB	Transcription factor	Western blotting (nuclear/cytoplasmic fractions)	HMEC-1 cells	[28]
		NFkB GFP-p65	HeLa	[29]
		Immunohistochemistry (nuclear translocation) with confocal microscopy	Human monocyte-derived dendritic cells	[30]
			Human breast cancer tissue	[31]
		Electrophoretic mobility shift assay (EMSA) of nuclear extracts	Human colon cancer tissue	[32]
		IFC (nuclear translocation)	THP-1 cells, primary murine lymph node cells	[13]
			Leukemic cell lines	[14]

(continued)

Table 1
(continued)

Protein	Function	Detection method	Type of sample	Reference
FOXO	Transcription factor	Western blotting (nuclear/cytoplasmic fractions)	Cultured adult flexor digitorum brevis fibers	[33]
		Western blot (phosphorylated protein)	C2C12 cells	[34]
		Immunohistochemistry (nuclear translocation) with confocal microscopy	C2C12 cells	[34]
		GFP- forkhead family of transcription factors (FOXO)3a	ASTC-a-1 cells	[35]
β-catenin	Multifunctional	Western blotting, Fluorescence recovery after photobleaching (FRAP)	Cell lines	[36]
RAN	Small GTPase	Immunohistochemistry/Intensity scoring	Human primary cancer samples	[37]
Oligodendrocyte basic helix-loop-helix transcription factor (Olig)2	Oligodendrocyte transcription factor	Immunohistochemistry/Intensity scoring	Tissue sections, transgenic mice	[38]
TRIM8	RING family of ligases	TRIM8-GFP by confocal microscopy, nuclear fractionation, and western blotting	Transfected HEK293 cells	[39]

lines [13, 18] (summarized in Table 1), it was never successfully applied for analysis of primary human solid tissues. In order to develop and optimize the staining procedure for IRF3 and the data analysis, we used human primary macrophages stimulated with lipopolysaccharide (LPS) (Fig. 2). First, we tested two different procedures for intracellular staining using the BD Cytofix/Cytoperm Fixation/Permeabilization Kit (BD Biosciences) for staining intracellular proteins and the BD Pharmingen Transcription Factor Buffer Set (BDPT) (BD Biosciences) optimized for staining intranuclear proteins (data not shown). We have previously compared other protocols for intracellular staining such as (1) fixation with 2% paraformaldehyde (PFA) for 10 min RT and permeabilization with 0.2% Triton (TX)-100, (2) fixation with cold acetone for 10 min at −20 °C, and (3) the Fix/Perm staining kit (Invitrogen). However, we observed higher background with these protocols compared to the BD staining kits (data not shown). Since a

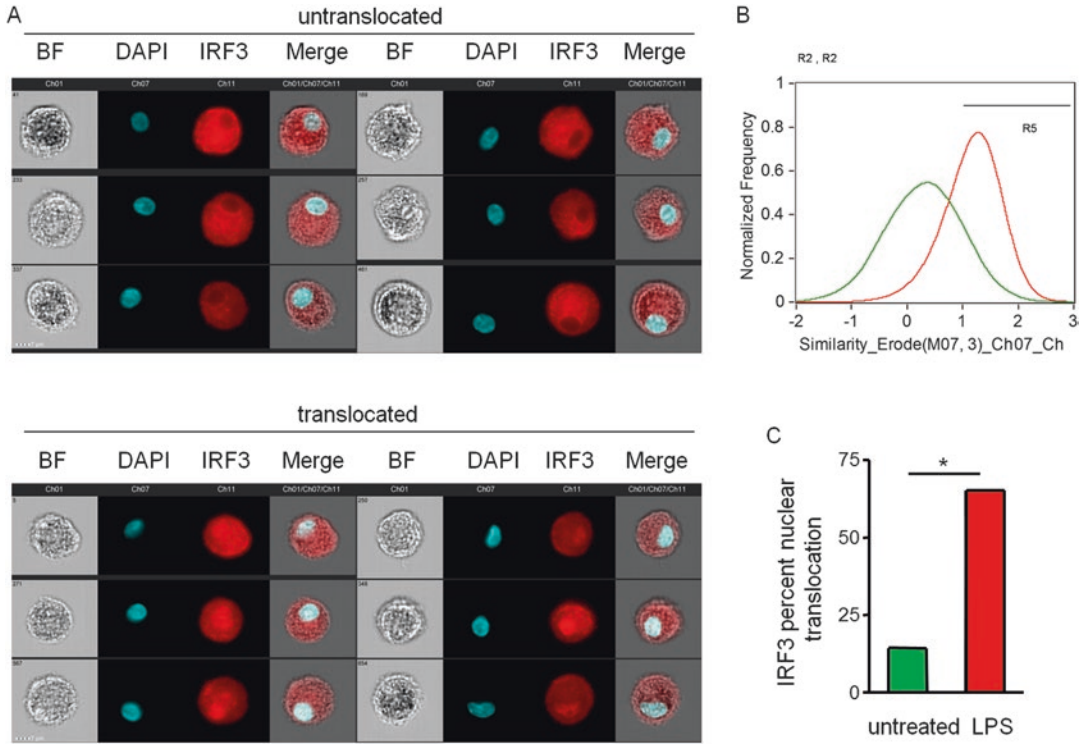

Fig. 2 IRF3 nuclear translocation in primary human macrophages measured by imaging flow cytometry 1 h after activation with 100 ng/ml LPS. (**a**) Shown are representative images of MDMs without or with nuclear IRF3 (BF, brightfield; DAPI, nuclear stain). (**b**) Histograms representing the similarity score parameter that correlates the location of IRF3 staining and the nuclear dye and the percent of cells with nuclear translocation (similarity score higher than 1, R5) for untreated (green) and LPS-stimulated (red) cells. (**c**) The bar graph represents the percent cells with nuclear IRF3. The data were obtained from at least 20,000 events analyzed for each condition with Amnis ImageStream X Mark II at multiplication 60×. *p* value was calculated by chi-squared test (*, $p < 0.0001$)

conjugated anti-IRF3 antibody was not available, we did indirect staining with a rabbit monoclonal antibody (Abcam) and a donkey anti-rabbit Alexa fluor 647 (AF647) conjugated antibody (molecular probes). We used a rabbit IgG isotype control to evaluate any non-specific background staining. Samples fixed with BD Cytofix/Cytoperm Fixation/Permeabilization Kit had reduced the background with IgG isotype antibody compared to BDPT fixed samples (data not shown). We determined the optimal concentration of the primary and the secondary antibody to get a specific staining with a minimal background (*see* **Experimental Design** for details). This protocol was successfully used both in primary human MDMs and with $CD4^+$ T cells [7]. We then adapted the IRF3 staining protocol for use with primary myeloid cells from human cervical mucosal tissue explants. We treated cervical tissue with LPS to induce IRF3 nuclear translocation and then prepared a single cell

suspension from the tissue using a protocol that we have previously developed for these types of samples [18]. Since we expected a higher background with the cells derived from the mucosal tissue, we optimized the IRF3 staining procedure by modifying the fixation step. Using spectral flow cytometry approach, we determined that fixation with 4% PFA preheated at 80 °C [40] significantly reduced the background for analysis of myeloid cells from cervical tissue samples and separated positive from negative signal (Fig. 3a, b).

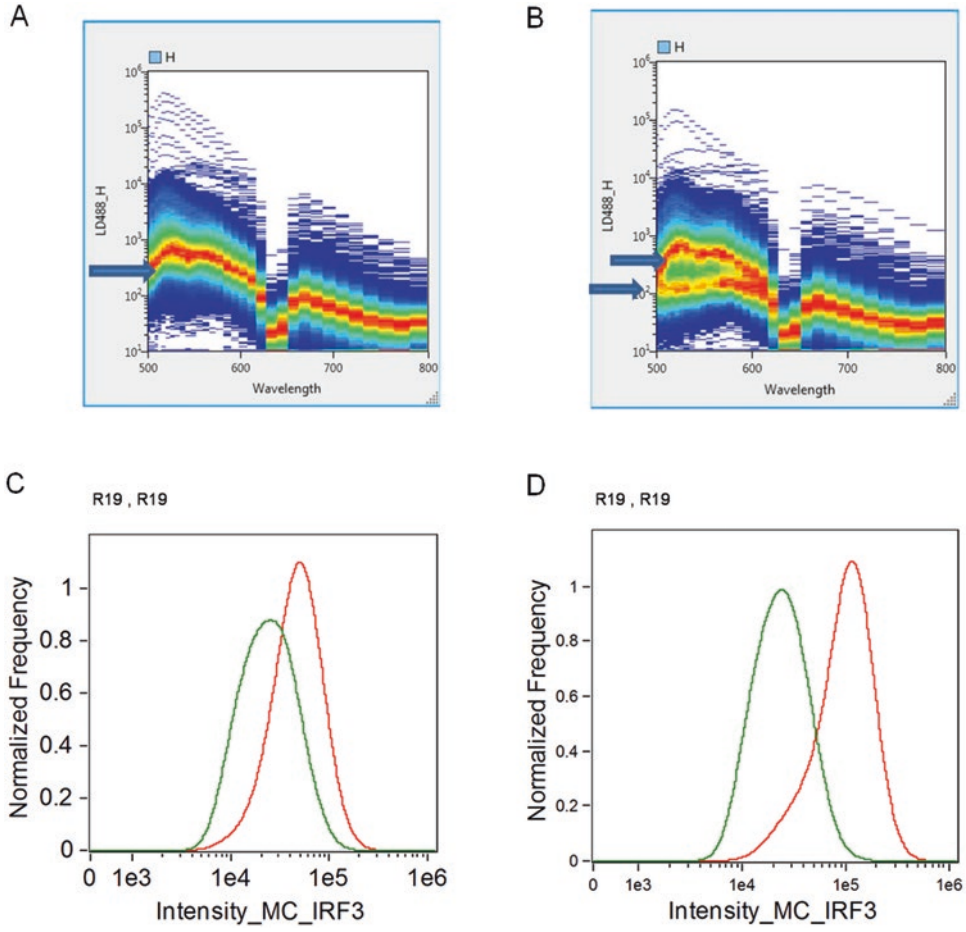

Fig. 3 Comparison of different fixation conditions for analysis of cervical tissue myeloid cells. (**a, b**) Spectral flow cytometry comparing cells derived from cervical tissue samples, fixed with BD Cytofix/Cytoperm Fixation Solution (**a**) and 4% PFA preheated at 80 °C (**b**) after staining with Alexa488-CD14 antibody. Arrows in (**b**) are pointing to positive (upper arrow) and negative signal (lower arrow) levels. Autofluorescent background at spectral flow cytometry histogram depicting cells fixed with BD Cytofix/Cytoperm Fixation Solution cannot be separated from positive signal. (**c, d**) Imaging flow cytometry of $CD14^+$ mucosal tissue cells fixed with BD Cytofix/Cytoperm Fixation Solution (**c**) or 4% PFA preheated at 80 °C (**d**) and stained with anti-IRF3 antibody (red) or IgG isotype control (green). Data on C and D is acquired by Amnis ImageStream X Mark II with multiplication 60×

Indeed, we observed a better discrimination between the background signal in isotype IgG control stained samples and samples stained with anti-IRF3 after fixation with 4% PFA at 80 °C (Fig. 3c, d). Therefore, the intracellular staining for IRF3 with cervical tissue samples was performed after fixation with PFA at 80° instead of fixation with BD Fix/Perm solution. The following incubation with antibodies was performed in the BD Perm/Wash solution. Representative data for IRF3 nuclear translocation in myeloid cells from cervical explants treated with LPS is shown in Fig. 4.

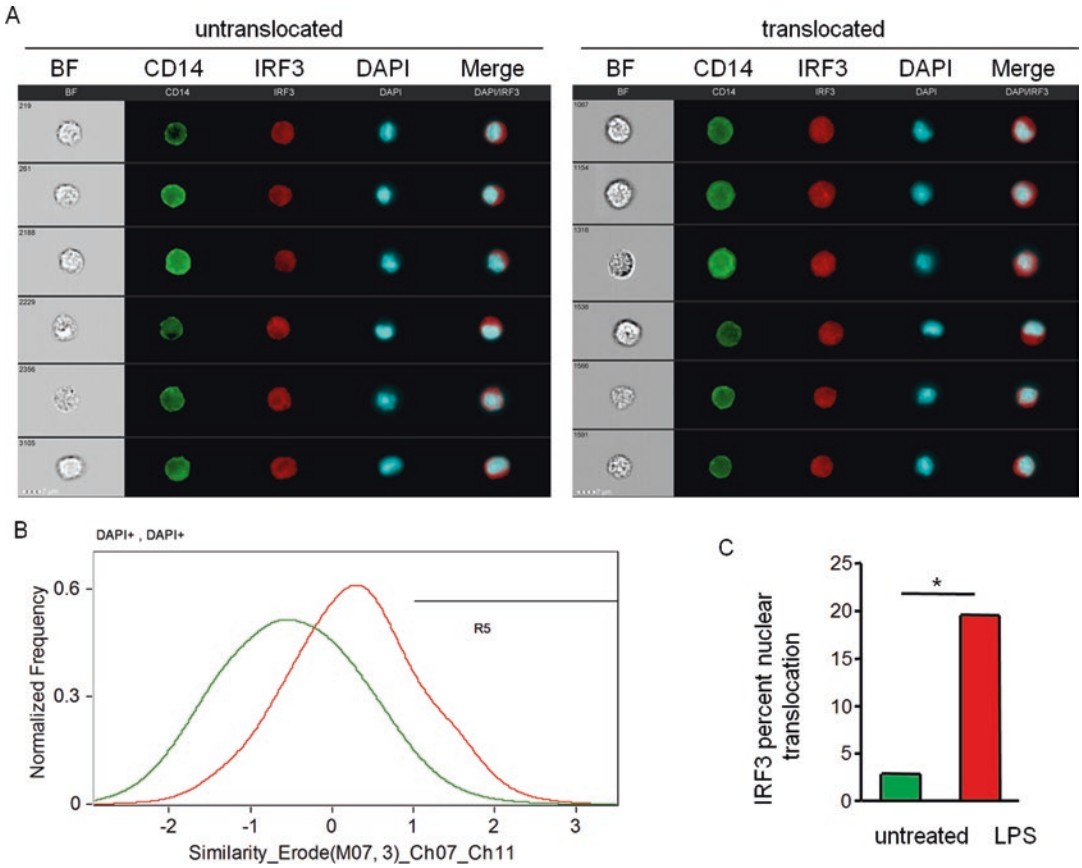

Fig. 4 Measurement of IRF3 nuclear translocation in cervical myeloid cells by imaging flow cytometry. (**a**) Representative images of cervical CD14$^+$ cells without or with nuclear IRF3 (BF, brightfield; DAPI, nuclear stain) from a single-cell suspension prepared by collagenase digestion of the tissue sample prior to analysis with Amnis ImageStream X Mark II. (**b**) Histogram representing the similarity score parameter that correlates the location of IRF3 staining and the nuclear dye and the percent of cells with nuclear translocation (similarity score higher than 1, R5) for CD14$^+$ cells in untreated tissue samples (green) versus samples stimulated with 1000 ng/ml LPS for 1 h (red). (**c**) The bar graph represents the percent CD14$^+$ cells with nuclear IRF3. The data were obtained from at least 20,000 events analyzed for each condition. *p* value was calculated by chi-squared test (*, $p < 0.0001$)

1.2 Applications of the Method

This protocol provides an objective measurement of IRF3 activation at a single cell level. It can be used with any cell type, including cells with a small cytoplasm-to-nuclear ratio such as primary T lymphocytes [7]. It can also be applied to tissue samples and to cell types with a relatively low abundance. The technique is very sensitive and can detect even subtle changes allowing analysis for statistical significance since a very high number of cells are analyzed. The method can be adapted to analyze other proteins in the IRF family (IRF4, IRF5, IRF7) as well as nucleocytoplasmic shuttling of other transcriptional regulators in heterogeneous primary human solid tissues and tumor samples.

1.3 Comparison with Other Methods

Nucleocytoplasmic localization and trafficking were studied for a long time using traditional biochemical methods and transmission electron microscopy (TEM) of cultured cell lines and tissue sections [41–43] and lately by high-content microscopy of proteins tagged with fluorescent sensors [44]. Thus, IRF3 activation has been studied by measuring nuclear translocation or phosphorylation, and it is routinely measured by Western blot or by measuring dimerization of native gel (summarized in Table 1). However, these methods are semiquantitative and require a relatively large number of cells to obtain cell lysates (typically 1–1.5 $\times 10^6$ cells required). A separation of nuclear and cytosolic cell fraction is required if nuclear translocation is measured. Isolation of nuclear cellular fractions without contamination with perinuclear organelles (e.g., mitochondria, endoplasmic reticulum) represents a practical challenge [45, 46]. These techniques are laborious and time-consuming and require larger amounts of cells (800–1000 K per strip for Western blotting). Maguire and coauthors [47] performed a correlative study in order to compare results for nucleocytoplasmic translocation of NFkappaB in leukemic cell lines evaluated by Western blotting, conventional flow cytometry, and IFC and concluded that IFC allows for quantitative and statistically robust analysis in immunophenotypically defined subpopulations. Also, Western blot might not be sensitive enough to detect subtle effects or evaluate heterogeneous cellular populations because it provide averaged information about cellular population, and IRF3 is usually translocated to the nucleus only in a small percent of the cells at a given time since the event is transient. Therefore, it is important to look at a single cell level and determine the percent of cells with IRF3 activation. Another method used to measure nuclear translocation of IRF3 and other transcription factors is immunohistochemistry or immunofluorescent microscopic analysis of cellular lines and/or tissue sections [15, 16]. However, analyzing the images and getting objective quantitative data with this technique are difficult and require a significant amount of post-acquisition analysis. With immunofluorescent microscopy, it is feasible to analyze only

up to hundreds of cells (in average 20–100 cells per slide), while the IFC technique provides objective data for up to tens of hundreds of thousands of cells at a high speed and can be considered a high-content method of analysis. IFC also obtains data even for relatively rare cell types in tissue samples (<0.01% from population). In addition, immunostaining would be difficult to do with certain cell types such as suspension cells or with primary cells because the cells would have to be fixed on a slide first and primary cells might be more difficult to culture on a slide or attach by cytospin than immortalized cell lines. Analysis of nuclear-cytoplasmic distribution in primary tissues is usually limited by confirming nuclear or cytoplasmic localization in tissue samples by TEM or immunohistochemical staining in combination with fluorescent microscopy [37]. Both Western blot and immunohistochemistry are not high-throughput methods and cannot be used when working with large numbers of samples.

Recently, a new reporter systems measuring IRF3 activation were described [25]; however, they require cell transfection or transduction, and the primary immune cells such as T cells are difficult to transfect. In addition, a transfection or lentiviral transduction could trigger activation of IRF3 and IFN response on its own. ELISA assays measuring phosphorylated IRF3 are available as an alternative quantitative method for IRF3 analysis; however, they also require a preparation of cell lysates (averaged cell population) and are laborious when working with a large number of samples. None of these assays measures IRF3 activation at a single cell level.

In contrast, the protocol which we describe to measure IRF3 nuclear translocation using IFC is applicable to heterogenous cell populations and easy and fast to perform. The procedure of sample preparation is no different than that for intracellular staining for flow cytometry. The samples are acquired by ImageStream instrument at a fast rate of 1000–5000 cells/s, and a large number of samples can be analyzed at a time. The samples are fixed after the staining and the signal is stable as long as the samples are protected from light prior to analysis. The method is quantitative and allows statistical analysis of the data obtained from thousands of cells analyzed at a single cell level (medium file size 10–20,000 events). In contrast to microscopy, IFC allows reliable compensation and elimination of non-specific signals. The protocol can be used also with a single cell suspension prepared from human tissue samples.

1.4 Experimental Design

The described protocol for detection of nuclear translocation of IRF3 can be applied to any cell type including primary immune cells, and it works reliably even in cells with a small cytoplasm-to-nucleus ratio, such as T cells. For analysis of solid tissue samples, the tissue has to be digested first to prepare a single cell suspension.

We have previously published an optimized procedure for detection of immune cells from genital tract mucosal tissue preserving the immune cells' surface markers by a combination of mechanical and enzymatic digestion [17]. The protocol is relatively easy and fast. A critical point with this procedure is that undigested cells can be lost from the analysis, which can affect interpretation of results. We have optimized the procedure to maximize recovery of myeloid cells from the stroma of cervical mucosal samples; however, the procedure might have to be optimized for different tissue and cell types (*see* Table 2).

Table 2
Troubleshooting of the procedure for preparation of single-cell suspension from tissue samples

Step	Problem	Possible reason	Possible solution
Preparation of a single-cell suspension from human tissue samples	Small pellet size	Not enough starting material (small tissue sample)	Increase a size of starting sample; decrease the number of treatment conditions
		Loss of cells during cell purification	Optimize the tissue digestion procedure by determining the best program used for mechanical dissociation for the specific tissue type, the length of enzymatic digestions, and removal of adipose tissue that decreases efficiency of enzymatic dissociation
	Sample size is large, yield of isolated cells is low	Incomplete digestion	Occurs with new lots of digestion enzyme; may require adjustment of enzyme concentrations
	Viscous cell pellet	Nuclei have burst due to fixation/permeabilization conditions	Modify fixation/permeabilization buffer conditions (change to milder conditions)
	Low viability	Overdigestion	Reduce the amount of enzyme or the time of incubation with the enzyme
		Temperature of solution during digestion	Monitor temperature during digestion; ensure that temperature of digestive mixture is 37 °C, when digestion starts (preheat enzymatic mixture)
	Loss of cell surface markers signal	Cleavage during enzymatic digestion (e.g., CD56, CD4, and CD209 are cleaved when crude collagenase is used for digestion)	The use of mechanical digestion allows to reduce the time of enzymatic digestion to preserve cell surface markers; alternatively purified enzymes can be used, such as Liberase^{TL} and Liberase^{DL} enzyme blends (Roche applied science); however, the digestion efficiency and cell recovery from the tissue might decrease

As with all immunofluorescent methods of analysis, the IFC-based approach relies on the availability of antibodies recognizing the target antigen of interest. The advantage of IFC analysis is that not only flow cytometry tested monoclonal antibodies can be used, but so can a wider panel of polyclonal antibodies that positively tested for fluorescent microscopy analysis of the target antigen. A fluorescent microscopy can provide a quick preliminary way to check the quality of the antibody. The direct conjugate of ant-IRF3 is not commercially available, and an indirect staining with a secondary conjugated antibody has to be used. Alternatively, the antibody of interest can be conjugated in-house using commercially available conjugation kits (such as antibody labeling kits by BIO-RAD Laboratories).

In our protocol, cells are stained with a nuclear dye (DAPI) and IRF3 rabbit monoclonal antibody or rabbit IgG as controls and then stained with a donkey anti-rabbit Alexa fluor (AF) 647 conjugated antibody. MDMs stimulated with LPS for 1 h serve as a positive control since this time point is the peak of IRF3 nuclear translocation [21]. Single positive controls stained for DAPI or IRF3 alone are used for compensation. When working with tissue samples, a single cell suspension has to be prepared first and then stained for cell surface markers to allow the identification of the cells of interest such as $CD14^+$ myeloid cells [17]. In this case, compensation beads can be used as a single positive control for the cell surface staining since the amount of tissue is limited. The high signal-to-noise ratio and low background are important, and therefore some preliminary optimizations of fixation/permeabilization conditions are required in order to decrease the background level (*see* **Note 1**).

Nuclear translocation of IRF3 is then assessed using a high-content imaging flow cytometer ImageStream X Mark II. After optimization of cellular masks, cell populations are sequentially gated on single cells positive for DAPI and IRF3 staining. Image analysis is performed using a nuclear mask, and the similarity score parameter, a log-transformed Pearson correlation coefficient of the pixel values of two images, is used to correlate the location of IRF3 staining and the nuclear dye (DAPI) to identify cells with nuclear IRF3. Caution should be taken with an increase of the number of cell surface markers that need to be used to identify different cell populations such as myeloid cells and lymphocytes, as signal-to-noise level of detected IRF3 expression is affected by increasing the level of background. Finally, the suggested protocol is a first attempt to analyze nucleocytoplasmic translocation in heterogenous primary solid tissue samples in high content and statistically robust manner particularly important for transcriptomics and signal transduction fields.

2 Materials

2.1 Reagents

1. Anti-IRF3 rabbit monoclonal antibody (Abcam, cat. no. ab68481, 1.038 mg/ml).
2. Rabbit IgG monoclonal isotype control (Abcam, cat. no. ab172730, 1.858 mg/ml).

   The antibodies have to be aliquoted upon delivery and stored at −20 °C. Avoid freeze/thaw cycle.
3. AF647 labeled donkey anti-rabbit IgG (H + L) 2 mg/ml. It is important to centrifuge the vial with antibody conjugate solution briefly in a microcentrifuge before use to eliminate protein aggregates which could interfere with the quality of the immunostaining. Protect from light.
4. 4′,6-Diamidino-2-phenylindole (DAPI). Reconstitute in distilled water at 10 mg/ml and store at −20 °C. Protect from light.
5. 4% paraformaldehyde solution in PBS.
6. BD Cytofix/Cytoperm Fixation/Permeabilization Kit (BD Biosciences (BD).
7. BD Pharmingen Transcription Factor Buffer Set (BD).
8. Distilled water.
9. FACS buffer: Dulbecco's PBS (D-PBS 1×), 1 mM EDTA, 25 mM 4-(2-hydroxyethyl)-1-piperazineethanesulfonic acid (HEPES), 0.5% bovine serum albumin (BSA) prepared in the laboratory and stored at 4 °C filtered sterile using 500 ml 0.45 μM filter unit.
10. Zombie Green™ Fixable Viability Kit (BioLegend): The lyophilized Zombie Green™ dye has to be reconstituted in DMSO prior to use as per manufacturer's instructions. 100 μl of DMSO are added to one vial of Zombie Green™ dye until fully dissolved. The reconstituted dye can be stored at −20 °C.
11. CD14-PE clone HCD14 (BioLegend).
12. Human TruStainFCX™ (BioLegend).
13. BD CompBead Plus Anti-Mouse Ig, k/Negative Control (BSA) Compensation Plus (7.5 μm) Particle Set (BD Biosciences).
14. Ficoll-Paque PLUS.
15. LPS *E. coli* 1 mg/ml.
16. Scalpel handle size 3 (Surgical Design).
17. Surgical blade no. 10.
18. GentleMACS C Tubes (MACS Miltenyi Biotec).

19. Collagenase IV: 1 g of collagenase IV is dissolved in 100 ml of RPMI-1640 containing 10% FBS. The resulting 2× stock of collagenase IV is aliquoted and stored at −80 °C prior to use.
20. Accutase enzyme cell detachment medium.
21. Multiwell Primaria 6 well (Falcon, BD).
22. Primaria cell culture dish 100 × 20 mm style dish (Corning).
23. 12-well flat bottom tissue culture plates (Falcon, BD).
24. Microtubes (Axygen).
25. 1.5 ml low retention Clear-view™ Snap-Cap microtubes (Sigma-Merck).

2.2 Equipment

1. 5-laser ImageStream X Mark II imaging cytometer (Amnis-EMD-Millipore-Sigma) equipped with 120 milliwatt (mW) 405 nm laser, 200 mW 488 nm blue laser, 200 mW 561 nm green–yellow laser, 150 mW 658 nm laser, and 8.75 nm 765 nm infrared laser, Multimag upgrade (up to 60× magnification), two CCD cameras with ten fluorescent, and two brightfield channels. The system is calibrated daily using a microbeads fluorescent set (Spherotech) and Assist™ program (Amnis-EMD-Millipore-Sigma).
2. Spectral flow cytometer SP6800 (SONY Biotechnology Inc., USA) equipped with 60 mW violet 405 nm, 40 MW blue 488 nm, and red 638 nm lasers, as well as a 32-channel linear array photomultiplier (500–800 nm range for 488 nm excitation and 420–800 nm for 405/638 laser combination). The scheme of spectral flow cytometer is provided in Fig. 5. Alignment of the instrument is performed with Ultra Rainbow calibration beads (Spherotech) as described [48].
3. gentleMACS™ Dissociator (Miltenyi Biotec) is a benchtop instrument which allows the semiautomated dissociation of tissues into single-cell suspensions with high viability rates, yields, and preserved cell surface epitopes.
4. 37 °C incubator/shaker.
5. 80 °C water bath.
6. Centrifuge Allegra X-15R (Beckman Coulter) or similar benchtop refrigerated centrifuge.
7. Eppendorf refrigerated centrifuge 5430.

3 Methods

3.1 Cell Suspension Preparation

Donor blood or tissue sample initial processing is done following universal precautions. All work should be carried out in a class II biological safety cabinet.

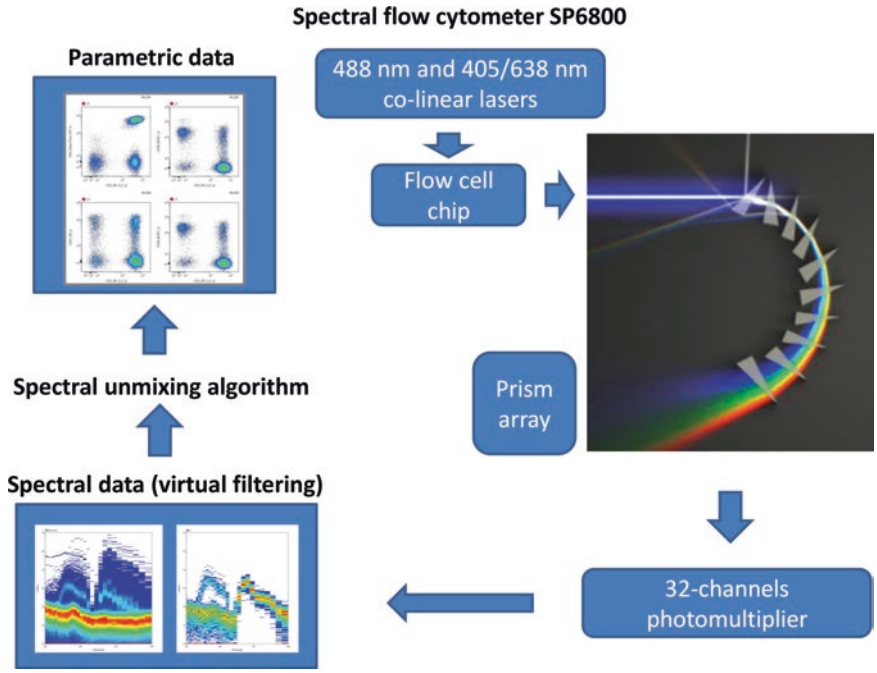

Fig. 5 Scheme of spectral flow cytometer analysis

3.1.1 Donor Blood Sample

Human blood samples are obtained from the Brigham and Women's Hospital Specimen Bank, Boston, MA, with Institutional Review Board approval.

1. Human PBMCs are separated using Ficoll-Paque density gradient centrifugation following manufacturer's recommendations [49].
2. Mononuclear cells are cultured in RPMI 1640 media (Cellgro) containing 10% human serum (AB) (GemCell), 100 U/ml penicillin, and 100 mg/ml streptomycin sulfate (H10 medium).
3. MDMs are differentiated by culturing on pre-coated 6-well Primaria plates (Falcon) for 5–7 days as previously described [50].
4. To induce IRF3 nuclear translocation, the MDMs are activated for 1 h with 100 ng/ml LPS in serum-free media.
5. MDMs are then detached from the tissue culture plate by incubation with Accutase (Ebiosciences) for 30 min at room temperature following a wash with D-PBS.

3.1.2 Human Tissue Samples

Human cervical tissue is obtained from patients undergoing hysterectomy for benign conditions such as fibroids and without cervical pathology and signs of cervical infection or inflammation following

Institutional Review Board (IRB) approval. Cervical tissue samples were provided by the Tissue and Tumor Bank at the University of Massachusetts Medical School (Worcester) and by the Cooperative Human Tissue Network which is funded by the National Cancer Institute. The tissue sample is transported on ice in 15 ml tube (Falcon, BD Biosciences) filled with H10 medium and stored at 4 °C in H10 medium until processing within 24 h of surgery. The time between obtaining of sample and starting of processing has to be minimized.

We have previously developed the procedure for preparing a single-cell suspension from cervical tissue samples to increase the recovery of cells from the deeper tissue layers and prevent cleavage of cell surface markers [17]. Disaggregation typically achieved by combining enzymatic and mechanical techniques, and the choice of enzymatic and/or mechanical technique may profoundly influence the results [51–53]. We describe a disaggregation method for cervix tissue that consists of non-traumatic, mild mechanical dissociation step followed by enzymatic dissociation with collagenase IV (*see* **Note 2**).

1. The cervical mucosa is first separated from the underlying stroma by cutting 5 mm below the epithelial surface, and the tissue is minced into 5 mm^3 pieces using a surgical scalpel.
2. The tissue is then placed in a 12-well tissue culture plate in serum-free media. To induce IRF3 nuclear translocation, the tissue is treated for 1 h with 1000 ng/ml LPS. Serum-free media can be used for short-term culture prior to digestion for flow cytometry imaging in order to reduce the background. Longer cell culture requires the use of H10 media.
3. A single-cell suspension is prepared as previously described [17]. Briefly, the tissue is placed in pre-warmed 5 mg/ml collagenase IV (Life Sciences) in H10 media in a gentleMACS C Tube and subjected to mechanical dissociation for 1 min using mouse spleen 01.01 program of the gentleMACS Dissociator (MACS Miltenyi Biotec) (*see* **Note 2**).
4. The sample is then incubated for 30 min at 37 °C with shaking at 150 rpm, followed by another cycle of mechanical dissociation.
5. The suspension is filtered through a 100 μm cell strainer (BD Biosciences), and viable cells are collected by centrifugation at 500 × *g* for 5 min at 4 °C.

3.2 Direct Immunostaining for CD14

Direct immunostaining for CD14 is performed using phycoerythrin (PE) conjugated mouse monoclonal antibody (BioLegend) at 1/20 dilution following an incubation with a Fc-receptor (FcR) block (TruStain) for 10 min at 4 °C in FACS buffer. The antibody is incubated for 30–60 min at 4 °C followed by a wash with 2 ml of FACS buffer and centrifugation to pellet the cells.

Timing: The timing for cell preparation varies based on the cell type used. If MDMs are used, they have to be detached from the culture plate using Accutase as described above. The total time for processing in that case is 1 h. Cell surface staining is not necessary when working with a pure population of cells such as MDMs.

If a cervical tissue sample is used, it has to be digested with collagenase to prepare a single-cell suspension, as described above, which takes approximately 1 h. Cell surface staining of the single-cell suspension is necessary to identify the cell of interest such as $CD14^+$ myeloid cells before proceeding with the intracellular IRF3 staining. The samples should be protected from light after the cell surface staining has been done. The total processing time for the cervical tissue is approximately 2 h.

3.3 Fixation-Permeabilization Procedure

3.3.1 Cell pellets preparation

A minimum of 1×10^5 cells by centrifugation at $500 \times g$ for 5 min at 4 °C. Prepare additional pellets for single positive staining controls with IRF3 and with 4′,6-diamidino-2-phenylindole (DAPI), respectively. It is not possible to use a single positive staining control for compensation when working with tissue samples because of the sample size limitation and also because gating on certain cell types requires staining for additional markers. Therefore, we recommend the use of compensation beads when working with tissue samples.

3.3.2 Optional

Before fixation LIVE/DEAD cells discrimination can be performed (*see* **Note 3**). A fixable dead cell stain, such as LIVE/DEAD dye family (Invitrogen-Thermo Fisher Scientific) or Zombie dyes (BioLegend), can be used for dead cell exclusion. These dyes bind to amines on the cell surface of live cells and are permanent to the cells with compromised cell membrane integrity allowing the exclusion of nonviable cells from the downstream analyses.

We have used the following procedure for Zombie Green™ dye: Use prior to cell surface staining of the cells. Pellet 1×10^6 cells, following a D-PBS wash. Add 100 μl of D-PBS with Zombie Green™ at 1:1000 and incubate at room temperature for 15–30 min. Wash with FACS buffer and proceed with staining for cell surface markers and fixation. Protect from light.

3.3.3 Fixation with 4% Paraformaldehyde (PFA)

It is critical to choose fixation-permeabilization protocol compatible with each antibody of interest in the staining panel. We performed an extensive optimization of the many variables involved in sample staining for IRF3 protein using spectral flow cytometry analyzer (SP6800, SONY Biotechnology Inc., USA). In contrast to conventional flow cytometry that distinguishes parts of emission peaks defined by a preselected combination of hardware bandpasses, spectral flow cytometry allows to analyze emission spectra along a range of continuous wavelengths (500–800 nm) (Fig. 3a, b). This approach

allows to compare and to optimize antibody staining in cells with high intrinsic autofluorescence that is overlapping with fluorochrome-conjugated antibody emission signal [54] (*see* also **Note 4**).

1. Add 500 µl of 4% PFA preheated at 80 °C in a water bath to each cell pellet for 2 min (*see* **Note 5**). The pellet should be loosened before that by a quick vortexing. Heating the PFA solution at >60 °C is important, since the monomeric formaldehyde is a more potent fixative than polymeric formaldehyde and better penetrates into the cell [40]. Add fixative in a dropwise fashion while vortexing slowly, in order to prevent aggregation of cells during fixation. Alternatively, vortex the cellular pellet prior to adding the fixative. We recommend cell surface staining to be done before fixation because many antibodies that are working on viable cells do not separate cell populations after cells have been fixed and permeabilized. If staining for additional cell surface markers is required after fixation, it is absolutely necessary to validate surface marker antibodies for use in fixed and permeabilized cells [55].
2. Pellet the fixed cells by centrifugation as above to remove the fixative.

   Timing: 10 min.

   Optional: After the fixation, the samples can be kept overnight or longer before proceeding with the intracellular staining. The pellet should be resuspended in 100 µl FACS buffer and stored at 4 °C protected from light.

3.4 Intracellular IRF3 Staining

1. Pellet the cells by centrifugation as above if they have been stored overnight in FACS buffer. Prepare pellets for single positive control for DAPI and IRF3 alone (*see* **Note 6**).
2. Wash with 200 µl BD Perm/Wash Buffer (BD) per pellet. BD Perm/Wash Solution (BD, USA) is provided as a 10× stock, and the amount of the buffer necessary for each experiment has to be prepared prior to use by mixing one part of the stock solution with nine parts of distilled water (vol/vol). If working with a small cell number, skip this step to avoid loss of cells. Instead, carefully aspirate completely the fixation solution or the FACS buffer.
3. Add the anti-IRF3 antibody diluted at 1:200 (5.19 µg/ml from a stock at 1.038 mg/ml) in BD Perm/Wash Buffer. For the isotype control, use rabbit IgG at the same protein concentration (dilution at 1:360 of a 1.858 mg/ml stock) (*see* **Note 7**). Use 100 µl of the diluted primary antibody per pellet. Do not add antibodies to the sample which will serve as a DAPI single positive control. Vortex to mix and incubate for 30 min at room temperature.
4. Add 1 ml of BD Perm/Wash Buffer to wash and centrifuge as above.

5. Aspirate the supernatant and add donkey anti-rabbit AF647 conjugated antibody diluted at 1:1200 (1.66 μg/ml) in BD Perm/Wash Buffer. Vortex to mix and incubate for 20 min at room temperature. Protect the samples from light. If cell surface staining has not been done before, protect the samples from light at all times after this step.
6. Add 1 ml of BD Perm/Wash Buffer to wash and centrifuge as above.
7. Aspirate the supernatant and repeat the wash with another 1 ml of BD Perm/Wash Buffer. Vortex and centrifuge as above.
8. Aspirate the supernatant and add 500 μl per pellet of the nuclear stain DAPI diluted at 1:10,000 (1 μg/ml) in DPBS. Do not add DAPI to the sample which will serve as an IRF3 single positive control. Incubate for 10 min at room temperature. Protect from light.
9. Centrifuge as above.
10. Aspirate the supernatant and resuspend the pellet in 50 μl of FACS buffer.
11. Transfer the suspension into a 1.5 ml protein low retention tube for acquisition with ImageStream. The samples should be protected from light.

    Timing: 1 h and 30 min.

    Optional: The samples can be stored at 4 °C protected from light, if not imaged immediately. The samples are stable for at least a week (*see* **Note 8**).

3.5 Data Acquisition with ImageStream

Acquire data with the ImageStream X Mark II (IS-X) imaging cytometer.

1. Start IS-X instrument and Inspire™ software (Amnis-EMD-Millipore-Sigma).
2. To initialize fluidics from Inspire™ file menu, choose "Load Default Template." Use ASSIST tab to start calibrations and testing of the instrument. Click "Start all" and verify that calibrations are successful.
3. Turn all lasers used in the experiment. Briefly, for described IRF staining, turn next lasers: (a) 405 nm violet laser for DAPI, (b) 488 nm laser, (c) 658 nm laser for IRF staining, and (d) 785 nm laser at 0.5 mW for side scatter; brightfield (BF) for all samples with exception of compensation controls was acquired at channel 1.
4. Press "Flush Lock and Load" to load a first sample and adjust laser power for each of the fluorochromes.
5. Using area vs aspect ratio parameters, eliminate acquisition of unwanted debris. To collect only cells, set Area Low Limit in BF channel to size of cell (7–8 μm for lymphocytes and can be

20–50 μm for different cell lines). For primary human cells due to their heterogeneity, consider excluding only erythrocytes and platelets (>2–4 μm). Select fluorescent channels to be collected or collect all channels.

6. Enter the File name and Destination Folder for your experiment.
7. Press "Run Acquire" to collect and save experimental data file.
8. Acquire single fluorescent sample controls as compensation controls (need to be acquired with 785 nm laser (side scatter laser) off and with brightfield channel off. Collect at least 400–500 single events (more events may help with manual adjustment of spectral compensation). Only events exhibiting a positive signal in the fluorescent channel of interest have to be collected (e.g., DAPI control has to be positive at channel 7). Use the brightest sample in the experiment to set the laser power for each fluorochrome to prevent saturation of images (choose max pixel values between 100 and 4000 counts). After you save the data file with the adjusted laser power for the first sample, do not change these parameters for the entire experiment.
9. Press "Flush, Lock and Load" to acquire the next sample, and repeat this procedure till all experimental samples will be collected.

   Timing: The time of sample acquisition varies based on the cell concentration of the samples, but it is up to 20–30 min per sample when working with low cell numbers (less than 1×10^5 in 50 μl) and 5–10 min per sample when working with more concentrated samples (1×10^6 in 50 μl).

3.6 Data Analysis of ImageStream

1. Perform analysis using ImageStream Data Exploration and Analysis Software (IDEAS) vs. 6.1 (Amnis-EMD-Millipore-Sigma) or current version of software.
2. Launch IDEAS software (Amnis-EMD-Millipore-Sigma) and load one of the sample raw (.rif) files.
3. Create a compensation matrix by launching Compensation Wizard. Click on "new matrix" and add files acquired as single compensation controls during the experiment.
4. Follow through the Compensation Wizard directions until the end. The finished compensation matrix will be saved and used for generation data analysis file (.daf).
5. Generate .daf file using a new created compensation matrix.
6. Use a scatter plot area vs aspect ratio (brightfield; channel 1; filter: 480–500 nm) of all the cellular events in the data file to distinguish single cells from debris or multicellular events.
7. Define the single-cell population and gate around singlets. Verify created gate by clicking on individual dots and corresponding images.

8. Roundish single cells expected to have an aspect ratio app 1 (ratio of two cell diameters); however, it can be <1 for elongated cells and around 0.5 for doublets.
9. Alternatively, histogram of fluorescent intensity of nuclear dye (DAPI) can be used to identify single events (one nucleus in the single cell vs. multiple nuclei in cell clusters (Fig. 6, sequence of IFC analysis).
10. Single "focused" images were gated out using Gradient RMAX (focused events).
11. Quantitate similarity (or co-localization) of the IRF3 with nuclear dye DAPI to determine translocation of IRF into the nucleus. A high degree of IRF/DAPI co-localization corresponds to high similarity score (SS) and a predominant nuclear distribution of IRF3 factor. The SS score is a log-transformed Pearson's correlation coefficient between the pixel values of nucleus image and fluorescence image of translocated protein (IRF3-AF647, channel 11) as described previously [13, 18].
12. Setting correct mask for analysis.

    Selecting the best mask is a crucial step for performing IFC assays. Examples of morphology and erode masks can be seen

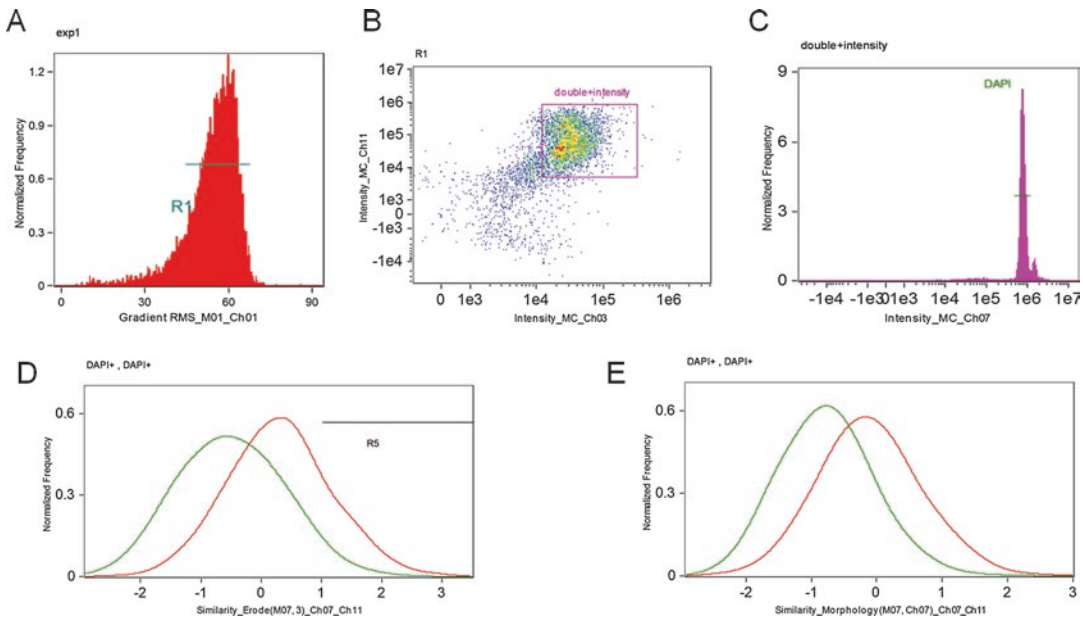

Fig. 6 Sequence of imaging flow cytometry analysis used in the protocol with data acquired with Amnis ImageStream X Mark II in 60× magnification. (**a**) Focused cells defined by gating at highly contrasted cells at Gradient RMS histogram (which measures the sharpness quality of image). Unfocused cells are excluded due to a low Gradient RMS values; (**b**) IRF3^{+}CD14^{+} double intensity cells gated at IRF3 and CD14 fluorescent intensities biparametric dotplot; (**c**) Single cells defined by nuclear staining (gated at histogram of DAPI fluorescent intensity). Similarity histograms based on nuclear morphology (M07, Ch7, **d**) and erode (M07,3, **e**) mask and cellular mask, optimized for IRF3 fluorescent intensity parameter (fluorescent channel 11)

in publications by McGrath et al. [56] and George et al. [13] and threshold mask with different cutoffs in the study by Henery and colleagues [57] and recent detailed review by Dominical et al. [58].

Masks in IFC experiment can be divided in three major types, default masks, function masks, and combined masks; can be created on the basis of brightfield, side scatter, and fluorescence images; and can be combined in a Boolean manner and customized (IDEAS—ImageStream Data Exploration and Analysis Software, Amnis-EMD-Millipore-Sigma). For analysis of nucleocytoplasmic shuttling, a nuclear mask, generated using a nuclear dye (in our approach DAPI), is essential [58]. Alternatively, cytoplasmic mask excluding the nuclear and membrane regions can be created, especially, if probe is specific for the cytoplasmic region of the cell. In order to optimize mask in our experiments, we visually inspected and compared morphology, object, threshold with different cutoffs, and erode (−2 pixel) masks (Fig. 7) and in further experiments used erode (−2 pixel) mask and morphology mask in parallel. Different masks were visualized on the cells and/or cellular nuclei (example in Fig. 7) to check their relevance and suitability for analysis.

IDEAS has wizard predefined sequences of algorithms allowing for straightforward way to set spectral compensation and quantify % of translocation. However, in some cases, it might be necessary to perform additional analysis based on the fluorescence intensity per cell and percentage of cells displaying fluorescence in combination with morphological features.

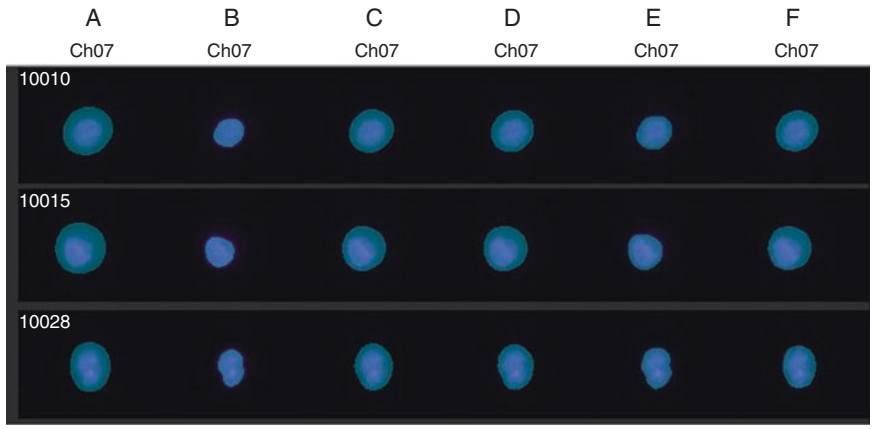

Fig. 7 Representative images of respective cellular nuclear masks created with IDEAS (DAPI fluorescent channel). Cells were acquired by Amnis ImageStream X Mark II at 60× magnification. (**a**) Default mask channel 7 (DAPI); (**b**) Morphology mask (M07, Ch07); (**c**) Object mask (M07, Ch07, tight); (**d**) Threshold mask (M07, Ch07, 95); (**e**) Dilate mask (threshold (M07, Ch 07, 70), 2); (**f**) Erode mask (M07,3)

13. Once all plots are created for the certain experimental condition, create "a statistical report template," save it as .ast file, and batch all appropriate files. Export data from IDEAS as Excel files to perform statistical analysis.
14. Statistical analysis can be done using GraphPad Prism (GraphPad) or alternative software (STATISTICA and/or SPSS). Data for the similarity score values can be analyzed by one-way analysis of variance (ANOVA) with Bonferroni multiple comparison test. Data for the percent cells positive for nuclear IRF3 stain can be analyzed by chi-squared test using the absolute number of positive cells compared to the control. P values below 0.05 are considered significant.

3.7 Anticipated Results

An overview of the protocol is given in Fig. 1. The representative images in Figs. 2 and 4 demonstrate that the percentage of cells with nucleocytoplasmic translocation can be successfully quantified in blood-derived MDMs and in primary myeloid cells derived from human cervical mucosa. The percentage of translocation in response to LPS increased from 14.4 to 65.27% in MDMs (Fig. 2b, c) and from 2.9 to 19.6% in cervical $CD14^+$ cells (Fig. 4b, c). We have previously used this technique to determine the effect of knocking down TREX1 on the interferon (IFN) pathway induction by HIV infection both in primary human MDMs and $CD4^+$ T cells [7]. TREX1 knockdown did not significantly change IRF3 localization in uninfected cells; however, IRF3 translocated to the nucleus after HIV infection in cells knocked down for TREX1. This was consistent with previously reported data of IFN production after HIV infection in TREX-1 knockout cells [59]. IRF3 activation was suppressed after we knocked down the DNA sensors that recognize HIV reverse transcripts, cGAS and IFI16, demonstrating that the IFN induction by HIV was dependent on these DNA sensors. In contrast, the knockdown of another DNA sensor AIM2 or the RNA sensor RIG-I, which are not required for the induction of type I IFN by HIV, did not suppress IRF3 nuclear translocation. Furthermore, we detected a significant increase in the levels of IRF3 nuclear translocation in cells knocked down for AIM2 which is in agreement with findings published at the same time by another group suggesting a negative regulation of the STING-IRF3 pathway by the AIM2 inflammasome [60]. Thus, our IRF3 activation assay using IFC is sensitive and allowed us to dissect the mechanisms of IRF3 activation and IFN induction in response to HIV infection with statistical significance. It was powerful even when used with human primary T cells, which have a low nuclear-to-cytosolic ratio.

The level of IRF3 activation might vary between donors; however, due to the high number of analyzed events, statistically significant changes can be determined even for donors with a weaker response.

The staining performs well each time with all cell types that we have tested including human cervical tissue samples. Preliminary optimization of fixation/permeabilization conditions specific for cell types and tissues is required. We recommend using a spectral flow cytometer (SP6800, Sony Biotechnology Inc., USA) for this purpose. A negative control sample (e.g., samples where the expression of the target protein has been silenced) is recommended to confirm the specificity of antibodies used and whether it is possible to accurately detect the level of nucleocytoplasmic translocation. A positive control sample (such as LPS-activated sample for IRF3; Fig. 4) is required in order to troubleshoot problematic steps and confirm that the technique has been run correctly. We recommend statistical analysis data following validation and optimization of different masks to ensure that subtle changes in protein translocation are not overlooked. This IFC protocol is readily applicable for different experimental settings within the field of signal transduction and transcriptional analysis. Combining the detection of target proteins with morphological and fluorescent labeling-defined cellular subpopulations assigns the percent of nucleocytoplasmic translocation to specific subpopulations. When the amount of the starting material (blood volume or weight of tissue) is known, absolute numbers of cellular subpopulations can be obtained and combined with the exact percent of nucleocytoplasmic translocation.

4 Notes

1. *Sample fixation and permeabilization*. Immunostaining of different intracellular proteins may require different fixation and permeabilization protocols. As alternative to the provided protocol, one may consider modifying permeabilization by varying duration of permeabilization, permeabilization with Triton X-100, or combining fixation and permeabilization in one step [61].
2. *Tissue digestion optimization*. We recommend the use of semi-automatic tissue dissociator (we used gentleMACS™ dissociator, Miltenyi Biotec) to increase the yield of dissociated cells. The use of gentleMACS™ dissociator is critical with difficult to digest fibrous samples such as the human cervical tissue samples. For this type of tissue, enzymatic dissociation alone does not allow sufficient recovery of cells located deeper in the stroma, such as the myeloid cells. Also, the combination of enzymatic digestion and mechanical dissociation allows reducing the time of incubation with the enzymes which can cleave certain cell surface markers (such as CD56, CD4, CD209 (DC-DIGN)). The choice of the type and the concentration of dissociation enzyme is important for keeping integrity of antigen epitopes and depends on the epitope of interest. It is also

important to not exceed 30 min of incubation with collagenase IV to prevent loss of cell viability and loss of certain cell surface markers due to enzymatic digestion. In addition, we recommend the use of a semiautomatic tissue dissociator versus manual mechanical tissue dissociation in order to increase reproducibility since manual mechanical tissue dissociation may yield significant fluctuations in the yield of viable cells.

3. *Dead cell discrimination*. Dead and damaged cells often cause increased autofluorescence. Staining for dead cell discrimination enables exclusion of dead cells from analysis. Amino-reactive dyes (LIVE/DEAD fixable dead cell stains) are suitable for fixed cells [62]. Titrate Zombie Green™ to determine the optimal dilution for each sample type. Heat-shocked cells (incubated at 65 °C for 1 min, followed by 1 min incubation on ice) can be used as a single positive control for viability dye.
4. *Choice of fluorochromes*. IS-X instrument has colinear lasers, and fluorescence may require higher spectral compensation than conventional flow cytometer with optical pathways separated from different lasers. Therefore, the choice of fluorochromes including DNA dyes is important. For example, propidium iodide (PI) would intensively bleed in neighboring channels and create spectral compensation problems and distort images. The use of DNA dyes with a narrow emission profile, such as DAPI, is recommended.
5. *Safety precaution*. Paraformaldehyde is a suspected carcinogen and skin/eye irritant. Wear suitable protective clothing, gloves, and eye protection while handling and use in well-ventilated areas. Avoid contact of material with the skin or eyes. Wash thoroughly after handling.
6. *Large number of samples*. When working with a large number of samples, the staining protocol can be performed in a 96-well V-bottom plate. The plate can be centrifuged to pellet the cells. The pipetting can be done with a multichannel pipette.
7. *Optimization of staining conditions*. Antibody titration is required. Directly conjugated and flow cytometry-validated antibodies are preferential. However, as we have demonstrated above, the use of non-directly conjugated antibody is possible. Antibody selection is paramount. Antibodies not used for flow cytometry can be acceptable after preliminary validation. To prevent non-specific staining, it can be useful to increase the amount of blocking serum and/or to add a detergent such as 0.05% Tween 20 or Triton X-100 to the wash buffer. Also, cells can be cultured in media with reduced serum to reduce the background.
8. *Sample storage*. The fixed samples are stable and can be stored with minimal loss of signal (depending on fluorochrome) until

transported for analysis, or they can potentially be shipped to an IFC core facility or collaborative laboratory equipped with ImageStream X instrument for analysis.

Acknowledgments

Support for this work was provided by Harvard University CFAR (P30 AI060354) to R.T. and PCMM – Boston Children's Hospital and grants from MES of Republic of Kazakhstan PI NURIS 055 project #100/14 to N.S.B. The authors thank Judy Lieberman for her continuing support and Kenneth Ketman at the Flow and Imaging Cytometry Resource at PCMM-BCH for his technical assistance.

References

1. Görlich D, Kutay U (1999) Transport between the cell nucleus and the cytoplasm. Annu Rev Cell Dev Biol 15:607–660
2. Tran EJ, King MC, Corbett AH (2014) Macromolecular transport between the nucleus and the cytoplasm: advances in mechanism and emerging links to disease. Biochim Biophys Acta 1843:2784–2795. https://doi.org/10.1016/j.bbamcr.2014.08.003
3. Stelma T, Chi A, van der Watt PJ, Verrico A, Lavia P, Leaner VD (2016) Targeting nuclear transporters in cancer: diagnostic, prognostic and therapeutic potential. IUBMB Life 68:268–280. https://doi.org/10.1002/iub.1484
4. Marchi M, Parra R, Costa M, Ratto GM (2010) Localization and trafficking of fluorescently tagged ERK1 and ERK2. Methods Mol Biol 661:287–301. https://doi.org/10.1007/978-1-60761-795-2_17
5. Barteneva NS, Fasler-Kan E, Vorobjev IA (2012) Imaging flow cytometry: coping with heterogeneity in biological systems. J Histochem Cytochem 60:723–733
6. Basiji DA (2016) Principles of Amnis imaging flow cytometry. Methods Mol Biol 1389: 13–21.https://doi.org/10.1007/978-1-4939-3302-0_2
7. Wheeler LA, Trifonova RT, Vrbanac V, Barteneva NS, Liu X et al (2016) TREX1 knockdown induces an interferon response to HIV that delays viral infection in humanized mice. Cell Rep 15:1715–1727. https://doi.org/10.1016/j.celrep.2016.04.048
8. Haridas V, Ranjbar S, Vorobjev IA, Goldfeld AE, Barteneva NS (2017) Imaging flow cytometry analysis of intracellular pathogens. Methods 112:91–104. https://doi.org/10.1016/j.ymeth.2016.09.007
9. Hill R, Cautain B, de Pedro N, Link W (2014) Targeting nucleocytoplasmic transport in cancer therapy. Oncotarget 5:11–28
10. Ikushima H, Negishi H, Taniguchi T (2013) The IRF family transcription factors at the interface of innate and adaptive immune responses. Cold Spring Harb Symp Quant Biol 78:105–116. https://doi.org/10.1101/sqb.2013.78.020321
11. McNab F, Mayer-Barber K, Sher A, Wack A, O'Garra A (2015) Type I interferons in infectious disease. Nat Rev Immunol 15:87–103. https://doi.org/10.1038/nri3787
12. Reich NC (2002) Nuclear/cytoplasmic localization of IRFs in response to viral infection or interferon stimulation. J Interf Cytokine Res 22:103–109
13. George TC, Fanning SL, Fitzgerald-Bocarsly P, Medeiros RB, Highfill S et al (2006) Quantitative measurement of nuclear translocation events using similarity analysis of multispectral cellular images obtained in flow. J Immunol Methods 311:117–129
14. Woo SR, Fuertes MB, Corrales L, Spranger S, Furdyna MJ et al (2014) STING-dependent cytosolic DNA sensing mediates innate immune recognition of immunogenic tumors. Immunity 41:830–842. https://doi.org/10.1016/j.immuni.2014.10.017
15. Xu J, Mercado-López X, Grier JT, Kim WK, Chun LF et al (2015) Identification of a natural viral RNA motif that optimizes sensing of viral RNA by RIG-I. MBio 6:e01265-15. https://doi.org/10.1128/mBio.01265-15
16. Lau DT, Fish PM, Sinha M, Owen DM, Lemon SM, Gale M Jr (2008) Interferon regulatory factor-3 activation, hepatic interferon-stimulated gene expression, and immune cell infiltration in hepatitis C virus patients. Hepatology

47:799–809. https://doi.org/10.1002/hep.22076
17. Trifonova RT, Lieberman J, van Baarle D (2014) Distribution of immune cells in the human cervix and implications for HIV transmission. Am J Reprod Immunol 71:252–264. https://doi.org/10.1111/aji.12198
18. Fasler-Kan E, Baiken Y, Vorobjev IA, Barteneva NS (2016) Analysis of nucleocytoplasmic protein shuttling by imaging flow cytometry. Methods Mol Biol 1389:127–137. https://doi.org/10.1007/978-1-4939-3302-0_8
19. Doyle S, Vaidya S, O'Connell R, Dadgostar H, Dempsey P et al (2002) IRF3 mediates a TLR3/TLR4-specific antiviral gene program. Immunity 17:251–263
20. Ysebrant de Lendonck L, Tonon S, Nguyen M, Vandevenne P, Welsby I et al (2013) Interferon regulatory factor 3 controls interleukin-17 expression in CD8 T lymphocytes. Proc Natl Acad Sci U S A 110:E3189–E3197. https://doi.org/10.1073/pnas.1219221110
21. Reimer T, Brcic M, Schweizer M, Jungi TW (2008) Poly(I:C) and LPS induce distinct IRF3 and NF-kappaB signaling during type-I IFN and TNF responses in human macrophages. J Leukoc Biol 83:1249–1257. https://doi.org/10.1189/jlb.0607412
22. Rajput A, Kovalenko A, Bogdanov K, Yang SH, Kang TB et al (2011) RIG-I RNA helicase activation of IRF3 transcription factor is negatively regulated by caspase-8-mediated cleavage of the RIP1 protein. Immunity 34:340–351. https://doi.org/10.1016/j.immuni.2010.12.018
23. Liu S, Cai X, Wu J, Cong Q, Chen X et al (2015) Phosphorylation of innate immune adaptor proteins MAVS, STING, and TRIF induces IRF3 activation. Science 347:a2630. https://doi.org/10.1126/science.aaa2630
24. Fitzgerald KA, Rowe DC, Barnes BJ, Caffrey DR, Visintin A et al (2003) LPS-TLR4 signaling to IRF3/7 and NF-kappaB involves the toll adapters TRAM and TRIF. J Exp Med 198:1043–1055
25. Wang Z, Ji J, Peng D, Ma F, Cheng G, Qin FX (2016) Complex regulation pattern of IRF3 activation revealed by a novel dimerization reporter system. J Immunol 196:4322–4330. https://doi.org/10.4049/jimmunol.1502458
26. Li Q, Tang L, Roberts PC, Kraniak JM, Fridman AL, Kulaeva OI et al (2008) Interferon regulatory factors IRF5 and IRF7 inhibit growth and induce senescence in immortal li-Fraumeni fibroblasts. Mol Cancer Res 6:10.1158
27. Marié I, Smith E, Prakash A, Levy DE (2000) Phosphorylation-induced dimerization of interferon regulatory factor 7 unmasks DNA binding and a bipartite transactivation domain. Mol Cell Biol 20:8803–8814
28. Cao N, Chen T, Guo ZP, Qin S, Li MM (2014) Monoammonium glycyrrhizate suppresses tumor necrosis factor-α induced chemokine production in HMEC-1 cells, possibly by blocking the translocation of nuclear factor-kappaB into the nucleus. Can J Physiol Pharmacol 92:859–865
29. King CC, Sastri M, Chang P, Pennypacker J, Taylor SS (2011) The rate of NF-κB nuclear translocation is regulated by PKA and a kinase interacting protein 1. PLoS One 6:e18713. https://doi.org/10.1371/journal.pone.0018713
30. Blaecke A, Delneste Y, Herbault N, Jeannin P, Bonnefoy JY et al (2002) Measurement of nuclear factor-kappa B translocation on lipopolysaccharide-activated human dendritic cells by confocal microscopy and flow cytometry. Cytometry 48:71–79
31. Montagut C, Tusguets I, Ferrer B, Corominas JM, Bellosillo B et al (2006) Activation of nuclear factor-kappa B is linked to resistance to neoadjuvant chemotherapy in breast cancer patients. Endocr Relat Cancer 13:607–616
32. Kojima M, Morisaki T, Sasaki N, Nakano K, Mibu R et al (2004) Increased nuclear factor-kB activation in human colorectal carcinoma and its correlation with tumor progression. Anticancer Res 24:675–681
33. Schachter TN, Shen T, Liu Y, Martin F, Schneider MF (2012) Kinetics of nuclear-cytoplasmic translocation of Foxo1 and Foxo3A in adult skeletal muscle fibers. Am J Physiol Cell Physiol 303:C977–C990. https://doi.org/10.1152/ajpcell.00027.2012
34. Clavel S, Siffroi-Fernandez S, Coldefy AS, Boulukos K, Pisani DF, Derijard B (2010) Regulation of the intracellular localization of Foxo3a by stress-activated protein kinase signaling pathways in skeletal muscle cells. Mol Cell Biol 30:470–480. https://doi.org/10.1128/MCB.00666-09
35. Wang X, Chen WR, Xing D (2012) A pathway from JNK through decreased ERK and Akt activities for FOXO3a nuclear translocation in response to UV irradiation. J Cell Physiol 227:1168–1178. https://doi.org/10.1002/jcp.22839
36. Krieghoff E, Behrens J, Mayr B (2006) Nucleocytoplasmic distribution of β-catenin is regulated by retention. J Cell Sci 119:1453–1463
37. Caceres-Gorriti KY, Carmona E, Barres V, Rahimi K, Letourneau IJ et al (2014) RAN nucleo-cytoplasmic transport and mitotic spindle assembly partners XPO7 and TPX2 are new prognostic biomarkers in serous epithelial

ovarian cancer. PLoS One 9:e91000. https://doi.org/10.1371/journal.pone.0091000

38. Marumo T, Takagi Y, Muraki K, Hashimoto N, Miyamoto S, Tanigaki K (2013) Notch signaling regulates nucleocytoplasmic Olig2 translocation in reactive astrocytes differentiation after ischemic stroke. Neurosci Res 75:204–209. https://doi.org/10.1016/j.neures.2013.01.006
39. Tomar D, Sripada L, Prajapati P, Singh R, Singh AK, Singh R (2012) Nucleo-cytoplasmic trafficking of TRIM8, a novel oncogene, is involved in positive regulation of TNF induced NF-kB pathway. PLoS One 7:e48662. https://doi.org/10.1371/journal.pone.0048662
40. Dissing-Olesen L, MacVicar BA (2015) Fixation and immunolabeling of brain slices: SNAPSHOT method. Curr Protoc Neurosci 71:1.23.1-12. https://doi.org/10.1002/0471142301.ns0123s71
41. Domingues I, Rino J, Demmers JA, de lanerolle P, Santos SC (2011) VEGFR2 translocates to the nucleus to regulate its own transcription. PLoS One 6:e25668. https://doi.org/10.1371/journal.pone.0025668
42. Kojima Y, Nalayama M, Nishina T, Nakano H, Koyanagi M, Taked K et al (2011) Importin β1 protein-mediated nuclear localization of death receptor 5 (DR5) limits DR5/tumor necrosis factor (TNF)-related apoptosis- inducing ligand (TRAIL)-induced cell death of human tumor cells. J Biol Chem 286:43383–43393. https://doi.org/10.1074/jbc.M111.309377
43. Bhosle VK, Rivera JC, Zhou TE, Omri S, Sanchez M et al (2016) Nuclear localization of platelet-activating factor receptor controls retinal neovascularization. Cell Discov 2:16017. https://doi.org/10.1038/celldisc.2016.17
44. Heydorn A, Lundholt BK, Praestegaard M, Pagliaro L (2006) Protein translocation assays: key tools for accessing new biological information with high-throughput microscopy. Methods Enzymol 414:513–530
45. Huber LA, Pfaller K, Vietor I (2003) Organelle proteomics: implications for subcellular fractionation in proteomics. Circ Res 92:962–968
46. Bhosle VK, Gobeil F Jr, Rivera JC, Ribeiro-da-Silva A, Chemtob S (2015) High resolution imaging and function of nuclear G protein-coupled receptors (GPCRs). Methods Mol Biol 1234:81–97. https://doi.org/10.1007/978-1-4939-1755-6_8
47. Maguire O, Collins C, O'Loughlin K, Miecznikowski J, Minderman H (2011) Quantifying nuclear p65 as a parameter for NF-κB activation: correlation between ImageStream cytometry, microscopy, and western blot. Cytometry 79:461–469. https://doi.org/10.1002/cyto.a.21068
48. Futamura K, Sekino M, Hata A, Ikebuchi R, Nakanishi Y, Egawa G, Kabashima K et al (2015) Novel full-spectral flow cytometry with multiple spectrally-adjacent fluorescent proteins and fluorochromes and visualization of in vivo cellular movement. Cytometry 87:830–842. https://doi.org/10.1002/cyto.a.22725.
49. Böyum A (1968) Isolation of mononuclear cells and granulocytes from human blood. Isolation of mononuclear cells by one centrifugation, and of granulocytes by combining centrifugation and sedimentation at 1g. Scand J Clin Lab Invest Suppl 97:77–89
50. Song E, Lee SK, Dykxhoorn DM, Novina C, Zhang D et al (2003) Sustained small interfering RNA-mediated human immunodeficiency virus type 1 inhibition in primary macrophages. J Virol 77:7174–7181
51. Allalunis-Turner MJ, Siemann DW (1986) Recovery of cell subpopulations from human tumour xenografts following dissociation with different enzymes. Br J Cancer 54:615–622
52. Chang Q, Hedley D (2012) Emerging applications of flow cytometry in solid tumor biology. Methods 57:359–367. https://doi.org/10.1016/j.ymeth.2012.03.027
53. Quatramoni JG, Singhal S, Bhojnagarwala P, Hancock WW, Albeda SM, Eruslanov E (2015) An optimized disaggregation method for human lung tumors that preserves the phenotype and function of the immune cells. J Leukoc Biol 97:201–209
54. Dashkova V, Segev E, Malashenkov D, Kolter R, Vorobjev I, Barteneva NS (2016) Microalgal cytometric analysis in the presence of endogenous autofluorescent pigments. Algal Res 19:370–380
55. Krutzik PO, Trejo A, Schulz KR, Nolan GP (2011) Phospho flow cytometry methods for the analysis of kinase signaling in cell lines and primary human blood samples. Methods Mol Biol 699:179–202. https://doi.org/10.1007/978-1-61737-950-5_9
56. McGrath KE, Bushnell TP, Palis J (2008) Multispectral imaging of hematopoietic cells; where flow meets morphology. J Immunol Methods 336:91–97. https://doi.org/10.1016/j.jim.2008.04.012
57. Henery S, George T, Hall B, Basiji D, Ortyn W, Morrissey P (2008) Quantitative image based apoptotic index measurement using multispectral imaging flow cytometry: a comparison with standard photometric methods. Apoptosis 13:1054–1063. https://doi.org/10.1007/s10495-008-0227-4
58. Dominical V, Samsel L, McCoy JP Jr (2017) Masks in imaging flow cytometry. Methods 112:9–17. https://doi.org/10.1016/j.ymeth.2016.07.013

59. Yan N, Regalado-Magdos AD, Stiggelbout B, Lee-Kirsch MA, Lieberman J (2010) The cytosolic exonuclease TREX1 inhibits the innate immune response to human immunodeficiency virus type 1. Nat Immunol 11:1005–1013. https://doi.org/10.1038/ni.1941
60. Corrales L, Woo SR, Williams JB, McWhirter SM, Dubensky TW, Gajewski TF (2016) Antagonism of the STING pathway via activation of the AIM2 inflammasome by intracellular DNA. J Immunol 196:3191–3198. https://doi.org/10.4049/jimmunol.1502538
61. Artym VV, Matsumoto K (2010) Imaging cells in three-dimensional collagen matrix. Curr Protoc Cell Biol. Chapter 10: Unit 10.18.1-20. https://doi.org/10.1002/0471143030.cb1018s48
62. Perfetto SP, Chattopadhyay PK, Lamoreaux L, Nguen R, Ambrozak D, Koup RA, Roederer M (2010) Amine-reactive dyes for dead cell discrimination in fixed samples. Curr Protoc Cytom. Chapter 9, Unit 9.34. https://doi.org/10.1002/0471142956.cy0934s53

Chapter 9

Methods of Study of Neuron Structural Heterogeneity: Flow Cytometry vs. Laser Interferometry

Ekaterina Kopeikina, Marina Dukhinova, and Eugene D. Ponomarev

Abstract

Neuronal cells are probably the less studied cells regarding their heterogeneity on a single cell or population levels. One of the main problems of studying of individual neurons is the presence of long processes (axons) on differentiated adult neurons that hamper their isolation without significant damage to the cells. Therefore, the most common method to study neuronal cells is immunofluorescent microscopy of sections of the brain, which remains poorly quantitative and allows analyzing a small number of fixed cells. Also, immunofluorescent microscopy has a number of staining artifacts since histology section has high level of autofluorescence and non-specific binding of fluorescent probes. Alternative methods that could overcome disadvantages of immunofluorescent histology include flow cytometry, scanning cytometry, and laser interferometry. Flow cytometry and, to some extent of degree, scanning cytometry allow performing analysis of multiple markers with a low level of non-specific background and very robust statistics. Laser interferometry allows studies intact, alive neurons without staining. Limitations and advantages of these methods are discussed in this chapter.

Key words Neurons, Flow cytometry, Laser interferometry

1 Introduction

Morphological, physiological, and biochemical heterogeneity of neurons allows to differentiate them into several subpopulations with distinct functions. Morphologically neurons differ in size and ultrastructural characteristics. Physiologically, there is a direct relationship between the size with a diameter of nerve fibers and the speed they conduct a nerve impulse [1]. Finally, the use of specific markers (e.g., receptors for neurotransmitters) makes it possible to identify the biochemical properties and functions [2]. Neurons in the brain have a broad range of heterogeneities, even within the same morphological or physiological types of the cells. Speaking about heterogeneity, it is important to distinguish biochemical heterogeneity, which relates to neuronal structure, and dynamic heterogeneity, which refers to measurements of continuing

Natasha S. Barteneva and Ivan A. Vorobjev (eds.), *Cellular Heterogeneity: Methods and Protocols*, Methods in Molecular Biology, vol. 1745, https://doi.org/10.1007/978-1-4939-7680-5_9,

neuronal electrophysiological activity [3, 4]. Heterogeneity is observed in virtually every aspect of neuronal physiology [5].

One of the increasingly used methods for studying the heterogeneity of neurons is flow cytometry. As a modern technology for measuring multiple characteristics of cells, flow cytometry appeared as a result of the development of traditional cytochemical and histochemical methods of analysis. This technology, designed to accelerate analysis in cytodiagnostic and clinical cytology, has gradually evolved into an effective approach to solving many problems of immunology, cell biology, cell engineering, etc. [6].

This technology is based on the entire arsenal of cytochemical fluorescence methods for analyzing the structural components of cells, as well as intracellular organelles [6]. Flow cytometry differs from classical cytochemistry by higher productivity and effectiveness. Flow cytometry examines samples from several thousand to millions of cells at high speed, which guarantees the statistical reliability of the results [7]. In turn, modern cytometry differs from molecular biology and classical biochemistry by the ability to analyze not only the averaged molecular characteristics of the entire population but the individual parameters of each cell [8].

There are two main directions of modern conventional flow cytometry: (1) analytical flow cytometry and (2) cell sorting with subsequent biochemical analysis (e.g., RNA-seq). A first direction is an analytical approach; the second path allows to select the cell subpopulations of interest or even single cells based on the analytical capabilities of analytical flow cytometry and then to proceed to the biochemical analysis of the selected subpopulations or each single cell. Essential features of flow cytometry make this method valuable for clinical practice (Fig. 1) [7, 9].

Modern cytometers record a number of parameters for each cell at a rate of up to 10,000 cells per second [10]. Despite the complexity of modern flow cytometers, the central principle of flow cytometry is quite simple. Under a certain pressure, a constant “squeezing” current of the isotonic solution moves through the flow cell. Inside the flow cell, there is a probe stream with analyzed cells. The conditions are chosen so that due to the difference in pressure in the “squeezing” and the probe streams, the flow is hydrodynamically focused, and therefore the cells line up one after the other. Cells cross a beam of the laser beam of light in a particular place, and their characteristics are measured [10].

To apply the principle of flow cytometry, it is required to receive the suspension of individual neurons, even though they tend to form a network of axons and dendrites in which the outgrowths of cells form synapses. To avoid neuronal damage during preparation of cell suspension, neurons from the brain of juvenile animals are used. In juvenile or newborn animals, interneuronal connections have not yet completely formed, but neuronal cells have already been differentiated and specialized [11]. For flow

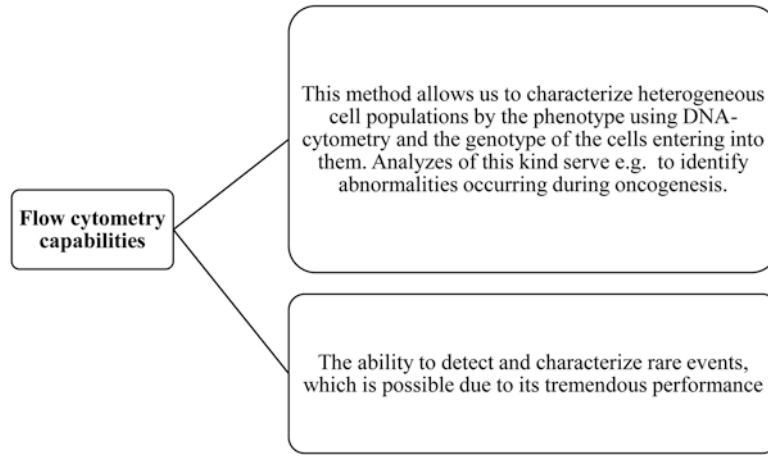

Fig. 1 Advantages of flow cytometry in clinical practice

cytometry, it is convenient to use the tissue of the cerebellum, obtained from rodents at the age of 9–12 days or cortex obtained at the age of 3–7 days [12]. Treatment of tissue with enzymes (e.g., trypsin or papain) that loosens the intercellular environment, followed by interfusion of the suspension, allows you to separate the cells. After losing links with neighboring cells, neurons become spherical and remain viable for several hours. During this time, they can be stained and analyzed by flow cytometry. However, it is important to remember that from 5% to 15% of the total suspension of cells usually do not survive even within several hours. Therefore, dyes that separate alive from dead cells are necessary to use during analysis.

To investigate the heterogeneity of neurons, the following cell parameters could be measured:

(a) Scattering of light at an angle of 90° (so-called side scatter—SSC). The use of this parameter allows analyzing the relationship between the size of the cytoplasm and the nucleus, as well as the granularity or heterogeneity of the cytoplasm.

(b) Scattering of light at small angles (1–10°)—forward scatter (FSC). This parameter is used to determine the size of cells.

(c) Measurement of the fluorescence intensity of the object. It is the ability to analyze fluorescence intensity that has made flow cytometry highly informative and widely used.

As a rule, modern cytometers are equipped with several photoelectronic multipliers, which allow recording several types of fluorescence simultaneously. In addition to fluorescence intensity, it is possible to measure the time of a particle flight through the analysis zone and the polarization of fluorescence. The first one allows investigators to make conclusions about the asymmetry level of the

organelles or cells in the study and the second—about the level of viscosity of cell membranes which changes the functional state [10].

The information obtained from the measurement of the time of flight of cells through the analysis zone and light scattering signals makes it possible to examine the morphological characteristics of cells (cytoplasm granularity, the size of the cytoplasm and nucleus, the size and the degree of asymmetry of the cells) [2]. This capability, in turn, allows analyzing the cells without the use of fluorescent dyes. It may be particularly useful to distinguish different neuronal subpopulations (e.g., pyramidal neurons and interneurons).

The development of hybridoma technology has led to the broad usage of monoclonal antibodies [13]. Monoclonal antibodies allow the classification of cells not only by their morphological differences but also by a set of receptors and surface (or intracellular) antigens characteristics of individual cells and functional states [14]. Fluorochrome-labeled monoclonal antibodies allow both quantitative and qualitative analysis of intracellular and surface antigens.

The use of several monoclonal antibodies, which are labeled with different fluorescent dyes, allows investigators to obtain information about several antigens on the cell surface in one experiment. Therefore, this allows analyzing the subpopulation composition of cells, the presence of various anomalies, and the activity of cells within the subpopulation [12]. A good example of surface markers are receptors for neurotransmitters that would allow distinguishing dopaminergic or serotoninergic neurons or their subsets based on expression of dopamine receptors DR1 or DR2 and serotonin (5-HT) receptors (5-HTR1, 5-HTR2, etc.). In addition, intracellular expression of 5-HT could also be performed using anti-5-HT serum [15].

In flow cytometry, the study of the activity of intracellular enzymes with the help of fluorescent probes is currently widely used. Certain reagents have been established, which are the synthetic substrates that can be used to measure the activity of intracellular enzymes. These substrates penetrate the membrane of a living cell and have significant advantages over previously synthesized substrates, including increased resolving power and reduced analysis time.

A whole set of different fluorochromes made it possible to perform quantitative analysis of variety of parameters such as intracellular pH (7-hydroxycoumarin and fluorescein) and reactive oxygen species (ROS) including nitric oxide (NO) (using DAF-FM probe). Moreover, a concentration of free calcium ions (Indo-1, Fluo-3 probes), mitochondrial membrane potential (JC-1 probe), apoptosis (caspase-3 activity), and many others can be measured [10].

Nevertheless, the lack of standard approaches to tune cytometers for analysis of neuronal cells, preparing samples and creating

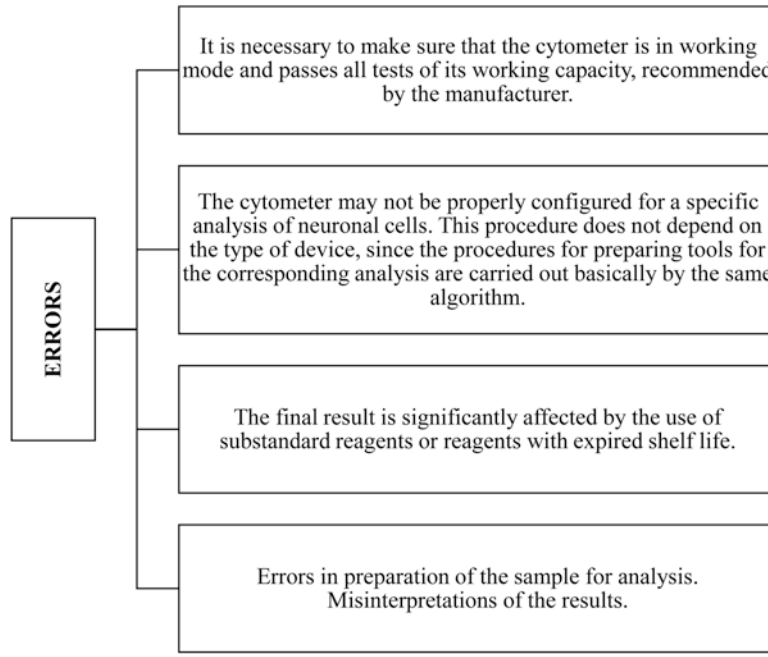

Fig. 2 Possible errors in using the flow cytometry analysis for neuronal cells

research protocols, still makes this method rather subjective and dependent on the researcher experience. During the analysis, errors and misinterpretations could be done at different stages (Fig. 2).

Thus, the advantages of flow cytometry in the study of heterogeneity of neurons include:

(a) Ability to measure membrane potential, intracellular calcium level, NO, 5-HT, etc. All these parameters can be recorded if appropriate fluorescent labels are used.

(b) Ability to simultaneously measure several parameters in the same cell. It is possible to reveal a correlation between changes in these parameters at the same time for almost every cell, not just with statistical (integral, averaged) parameter value, but with individually measured values for individual neurons.

One of the major drawbacks of flow cytometry is the need to use neurons from tissue that does not yet have all the characteristic properties of the adult brain. Nevertheless, the development of modern biotechnological methods has made it possible to solve even this problem. A laser scanning cytometers (LSC) was developed by CompuCyte Corp (Cambridge, MA, USA). In LSC, instead of pumping a cell suspension through a capillary, a laser beam is used to "sweep" a monolayer culture of grown neurons or brain slice (histology section) and conduct cytometric measurements as done by conventional flow cytometer. Using this approach,

the same morphological and fluorescent features could be studied on neurons of adult age without additional processing of neuronal cells and destruction of intercellular contacts and processes [4]. However, LSCs inherited problems associated with immunofluorescent histology such as high level of background due to autofluorescence and non-specific labeling when using antibodies. Moreover, it is very difficult to identify individual neurons with multiple processes across neuronal tissue.

Another modern technique for studying the heterogeneity of neurons is laser interferometry, in which a low-power laser radiation acts as a light source. Laser interferometry is used to study the dynamics of the cellular structure and the shape of biological objects [16]. The profilometer-based microscopes create images due to a change in the optical density of the biological object. The magnitude of this change is quantified [17].

Laser interference microscopy is currently used to assess changes in individual cells (changes in its shape and volume) and subcellular organelles (changes in the shape, volume, and movement of subcellular organelles, e.g., cytoplasmic actomyosin complexes) [18].

However, the possibilities of laser interference microscopy are clearly not fully used in the study of functions of neuronal cells. The specificity of this object is the exclusive dependence of the functional state and cellular dynamics on the method of investigation. Numerous artifacts are known to be connected with tissue fixation and staining procedure when using standard or confocal immunofluorescence microscopy. In case of laser interference microscopy, the distribution of the phase change in the optical density of an object is investigated. The principle of operation of laser interference microscopy is based on measuring the local phases of the light wave reflected by the object [13]. As a result of superposition of the wave from the reference mirror and the reflected wave, an interference pattern of the object is created. Then the signal is normalized along the wavelength, and the difference in the optical path of two waves or the phase height (thickness) of the object at a given point is determined. Thus, the phase portrait of the cell consists of the distribution of the phase shifts in different regions of the object. The obtained values of the phase shifts are used to reconstruct a 3D image of the cell.

Using the method of laser interference microscopy, cells as well as isolated organelles of neuronal cells (e.g., axons, vesicles) are studied. Other methods of microscopy could be also used to study these objects, but in comparison with them, the method of laser interference microscopy has several important advantages such as analysis of live cells without staining (Fig. 3).

Thus, when using laser interference microscopy, it is important to obtain an image of a neuron that has a number of additional characteristics in comparison with the image obtained with the

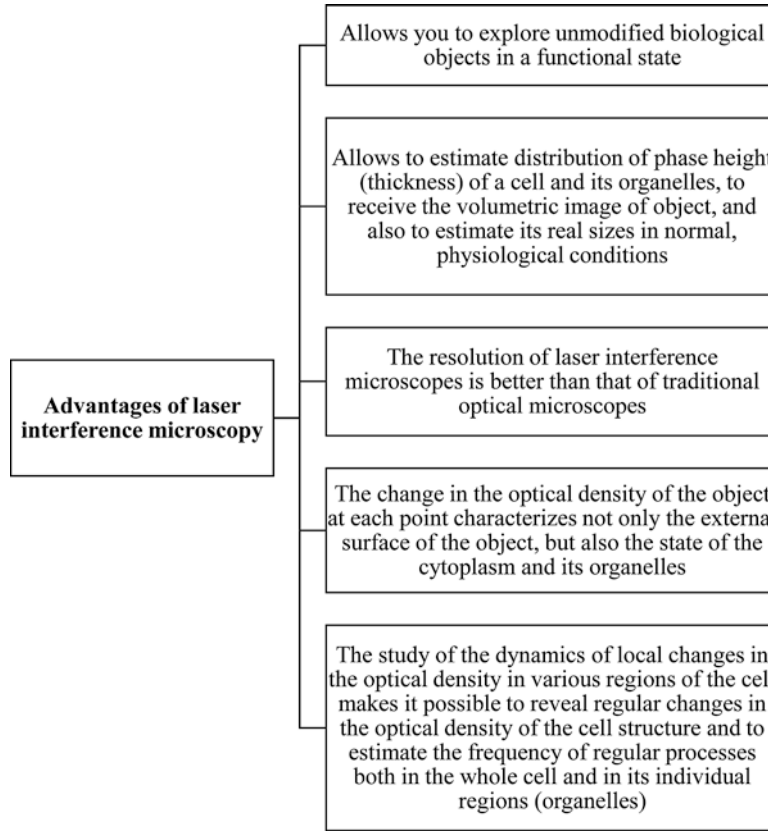

Fig. 3 Advantages of laser interference microscopy

help of traditional light microscopy. It is possible to obtain a volumetric image of neurons and distribution of subcellular structures, as well as to estimate their vertical dimensions, which is inaccessible to most other microscopic methods.

In addition, laser microinterferometry makes it possible to examine a non-fixed alive neurons without additional contrasting of the cell image with the help of dyes and therefore not to interfere with the coordinated functioning of the cell. This suggests that the method of laser interference microscopy could be used to study changes in lateral sizes and cell volume with a homogeneous cytoplasmic structure and subcellular structure of the cytoplasm and organelles of cells with a heterogeneous cytoplasmic structure in different functional states of a neuron [18, 19].

2 Materials

Prepare solutions at room temperature and store them at +4 °C. To work with cell suspensions, use refrigerated bracket centrifuge suitable for cell culture work (e.g., Eppendorf 5810R).

2.1 Preparation of Neuronal Cell Suspension

1. Prepare digesting medium. Add to 10 ml of DMEM medium 1.8 mg of L-cysteine, 1.8 mg EDTA, and 200 μl of papain (dissolved at a concentration of 1 U/μl in water; from Sigma). Warm digesting medium at water bath at +37 °C for 15 min.
2. To remove cell aggregates, we used 70 μm nylon mesh (cell strainer from Falcon).
3. To wash cells after digestion, we used PBS with 20% FBS (Gibco) to inhibit papain enzyme during the washing procedure.

2.2 Staining for the Surface Markers and Cell Viability

1. To block non-specific staining, we used normal goat serum.
2. Prepare FACS buffer: PBS with 10% FBS and 0.1% sodium azide.
3. Antibodies for surface markers should be diluted in FACS buffer to make a 2× solution of antibodies that will be added 1:1 to neuronal cells suspended in 100% goat serum to make final 1× concentration of antibodies in FACS buffer with 50% goat serum. It is preferable to make direct conjugates with fluorophores; however, secondary antibodies could also be used. To do that, use secondary antibodies in FACS buffer with 50% goat serum.
4. To analyze alive cells, we used 7-amino-actinomicine D (7-AAD) viability dye. To distinguish dead and live cells in fixed neuronal cells, we used LIVE/DEAD™ Fixable Dead Cell Stains from Molecular Probes/Thermo Fisher.
5. To fix cell, we used 1% paraformaldehyde. To prepare cell fixative, dissolve 10 ml of 16% paraformaldehyde solution (Electron Microscopy Sciences Inc.) in 150 ml of PBS. Mix thoroughly and store at +4 °C for 1 month.

3 Methods

3.1 Protocol for Preparation of Neuronal Cells for Flow Cytometry

1. Dissect brains (whole brains or specified anatomical location such as the cerebellum, hippocampus, or cortex) from 3 to 5 C57BL/6 (or other strain) mice of 1–12 days old (*see* **Note 1**).
2. Incubate brains in digesting media for 20–30 min at +37 °C.
3. Pipet several times digested brain tissue using 10 ml Pasteur pipet to receive single cell suspension.
4. Pass cell suspension through filter or cell strainer to remove cell aggregates.
5. Wash cells. Transfer 10 ml of cell suspension to 50 ml tube and add 40 ml of PBS with 20% FBS. Spin the cells at 2000 rpm (400×*g*) for 5 min at room temperature.

6. Second wash. Resuspend cells with 50 ml of PBS with 20% FBS. Spin cells at 2000 rpm for 5 min at room temperature.
7. Perform blocking to eliminate non-specific staining. Resuspend Cells in 100 μl of normal goat serum (*see* **Note 2**)
8. Incubate cells for 15 min on ice.
9. Add 100 μl of properly diluted antibodies in FACS buffer to stain for surface markers (*see* **Note 3**) and dye to eliminate dead cells from analysis (*see* **Note 4**)
10. Incubate cells for 15 min on ice.
11. Wash cells in 1–5 ml of PBS at +4 °C.
12. In the case of indirect antibody staining, incubate cells with secondary antibodies diluted in FACS buffer with 50% goat serum for 10–15 min on ice. Wash cells in 1–5 ml of PBS (Optional).
13. Resuspend cells in PBS for cell sorting (for analysis *see* **step 13** of Subheading 3.1). For cell sorting of neurons, it is important to use large nozzle size of 100 μm or even 150 μm and use the lower speed of sorting. In addition, non-cuvette- based flow cytometers have an advantage when compared to cuvette-based cell sorters regarding cell viability and integrity after sorting. Due to large size of neurons, sorting of 2000–5000 cells allows reasonable RNA isolation to perform real-time RT-PCR (*see* **Note 5**).
14. Fix the cells in 1% paraformaldehyde in PBS. It is possible to keep fixed samples at +4°C for 2–3 weeks (optional) (*see* **Note 6**).
15. Analyze on a flow cytometer.

3.2 Protocol for Preparation of Neuronal Cells for Laser Scanning Cytometry and Laser Interferometry

1. Use either newborn or adult mice 6–8-week old C57BL/6 (or other strain) mice.
2. Remove brains from the skull.
3. Transfer brains to ice-cold PBS.
4. Create brain slices using a razor blade.
5. Place each slice between two thin glass coverslips.
6. For laser scanning cytometer, sections should be fixed overnight with 1% paraformaldehyde in PBS, washed in PBS and blocked with 100% normal goat serum, and stained with proper antibodies diluted in FCAS buffer with 50% goat serum similar to staining procedure in Subheading 3.1. Otherwise standard protocols for preparation and staining for immunofluorescence histology could also be applied (*see* **Note 7**).
7. No further sample preparation is needed before the analysis for laser interferometry (*see* **Note 8**).

4 Notes

1. Flow cytometry has a significant advantage over other methods in modern neuroscience in its ability to analyze multiple parameters of a vast number of neuronal cells (2000–10,000) and significantly reduce non-specific background staining associated with the analysis of brain slices or histology sections. Moreover, single cell sorting combined with modern transcriptomic technologies (e.g., RNA-seq) enables to examine gene expression in neurons in single cell level [20]. We received best results when P3 (3-day-old) C57BL/6 mice are used.
2. To reduce background for surface marker staining with antibodies, blocking with 50% normal goat serum on ice for 15–20 min gives very good results.
3. Advantages of flow cytometry in the study of heterogeneity of neurons include the following: ability to measure membrane potential, intracellular calcium level, ROS, etc. with the usage of appropriate fluorescent probes. For staining of the cells with other fluorescent probes (e.g., to detect Ca^{2+}), use proper buffer and protocol for staining from the manufacturer.
4. Since dying cells are always present in neuronal cell preparations, specific dyes to eliminate dead cells are required. To analyze alive cells, traditional dyes such as 7AAD could be used. For usage of fixed neuronal cells, LIVE/DEAD™ Fixable Dead Cell Stains from Molecular Probes showed good results.
5. Preparations of neuronal cells tend to aggregate; therefore, all precautions must be taken to avoid aggregation (e.g., 70 nylon mesh filtration of cell suspension, dilution of the sample, low speed of stream). For cell storing, usage of large nozzle size of 100 μm and 150 μm is recommended. Also, from our experience, non-cuvette-based flow cytometers (e.g., BD FACSAria™) have an advantage over cuvette-based cell sorters (e.g., MoFlo® Astrios™) regarding cell viability and integrity of neuronal cells after sorting. However, we successfully used BD FACSAria III for sorting of neuronal cells.
6. To perform intracellular staining, after staining of the cells for surface markers, the addition of LIVE/DEAD™ Fixable Dead Cell Stains, we further use standard fixation/permeabilization kit (e.g., from BD Biosciences) for intracellular cytokine staining.
7. For laser scanning cytometer (iCyte™ from CompuCyte), the main problem remains to identify single neuronal cells. Traditional neuronal marker β3-tubulin stain neuronal processes that make it very problematic to discriminate individual neuronal cells. To overcome this problem, we used neuronal

markers that label neuronal bodies (e.g., MAP2). A combination of MAP2 and nuclei (DAPI) staining allowed us to identify large neuronal bodies with limited success.

8. When using laser interference microscopy, it is possible to obtain a volumetric image of neurons and the distribution of subcellular structures and obtain information about the cell and tissue structure in all three dimensions. Also, laser micro-interferometry makes it possible to examine alive neurons without additional contrasting of the cell image with the help of dyes, which eliminate many artifacts. Thus, there is no clear winner in the methods of flow cytometry and laser interference microscopy in application to study the neuron heterogeneity. Investigators should choose the method according to the purposes of the study, along with other supporting electrophysiological and molecular techniques.

Acknowledgments

The work was supported by Research Grant Council-General Research Fund grant Ref. No. 14113316 (Hong Kong) to E.D.P.

References

1. Wang SS-H, Shultz JR, Burish MJ, Harrison KH, Hof PR, Towns LC et al (2008) Functional trade-offs in white matter axonal scaling. J Neurosci 28:4047–4056
2. Martínez M, Quiroga NY, Castellanos JE, Hurtado H, Hurtado H (2000) Subpoblaciones neuronales presentes en el ganglio de la raíz dorsal. Biomedica 20:248–260
3. Mejias JF, Longtin A (2014) Differential effects of excitatory and inhibitory heterogeneity on the gain and asynchronous state of sparse cortical networks. Front Comput Neurosci 8:107. https://doi.org/10.3389/fncom.2014.00107
4. Pennartz CMA, De Jeu MTG, Geurtsen AMS, Sluiter AA, Hermes ML (1998) Electrophysiological and morphological heterogeneity of neurons in slices of rat suprachiasmatic nucleus. J Physiol 506:775–793
5. Baroni F, Mazzoni A (2014) Heterogeneity of heterogeneities in neuronal networks. Front Comput Neurosci 8:161. https://doi.org/10.3389/fncom.2014.00161
6. Givan AL (2011) Flow cytometry: an introduction. Methods Mol Biol 699:1–29. https://doi.org/10.1007/978-1-61737-950-5_1
7. Di Nicola M, Siena S, Bregni M, Peccatori F, Magni M, Ravagnani F et al (1993) Quantization of CD34+ peripheral blood hematopoietic progenitors for autografting in cancer patients. Int J Artif Organs 16(Suppl 5):80–82
8. Sack U, Scheibe R, Wötzel M, Hammerschmidt S, Kuhn H, Emmrich F et al (2006) Multiplex analysis of cytokines in exhaled breath condensate. Cytometry A 69A:169–172
9. Stratieva-Taneeva PA, Khaidukov SV, Kovalenko VA, Nazimov IV, Samokhvalova LV, Nesmeyanov VA (1993) Bispecific monoclonal antibodies to human interleukin 2 and horseradish peroxidase. Hybridoma 12:271–284
10. Shapiro HM (2003) Practical flow cytometry. Wiley, New York
11. Biggio M, Storace M, Mattia M (2013) Non-instantaneous synaptic transmission in spiking neuron networks and equivalence with delay distribution. BMC Neurosci 14:P267
12. Somers D, Panneton WM (1984) Heterogeneity of neurons in the subnucleus interpolaris of the cat. Brain Res 309:335–340
13. Luider J, Cyfra M, Johnson P, Auer I (2004) Impact of the new Beckman Coulter cytomics FC 500 5-Color flow cytometer on a regional

flow cytometry clinical laboratory service. Lab Hematol 10:102–108

14. Fritschy J-M (2015) Significance of GABA(A) receptor heterogeneity: clues from developing neurons. Adv Pharmacol 73:13–39. https://doi.org/10.1016/bs.apha.2014.11.006
15. Walsh JJ, Han MH (2014) The heterogeneity of ventral tegmental area neurons: projection functions in a mood-related context. Neuroscience 282:101–108. https://doi.org/10.1016/j.neuroscience.2014.06.006
16. Brazhe (Ulyanova) NA, Erokhova LA, Churin AA, Maksimov GV (2005) The relation of different-scale membrane processes under nitric oxide influence. J Biol Phys 31:533–546. https://doi.org/10.1007/s10867-005-2043-1
17. Tychinsky VP, Kretushev AV, Vyshenskaya TV, Tikhonov AN (2005) Coherent phase microscopy in cell biology: visualization of metabolic states. Biochim Biophys Acta Bioenerg 1708:362–366
18. Brazhe AR, Brazhe NA, Maksimov GV, Ignatyev PS, Rubin AB, Mosekilde E et al (2008) Phase-modulation laser interference microscopy: an advance in cell imaging and dynamics study. J Biomed Opt 13:0340004. https://doi.org/10.1117/1.2937213
19. Dobrunz LE, Stevens CF (1997) Heterogeneity of release probability, facilitation, and depletion at central synapses. Neuron 18:995–1008
20. Cembrowski MS, Bachman JL, Wang L, Sugino K, Shields BC, Spruston N (2016) Spatial gene-expression gradients underlie prominent heterogeneity of CA1 pyramidal neurons. Neuron 89:351–368. https://doi.org/10.1016/j.neuron.2015.12.013

Chapter 10

Usage of Multiparameter Flow Cytometry to Study Microglia and Macrophage Heterogeneity in the Central Nervous System During Neuroinflammation and Neurodegeneration

Marina Dukhinova, Ekaterina Kopeikina, and Eugene D. Ponomarev

Abstract

The resident macrophages of the central nervous system (CNS), also known as microglia, and blood-derived macrophages play an important role in the functional activity of the normal CNS, as well as in the development of neuroinflammation during various neurodegenerative disorders. Microglia and macrophages represent heterogeneous populations, which can modulate CNS environment and have different effects on neuronal regeneration. In this chapter, the main features of microglial and macrophage subsets and current methods for investigation of their heterogeneity will be discussed.

Key words Microglia, Macrophages, Neuroinflammation, Neurodegeneration

1 Introduction

The central nervous system (CNS) is unique when compared to other organs. First, the CNS has restricted potential for self-renewal or regeneration. Second, the CNS is isolated from blood and immune cells by the blood-brain barrier (BBB), which restrains the interactions between CNS-resident and peripheral cells. Third, the lymphatics of the CNS, recently found in the dura mater, has still very limited influence on CNS parenchyma [1]. Unless BBB remains intact, CNS-resident microglia represent the major immune cells of the CNS parenchyma, which participate in neurodevelopment and constantly monitor the surrounding environment in search of any damage or pathogen invasion [2]. During neuroinflammatory and neurodegenerative conditions, peripheral immune cells, such as dendritic cells, macrophages, lymphocytes, and neutrophils, invade the CNS and provide various immune responses that contribute to neurodegeneration and/or neuronal repair. Nevertheless, the self-renewal of the CNS after damage is

Natasha S. Barteneva and Ivan A. Vorobjev (eds.), *Cellular Heterogeneity: Methods and Protocols*, Methods in Molecular Biology, vol. 1745, https://doi.org/10.1007/978-1-4939-7680-5_10,

very restricted. Several researchers link this fact with the unique phenotype of microglia and macrophages in the CNS [3].

Microglia represent brain-resident mononuclear cells of myeloid lineage although their exact origin remains unclear and controversial. It was recently established that microglia originate not from the bone marrow as all other immune and blood-derived cells but from the yolk sac and populate the brain early in development. Microglia account for 10–20% of all CNS glial cells and about 5–10% of all CNS cells [4]. Thus, the number of microglial cells in the CNS is quite low when compared to neuronal or astroglial cells. To isolate CNS mononuclear cells, Percoll™ gradient is widely used. This technique is very efficient for isolation and enrichment of microglia cells from the CNS [5]. Other macrophages associated with the CNS besides microglia (e.g., perivascular macrophages) have distinct anatomic localizations with certain distinguishing features and functions (Table 1) [6, 7]. A detailed protocol for isolation of CNS mononuclear cells will be described below.

In the normal adult CNS, the predominant population of mononuclear cells is microglia that constitute more than 95% of all

Table 1
Populations of myeloid cells associated with the adult CNS under physiological and pathological conditions

Population	Localization	Marker	Origin	Maintenance
Microglia	Parenchyma	CX3C chemokine receptor 1 (CX3CR1)^{high}, Ionized calcium-binding adapter molecule 1 (Iba1), F4/80	Yolk sac	Self-renewal
Perivascular macrophages	Perivascular space	CX3CR1^{high}, F4/80, cluster of differentiation 45 (CD45)$^{high/low}$	Blood	Self-renewal, no significant exchange with blood-derived cells
Meningeal macrophages	Subarachnoid space, pia matter	CX3CR1^{high}, F4/80, CD45^{high}	Blood	Exchange with blood-derived macrophages
Choroid plexus macrophages	Choroid plexus	CX3CR1^{high}, F4/80, CD45^{high}	Blood	Self-renewal, no significant exchange with blood-derived cells
Monocyte-derived macrophages	Blood	Lymphocyte antigen 6 complex (Ly6C)^{high}, CX3CR1^{low}, CD45^{high}	Bone marrow	Originated from bone marrow, differentiated from monocytes into macrophages in the CNS

mononuclear cells. However, mononuclear cells that are isolated from the inflamed CNS are very heterogeneous and include CNS-resident microglia and peripheral macrophages and lymphocytes [5]. Different strategies can be further used to distinguish microglia from macrophages and other infiltrated cells. Well-known markers of microglia and macrophages used for flow cytometry include CD11b, CD45, Ly6C, and Iba-1 for immunofluorescence (Fig. 1). Recent studies described the comparison of gene expression profiles between certain cell populations and discovered more specific targets, such as transmembrane protein 119 (Tmem119) or Siglec-H, which are expressed in microglia but not peripheral macrophages (Table 2) [4, 8–11].

Another strategy to separate microglia from macrophages is the application of mouse models with target expression of a fluorescent marker on a certain cell populations. Two common examples include:

1. LysM-GFP knock-in mice. In these mice, GFP is expressed in hematopoietic cells of myeloid lineage, but not in microglia [12].
2. Bone marrow chimera. As a donor for the bone marrow, use mice that ubiquitously express GFP under actin promoter. Recipient mice are lethally irradiated (950 rads) to remove all hematopoietic stem cells in the bone marrow. After 8 weeks of reconstitution with donor bone marrow, GFP will be expressed in peripheral monocytes/macrophages but not microglia, which is irradiation resistant [13].

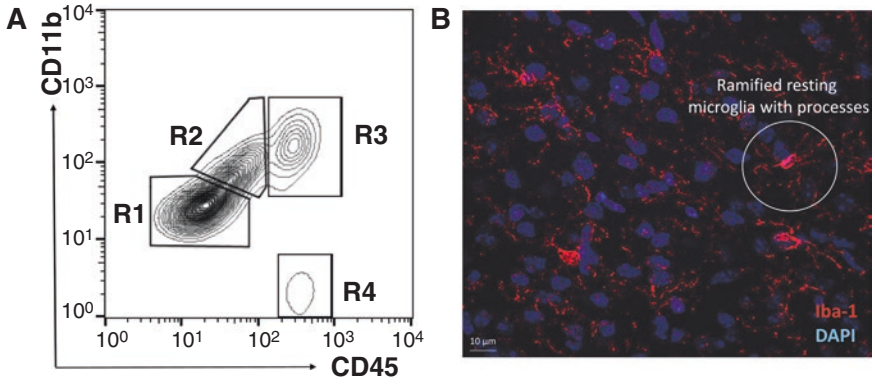

Fig. 1 Analysis of heterogeneity of microglia and macrophages in the CNS using flow cytometry and microscopy. (**a**) Example of flow cytometry analysis of mononuclear cells isolated from the CNS with inflammatory status and stained for CD11b and CD45. Gate R1 represents $CD11b^{+}CD45^{low}$ resting microglia. Gate R2 represents $CD11b^{+}CD45^{int}$ activated microglia. Gate R3 represents $CD11b^{+}CD45^{high}$ macrophages. Gate R4 represents $CD11b^{-}CD45^{high}$ lymphocytes. (**b**) Confocal image of brain histology section stained for microglia with Iba1 (shown in red) and for nuclei (DAPI, shown in blue)

Table 2
Distinctive markers of microglia and macrophages applied in experimental approaches

Marker	Expression on microglia	Expression on macrophages
CD11b	Yes	Yes
CD45	Yes, low or intermediate[a]	Yes, high
F4/80	Yes	Yes
Ly6C	No	Yes[b]
Iba1	Yes	Yes
Tmem119	Yes	No
Siglec-H	Yes	No
P2Y G-protein coupled 12 (P2YG12)	Yes	No

[a]The level of CD45 expression becomes intermediate in activated microglia in the inflamed CNS
[b]Subset of peripheral macrophages recruited to the CNS obtain different phenotype over the time and downregulate Ly6C within CNS microenvironment

Both microglia and macrophages within the CNS represent heterogeneous populations and could have different functional states. The only feasible approach to distinguish the subsets of macrophages associated with the CNS (Table 1) is a combination of the cell localization (perivascular and subarachnoid space, pia mater, or choroid plexus) and monocyte marker expression. Currently, there are no specific molecular markers to distinguish perivascular, meningeal, choroid plexus, and bone marrow-derived macrophages. In the future, genetic profiling of these populations can serve as a tool to highlight the question.

The most recent way to characterize macrophage activation stage is to name the trigger of activation (e.g., interleukin 4 (IL-4), lipopolysaccharides (LPS), etc.). Otherwise, macrophages could be classified as resting, or M0, and classically (M1) or (M2) activated. Resting macrophages circulate in the bloodstream and do not exhibit any activity, while activated macrophages can obtain pro- (M1) or anti- (M2) inflammatory features secreting various cytokines and chemokines and recruiting other cells to the site of neuronal damage.

States of microglia activation are somewhat similar to that of macrophages. In the healthy CNS, microglia is found in so-called non-activated state, when the ramified cells are monitoring the CNS with long processes (Fig. 1b) in search for any damages or pathogen invasion and are in constant contact with neurons (Fig. 2).

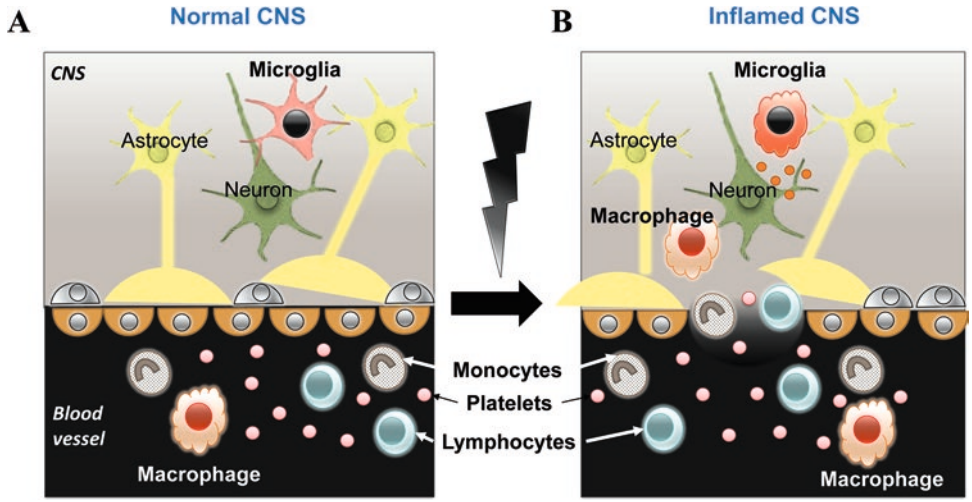

Fig. 2 Functional activity of microglia and macrophages. in the healthy and inflamed CNS. (**a**) Ramified microglia contact with neurons and scan the surrounding environment in search for cell damage or pathogen invasion. (**b**) Activated microglia and infiltrating macrophages secrete pro- and anti-inflammatory factors, recruit other peripheral immune cells to the CNS, and participate in regeneration after neuronal damage

In the healthy CNS, neurons interact with microglia and suppress its pro-inflammatory activity and M2-like state via stimulation of microRNA-124 (miR-124) expression [14, 15]. Another axis of regulation is an interaction between fractalkine receptor CX3CR1, in which expression is reduced in activated microglia, and its ligand, neuronal-expressed C-X3-C motif ligand 1 (CX3CL1) [16]. The markers of non-activated microglia include IL-4, Ym1, and transforming growth factor beta 1 (TGFβ1).

Once activated by a trigger, microglia loses its processes and obtains a functionally and morphologically different phenotype with upregulation of CD45 and CD11b (Figs. 1a and 2b), which some researchers tend to distinguish as pro-inflammatory (M1) and neuroprotective (M2). However, these two subtypes are very distinct in in vitro rather than in vivo systems [17]. Under inflammatory conditions in vivo, such as experimental autoimmune encephalomyelitis, activated microglia (which express M1 markers MHC class II and CD86) also represent M2 phenotype, which produces high levels of Ym1 (anti-inflammatory), but not pro-inflammatory nitric oxide (NO) [18–20].

Any CNS damage or pathogen may cause microglial activation. In addition to microglia activation, peripheral macrophages are also recruited to the CNS, and BBB becomes compromised. The major function of myeloid cells in the inflamed CNS is the phagocytosis of pathogens and/or cellular debris and recruitment of other cells to the site of damage. Additionally, activated microglia and peripheral macrophages secrete pro-inflammatory cytokines, matrix metalloproteases, and reactive oxygen species

including nitric oxide (NO) that contribute to further BBB disruption and neuronal loss. In the context of different neuroinflammatory conditions and through the course of the same disease, these myeloid cells or their subpopulations of them can contribute to neuronal damage or regenerative events (Tables 3 and 4) [21–26]. For example, one week after stroke, initial acute damage skews infiltrating macrophages toward pro- or anti-inflammatory M1 and M2 phenotypes in 1:1 ratio. However, at later time points, macrophages with alternative M2 activation start to dominate in their numbers. These data are supported by the evidence of impaired recovery in mice with blocked macrophage infiltration [27]. A specific population of microglia located in subventricular zone is essential for neurogenesis [24]. Considering these facts, we came to conclusions that (1) microglia and macrophages are key structural and functional players of the normal and inflamed CNS; (2) the role of mononuclear cells in the CNS varies between different subsets and under various pathogenic conditions. Different subunits of macrophages and microglia can contribute to neuronal damage [28–31] or assist in neuronal repair within the CNS [13, 18]. Thus, it is essential to investigate these cells on populational and single cell levels to investigate their role and use them as therapeutic targets.

2 Materials

2.1 Equipment

1. Refrigerated cell culture centrifuge (bucket rotor) with the option to switch off bake such as Eppendorf 5810R or equivalent.
2. Flow cytometer with an option to perform at least 2–3 fluorescence color analyses is also required. We used BD LSRFortessa cytometer and routinely performed four- or five-color cytometric analysis.

2.2 Animals

We used 8–12-week-old C57BL/6 mice. CNS inflammation (experimental autoimmune encephalitis) was induced as described earlier [14].

2.3 Cell Homogenization

15 ml Teflon-glass Dounce homogenizer was acquired from Wheaton Inc. Cell strainer (70 μ) was purchased from Falcon.

2.4 Reagents for Mononuclear Cell Isolation

Prepare fresh solutions at room temperature. To prepare 100% Percoll solution, the original Percoll solution is mixed with 10× PBS at 10:1 ratio. To prepare 10 ml of 70% Percoll, take 7 ml of 100% Percoll and add 3 ml of DMEM medium mix thoroughly (vortex). To prepare 10 ml of 40% Percoll, take 4 ml of 100% Percoll and add 6 ml of 1× PBS; mix thoroughly.

Table 3
Morphological and functional subsets of infiltrating peripheral macrophages in the CNS

Subset	Markers	Functional role in the CNS
Ly6C^{high}	CX3CR1^{low}, CD43^{low}, C-C chemokine receptor type 2 (CCR2^{+})	Pro-inflammatory activity, peripheral cell recruitment, neuronal damage
Ly6C^{low}	CX3CR1^{high}, CD43^{high}	Anti-inflammatory [26]. These phenotype is obtained by peripheral macrophages in the CNS
M1 = M (IFNγ/ LPS)	CD32, CD16, CD11b, CD86, MHC class II, Inducible nitric oxide synthase (iNOS)	Pro-inflammatory activity, peripheral cell recruitment, neuronal damage
M2 = M (IL-4)	Ym1, IL-4, TGFβ, Arginase 1(Arg1)	Recruitment of regulatory T-cells Hematoma resolution after intracerebral hemorrhage

Table 4
Functional subsets of CNS-resident microglia

Marker	Functional role	Characteristics
CD45	Scan the CNS environment; Phagocyte pathogens or cell debris, recruit other blood/immune cells	Ramified (CD45^{low}): IL-4, Ym1, TGFβ1 Activated (CD45^{high}): MHC class II^{high}, Ym1^{high}
No specific markers	Link the immune and neuronal cells	Respond to neurotransmitters
CD11c	Induce CD4^{+} T-cell proliferation; Have less potential for inflammation	CD11c^{+}: IGF1^{high}, MHC class II, CD86; CD11c^{-}: YM1^{high}
Signal transducer and activator of transcription 6 (STAT6)	Participate in adult neurogenesis	Location in subventricular zone, reduced Iba1 expression

2.5 Antibodies

Directly conjugated rat anti-mouse monoclonal anti-CD11b-AF488 (used in dilution 1:200), anti-Ly6C-PE (dilution 1:200), and anti-MHC class II-PE-Cy5 (dilution 1:200) were from BD Biosciences, and anti-CD45-APC-Cy7 (dilution 1:100) was purchased from BioLegend. For blocking of Fc receptors rat anti-mouse, CD16/CD32 antibodies (dilution 1:50) were used. For antibody labeling, we used FACS buffer: PBS with 5% FBS and 0.01% sodium azide.

2.6 Fixative

To prepare cell fixative, dissolve 10 ml of 16% paraformaldehyde solution (Electron Microscopy Sciences Inc.) in 150 ml of 1× PBS, mix thoroughly, and store at +4 °C for 1 month.

3 Methods

1. Perform the whole-body intracranial perfusion of an anesthetized mouse with ice-cold PBS. This step allows removing blood cells from the brain/spinal cord microvasculature (*see* **Note 1**).
2. Dissect the brain and spinal cord, homogenize tissue in ice-cold PBS, and filter the cell suspension through 70 μm cell strainer to remove aggregates.
3. Centrifuge cells for 5 min at 650 × *g* at +4 °C.
4. Use either continuous (a) or discontinuous (b) Percoll gradients for further enrichment of mononuclear cells from the CNS. All procedures were performed at room temperature.
5. (a) To isolate mononuclear cells using continuous gradient, resuspend the cell precipitate from one mouse brain/spinal cord in 1× PBS (10 ml, room temperature), and add 5 ml of 100% Percoll to the cell suspension at 1:2 ratio. Mix gently by inverting the tube several times.

   (b) To isolate mononuclear cells using discontinuous gradient, resuspend the cell precipitate from one mouse brain/spinal cord in 5 ml of 70% Percoll, and gently overlay 10 ml of 40% Percoll. Avoid disturbing the gradient to have two distinct layers of 70% Percoll (bottom) and 40% Percoll (up).
6. (a) Centrifuge cells in continuous Percoll gradient without breaking for 30 min at 1000 × *g* (room temperature). Remove the cell debris at the top, and collect the mononuclear cell suspension at the bottom (Fig. 3a).

   (b) Centrifuge cells in discontinuous 40%/70% Percoll gradient without breaking for 30 min at 1000 × *g* (room temperature). Remove the cell debris on the top, and collect the mononuclear cell suspension in the 40%/70% interphase (Fig. 3b).

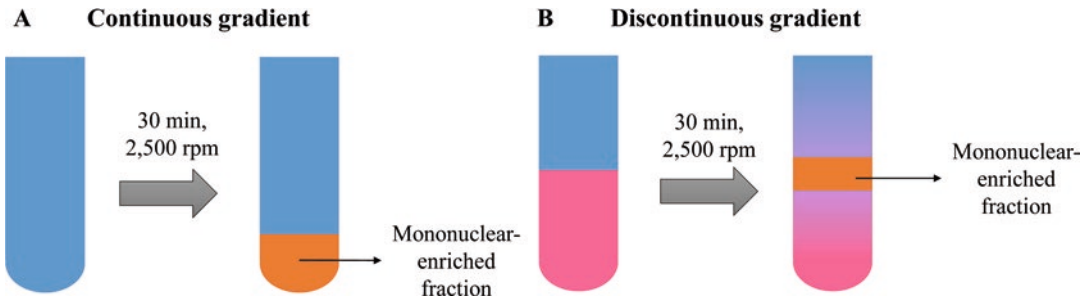

Fig. 3 Scheme of application of continuous and discontinuous Percoll gradients for isolation of mononuclear cells from the CNS

7. Dilute collected cell suspension with PBS to wash cells (add at least two parts of PBS to one part of collected cell suspension (by volume), mix thoroughly, and centrifuge for 7 min at 650 × *g*).
8. Decant the supernatant and collect cell precipitate, which contains isolated CNS mononuclear cells.
9. Resuspend cells in 100 μl of FACS buffer. Incubate the cells with FcR blocking antibodies (1:50) to avoid non-specific antibody binding via Fc receptors on microglia and macrophages (15 min on ice).
10. After FcR blocking, add the required antibodies for surface markers diluted in the suitable amount of FACS buffer (*see* Subheading 2 for antibody dilutions), and incubate for 15 min on ice (*see* **Notes 2** and **3**).
11. Wash the samples with 1 ml of PBS.
12. Centrifuge at 650 × *g* for 5 min and resuspend the precipitate in 1% paraformaldehyde in PBS, vortex cells immediately, and store the samples at +4°C for 2–3 weeks before analysis on flow cytometer (*see* **Notes 4–6**).

4 Notes

1. One mouse brain with spinal cord yields 200,000–400,000 mononuclear cells from normal CNS and up to 1,000,000 cells from inflamed CNS during inflammation (e.g., experiential autoimmune encephalomyelitis, traumatic brain injury).
2. The combination of markers CD11b-AF488, Ly6C-PE, MHC class II-PE-Cy5, and CD45-APC-Cy7 (all from BD Biosciences) allowed us to perform four-color flow cytometry and distinguish peripheral macrophages ($CD11b^{+}Ly6C^{+}$), non-activated microglia ($CD11b^{+}Ly6C^{-}$MHC class $II^{-}CD45^{low}$), and activated microglia ($CD11b^{+}Ly6C^{-}$MHC class $II^{+}CD45^{int/high}$).
3. For compensation controls, we successfully used compensation anti-rat beads from BD Biosciences.
4. In addition to surface markers, intracellular staining in combination with surface staining could also be performed to analyze M2 vs. M2 type of activation of microglia or macrophages in the CNS. We successfully identified M2 marker Ym1 (M2 marker) and NO (M1 marker) on microglia in combination with surface staining for CD11b and CD45. To identify Ym1, polyclonal antibodies were used and for NO molecular probe DAF-FM (Molecular Probes) [18].
5. The proliferation of microglia during neuroinflammation can also be measured by performing intraperitoneal injection of

1–2 mg BrdU 14 h before the isolation of CNS mononuclear cells that were stained for surface markers CD11b, CD45, and anti-BrdU fluorochrome-labeled antibody using a kit from BD Biosciences.

6. $CD11b^{+}CD45^{low}$ microglia can be sorted on single cell or population levels [32]. Since microglia is fragile, lower pressure and low sorting speed are recommended. For collection, use Eppendorf tubes with 500 μl of DMEM media with 10% FBS (population sorting) or U-shaped 96-well plates for real-time PCR with 50 μl of DMEM media with 10% FBS (single cell sorting). We successfully used BD FACSAria II and III for sorting and further mRNA expression profiling.

Acknowledgments

The work was supported by Research Grant Council-Early Career Scheme grant reference 24100314 (Hong Kong) to E.D.P.

References

1. Louveau A, Smirnov I, Keyes T, Eccles J, Rouhani S et al (2015) Structural and functional features of central nervous system lymphatics. Nature 523(7560):337–341. https://doi.org/10.1038/nature14432
2. Edmonson C, Ziats M, Rennert OM (2016) A non-inflammatory role for microglia in autism-spectrum disorder. Front Neurol 7:9. https://doi.org/10.3389/fneur.2016.00009
3. Gensel J, Zhang B (2015) Macrophage activation and its role in repair and pathology after spinal cord injury. Brain Res 1619:1–11. https://doi.org/10.1016/j.brainres.2014.12.045
4. Prinz M, Erny D, Hagemeyer N (2017) Ontogeny and homeostasis of CNS myeloid cells. Nat Immunol 18:385–392
5. Campanella M, Sciorat C, Tarozzo G, Beltramo M (2002) Flow cytometric analysis of inflammatory cells in ischemic rat brain. Stroke 33:586–592
6. Goldmann T, Wieghofer P, Jordão M, Prutek F, Hagemeyer N, Frenzel K et al (2015) Origin, fate and dynamics of macrophages at central nervous system. Nat Immunol 17:797–805. https://doi.org/10.1038/ni.3423
7. Prinz M, Priller J, Sisodia S, Ransohoff R (2011) Heterogeneity of CNS myeloid cells and their roles in neurodegeneration. Nat Neurosci 14:1227–1235. https://doi.org/10.1038/nn.2923
8. Starossom S, Veremeyko T, Yung A, Dukhinova M, Au C, Lau A, Weiner H, Ponomarev E (2015) Platelets play differential role during the initiation and progression of autoimmune neuroinflammation. Circ Res 117(9):779–792. https://doi.org/10.1161/CIRCRESAHA.115.306847
9. Garcia-Bonilla L, Faraco G, Moore J, Murphy M, Racchumi G, Srinivasan J et al (2016) Spatio-temporal profile, phenotypic diversity, and fate of recruited monocytes into the post-ischemic brain. J Neuroinflammation 13:285
10. Bennett M, Bennett F, Liddelow S, Ajami B, Zamanian J, Fernhoff N et al (2016) New tools for studying microglia in the mouse and human CNS. Proc Natl Acad Sci U S A 113(12):E1738–E1746
11. Chiu I, Morimoto E, Goodarzi H, Liao J, O'Keeffe S, Phatnani H et al (2013) A neurodegeneration-specific gene expression signature and immune profile of acutely isolated microglia from an ALS mouse model. Cell Rep 4(2):385–401
12. Faust N, Varas F, Kelly L, Heck S, Graf T (2000) Insertion of enhanced green fluorescent protein into the lysozyme gene creates mice with green fluorescent granulocytes and macrophages. Blood 96:719–726
13. Shechter R, London A, Varol C, Raposo C, Cusimano M, Yovel G et al (2009) Infiltrating

blood-derived macrophages are vital cells playing an anti-inflammatory role in recovery from spinal cord injury in mice. PLoS Med 6(7):e1000113

14. Ponomarev E, Veremeyko T, Barteneva N, Krichevsky A, Weiner H (2011) MicroRNA-124 promotes microglia quiescence and suppresses EAE by deactivating macrophages via the C/EBP-α–PU.1 pathway. Nat Med 17(1):64–70
15. Hamzei Taj S, Kho W, Aswendt M, Collmann F, Green C, Adamczak J, Tennstaedt A, Hoehn M (2016) Dynamic modulation of microglia/macrophage polarization by miR-124 after focal cerebral ischemia. J Neuroimmune Pharmacol 11(4):733–748
16. Wolf Y, Yona S, Kim K, Jung S (2013) Microglia, seen from the CX3CR1 angle. Front Cell Neurosci 7:26. https://doi.org/10.3389/fncel.2013.00026
17. Haga A, Takahashi E, Inomata Y, Kawahara K, Tanihara H (2016) Differentiated expression patterns and phagocytic activities of type 1 and 2 microglia. Invest Ophthalmol Vis Sci 57:2814–2823
18. Ponomarev E, Maresz K, Tan Y, Dittel B (2007) CNS-derived interleukin-4 is essential for the regulation of autoimmune inflammation and induces a state of alternative activation in microglial cells. J Neurosci 27(40):10714–10721
19. Ransohoff R (2016) A polarizing question: do M1 and M2 microglia exist? Nat Neurosci 19:987–991
20. Shemer A, Erny D, Jung S, Prinz M (2015) Microglia plasticity during health and disease: an immunological perspective. Trends Immunol 36(10):614–624. https://doi.org/10.1016/j.it.2015.08.003
21. Miró-Mur F, Pérez-de-Puig I, Ferrer-Ferrer M, Urra X, Justicia C, Chamorro A, Planas A (2016) Immature monocytes recruited to the ischemic mouse brain differentiate into macrophages with features of alternative activation. Brain Behav Immun 53:18–33. https://doi.org/10.1016/j.bbi.2015.08.010
22. Walker P, Bedi S, Shah S, Jimenez F, Xue H, Hamilton J, Smith P, Thomas C, Mays R, Pati S, Cox CS Jr (2012) Intravenous multipotent adult progenitor cell therapy after traumatic brain injury: modulation of the resident microglia population. J Neuroinflammation 9:228. https://doi.org/10.1186/1742-2094-9-228
23. Chang C, Wan J, Li Q, Renfroe S, Heller N, Wang J (2017) Alternative activation-skewed microglia/macrophages promote hematoma resolution in experimental intracerebral hemorrhage. Neurobiol Dis 103:54–69
24. Xavier R, Kress B, Goldman S, de Menezes L, Nedergaard M (2015) A distinct population of microglia supports adult neurogenesis in the subventricular zone. J Neurosci 35(34):11848–11861
25. Pannell M, Szulzewsky F, Matyash V, Wolf S, Kettenmann H (2014) The subpopulation of microglia sensitive to neurotransmitters/neurohormones is modulated by stimulation with LPS, interferon-c, and IL-4. Glia 62:667–679
26. London A, Benhar I, Mattapallil M, Mack M, Caspi R, Schwartz M (2013) Functional macrophage heterogeneity in a mouse model of autoimmune CNS pathology. J Immunol 190(7):3570–3578
27. Wlodarczyk A, Cédile O, Jensen K, Jasson A, Mony J, Khorooshi R et al (2016) Monocyte-derived macrophages contribute to spontaneous long-term functional recovery after stroke in mice. J Neurosci 36(15):4182–4195
28. Horn K, Busch S, Hawthorne AL, van Rooiinen N, Silver J (2008) Another barrier to regeneration in the CNS: activated macrophages induce extensive retraction of dystrophic axons through direct physical interactions. J Neurosci 28(38):9330–9341. https://doi.org/10.1523/JNEUROSCI.2488-08.2008
29. Ponomarev E, Veremeyko T, Weiner H (2013) MicroRNAs are universal regulators of differentiation, activation and polarization of microglia and macrophages in normal and diseased CNS. Glia 61(1):91–103
30. Barakat R, Redzic Z (2015) Differential cytokine expression by brain microglia/macrophages in primary culture after oxygen glucose deprivation and their protective effects on astrocytes during anoxia. Fluids Barriers CNS 12:6. https://doi.org/10.1186/s12987-015-0002-1
31. Wlodarczyk A, Cédile O, Jensen KN, Jasson A, Mony JT, Khorooshi R, Owens T (2015) Pathologic and protective roles for microglial subsets and bone marrow- and blood-derived myeloid cells in central nervous system inflammation. Front Immunol 6:463
32. Doorn KJ, Breve JJP, Drurkach B, Boddeke H, Huitinga I, Lucassen PJ, van Dam A-M (2015) Brain-region specific expression profiles in freshly isolated rat microglia. Front Cell Neurosci 9:84. https://doi.org/10.3389/fncel.2015.00084

Part III

Imaging and Spectroscopy Methods in Heterogeneity Studies

Chapter 11

Analysis of Microtubule Dynamics Heterogeneity in Cell Culture

Anara Serikbaeva, Anna Tvorogova, Sholpan Kauanova, and Ivan A. Vorobjev

Abstract

Microtubules (MTs) are dynamic components of the cytoskeleton playing an important role in a large number of cell functions. Individual MTs in living cells undergo stochastic switching between alternate states of growth, shortening and attenuated phase, a phenomenon known as tempered dynamic instability. Dynamic instability of MTs is usually analyzed by labeling MTs with +TIPs, namely, EB proteins. Tracking of +TIP trajectories allows analyzing MT growth in cells with a different density of MTs. Numerous labs now use +TIP to track growing MTs in a variety of cell cultures. However, heterogeneity of MT dynamics is usually underestimated, and rather small sampling for the description of dynamic instability parameters is often used. The strategy described in this chapter is the method for repetitive quantitative analysis of MT growth rate within the same cell that allows minimization of the variation in MT dynamics measurement. We show that variability in MT dynamics within a cell when using repeated measurements is significantly less than between different cells in the same chamber. This approach allows better estimation of the heterogeneity of cells' responses to different treatments. To compare the effects of different MT inhibitors, the protocol using normalized values for MT dynamics and repetitive measurements for each cell is employed. This chapter provides detailed methods for analysis of MT dynamics in tissue cultures. We describe protocols for imaging MT dynamics by fluorescent microscopy, contrast enhancement technique, and MT dynamics analysis using triple color-coded display based on sequential subtraction analysis.

Key words Microtubule dynamics, Fluorescent microscopy, Dual color-coded display, End-binding protein

1 Introduction

1.1 Microtubules in the Interphase Cells

Microtubules (MTs) are dynamic long polymer structures consisting of α- and β-tubulin dimers polymerized at the expense of GTP hydrolysis [1]. MTs play an important role in the organization of cell shape, providing a structural basis for the anisotropic transport in the cytoplasm [2, 3]. While MTs contribute to the spatial organization of cells, they are highly dynamic themselves. MT dynamics is essential for cell division as well as for the proper organization of interphase cells. In the interphase cells, dynamic MTs regulate

Natasha S. Barteneva and Ivan A. Vorobjev (eds.), *Cellular Heterogeneity: Methods and Protocols*, Methods in Molecular Biology, vol. 1745, https://doi.org/10.1007/978-1-4939-7680-5_11,

cell polarization [4], cell migration [5], focal adhesion turnover [6], and even synaptic plasticity [7–9]. Overall, dynamic instability of MTs is an efficient way for their plus ends to search in the intracellular space [10].

MTs are the primary target for several anticancer drugs, widely used in chemotherapy. All MT-binding drugs share antiproliferative activity directly inhibiting cell division [11] and have been reported to demonstrate anti-metastatic properties, i.e., inhibition of the dissemination of tumors [12–15]. This makes an analysis of MT dynamics of great practical importance.

1.2 Dynamic Instability of Microtubules in Vivo

To be able to fulfill diverse functions, MTs are arranged into specific patterns, and MT arrays are remodeled according to extra- and intracellular signals. MT remodeling occurs through their intrinsic property—dynamic instability. The precise regulation of MT dynamics and the dynamic interactions with subcellular structures, such as plasma membrane and adhesion sites, appear to be of crucial importance to normal cell function.

Dynamic instability is an intrinsic property of tubulin polymer, characterized by the apparently non-equilibrium behavior of individual MTs undergoing prolonged phases of growth (polymerization) or shortening (depolymerization). Switching between phases is abrupt and stochastic. Besides growth and shortening, MTs in living cells often spend significant time in the attenuated state (pause), when changes in MT length are at the level below the resolution of light microscope [16–18].

Dynamic behavior of MTs is modulated by posttranslational modification of tubulin [19] and a large number of MT-associated proteins, including MAPs [20, 21], +TIPs [22, 23], and some motor proteins like kinesins [24, 25], Rho proteins [26], and others [27].

MT dynamics could be modeled in vitro using purified tubulin and accessory proteins [1, 28, 29]. However, MT behavior in vitro and in vivo is significantly different. MTs in living cells have several times higher growth rate and frequencies of catastrophes and rescue and spend significant time in an attenuated state (pauses). MT growth rate determined in cultured cells (at 37 °C) is in the range of 10–30 μm/min and shortening rate—in the range 15–40 μm/min [18–33]. Duration of pauses is usually in the range from few to tens of seconds, and percentage of time spent by MTs in pauses is highly variable [34, 35].

MTs near the cell margin undergo rather short excursions of growth and shortening with an amplitude about 1–4 μm [17, 18, 34, 35], while in the internal cytoplasm, behavior might be different. MTs in the internal cytoplasm cannot be assessed directly after tubulin labeling because the high spatial density precludes direct tracing of MT ends. Successful analysis of labeled MT is only possible for a limited time after path photobleaching [30, 36], and it was

shown that MTs in the internal cytoplasm sometimes undergo uninterrupted growth that can continue for 10–15 μm [30].

Discovery of plus-end labeling to visualize MTs [37, rev. 23] made it possible to overcome the problems with labeling whole MTs. The most robust label appears to be EB proteins [38, 39]. EB proteins, directly or in complex, accumulate at the MT plus end, serving as a fine tool for tracking growing MTs [30, 40]. The plus-end binding proteins EB1 and EB3 bind to the growing end of MTs [41] and rather rapidly dissociate from it when MT growth is stopped [23, 42]. The advantage of the plus-end labeling approach is evident since it allows nearly unlimited observations of MTs in the cell interior and it is now a gold standard for the analysis of MT growth.

1.3 Analysis of MT Dynamics in Cells

MTs display intrinsically variable rates of growth and shortening. Dynamic instability of MTs can be described in full when using not less than ten parameters [17, 18, 31, 34, 35, 43]: the rates of microtubule growth and shortening, the frequency of transition from growth to shortening or from pause to shortening (both usually named catastrophe), and the frequency of transition from shortening to growth or pause (Table 1).

In some cases, a reduced set of five parameters (rates of growth and shortening, catastrophe and rescue frequencies, and duration of attenuated phases) is applied [44].

MTs dynamics could also be approximated as a one-dimensional random walk in the confined space [18, 26, 45, 46] with apparent stabilization near the cell edge [30, 47]. Using random walk approach, MT dynamics could be described by two parameters, i.e., drift and diffusion. The coefficient of drift, v_d, is defined as the average (mean) rate of displacement of the plus ends of a population of MTs. The coefficient of diffusion, D, is defined as a variance (mean square displacement) of MT ends about the drift component. It is a measure of the dynamic activity

Table 1
Parameters of the dynamic instability of MTs

Rate (μm/min)	Growth (μm/min) Shortening (μm/min)
Duration of phase (min)	Growth (min) Shortening (min) Attenuation phase (min)
Percent of time spend in	Growth (%) Shortening (%) Attenuation phase (%)
Frequency (events/min)	Catastrophe Rescue

or "random walk" of the MT ends [30, 36, 45]. Another global parameter used to describe MT behavior is "dynamicity" that is a measure of overall tubulin exchange at the plus ends per unit time [17, 31, 43, 48, 49]. This parameter also represents to some extent random search by the plus ends.

Detailed analysis of EB-labeling shows [23] that comets disassemble not immediately upon cessation of MT growth but remained some time when MT is pausing. This feature made it possible to analyze pauses using plus-end TIPs [44, 50, 51]. Analysis of pauses is important since many inhibitors convert dynamic MTs to the attenuated state as described below.

1.4 Microtubule-Targeting Drugs Suppress Dynamic Instability

MTs are targets for numerous anticancer drugs widely used as a treatment against tumor progression. All of these drugs directly interact with tubulin affecting MT dynamics [11, 52, 53]. Based on the effect at relatively high concentrations, MT-binding drugs can be divided into two categories: MT-stabilizing agents (taxanes) that promote tubulin polymerization and stabilize MTs thus increasing polymer mass in interphase cells and MT-destabilizing agents (vinca alkaloids, nocodazole, colchicine) inhibiting tubulin polymerization [11, 54]. Drugs promoting MT depolymerization like colcemid, nocodazole, and some others bind to the colchicine domain, at the interface between α- and β-tubulin [55], while drugs of vinblastine family bind to the so-called vinca domain on β-tubulin [56]. Taxanes promoting MT polymerization bind to the taxane pocket also on β-tubulin, to stabilize lateral α-/β-tubulin dimer contacts [57].

Despite having opposite effects on net MT assembly at high concentrations, all types of drugs share common in vivo phenotype that is the dramatic inhibition of MT dynamic instability achieved by suppression of both growth and shortening events while increasing the percentage of time MTs spend in attenuated or "paused" state ([52, 58, 59]; rev. 53). The overall effect of MT-binding drugs is in a large decrease of dynamicity of MTs [rev. 60].

The range of concentrations effective for MT stabilization has been determined in different studies, varies significantly (Table 2) even for the same cell type. More than that, endothelial and neuronal cells and some tumor cells demonstrate biphasic effects, i.e., increased dynamic instability at low concentrations (with increased growth rate) and suppressed dynamic instability (decreased growth rate) at higher concentrations of the drugs [61, 62].

This invokes a question about reproducibility of measurements of MT dynamics.

1.5 Approaches and Requirements for the Evaluation of MT Dynamics Alteration

MT dynamics is evaluated by tracking the ends of MTs. Sufficient spatial resolution for determining fluorescently labeled MT ends is achieved when using oil immersion ×60 or ×100 objective lens with high numerical aperture when equivalent pixel size of the camera is below a Nyquist limit, i.e., around 100 nm, and a further

increase of magnification is not important [71]. The next question is what temporal frequency tracking of MTs needs to be performed to minimize random errors and avoid bias in the measurements. The experimental consensus does not exist, and measurements were performed at time intervals ranging between 0.3 s [44] and 5 s [17, 18, 35, 45] with the exposure time varying between 200 and 1500 ms [60].

When using manual tracking, 2 s time interval gives satisfactory results when mean growth rate of MTs is around 15–20 μm/min, while for slower MTs, even longer time intervals (4–5 s) are sufficient. Using longer time intervals between frames with relatively short exposure times allows one diminishing the irradiation load and facilitates prolonged observations.

More frequent sampling allows growth-track clustering, and subsequent analysis semi-automated or automated analysis of the MT plus-end dynamics [33, 44, 50]. However, there are still limitations in automated algorithms. Because the definition of pause is different in computer-based and hand-tracked method, automatic approach detects growth rate and pauses at lower accuracy in comparison with the hand-tracked method. In particular, in Matov's approach [44], tiny displacements were assigned into MT growth rate measurements, while manually it is recognized as pauses (*see* protocol below for details). Thus, the mean value of MT growth rate is lower, and pauses appear to be less frequent when using automated method compared to manual tracking.

Summarizing, the most accurate measurement is achieved by manual tracking of the ends of MTs on the time-lapse sequences recorded with equivalent pixel size ~100 nm at 2–4 s time intervals and building so-called life histories for individual MTs.

1.6 Heterogeneity of MT Dynamics within Cell Culture

MT behavior in the cell population is often assumed as a homogeneous one; however, a growing body of evidence shows that it is oversimplification. Local regulation of MT dynamics in some parts of cells has been shown long ago [30, 35, 72]. The next question is whether MTs in a population of cells have the same dynamics and response to different external treatments in the same way. These questions are especially interesting regarding cancer cells.

Cancer is a highly heterogeneous disease with numerous subpopulations of cells within the same tumor [73–75]. It is well known that cancer cells demonstrate profound intra-and interline variation after prolonged exposure to antimitotic drugs [76]. One of the interesting questions about MT dynamics is that mammalian cells might have MTs composed of several β-tubulin isotypes [77–79], while composition of MTs predicts cellular response to anti-microtubule drugs [80, 81]. Heterogeneous response to taxol was directly observed in a population of HeLa cells [81].

Table 2
Alteration of microtubule growth by microtubule-targeting agents in vivo

Drug	Concentration (nM)	Cell line	Control growth rate (μm/min)	Final growth rate (μm/min)	Growth rate change (%)[a]	Method	Reference
Vinblastine	8	BS-C-1	6.9 ± 3.9	9.5 ± 7.6	+37	Rhodamine-labeled tubulin	[49]
Vinblastine	32	BS-C-1	6.9 ± 3.9	5.5 ± 3.4	−20	Rhodamine-labeled tubulin	[49]
Vinblastine	15	CHO	16.2 ± 0.8	10.2 ± 0.7	−37	EGFP-MAP4	[63]
Vinblastine	2.5	CHO	16.2 ± 0.9	11.6 ± 0.7	−28	EGFP-MAP4	[63]
Vinblastine	3	HeLa	17.8 ± 0.4	10.5 ± 0.3	−41	EB3-GFP	[64]
Taxol	30	Caov-3	8.27 ± 4.5	6.30 ± 3.7	−24	Rhodamine-labeled tubulin	[65]
Taxol	2	HUVEC	7.2 ± 0.2	10.224[a]	+42	Rhodamine-labeled tubulin	[62]
Taxol	1	HMEC-1	4.9 ± 0.6	7.0 ± 0.4	+42	Rhodamine-labeled tubulin	[62]
Taxol	5	HMEC-1	4.9 ± 0.6	9.7 ± 0.6	+98	Rhodamine-labeled tubulin	[62]
Taxol	2	A549	12 ± 0.6	9.4 ± 0.7	−22	Rhodamine-labeled tubulin	[62]
Taxol	20	NSCLC H460	10.6 ± 0.2	8.056[a]	−24	GFP-βI-tubulin	[66]
Taxol	50	NRK fibroblast	18.4 ± 8.0	10.5 ± 4.9	−43	Rhodamine-labeled tubulin	[67]
Nocodazole	50	NRK fibroblast	18.4 ± 8.0	8.4 ± 8.4	−54	Rhodamine-labeled tubulin	[67]
Nocodazole	100	BS-C-1	9.2 ± 0.76	3.0 ± 0.27	−67	Rhodamine-labeled tubulin	[68]

(continued)

Table 2 (continued)

Drug	Concentration (nM)	Cell line	Control growth rate (μm/min)	Final growth rate (μm/min)	Growth rate change (%)[a]	Method	Reference
Nocodazole	500	BS-C-1	9.2 ± 0.76	5.4 ± 0.97	−41	Rhodamine-labeled tubulin	[68]
Nocodazole	100	Newt lung cells	4.9 ± 0.14	1.7 ± 0.25	−35	Rhodamine-labeled tubulin	[68]
Nocodazole	80	U2OS	16	6.5	−59[b]	EB3-mCherry	[69]
Nocodazole	80	LLCPK1	14	6	−57[b]	EB3-mCherry	[69]
Colchicine	0.2	HUVEC	12 ± 0.6	15,9 ± 0.8	+33	GFP-MAP4	[70]

[a]"+" means increased rate; "−"means decreased rate
[b]Changes calculated from the plots given in [69]

The subpopulations that contribute unequally to disease progression or response to therapeutic intervention become the subject of recent studies, but to the best of our knowledge, this question was not addressed to the properties of MTs.

Our direct observations clearly demonstrate that MT dynamics in cultured cells could be heterogeneous, both in nearly normal and cancer ones. When large sampling size is used (overall >500 track measurements in >20 cells), the distribution of MT growth rates appears as a nearly normal one (Fig. 1), just hiding heterogeneity at the individual cell level. Heterogeneity at the single cell level is observed both in stably expressing EB-3-RFP 3T3 cells where growth rate of MTs is differently more than twofold (Fig. 2a) and in temporarily transfected cells (Fig. 2b–d).

Cell responses to the treatment with MT inhibitors also are heterogeneous in a wide range of concentrations of drugs. At low concentrations of inhibitors, heterogeneity is manifested in opposite changes of MT growth rate in individual cells (Fig. 3). At high concentrations, heterogeneity in a cell population can also be observed qualitatively from changes of MT growth tracks, when growth was still observed in some cells while completely absent in others (data not shown).

Fortunately, MT dynamics in a given interphase cell does not fluctuate significantly with time (Fig. 4), while a standard deviation between different cells grown on the same coverslip ranged between 10% and 60% of the mean. This gives one opportunity to analyze cells' response at a single cell level. Data obtained from dif-

ferent cells before and after drug treatment could be further evaluated quantitatively.

We found that, without the drug, cells showed moderate intracellular variability in MT growth rate of no more that 20% (Fig. 4). To minimize the deviation in MT growth parameters, we suggest using single cell analysis before and after the treatment. This approach allows one to determine subtle changes in MT dynamics. Sequential analysis of MT dynamics on individual cell level opens the way to understanding molecular responses to drugs in individual cells.

Here, we provide a detailed protocol for quantitative analysis of MT growth rates from EB3-RFP time-lapse fluorescent images. We detect EB3-RFP comets, then select appropriate areas for detailed analysis, and then track the comets manually to measure MT growth rates on FIJI/ImageJ software. This method allows analysis of MT growth rates on individual cell level that makes it possible to analyze heterogeneity in MT behavior.

2 Materials

2.1 Choice of Cell Line

NIH3T3 permanently transfected with EB-3-RFP was custom prepared in our laboratory. U118 glioblastoma cell line, A549 lung carcinoma, and HT1080 were obtained from ATCC.

Using transfection reaction with EB-3-RFP plasmid, almost all types of cultured cells are suitable. However, for further analysis, cells must (1) have a flat morphology allowing observation of growing MTs both in control and under the action of drugs and (2) keep flattened morphology with sufficiently large lamellae when transferred to CO_2-independent medium for microscopy.

2.2 Culture Media

1. Growth medium: complete DMEM medium supplemented with 5% fetal bovine serum (FBS), L-glutamine, 100 U/ml penicillin, and 100 μg/ml streptomycin.
2. Cell detachment medium: Trypsin-EDTA 0.25% is stored at 4 °C.
3. Sterile Dulbecco's phosphate-buffered saline (DPBS) is stored at 4 °C.

2.3 Transfection Reagent

X-tremeGENE HP DNA transfection reagent (Roche) stored at –20 °C or lower temperature.

2.4 EB-3-RFP Plasmid

EB-3-RFP plasmid for cell transfection was donated by Dr. A. Akhmanova. Plasmid should be stored at –20 °C or lower temperature in small aliquots.

2.5 Observation vials

8 well or 24 well glass bottom plate dishes are used (*see* **Note 1**).

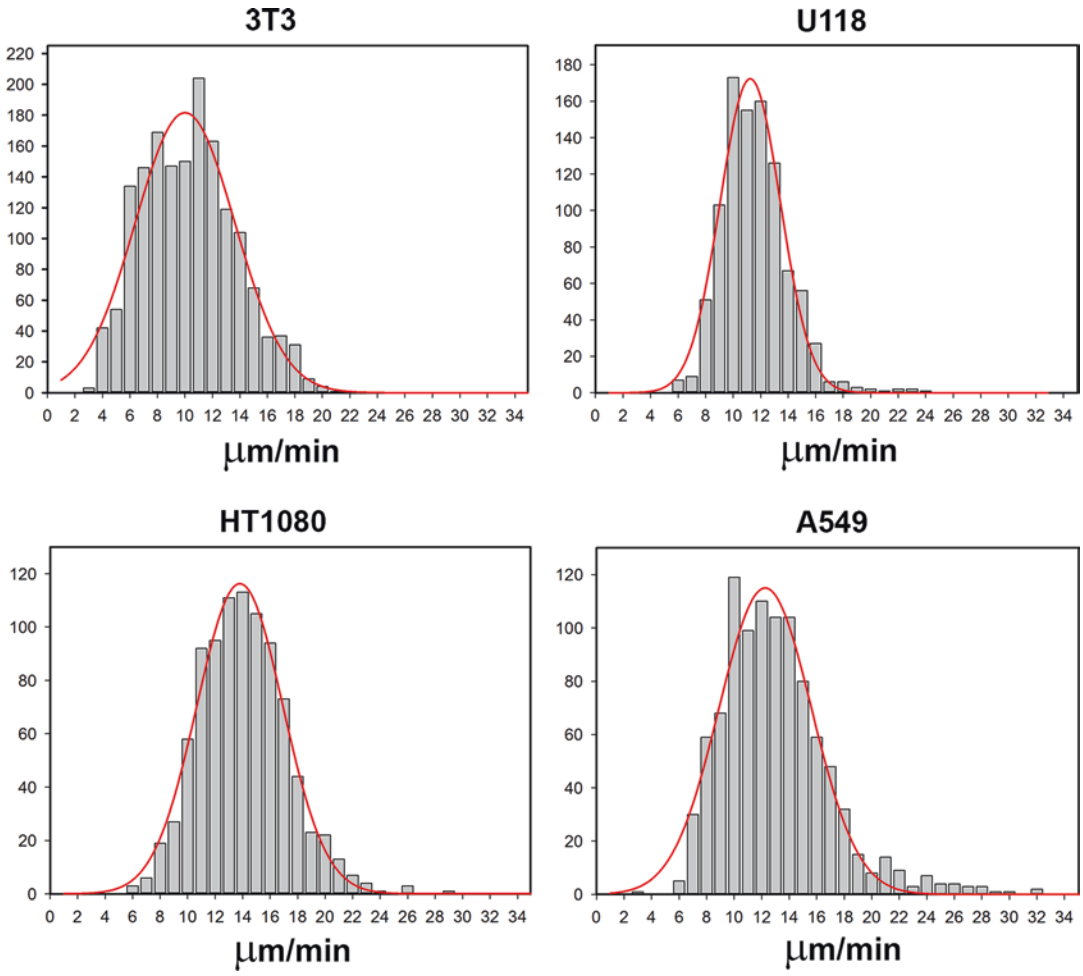

Fig. 1 MT growth rate averaged for cell populations (NIH 3T3, HT1080, A549, and U118 cells). All distributions could be approximated by Gaussian fit (red line). However, SD is different and depends on the cell line

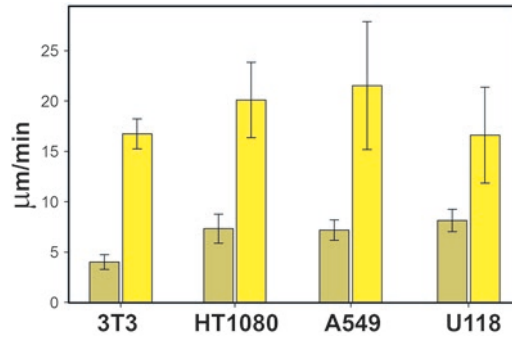

Fig. 2 Heterogeneity of MT growth rate within one population of cells. The minimal and maximal growth rates of MTs ($n > 15$) within "slow" and "fast" U118 cells are statistically significant ($p < 0.01$)

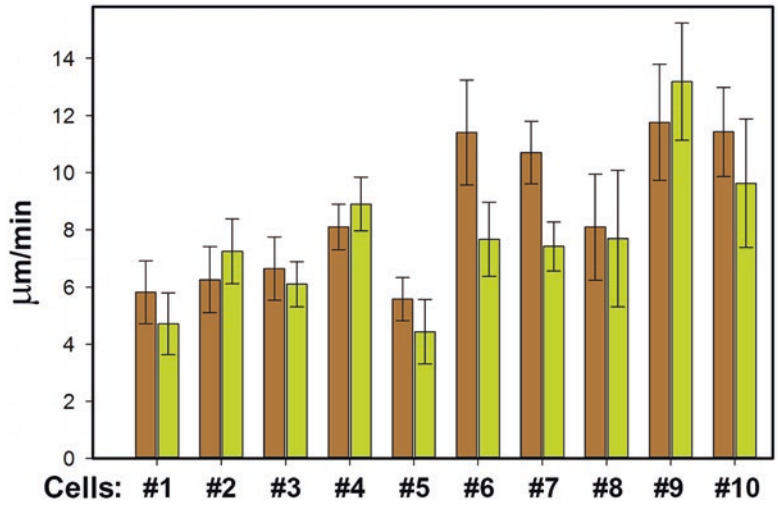

Fig. 3 Cells' response to the low concentration of MT inhibitor is heterogeneous. MT growth rate increased in cells (2, 4, and 9) while decreased in other cells. A significant decrease ($p < 0.01$) was observed in cells 1, 6, 7, and 10

2.6 MT Inhibitors

Stock solutions of nocodazole, Taxol, and vinorelbine are prepared in DMSO and stored at –20 °C. Final working solutions are prepared immediately before the experiment and cannot be stored for more than few hours.

2.7 Drugs

Nocodazole, Taxol, and vinorelbine could be obtained from different sources. We purchased all drugs as powders from Sigma-Aldrich. Stock solutions are prepared in DMSO and stored at –20 °C in aliquots to avoid numerous thawing cycles. When drugs are used in nanomolar concentrations, intermediate working solution at a concentration < 1 μg/ml is prepared instantaneously in complete culture medium.

2.8 Microscope

Time-lapse images of MT plus ends were obtained on AxioObserver fully motorized microscope having Perfect Focus System with a temperature control box (Carl Zeiss, Oberkochen, Germany) and fully motorized stage with Hamamatsu ORCA FLASH 2 camera using ×63/1.4 PlanApo oil immersion objective operating under ZEN software. For optimal recording equivalent pixels size should be around 100 nm (*see* **Note 2**). The microscope is operating under ZEN software (*see* **Note 3**).

3 Methods

3.1 Cell Culture

All four cell lines NIH 3T3 fibroblasts, HT1080, A549, and U118 are cultivated under standard conditions in 25 cm^2 plastic flasks using 6 ml of DMEM medium supplemented with 5% FBS, L-glutamine, 100 U/ml penicillin, and 100 μg/ml streptomycin in a

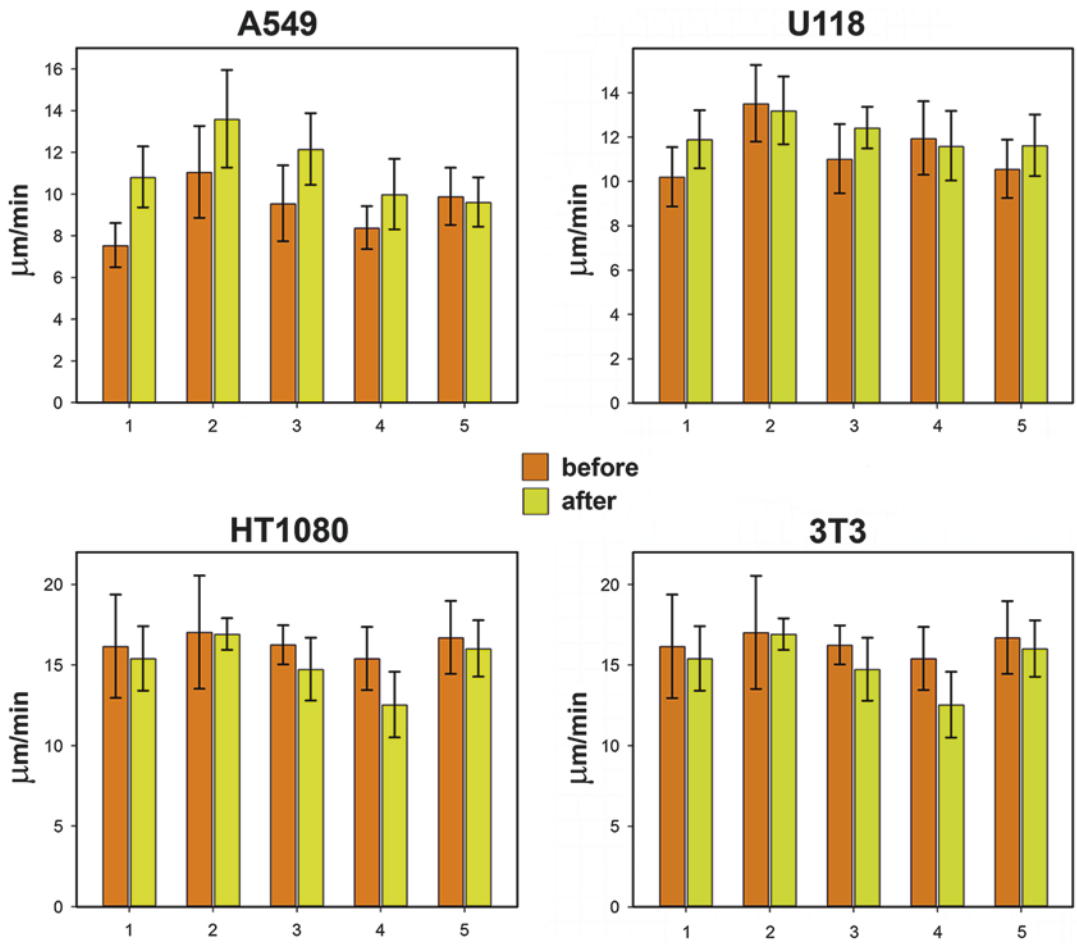

Fig. 4 MT dynamics in NIH 3T3, HT1080, A549, and U118 cells does not change with time. Measurements were taken with 1-h interval. The coefficient of variation (SD/mean) for each 3T3 cell is very lower than in the population

CO_2 incubator with 5% CO_2 at 37 °C. Experimental cell lines should be split 2–3 times per week to avoid overgrowth in the tissue culture flasks. For cell detachment, we use trypsin-EDTA in concentration 0.25%.

3.2 Splitting and Seeding Cells

1. Detach cells from flasks by trypsinization and resuspend them in growth media. To do this, after removal of an old medium in the 25 cm^2 flask wash cells with pre-warmed 3 ml of PBS. Use 1 ml of 0.25% trypsin-EDTA to detach cells in 25 cm^2 flask with the following incubation at 37 °C for no more than 3 min.
2. Resuspend detached cells in DMEM medium supplemented with 5–10% FBS, L-glutamine, 100 U/ml penicillin, and 100 µg/ml streptomycin.
3. Then transfer cells into (the concentration of cells per well should be adjusted by changing dilution to 2–4 × 10^4 cells/

ml—*see* **Note 4**) the eight-chambered cover glass system (final volume of cell suspension per well is 500 μl) or 24-well glass bottom plate (final volume of cell suspension per well is 1000 μl).

4. To allow cells to spread on the substrate, place the experimental sample into an incubator at 37 °C for at least 24 h until a necessary density of cell monolayer is obtained.

3.3 Transfection

Cell cultures of NIH 3T3 fibroblasts, HT1080, A549, and U118 expressing EB-3-RFP are transfected with 1 μg/μl of EB-3-RFP plasmid using X-tremeGENE HP DNA transfection reagent according to manufacturer's instructions. The optimal ratio of plasmid to transfection agent is 1:2.

When using 24-well dish, the final volume of culture medium is 1 ml per well. When using eight-chambered cover glass system, the final volume is 0.5 ml per well (*see* **Note 5**).

1. For cell transfection firstly, for one well of 24-well plate, take a 1 ml (or smaller) Eppendorf tube.
2. Add 1 μl transfection reagent into 50 μl of sterile PBS and then 0.5 μl of EB-3-RFP plasmid (concentration 1000 ng/μl) to form a plasmid-agent complex. The sequence of the mixture to be added is important.
3. Incubate transfection mixture for 25 min on average to allow the formation of transfection agent-plasmid complex.
4. Add the mixture dropwise to the wells containing cell monolayer.
5. 24 h after transfection has started, change culture medium for the fresh full culture medium, and keep cells growing in the CO_2 incubator for additional 12–24 h (based on the expression state of EB-3-RFP in cells). The optimal level of the expression of the EB-3 plasmid with individual observable comets is usually obtained in 48 h after transfection.
6. For analysis cells have to be selected based on the relative brightness of EB comets—preferable cells are with the minimal detectable level of EB fluorescence.

3.4 Data Acquisition

For live cell imaging, transiently or stably transfected cells are placed in a recording media, usually CO_2-independent culture Leibowitz media supplemented with 5% FBS, 100 U/ml penicillin, 100 μg/ml streptomycin, and L-glutamine (1 ml per well) and incubating at 37 °C for at least 2 h before the beginning of recording (*see* **Note 6**).

1. Warm up microscope to 37.0 °C (*see* **Note 7**), then place multiwell chamber on the microscope stage, and set up the ×63/1.4 oil immersion PlanApo objective.

2. To start recording open ZEN software and run ZEN setup.
3. Initialize ZEN "Blue" software for microscope control from a shortcut, and then choose "ZEN system" in the selection window. Chose an "Acquisition" tab for experiment setup from the upper left corner containing "Locate," "Acquisition," "Processing," and "Analysis" tabs. In "Experiment manager" block, choose a desired experiment setup. This will upload last saved settings including camera, channel and exposure setup, light path hardware settings, position and time settings ("Tiles" and "Time Series" boxes must be activated), focus strategy, and file name for autosave mode.
4. Make focus adjustment and ROI positions setup. Go to "Channels" window, and select field DIC (or any transmitted light option). Then go to "Experiment manager" box, and press "Live" button for camera live mode.
5. After activating this button, switch it to "Start" and it will be used to turn on/off real-time mode. Adjust focus by coarse and fine knobs on microscope. Press "Stop."
6. Go to "Channels," and select field RFP LED (this will initialize LED illumination mode to prevent cell damage due to intensive light exposure from mercury lamp).
7. Go to "Live" mode and search for at least one object of interest. Adjust fine focus and find appropriate cell (*see* **Note 8**).
8. Go to "Tiles" window in "Multidimensional Acquisition" block, and set position "1" in Position window, by pressing "+" symbol. This action creates a XYZ-position beacon for the desired ROI. Search for other appropriate cell adding, and then "save XYZ" of each of them.
9. Set exposure settings for time-lapse. Go to "Channels" and select field with RFP Lamp for reflection light method. This will initialize HXP-120 metal halide light source. Adjust lamp intensity to 100% and set exposure to 200–300 ms. Transfected cells contained EB-3-RFP plasmid that enabled fluorescent light capture from growing plus end of MTs under 555 nm (green) excitation. Standard band-pass or long-pass Cy-3/TRITC filter cube is used.
10. Go back to "Live" mode and check every ROI for XYZ coordinates. Turn off "Live." Go to "Focus strategy" mode, select "Absolute fixed Z-Position," and put marker at "Use Z-position from Tiles Setup" box.
11. Go to "Time Series" window and set duration to 100 cycles and frame interval to 2 s. Activate "Autosave" window and check for correct path and filename. Go to "Channels" window and check for desired illumination mode. There must be a marker in "RFP Lamp" field and none in other fields. Go to

Experiment manager and press button "►Start Experiment." It will initialize time-lapse recording, and the stack of images will be recorded to the selected folder. To stop experiment, use animated "Stop" button that appears in the box above.

12. Image acquisition is performed with adjusted microscopy parameters. Exposure time depends on the intensity of the fluorescence signal (300 ms was optimal in our set of experiments; however, it could be reduced to 200 ms with bright enough light source). To accurately measure MT growth rate, 100 frames at 2 s time interval are collected.

13. Sequential Image Acquisition

    Figure 5 shows the major steps schematically. Briefly, incubated transfected cells in each well ($N \geq 5$) are first imaged and recorded before adding the drug. We typically acquired 100 sequential images at 2 s intervals for each cell using 300–500 ms exposure time. Time-lapse settings will vary depending on the sensitivity of the camera, the brightness of the specimen, the fluorophore used for labeling, and the amount of photobleaching. Using RFP excited by the green light allows significantly minimizing photobleaching compared to the use of EGFP (data not shown). After recording drugs are added to each well, and cells are returned to the microscope stage and incubated for at least 1 h on at 37 °C.

14. Data acquisitions are repeated after drug treatment within the same cells using saved positions in ZEN after 1 h incubation with drugs (*see* **Note 9**). For the analysis of MT dynamics, at least five cells before and after the treatment have to be recorded.

3.5 Data Analysis

ImageJ software package can be used for data analysis. File conversion from ZEN software (goes along with Zeiss microscopes) could be performed in two ways. Firstly, all captured images should be exported from ZEN (*.czi format) to 16 bit grayscale multilayer *.tif files for further analysis on ImageJ software.

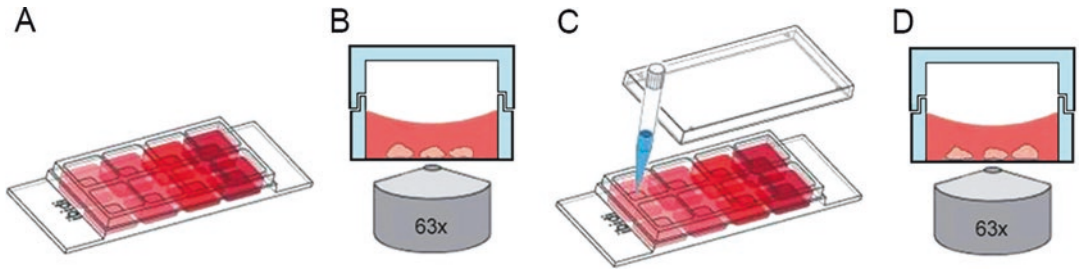

Fig. 5 General experimental setup. (**a**) Seed cells into the observation chamber and incubate. (**b**) Microscopy of transfected cells (first time-lapse recording). (**c**) Add MT-binding drug. (**d**) Microscopy of the same transfected cells (second time-lapse recording)

Another way is to open *.czi images directly in ImageJ using "Import" function.

3.5.1 Contrast Enhancement

1. Open images from the appropriate folder in ImageJ using "Virtual stack," and save stack as a multilayer TIFF file.
2. Create two copies of Stack obtained by right-clicking on the movie and selecting "Duplicate"; tick the "Duplicate stack."
3. Apply Gaussian blur with sigma radius of 0.6 to the Stack 1 (*Process* → *Filters* → *Gaussian Blur*). Apply to the entire image sequence (Fig. 6).
4. Apply Gaussian blur with sigma radius of 5.0 to the Stack 2 (*Process* → *Filters* → *Gaussian Blur*). Apply to the entire image sequence (Fig. 6) (*see* **Note 10**).
5. Make image subtraction (*Process* → *Image calculator*). In the "Image 1" box, select an image with a small sigma radius, select the image with a large sigma radius in the "Image 2" box, select "Subtract" in the "Operation" field, and check the boxes "Create new window" and "32 bit (float) result." Apply to the entire image sequence (Fig. 6).
6. Save the new image under the appropriate name. This image is your stack for further analysis (*see* **Note 11**).

3.5.2 Generation of Maximal Intensity Projections (MIP)

To generate MIP go to the Stack menu (*Image* → *Stacks* → *Z-Project*), select Maximal Intensity. The whole stack will be converted into a single image representing all tracks of MT plus ends (Fig. 6) (*see* **Note 12**).

3.5.3 Manual Tracking

The plus ends of MTs are tracked over time using the manual tracking function (*Plugins* > *Tracking* > *Manual tracking)* using the stack obtained in Subheading 3.5.1 (Fig. 7).

Before tracking adjust the calibration for images by proceeding to *Analyze* > *Set scale*. Use the following parameters for manual tracking: distance in pixels, 1.0; known distance, according to your equivalent pixel size, in nm; pixel aspect ratio, 1.0; unit of length, nm; set global.

Initiate the tracking of the growing MT from the first frame showing spatial EB displacement. As you have found the point of initial growth of MT, click on *Add track*, and table with the results of tracking will pop up, indicating with XY coordinates, distance traveled by EB during the time interval between two frames, velocity of movement, and intensity of the corresponding pixel. The next frame will appear automatically as you proceed with the tracking of moving comet of the MT (*see* **Note 13**).

If MT goes into pause state or to shortening, terminate tracking by clicking on *End track*, and select next MT from the image sequence for the analysis (*see* **Note 14**). Pause in the manual tracking

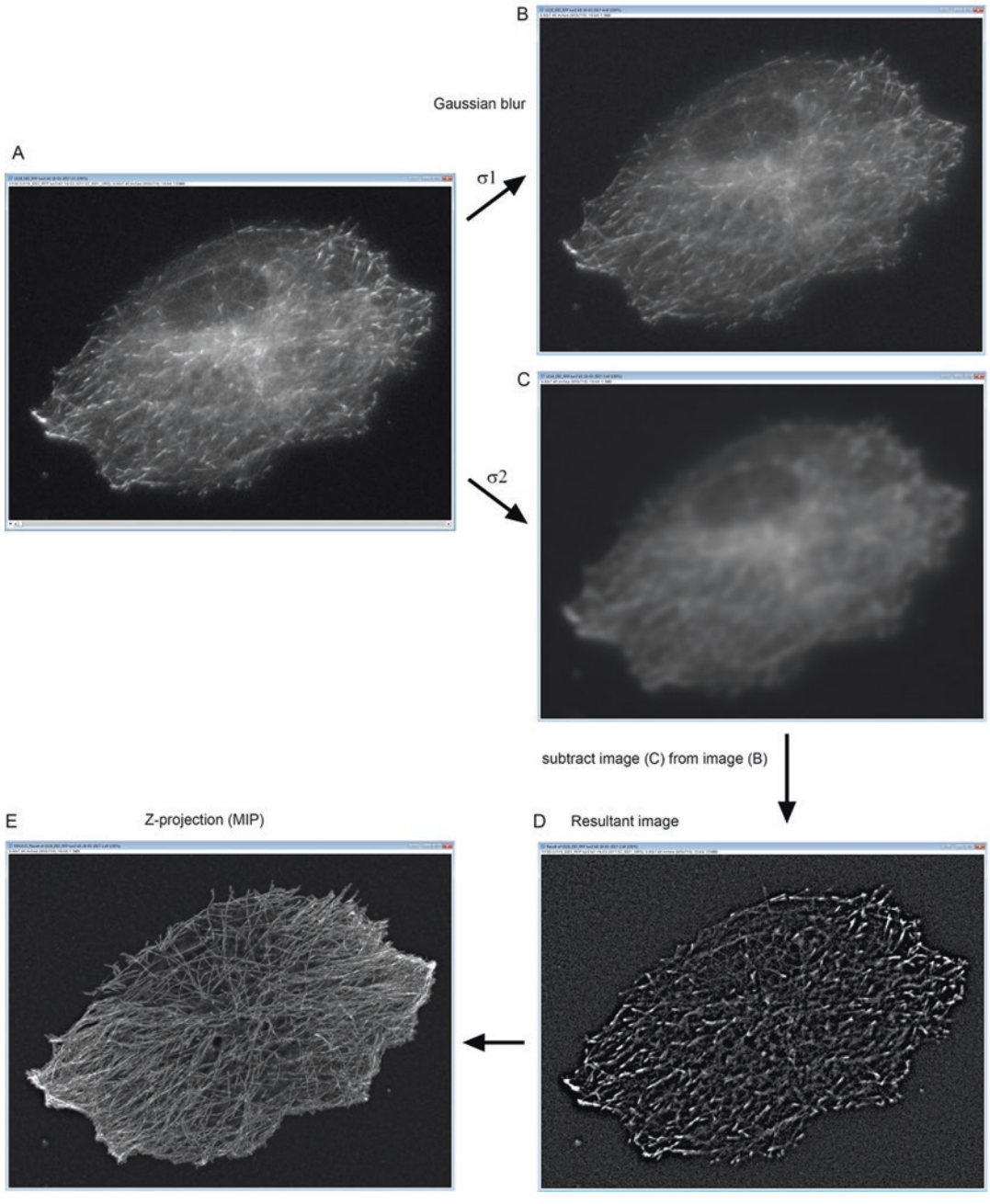

Fig. 6 Microscopy image sequence. (**a**–**c**) Extraction of comets using Gaussian blurring ($\sigma1 = 0.7$ and $\sigma2 = 6.0$). (**d**) Contrast enhancement to identify individual comets. (**e**) MIP (maximal intensity projection) obtained for 100 frames. HT1080 cell

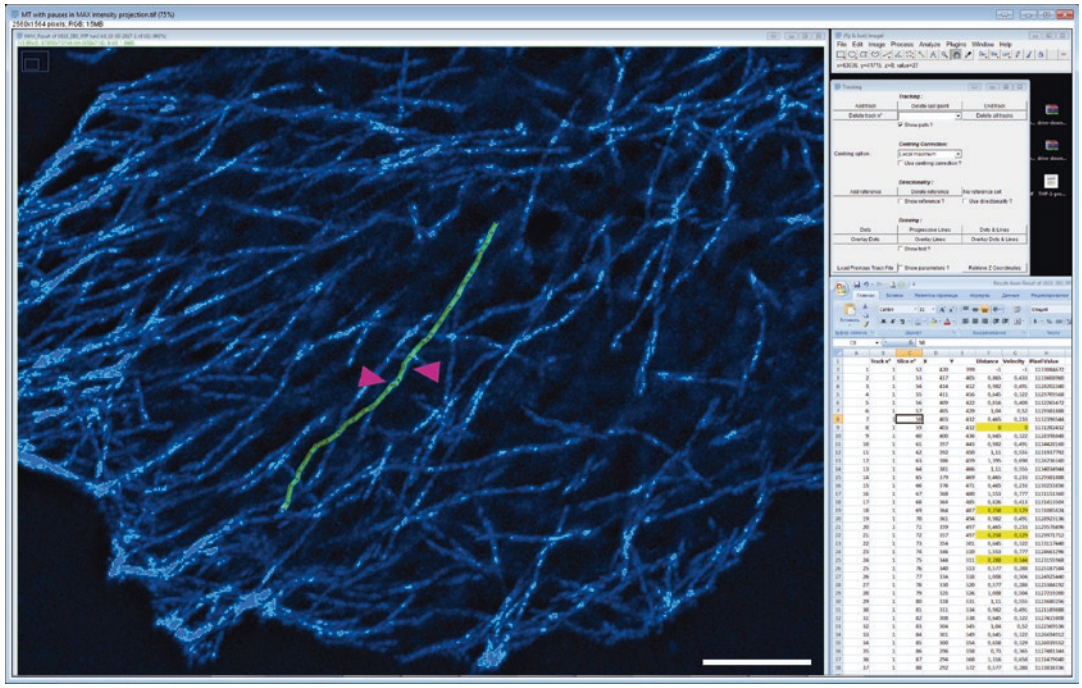

Fig. 7 Manual tracking of MT end. Overlay of a track (yellow) on MIP image. Arrowheads point insignificant displacements between two frames. This track for further analysis is split into three. Scale bar 10 μm

is interpreted if velocity is close to zero, i.e., the displacement of EB is less than 0.23 μm (2.236 pix). Then, further growth is tracked separately starting from the pausing state of MT end.

From the ImageJ dataset, export the column Velocity with eliminated initial −1 value into separate Excel spreadsheet, and convert to necessary unit (*see* **Note 15**).

In case of making mistake while clicking the growing MT end, you can remove the last tracked point by clicking on *Delete last point* that returns the image on one slice back.

3.5.4 Control of Manual Tracking

For the internal control, it is useful to transfer manually build track onto MIP image using ROI manager window to make sure that you did not track events belonging to the different MTs.

If the beginning or end of an event cannot be determined clearly from image sequence, generate maximal intensity projection image by combining all frames. Click on *Image* → *Stack* → *Z project* → *Choose Maximal intensity* → *press Ok*. Appeared image shows tracks of MTs for all frames and allows one to determine the beginning and end of MT. If the ambiguity is not resolved, then end tracking at the very last clear place of the growing MT end but only in case of sufficient number of frames is reached. Subsequent analysis of growing MT end only includes growth tracks with a

lifetime of four frames and greater, since short tracks are associated with unambiguity resulting in larger S.D. value [44] (*see* **Note 16**).

3.5.5 Visualization by Triple Color-Coded Display Analysis

Color-coded images represent semi-qualitative measurements of different dynamics events validating quantitative manual tracking method [51]. The triple color approach that is based on sequential subtraction approach [45] provides a rapid way to visually inspect the frequency of pauses of MTs and to select areas of high concentration of growing MT ends where tracking should not be taken (Fig. 8).

Triple color visualization is done using the following steps: (1) convert image stack obtained for manual tracking into RGB mode and duplicate it; (2) then convert one stack into green (suppressing red and blue channels) and another stack into red (suppressing green and blue channels).

To generate color-coded image sequence with 4 s interval from fluorescent frames obtained with 2 s interval, subtract first two frames from the green stack and last two frames from the red stack to keep both stacks of equal size. After subtraction of frames merges two-colored stacks (*Process* → *Image calculator* → *Add*) to generate the triple color (green-yellow-re d) image sequence.

To identify ends of growing MTs (comets) in color, apply threshold by adjusting brightness and contrast in menu *Image-Adjust-Brightness/Contrast* to the narrow range in merged time-lapse images. The resulting color images provide a simple way to identify qualitatively two different events in MT dynamic behavior: growing green-red (red-head, green-tail) comet and pausing MT by a yellow merged zone (*see* **Notes 14** and **17**).

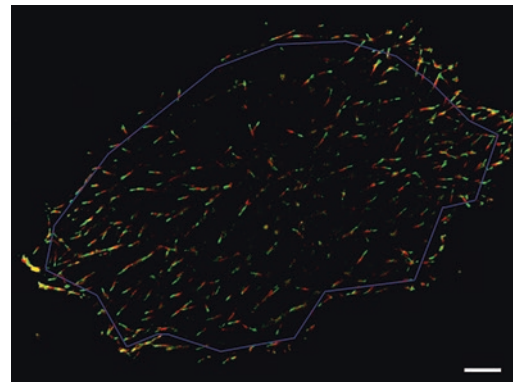

Fig. 8 The triple color assay is showing individual comets to extract dynamic information (pauses) from two images taken at 4 s interval. Blue contour shows the area where MT dynamics is analyzed. Scale bar, 10 μm

4 Notes

1. Eight-chambered cover glass system has a size of a regular coverslip, while 24-well plates have a size of a standard plate (110 × 85 mm) and might not fit some microscopic stages. For life imaging of transfected cells, we used eight-chambered cover glass system #1.5 high-performance cover glass (0.17 ± 0.005 mm) (In Vitro Scientific—www.invitrosci.com) or MatTek Corporation Glass Bottom 24-well plates No. 1.5.
2. The precision of the rate measurement depends on the pixel size. The maximal equivalent pixel size when an error is reasonable is around 100 nm. It is usually equivalent to the use of ×60 (×63) objective along with digital camera having pixels of 6.45 μm (standard for sCMOS cameras of Andor and Hamamatsu and some other CCDs). Pixels of less size (i.e., 60–70 nm) give slightly better precision, but it decreases the sensitivity of the microscopic system and requires excessive illumination of cells. When using EMCCD cameras with larger pixel size (9–11 μm), the intermediate lens is required, or recording could be performed using 100× immersion objective.
3. Any kind of inverted motorized fluorescent microscope from major manufacturers (Carl Zeiss, Nikon, Olympus, Leitz) could be used operating under different software (MetaMorph Micromanager and others). The requirements are (1) large temperature control unit covering the specimen, microscope stage, and objective, (2) fully motorized stage with a system allowing keeping selected focal plane (*Z*-axis position) during time lapse, (3) scientific CMOS or EMCCD camera with high quantum yield (>70%), and (4) appropriate software making it possible to "remember" multiple stage positions and record large files for time-lapse observations.
4. It is easy to image when cells are very well spread and flat; a dense culture with confluence >70% should be avoided. Taking into account that cells are dividing during transfection the initial density of 1 day culture should be not more than 20–30%.
5. For 24-well plate with the diameter of the well 10–13 mm, 50 μl of transfection mixture is sufficient; the amount of DMEM medium per one well is 1 ml. The larger amount of plasmid might be toxic for cells or cause overexpression of the plasmid. Shake slightly back and forth the 24-well plate with cells to allow transfection complex mix with culture medium. Cells are then incubated with the transfection mixture overnight.

6. CO_2-independent medium (L-15 ort from other sources) is capable of maintaining long-term pH stability under atmospheric CO_2 (0.03%).
7. For AxioObserver the fluctuation of temperature is ±0.1 °C. For other heating systems with higher possible fluctuations, it is safer to set the temperature a little bit less than 37.0 °C (e.g., 36.0 °C when deviation might be 1 °C).
8. To select the cells, the following criteria are useful: level of labeling should be low enough, just to make comets clearly visible under the camera with 200–300 ms exposure. The image might look dim for the nonadapted eye. Rather bright comets represent overexpression of EB protein, and MT dynamics might be diminished in such cells.
9. Since cells might slightly move from the original position, field of view has to be shifted subsequently. According to our experience within 60–90 min, no cell traveled away from its initial position more than 10 μm; however, it could change its shape. After imaging cells in the first well, the chamber on the stage is transferred to view and record the second well.
10. Depending on your settings, σ (sigma) can be adjusted according to the magnification of the camera chip. The preferred equivalent value of σ1 is about 0.06 μm (60 nm) and σ2 is about 0.5–0.6 μm.
11. To decrease the image size, you can change it to 16-bit image. To do this, adjust brightness and contrast first, and then convert the image to 16-bit format and save it.
12. In some cells, the number of tracks in the whole time-lapse series might be too high for subsequent analysis. It is recommended then to make MIP from a reduced number of frames (say 1–50 and 51–100).
13. Displacement of EB-3-RFP comets over time is tracked until growing MT plus ends reach approximately 1–2 μm from cell periphery (Fig. 8), because of the difference in MT behavior in the cell interior compared with that near the cell margin [30].
14. Before the displacement of MT end is observed, there is usually a gradual increase of EB signal at stationary plus end of MT between two successive frames. Also before EB comet disappears completely, it usually demonstrates negligible displacement (less than 0.3 μm), and its brightness goes down. That means that the real catastrophes (switch from growth into shortening) are very rare, and the real pause converts into small displacement. Thus, once MT stops growing, simply click on *End track* and proceed to the next MT.
15. To convert results of your measurements to μm/min rate, multiply all numbers 30 times for 2 s interval images or 15

times for 4 s intervals. MT growth rate for every experimental condition is represented by calculating the mean of converted data.

16. Tracking no less than $n = 15$ MTs per cell (in no less than five cells) is usually sufficient to get reproducible results between sets of experiments, but it is not enough to analyze heterogeneity.
17. Qualitatively, we consider that MT is in pause when persistently growing MT end shows no shift or insignificant between two successive frames in the image sequence. Because the triple color method is based on the relative displacement of color-coded labels, accurate visualization of pausing MTs depends on the time interval between two sequential images. Since the duration of MT pausing may vary, the color criteria for the measurement of MT pause may be green-overlapping yellow-red in addition to only yellow. We obtained 6–10-pixel-long EB-3-RFP comets. Taking into account the resolution of the microscope 220–250 nm, the minimal displacement that can be considered to be meaningful is 3 and more pixels (>300 nm). With this limit, a minimal growth rate that could be determined on the triple color image at 4 s interval is 4.5 μm/min. According to our observations, the interval of 4 s is sufficient since >95% of MTs in 3T3 cells and nearly 100% in cancer cell cultures are growing faster than a threshold value.

References

1. Desai A, Mitchison TJ (1997) Microtubule polymerization dynamics. Annu Rev Cell Dev Biol 13(1):83–117
2. Rodionov VI, Gyoeva FK, Tanaka E et al (1993) Microtubule-dependent control of cell shape and pseudopodial activity is inhibited by the antibody to kinesin motor domain. J Cell Biol 123(6):1811–1820
3. Alberts B et al (2014) Molecular biology of the cell. Garland Science, New York
4. Lauffenburger DA, Horwitz AF (1996) Cell migration: a physically integrated molecular process. Cell 84(3):359–369
5. Etienne-Manneville S (2013) Microtubules in cell migration. Annu Rev Cell Dev Biol 29: 471–499
6. Broussard JA, Webb DJ, Kaverina I (2008) Asymmetric focal adhesion disassembly in motile cells. Curr Opin Cell Biol 20:85–90
7. Fanara P, Husted KH, Selle K et al (2010) Changes in microtubule turnover accompany synaptic plasticity and memory formation in response to contextual fear conditioning in mice. Neuroscience 168(1):167–178
8. Atarod D, Eskandari-Sedighi G, Pazhoohi F et al (2015) Microtubule dynamicity is more important than stability in memory formation: an in vivo study. J Mol Neurosci 56(2): 313–319
9. Dent EW (2017) Of microtubules and memory: implications for microtubule dynamics in dendrites and spines. Mol Biol Cell 28(1): 1–8
10. Holy TE, Leibler S (1994) Dynamic instability of microtubules as an efficient way to search in space. Proc Natl Acad Sci U S A 91(12): 5682–5685
11. Jordan MA, Wilson L (2004) Microtubules as a target for anticancer drugs. Nat Rev Cancer 4(4):253–265
12. Stearns ME, Wang M (1992) Taxol blocks processes essential for prostate tumor cell (PC-3 ML) invasion and metastases. Cancer Res 52(13):3776–3781
13. Hotchkiss KA, Ashton AW, Mahmood R et al (2002) Inhibition of endothelial cell function in vitro and angiogenesis in vivo by docetaxel (Taxotere): association with impaired reposi-

tioning of the microtubule organizing center. Mol Cancer Ther 1(13):1191–1200

14. Hayot C, Farinelle S, De Decker R et al (2002) In vitro pharmacological characterizations of the anti-angiogenic and anti-tumor cell migration properties mediated by microtubule-affecting drugs, with special emphasis on the organization of the actin cytoskeleton. Int J Oncol 21(2):417–426
15. Pasquier E, Honoré S, Braguer D (2006) Microtubule-targeting agents in angiogenesis: where do we stand? Drug Resist Updat 9(1): 74–86
16. Gliksman NR, Skibbens RV, Salmon ED (1993) How the transition frequencies of microtubule dynamic instability (nucleation, catastrophe, and rescue) regulate microtubule dynamics in interphase and mitosis: analysis using a Monte Carlo computer simulation. Mol Biol Cell 4(10):1035–1050
17. Yvon AM, Wadsworth P (1997) Non-centrosomal microtubule formation and measurement of minus end microtubule dynamics in A498 cells. J Cell Sci 110(19):2391–2401
18. Vorobjev IA, Svitkina TM, Borisy GG (1997) Cytoplasmic assembly of microtubules in cultured cells. J Cell Sci 110(21):2635–2645
19. Song Y, Brady ST (2015) Post-translational modifications of tubulin: pathways to functional diversity of microtubules. Trends Cell Biol 25(3):125–136
20. Howard J, Hyman AA (2007) Microtubule polymerases and depolymerases. Curr Opin Cell Biol 19(1):31–35
21. Dumontet C, Jordan MA (2010) Microtubule-binding agents: a dynamic field of cancer therapeutics. Nat Rev Drug Discov 9(10):790–803
22. Schuyler SC, Pellman D (2001) Microtubule "plus-end-tracking proteins": the end is just the beginning. Cell 105(4):421–424
23. Akhmanova A, Steinmetz MO (2008) Tracking the ends: a dynamic protein network controls the fate of microtubule tips. Nat Rev Mol Cell Biol 9(4):309–322
24. Walczak CE (2003) The Kin I kinesins are microtubule end-stimulated ATPases. Mol Cell 11(2):286–288
25. Moore A, Wordeman L (2004) The mechanism, function and regulation of depolymerizing kinesins during mitosis. Trends Cell Biol 14(10):537–546
26. Grigoriev I, Borisy G, Vorobjev I (2006) Regulation of microtubule dynamics in 3T3 fibroblasts by Rho family GTPases. Cell Motil Cytoskeleton 63(1):29–40
27. Dogterom M, Kerssemakers JW, Romet-Lemonne G et al (2005) Force generation by dynamic microtubules. Curr Opin Cell Biol 17(1):67–74
28. Kinoshita K, Arnal I, Desai A et al (2001) Reconstitution of physiological microtubule dynamics using purified components. Science 294(5545):1340–1343
29. Li W, Moriwaki T, Tani T et al (2012) Reconstitution of dynamic microtubules with Drosophila XMAP215, EB1, and Sentin. J Cell Biol 199(5):849–862
30. Komarova YA, Vorobjev IA, Borisy GG (2002) Life cycle of MTs: persistent growth in the cell interior, asymmetric transition frequencies and effects of the cell boundary. J Cell Sci 115(17):3527–3539
31. Azarenko O, Okouneva T, Singletary KW et al (2008) Suppression of microtubule dynamic instability and turnover in MCF7 breast cancer cells by sulforaphane. Carcinogenesis 29(12): 2360–2368
32. Zilberman Y, Ballestrem C, Carramusa L et al (2009) Regulation of microtubule dynamics by inhibition of the tubulin deacetylase HDAC6. J Cell Sci 122(19):3531–3541
33. Applegate KT, Besson S, Matov A et al (2011) plusTipTracker: quantitative image analysis software for the measurement of microtubule dynamics. J Struct Biol 176(2):168–184
34. Shelden E, Wadsworth P (1993) Observation and quantification of individual microtubule behavior in vivo: microtubule dynamics are cell-type specific. J Cell Biol 120:935–945
35. Waterman-Storer CM, Salmon ED (1997) Actomyosin-based retrograde flow of microtubules in the lamella of migrating epithelial cells influences microtubule dynamic instability and turnover and is associated with microtubule breakage and treadmilling. J Cell Biol 139(2): 417–434
36. Alieva IB, Berezinskaya T, Borisy GG et al (2015) Centrosome nucleates numerous ephemeral microtubules and only few of them participate in the radial array. Cell Biol Int 39(11):1203–1216
37. Perez F, Diamantopoulos GS, Stalder R et al (1999) CLIP-170 highlights growing microtubule ends in vivo. Cell 96:517–527
38. Bieling P, Laan L, Schek H et al (2007) Reconstitution of a microtubule plus-end tracking system in vitro. Nature 450(7172):1100–1105
39. Tirnauer JS, Grego S, Salmon ED et al (2002) EB1–microtubule interactions in Xenopus egg extracts: role of EB1 in microtubule stabilization and mechanisms of targeting to microtubules. Mol Biol Cell 13(10):3614–3626
40. Piehl M, Cassimeris L (2003) Organization and dynamics of growing microtubule plus

ends during early mitosis. Mol Biol Cell 14(3):916–925

41. Schuster M, Kilaru S, Latz M et al (2015) Fluorescent markers of the microtubule cytoskeleton in Zymoseptoria tritici. Fungal Genet Biol 79:141–149
42. Zanic M, Stear JH, Hyman AA (2009) EB1 recognizes the nucleotide state of tubulin in the microtubule lattice. PLoS One 4(10):e7585
43. Kapoor S, Panda D (2012) Kinetic stabilization of microtubule dynamics by indanocine perturbs EB1 localization, induces defects in cell polarity and inhibits migration of MDA-MB-231 cells. Biochem Pharmacol 83(11):1495–1506
44. Matov A, Applegate K, Kumar P et al (2010) Analysis of microtubule dynamic instability using a plus-end growth marker. Nat Methods 7(9):761–768
45. Vorobjev IA, Rodionov VI, Maly IV et al (1999) Contribution of plus and minus end pathways to microtubule turnover. J Cell Sci 112(14):2277–2289
46. Gregoretti IV, Margolin G, Alber MS (2006) Insights into cytoskeletal behavior from computational modeling of dynamic microtubules in a cell-like environment. J Cell Sci 119(22): 4781–4788
47. Mimori-Kiyosue Y, Grigoriev I, Lansbergen G et al (2005) CLASP1 and CLASP2 bind to EB1 and regulate microtubule plus-end dynamics at the cell cortex. J Cell Biol 168(1):141–153
48. Toso RJ, Jordan MA, Farrell KW et al (1993) Kinetic stabilization of microtubule dynamic instability in vitro by vinblastine. Biochemistry 32(5):1285–1293
49. Dhamodharan R, Wadsworth P (1995) Modulation of microtubule dynamic instability in vivo by brain microtubule associated proteins. J Cell Sci 108:1679–1689
50. Sironi L, Solon J, Conrad C et al (2011) Automatic quantification of microtubule dynamics enables RNAi-screening of new mitotic spindle regulators. Cytoskeleton 68(5): 266–278
51. Garrison AK, Shanmugam M, Leung HC et al (2012) Visualization and analysis of microtubule dynamics using dual color-coded display of plus-end labels. PLoS One 7(11):e50421
52. Jordan MA, Kamath K (2007) How do microtubule-targeted drugs work? An overview. Curr Cancer Drug Targets 7(8):730–742
53. Castle BT, McCubbin S, Prahl LS et al (2017) Mechanisms of kinetic stabilization by the drugs paclitaxel and vinblastine. Mol Biol Cell 28(9):1238–1257
54. Wilson L, Jordan MA (1995) Microtubule dynamics: taking aim at a moving target. Chem Biol 2(9):569–573
55. Dorléans A, Gigant B, Ravelli RB et al (2009) Variations in the colchicine-binding domain provide insight into the structural switch of tubulin. Proc Natl Acad Sci U S A 106(33): 13775–13779
56. Gigant B, Wang C, Ravelli RB et al (2005) Structural basis for the regulation of tubulin by vinblastine. Nature 435(7041):519–522
57. Nogales E, Whittaker M, Milligan RA (1999) High-resolution model of the microtubule. Cell 96(1):79–88
58. Honore S, Kamath K, Braguer D et al (2004) Synergistic suppression of microtubule dynamics by discodermolide and paclitaxel in non-small cell lung carcinoma cells. Cancer Res 64(14):4957–4964
59. Smith JA, Wilson L, Azarenko O et al (2010) Eribulin binds at microtubule ends to a single site on tubulin to suppress dynamic instability. Biochemistry 49(6):1331–1337
60. Honore S, Braguer D (2011) Investigating microtubule dynamic instability using microtubule-targeting agents. In: Straube A (ed) Microtubule dynamics: methods and protocols, Methods in molecular biology, vol 777. Springer, New York, pp 245–260
61. Yang H, Ganguly A, Cabral F (2010) Inhibition of cell migration and cell division correlates with distinct effects of microtubule inhibiting drugs. J Biol Chem 285(42):32242–32250
62. Mohan R, Katrukha EA, Doodhi H et al (2013) End-binding proteins sensitize microtubules to the action of microtubule-targeting agents. Proc Natl Acad Sci U S A 110(22): 8900–8905
63. Yvon AM, Wadsworth P, Jordan MA (1999) Taxol suppresses dynamics of individual microtubules in living human tumor cells. Mol Biol Cell 10(4):947–959
64. Pasquier E, Honore S, Pourroy B et al (2005) Antiangiogenic concentrations of paclitaxel induce an increase in microtubule dynamics in endothelial cells but not in cancer cells. Cancer Res 65(6):2433–2440
65. Gan PP, McCarroll JA, Po'uha ST (2010) Microtubule dynamics, mitotic arrest, and apoptosis: drug-induced differential effects of βIII-tubulin. Mol Cancer Ther 9(5): 1339–1348
66. Mikhailov A, Gundersen GG (1998) Relationship between microtubule dynamics and lamellipodium formation revealed by direct imaging of microtubules in cells treated with

nocodazole or taxol. Cell Motil Cytoskeleton 41(4):325–340

67. Vasquez RJ, Howell B, Yvon AM (1997) Nanomolar concentrations of nocodazole alter microtubule dynamic instability in vivo and in vitro. Mol Biol Cell 8(6):973–985
68. Wieczorek M, Bechstedt S, Chaaban S (2015) Microtubule-associated proteins control the kinetics of microtubule nucleation. Nat Cell Biol 17(7):907–916
69. Ganguly A, Yang H, Zhang H (2013) Microtubule dynamics control tail retraction in migrating vascular endothelial cells. Mol Cancer Ther 12(12):2837–2846
70. Pourroy B, Honoré S, Pasquier E (2006) Antiangiogenic concentrations of vinflunine increase the interphase microtubule dynamics and decrease the motility of endothelial cells. Cancer Res 66(6):3256–3263
71. Thompson RE, Larson DR, Webb WW (2002) Precise nanometer localization analysis for individual fluorescent probes. Biophys J 82(5): 2775–2783
72. Wadsworth P (1999) Regional regulation of microtubule dynamics in polarized, motile cells. Cell Motil Cytoskeleton 42(1):48–59
73. Heppner GH (1989) Tumor cell societies. J Natl Cancer Inst 81(9):648–649
74. Fisher R, Pusztai L, Swanton C (2013) Cancer heterogeneity: implications for targeted therapeutics. Br J Cancer 108(3):479–485
75. Meacham CE, Morrison SJ (2013) Tumour heterogeneity and cancer cell plasticity. Nature 501(7467):328–337
76. Gascoigne KE, Taylor SS (2008) Cancer cells display profound intra-and interline variation following prolonged exposure to antimitotic drugs. Cancer Cell 14(2): 111–122
77. Joshi HC, Yen TJ, Cleveland DW (1987) In vivo co-assembly of a divergent beta-tubulin subunit (c beta 6) into microtubules of different function. J Cell Biol 105(5): 2179–2190
78. Lewis SA, Gu W, Cowan NJ (1987) Free intermingling of mammalian β-tubulin isotypes among functionally distinct microtubules. Cell 49(4):539–548
79. Lopata MA, Cleveland DW (1987) In vivo microtubules are copolymers of available 13-tubulin isotypes: localization of each of six vertebrate 13-tubulin isotypes using polyclonal antibodies elicited by synthetic peptide antigens. J Cell Biol 105:1707–1720
80. Stengel C, Newman SP, Leese MP et al (2010) Class III β-tubulin expression and in vitro resistance to microtubule targeting agents. Br J Cancer 102(2):316–324
81. Ganguly A, Yang H, Cabral F (2011) Class III β-tubulin counteracts the ability of paclitaxel to inhibit cell migration. Oncotarget 2(5): 368–377

Chapter 12

Heterogeneity of Focal Adhesions and Focal Contacts in Motile Fibroblasts

Aleena Gladkikh, Anastasia Kovaleva, Anna Tvorogova, and Ivan A. Vorobjev

Abstract

Cell-extracellular matrix (ECM) adhesion is an important property of virtually all cells in multicellular organisms. Cell-ECM adhesion studies, therefore, are very significant both for biology and medicine. Over the last three decades, biomedical studies resulted in a tremendous advance in our understanding of the molecular basis and functions of cell-ECM adhesion. Based on morphological and molecular criteria, several different types of model cell-ECM adhesion structures including focal adhesions, focal complexes, fibrillar adhesions, podosomes, and three-dimensional matrix adhesions have been described. All the subcellular structures that mediate cell-ECM adhesion are quite heterogeneous, often varying in size, shape, distribution, dynamics, and, to a certain extent, molecular constituents. The morphological "plasticity" of cell-ECM adhesion perhaps reflects the needs of cells to sense, adapt, and respond to a variety of extracellular environments. In addition, cell type (e.g., differentiation status, oncogenic transformation, etc.) often exerts marked influence on the structure of cell-ECM adhesions. Although molecular, genetic, biochemical, and structural studies provide important maps or "snapshots" of cell-ECM adhesions, the area of research that is equally valuable is to study the heterogeneity of FA subpopulations within cells. Recently time-lapse observations on the FA dynamics become feasible, and behavior of individual FA gives additional information on cell-ECM interactions. Here we describe a robust method of labeling of FA using plasmids with fluorescent markers for paxillin and vinculin and quantifying the morphological and dynamical parameters of FA.

Key words Focal adhesions, Fluorescence microscopy, Paxillin, Vinculin, Image processing, Heterogeneity

1 Introduction

Cell migration in multicellular organisms is involved in normal development and tissue homeostasis, as well as pathological processes such as inflammation, tumor formation, and progression. Aberrant mechanisms of cell-ECM adhesion and cell migration are considered to be the main reason of metastatic tumor growth [1, 2]. Cell adhesion to extracellular matrix (ECM) is governed by adhesion of integrin-like receptors that are prominently expressed in the

Natasha S. Barteneva and Ivan A. Vorobjev (eds.), *Cellular Heterogeneity: Methods and Protocols*, Methods in Molecular Biology, vol. 1745, https://doi.org/10.1007/978-1-4939-7680-5_12,

plasma membrane and rapidly assemble in cell matrix adhesion sites. Focal adhesions are cornerstone structures regulating cell motility and coupling interaction of cytoskeleton with the extracellular matrix. The components of focal adhesions are diverse and include scaffolding molecules, special GTPases, and enzymes such as kinases, phosphatases, proteases, and lipases [3, 4]. Different types of focal adhesions are defined by their subcellular location, size, and composition. Commonly these structures are classified into initial adhesions (or nascent adhesions), focal complexes, focal adhesions, fibrillar adhesions, podosomes, and three-dimensional (3D) matrix adhesions [3, 5].

The number of cell-ECM adhesion sites, their size, and distribution can vary considerably from one cell to the other or even within a single cell, and their morphological diversity may be affected by multiple factors including the nature of the substratum, composition of the culture medium, incubation time after plating, and cell density. Maturation of cell-ECM adhesion structures begins with the appearance of initial focal complexes in the lamellipodia, at a distance of 1–2 μm from the leading edge, both during the spreading process and during cell migration [6, 7]. The half-life of the initial focal complex might be as short as 60 s [6, 8]. When the initial focal complex is located behind the lamellipodia, it either disappears encountering the zone of depolymerizing actin [9] or on opposite increases in size and assembles into focal adhesions. Focal adhesions are point adhesion structures of 0.5–1 μm in size that exist for several minutes and can then be disassembled [10]. When stable, focal adhesions assemble into focal contacts—membrane-associated structures of oval shape, reaching 3–10 μm in length, the lifetime of which is 10–120 min. Initial focal complexes are located in the lamellipodia zone, focal adhesions and focal contacts—at the lamellipodia-lamella border—and fibrillar adhesions predominantly are located in the central part of the cell. During the development of focal contacts in a cell migrating on the substrate, treadmilling phenomenon is observed: focal adhesions disappear at the posterior margin or in the central part of the cell, and new ones appear on the leading edge of the cell [11]. The formation, turnover, maturation, and senescence or disassembly of FAs are subject to regulation by some signaling pathways including the phosphorylation of FAK and paxillin [12]. FA growth and elongation (maturation) is a tension-sensitive process in which the molecular composition changes due to recruitment and activation of other FA proteins like vinculin, talin, and zyxin [13, 14].

The size and number of individual FA are measured using time-lapse fluorescent microscopy of cells transfected by some of the FA proteins or on the fixed specimens using antibody staining [15–17]. Due to heterodimeric nature of integrins forming a large number of complexes, it is reasonable to use more conservative proteins as markers of focal adhesions; in this case, linker proteins

would be the obvious variant [16]. However, when using antibody staining, it is important to understand the biochemical nature and functional role of these proteins in focal adhesions; reproducibility of labeling and ubiquitous expression in different cell types should also be taken into account.

In that respect, paxillin and vinculin are the best choices to trace both morphology and dynamics of different cell-ECM adhesions due to extensive studies of their structure, functions, and regulation patterns [17–20].

Paxillin is a 68-kDa focal adhesion-associated adaptor protein containing tyrosine that is phosphorylated when protein comes to the FA. The C-terminal region of paxillin targets it to focal adhesions through a direct association with the cytoplasmic tail of beta-integrin. The N-terminal region of paxillin binds to protein tyrosine kinases, such as Src and focal adhesion kinase (FAK), as well as with structural proteins, such as vinculin, and regulators of actin organization. Paxillin is tyrosine-phosphorylated by FAK and Src upon integrin engagement [20] creating binding sites for the adapter protein Crk. Thus paxillin inside FA serves as a docking site to recruit specific combinations of signaling molecules to coordinate downstream signaling pathways [21].

Vinculin is an 117-kDa protein consisting of a globular head domain and the tail region. Vinculin is recruited to the already formed nascent FA and controls its stability through direct interactions with talin and actin in the central layer of FA [22, 23]. Head domain contains binding sites for talin and α-actinin and a tyrosine phosphorylation site, whereas the tail region contains binding sites for F-actin and paxillin [22]. Vinculin is recruited to the surface layer of FA by phosphorylated paxillin where it also interacts with integrins. Upon entering into the surface layer of FA, vinculin changes its conformation and then is relocated into upper layer of FA, where it further interacts with talin by the head domain and with polymerized actin via tail domain [22–24]. When vinculin switches to open conformation, it regulates the accessibility of paxillin for the phosphorylation by focal adhesion kinase (FAK) providing a feedback in FA composition [25].

2 Dynamics and Heterogeneity of FA

Essential characteristics for evaluating heterogeneity of focal adhesions include their size, lifetime, and intensity parameters. To assess this, time-lapse microscopy with high spatial and temporal resolution is required. Despite the information concerning the molecular heterogeneity of focal adhesions and expanding list of focal adhesion compounds [26], little is known about the diversity of morphology and dynamics of focal adhesions and focal complexes within one cell.

Time-lapse microscopy shows that overall intensity of individual FA (representing the amount of a given fluorescent protein within FA) changes versus time according to a bell-shaped plot, and thus periods of FA growth, relative stability, and disassembly could be determined [27]. Based on these parameters, Spanjaar et al. [28] distinguished three different populations of paxillin FA within one cell. Our observations show that both average FA size and FA intensity increase in a long-lived population of FA. At the same time, some of the long-lived FAs have an average size, and some of the short-lived FAs are very large. This data is in agreement with the study of Hernandez-Varas et al. [29], who revealed a subpopulation of relatively stable vinculin-traced focal adhesion sites that were highly heterogeneous on their area and overall intensity values. It is noteworthy that in almost all cases datasets of FA variables demonstrate non-normal distribution [28], so range and median values better describe heterogeneity in values of FA parameters.

Since it remains unclear whether different parameters of FA, namely, size, duration of existence, and maximal intensity correlate with each other, it is worthwhile to determine them independently. To make these measurements possible, we provide a detailed protocol for visualization and quantitative analysis of FAs using paxillin and vinculin as markers of focal complexes and focal adhesions, respectively (Fig. 1). The transfected cell line of 3T3 fibroblast was taken as a model object; however, these approaches could be used

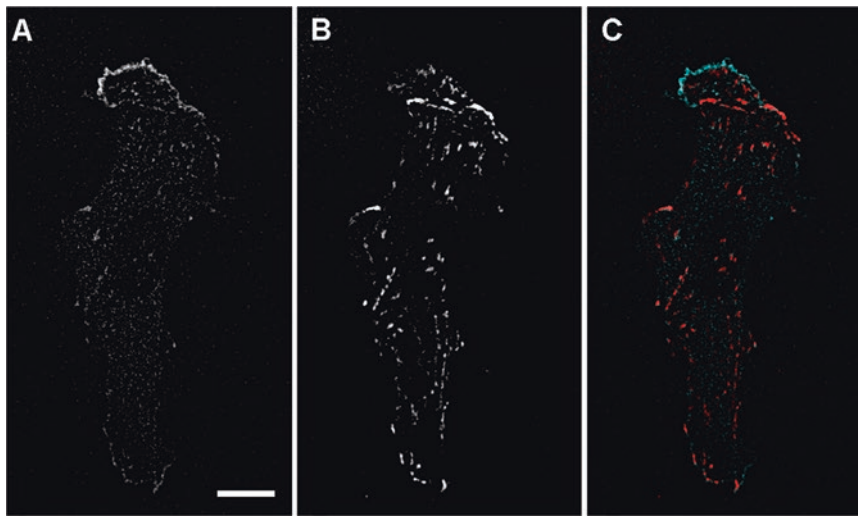

Fig. 1 Heterogeneity of focal adhesion structures in motile cell determined by double transfection. (**a**) Cell transfection with Ptag-GFP2-paxillin vector enables to visualize focal adhesions on the active edge of the cell. (**b**) Cell transfection with Ptag-RFP-vinculin vector enables to visualize mature focal adhesions both on the active edge of the cell and in the cell body. (**c**) Merged picture demonstrates heterogeneity of protein structure and dynamics of FA subpopulations within one cell with paxillin (cyan) located predominantly at the leading edge and vinculin (red) located mainly in the cell body. Scale bar 10 μm

for a variety of cultured cells. So far we provide a protocol to address the issue of heterogeneity of morphology and dynamics of FA in live and motile cells.

3 Materials

3.1 Buffers and Cell Culture Media

1. Isotonic phosphate-buffered saline PBS (sterile) contains 137 mM NaCl, 2.7 mM KCl, 4.3 mM Na_2HPO_4, 1.4 mM KH_2PO_4 (*see* **Note 1**).
2. DMEM/F12 culture media with 2 mM L-glutamine and gentamicin (*see* **Note 2**).
3. Trypsin-EDTA sterile solution (0.05% EDTA) (*see* **Note 3**).
4. Fetal calf serum (FCS): aliquot into individual 50 ml fractions to avoid contamination and keep frozen (below −20 °C).
5. CO_2-independent medium for cell imaging (*see* **Note 4**).

3.2 Cell Culture

1. 3T3 cell culture information: cells become confluent at a density of app. 40,000 cells/cm^2, and a saturation density of about 50,000 cells/cm^2 can be reached. However, in culture, cells should not be allowed to become completely confluent. Cells will double every 18 h. Culture cells in a plastic flask (they do not adhere well to certain types of glass) (*see* **Note 5**).

3.3 Transfection Reagents

1. Plasmids.
   Ptag-RFP-vinculin vector (Eurogen, Russia, cat # FP372), (500 ng/μl) (*see* **Note 6**).
   Ptag-GFP2-paxillin vector (Eurogen, Russia, cat # FP373), (500 ng/μl) (*see* **Note 7**).
2. X-tremeGENE HP DNA transfection reagent (Roche, Switzerland).

3.4 Additional Materials

1. Glass bottom Petri dishes (35 mm, MatTek Corporation, USA) (*see* **Note 8**).

3.5 Instrumentation

1. CO_2 incubator (Sanyo, Japan).
2. Laminar flow cabinet.
3. Fluorescence inverted microscope Nikon-Eclipse TI with perfect focus system equipped with mercury arc lamp, motorized stage, and temperature control system. The following filter cubes were used: FITC (excitation filter wavelength 450–490 nm, dichroic mirror wavelength 500 nm, emission filter 525/30 nm), RFP (excitation filter 530–560 nm, a dichroic mirror 570 nm, emission 585/46 nm), and DIC in the third channel. The microscope was equipped with Orca Flash 4.0

camera (Hamamatsu) and supplied with PC, equipped with MicroManager data acquisition software and ImageJ data analysis software.

4 Methods

4.1 Cell Culture

1. Culture 3T3 cells in 75 cm^2 flasks using DMEM/F12 medium supplemented with 10% fetal calf serum (FCS), glutamine, and gentamicin. Place flasks in a CO_2 incubator with 5% CO_2 at 37 °C.
2. For subculturing remove medium and rinse with Trypsin-EDTA.
3. Add 200–300 μl of trypsin-EDTA and allow flask to sit at 37 °C until cells begin to disperse (round up).
4. Add 2 ml of medium and dispense suspended cells into glass bottom Petri dishes at a density of 3×10^5 cells per plate (*see* **Note 9**).
5. Incubate overnight at 37 °C in a CO_2 incubator.

4.2 Transfection

1. Prepare the plasmid DNA solution using sterile TE (Tris/EDTA) buffer or sterile water at a concentration from 0.1 to 2.0 μg/μl.
2. Prepare the transfection mix: put 100 μl of PBS into 1.5 ml Eppendorf; add 1 μl of plasmid vector (initial concentration 0.5–0.7 mg/ml). Add transfection reagent in a volume twice to the volume of a plasmid vector (*see* **Note 10**). Incubate at room temperature for 25 min.
3. Discard cell medium (by aspiration).
4. Rinse 1× with warm 1× PBS.
5. Add 2 ml of fresh warm medium.
6. Add the transfection mix to the Petri dish.
7. Incubate overnight at 37 °C and 5% CO_2.
8. The cell can be visualized in the time interval from 24 to 72 h after transfection.

4.3 Data Acquisition

1. Warm up a microscope to 37 °C (*see* **Note 11**).
2. Place the Petri dish on the microscope stage, set up the x60 oil immersion PlanApo objective, and insert the ×1.5 intermediate lens into the lightpass.
3. Open MicroManager Software.
4. Set the appropriate channels in Preset menu (Configuration settings → Channels) (*see* **Note 12**) (Fig. 2b).

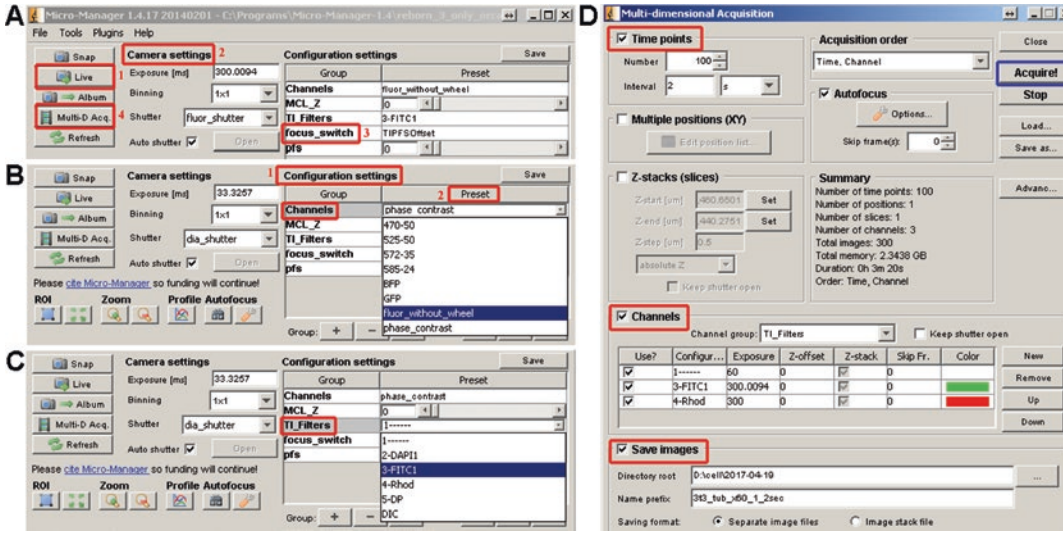

Fig. 2 Microscope configuration settings under MicroManager control. (**a**) Adjustment of camera settings. Click the "Live" button (1), and then in Camera settings menu (2), adjust the exposure, choose the shutter, switch on the PFS system (3), close "Live" menu, and open "Multi-D acquisition" menu (4). (**b**) Setting channels in configuration settings. (1) Preset menu (2). (**c**) Setting filters in configuration settings. (**d**) Defining the image acquisition parameters in Multi-D acquisition control menu

5. Set the appropriate filters in the Preset menu (Configuration settings → TI_Filters) (*see* **Note 13**) (Fig. 2c).
6. Transfer the optical path from eyepieces to the camera (R100 button on the forward microscope panel).
7. Introduce two ND filters into the optical path (optical density of filters will be equal to 4 and 8, respectively) (*see* **Note 14**).
8. Click the "Live" button, and live image of cells in a field of view will appear on the monitor (Fig. 2a).
9. Find the spreading cell with normal fibroblast morphology, visible focal contacts, and low cytoplasmic fluorescence (high signal/noise ratio).
10. Adjust the microscope focus.
11. In Camera settings menu, set the exposure (300 ms) and choose active shutter (*see* **Note 15**).
12. Set microscope focus and switch on the PFS system.
13. Close "Live" menu.
14. Open Multi-D acquisition control (Fig. 2d).
15. In Multi-D acquisition control menu, define the number of time points and the time interval between frames; set the appropriate sequence of image acquisition in the channels, and set the file to save path and click "Acquire" button (Fig. 2d). The stack of images will be recorded to the selected folder.

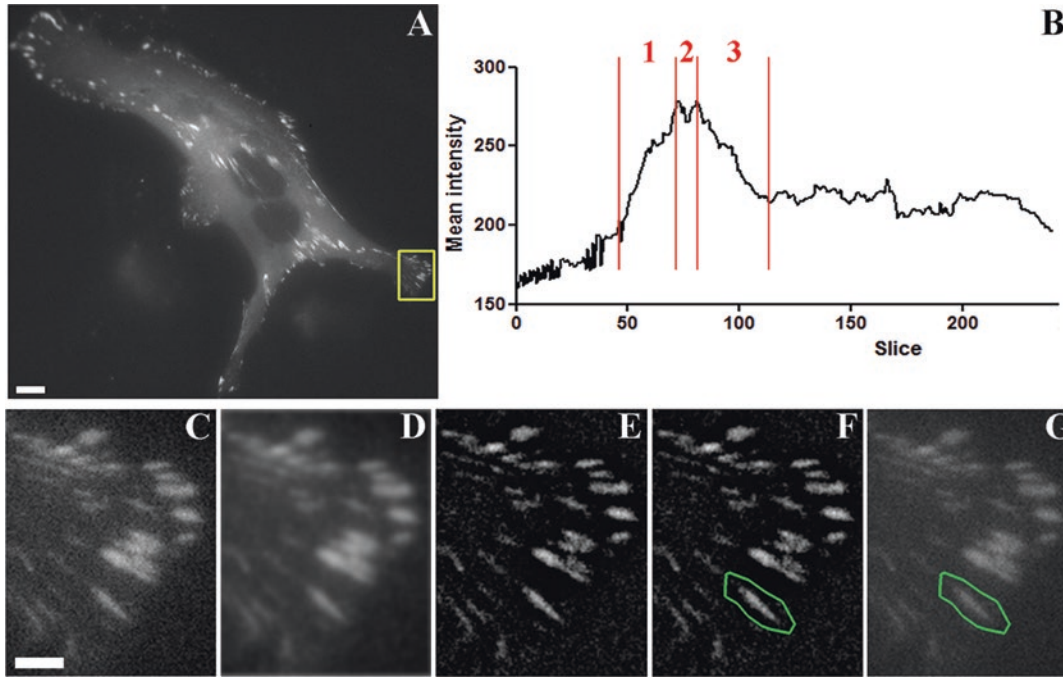

Fig. 3 Selection of the area for analysis of intensity. (**a**) Crop the area of the cell with active membrane ruffling and dynamic FA. (**b**) Graph of mean fluorescence intensity of the selected area (vinculin contact) versus lifetime (one frame was taken in 3 s), 1 assembly stage, 2 steady state, 3 disassembly. (**c**) Applying the Gaussian blur filter to the image sequence. Sigma radius is equal to 0.5. (**d**) Applying the Gaussian blur filter to the image sequence. Sigma radius is equal to 5.0. (**e**) Visualization of FA by increasing the contrast of Stack 2. (**f**) Selection of required FA area on Stack 1. (**g**) Result of restoration of selected area to Stack 1. Scale bars are 10 μm

4.4 Data Analysis

1. Open the acquired stack in ImageJ software (*see* **Note 16**), convert it to 8-bit format (Image → Type → 8-bit), and select the area in the image with dynamic FAs (*see* **Note 17**). Then highlight it with the "Rectangular" frame tool on the toolbar, then crop the movie (Image → Crop), and save it as Stack 1 (Fig. 3a).
2. Create two copies of Stack 1 by right-clicking on the movie and selecting "Duplicate"; tick the "Duplicate stack."
3. Apply Gaussian blur with sigma radius of 0.5 to the first copy of Stack 1 (Process → Filters → Gaussian Blur). Apply to the entire image sequence (Fig. 3c).
4. Apply Gaussian blur with sigma radius of 5.0 to the second copy of Stack 1 (Process → Filters → Gaussian Blur). Apply to the entire image sequence (Fig. 3d).
5. Perform subtraction (Process → Image calculator). In the "Image 1" box, select an image with a small sigma radius, select the image with a large sigma radius in the "Image 2" box, select "Subtract" in the "Operation" field, and check the boxes "Create new window" and "32-bit (float) result." Apply to the entire image sequence (Fig. 3e).

6. Save the new image stack as Stack 2.
7. Close all Stacks except for Stack 1 and Stack 2.
8. Adjust Contrast Settings on Stack 2 (Image → Adjust → Brightness/Contrast) by changing the "Minimum" and "Maximum" parameters (Fig. 3e).
9. Browse the movie, find the FA that appears and disappears during the movie, and record the frame number in which the FA appears, the number of the previous frame (will be taken as the background), and the frame number in which the contact disappears.
10. Select the required area of the focal contact using the "Polygon selections" on the toolbar, and remember this selection by pressing the "T" key; after that "ROI Manager" window will appear (Fig. 3f).
11. Copy the selected area into Stack 1 (Edit → Selection → Restore selection) (Fig. 3g).
12. Plot a graph of the selected area intensities for each frame (Image → Stacks → Plot *Z*-axis Profile) (*see* **Note 18**). In the appeared window, click "Live" and determine the frame number with maximal intensity; remember the value. Using the "List" command, get and save the received intensity values (Fig. 3b).
13. Find the plateau area on the graph and record the numbers of its first and last frame. The length of the plateau segment presents the stable stage, everything before the plateau is the assembly stage, and everything after is the disassembly stage (*see* **Note 19**).
14. On Stack 2, select the area of FA in the frame where it has just appeared, and remember this value by pressing the "T" key. Repeat for frames where the steady state begins, for the frame with maximal MFI, and for the frame where the FA disappears. Save the selection (ROI Manager → More → Save).
15. Calculate the area values (ROI Manager → Measure). Representative results are shown in Fig. 4.
16. Calculate lifetime values; subtract the last frame number from the first frame number, and multiply this value by the time interval between frames (3 s for paxillin-labeled contacts and 1 min for vinculin-labeled contacts in our case). Representative results are shown on Fig. 5a–b (*see* **Note 20**).
17. Plot a histogram of maximal mean fluorescence intensities. Representative results are shown in Fig. 5c, d.
18. Normalize the intensity using the formula:

$$I_n = I / I_b,$$

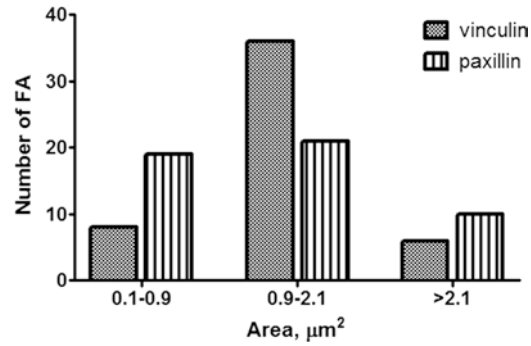

Fig. 4 Heterogeneity of FA area measured for paxillin- and vinculin-labeled contacts. FA area is the key parameter to distinguish the subpopulations of FAs. Here we demonstrate that three subpopulations of FAs can be distinguished in both vinculin- and paxillin-labeled cells, but the percentage of small FAs will be higher in paxillin-labeled cell, whereas most of vinculin-labeled FAs will be in a medium FA group. This data was collected from five EGFP-paxillin and five RFP vinculin cells

where I_n is the normalized intensity, I raw intensity, and I_b background intensity (*see* **Note 21**).

19. Calculate the integral fluorescence intensity by the formula:

$$I_I = I_{av} \times S,$$

where I_{av} is the average fluorescence intensity at a given frame and S is the area of the FA on this frame (*see* **Note 22**).

5 Notes

1. Adjust to pH = 7.3–7.5 in ddH_2O and filter sterile. Store at +4 °C up to a year.
2. Make fresh on the first day of the experiment. For 500 ml final volume, start with 450 ml of DMEM/F12 media and add 146 mg of L-glutamine, 80 mg of gentamicin, and 50 ml of heat-inactivated FCS. Let culture medium warm up in an incubator at 37 °C before use. Complete culture medium is stored at 4 °C.
3. This solution is stored frozen between −20 and −40 °C. Repeated cycles of freezing and thawing should be avoided, so aliquot stock solution into individual 5 ml fractions. Before the experiment, warm the appropriate number of aliquots in the incubator.
4. CO_2-independent medium contains a buffering system composed of mono- and di-basic sodium phosphate and β-glycerophosphate. A small amount of sodium bicarbonate

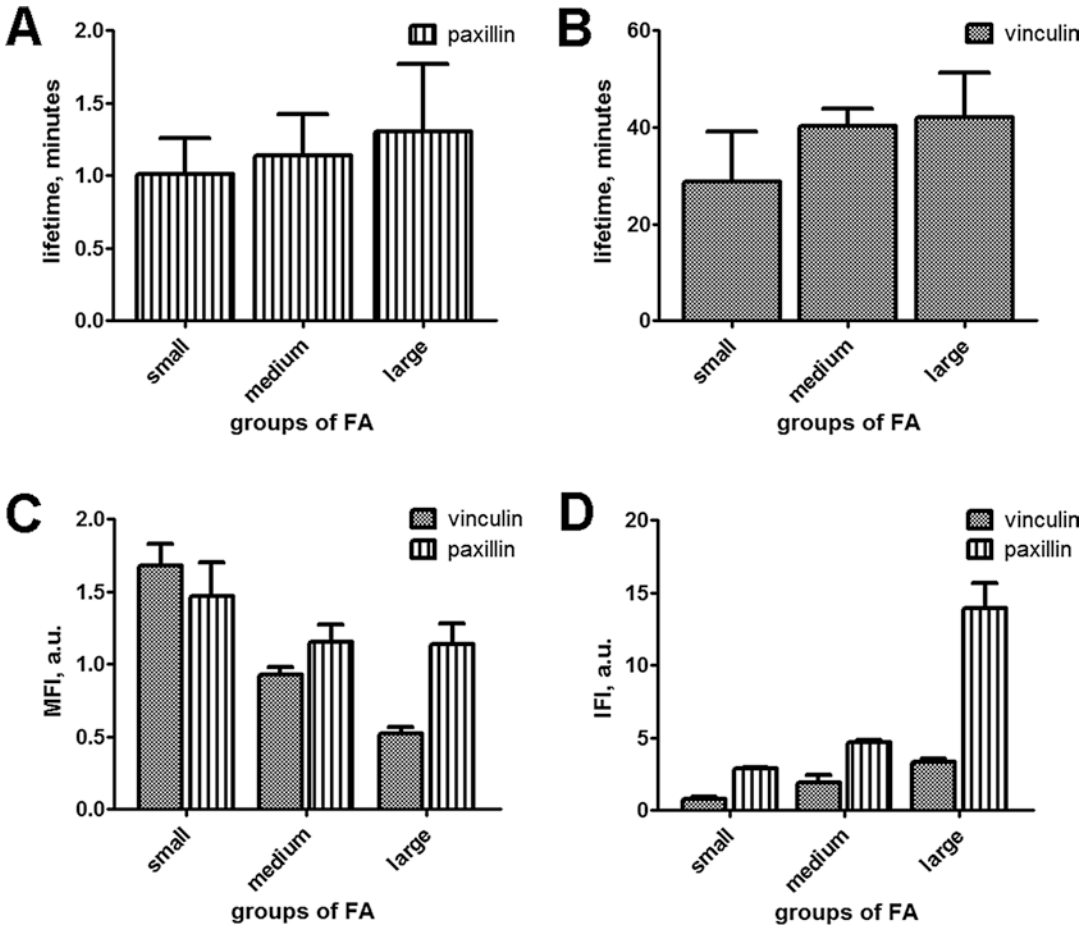

Fig. 5 Heterogeneity in different groups of FA. (**a**) The majority of paxillin-labeled adhesions have the mean lifetime between 1 and 1.5 min that corresponds to nascent adhesions, while (**b**) different groups of vinculin-labeled FAs have the mean lifetimes from 28 to 42 min that correspond to mature focal complexes. These data also demonstrate that FA lifetime does not depend on its area. (**c**) Mean fluorescent intensity corresponds to the density of a given protein; thus, small vinculin-labeled FAs are denser, than medium and large FAs, with the same trend in paxillin-labeled contacts. (**d**) Integral fluorescence intensity corresponds to the total amount of a given protein in FA; thus, protein amount in both paxillin- and vinculin-labeled FAs increases with their size. All data are presented as median ± SEM

has been included in the formulation to meet essential bicarbonate-dependent cell functions. Make fresh on the day of experiment; full media composition is the same as for DMEM/F12.

5. To preserve, freeze cells in conditioned growth medium supplemented with 5% (v/v) DMSO and store in liquid nitrogen vapor phase or at −135 °C. For the limited time, cells could be stored at −80 °C.
6. pTagRFP-vinculin is a mammalian expression vector encoding TagRFP-vinculin fusion protein. The vector can be used for

fluorescence labeling of vinculin in live cells. This vector can be transfected into 3T3 cells by X-tremeGENE HP DNA transfection reagent (Sigma-Aldrich) or any common transfection method. DH5alpha strain was chosen for propagation of plasmid in *E. coli*. The vector is resistant to kanamycin (50 μg/ml).

7. pTagGFP2-paxillin is a mammalian expression vector encoding GFP2-paxillin fusion protein. The vector can be used for fluorescence labeling of paxillin in live cells. Chicken paxillin is fused to the GFP2 N-terminus. This vector can be transfected into 3T3 cells by X-tremeGENE HP DNA transfection reagent (Sigma-Aldrich) or any common transfection method. DH5alpha strain was chosen for propagation of plasmid in *E. coli*. The vector is resistant to kanamycin (50 μg/ml).
8. 3T3 cells are shown to be low adhesive to certain types of glass, but the chosen Petri dishes have the appropriate glass thickness (#1.5 or 170 μm) and good adhesive properties that allows the use of oil immersion ×60 objective.
9. For transfection of 3T3 fibroblasts, we used cells that reached about 70% confluency, as few cells in culture without cell-cell contacts are poorly transducable, and high cell density results in contact inhibition and entrance to G0 phase when cells avoid the uptake of nucleic acids.
10. A ratio of 2:1 of a microliter of X-tremeGENE HP DNA transfection reagent is optimal for 3T3 fibroblasts, as for other cell types. However, for non-adherent cells, we prefer to take 1:1 (v/w) ratio.
11. Warming up the microscope takes not less than 45–60 min; otherwise the residual drift because of the non-uniform temperature of different parts of the microscope might impede time-lapse recording.
12. In this case, "fluor without wheel" channel was chosen to open light path from the mercury arc.
13. In this case, FITC filter set for visualization of paxillin and rhodamine filter set for visualization of vinculin were chosen.
14. This will decrease the degree of photo damage through live imaging.
15. This exposure value is adjusted by the set of neutral filters (ND4 and ND8) that allows to retain high signal/noise ratio and minimize photo damage.
16. If you have captured the image sequence, then open menu File → Import → Image sequence (open as a virtual stack); if the captured file is already a single TIFF file, then proceed to File → Import → TIFF Virtual Stack.
17. Most of paxillin-labeled FAs are visualized within 5 μm from the cell edge (Fig. 6a), whereas vinculin-labeled mature focal adhesions can be found also in the body of the cell (Fig. 6b).

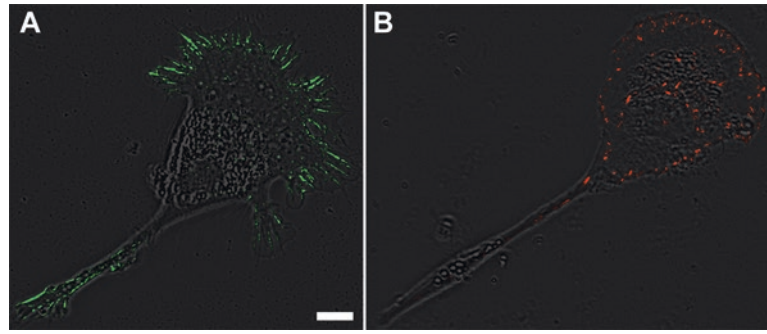

Fig. 6 (**a**) Most of paxillin-labeled FAs are located near the cell edge. (**b**) Vinculin-labeled contacts are visualized in the cell body. Scale bars 10 μm

18. "Plot *Z*-axis profile plug-in" is intended to calculate mean fluorescence intensity of a given area on the whole image stack.
19. Sometimes when calculating MFI for paxillin FA, the steady state of the contact cannot be determined (thus, the FA assembles and immediately begins to disassemble); if so, just record the maximal intensity value.
20. Since most of the dataset do not pass D'Agostino-Pearson omnibus normality test, we recommend describing the parameter values using median ± SEM.
21. Background intensity is the value of MFI for the selected area on N-1 frame (the frame before the FA appears).
22. Specific fluorescence intensity corresponds to the density of FA, e.g., to the distribution of a given protein in FA.

References

1. Rooney C, White G, Nazgiewicz A, Woodcock SA, Anderson KI, Ballestrem C, Malliri A (2010) The Rac activator STEF (Tiam2) regulates cell migration by microtubule-mediated focal adhesion disassembly. EMBO Rep 11(4):292–298
2. Maziveyi M, Alahari SK (2017) Cell matrix adhesions in cancer: the proteins that form the glue. Oncotarget. 10.18632/oncotarget.17265
3. Geiger B, Bershadsky A, Pankov R, Yamada KM (2001) Transmembrane crosstalk between the extracellular matrix–cytoskeleton crosstalk. Nat Rev Mol Cell Biol 2(11):793–805
4. Wehrle-Haller B, Imhof B (2002) The inner lives of focal adhesions. Trends Cell Biol 12(8): 382–389
5. Larsen M, Artym VV, Green JA, Yamada KM (2006) The matrix reorganized: extracellular matrix remodeling and integrin signaling. Curr Opin Cell Biol 18:463–471
6. Alexandrova AY, Arnold K, Schaub S, Vasiliev JM, Meister JJ, Bershadsky AD, Verkhovsky AB (2008) Comparative dynamics of retrograde actin flow and focal adhesions: formation of nascent adhesions triggers transition from fast to slow flow. PLoS One 3(9):e3234
7. Nayal A, Webb DJ, Brown CM, Schaefer EM, Vicente-Manzanares M, Horwitz AR (2006) Paxillin phosphorylation at Ser273 localizes a GIT1-PIX-PAK complex and regulates adhesion and protrusion dynamics. J Cell Biol 173(4):587–589
8. Choi CK, Margraves CH, English AE, Kihm KD (2008) Multicontrast microscopy technique to dynamically fingerprint live-cell focal contacts during exposure and replacement of a cytotoxic medium. J Biomed Optics 13(5): 054069
9. Mekhdjian AH, Kai F, Rubashkin MG, Prahl LS, Przybyla LM, McGregor AL, Bell ES,

Barnes JM, DuFort CC, Ou G et al (2017) Integrin-mediated traction force enhances paxillin molecular associations and adhesion dynamics that increase the invasiveness of tumor cells into a three-dimensional extracellular matrix. Mol Biol Cell 28:1467–1488

10. Beningo KA, Dembo M, Kaverina I, Small JV, Wang YL (2001) Nascent focal adhesions are responsible for the generation of strong propulsive forces in migrating fibroblasts. J Cell Biol 153(4):881–888
11. Vicente-Manzanares M, Horwitz AR (2011) Adhesion dynamics at a glance. J Cell Sci 124(Pt 23):3923–3927
12. Webb DJ, Donais K, Whitmore LA, Thomas SM, Turner CE, Parsons JT, Horwitz AF (2004) FAK-Src signalling through paxillin, ERK and MLCK regulates adhesion disassembly. Nat Cell Biol 6(2):154–161
13. Ballestrem C, Erez N, Kirchner J, Kam Z, Bershadsky A, Geiger B (2006) Molecular mapping of tyrosine-phosphorylated proteins in focal adhesions using fluorescence resonance energy transfer. J Cell Sci 119(Pt 5):866–875
14. Zaidel-Bar R, Cohen M, Addadi L, Geiger B (2004) Hierarchical assembly of cell-matrix adhesion complexes. Biochem Soc Trans 32(Pt3):416–420
15. Omachi T, Ichikawa T, Kimura Y, Ueda K, Kioka N (2017) Vinculin association with actin cytoskeleton is necessary for stiffness-dependent regulation of vinculin behavior. PLoS One 12(4):e0175324
16. Owen GR, Meredith DO, Gwynn I, Richards RG (2005) Focal adhesion quantification – a new assay of material biocompatibility? Rev Eur Cell Mater 9:85–96
17. YL H, Lu S, Szeto KW, Sun J, Wang Y, Lasheras JC, Chien S (2014) FAK and paxillin dynamics at focal adhesions in the protrusions of migrating cells. Sci Rep 4:6024
18. Carisey A, Ballestrem C (2011) Vinculin, an adapter protein in control of cell adhesion signaling. Eur J Cell Biol 90(2-3):157–163
19. Nagasato AI, Yamashita H, Matsuo M, Ueda K, Kioka N (2017) The distribution of vinculin to lipid rafts plays an important role in sensing stiffness of extracellular matrix. Biosci Biotechnol Biochem 81(6):1136–1147
20. Lopez-Colome AM, Lee-Rivera I, Benavides-Hidalgo R, Lopez E (2017) Paxillin: a crossroad in pathological cell migration. J Hematol Oncol 10(1):50
21. Schaller MD (2001) Paxillin: a focal adhesion-associated adaptor protein. Oncogene 20(44): 6459–6472
22. Humphries JD, Wang P, Streuli C, Geiger B, Humphries MJ, Ballestrem C (2007) Vinculin controls focal adhesion formation by direct interactions with talin and actin. J Cell Biol 179(5):1043–1057
23. Dumbauld DW, Shin H, Gallant ND, Michael KE, Radhakrishna H, Garcia AJ (2010) Contractility modulates cell adhesion strengthening through focal adhesion kinase and assembly of vinculin-containing focal adhesions. J Cell Physiol 223(3):746–756
24. Giannone G (2015) Super-resolution links vinculin localization to function in focal adhesions. Nat Cell Biol 17:845–847. https://doi.org/10.1038/ncb3196
25. Subauste MC, Pertz O, Adamson ED, Turner CE, Junger S, Hahn KM (2004) Vinculin modulation of paxillin-FAK interactions regulates ERK to control survival and motility. J Cell Biol 165(3):371–381
26. Zamir E, Geiger B (2001) Molecular complexity and dynamics of cell-matrix adhesions. J Sci 114(Pt 20):3583–3590
27. Berginski ME, Vitriol EA, Hahn KM, Gomez SM (2011) High-resolution quantification of focal adhesion spatiotemporal dynamics in living cells. PLoS One 6(7):e22025
28. Spanjaard E, Smal I, Angelopoulos N, Verlaan I, Matov A, Meijering E, Wessels L, Bos H, de Rooij J (2015) Quantitative imaging of focal adhesion dynamics and their regulation by HGF and Rap1 signaling. Exp Cell Res 330(2): 382–397
29. Hernandez-Varas P, Berge U, Lock JG, Stromblad S (2015) A plastic relationship between vinculin-mediated tension and adhesion complex area defines adhesion size and lifetime. Nat Commun 6:7524

Chapter 13

Laser Tweezers Raman Microspectroscopy of Single Cells and Biological Particles

Maria Navas-Moreno and James W. Chan

Abstract

Laser tweezers Raman spectroscopy (LTRS) is a variation of micro-Raman spectroscopy that is used to analyze single cells and biological particles suspended in an aqueous environment. The Raman spectrum of the cell/particle reflects its intrinsic biochemical composition and molecular structures. The technique utilizes a laser trap generated by a tightly focused Gaussian laser beam to physically manipulate individual cells and immobilize them in the laser focal volume. The same laser that is used for optical trapping also simultaneously excites Raman signals from the trapped cell, which are detected using a spectrometer and a confocal detection setup. LTRS offers unique capabilities not commonly found in other optical cytometry methods, such as label-free chemical analysis, multi-parametric chemical detection with a single excitation laser, and a non-photobleaching signal that can be used to quantitate and monitor dynamic chemical changes. This chapter provides guidelines on the design of a single beam LTRS microscope and methods for building and aligning the system. Operating procedures for trapping particles and acquiring spectra and a summary of data analysis techniques are provided.

Key words Raman scattering, Optical tweezers, Laser trapping, Single cells, Vibrational spectroscopy, Laser, Cytometry

1 Introduction

Biological research has, for the longest time, been performed on groups of cells under the assumption that all cells in a population are identical. It is now recognized that individual cells can behave very differently. As such, the importance of obtaining quantitative measurements of single cells rather than bulk-averaged data cannot be overstated. Critical information on the behavior of a small number of specific cells can be hidden in a bulk measurement. Bulk measurements that yield parameters averaged over a large population can also provide misleading information about a biological process, while single cell measurements can yield more accurate information about the heterogeneity in a system. The growing need to transition from population-based experimental methods to

Natasha S. Barteneva and Ivan A. Vorobjev (eds.), *Cellular Heterogeneity: Methods and Protocols*, Methods in Molecular Biology, vol. 1745, https://doi.org/10.1007/978-1-4939-7680-5_13,

single cell methods motivates the development of new cytometry methods. New methods are needed that can measure the biochemistry of cells in their natural state and monitor their dynamics and response to environmental perturbations.

Optical methods are very attractive for single cell analysis because they enable biochemical analysis of living specimens in a minimally invasive and nondestructive manner. Many cytometric methods rely on exogenous fluorescent labels to obtain biochemical information of a cell. There are, however, several drawbacks and limitations with using exogenous labels. They can be cytotoxic to the cell, which can alter the cellular chemistry and affect cell function. Photobleaching of the fluorescence signal is another issue that makes it challenging to perform prolonged studies on the same cell. The procedure of labeling cells is time-consuming, which can lead to long clinical turnaround times or affect time-sensitive samples. Moreover, the multiple steps involved in the labeling process can result in the loss of valuable cells from the sample. Labeled cells can also be unsuitable for clinical use. Cells that are genetically modified to express fluorescent reporters may be useful for research purposes, but these cells are not applicable for human transplantation due to clinical safety concerns because of the use of lentiviral transduction. Similar concerns preclude using cells labeled with fluorescent molecules conjugated to animal-derived antibodies. Regulatory agencies have highlighted the necessity of obtaining xeno-free cells for therapeutic use, since exposure of human cells to the products of animal origin may increase the risk of nonhuman pathogen transmission (e.g., viruses, prions), making them unsuitable as clinical-grade cells for research and human clinical trials. Label-free cytometry, in which optical signals reflecting the intrinsic biochemical properties of a cell are directly obtained without the addition of exogenous probes, is very attractive because of its potential to address many of medical issues.

A wide range of optical techniques is available for label-free interrogation of intrinsic molecular species in a cell. Harmonic generation [1, 2], autofluorescence [3], fluorescence lifetime [4], and Raman scattering are a few examples of label-free modalities that have been explored for single cell analysis. In particular, Raman spectroscopy [5] has, over the past decade, emerged as a promising single cell analytical technique. Based on the inelastic scattering of photons by molecular bonds, Raman spectroscopy has the unique capability of direct detection of molecules inside cells without the use of exogenous labels (Fig. 1). In Raman scattering, incident photons from a light source scatter inelastically off of molecules in the sample, gaining or losing amounts of energy equivalent to those of the vibrational levels of the molecules. Note that because Raman scattering is a nonresonant process (i.e., the green arrow in Fig. 1b describes a transition to a virtual state), any excitation wavelength can, in principle, be used to generate the

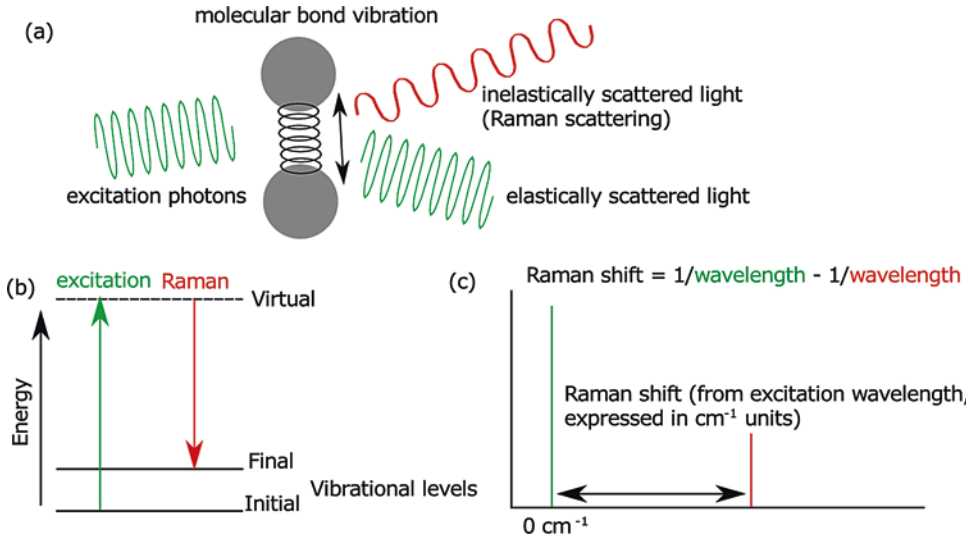

Fig. 1 (**a**) Illustration of the Raman scattering process. Excitation photons interacting with molecular bonds are mainly elastically scattered resulting in no change in the wavelength of the scattered light. A small fraction of photons is inelastically scattered, which results in Raman scattered light whose wavelength is red-shifted. (**b**) Energy diagram showing the Stokes-shifted Raman transition from an initial to a final vibrational level. The shift in wavelength of the excitation and Raman scattered photon corresponds to the specific vibrational energy of the molecular bond. (**c**) The signal is presented in a Raman spectrum as a shift (in wavenumber units/cm) from the excitation wavelength, as shown in the equation

Raman spectrum. However, factors such as the Raman efficiency and the generation of undesired fluorescent background, which are wavelength dependent, need to be considered. These issues are discussed later in the chapter. Because different bonds have unique characteristic vibrational frequencies (or energies), the inelastically scattered photons generated from the interaction between the incident light and the bonds will have different frequencies. Detection of all scattered photons yields a Raman spectrum with Raman peak shifts (in wavenumber units, *see* Fig. 1c) corresponding to the different molecular bond vibrations in the biological particle (Fig. 2). As such, a Raman spectrum serves as a highly multiplexed and detailed chemical fingerprint of the endogenous biomolecules in a cell (i.e., lipids, cholesterol, protein, DNA, RNA). Raman spectroscopy can also be used to detect and measure exogenous chemicals (e.g., anticancer drugs, antibiotics) introduced into the cell. Raman spectroscopy is a quantitative technique because peak intensities are linearly proportional to molecular concentration. Furthermore, because the signals do not photobleach, Raman spectroscopy can be used to make quantitative measurements of dynamic chemical changes in a cell over time. Existing cytometry instruments and methods do not commonly offer the ability to probe cells intracellularly without the need for external reporters, nor are they capable of real-time,

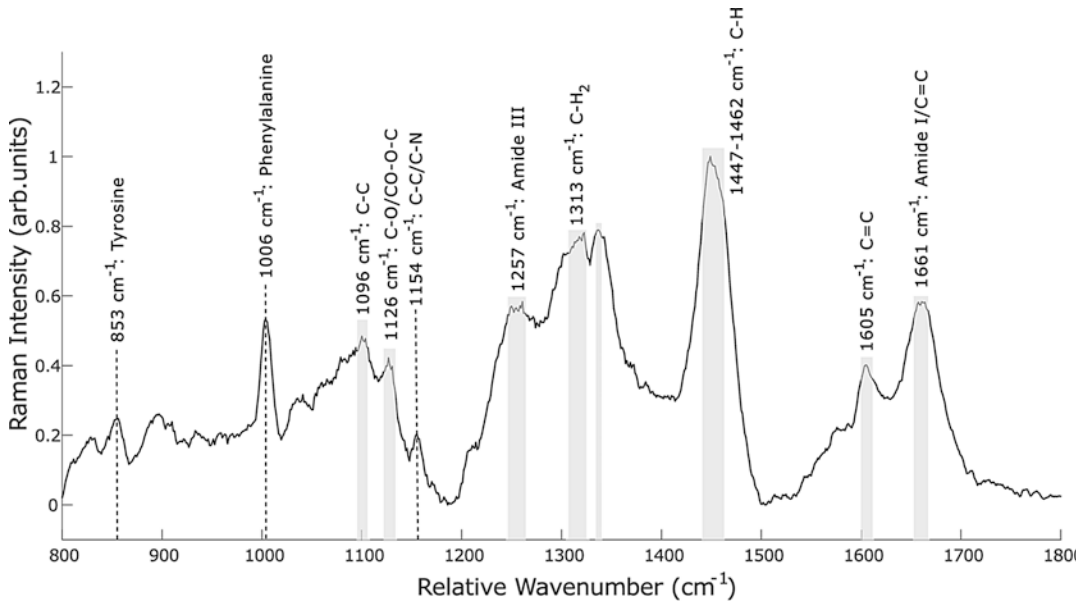

Fig. 2 An example of Raman spectrum of a biological sample. Average of ten laser-trapped baker yeast (*S. cerevisiae*) cells (smoothed and background corrected). Relevant Raman bands are labeled

quantitative measurements on single cells. Direct intracellular chemical detection and real-time, quantitative measurements of the biochemistry in single cells are unique capabilities not easily found in existing cytometry instruments and methods. These capabilities can potentially enable new discoveries in biology and improve the detection and diagnosis of disease in clinical applications.

Raman microscopes consist of several main components: a laser excitation source, a microscope with various objectives, a scanning stage for sample positioning, a pinhole aperture for confocal detection, and a spectrometer and charge-coupled device (CCD) camera for acquiring the spectra. With commercial confocal Raman microscopes, the sample often needs to be immobilized onto a substrate. The focused laser beam can be used to probe a specific region of the sample (i.e., point sampling) with diffraction-limited spatial resolution or to acquire a full Raman chemical image. The latter is accomplished by scanning the sample relative to the laser focus such that a full spectrum is collected at every *x*–*y* coordinate in the sample to obtain spatial information. This is commonly referred to as hyperspectral Raman imaging. Images can be reconstructed of the different chemical species, with image contrast being based on the intensities of the different Raman vibration peaks. Although these instruments can analyze a broad range of materials, the analysis of small particles, such as single cells and biological particles (e.g., cellular vesicles), is challenging. Issues such as ensuring optimal overlap of the laser

focus with the small cell/particle to maximize the signal-to-noise ratio (SNR) of the spectra, avoiding background noise and signals from the substrate that interferes with the Raman signal of the cell, and finding suitable methods to prepare the sample onto the substrate that minimize sample perturbation and damage are often encountered.

Laser tweezers Raman spectroscopy (LTRS) was developed over 15 years ago. The unique capabilities offered by this technique enabled Raman spectroscopy to be more readily applicable to single cell and microparticle analysis. LTRS combines optical trapping with micro-Raman spectroscopy to facilitate the analysis of individual small cells (e.g., bacteria) in suspension and improves the signal-to-noise ratio of the acquired Raman spectra, allowing for shorter spectral acquisition times. Laser trapping is the key technology that allows Raman spectroscopy to be performed on suspension cells and particles floating in an aqueous solution without needing to immobilize them to a substrate. In its simplest configuration, LTRS uses a single tightly focused laser beam that optically traps and immobilizes an individual cell floating in solution within the laser focus (Fig. 3a). A tight laser waist, achieved by using a high numerical water- or oil-immersion objective, generates a very strong electric field gradient that exerts small forces on dielectric particles. Dielectric particles are therefore attracted to the center of the beam near the focus, where the equilibrium in the

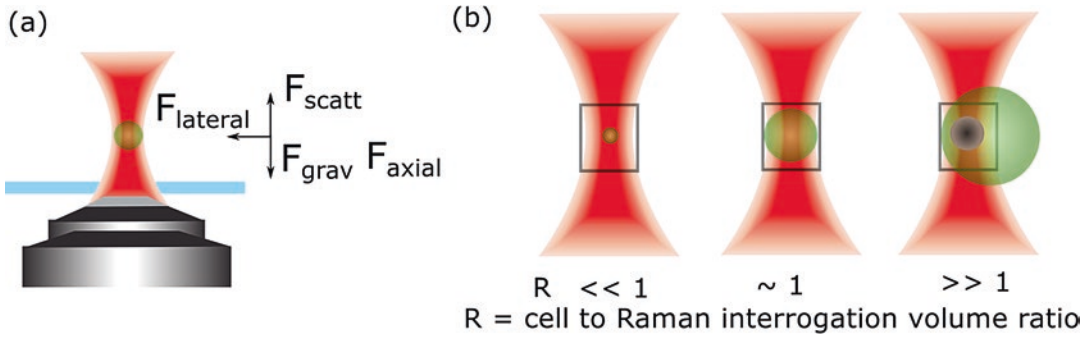

Fig. 3 (**a**) Laser tweezers use a tightly focused laser beam to optically manipulate small particles. The strong electric field gradient at the laser beam focus results in the generation of small lateral, scattering, and axial forces ($F_{lateral}$, F_{scatt}, F_{axial}, see arrows) that, when applied to dielectric particles, results in the particle being attracted to the laser focus, which is the region of strongest electric field. (**b**) When performing LTRS on single cells (or biological particles), it is important to consider the effect of the cell size/volume on the spectra that is acquired. For a particle much smaller than the Raman interrogation focal volume (denoted by the rectangle) ($R \ll 1$), the acquired spectrum reflects the chemical composition of the entire particle. However, multiple particles may become trapped in the focal volume, resulting in a spectrum that represents a particle cluster. For $R \sim 1$, a single cell occupies most of the focal volume, and the acquired spectrum represents the chemistry of the entire cell. For $R \gg 1$, only a fraction of the cell is trapped. Therefore, the spectrum represents only that specific region of the cell that is trapped (e.g., an organelle or subcellular particle, represented by the dark circle in the picture) and NOT of the entire cell

lateral and axial forces is achieved. The same laser that is used for trapping is also used to simultaneously excite Raman signals from the trapped particle. The signal collection is performed in the epi-direction, i.e., microscope objective is used for both delivering light to the particle and collecting the scattered Raman signal. This signal is then delivered through a confocal aperture to a spectrometer/detector, as in a conventional Raman microscope. Another advantage of the laser trapping feature is that the cell can be positioned far enough from any surfaces to minimize that material's high autofluorescence and/or Raman background signals that would interfere with the Raman signals of the trapped cell.

Other variations of the LTRS technique have been developed over the past several years. Still based on the fundamental concept of combining an optical trap with confocal Raman detection, these techniques integrate more sophisticated designs and methods for offering additional, unique capabilities to improve system performance. For example, multifocal LTRS systems [6, 7] have been developed that split a laser beam into several beams to generate multiple foci that trap and spectrally analyze many cells simultaneously, which increases the analytical throughput. Other systems add optical modalities such as differential interference contrast (DIC) [8] or fluorescence [9] to provide additional information. Multi-beam systems that use one laser (at one wavelength) to optically trap the cell and a second laser (at a second wavelength) to perform the Raman interrogation have been demonstrated [10]. Such a system can use a low-power and far-infrared wavelength laser for trapping to minimize any potential photodamage and a higher-powered, visible wavelength laser as a Raman excitation source to generate a strong Raman spectra. Detailed discussions of these variations are beyond the scope of this chapter, but references are provided for readers interested in learning about them.

Numerous studies have shown that LTRS can trap and analyze many different cell types and different-sized particles for many biological and biomedical applications. This section is not intended to be a comprehensive review of these studies; rather, it serves to briefly highlight several applications to give a sense of the broad utility of this method by which a variety of particles can be analyzed (Fig. 3b). Because LTRS requires a tightly focused laser beam to generate intensity gradients strong enough to trap and manipulate the particle, the laser focal volume from which Raman signals can be generated is roughly 1 μm^3. Therefore, small particles with a similar volume (i.e., a cell to focal volume ratio $R \sim 1$) are ideal for the LTRS technique because they can be most easily trapped and the acquired Raman spectrum reflects the overall biochemical composition of the entire particle. Bacteria are the example of an ideal biological particle for LTRS analysis. Bacterial spores are a structure produced by bacteria to survive harsh environmental conditions. Chan et al. [11] demonstrated that individual spores

in suspension could be analyzed by LTRS. The Raman spectrum was comprised of Raman bands primarily associated with calcium dipicolinic acid (CaDPA), a chemical compound found in the spore core that protects and stabilizes DNA, at 324, 1017, 1395, and 1572 cm^{-1}. Using this unique chemical fingerprint, spores were identified and discriminated from other non-biological microparticles in a label-free, reagentless manner. LTRS has also been used to study the dynamics of spore germination [12]. By following the evolution of the Raman peak intensities of CaDPA, the release of CaDPA as the spore germinates into a bacteria cell can be monitored. Quantitative parameters such as the lag time (time from nutrient exposure and initiation of release) and release time (time for the complete release) of CaDPA can be determined from these time plots. Additional studies [13, 14] have then analyzed changes in the germination times as spores are subjected to different environmental perturbations (i.e. chemicals, temperature). LTRS has been used to analyze other types of bacteria, such as *E. coli* [15, 16]. The responses of bacteria to different concentrations of antibiotic drugs were monitored by recording time-dependent changes in the intensities of protein- and DNA-associated Raman peaks. Biological particles smaller than bacteria can also be stably trapped and analyzed with LTRS. For example, triglyceride-rich lipoprotein (TGRL) particles, submicron lipid particles responsible for transporting hydrophobic lipid molecules in the bloodstream and implicated in the onset of atherosclerotic cardiovascular disease, have been analyzed by LTRS. The Raman spectra of these particles reveal detailed information about the composition of fatty acids, proteins, lipids, and structural rearrangements of lipids [17]. In particular, the breakdown of triacylglycerols and the formation of a highly ordered core of free saturated fatty acids were reflected in the Raman spectra of pre- and postprandial particles isolated from human subjects. Another example of LTRS analysis of submicron particles is a more recent work [18] devoted to the analysis of exosomes, extracellular vesicles secreted from cells that have drawn considerable interest recently because they carry chemical information and markers that can be used for disease detection and diagnosis. LTRS was used to study the chemical composition of exosomes from eight cell lines [18]. Cell-type-averaged Raman spectra results made it possible to reveal variations in total exosomal protein, lipid, genetic, and cytosolic content. Spectral differences between different cell lines were due to cholesterol content, surface protein, and phospholipids. Exosomes derived from cancerous and noncancerous cell lines were discriminated based on their relative expression of cholesterols and phospholipids. Note that a challenge with analyzing particles much smaller than the Raman interrogation volume ($R \ll 1$) is the risk of trapping multiple particles simultaneously in the focal volume. Therefore, the acquired spectra represent chemical information averaged over

many particles. To avoid such a situation, appropriate dilution of the solution is needed to ensure that only a single particle is in the trap during the time it takes to acquire the spectra.

Suspension cells larger than the focal volume can also be trapped and analyzed with LTRS. There is an upper limit to this cell size, however, since it becomes increasingly more difficult to trap and manipulate larger objects. Anecdotal evidence suggests that cells as large as ~8–10 μm in diameter can be analyzed with LTRS. However, it should be noted that the small focal volume can only interrogate a fraction of the cell volume (i.e., $R \gg 1$). Consequently, the Raman spectrum that is acquired only reflects the chemical composition in that particular region of the cell and cannot be considered an accurate representation of the entire cell's biochemistry. A study by Fore et al. [19] showed that when trapping mononuclear cells such as monocytes, LTRS acquires Raman spectra primarily from the nucleus, since it is the nuclear region that is optically trapped. Examples of applications using LTRS for single cell analysis include cancer detection [20] and analysis of red blood cell oxygenation and mechanics [21].

This chapter focuses on the single beam LTRS microscope, the most common optical trapping Raman system that is used for analyzing single cells and biological particles. This section provides information on the design, layout, and components of a system for readers who are interested in building their own LTRS microscope. Methods for setting up and aligning the system are provided. This chapter also provides detailed operating procedures for a user to trap and acquire spectra and methods to process, analyze, and interpret the spectral data.

2 Materials

2.1 Instrument Description

A conventional LTRS system consists of several key components:

1. *Microscope base*. Although not essential, a good microscope base, commonly inverted, provides a robust scaffold for the other components while providing basic features like focusing and imaging. An ideal microscope base will have at least one extra available light path, which will be used to add the LTRS capability (*see* **Note 1**). If a microscope base is not available, an equivalent apparatus can be constructed from optomechanical and motion control components for stable mounting of microscope objectives and optical elements.
2. *Excitation source*. The observed width of a Raman band is a function of the natural linewidth of the vibrational level probed and the linewidth of the excitation source. Thus, a monochromatic laser with a narrow linewidth is commonly used. To select the optimal wavelength, there are few factors that need

to be considered. The intensity of the Raman bands is proportional to λ^{-4}, where λ is the excitation wavelength. Because of this property, shorter wavelengths (e.g., green) are preferred, but with such wavelengths, excitation of autofluorescent signals from the sample may become an important issue, and it could overwhelm the much weaker Raman signal. In such cases, near-infrared (NIR) wavelengths are used to avoid a high fluorescent background. Photodamage and the resonant Raman effect are additional factors to consider when selecting the wavelength. Photodamage in biological samples is due to heating and photochemical reactions (e.g., photooxidation, photo-fragmentation, etc.) that follow the absorption of laser light by water and other molecules in the sample. A NIR laser will minimize photodamage, although laser power and time of exposure also play an important role and should be carefully considered and tested. Finally, when the excitation wavelength lies in the absorption spectrum of a molecule, a phenomenon called resonant Raman scattering (RRS) can be observed which results in very strong Raman peaks. For more information on RRS, refer to [22]. Typically, a single laser is used for trapping and probing Raman spectra, although trapping and probing with two different sources [10] or trapping using two counter-propagating beams can be advantageous in order to avoid photodamage under other circumstances [23]. Additionally, it is highly desirable to have a laser source that is frequency stable. Raman band positions are relative to the excitation source. Thus, having a laser source which does not have a stable wavelength will deteriorate the precision of the Raman band position.

3. *High numerical aperture (NA) lens*, typically a water- or oil-immersion microscope objective with NA > 1.2, is needed to tightly focus the laser beam to achieve forces for optical trapping and to excite and collect the Raman scattered light.
4. *Filters* are needed (1) to block any unwanted wavelengths coming from the excitation source (i.e., a laser cleanup filter) and (2) to separate the Raman spectrum from the excitation wavelength, commonly achieved using one or a combination of dichroic mirror, and long-pass or notch filter.
5. *Confocality element*, such as a pinhole or an optical fiber, is used in confocal LTRS systems to minimize the background due to fluorescence or light scattered outside the focal plane.
6. *Dispersive device*, such as a spectrometer or a monochromator, to disperse the Raman scattered light and thus observe the individual spectral features. The main element of a spectrometer or a monochromator is the grating, an element with an engineered periodic pattern that diffracts and splits the light

into the different wavelengths. The selection of gratings depends on the desired spectral resolution (i.e., how well adjacent Raman bands are resolved), the spectral range that needs to be covered, and the excitation wavelength.

7. *Detector*, such as a charge-coupled device (CCD), an electron-multiplying CCD (EMCCD), a photomultiplier tube (PMT), or an avalanche photodiode (APD), to transduce the light into an electric signal. There are three main factors to consider when selecting the right detector: speed, efficiency, and noise. They are all interconnected, but speed narrows down to how fast a spectrum can be measured and recorded, efficiency to how many photons are turned into electrons in the detector (i.e., quantum efficiency), and noise to how much background signals does the detector add to the spectrum due to multiple sources (i.e., thermal, shot, and readout noise).

   The protocol described in this chapter for setting up an LTRS system uses a CCD camera. CCD cameras are more commonly used than PMTs or APDs because they can capture the full spectrum at once, which is more convenient than measuring the light intensity at each wavelength, although PMTs and APDs do offer advantages in the case of very fast or very dim applications. For more information on PMTs and APDs, and their use, refer to [24].

   Since Raman scattering is an inherently weak phenomenon, minimizing the noise added during detection and readout is very important. In CCDs, thermal noise or dark current is significantly reduced by lowering the temperature of the detector, usually done by thermo-electrical or liquid nitrogen cooling. Shot noise or random noise can be minimized by collecting more photons, in other words, by increasing the exposure time or the laser power. Finally, readout noise combines many sources of noise. It is a characteristic of the CCD provided by the manufacturer, used to quantify the noise that is added to the measurement during the reading of the detector and the digitization of the data. Readout noise is a function of the readout rate, so the faster the signal is read out from the CCD, the higher the noise contribution. Additionally, depending on the excitation wavelength, the proper CCD needs to be selected for its quantum efficiency is often optimized for either ultraviolet/visible or NIR ranges. Last but not least, etaloning, an optical phenomenon that occurs with CCD cameras especially when working in the NIR, must be considered when selecting the CCD camera. To avoid etaloning, a front-illuminated or a deep-depletion back-illuminated camera, and a CCD chip (i.e., the active region of the CCD camera) with the appropriate antireflective coating and thicker (~40–50 μm) than that of a UV/VIS optimized camera (usually around ~10–20 μm), should be used.

EMCCDs are newer types of detectors that allow faster readout rates with signal-to-noise ratios (SNR) comparable to that of a CCD under conditions in which the exposure time can be very short. Hence, these detectors are particularly useful when dealing with very strong Raman scatterers. If long exposure times are required, such as in the case of weak Raman scatterers or samples with low concentrations, EMCCDs must be carefully evaluated as they could result in a lower SNR.

8. *Brightfield imaging*. Second port for white light/brightfield imaging to view the laser focus position and the trapped cells.
9. *Computer/workstation* to record and analyze the spectra.

2.2 Equipment and Materials (See Note 2)

2.2.1 Major Equipment

1. Vibration isolating optical table or breadboard.
2. Inverted microscope base; transmitted white light source and condenser.
3. Power meter.
4. Color CCD camera for brightfield imaging.
5. Microscope objective—Olympus UPLSAPO 60× 1.2NA water immersion or similar (*see* **Note 3**).
6. 785 nm laser—CrystaLaser (power = 120 mW, beam diameter ($1/e^2$) = 1.2 mm) or similar.
7. Laser mount (*see* **Note 4**).
8. Spectrometer with adjustable manual slit entrance and at least one grating (600 grooves/mm grating recommended)—Princeton Instruments.
   (a) Slit cover plate with 4–40 threaded holes compatible with 30 mm cage systems (*see* **Note 5**)—Princeton Instruments (pinhole configuration).
   (b) Fiber coupler with X–Y micrometer control—Princeton Instruments (optical fiber configuration).
9. Deep-depletion back-illuminated CCD camera with appropriate flange to mount onto the spectrometer—Princeton Instruments PIXIS 100.

2.2.2 Optics

1. Neutral density filters (*see* **Note 6**).
2. Laser cleanup filter—Semrock 785 nm MaxLine Filter.
3. Dichroic mirror—Semrock 785 nm RazorEdge Dichroic Beamsplitter.
4. Long-pass filter—Semrock 785 nm RazorEdge Long-Pass Edge Filter.
5. Hot mirror.
6. 20 μm pinhole.

7. Achromatic doublet IR-coated lenses $f1 = 300$ mm, $f2 = 30$ mm (*see* **Note 7**).
8. Four IR-coated mirrors.
9. One-hundred micron pinhole (pinhole configuration).
10. Achromatic doublet IR-coated lenses $f3 = 45$ mm, $f4 = 100$ mm, $f5 = 60$ mm (pinhole configuration).
11. Optical fiber (50 μm core, 0.22NA; optical fiber configuration).
12. Achromatic doublet IR-coated lens $f6 = 40$ mm (optical fiber configuration).

2.2.3 Optomechanical Components

1. Appropriate empty filter cube.
2. Assortment of posts and post holders.
3. Two lens mounts.
4. Four kinematic mirror mounts.
5. XY translation mount.
6. Translation stage (optional).

2.2.4 Pinhole Configuration

1. Two additional lens mounts.
2. Additional translation stage (optional).
3. Thirty millimeter cage plate.
4. XY translating lens mount for cage system.
5. Two rods 6 in. long with 4–40 internal threading.

2.2.5 Optical Fiber Configuration

1. One additional lens mount.
2. Two FC/PC fiber adapter plates.
3. Additional translation stage.

2.2.6 Alignment Tools

1. Silver mirror.
2. Infrared sensor card.
3. Fluorescing alignment disc.
4. Two long lens tubes.
5. RMS to SM1 thread adapter.
6. SM1 to RMS thread adapter.
7. Two iris diaphragms.
8. Alignment target for cage system.
9. IR viewer.
10. Small fiber-coupled laser.
11. Piece of polystyrene, for example, a plastic petri dish or cuvette, or a piece of silicon wafer.
12. 1 μm polystyrene beads.

2.2.7 Sample Preparation

1. Uncoated #1 coverslip bottom petri dishes.
2. Stainless steel cell chamber for glass or quartz coverslips.
3. 25 mm (1 in.) diameter round quartz #1 coverslips.

3 Methods

3.1 Construction and Alignment of the LTRS Microscope

In this section protocols for the construction, alignment, and spectral calibration of the LTRS system are described. Figure 4 shows the schematics of the excitation light path and the detection light path. The detection light path can be constructed using a pinhole or an optical fiber to achieve confocality, and procedures for using both are described. Which option to choose depends on space availability and signal levels. Using an optical fiber may result in a more compact system, and in some cases, the system is easier to set up since some spectrometers may be difficult to align in free space (i.e., using a pinhole). On the other hand, using a pinhole results in a more efficient system, meaning there is less photon loss from the sample to the detector because the loss associated with optical fibers can be avoided.

3.1.1 Setup of the Excitation Light Path

WARNING: Laser exposure of the skin or the eyes may result in injury. Please wear appropriate goggles and exercise safety measures to prevent harming yourself or others.

1. Fix the microscope base (*see* **Note 8**) to the optical table or breadboard. Position the microscope, so there is enough space in the back and around it for the laser, optics, and spectrometer (*see* **Note 9**).
2. Follow microscope manufacturer instructions to mount bright-field light source and condenser.
3. Add one drop of water on top of the objective, and place the 20 μm pinhole mounted on a glass slide (*see* **Note 10**) in the sample holder of the microscope. Using transmitted light, find its image on the eyepiece, focus, and center it. The image of the pinhole will help position the mirrors behind the microscope.
4. Set the dichroic mirror in the empty filter cube, set the filter cube in the filter turret, and turn the turret so the dichroic mirror is in place and the image from the pinhole exits through the rear port.
5. With the mirror holder not tilted (*see* **Note 11**), place the first IR-coated mirror (M1) right behind the microscope with the pinhole light centered on it and reflecting the light at approximately 45° (Fig. 4). Secure the holder onto the table or breadboard.

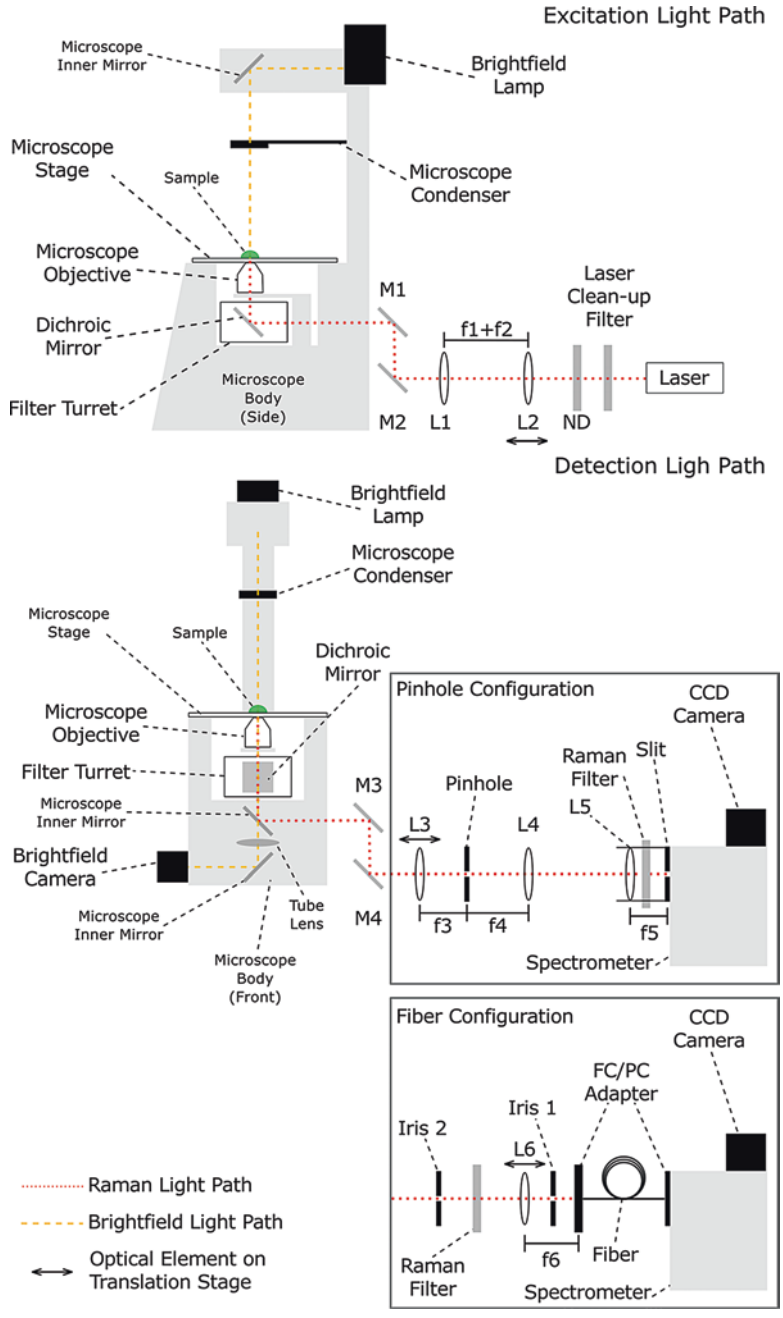

Fig. 4 A detailed schematic of excitation and detection light paths of an LTRS system. Both pinhole and optical fiber-based detection light paths are shown

6. Place the second IR-coated mirror (M2, holder not tilted) with the pinhole light centered on it and reflecting the light at approximately 45° (*see* **Note 12**). The purpose of the two mirrors set in a periscope configuration is to add the capability to

steer the laser beam so it can be set centered and straight through the objective.

7. Place the achromatic doublet lens (*see* **Note 13**) L1 (f = 300 mm) with the pinhole light centered and traveling perpendicular to the lens, right after the second mirror M2 (*see* **Note 14**).
8. (Optional) Place the translation stage so it travels parallel to the light and that the center of the motion range is approximately $f1 + f2$ apart from the first lens L1.
9. Place lens (*see* **Note 14**) L2 (f = 30 mm) approximately $f1 + f2$ apart from the first lens and positioned so that the pinhole light is centered and traveling perpendicular to it (*see* **Note 15**).

NOTE: At this point, all of the optics have been placed at their coarse position and angle. The following steps describe placement of the laser and performing fine adjustments. Please wear appropriate goggles and exercise safety measures to prevent harm to yourself and others.

10. With the laser off, place it so that the laser beam will travel (a) parallel to the table/breadboard, (b) at the same height as the rest of the optics, and (c) perpendicular to the lenses L1 and L2. Leave enough room in between the laser and L2 to place the laser cleanup filter and the neutral density (ND) wheel. If space is a concern, more mirrors like the ones set in **steps 5** and **6** can be used.
11. Place the laser cleanup filter in front of the laser. Make sure the laser will travel in the direction indicated by the arrow on the rim of the filter.
12. Set up the filter wheel in front of the cleanup filter so that the beam will be perpendicular to and centered on the ND filter.
13. Set up a sensor card in front of the ND filter (*see* **Note 16**). Turn on the laser and verify that the beam is centered on the filter. Do not remove the card in front of the ND filter, yet.
14. Set up the power meter behind the ND filter so that it also is centered on the beam path. Set up the ND filter with an optical density (OD) that will result in a few milliwatts laser power (*see* **Note 17**).
15. Block the laser beam and remove the power meter.
16. Set a card in front of L2. Unblock the laser and verify that (a) the beam is traveling parallel to the table by checking the height at different positions along the beam path and (b) the beam hits L2 at the center. To check if the beam is centered, set the second card behind L2, and move the first one close enough to the lens so you can see whether the beam is roughly centered. If (a) and (b) are achieved, set the second card in

front of L1, remove the card in front of L2, and make the necessary fine adjustments with the lens mount so that the lens is well centered with the laser. If the beam doesn't fulfill (a) and/or (b), adjust the laser mount until it does.

17. Make sure the beam is centered on L1. Follow the same procedure as for L2 (**step 16**), but this time set one card in front of mirror M2 and the other one in front of L1.
18. IMPORTANT STEP. Collimate the laser beam by moving L2 using the translation stage. Collimation is achieved when the laser spot diameter is the same at various points along the beam path (*see* **Note 18**). If the beam diverges (i.e., becomes larger) after L1, it means the lenses are too far apart. On the other hand if there is an observable focal point after L1, the lenses are too close to each other. Another way to check for collimation is using a shearing interferometer.
19. Put a card in front of M1. Make sure the beam is centered on M2, and it is incident at approximately 45°. Adjust the mirror if necessary.
20. Put a card right at the rear port of the microscope to block the beam from going inside. Make sure the beam is centered on M1, and it is incident at approximately 45°. Adjust the mirror if necessary.

    CAUTION: At this point, the beam is going to be reflected UPWARD by the dichroic mirror inside the microscope. Do not use the eyepiece with the laser on and take necessary precautions.

21. Using a card, make sure the beam is going inside the microscope roughly center through the rear port. If it is too far off, mirrors M1 and M2 need to be coarsely moved, so the beam is centered at the three points: M1, M2, and the rear port. During this step, avoid changing the tilt of the mirror holder.
22. Block the beam and replace the microscope objective with the IR alignment disc.
23. Unblock the beam and locate the beam's position on the IR disc. Using M1 center the beam on the disc. At this point, the beam is entering the back aperture or pupil of the objective through the center, but it may very likely be tilted.
24. Block the beam and replace the IR alignment disc with the lens tubes using the thread adapter. Place the IR disc at the top of the lens tubes, using the second thread adapter. Check the beam position on the disc.
25. IMPORTANT STEP. It is now necessary to make sure that the beam is centered at both the top and bottom positions of the lens tube. The slightest tilt in the beam will severely affect

the ability of the focused beam to trap a particle. To straighten the beam, change the tilt of M1 and M2, and repeat **steps 22–24** until the beam is centered at both locations.

26. Install the small CCD camera on the left side port of the microscope for brightfield imaging.
27. Place a piece of polystyrene on the microscope stage, and focus on its surface using the brightfield camera. The laser spot should be visible, and as the objective is moved slightly in and out of focus, the spot size should become smaller and larger but should not move from its central position. If it does, this means the laser is not going straight up through the objective. Repeat **step 25** until the laser spot doesn't move on the image (*see* **Note 19**).

NOTE: At this point the excitation light path is complete. The next step is to align the detection light path. Confocality can be achieved using either a pinhole or an optical fiber coupled to the spectrometer. Both are described below.

3.1.2 Setup of Detection Light Path Using a Pinhole

1. Place and secure the spectrometer (*see* **Note 20**). Mount the entrance slit and the cover plate.
2. Use a silver mirror as a sample and focus on it. Set the pull knobs on the microscope base in the correct positions to make sure the reflected light exits through the right-side port. It might be necessary to increase the laser power so the light can be observed with the IR sensor card.
3. Mount the 100 μm pinhole on the XY translation mount, and place it perpendicular and roughly centered with the reflected light path, leaving enough space to place L3 (and the optional translation stage) before; and L4 after. Using the sensor card, make sure some light goes through the pinhole.
4. Place the translation stage so it travels parallel to the light and that the center of the motion range is approximately $f3 = 45$ mm behind the pinhole (optional).
5. Set L3 ($f = 45$ mm) (*see* **Note 14**) in front of the pinhole (i.e., the focal length) apart, making sure it is centered and perpendicular to the light path. It is very likely that after placing L3 no light will go through the pinhole. The exact position from the pinhole and the centering of L3 need to be finely adjusted until light is observed with the sensor card on the other side of the pinhole (*see* **Note 21**).
6. Set the power meter sensor in the back of the pinhole, and maximize the power going through by finely adjusting L3 in all three directions (*see* **Note 22**).
7. Place lens L4 ($f = 100$ mm) (*see* **Note 14**) approximately $f3 + f4 = 145$ mm apart from L3, and position it so that the

light is centered and traveling perpendicular to it (*see* **Note 23**). Adjust the position of L4 until collimation is achieved (*see* **step 18** in section 3.1.1).

8. Cover the entrance to the spectrometer to prevent laser light from going in.
9. Screw in the 6-in.-long rods to the plate that covers the slit of the spectrometer.
10. Set mirrors M3 and M4 in a similar way as in **steps 5** and **6** in section 3.1.1) to direct the light toward the entrance of the spectrometer.
11. Using the alignment target for cage system on the 6-in. rods and mirrors M3 and M4, make sure that the beam is going straight and centered through the entrance slit of the spectrometer. If the light is too dim, it may be necessary to use an IR viewer in combination with the sensor card (*see* **Note 24**).
12. Using the cage plate, set the long-pass filter in front of the spectrometer as close to the slit as possible. Make sure the filter is in the right direction so the laser light will travel in the direction indicated by the arrow on the rim of the filter.
13. Mount L5 (f = 60 mm) (*see* **Note 14**) on the cage system lens holder, and make note of the direction that the light travels. Set the lens holder on the rods, placing the lens in the appropriate direction and approximately 60 mm from the slit (*see* **Note 25**). Center the lens using the adjustment knobs on the holder so that the spot position on the long-pass filter is the same as without the lens.
14. Start the CCD and spectrometer controlling software. Set the CCD camera temperature to −80 °C, and if available, select the desired grating and center wavelength.
15. Lower the laser power to a few milliwatts, and completely open the spectrometer entrance slit. Using the CCD/spectrometer software, center the grating at 785 nm (*see* **Note 26**), and start a short integration time acquisition (e.g., a few milliseconds) binning vertically the entire CCD chip. At this point, it is only necessary to check that laser light is going into the spectrometer, which can be done by acquiring spectra (*see* **Note 27**) blocking and unblocking the light path in front of the spectrometer. A remarkable difference should be observed between the two spectra.
16. Set a thick piece of polystyrene in the sample holder, instead of the silver mirror, and use the image on the brightfield camera to find the focus.
17. Acquire a spectrum using an integration time of a few milliseconds to a few seconds, until the polystyrene Raman spectrum (Fig. 5) is observed. If no spectrum is observed, adjust mirrors M3 and M4 until the spectrum is observed.

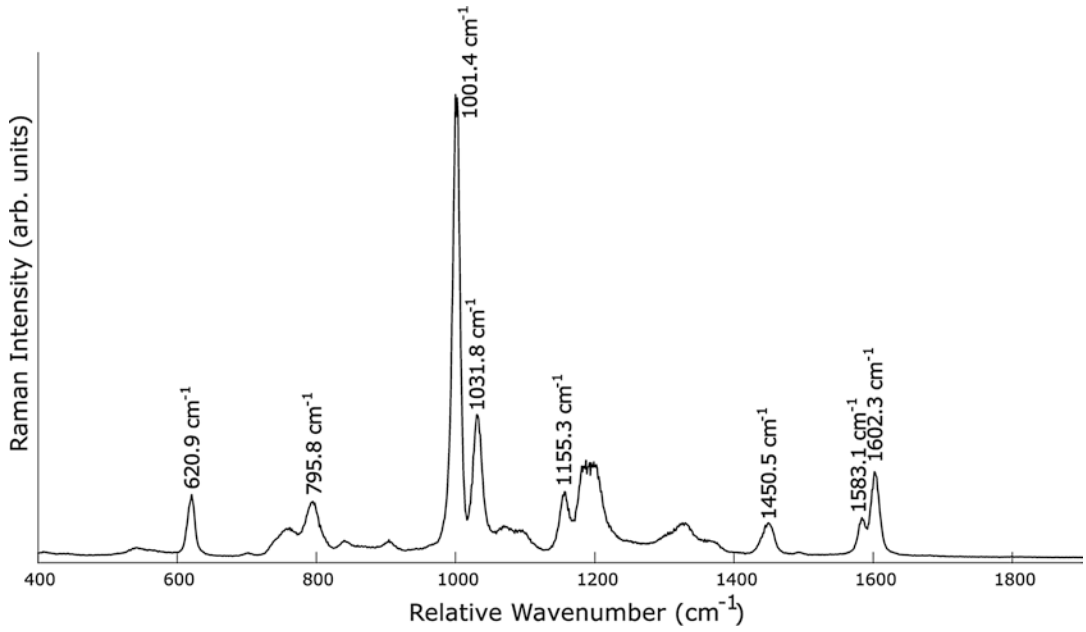

Fig. 5 Reference polystyrene Raman spectrum shown with main Raman band positions labeled [41]

18. Close the slit 5 μm and make sure the light still goes through. If it doesn't, steer mirror M4 sideways until the spectrum is observable again.
19. Open the slit until it is about 15 um wide. The scattered light is now centered horizontally on the spectrometer.
20. Set the software, so the image of the entire CCD is acquired, as opposed to binning and obtaining a single spectrum. Acquire an image. It might be necessary to play around with the integration time until you get a good image. The image acquired should consist of a row of points that correspond to the Raman bands of polystyrene. It is very likely that the points are not straight on a horizontal line and are not as tight as they should be. Hence, the CCD camera needs to be focused and rotated to fix these issues that will result in wider spectral features.
21. Set the laser power to 50 mW.
22. Drop 20 μL of a 1:1 mix of the 1 μm polystyrene beads and water on a glass coverslip. Place the coverslip on the microscope stage, and focus on it. Trap one of the beads by a laser beam (*see* Subheading 3.2.2, optical trapping protocol for more details). The polystyrene Raman spectrum should be observed just as before; the advantage of using a bead is that it is easier to have the brightfield image focus and the scattered light detection light path focus coincide since the trapped bead will position itself at the laser beam focus.

23. Setting the shortest integration time that will allow observation of the dots, and adjusting the contrast of the image, so it is easier to see, start the camera on live mode (i.e., a mode that gets images continuously). Loosen the CCD camera just enough to rotate it. Very gently rotate the camera until all the dots are in a straight line.
24. Using the focusing dial on the spectrometer, focus the CCD. The optimal position is where the spots are the tightest along the vertical axis (*see* **Note 28**).
25. The small CCD camera used for brightfield imaging can easily be damaged if routinely exposed to the laser light. To avoid that, set the hot mirror in front of the camera to block the laser.
26. It is optional but highly recommended to enclose the excitation and detection light paths outside of the microscope and the microscope itself. The purpose is twofold: (a) to protect users from accidental laser exposure and (b) to minimize background due to other sources of light like room lights and computer monitors. Design the encasing such that access to critical components is easy, such as the mirrors M1–M4, the pinhole, and of course, the microscope stage, and focusing and adjusting knobs.

3.1.3 Setup of Detection Light Path Using an Optical Fiber

1. Set the silver mirror as a sample and focus on it. Set the pull knobs on the microscope base in the correct positions to make the reflected light exit through the right-side port. It might be necessary to increase the laser power so the light can be observed with the IR sensor card.
2. Set mirrors M3 and M4 in a periscope configuration, like in **steps 5–6** in subheading 3.1.1. These two mirrors will be used to steer the light, so it couples correctly with the fiber.
3. Mount the FC/PC fiber adapter plate on an XY translation mount and top of a translation stage. Screw in the fiber onto the FC/PC adapter. Make sure the light is centered and travels perpendicular to the plate (*see* **Note 29**). Leave enough space in between M4 and the fiber adapter to set two irises 10 cm apart.
4. Screw in the fiber onto the FC/PC adapter.
5. Connect the free end of the fiber to the alignment laser. The light from this laser, traveling toward the microscope, will be used to aid the coupling of the signal (traveling away from the microscope) to the fiber.
6. Set and fix the two irises, the first one ~20 mm from the FC/PC adapter and the second one at least 10 cm apart, centered on the light from coming out of the fiber. Close the iris a little but still letting pass some of the light.

7. Set lens L6 (f = 40 mm) (*see* **Note 14**) in between the irises, roughly 40 mm apart from the fiber. Center the lens, so the light still goes through both irises.
8. Unscrew the fiber from the alignment laser, and using a second FC/PC adapter, screw together with the power sensor.
9. Using mirrors M3 and M4, make the light coming from the microscope go centered through both irises.
10. Using the knobs on the XY mount and the translation station on which the fiber is fixed, maximize the power measured. It might take some time to get an initial reading, but once found, turn one knob at time, and rotate through the three knobs until the signal is maximized.
11. Set the long-pass filter on a mount and fixed in between M4 and L6, making sure the light is perpendicularly incident.
12. Place and secure the spectrometer (*see* **Note 30**). Mount on the spectrometer, the entrance slit, and fiber coupler with X–Y micrometer control fitted with the FC/PC adapter.
13. Set a thick piece of polystyrene in the sample holder, instead of the silver mirror, and using the image on the brightfield camera, find the focus.
14. Start the CCD and spectrometer controlling software. Set the CCD camera temperature to −80 °C, and if available, select the desired grating and center wavelength.
15. Acquire a spectrum using an integration time of a few milliseconds to a few seconds, until the polystyrene Raman spectrum (Fig. 5) is observed.
16. Close the slit 5 μm and make sure the light still goes through. If it doesn't, adjust the X micrometer control of the fiber adapter on the spectrometer until it does.
17. Open the slit until it is about 15 um wide. The scattered light is now centered horizontally on the spectrometer.
18. Set the software, so the image of the entire CCD is acquired, as opposed to binning and obtaining a single spectrum. Acquire an image. It might be necessary to play around with the integration time until you get a good image. The image acquired should consist of a row of points that correspond to the Raman bands of polystyrene. It is very likely the points are not straight on a horizontal line and are not as tight as they should be. Hence, the CCD camera needs to be focused and rotated to fix these issues that will result in wider spectral features.
19. Set the laser power to 50 mW.
20. On a glass coverslip, drop 20 μL of a 1:1 mix of the 1 μm polystyrene beads and water. Set the coverslip on the microscope and focus on it. Trap one of the beads (*see* Subheading 3.2.2,

optical trapping protocol for more details). The polystyrene Raman spectrum should be observed just as before. The advantage of using a bead is that it is easier to have the brightfield image and the scattered light detection path foci coincide since the trapped bead will position itself at the laser focus.

21. Setting the shortest integration time that will allow observation of the dots, and adjusting the contrast of the image so it is easier to see, start the camera on focus mode (i.e., a mode that gets images continuously). Loosen the CCD camera just enough to rotate it. Very gently rotate the camera until all the dots are on a straight line.
22. Using the focusing dial on the spectrometer, focus the CCD. The optimal position is where the spots are the tightest along the vertical axis (*see* **Note 31**).
23. The small CCD camera used for brightfield imaging can easily get damaged if routinely exposed to the laser light. To avoid that, set the hot mirror in front of the camera to block the laser.
24. It is optional, but highly recommended, to enclose excitation and detection light paths outside of the microscope and the microscope itself. The purpose is twofold: (1) to protect users from accidental laser exposure and (2) to minimize background due to other sources of light like room lights and computer monitors. Design the encasing such that access is easy to key components, such as the mirrors M1–M4, the fiber ends, and of course, the microscope stage, focusing and adjusting knobs.

3.1.4 System Calibration

The purpose of the calibration procedure is to find the relationship between the wavelength (or wavenumber) of the dispersed light entering the spectrometer and the pixels on the CCD. This calibration can be performed in wavelength units (i.e., nm) using a reference light source (e.g., a neon lamp) or in relative wavenumber units (i.e., cm^{-1}) using a sample with well-known Raman peaks (e.g., polystyrene).

1. Set the reference light source or polystyrene sample on the microscope. Acquire a spectrum with a good SNR.
2. Find the pixel position of each of the most prominent spectral peaks.
3. Create a table with the peak pixel positions and the corresponding known wavelength or wavenumber value for each peak in the spectrum. *See* Fig. 5 for the example with polystyrene. For a reference light source, refer to the manual or the National Institute of Standards and Technology (NIST) atomic spectra database [25].
4. Fit the data to a second-order polynomial, which will be used to determine the spectral value for all pixel positions.

5. Check that the fit is accurate for those pixel positions with known spectral values. Calculated values should not differ more than a few hundredths of a nanometer (*see* **Note 32**). If the difference is significant, review the values. When using a low grooves/mm grating, hence a longer wavenumber range, it is possible that the fit works well only for some region on the CCD. In that case, try a higher-order polynomial fit, and make sure to have a reference sample that exhibits spectral features covering the entire spectral range. In this case, reference light sources can be more useful since Raman spectra of common reference samples (e.g., polystyrene and organic solvents) tend to have regions without any spectral features.

3.2 Collecting LTRS Raman Data

3.2.1 Sample Preparation

Sample preparation protocols for LTRS measurements are similar to those used for flow cytometry, except there is no need for external labels. In this section, information to consider when preparing samples and trapping cells/particles for LTRS measurements is provided. Measurements can be done on live or fixed cells, whether mammalian [26], yeast [27], or bacteria [15].

1. *Samples need to be in a solution* that is not fluorescent and doesn't have strong Raman signals. For example, phenol red, a chemical commonly used as a proxy for pH in cell culture, is highly fluorescent, and thus it should be avoided. Also, organic solvents commonly used for cell fixation, like methanol, have a very strong Raman signature and should also be avoided. On the other hand, water, phosphate buffers, and cell culture media (without phenol red) are weak Raman scatterers and are the media of choice. In general, routine cell handling and preparation procedures can be used prior to LTRS measurements, but an extra wash step should be taken to suspend the samples in the proper medium.
2. *Sample concentration* is an important consideration for optical trapping. A sample too dilute will result in long times searching for cells/particles that will make the LTRS measurements long and laborious. Too concentrated a sample will result in particles kicking out a trapped particle during the Raman spectral analysis as well as possible particle aggregation.
3. Choose the *right coverslip*. Coverslips are made from different material: plastic, glass, and quartz. Plastic coverslips should be avoided as plastics are very strong Raman scatterers and will result in a strong background. On the other hand, glass and quartz are both weak Raman scatterers, but selecting one or the other depends on the sample and the excitation wavelength used. It all comes down to selecting the material that will provide the weakest background with respect to the sample's Raman features. If dealing with a sample that is a strong Raman scatterer, there might not be a difference between selecting quartz or glass slides (besides price). In case the sample is a

weak Raman scatterer, selection of the coverslip will depend on the excitation wavelength that is used, as glass fluoresces when excited with near-IR light. So, if using a visible laser as the excitation source, glass is a good inexpensive choice. If using a near-IR excitation source, quartz is the best option.

4. *Evaporation of the solution* can be a potential concern. Take necessary measures, so the sample will not dry out during the LTRS measurements. Some suggestions are (a) don't use a coverslip alone; instead use a glass bottom petri dish or a quartz coverslip set in a stainless steel cell chamber covered with a lid. (b) If a small volume is being used, place a dampened lint-free tissue inside the petri dish/chamber. If (b) it does not work, glass or quartz capillaries may be employed.

3.2.2 Optical Trapping

1. Set the sample on a glass bottom petri dish or a cell chamber with a quartz coverslip.
2. Add a drop of the right immersion medium (e.g., water, oil) to the objective, and place the dish on the microscope stage.
3. Focus on the sample using the brightfield channel camera.
4. If the position of the laser spot on the brightfield field of view is not known, remove the filter in front of the brightfield camera to view the laser spot. Note the laser position and put back the filter.
5. Identify a target cell/particle to trap, and very gently move the microscope stage to bring the particle close to the laser spot. As the particle approaches the laser spot, one of two things can happen:
   (a) The particle is trapped, which can be checked by gently moving the microscope stage and verifying that the other particles move, except for the trapped one, which remains in place where the laser spot is.
   (b) The particle is kicked out by the laser. This is unavoidable from time to time, but if it happens consistently, there are a few things to check. If the sample is too concentrated, diluting it might help. If this does not help, try approaching a particle that is slightly above of the focus and/or increasing the laser power to 30–50 mW. Higher powers can be used, but consider photodamage of the sample. If all of the above fails, check that a high NA (>1) objective is being used and that the laser is not tilted on the axis of the objective, which will result in an unstable trap (**steps 22–25** of protocol in Subheading 3.1.1).
6. In some cases, for example, when dealing with weak Raman scatterers or when using glass coverslips, it might be convenient to move the particle away from the coverslip using the

force of the trap. Trap the particle and gently move the focus upward. Take into account that the particle cannot be taken out of the working distance of the objective, which is very short for high NA objectives.

7. Darken the room. Since Raman scattering is such a weak phenomenon, it is necessary to turn off the room lights and in some cases even computer monitors. Encasing the microscope helps reduce the interference from unwanted light sources.
8. Using the deep-depletion CCD/spectrometer software, set the integration time that is needed to get a spectrum with a good SNR. Depending on your sample, it can be in the order of seconds to a few minutes. Additionally, as part of the spectroscopy software, there are other parameters that can be set such as averaging or number of frames. Averaging is used to improved SNR by collecting multiple, consecutive spectra of the same sample and averaging them. Multiple frames can be used to acquire a time sequence if the sample's behavior over time is of interest. More details about the camera and spectrometer settings are provided below.
9. It is optional, but highly recommended, to acquire a spectrum of the surrounding medium without anything trapped at the same focal distance from the coverslip. This spectrum can later be used to do a background subtraction. More information regarding background subtraction is provided in Subheading 3.3.1.

3.2.3 Spectrometer and Camera Settings

As part of any software specialized for the acquisition of spectra, various parameters of the camera/detector and spectrometer can be adjusted to optimize the acquired spectrum. In this section, we discuss the parameters that can be set in a system with a CCD camera.

Grating. Many spectrometers come with more than one grating. The gratings are usually blazed for a particular wavelength. The number of grooves per millimeter of the grating will determine the spectral resolution of the system. The higher the number of grooves per millimeter, the higher the spectral resolution but the shorter the spectral range is. Choose the grating that provides the desired spectral resolution and spectral range for the experiment.

Center wavelength is the value at which the grating will be centered, and it can be set to any value starting at zero to the spectrometer/grating limit. When set at zero, dispersion won't be detected. Instead, the CCD camera will capture a picture of the sample just as a camera mounted on the microscope would. The grating will behave more efficiently regarding reflectance, the closer the center wavelength is to the blaze wavelength of the grating.

Camera temperature. Most CCD cameras can be cooled thermoelectrically or by using liquid nitrogen. The purpose of cooling the camera is to reduce the dark current or thermal noise. Thermoelectrically cooled cameras usually reach and are stabilized at temperatures close to −80 °C.

Camera gain. It is a value provided by the manufacturer that characterizes the number of electrons collected by the CCD and values generated after digitization, sometimes known as CCD counts. When multiple values are available, the optimal value is determined by the strength of the signal measured. Use low gain values for high-intensity signals (i.e., strong Raman scatterers) and vice versa.

Camera readout rate. Readout rate is the inverse of the time it takes to digitize the signal and correlates with the level of noise added to the data by the detector and the electronics. CCD cameras that have been optimized for spectroscopic applications allow the user to set the readout rate to a few preset values. It is recommended to use the slowest readout rate, which would result in less noise, unless there are reasons to increase the frame rate (i.e., reduce the total time it takes the system to digitize the data) such as when studying the dynamics of a fast process.

3.3 Pre-processing of Raman Spectra

Inevitably, the collected Raman spectra will still contain unwanted signal contributions such as from background fluorescence and noise. It is therefore very important not only to know how to avoid such contributions during the experimental acquisition but also how to overcome them when they cannot be avoided. In this section, we discuss the most popular methods used to remove these undesired contributions and to mathematically improve the SNR of the spectra. We also discuss normalization approaches used to aid the interpretation and comparison of spectra.

3.3.1 Background Removal

When dealing with LTRS, spectra sources of background can be grouped into four types: (1) the laser-induced background that originates from the solution and the sample holder (i.e., a coverslip or capillary tube), (2) the laser-induced background that originates from the sample itself, most commonly autofluorescence, (3) light sources other than the Raman excitation laser, and (4) a baseline due to the dark current of the CCD detector.

The simplest way to deal with external background, i.e., the background due to external light sources, solution, and/or coverslip, is to acquire accompanying spectra under identical conditions to those used to acquire the sample's spectrum, but without the trapped particle (i.e., a blank control). In this case, a simple subtraction of the background from the sample spectrum usually provides satisfactory results if the two spectra were acquired at approximately the same distance from the coverslip and using the same acquisition parameters, such as integration time, averaging

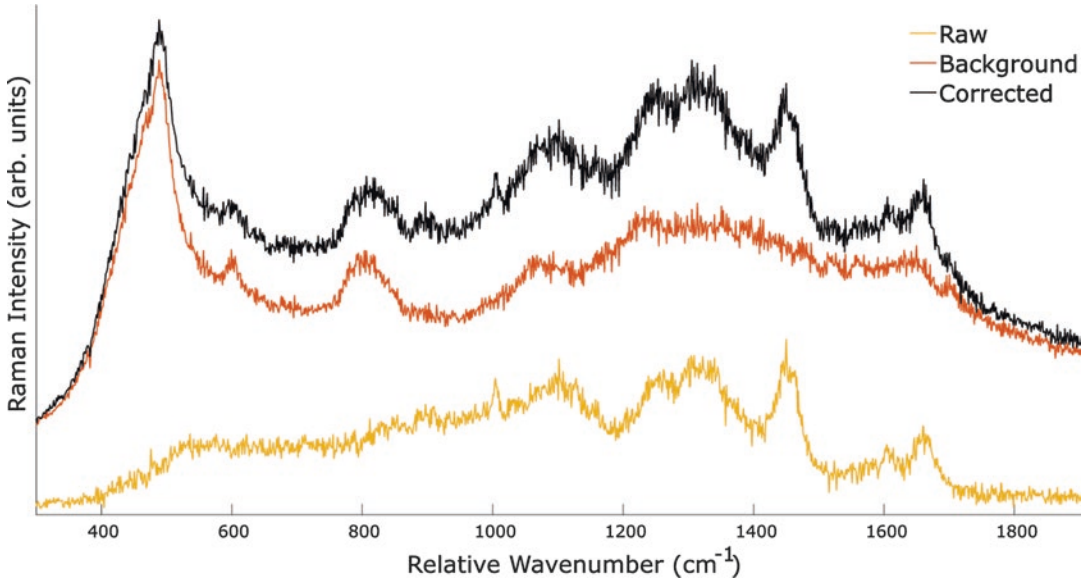

Fig. 6 Raman spectrum of a single trapped yeast cell and its corresponding acquired background and corrected spectra

frames, camera settings, etc. Figure 6 shows the raw Raman spectrum of a single trapped yeast cell and its corresponding background and the corrected spectra.

Tip: After the subtraction, the resulting spectrum should consist of positive values and some negative values that shouldn't be outside of the noise range, which can be estimated as the standard deviation of all values in a flat region of the spectrum (e.g., between 1700 and 2200 cm^{-1} in the Raman spectrum of polystyrene). If large negative values are obtained, the background spectrum might not have been obtained under identical conditions as the sample and shouldn't be used.

A more robust background removal can be done by fitting two or more known background spectra (e.g., background spectra collected at two different focal distances from the coverslip) to the sample spectrum. Asymmetric or weighted least squares algorithms can be implemented for that purpose [28].

On the other hand, laser-induced sources of background, such as sample's autofluorescence or phosphorescence, would not be eliminated by subtracting a blank control spectrum from the sample's measurement. Many algorithms have been developed to estimate the unknown background and correct Raman spectra in this situation. They all achieve the desired correction by fitting the baseline to an analytical function and subtracting the fit from the spectrum. The slope of the background and the function used to fit it are key factors that influence the quality of the correction. The correction of concave-like backgrounds with high slopes may result

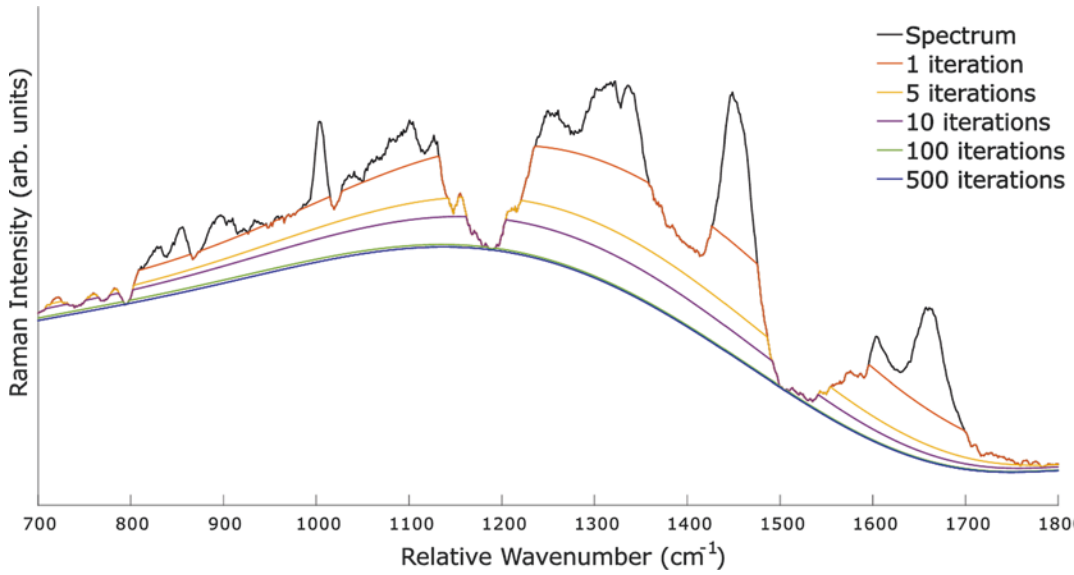

Fig. 7 Baseline update of the Lieber polynomial fit background correction algorithm for a given number of iterations

in the appearance of artificial spectral features (i.e., artifacts). Additionally, the function used to fit the background can also adversely impact the resulting spectrum resulting in an uneven baseline.

A common algorithm uses polynomials to fit the baseline, and the baseline is iteratively redefined and fitted so that the Raman peaks influence the fit the least [29]. Figure 7 shows how the baseline is updated for a given number of iterations.

In some cases, the background is constant throughout the spectrum, like in the case of background due to the dark current in CCDs, or has a simple linear form. In those cases taking the mathematical first and second derivatives of the spectrum will very effectively remove the background.

Background correction of Raman spectra has to be done carefully to avoid artifacts in the final spectra. Which method to use depends on the range of the data and the nature and shape of the background. In addition to the methods discussed in this section for background correction, multivariate analysis methods exist that can also help to identify unknown background in spectroscopic data. Those techniques will be discussed in Subheading 3.4.2.

3.3.2 Denoising

Noise is an important aspect to understand and consider when dealing with Raman spectra. Since Raman is an inherently weak phenomenon, it can be easily overwhelmed by any of the three types of noise: thermal, readout, and shot noise (*see* **Note 33**). Thermal and readout noise can be controlled by changing the

temperature and the readout rate of the detector, respectively, and are minimized, thanks to the availability of better detector and deep cooling systems. Shot noise, on the other hand, is random in nature and unavoidable. In this section, we discuss the various ways to lower the effect of noise on the final measurement, from acquisition parameters to mathematical processing of the spectra.

The first line of defense against noise is increasing the number of photons collected. That can be done by either using longer exposure times, increasing the laser power, or acquiring multiple frames (i.e., consecutive acquisitions of the same spectrum). Which approach to use depends on the characteristics of the detector and the sample. In the case of an LTRS system that is shot-noise limited (i.e., a system in which thermal and readout noise are low compared to shot noise), increasing the exposure time, or the laser power, would help improve the SNR [32]. On the other hand, for a system that is readout-noise limited, averaging over multiple frames will result in a better SNR. The underlying reason is that the readout noise for most CCD cameras is very well described by a random Gaussian noise. Thus, averaging short exposure time frames narrows down the error in the measurement due to readout. There are cases in which either of those approaches is not suitable, for example, due to photodamage or the timescale of the phenomenon of interest, and mathematical corrections need to be used.

Tip: Before doing the final measurements, perform a control experiment to understand the effect of laser power, readout rate, integration time, and averaging on SNR, estimated as the intensity at the peak of one of the Raman bands divided by the standard deviation of all values in a flat region of the spectrum.

Even under proper experimental conditions, noise will still be present. In that case, mathematical algorithms, sometimes referred to as filters, exist to smooth the spectroscopic data. Perhaps the most popular one is the Savitzky-Golay algorithm [30], which fits polynomials of order p to small subsets of k adjacent data points. Figure 8 shows the effect the polynomial order p and the window size k chosen to smooth the data have on the spectra. When selecting p and k for a Savitzky-Golay smoothing routine, it is important to be aware of the possible loss of spectral features due to oversmoothing and the broadening of the Raman bands with increasing window size.

Other common algorithms to smooth data are the moving average, which averages the values of adjacent data points, a Gaussian algorithm, which fits small subsets of adjacent data points to Gaussian functions, and Fourier transform filters that get rid of the high-frequency features of the spectrum, among others [31]. Figure 9 shows a comparison of the different smoothing methods and their effect on spectral features.

Tip: Regardless of the denoising method chosen, attention should be paid to the Raman bands broadening and shifting caused by the smoothing algorithm.

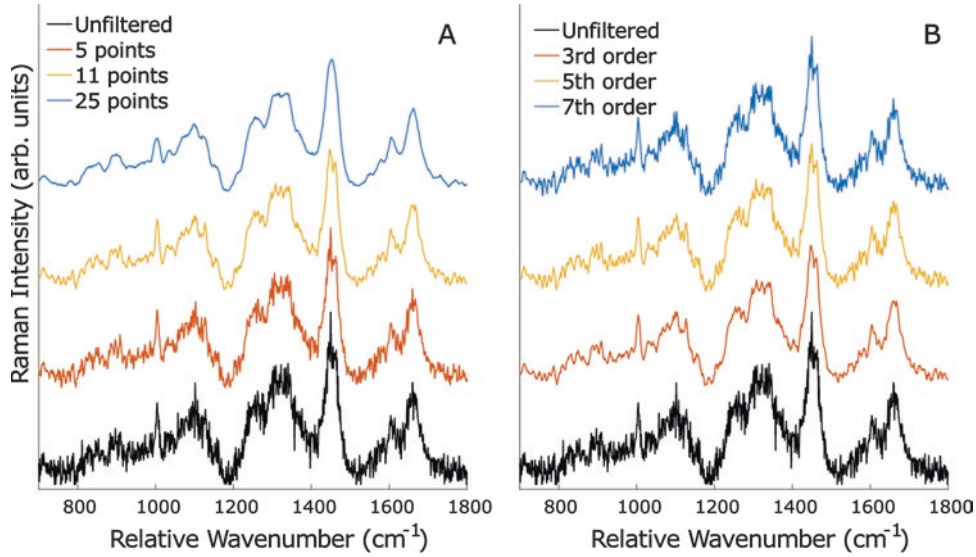

Fig. 8 (**a**) Effect of the window size k on the final spectrum when using a Savitzky-Golay filter with a third-order polynomial. (**b**) Effect of the polynomial order p on the final spectrum when using a Savitzky-Golay filter with an 11-point window

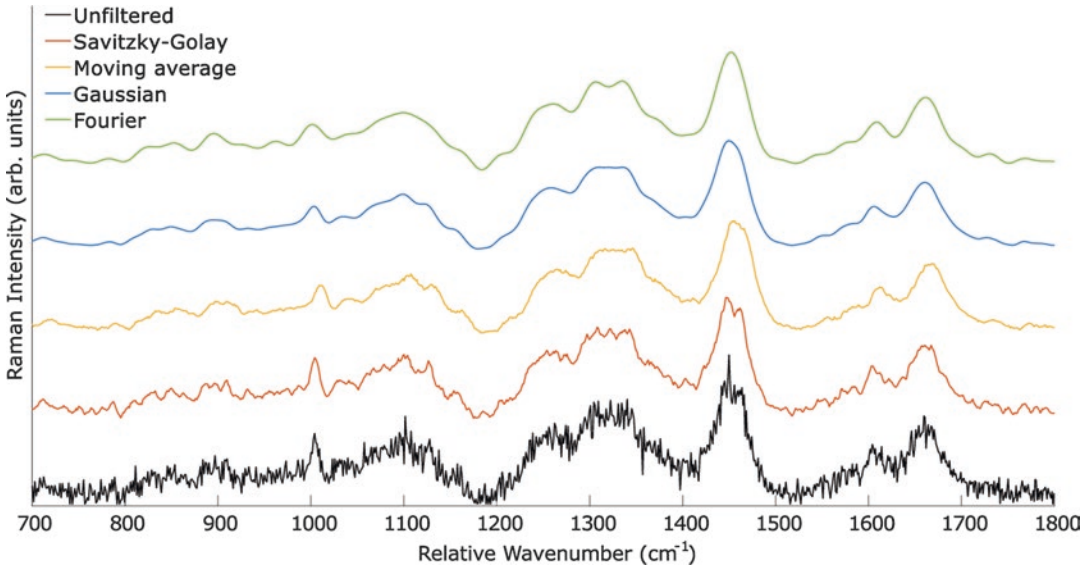

Fig. 9 Comparison of the different smoothing methods and their effect on spectral features. Savitzky-Golay filter (11-point window, third-order polynomial), moving average (11-point window), Gaussian filter (11-point window, $\sigma = 5$), and Fourier filter (preserving 50 frequencies)

In addition to the methods discussed in this section for data smoothing, multivariate analysis methods exist that can separate uncorrelated noise from the actual data, effectively smoothing the spectra. Those techniques will be discussed in Subheading 3.4.2.

3.3.3 Normalization

Many LTRS studies aim to investigate relative changes in Raman band intensities for sample classification and identification or to monitor chemical changes in dynamic biological processes. Hence, normalization of the spectra is required so that spectral features can be compared. Absolute intensity values, which may vary due to systematic fluctuations (e.g., varying laser intensities from one measurement to the next or variations in the interrogated volume), are unreliable and not often used for comparing spectra. Which normalization method to use, if any, depends on the samples and the goal of the experiment. The most common types of normalization are total spectral intensity normalization and single band normalization, but there are some other methods like standard normal variance (SNV) [32] which normalizes the data, so the standard deviation of all the points in a single spectrum is one, and multiplicative scatter correction (MSC) [33] that aims to correct spectra, so they resemble a reference spectrum (e.g., the average spectrum). Both SNV and MSC are particularly useful with datasets of multiple spectra and with spectra that have background which are difficult to correct.

In the case of total intensity normalization, the intensity value of each point on the spectrum is divided by the sum of all intensity values of all the points. Single band normalization is done by dividing the spectrum by the area, the peak value of a given Raman band, or the maximum value of the spectrum. The advantage of total intensity and single band normalization approaches is their simplicity, but they may not be the best option if the background is prevalent, changes overtime, or cannot be completely removed, which are common situations in complex biological samples.

3.4 Analysis of Raman Spectra

Studies using LTRS to characterize single cell populations often aim to use the multidimensional Raman spectra to identify key chemical components and their concentrations (e.g., quantifying drug concentrations after exposure) or to identify molecular differences between different populations (e.g., identifying normal and cancerous cells). Such studies require analytical tools that allow for the comparison, quantification, and sorting of the spectra collected from individual cells. This section is intended to be a brief introduction to the different kinds of techniques that can be used for analyzing Raman data sets. For more comprehensive, in-depth reviews, please refer to [31, 34, 35].

3.4.1 Single Variable Analysis

Single variable methods are those that make use of a single data point per cell or sample. Such is the case when using the peak intensity of a Raman band or the relative intensity of two Raman bands of interest. In either case, the experiment could aim to characterize a sample or to identify differences between different populations.

In terms of sample characterization, Raman spectroscopy offers an outstanding advantage as it can quantify the concentration of molecules. In LTRS, the intensity of the Raman peaks for a molecule is proportional to the number of molecules in the focal volume probed. In homogenous solutions, where the average number of molecules in the focal volume is constant, or very small cells, such as bacterial cells that fit inside the laser focal volume, (*see* **Note 34**) such that the entire cell is being probed at once, the analysis of the spectra is straightforward. The inferences regarding concentrations of molecules using peak intensities will be accurate [29, 38] and only vary due to the inherent variation of biological samples [27]. On the other hand, in the case of inhomogeneous solutions or larger cells, such as mammalian cells, only a fraction of the volume is being probed, thus limiting the analysis based on single Raman peak intensities. In those cases, analysis of relative intensities or intensity ratios between two independent Raman bands can provide a more accurate result [36].

Hypothesis tests, such as the analysis of variance (ANOVA) in the case of normally distributed (i.e., parametric) populations or the Kruskal-Wallis for nonparametric distributions, can be used to determine if the Raman differences between two, or more, cell populations are statistically significant.

3.4.2 Multivariate Analysis

Multivariate analysis, also known as chemometrics and a subset of machine learning, refers to the analysis techniques that take advantage of all the information carried by the Raman spectra. They are divided into unsupervised methods, in which no prior knowledge of the spectra is required, and supervised methods, which offer a way to quantify or classify new unknown samples based on information acquired from a training dataset of well-characterized samples.

Unsupervised methods are used to explore the spectral dataset in search for differences between the various spectra and/or to identify those features that make the spectra different or similar.

The most widely used technique is called principal component analysis (PCA). In PCA, each spectrum is represented as a point in an n-dimensional space, where n is the number of variables, e.g., the number of points each spectrum has. The spectra dataset is then represented as a cloud of points in that n-dimensional space. PCA finds a new set of axes that better describes the variance among the data set. In mathematical terms, PCA works as a linear transformation from the space of variables with n dimensions (where n is the number of variables) to a new space that represents the data in a more meaningful way. The problem is that there are many changes of basis that could be used. This problem is solved

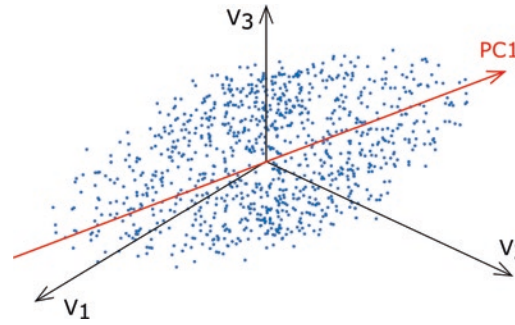

Fig. 10 Data points (blue) in a three-dimensional variable space. Red line shows the direction of most variability within the data, known as principal component 1 (PC1)

by assuming that the directions within the data with maximum variance are the ones that carry most of the information. Each of the axes in the new space is called a principal component (PC), and the first PC is the axis along which variance is the largest. A more intuitive way to understand PC is depicted in Fig. 10 where each data point is represented by three coordinates (i.e., only using three variables). The dataset displays most of the variability along the line depicted in red or PC1.

One of the most useful aspects of PCA is the reduction of dimensionality. In other words, PCA finds out which of the variables contribute the most to the data variance. In Raman spectra, this can mean that instead of thousands of variables per spectrum, each spectrum can be reduced to just a few variables that are most relevant for determining differences among all the spectra analyzed. Hence, PCA is often used as an initial step to test if there are differences among the dataset that can be used to classify the spectra.

Clustering methods such as hierarchical clustering analysis and k-means are also unsupervised techniques that allow for the exploration of spectra and whether they can be classified without prior knowledge of the samples.

Unsupervised techniques are often followed by supervised ones. Supervised techniques are those that work based on known information in the form of a training dataset to predict a class or composition of a new unknown sample. Such problem can be addressed by classification and predictive models such as support vector machine (SVM) [37, 38],partial least squares-regression (PLS-R) [39, 40], or principal component regression (PCR) [40] among others.

4 Notes

1. The ideal situation is to select a light path inside the microscope that avoids the tube lens, but if not possible, the tube lens can be carefully taken out of the microscope. The downside of doing so is that the eyepiece won't focus at the right focal plane.
2. Information on specific providers and products are included merely as suggestions for the reader and are not intended to be endorsements by the authors. Other providers and products also match the required specifications. Here we present the setup of an NIR 785 nm LTRS system, but other wavelengths could also be used. Be aware that most optics are designed for a specific wavelength range (e.g., ultraviolet, visible, or IR).
3. The strength of the forces exerted on the trapped particle is proportional to the NA of the objective. Hence objectives with NA higher than 1 are recommended.
4. The laser mount will depend on the specific laser used. For example, for a tube laser, a v-clamp could be used. Choose a mount that will allow the height and tilt to be adjusted so the laser beam can be set at the proper height and traveling parallel to the surface of the table/breadboard.
5. Thirty millimeter cage systems are standard systems designed to ease the construction of optomechanical setups. They are available from most optomechanical component providers.
6. Neutral density filters are used to control the intensity of the laser, but the discrete optical densities of the filters limit tunability of the laser intensity to specific values. The use of a $\lambda/2$ plate and a polarizer beam splitter combination will allow the intensity to be tuned over a continuous range.
7. The exact $f1$ and $f2$ focal lengths have to be determined depending on the diameter of the laser beam and the diameter of the back aperture (i.e., pupil) of the objective used. The original beam diameter needs to be expanded to slightly overfill the rear aperture of the objective; in this way the focused light results in a diffraction-limited spot and a tighter trap.
8. For the LTRS alignment, we recommend using a port in the microscope base that doesn't go through the tube lens (i.e., the lens inside the body of the microscope placed between the objective and the eyepiece and/or camera port). With a base like the Olympus IX71, the rear port (normally used for a fluorescence lamp) is ideal to set up the excitation light path and the right-side port to set up the detection light path. Using the rear and right-side ports is convenient as they do not make use of the tube lens, and the dichroic mirror can be set in an empty

filter cube and placed inside the turret. Alternatively, in the Olympus IX71, there is enough space between the turret and the objective to place a dichroic mirror using a machined holder. This way it would be possible to have both wide-field fluorescence and LTRS in the same microscope.

9. Use the screw holes drilled on the optical table/breadboard as a guide, and during the initial coarse alignment, try to keep the beam traveling parallel to the rows of holes.
10. Unmount the thin metal sheet, onto which the pinhole is made, from the holder. Take care not to puncture or bend the sheet. On a regular microscope slide, set the sheet flat and cover it with a #1 coverslip. To glue the coverslip to the slide, use four very small dots of nail polish making sure it isn't dragged toward the pinhole by surface tension.
11. The easiest way to level a tilted mount is by turning each of the screws so the first plate is approximately in the middle of the screw's range and the distance between the two plates is the same at each of the two or three screw positions.
12. At this point, the light from the pinhole might be very dim. If that is the case, measure the distance from the surface of the optical table or breadboard, and estimate the direction of the light to set the mirror at the approximate height and perpendicular to the light.
13. Achromatic doublet lenses achieve a tighter focus and are less sensitive to off-center alignment than other types of lenses and have a constant focal length across multiple wavelengths.
14. If using an achromatic doublet, the lens should be set so that the laser beam will encounter the face with the lowest radius of curvature first.
15. It is recommended but not necessary to set the lens on a translation stage as it will make laser collimation easier.
16. This is a precaution step done in case the beam is not centered on the lens and scatters light in various directions. It is suggested to continue this safety practice as the alignment continues.
17. OD is defined as $\mathrm{OD} = \log_{10}\left(1/T\right)$, where T is the transmittance, defined as the ratio between the power before and after the ND. The laser used in this alignment provides a 120 mW nominal power. To lower the intensity to 10 mW (or $T = 0.083$), an ND filter with an OD of 1.0 is appropriate.
18. The nominal $1/e^2$ diameter of the laser is 1.2 mm, and the magnification obtained with L1 and L2 is 10×. Hence the resulting beam diameter is approximately 12 mm.

19. Alternatively, the adjustment can be made using the spot observed on the camera. Hence, instead of using the IR disc at two different positions, the image of the laser spot at two different focal points should be used. With this option, only minimal adjustments should be made at each iteration, and it is important to make sure that the beam still goes centered through the objective.
20. It will be necessary to place lenses L3 and L4 and mirrors M3 and M4 in between the microscope and the spectrometer as shown in Fig. 3. Position the spectrometer, so there is enough space to do so.
21. If too much adjustment is necessary, it could be due to the lens not being centered or not perpendicular enough to the light path. Make sure that when the lens is placed, the resulting spot is on the pinhole (to the best of your ability to see the spot and the pinhole).
22. It is recommended but not necessary to set the lens on a translation stage as it will make it easier to maximize the power.
23. It is recommended but not necessary to set the lens on a translation stage as it will make laser collimation easier.
24. If an IR viewer is not available, the power of the laser might be increased, but additional care needs to be taken not to be exposed to direct, scattered, or reflected laser light.
25. With the Princeton Instruments slits, the position of the slit is roughly at the center of the adjusting knob.
26. If using another excitation wavelength, center the grating to that value. It is common in spectrometers with a nonadjustable grating for the grating to be set, so a little bit of the laser light is still observable at the edge of the CCD pixel array.
27. The spectral features, whether from the laser or room light, are going to be wide since the slit is opened all the way.
28. Most spectrometers suffer from a distortion that causes features on the edge of the CCD to appear elongated on the vertical axis, thus making like a bow tie. Use the dots (i.e., Raman bands) in the middle of the CCD when focusing.
29. Using the sensor card, the light should be observable on the back side of the plate.
30. Take into consideration the space needed to place the mirrors, filter, and lens to couple to the fiber and the fiber itself.
31. Most spectrometers suffer from a distortion that causes features on the edge of the CCD to appear elongated on the vertical axis, thus making like a bow tie. Use the dots (i.e., Raman bands) in the middle of the CCD when focusing.

32. This value is the spectral resolution of the system, and it depends on the CCD pixel size, the grating, and the size of the slit used. Refer to the equipment manual to get a better idea of what values are acceptable.
33. Shot noise can be described by a Poisson process that for large numbers approaches a normal distribution with standard deviation $\sqrt[2]{n}$, where n is the number of photons collected. Hence, the SNR associated with shot noise can be expressed as $\sqrt[2]{n}$, and it improves as the number of photons collected increases.
34. The focal volume depends on the NA of the objective and the laser wavelength. The spot size (i.e., the diameter of the laser beam at the focal length) is given by $\frac{1.22\lambda_{exc}}{NA_{Obj}}$.

References

1. Awasthi S, Izu LT, Mao Z, Jian Z, Landas T, Lerner A, Shimkunas R, Woldeyesus R, Bossuyt J, Wood B, Chen YJ, Matthews DL, Lieu DK, Chiamvimonvat N, Lam KS, Chen-Izu Y, Chan JW (2016) Multimodal SHG-2PF imaging of microdomain Ca^{2+}-contraction coupling in live cardiac myocytes. Circ Res 118(2):e19–e28. https://doi.org/10.1161/CIRCRESAHA.115.307919
2. Awasthi S, Matthews DL, Li RA, Chiamvimonvat N, Lieu DK, Chan JW (2012) Label-free identification and characterization of human pluripotent stem cell-derived cardiomyocytes using second harmonic generation (SHG) microscopy. J Biophotonics 5(1):57–66. https://doi.org/10.1002/jbio.201100077
3. Huang S, Heikal AA, Webb WW (2002) Two-photon fluorescence spectroscopy and microscopy of NAD(P)H and flavoprotein. Biophys J 82(5):2811–2825. https://doi.org/10.1016/S0006-3495(02)75621-X
4. Squirrell JM, Fong JJ, Ariza CA, Mael A, Meyer K, Shevde NK, Roopra A, Lyons GE, Kamp TJ, Eliceiri KW, Ogle BM (2012) Endogenous fluorescence signatures in living pluripotent stem cells change with loss of potency. PLoS One 7(8):e43708. https://doi.org/10.1371/journal.pone.0043708
5. Chan JW (2013) Recent advances in laser tweezers Raman spectroscopy (LTRS) for label-free analysis of single cells. J Biophotonics 6(1):36–48. https://doi.org/10.1002/jbio.201200143
6. Kong LB, Chan J (2014) A rapidly modulated multifocal detection scheme for parallel acquisition of Raman spectra from a 2-D focal array. Anal Chem 86(13):6604–6609. https://doi.org/10.1021/ac5012188
7. Liu R, Taylor DS, Matthews DL, Chan JW (2010) Parallel analysis of individual biological cells using multifocal laser tweezers Raman spectroscopy. Appl Spectrosc 64(11):1308–1310. https://doi.org/10.1366/000370210793334972
8. Zhang PF, Kong LB, Wang GW, Setlow P, Li YQ (2010) Combination of Raman tweezers and quantitative differential interference contrast microscopy for measurement of dynamics and heterogeneity during the germination of individual bacterial spores. J Biomed Opt 15(5):Artn 056010. https://doi.org/10.1117/1.3494567
9. Moritz TJ, Brunberg JA, Krol DM, Wachsmann-Hogiu S, Lane SM, Chan JW (2010) Characterisation of FXTAS related isolated intranuclear protein inclusions using laser tweezers Raman spectroscopy. J Raman Spectrosc 41(1):33–39. https://doi.org/10.1002/jrs.2436
10. Creely CM, Singh GP, Petrov D (2005) Dual wavelength optical tweezers for confocal Raman spectroscopy. Optics Commun 245(1–6):465–470. https://doi.org/10.1016/j.optcom.2004.10.011
11. Chan JW, Esposito AP, Talley CE, Hollars CW, Lane SM, Huser T (2004) Reagentless identification of single bacterial spores in aqueous solution by confocal laser tweezers Raman spectroscopy. Anal Chem 76(3):599–603. https://doi.org/10.1021/ac0350155
12. Chen D, Huang SS, Li YQ (2006) Real-time detection of kinetic germination and heterogeneity of single Bacillus spores by laser tweezers

Raman spectroscopy. Anal Chem 78(19):6936–6941. https://doi.org/10.1021/ac061090e

13. Kong L, Zhang P, Wang G, Yu J, Setlow P, Li YQ (2011) Characterization of bacterial spore germination using phase-contrast and fluorescence microscopy, Raman spectroscopy and optical tweezers. Nat Protoc 6(5):625–639. https://doi.org/10.1038/nprot.2011.307
14. Wang S, Shen A, Setlow P, Li YQ (2015) Characterization of the dynamic germination of individual clostridium difficile spores using Raman spectroscopy and differential interference contrast microscopy. J Bacteriol 197(14):2361–2373. https://doi.org/10.1128/JB.00200-15
15. Moritz TJ, Polage CR, Taylor DS, Krol DM, Lane SM, Chan JW (2010) Evaluation of *Escherichia coli* cell response to antibiotic treatment by use of Raman spectroscopy with laser tweezers. J Clin Microbiol 48(11):4287–4290. https://doi.org/10.1128/JCM.01565-10
16. Moritz TJ, Taylor DS, Polage CR, Krol DM, Lane SM, Chan JW (2010) Effect of cefazolin treatment on the nonresonant Raman signatures of the metabolic state of individual *Escherichia coli* cells. Anal Chem 82(7):2703–2710. https://doi.org/10.1021/ac902351a
17. Chan JW, Motton D, Rutledge JC, Keim NL, Huser T (2005) Raman spectroscopic analysis of biochemical changes in individual triglyceride-rich lipoproteins in the pre- and postprandial state. Anal Chem 77(18):5870–5876. https://doi.org/10.1021/ac050692f
18. Smith ZJ, Lee C, Rojalin T, Carney RP, Hazari S, Knudson A, Lam K, Saari H, Ibanez EL, Viitala T, Laaksonen T, Yliperttula M, Wachsmann-Hogiu S (2015) Single exosome study reveals subpopulations distributed among cell lines with variability related to membrane content. J Extracell Vesicles 4:28533. https://doi.org/10.3402/jev.v4.28533
19. Fore S, Chan J, Taylor D, Huser T (2011) Raman spectroscopy of individual monocytes reveals that single-beam optical trapping of mononuclear cells occurs by their nucleus. J Opt 13(4):44021. https://doi.org/10.1088/2040-8978/13/4/044021
20. Chan JW, Taylor DS, Lane SM, Zwerdling T, Tuscano J, Huser T (2008) Nondestructive identification of individual leukemia cells by laser trapping Raman spectroscopy. Anal Chem 80(6):2180–2187. https://doi.org/10.1021/ac7022348
21. Liu R, Mao Z, Matthews DL, Li CS, Chan JW, Satake N (2013) Novel single-cell functional analysis of red blood cells using laser tweezers Raman spectroscopy: application for sickle cell disease. Exp Hematol 41(7):656–661. e651. https://doi.org/10.1016/j.exphem.2013.02.012
22. Efremov EV, Ariese F, Gooijer C (2008) Achievements in resonance Raman spectroscopy: review of a technique with a distinct analytical chemistry potential. Anal Chim Acta 606(2):119–134. https://doi.org/10.1016/j.aca.2007.11.006
23. Dochow S, Krafft C, Neugebauer U, Bocklitz T, Henkel T, Mayer G, Albert J, Popp J (2011) Tumour cell identification by means of Raman spectroscopy in combination with optical traps and microfluidic environments. Lab Chip 11(8):1484–1490. https://doi.org/10.1039/C0LC00612B
24. Li Z, Deen M, Kumar S, Selvaganapathy P (2014) Raman spectroscopy for in-line water quality monitoring—instrumentation and potential. Sensors 14(9):17275
25. Kramida A, Ralchenko YU, Reader J, NIST ASD Team (2016) Atomic spectra database (version 5.4) Online edition. National Institute of Standards and Technology, Gaithersburg, MD. http://physics.nist.gov/PhysRefData/ASD/lines_form.html
26. Managò S, Valente C, Mirabelli P, Circolo D, Basile F, Corda D, De Luca AC (2016) A reliable Raman-spectroscopy-based approach for diagnosis, classification and follow-up of B-cell acute lymphoblastic leukemia. Sci Rep 6:24821. https://doi.org/10.1038/srep24821. http://www.nature.com/articles/srep24821#supplementary-information
27. Xie C, Chen D, Y-q L (2005) Raman sorting and identification of single living micro-organisms with optical tweezers. Opt Lett 30(14):1800–1802. https://doi.org/10.1364/OL.30.001800
28. Peng J, Peng S, Jiang A, Wei J, Li C, Tan J (2010) Asymmetric least squares for multiple spectra baseline correction. Anal Chim Acta 683(1):63–68. https://doi.org/10.1016/j.aca.2010.08.033
29. Lieber CA, Mahadevan-Jansen A (2003) Automated method for subtraction of fluorescence from biological Raman spectra. Appl Spectrosc 57(11):1363–1367. https://doi.org/10.1366/000370203322554518
30. Savitzky A, Golay MJE (1964) Smoothing and differentiation of data by simplified least squares procedures. Anal Chem 36(8):1627–1639. https://doi.org/10.1021/ac60214a047
31. Gautam R, Vanga S, Ariese F, Umapathy S (2015) Review of multidimensional data processing approaches for Raman and infrared

spectroscopy. EPJ Techn Instrument 2(1):8. https://doi.org/10.1140/epjti/s40485-015-0018-6

32. Barnes RJ, Dhanoa MS, Lister SJ (1989) Standard normal variate transformation and detrending of near-infrared diffuse reflectance spectra. Appl Spectrosc 43(5):772–777
33. Windig W, Shaver J, Bro R, Loopy MSC (2008) A simple way to improve multiplicative scatter correction. Appl Spectrosc 62(10): 1153–1159. https://doi.org/10.1366/000370208786049097
34. Long DA (2004) Handbook of Raman spectroscopy. From the research laboratory to the process line. Eds. Ian R. Lewis and Howell G. M. Edwards. Marcel Dekker, N-Y and Basel, 2001. J Raman Spectrosc 35(1):91–91. https://doi.org/10.1002/jrs.1117
35. Dörfer T, Schumacher W, Tarcea N, Schmitt M, Popp J (2010) Quantitative mineral analysis using Raman spectroscopy and chemometric techniques. J Raman Spectrosc 41(6):684–689. https://doi.org/10.1002/jrs.2503
36. Wu H, Volponi JV, Oliver AE, Parikh AN, Simmons BA, Singh S (2011) In vivo lipidomics using single-cell Raman spectroscopy. Proc Natl Acad Sci U S A 108(9):3809–3814. https://doi.org/10.1073/pnas.1009043108
37. Krafft C, Dochow S, Beleites C, Popp J (2014) Cell identification using Raman spectroscopy in combination with optical trapping and microfluidics. In: Mahadevan-Jansen A, Petrich W (eds) Biomedical vibrational spectroscopy VI: advances in research and industry. SPIE, San Francisco, CA, pp 893906–893907
38. Belousov AI, Verzakov SA, von Frese J (2002) Applicational aspects of support vector machines. J Chemometr 16(8–10):482–489. https://doi.org/10.1002/cem.744
39. Keating ME, Nawaz H, Bonnier F, Byrne HJ (2015) Multivariate statistical methodologies applied in biomedical Raman spectroscopy: assessing the validity of partial least squares regression using simulated model datasets. Analyst 140(7):2482–2492. https://doi.org/10.1039/C4AN02167C
40. Beebe KR, Kowalski BR (1987) An introduction to multivariate calibration and analysis. Anal Chem 59(17):1007A–1017A. https://doi.org/10.1021/ac00144a001
41. McCreery RL (2005) Calibration and validation. In: Raman spectroscopy for chemical analysis. John Wiley & Sons, Inc, Hoboken, NJ, pp 251–291. https://doi.org/10.1002/0471721646.ch10

Part IV

Metabolic and Molecular Biological Methods in Cell Heterogeneity Tracking

Chapter 14

Quantification of the Metabolic Heterogeneity in Mycobacterial Cells Through the Measurement of the NADH/NAD$^+$ Ratio Using a Genetically Encoded Sensor

Shabir Ahmad Bhat, Iram Khan Iqbal, and Ashwani Kumar

Abstract

NADH/NAD$^+$ levels are an indicator of the bacterial metabolic state. NAD(H) levels are maintained through coordination of pathways involved in NAD(H) synthesis and its catabolic utilization. Conventional methods of estimating NADH/NAD$^+$ require cell disruption and suffer from low specificity and sensitivity and are inadequate in providing spatiotemporal resolution. Recently, genetically encoded biosensors of the NADH/NAD$^+$ ratio have been developed. One of these sensors, Peredox-mCherry, was adapted for the measurement of cellular levels of NADH/NAD$^+$ in the slow-growing *Mycobacterium tuberculosis* (Mtb) and the fast-growing *Mycobacterium smegmatis*. Importantly, the use of the engineered reporter strains of Mtb demonstrated a significantly higher heterogeneity among the bacteria residing in macrophages compared to the bacteria grown in synthetic media. Previous estimations of NADH/NAD$^+$ levels have missed this important aspect of the biology of Mtb, which may contribute to the variable response of intracellular Mtb to different antimycobacterial agents. In this chapter, we describe the details of a method used in the generation of reporter strains for the measurement of the NADH/NAD$^+$ ratio in mycobacteria. Importantly, once the reporter strains are created, they can be exploited with fluorescence spectroscopy, FACS, and confocal microscopy to access the dynamic changes in the NADH/NAD$^+$ levels in intact individual bacterial cells. Although we have only described the method for the creation of reporter strains capable of measuring NADH/NAD$^+$ in mycobacteria in this chapter, a similar method can be used for generating reporter strains for other bacterial species, as well. We believe that such reporter stains can be used in novel screens for small molecules that could alter the metabolism of bacterial cells and thus aid in the development of new class of therapeutic agents.

Key words Bacterial metabolic state, Metabolic heterogeneity, Peredox, Tuberculosis pathogenesis

1 Introduction

The cellular metabolic balance is maintained by two important cofactors: nicotinamide adenine dinucleotide (NAD$^+$) and nicotinamide adenine dinucleotide phosphate (NADP$^+$) [1]. NADH and NADPH are the reduced forms of NAD$^+$ and NADP$^+$, respectively. The addition of a phosphate group to the 2′ position of the adenyl

Natasha S. Barteneva and Ivan A. Vorobjev (eds.), *Cellular Heterogeneity: Methods and Protocols*, Methods in Molecular Biology, vol. 1745, https://doi.org/10.1007/978-1-4939-7680-5_14, © Springer Science+Business Media, LLC 2018

nucleotide through an ester linkage converts NAD to NADP. The NAD(P)H species acts as a nodal point of metabolism in bacteria. About ~17% of the enzymatic reactions in bacteria and ~700 oxidoreductive reactions in living cells use NAD(P)H as a cofactor [2, 3]. The NAD(P)H species are indispensable parts of the oxidoreductive processes within the cell, which are essential for the survival and adaptation of a living cell. These processes include redox homeostasis, apoptosis, autophagy, cell death, cellular differentiation, and aging [4–6]. NAD^+ acts as an electron sink for the harvesting of energy during catabolism, and its reduced form NADH feeds electrons to the electron transport chain to generate the proton-motive force. On the other hand, NADPH is used as an electron donor for some vital anabolic reactions. The NADH/NAD^+ ratio is thus considered to be an indicator of the cellular redox and metabolic state [1].

In bacteria specifically, NADH homeostasis is involved in responding to environmental cues, regulating growth and biofilm development, and modulating the central metabolism in response to the availability of nutrients and the maintenance of the redox state during physiological stress, survival under antibiotic treatment, and persistence [7–9]. As an example, the decision of *Mycobacterium tuberculosis* (Mtb) cells to enter, maintain, or exit from the non-replicating persistent state is dependent on the prevailing metabolic state [10–12]. Bacterial levels of NAD^+ are maintained through the balance between its generation and its catabolic utilization. Mycobacteria utilize two main pathways to synthesize NADH: the salvage pathway and the de novo synthesis pathway. Both of the biosynthesis pathways play a vital role in mycobacterial adaptation to the changing environment [13, 14]. The de novo biosynthesis pathway is essential in Mtb in the absence of exogenous NAD^+, while the salvage pathway is important to survive the host-generated stress, such as hypoxia and the infection of animal models. In addition to its use in those pathways, NAD^+ is also consumed in cellular processes such as the repair of DNA and RNA, ADP-ribosylation, deacetylation, tRNA splicing, and the detoxification of antimicrobials [15]. Given the critical role of NAD homeostasis, its synthesis has been proposed as an important drug target [15, 16]. Furthermore, during adverse conditions (such as exposure to hypoxia), NADH accumulates inside the mycobacterial cells [9], and the accumulated NADH must be reoxidized to avoid the scarcity of NAD^+. Thus, the accurate measurement of the NADH/NAD^+ ratio is critical in understanding the bacterial response to varying environmental conditions.

Several conventional methods have been employed to estimate the NADH/NAD^+ ratio. These methods include the use of enzyme for indirect measurement of NADH/NAD^+, measurement of the lactate/pyruvate ratio using the assumption that it equilibrates with the NADH/NAD^+, the use of HPLC for the estimation of NADH and NAD^+, quantitation of autofluorescence of the

NAD(H) or NADP(H), the use of redox-active fluorogenic dyes, etc. [3, 17–19]. These methods have a number of limitations, such as (1) demanding disruption of the cells, (2) having low specificity, (3) lacking differentiation between free and protein-bound NADH or NAD^+, (4) lacking resolution at the single-cell level and thus not measuring the heterogeneity within the population, and (5) lacking spatiotemporal resolution [3, 20]. To overcome these disadvantages, noninvasive, reliable genetically encoded sensors were recently developed [21, 22]. These new sensors provide an accurate estimation of cellular NADH/NAD^+ levels with spatiotemporal resolution and thus are capable of measuring the metabolic dynamics in individual cells, reflecting metabolic heterogeneity within a population of cells. Both of these genetically encoded sensors are engineered based on the capability of the *Streptomyces* sensor protein Rex [21, 22]. Rex is a transcriptional regulator of *Streptomyces* that modulates transcription in response to the redox poise of the NADH/NAD^+ cellular pool [23]. The development of these sensors has opened a new arena in the study of cellular physiology. Unfortunately, most of these sensors have been originally developed for eukaryotic cells, and there are only a few studies wherein such probes have been used in bacteria. Recently, we have adapted the biosensor Peredox-mCherry [22] to determine the metabolic state of slow- and fast-growing mycobacterial species [24]. Peredox-mCherry was originally designed by Hung et al., and it integrates Rex domains with circularly permuted T-Sapphire protein to allow the sensing of cytosolic NADH/NAD^+ ratios (Fig. 1). We have demonstrated that stress generated by a plethora of physiologically relevant sources leads to the accumulation of

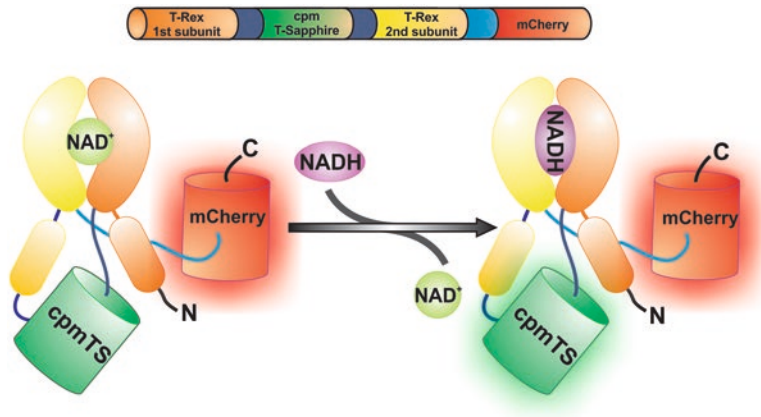

Fig. 1 Schematic illustration of NADH/NAD^+ sensor Peredox-mCherry. The circularly permuted T-Sapphire (cpTS) has been inserted between two T-Rex domains of *Thermus aquaticus* to generate the biosensor Peredox. Upon binding with NADH, the Peredox sensor transforms from an open to a closed conformation, which is accompanied by the increased green fluorescence of cpTS upon excitation with a 405 nm laser. The red fluorescence from the mCherry protein that is fused to the sensor, upon excitation with a 561 nm laser, is used for the normalization of the signal; the green/red ratio gives us the estimated NADH/NAD^+ ratio

NADH in mycobacterial cells [24]. A significant level of heterogeneity was observed the Mtb cells residing within the macrophages, compared with the Mtb cells growing in synthetic media. Importantly, immunological modulation of macrophages by interferon gamma resulted in the accumulation of NADH inside the Mtb cells. In this chapter, we describe an elaborate protocol for the estimation of the NADH/NAD^+ ratio in mycobacteria using Peredox-mCherry. A schematic workflow for using the Peredox sensor in mycobacterial cells is provided in Fig. 2. We are of the opinion that this probe could also be adapted for other bacterial cells for the measurement of their cellular NADH/NAD^+ levels. Such studies could reveal the metabolic heterogeneity of bacterial cells and its impact on the drug tolerance.

2 Materials

1. *Mycobacterium smegmatis* (mc^2155) (Msmeg) and *Mycobacterium tuberculosis* (H37Rv-ATCC 27294).
2. *RAW 264.7*® (ATCC® TIB-71™).
3. BD Difco™ Middlebrook 7H9 Broth.
4. BD Difco™ Middlebrook 7H10 Agar.
5. Middlebrook ADC Enrichment.
6. Middlebrook OADC Enrichment.
7. Tween™ 80.
8. 10% glycerol.
9. Hygromycin B, stock 50 mg/ml (G-Biosciences).
10. Phosphate-buffered saline (PBS).
11. Trypsin/EDTA solution.
12. Tissue culture media glutamax DMEM (Difco).
13. Cold freezing media (7H9 media with 20% glycerol).
14. Cryovials.
15. T25 culture flask.
16. 4% paraformaldehyde solution in PBS.
17. SlowFade® Gold Antifade Mountant.
18. Glass slides with frosted ends.
19. Cover glass (thickness, 0.13–0.17 mm).
20. Culture bottles, square (VWR).
21. 10 cm petri dishes.
22. 7H10 agar plates supplemented with 10% OADC and 50 μg/ml hygromycin B antibiotic (7H10-SUPPL plates).

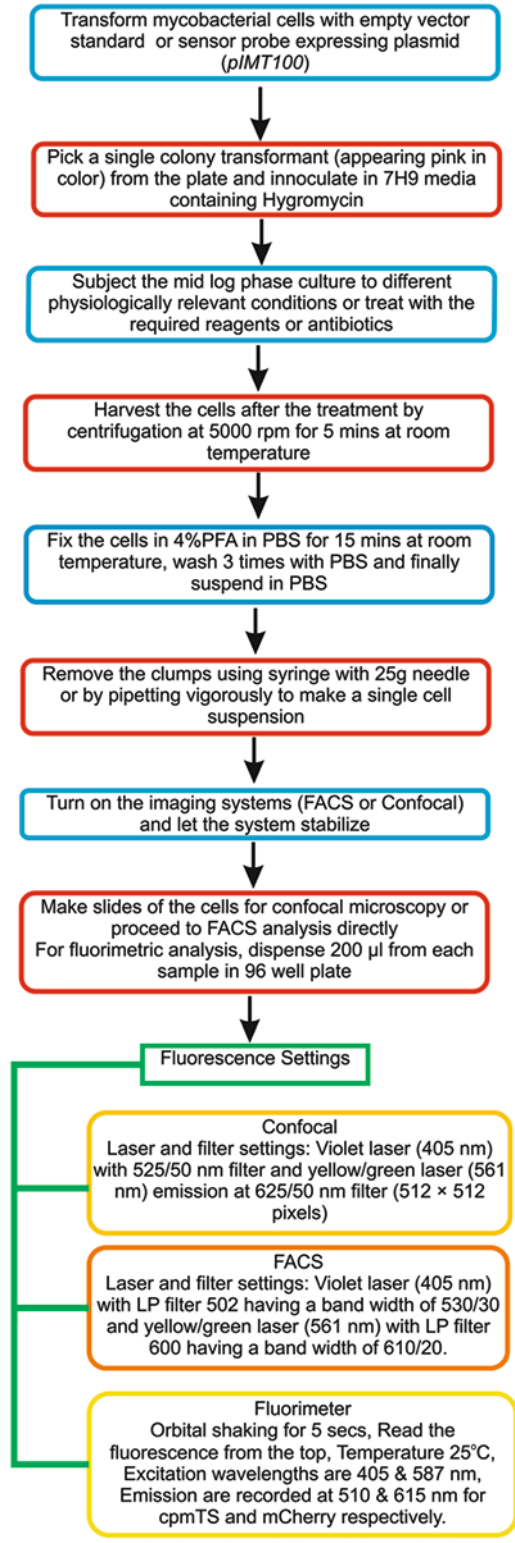

Fig. 2 Schematic workflow of the procedure for using the Peredox. The procedure starts with the transformation Fig. 2 (Continued) of the mycobacterial NADH sensor probe (IMT100) into mycobacteria. After the confirmation of the expression of the sensor, these cells are then subjected to different types of stresses (antibiotics or other environmental conditions). After the fixation and washing steps, the cells are subjected to different fluorescence analyses—fluorimetry, flow cytometry, and confocal microscopy

23. 7H9 broth supplemented with 10% ADC and 0.1% Tween 80 (7H9-SUPPL broth).
24. Electroporator (Eppendorf/Bio-Rad).
25. Electroporation cuvettes (Bio-Rad) with 1 and 2 mm gap sizes.
26. 37 °C shaker/incubator.
27. Black, 96-well assay plate with flat clear bottom.
28. Fluorescence spectrometer.
29. Confocal microscope equipped with 60× oil objective.
30. Flow cytometer with 488 nm (blue), 561 nm (green yellow), and 405 nm (violet) lasers and appropriate combination of optical filters.

3 Methods

3.1 Construction of Reporter Strain of Mycobacteria

3.1.1 Preparation of Electrocompetent Cells

1. Streak the mycobacterial stock (mc^2155 or H37Rv) on 7H10-SUPPL agar plates, and incubate the plate at 37 °C to get single colonies.
2. Pick up a single colony from the plate with the help of a sterile loop, and inoculate 5 ml of 7H9-SUPPL broth and incubate at 37 °C with a shaker speed of 90 rpm for Mtb (200 rpm for Msmeg).
3. At an OD_{600} of 1–2, add 5 ml of primary inoculum to 45 ml of 7H9-SUPPL broth, and allow it to grow as in **step 2** for 72 h for Mtb (12–16 h for Msmeg).
4. Harvest the cells from the culture by centrifugation at 3000 × *g* for 10 min at RT (4 °C for Msmeg), and resuspend the pellet in an equal volume of 10% glycerol kept at RT (ice-cold for Msmeg).
5. Repeat **step 4** twice, each time using half of the volume of 10% glycerol to resuspend the cell pellet.
6. Make the single-cell suspension in 1 ml of 10% glycerol, and aliquot the suspension in 1.5 ml microcentrifuge tubes, each containing 100 μl of cell suspension.
7. The aliquots can be stored at −80 °C until use.

3.1.2 Electroporation

1. Add 1–5 μg of plasmid DNA (pMT100: pMV762-Peredox-mCherry) to 100 μl of competent cells in a microcentrifuge tube, and incubate the sample on ice for 5 min.
2. Transfer the contents of the tube to a prechilled 2 mm electroporation cuvette without creating any froth.

3. Tap the cuvette to bring down the contents to the bottom, and place the cuvette in an electroporator whose parameters have already been set (**step 4**).
4. Deliver a single pulse at 2.50 kV, 25 μF, and with the controller resistance of 1000 Ω; immediately recover the cells by adding 1 ml of 7H9 media supplemented with 10% OADC and incubating the culture in a tube at 37 °C in a shaker for 16 h (4 h for Msmeg).
5. Harvest the cells, plate them on 7H10-SUPPL agar plates, and incubate the plates at 37 °C for ~15 days (5 days for Msmeg).
6. Let the colonies grow bigger in size so that they appear pinkish in color.
7. Pick up the pink-colored colonies, and streak them on another agar plate containing selective media. Inoculate in 7H9-SUPPL broth and incubate the inoculated broth at 37 °C for another 10 days (*see* **Notes 1** and **2**).
8. Grow the culture to the log phase (monitor the OD_{600}), make stocks in freezing media (7H9 media with 20% glycerol), and store the stocks at −80 °C until use.

3.1.3 Preparation of the Bacterial Reporter Strain Cells for the Fluorescence Assays: Fluorescence Spectroscopy, FACS, and Confocal Microscopy

These assays can be performed on live cells as well as fixed cells.

1. The Peredox-mCherry probe has two excitation and two emission maxima. The cpTS absorbs 405 nm laser light and emits at 510 nm, while the mCherry absorbs 587 nm light and emits at 615 nm.
2. The bacterial cultures of the reporter strain and the strain containing the backbone vector without insert are streaked on 7H10-SUPPL agar plates and allowed to grow for 4–5 days (1 day for Msmeg) (*see* **Notes 3** and **4**).
3. A loop full of bacterial culture (reporter strain and normal strain) from the agar plate is inoculated into 10 ml of 7H9-SUPPL media; the culture is incubated in a square bottle at 37 °C in a shaker for 24 h (12 h for Msmeg).
4. While still in 7H9 media with the appropriate antibiotic for selection, 3–5 ml aliquots of mid-log phase culture (OD_{600}~0.5–0.8) are removed and then treated with different reagents (antibiotics, toxicants, or oxidoreductants) or subjected to different abiotic conditions (pH change, heat, and low- or high-O_2 conditions) for the time periods that you have chosen in your experiment design. Untreated controls/vehicle controls shall be included in the experiment.
5. After treatment, the cells are immediately harvested from 1 ml cultures and fixed in 4% PFA at room temperature for 15 min. These samples are washed three times with 1× PBS to remove PFA and then resuspended in PBS (*see* **Note 5**).

6. Live cell assays can be performed in vitro in 96-well plates or on agar pads using fluorimetry or confocal microscopy respectively (*see* **Notes 6** and 7).
7. The clumps of mycobacterial cells are broken by pipetting in and out using a 1 ml pipette. This single-cell suspension is now ready for the fluorescence measurement assays.

3.2 Fluorimetry

1. Fluorimeter settings.
2. A fluorimeter with the 96-well plate reader module could be used here. However, the basic settings of the fluorimeter will remain the same. With this reporter strain, the probe gets excited at 405 nm, and the fluorescence is recorded at 510 nm. The corresponding second fluorescence excitation peak is at 587 nm, and the corresponding emission wavelength is 615 nm. The green/red (405/587) ratio corresponds to the ratio of $NADH/NAD^+$ in the cell.
3. Dispense 200 μl of each sample into the corresponding well of a 96-well white fluorescence plate, and keep one of the wells filled with the nonfluorescent strain to record the background fluorescence. Assign at least three wells for each sample. Record the fluorescence in the fluorimeter using the following settings: orbital shaking for 5 s, reading the fluorescence from the top, temperature 25 °C, excitation at 405 and 587 nm, and emission at 510 and 615 nm.
4. When performing the fluorescent plate reader assay on live cells, the cells are grown in 7H9 media with 10% OADC in a 96-well format under the desired conditions of the assay for the desired time. At the end of the treatment, the 96-well plate is put in the plate reader, which has already been set with the above parameters, and the fluorescence is recorded, as above.
5. The data are exported as an Excel sheet for analysis. Normalization can be done by subtracting the background fluorescence of the nonfluorescent strain from the sample wells; the green/red ratio, i.e., the intensity at 405 nm/intensity at 587 nm, is plotted, which corresponds to the $NADH/NAD^+$ ratio in the cell. We use GraphPad Prism® for plotting and performing the statistical analysis of the data using one-way ANOVA or Student's *t*-test.

3.3 Flow Cytometry

1. The flow cytometer instrument that will be used in this assay should be equipped with a violet laser (405 nm) and a green laser (560 nm) and should have separate detectors for each color in order to minimize the interference of the signals and lead to better a separation of the signals without compensation.
2. After the preparation of the samples as described above, 1 ml of fixed culture is then diluted to 5 ml in a FACS tube with PBS.

3. For the FACS assay with live cells, instead of fixing the samples with 4% PFA after their treatment, cells are directly washed three times with PBS and resuspended in PBS in FACS tubes. The samples should be kept on ice until analyzed. The time between the sample preparation and analysis in the cell sorter should be minimized.
4. The samples are then analyzed using a BD FACSAria Cell Sorter (BD Biosciences) with the following settings: violet laser (405 nm) with band-pass filter 502 (band width 530/30) and yellow/green laser (561 nm) with band-pass filter 600 (band width 610/20).
5. The bacterial strain containing the empty vector acts as the unstained control for gating of fluorescent cells. We also use cells treated with thioridazine hydrochloride as a positive control for the increase in the NADH/NAD^+ ratio.
6. The ratio of the (530/30 nm) emission to the (610/20 nm) emission upon excitation with 405 nm laser light and 561 nm laser light, respectively, is calculated. This ratio (green/red) corresponds to the estimated NADH/NAD^+ ratio in the bacterial cytoplasm. Figure 3 provides a representative image of analysis.

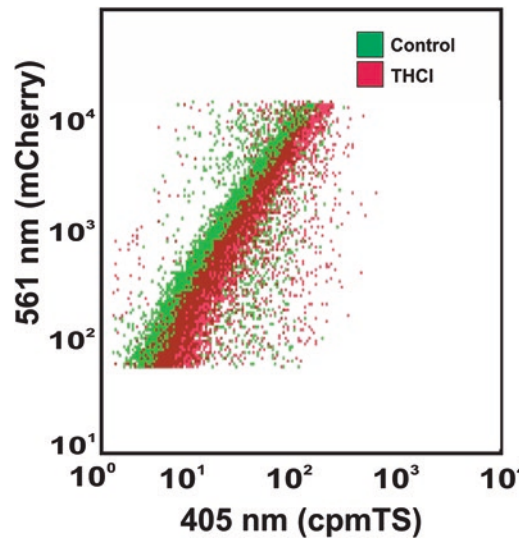

Fig. 3 Representative FACS data acquired using the NADH-reporter strain. The treated and untreated samples of the reporter strain, after taking necessary controls, are submitted to a FACSAria flow cytometer using lasers at 405 and 561 nm for excitation. The data are analyzed using FACSuite software in order to merge the ratiometric data in a single dot plot. The populations are color coded to easily distinguish between them in merged dot plot. In the above representation, the red represents the untreated control population, and the green represents the cells treated with thioridazine HCl, which clearly results in the increase of the green/red ratio that denotes the shifting of the population

3.4 Confocal Microscopy

1. Prepare the cover slips by washing them with 70% ethanol and wiping them clean using Kimwipes.
2. After preparing the samples (fixation and washing to remove the fixative) as described above, resuspend the sample in 200–400 μl of PBS.
3. Use a pipette or syringe with a needle to disrupt the cell clumps in order to make a single-cell suspension. Take 5 μl of this single-cell sample, mix it with 5 μl of SlowFade, and dispense a 10 μl drop of the mixture on a glass slide.
4. Carefully mount a clean coverslip over the sample without creating bubbles, followed by gently pressing the cover slip to squeeze the liquid out of it; use nail paint to seal the periphery.
5. After drying the slides for 1 h, image acquisition can be performed on the A1R Nikon confocal microscope equipped with 60× oil objective. It uses a CCD camera connected to a computer running NIS elements software.
6. Switch on the microscope, the violet laser (405 nm) with a 525/50 nm filter and the yellow/green laser (561 nm) with a 625/50 nm filter at least 15 min before image acquisition.
7. Prior to capturing the image, the cells in the sample should be in focus and fluorescent. This status can be confirmed by first focusing on the sample using low-resolution scanning (256 × 256 pixels) to avoid photobleaching of sample (*see* **Notes 8** and **9**).
8. Once focused, the images are captured at the resolution of 512 × 512 pixels and sometimes at 1024 × 1024 pixels with the pinhole of 1.0. The scan speed should be "half" and averaged four times to reduce the background signal (*see* **Note 10**).
9. The image captured by collecting the emission using the 525/50 nm filter upon excitation with the violet laser shows the Peredox (T-Sapphire) fluorescence, while the emission from excitation with the yellow/green laser using the 625/50 nm filter gives the mCherry fluorescence signal.
10. The T-Sapphire image window captured upon excitation with violet light is pseudocolored "green," while the mCherry image window captured upon excitation with yellow/green light is shown in "red."
11. Several programs, such as NIS elements, can also generate a pseudocolored ratiometric image by dividing the intensity of the 405 nm channel by that of the 561 nm channel in the image, pixel by pixel, to yield the image of the bacterial population with different green/red ratios that correspond to the different $NADH/NAD^+$ ratios inside the bacterial cells. Figure 4 provides representative confocal images along with ratiometric analysis.

3.5 Infection in Macrophages

1. In this study, we describe the protocol for the infection of RAW264.7 macrophages with the Mtb reporter strain expressing Peredox-mCherry, but this method can be extended to any other macrophages that can be cultured in vitro.
2. Streak the Mtb reporter strain stock on an agar plate, and then inoculate the resulting colony in 7H9 broth with the appropriate antibiotic, growing the resulting culture to mid-log phase (OD_{600}~0.8–1.0); make freezing stocks in freezing media (7H9 media with 20% glycerol), and keep them at −80 °C until use.
3. Thaw a stock of RAW264.7 macrophages, put the contents in a T25 flask containing warm (37 °C) Glutamax DMEM media supplemented with 10% FBS, and incubate the flask in a CO_2 incubator at 37 °C.
4. Before we begin, autoclave the coverslips after cleaning and wiping them dry by packing each separately in aluminum foil in an autoclavable box to prevent the coverslips from sticking to each other during autoclaving.
5. After 2 to 3 days, when the cells are 80–90% confluent, trypsinize and count the cells after washing them. Meanwhile, put autoclaved coverslips in 12-well plates, using tweezers, and seed the cells on coverslips at a density of 0.25×10^6 cells/well.

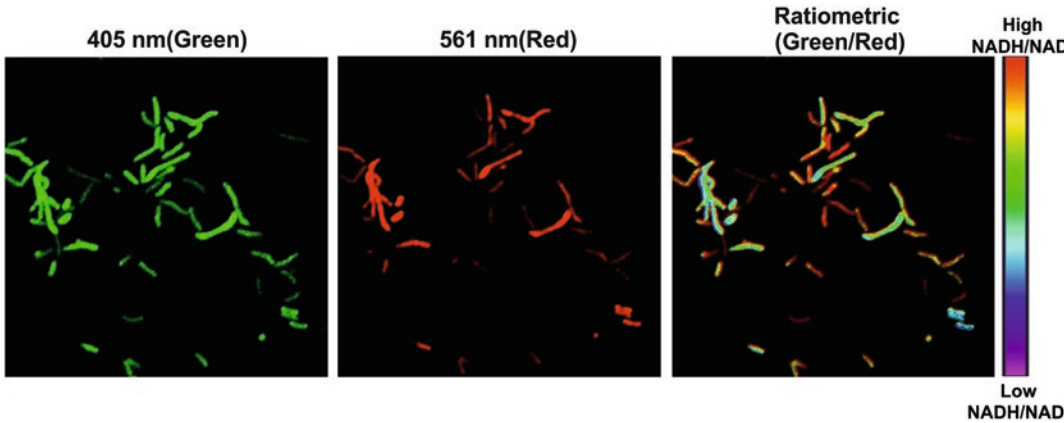

Fig. 4 Representative confocal image of the NADH-reporter strain of mycobacteria. The fixed cells of the reporter strain are imaged under a Nikon confocal microscope using NIS elements software for image acquisition upon excitation with a violet laser (405 nm, with a 525/50 nm filter) for cpTS and with a yellow/green laser (561 nm) for the mCherry protein, which emits at 625/50 nm. The obtained images are then subjected to analysis using the NIS analysis software from Nikon. The green channel image acquired using the 405 nm laser is then divided, pixel by pixel, by the 561 nm excited red channel image to obtain a ratiometric green/red image that represents the $NADH/NAD^+$ ratio. The bacterial cells are then selected individually to calculate the green/red ratio for each single bacterial cell, and the ratios are plotted using Graphpad Prism software

6. After 20 h of incubation in a CO_2 incubator at 37 °C, the DMEM complete media is replaced by DMEM media without antibiotics, followed by infection in the same media.
7. For infection, thaw 1 ml of the bacterial reporter strain stock, and spin it down to harvest the cells; wash once to remove the freezing media. Resuspend the cells in the same volume of DMEM without antibiotics, using a 1-ml disposable syringe fitted with a 25 G needle to make a single-cell suspension (*see* **Note 11**).
8. Add the bacterial suspension to the macrophage cells in the 12-well plate at a MOI of ~5 or 10 (depending on your infection efficiency), and incubate the plates in a CO_2 incubator at 37 °C for 2–3 h.
9. At the end of the incubation with the desired reagents or conditions, remove the media, fix the cells with 4% PFA for 15 min, and wash 3× with PBS to remove the PFA from the samples (*see* **Note 12**).
10. Using tweezers, mount the coverslips over a drop of SlowFade Antifade on a glass slide, seal the periphery using nail paint, and leave it to dry for 1 h in dark.
11. Proceed to confocal microscopy using the settings listed above for in vitro bacterial slide imaging (*see* **Note 13**).

4 Notes

1. The growth of transformants on the agar plates does not confirm the expression of the probe in the cytoplasm. The colonies shall be rechecked for the confirmation of expression under microscope. Fortunately, the Peredox probe-expressing colonies appear pink (due to expression of mCherry), making it easy to pick pink colonies for screening.
2. The colonies in which the expression of the protein is neither too low nor too high should be considered for use as a reporter strain.
3. While reviving the cultures from −80 °C, care must be taken to streak the stock on a 7H10 agar plate with the appropriate antibiotic prior to starting the liquid culture to avoid metabolic alterations of the bacterial stock in the liquid culture.
4. The control strain with the empty vector should be grown under similar conditions as the reporter strain to avoid the differences in the bacterial growth phases.
5. Handling too many samples together can lead to a long delay between the preparation of the first and last samples (mainly in

live cells), resulting in a difference in the incubation time and hence results.

6. The presence of discrete single cells on the image gives the data better resolution and helps in the single-cell analysis of the data by individuals when they are selecting bacteria using the NIS analysis software.
7. During the live cell analysis of the reporter strain using FACS and fluorimetry, try to avoid causing harsh mechanical stress to the cells, and minimize the time from the treatment to the analysis of the samples.
8. Prior to capturing the final confocal image, the samples should not be illuminated with high laser intensity; rather, the illumination of samples under low laser power could save the sample from photobleaching and photodamage.
9. Experiments with the Peredox probe (cpm T-Sapphire) use a high-power laser (405 nm), leading to the photobleaching of samples. One of the methods to avoid this photobleaching is to minimize the exposure of samples to this violet light, which can be achieved by compromising on the resolution to increase the scan speed, i.e., instead of capturing the images at 1084x1084 pixels, images could be captured at 512 × 512 or 256 × 256 pixel resolution.
10. Adjust the offset, PMT voltage, and laser power to make sure that the fluorescence intensity of the probe is not saturated during confocal microscopy, as the saturated fluorescence can result in artifacts due to the masking of fluorescence intensity distribution details.
11. During the infection of the macrophages, the breaking of cell clumps to form a single-cell suspension is essential to achieve homogeneous infection.
12. The fixative PFA should be removed completely from the sample by multiple washes with PBS, as it can result in autofluorescence signals during microscopy, which make the imaging difficult.
13. Before capturing the final confocal image, the samples should not be illuminated with high laser intensity; rather, the illumination of samples under low laser power could save the sample from photobleaching and photodamage.

Acknowledgments

This work was supported by funding from CSIR (OLP070) and Department of Biotechnology (BT/PR/5086/GBD/27/307/2011). We are thankful to Mr. Deepak Bhat for his help with

confocal microscopy. We are thankful to Dr. Hariom Kushwaha for managing the AK laboratory requirements. S.A.B. and I.K.I. are grateful to the CSIR for JRF and SRF. A.K. is supported by DST, India (DST/INT/AUS/GCP-7/13 and SR/SO/BB-0037/2013), and DBT, India (BT/PR15097/MED/29/237/2011), and CSIR through Supra Institutional Projects—BSC0210G (INFECT), BSC0211E (Bugs to drugs), and Network project BSC0119F (human microbiome).

References

1. Canto C, Menzies KJ, Auwerx J (2015) NAD(+) metabolism and the control of energy homeostasis: a balancing act between mitochondria and the nucleus. Cell Metab 22(1):31–53. https://doi.org/10.1016/j.cmet.2015.05.023
2. Beste DJ, Hooper T, Stewart G, Bonde B, Avignone-Rossa C, Bushell ME, Wheeler P, Klamt S, Kierzek AM, McFadden J (2007) GSMN-TB: a web-based genome-scale network model of *Mycobacterium tuberculosis* metabolism. Genome Biol 8(5):R89. https://doi.org/10.1186/gb-2007-8-5-r89
3. Sun F, Dai C, Xie J, Hu X (2012) Biochemical issues in estimation of cytosolic free NAD/NADH ratio. PLoS One 7(5):e34525. https://doi.org/10.1371/journal.pone.0034525
4. Dumollard R, Ward Z, Carroll J, Duchen MR (2007) Regulation of redox metabolism in the mouse oocyte and embryo. Development 134(3):455–465. https://doi.org/10.1242/dev.02744.
5. Chen S, Whetstine JR, Ghosh S, Hanover JA, Gali RR, Grosu P, Shi Y (2009) The conserved NAD(H)-dependent corepressor CTBP-1 regulates *Caenorhabditis elegans* life span. Proc Natl Acad Sci U S A 106(5):1496–1501. https://doi.org/10.1073/pnas.0802674106
6. Lin SJ, Ford E, Haigis M, Liszt G, Guarente L (2004) Calorie restriction extends yeast life span by lowering the level of NADH. Genes Dev 18(1):12–16. https://doi.org/10.1101/gad.1164804
7. Wolff KA, de la Pena AH, Nguyen HT, Pham TH, Amzel LM, Gabelli SB, Nguyen L (2015) A redox regulatory system critical for mycobacterial survival in macrophages and biofilm development. PLoS Pathog 11(4):e1004839. https://doi.org/10.1371/journal.ppat.1004839
8. Boshoff HI, Barry CE III (2005) Tuberculosis – metabolism and respiration in the absence of growth. Nat Rev Microbiol 3(1):70–80. https://doi.org/10.1038/nrmicro1065.
9. Rao SP, Alonso S, Rand L, Dick T, Pethe K (2008) The protonmotive force is required for maintaining ATP homeostasis and viability of hypoxic, nonreplicating *Mycobacterium tuberculosis*. Proc Natl Acad Sci U S A 105(33):11945–11950. https://doi.org/10.1073/pnas.0711697105
10. Bhat SA, Singh N, Trivedi A, Kansal P, Gupta P, Kumar A (2012) The mechanism of redox sensing in *Mycobacterium tuberculosis*. Free Radic Biol Med 53(8):1625–1641. https://doi.org/10.1016/j.freeradbiomed.2012.08.008
11. Trivedi A, Singh N, Bhat SA, Gupta P, Kumar A (2012) Redox biology of tuberculosis pathogenesis. Adv Microb Physiol 60:263–324. https://doi.org/10.1016/B978-0-12-398264-3.00004-8
12. Kumar A, Farhana A, Guidry L, Saini V, Hondalus M, Steyn AJ (2011) Redox homeostasis in mycobacteria: the key to tuberculosis control? Expert Rev Mol Med 13:e39. https://doi.org/10.1017/S1462399411002079
13. Vilcheze C, Weinrick B, Wong KW, Chen B, Jacobs WR Jr (2010) NAD+ auxotrophy is bacteriocidal for the tubercle bacilli. Mol Microbiol 76(2):365–377. https://doi.org/10.1111/j.1365-2958.2010.07099.x
14. Boshoff HI, Xu X, Tahlan K, Dowd CS, Pethe K, Camacho LR, Park TH, Yun CS, Schnappinger D, Ehrt S, Williams KJ, Barry CE III (2008) Biosynthesis and recycling of nicotinamide cofactors in *Mycobacterium tuberculosis*. An essential role for NAD in nonreplicating bacilli. J Biol Chem 283(28):19329–19341. https://doi.org/10.1074/jbc.M800694200
15. Sorci L, Ruggieri S, Raffaelli N (2014) NAD homeostasis in the bacterial response to DNA/RNA damage. DNA Repair (Amst) 23:17–26. https://doi.org/10.1016/j.dnarep.2014.07.014
16. Rodionova IA, Schuster BM, Guinn KM, Sorci L, Scott DA, Li X, Kheterpal I, Shoen C, Cynamon M, Locher C, Rubin EJ, Osterman AL (2014) Metabolic and bactericidal effects

of targeted suppression of NadD and NadE enzymes in mycobacteria. MBio 5(1). https://doi.org/10.1128/mBio.00747-13

17. Williamson DH, Lund P, Krebs HA (1967) The redox state of free nicotinamide-adenine dinucleotide in the cytoplasm and mitochondria of rat liver. Biochem J 103(2):514–527
18. Huang S, Heikal AA, Webb WW (2002) Two-photon fluorescence spectroscopy and microscopy of NAD(P)H and flavoprotein. Biophys J 82(5):2811–2825. https://doi.org/10.1016/S0006-3495(02)75621-X
19. Schneckenburger H, Wagner M, Weber P, Strauss WS, Sailer R (2004) Autofluorescence lifetime imaging of cultivated cells using a UV picosecond laser diode. J Fluoresc 14(5):649–654
20. Canelas AB, van Gulik WM, Heijnen JJ (2008) Determination of the cytosolic free NAD/NADH ratio in *Saccharomyces cerevisiae* under steady-state and highly dynamic conditions. Biotechnol Bioeng 100(4):734–743. https://doi.org/10.1002/bit.21813
21. Zhao Y, Jin J, Hu Q, Zhou HM, Yi J, Yu Z, Xu L, Wang X, Yang Y, Loscalzo J (2011) Genetically encoded fluorescent sensors for intracellular NADH detection. Cell Metab 14(4):555–566. https://doi.org/10.1016/j.cmet.2011.09.004
22. Hung YP, Albeck JG, Tantama M, Yellen G (2011) Imaging cytosolic NADH-NAD(+) redox state with a genetically encoded fluorescent biosensor. Cell Metab 14(4):545–554. https://doi.org/10.1016/j.cmet.2011.08.012
23. Brekasis D, Paget MS (2003) A novel sensor of NADH/NAD+ redox poise in *Streptomyces coelicolor* A3(2). EMBO J 22(18):4856–4865. https://doi.org/10.1093/emboj/cdg453
24. Bhat SA, Iqbal IK, Kumar A (2016) Imaging the NADH:NAD+ homeostasis for understanding the metabolic response of *Mycobacterium* to physiologically relevant stresses. Front Cell Infect Microbiol 6:145. https://doi.org/10.3389/fcimb.2016.00145

Chapter 15

Characterizing Cell Heterogeneity Using PCR Fingerprinting of Surface Multigene Families in Protozoan Parasites

Víctor Seco-Hidalgo, Antonio Osuna, and Luis Miguel de Pablos

Abstract

Parasites counteract the action of the immune system and other environmental pressures by modulating and changing the composition of their cell surfaces. Surface multigene protein families are defined not only by highly variable regions in length and/or sequence exposed to the outer space but also by conserved sequences codifying for the signal peptide, hydrophobic C-terminal regions necessary for GPI modifications, as well as conserved UTR regions for mRNA regulation. The method here presented exploits these conserved signatures for characterizing variations in the mRNA expression of clonal cell populations of protozoan parasites using a combination of nested PCR amplification and capillary electrophoresis. With this workflow, in silico gels from isolated cell clones can be generated, thus providing an excellent tool for analyzing cellular heterogeneity in protozoan parasites.

Key words Parasite, Cell heterogeneity, Gene expression, RNA, *Trypanosoma*, *Plasmodium*, *Leishmania*

1 Introduction

Cells are constitutively heterogeneous. In protozoan parasites, this heterogeneity is translated into a higher fitness and probability for surviving and hence for completing the life cycle. Conditions such as host immune pressure, drug pressure, vector and host metabolic and nutritional conditions, presence and magnitude of febrile episodes, host genetics, or presence of competing parasites are among the environmental pressures that protozoan parasites must counteract [1]. In unicellular protozoan parasites, the cell surface has a major role in protection and detection of all these changes, being many of its components key players in the communication of the cell with its outer space (cells, change in pH, nutrients or temperature, etc.). Although being highly packed and dense, many of these protozoan parasites are examples of dynamic cell surfaces with fluid plasma membranes, which are constantly changing in a combination of complexity and flexibility. This heterogeneity could be

Natasha S. Barteneva and Ivan A. Vorobjev (eds.), *Cellular Heterogeneity: Methods and Protocols*, Methods in Molecular Biology, vol. 1745, https://doi.org/10.1007/978-1-4939-7680-5_15,

either due to stochastic processes, where many molecular variants are constantly created and exposed to increase the long-term fitness of a cell population of parasites, or due to phenotypic plasticity processes where the variants are created in response to specific environmental signals [1].

In either case, these different molecular variants are components of multigene families of surface proteins that have been expanded in unicellular parasites and that have the ability of being degraded and/or replaced by new surface paralogs in short spaces of time. In such way, these rapid changes are reflected in cell-to-cell or cell population heterogeneity, which increases the chances of success within the parasite-host arms race. Examples of clonally variant gene expression have been found in STEVOR or RIFIN gene families of *Plasmodium falciparum* [2–4] or in the mucin-associated surface protein (MASP) multigene family of *Trypanosoma cruzi* [5]. Multigene surface protein families are widely extended within protozoan parasites as it is the case of var. family in *Plasmodium* spp. [6], smorf in *Babesia bovis* [7], SVSPs in *Theileria parva* [8], and *trans*-sialidase or mucin-like genes in *T. carassii* and *T. cruzi* [9, 10].

These multigene families are clear examples of how protozoan parasites maximize their genomes, where a rich repertoire of mechanisms leads to the amplification and diversification of surface molecules, including monoallelic expression, chromosome plasticity, aneuploidy, and/or a very promiscuous homologous recombination to generate surface polymorphic variants and expand its variability [11–13]. In the case of homologous recombination occurring between two similar or identical molecules of DNA, multigene families are specifically recombined due to the presence of conserved regions, which serve as unique scaffolds for recombination between homologous and nonhomologous chromosomes. Among these sequences, the N-(codifying for a signal peptide) and C-terminal (signal for GPI-anchoring) protein regions as well as 5′ or 3′UTR regions of the mRNAs are usually found to be the most conserved signatures. Thus, differences both in length and nucleotide compositions of hypervariable regions located between the conserved regions could be exploited and used to identify surface differences at the individual cell level [5–14]. Moreover, these differences can be further exploited for the isolation and characterization not only of cell heterogeneity but also of the antigenic content as it was shown for the IgM and IgG response against MASPs in *T. cruzi* experimental mice infections [15]. Here below, we presented a strategy for primer designing within multigene families, conserved regions, and further amplification of different clonal protozoan cell populations. In brief, the isolated mRNAs from clones or clonal populations of cells are resolved by capillary electrophoresis amplified after a semi-nested and nested PCR and finally analyzed and

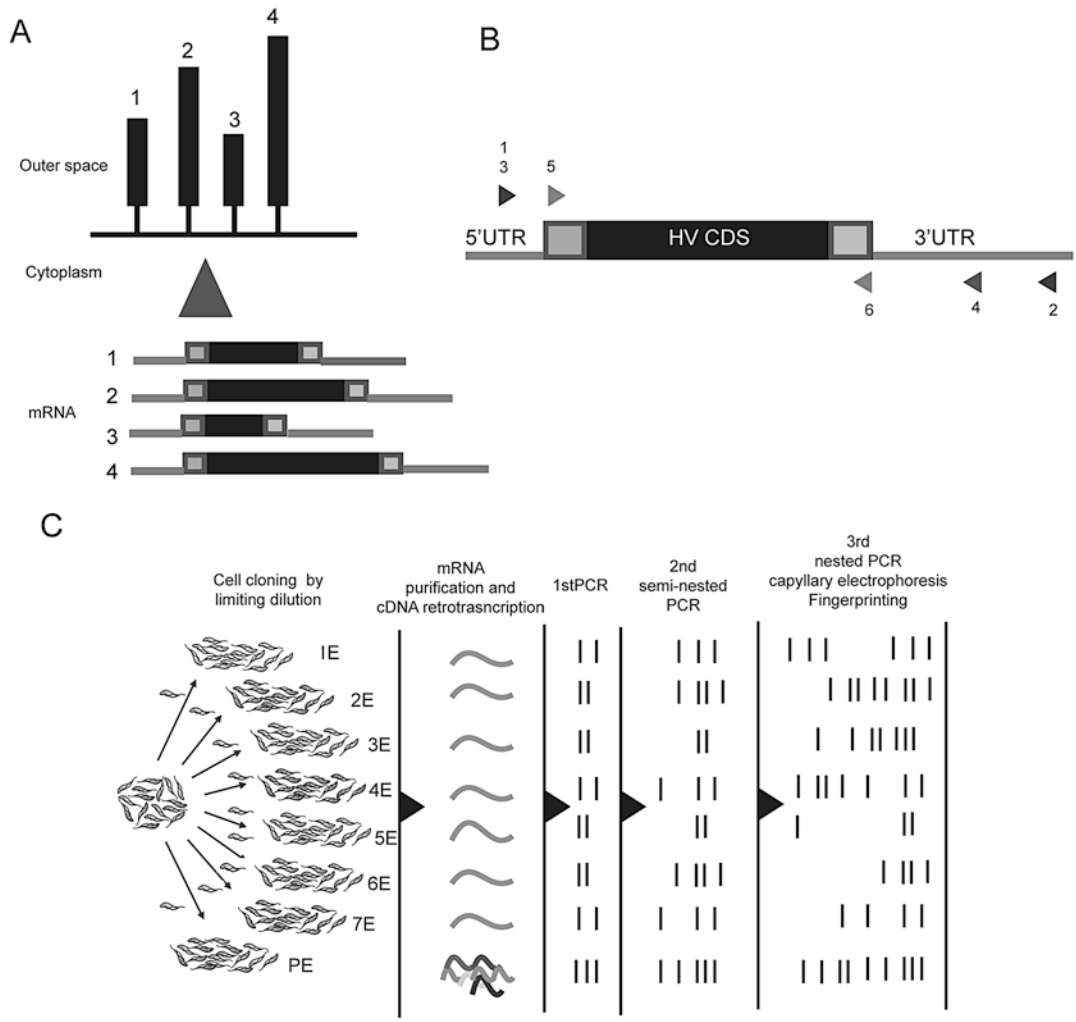

Fig. 1 Analysis of cellular heterogeneity using multigene family PCR fingerprinting. (**a**) Different mRNAs belonging to multigene surface proteins codify for different surface protein variants. Conserved regions are represented in gray and hypervariable regions in black. (**b**) Prototypical gene with potential conserved regions (in gray) for primer designing and amplification. First PCR, primers 1–2; second semi-nested PCR, primers 3–4; third nested PCR, primers 5–6. HV CDS: Hypervariable coding DNA sequence. (**c**) Workflow representing the five steps to obtain a final in silico gel of the expressed mRNA molecules belonging to targeted surface multigene family. In the example, 1E-7E represents seven different clonal populations of the epimastigote form of *T. cruzi* isolated by limiting dilution. PE means "parental" epimastigotes

compared using in silico gels (Fig. 1). With this protocol, we provide a detailed methodological description for the analysis of transcriptional variations using PCR fingerprinting among clonal cell populations of *Trypanosoma cruzi* as a unicellular protozoan parasite model organism. However, this methodology can be widely used for the study of other unicellular parasites expressing multigene protein families in their surfaces.

2 Materials

1. RPMI medium supplemented with 10% fetal bovine serum (FBS).
2. 96-well plates (Nunc).
3. Agarose.
4. RNeasy Mini Kit (Qiagen).
5. TURBO DNA-free™ Kit (Ambion).
6. Oligotex mRNA kit (Qiagen).
7. iScript Select cDNA synthesis kit (Bio-Rad Laboratories, Inc.).
8. ND-1000 spectrophotometer (Thermo Scientific).
9. Oligonucleotides labeled with 6-carboxyfluorescein (6-FAM).
10. Peak Scanner software (Applied Biosystems).
11. Interactive Binner (R script).
12. Fingerprinting II software (Bio-Rad).

3 Methods

3.1 Downloading the Genes of Interest

Download the sequences to be used as templates for nested PCR. In case of protozoan parasites, two main databases are frequently used for downloading sequences.

EupathDB: http://eupathdb.org/eupathdb/

GeneDB: http://www.genedb.org/Homepage

In this protocol example, the TriTrypDB database (http://tritrypdb.org/tritrypdb/, within EuPathDB database) was used for isolating conserved sequences within the genes belonging to the MASP multigene family of *T. cruzi*. To do so, introduce the term "MASP" keyword in the TriTrypDB gene text search box, and download the members of this family selecting "FASTA format" in the sequence retrieval tool. Within the download option, choose download mRNA sequences from transcription start to stop (MASP members have a conserved region not only the 5′ and 3′ ends of the CDS but also the 5′UTR and 3′UTR regions) (*see* **Note 1**).

3.2 Isolation of Conserved DNA Regions for Nested PCR Primer Designing

The main goal of this step would be to isolate conserved regions within the downloaded genes, so they can serve as templates for primer designing and further PCR fingerprinting. MEME Suite software (http://meme-suite.org/tools/meme) [16] is highly recommended for nucleotide motif discovery of ungapped regions (*see* **Note 2**). After the analysis, conserved regions of the desired longitude (we usually use between 50 and 100 Nts wide) are obtained and used for primer designing.

Finally and depending on the multigene complexity and depth of the analysis, two-step or three-step nested or semi-nested PCR could be employed for amplifying the maximum number of transcripts. For primer designing, use the isolated conserved regions above to isolate a sequence-tagged site (STS) using electronic PCR (https://www.ncbi.nlm.nih.gov/tools/epcr/) [17] and/or primer designing using programs such as eprimer3 (http://emboss.bioinformatics.nl/cgi-bin/emboss/eprimer3) for efficient PCR of the targeted multigene family.

Once conserve motifs and primers are designed, it is recommended to make a BLAST search within TriTryp or any other protozoan genome database to discard any potential off-targets.

In the case of MASP multigene family of *T. cruzi*, we used a semi-nested PCR (forward primer MASP 5′ Spliced Leader, reverse primer MASP 3′UTR) followed by a second step of nested PCR (forward primer 5′ end of MASP CDS, reverse primer 3′ end of MASP CDS) (Fig. 1b).

3.3 Cloning and Isolation of Cell Populations

Depending on the species, sample (in vitro culture or in vivo isolation of parasite cells), and/or conditions (temperature, pH, osmotic pressures, drug testing), multiple methods can be used for cell cloning such as cell sorting by FACS [18–20], agar colony formation [11, 21], microfluidics [22, 23], or cell cloning by limiting dilution [4, 5]. Since *T. cruzi* epimastigote cells are able to grow at concentrations down to one parasite/well, limiting dilution could be used as a method for the isolation of clonal populations of cells (*see* **Note 3**).

For cloning by limiting dilution, resuspend *T. cruzi* epimastigote cells at a concentration of ten parasites/ml in RPMI media, and seed 100 μl into 96-well plates (Nunc), leaving an empty well between samples to avoid cross-contaminations (*see* **Note 4**).

Grow the parasites at 27 °C for approximately 2 weeks (successful growth can be easily identified by a change in the pH (turning yellow) and density of the successful wells with clonal populations). Once the parasites reach the logarithmic phase of growth (approximately 1–5 × 10^6 cells/ml), the cultured 100 μl are transferred to 5 ml of RPMI media (1–5 × 10^4 cells/ml, labeled as Passage 1 (P1) culture). Finally, isolate the mRNA once the P1 culture reaches logarithmic growth (*see* **Note 5**).

3.4 mRNA Purification, RT-PCR, and Nested PCR

3.4.1 mRNA Purification and RT-PCR

Although the protocol used here follows what has performed in Seco-Hidalgo et al. [5], alternative methods for mRNA purification can be also used. In brief, RNA is extracted using the RNeasy Mini Kit (Qiagen, Hilden, Germany) and further treated with DNase I to avoid any DNA contamination (*see* **Note 6**). Next, the mRNA is purified using Oligotex mRNA kit (Qiagen, Hilden, Germany). The concentration and purity are measured using ND-1000 spectrophotometer (Thermo Scientific) (*see* **Notes 7** and **8**).

The mRNA is converted into cDNA using a reverse transcriptase step. To do so, any commercial kit could be used; in our hands, iScript cDNA synthesis kit (Bio-Rad Laboratories, Inc.) using random primers is efficient for a representative *T. cruzi* MASP cDNA population (*see* **Note 9**).

3.4.2 Nested Labeled PCR

Depending on the sensitivity, starting yields, and/or complexity of the target genes, a strategy of two-step or three-step nested PCR may be needed to obtain a broad spectrum of specific amplicons from the purified mRNA using the targeted conserved regions isolated as in Subheading 3.2.

In this example, we analyzed the heterogeneity of the MASP family of *T. cruzi* (close to 1500 members) [14], employing a three-step nested PCR, where the number of MASP amplicons was increased in each step (5) (Fig. 1a). An initial 25 μl PCR reactions were performed using 600 ng cDNA from each clonal population of cells and 3.3 μl of the amplified product for the second (semi-nested) and third (nested) PCR reaction, respectively (*see* **Note 10**).

To achieve a high-resolution identification of the amplicons, one of the primers used in the final nested PCR step (second or third) is linked to a fluorescent dye. As a result, fluorescently labeled amplicons are obtained for further analysis by capillary electrophoresis. One of the most common fluorescent dyes used for oligonucleotide labeling is the 6-carboxyfluorescein (6-FAM), although alternative fluorophores (JOE, VIC, NED, etc.) could be also employed (*see* **Note 11**). 6-FAM is reactive and water-soluble and has an absorbance maximum of 492 nm and an emission maximum of 517 nm.

3.5 Capillary Electrophoresis and Fingerprinting

Before proceeding with the capillary electrophoresis, it is essential to include an internal size standard in each sample (the last product of your nested labeled PCR) for achieving high run-to-run precision in sizing the DNA fragments. To distinguish between the targeted amplified products and the size standards, different fluorophores (like ROX, LIZ, or others) must be used. In our study, we employed the GeneScan™ 1200 LIZ size standard (Thermo) with a size range between 20 and 1200 bases (*see* **Note 12**).

The amplicons generated in the last step (third) of the nested labeled PCR are resolved in a capillary electrophoresis system (Fig. 1a); in this example, we worked with 3130 × 1 Genetic Analyzer (Applied Biosystems).

Next, peak identification and fragment sizing from electropherograms are obtained using Peak Scanner software (Applied Biosystems). Two different alternative analysis methods could be chosen: (1) Sizing Default, which assumes that primers have not been removed from the sample; and (2) Sizing Default_NPP

(NPP = no primer peak(s)), which should be used for your samples if the primers have been removed (*see* **Note 13**).

At this step, it is important to bear in mind the criteria for considering two close peaks as same or as different amplicons. To reduce the possible effects of this kind of potential error, there are available several free R scripts such as Interactive Binner or Automatic Binner. These algorithms implement a shifting window size binning strategy where the original data values (data from Peak Scanner; *see* **Note 14**) which fall in a specific interval, a bin or binning frame, are substituted by a representative value, often the central value of that interval. The distance between two consecutive binning frames is defined as the shift (Sh) value. Thereby, the mentioned scripts enable a user-defined choice of Sh and window size values to calculate the best binning frame for your data set. Thus, by submitting all the samples to the same analytic parameters, it is possible to optimally align the electrophoretic profiles getting a robust analysis without erroneous interpretations on the number of amplicons generated for each sample.

Finally, the edited data from the electropherograms are exported for a fingerprint analysis, where different software can be used. The example shown in Fig. 2 was performed using Fingerprinting II (Bio-Rad). This program creates a high-resolution in silico gel, including a cluster analysis which groups the samples according to their profile of bands based on (1) binary coefficients, considering the presence/absence of band (Jaccard, Dice, Jeffrey's x, or Ochiai coefficients), or (2) on more complete coefficients which calculate similarity based upon intensity bands (Pearson correlation or Cosine coefficient) (Fig. 2).

Fig. 2 Cellular heterogeneity of clonal populations compared using fingerprinting. The products of the three-step nested PCR of different samples (clonal populations of *T. cruzi*) were submitted to capillary electrophoresis and further processed using Fingerprinting II (Bio-Rad). The results window shows a dendrogram (left), the in silico gel (center), and the similarity matrix (right) that can be used for direct comparisons

In silico gels obtained using the protocol described above offers the possibility for multiple comparisons between cell clones and clonal populations, which are useful for showing cellular heterogeneities existing within the mRNA expression of a multigene family in the organism of interest.

4 Notes

1. The use of 5′UTR and 3′UTR regions as templates for amplification as they are often conserved in multigene surface protein families is recommended.
2. In MEME software, the sequences uploaded should not contain more than 60,000 characters and must be in FASTA format. If the characters of the sequences exceed the maximum, split the downloaded sequences into regions (for instance, 5′UTR + 5′ of the CDS by one hand and 3′ CDS + 3′UTR by the other) to make the analysis feasible.
3. Limiting dilution is highly recommended for isolating clonal populations parasites in in vitro optimized cultures, which are able to grow from concentrations of one cell per well.
4. To amplify clonal cultures of parasites, it is recommended to use highly replicative phases of the parasites, preferentially at logarithmic phase of growth.
5. For limiting dilution assays, it is recommended to test conditioned media mixing 1:1 fresh media with filtered supernatant from logarithmic-growing cultures and/or increase the concentration of fetal bovine serum (FBS) up to 20%.
6. We recommend TURBO DNA-free™ Kit (Ambion) as the method to be used to minimize potential mRNA lost.
7. For samples with limited starting material, RNeasy Micro Kit (Qiagen) or similar kits might be needed.
8. Check the mRNA purity and integrity by making PCR of a housekeeping gene with the eluted purified mRNA.
9. Depending on the source and the genes of interest, we recommend to perform trials using random, oligo-dT, or specific primers (i.e., specific to conserved region on 3′UTR of the genes of interest) to decide the most efficient method for obtaining the most representative cDNA population.
10. After two-step or three-step nested PCRs, the high numbers of amplicons obtained make the analysis of clonal differences among samples by conventional electrophoresis difficult. Despite of this limitation, the conventional agarose electrophoresis is necessary to check the quality of the amplifications and to determine the best step (second or third) of the nested PCR to be submitted for capillary electrophoresis.

11. The selection of the dye depends on the capillary electrophoresis system used and has to be considered prior to the primer designing before the last step in nested labeled PCR strategy.
12. As warned in **Note 11**, the selection of the fluorescent dye depends on the capillary electrophoresis system available but also on the estimated size of the amplicons to analyze.
13. Prior to the capillary electrophoresis, an important consideration has to be done. If the analysis of cellular heterogeneity is not focused on amplicons smaller than 100 bp, it is recommended to submit your amplified samples to a PCR Purification Kit, as QIAquick PCR Purification Kit (Qiagen). In this way, the excess of labeled primers, which could disturb the fluorescence signal from the specific amplicons, is removed increasing the quality of the analysis.
14. For shifting window size binning strategy, it is important to remove the lines that contain missing information from the Peak Scanner output file, being only necessary to copy to your favorite tabulation software the peak size area and height fields for importing to the Interactive Binner.

References

1. Seco-Hidalgo V, Osuna A, Pablos LM (2015) To bet or not to bet: deciphering cell to cell variation in protozoan infections. Trends Parasitol 31(8):350–356. https://doi.org/10.1016/j.pt.2015.05.004
2. Blythe JE, Surentheran T, Preiser PR (2004) STEVOR—a multifunctional protein? Mol Biochem Parasitol 134:11–15
3. Niang M, Yan Yam X, Preiser PR (2009) The *Plasmodium falciparum* STEVOR multigene family mediates antigenic variation of the infected erythrocyte. PLoS Pathog 5:e1000307
4. Rovira-Graells N, Gupta AP, Planet E et al (2012) Transcriptional variation in the malaria parasite *Plasmodium falciparum*. Genome Res 22:925–938
5. Seco-Hidalgo V, De Pablos LM, Osuna A (2015) Transcriptional and phenotypical heterogeneity of *Trypanosoma cruzi* cell populations. Open Biol 5:150190. https://doi.org/10.1098/rsob.150190
6. Kyes SA, Kraemer SM, Smith JD (2007) Antigenic variation in *Plasmodium falciparum*: gene organization and regulation of the var multigene family. Eukaryot Cell 6:1511–1520
7. Ferreri LM, Brayton KA, Sondgeroth KS et al (2012) Expression and strain variation of the novel "small open reading frame" (smorf) multigene family in *Babesia bovis*. Int J Parasitol 42:131–138
8. Schmuckli-Maurer J, Casanova C, Schmied S et al (2009) Expression analysis of the *Theileria parva* subtelomere-encoded variable secreted protein gene family. PLoS One 4:e4839
9. Freitas LM, dos Santos SL, Rodrigues-Luiz GF et al (2011) Genomic analyses, gene expression and antigenic profile of the trans-sialidase superfamily of *Trypanosoma cruzi* reveal an undetected level of complexity. PLoS One 6:e25914
10. Aguero F, Campo V, Cremona L et al (2002) Gene discovery in the freshwater fish parasite *Trypanosoma carassii*: identification of trans-Sialidase-like and mucin-like genes. Infect Immun 70:7140–7144
11. Ubeda JM, Raymond F, Mukherjee A et al (2014) Genome-wide stochastic adaptive DNA amplification at direct and inverted DNA repeats in the parasite *Leishmania*. PLoS Biol 12:e1001868
12. Sterkers Y, Crobu L, Lachaud L et al (2014) Parasexuality and mosaic aneuploidy in *Leishmania*: alternative genetics. Trends Parasitol 30:429–435
13. Reis-Cunha JL, Rodrigues-Luiz GF, Valdivia HO et al (2015) Chromosomal copy number

variation reveals differential levels of genomic plasticity in distinct *Trypanosoma cruzi* strains. BMC Genomics 16:499. https://doi.org/10.1186/s12864-015-1680-4

14. Bartholomeu DC, Cerqueira GC, Leao ACA et al (2009) Genomic organization and expression profile of the mucin-associated surface protein (masp) family of the human pathogen *Trypanosoma cruzi*. Nucleic Acids Res 37:3407–3417
15. dos Santos SL, Freitas LM, Lobo FP et al (2012) The MASP family of *Trypanosoma cruzi*: changes in gene expression and antigenic profile during the acute phase of experimental infection. PLoS Negl Trop Dis 6:e1779. https://doi.org/10.1371/journal.pntd.0001779
16. Bailey TL, Boden M, Buske FA et al (2009) MEME SUITE: tools for motif discovery and searching. Nucleic Acids Res 37:W202–W208
17. Schuler GD (1997) Sequence mapping by electronic PCR. Genome Res 7:541–550
18. Schulz D, Mugnier MR, Boothroyd CE et al (2016) Detection of *Trypanosoma brucei* variant surface glycoprotein switching by magnetic activated cell sorting and flow cytometry. J Vis Exp 116. https://doi.org/10.3791/54715
19. Boissière A, Arnathau C, Duperray C et al (2012) Isolation of *Plasmodium falciparum* by flow-cytometry: implications for single-trophozoite genotyping and parasite DNA purification for whole-genome high-throughput sequencing of archival samples. Malar J 11:163. https://doi.org/10.1186/1475-2875-11-163
20. Nair S, Nkhoma SC, Serre D et al (2014) Single-cell genomics for dissection of complex malaria infections. Genome Res 24:1028–1038
21. Akagi T, Sasai K, Hanafusa H (2003) Refractory nature of normal human diploid fibroblasts with respect to oncogene-mediated transformation. Proc Natl Acad Sci U S A 100:13567–13572
22. Geislinger TM, Chan S, Moll K et al (2014) Label-free microfluidic enrichment of ring-stage *Plasmodium falciparum*-infected red blood cells using non-inertial hydrodynamic lift. Malar J 13:375. https://doi.org/10.1186/1475-2875-13-375
23. Hochstetter A, Stellamanns E, Deshpande S et al (2015) Microfluidics-based single cell analysis reveals drug-dependent motility changes in trypanosomes. Lab Chip 15(8):1961–1968. https://doi.org/10.1039/c5lc00124b

Chapter 16

Assessing Carbon Source-Dependent Phenotypic Variability in *Pseudomonas putida*

Pablo I. Nikel and Víctor de Lorenzo

Abstract

The soil bacterium *Pseudomonas putida* is rapidly becoming a platform of choice for applications that require a microbial host highly resistant to different types of stresses and elevated rates of reducing power regeneration. *P. putida* is capable of growing in a wide variety of carbon sources that range from simple sugars to complex substrates such as aromatic compounds. Interestingly, the growth of the reference strain KT2440 on glycerol as the sole carbon source is characterized by a prolonged lag phase, not observed with other carbon substrates. This macroscopic phenomenon has been shown to be connected with the stochastic expression of the *glp* genes, which encode the enzymes needed for glycerol processing. In this protocol, we propose a general procedure to examine bacterial growth in small-scale cultures while monitoring the metabolic activity of individual cells. Assessing the metabolic capacity of single bacteria by means of fluorescence microscopy and flow cytometry, in combination with the analysis of the temporal takeoff of growth in single-cell cultures, is a simple and easy-to-implement approach. It can help to understand the link between macroscopic phenotypes (e.g., microbial growth in batch cultures) and stochastic phenomena at the genetic level. The implementation of these methodologies revealed that the adoption of a glycerol-metabolizing regime by *P. putida* KT2440 is not the result of a gradual change in the whole population, but it rather reflects a time-dependent bimodal switch between metabolically inactive (i.e., not growing) to fully active (i.e., growing) bacteria.

Key words *Pseudomonas putida*, Metabolic stochasticity, Phenotypic variability, Flow cytometry, Central carbon metabolism, Metabolic engineering

1 Introduction

The last few years have witnessed a significant increase in the number of microorganisms that can be metabolically engineered with dedicated tools of contemporary synthetic biology [1–5]. *Pseudomonas putida*, a soil bacterium originally isolated from a soil sample in Japan [6], has become an attractive host for metabolic engineering due to a number of reasons [7]. A fast growth, a low nutrient demand, an extremely versatile metabolism [8, 9], and a high capacity to supply redox power (e.g., NADPH) [10–13] are only a few advantages that render *P. putida* an interesting host for

Natasha S. Barteneva and Ivan A. Vorobjev (eds.), *Cellular Heterogeneity: Methods and Protocols*, Methods in Molecular Biology, vol. 1745, https://doi.org/10.1007/978-1-4939-7680-5_16,

biotechnological applications [14–20]. Furthermore, this species tolerates a wide operational process window, including very variable pH values, high temperature, as well as higher levels of toxic substances and organic solvents (some of them, e.g., toluene or *m*-xylene, can also be used as carbon sources by some strains of *P. putida* [21]).

The growth properties of the type strain KT2440 [22, 23] have been extensively studied in more or less *traditional* carbon sources, e.g., glucose, organic acids, and benzoate. Less attention has been paid, however, to the physiology and metabolism of *P. putida* when cells are grown on glycerol. From a biotechnological point of view, glycerol is an interesting substrate that is readily available since it constitutes a by-product of the biodiesel industry [24–27]. Cells grown on this substrate undergo a complex transcriptional response [28] that mostly affects genes involved in glycerol catabolism, central metabolic pathways, and those encoding components of the respiratory chain [29]. A noteworthy feature consistently detected in glycerol cultures is an anomalously long lag phase before any noticeable growth is observed. This particular situation is not perceived when the cells are cultured on glucose or succinate under the same conditions. We have demonstrated before that exposure of strain KT2440 to glycerol led to the appearance of two subpopulations that differ in their metabolic activity on the substrate and that the relative proportion of these bacterial subpopulations changes with time [30]. These observations challenge the customary view of prokaryotic growth and metabolism as a homogeneous and co-occurring process in space and time [31, 32]. In this context, the emergence of methodologies for studying bacteria at the single-cell level [33–35] revealed a complete repertoire of responses of individual microorganisms to specific environmental conditions, which cannot be captured by the traditional cultivation protocols [36]. Diversification of the metabolism in single cells within otherwise clonal populations can be seen as a particular case of phenotypic variation in which different regulatory or epigenetic traits lead to the stochastic manifestation of alternative features in otherwise isogenic individuals [37–39]. The phenomenon is broadly known as *persistence*, i.e., the occurrence of an alive but nongrowing fraction of cells in a bacterial pool is a prime example in this respect [40, 41].

In the present protocol, we present a general method to investigate the behavior of bacterial cells in single-cell cultures to disclose potential phenotypic variation phenomena. Using the distinctive growth pattern of *P. putida* KT2440 in glycerol cultures as an example, a combination of small-scale cultivation techniques and flow cytometry (FC)-assisted exploration of metabolic activities in individual bacteria is implemented to expose phenotypic variations related to the use of different carbon sources. This method can be extended to any other situation where the

occurrence of a given property in single bacterial cell results in a growth advantage with respect to the rest of the population.

2 Materials

General considerations and precautions. Always wear a laboratory coat, disposable gloves, and a protective eyewear whenever necessary. Clean the working areas with 70% (v/v) ethanol, before and after use. The guidelines provided below involving FC analysis should be considered a general procedure, and it may need further adjustments depending on the cytometer being used. Carefully follow the specific manufacturer's instructions when operating FC equipment. All chemicals are reagent or culture grade unless otherwise indicated. The following section lists specialty chemicals, reagents, kits, and equipment for the described applications and methods.

1. Glucose, glycerol, and reagents needed for the preparation of M9 minimal medium: $Na_2HPO_4{\cdot}7H_2O$, KH_2PO_4, NH_4Cl, and NaCl.
2. Lysogeny broth (LB) medium. LB medium: 15.5 g of the commercial medium in 1 L of DI water sterilized by autoclaving.
3. An M9 salt mixture is prepared as a 10× concentrated solution and autoclaved. 10× M9 solution: 128 g of $Na_2HPO_4{\cdot}7H_2O$, 30 g of KH_2PO_4, 5 g of NaCl, and 10 g of NH_4Cl. Just prior to use, this concentrated solution is diluted with sterile DI water and added with $MgCl_2$, a trace element solution, and glucose or glycerol as needed. $MgCl_2$ is added at 0.2 g/L from a filter-sterilized 2% (w/v) stock. A trace element solution is added at 2.5 mL/L. Glucose is added at 20 mM from a filter-sterilized 20% (w/v) stock, and glycerol is added at 40 mM from a filter-sterilized 0.8 M stock. If necessary, bacteriological agar (e.g., BD Biosciences cat. # BP1423-2) is added at a final concentration of 15 g/L when preparing solid culture media. All culture media are freshly prepared for each experiment.
4. M9 minimal medium is added with either glucose at 20 mM or glycerol at 40 mM as the only carbon source.
5. Glucose and glycerol enzymatic assay kits.
6. Deionized (DI) water, resistivity ≥18 MΩ/cm at 25 °C.
7. Benchtop microcentrifuge (capable of reaching at least 14,000 × *g*).
8. Microcentrifuge tubes (1.5 mL).

9. Disposable 12 × 75 mm BD Falcon™ capped polystyrene tubes (BD Biosciences, USA) or equivalent.
10. Nitrocellulose filters (0.45 μm).
11. UV-visible spectrophotometer [e.g., Ultrospec 3000 *Pro* UV-vis spectrophotometer (Biochrom Ltd., Cambridge, UK)].
12. Sterile serological pipettes. Micropipettes (including an eight-channel automatic pipette) and the appropriate tips.
13. Bio-Pure™ pipetting reservoir.
14. 0.9% (w/v) NaCl solution. This solution can be indefinitely stored at room temperature (*see* **Note 1**).
15. Erlenmeyer flasks (nominal volume = 50 mL).
16. Incubator shaker with temperature control and rotary agitation.
17. 10 mM sodium phosphate buffer (pH = 7.4): 8.4 mL of 1 M Na_2HPO_4 and 1.6 mL of 1 M NaH_2PO_4, diluted to 1 L; adjust the pH with the concentrated Na_2HPO_4 or Na_2HPO_4 solutions as appropriate before bringing the solution up to 1 L. Phosphate-buffered saline (PBS, composed of 137 mM NaCl, 2.7 mM KCl, 1.8 mM KH_2PO_4, and 10 mM Na_2HPO_4, pH = 7.4) can be used instead of or in addition to sodium phosphate buffer. These buffers can be stored for up to 3 months at room temperature.
18. Microplate reader.
19. Microtiter plates, 96 wells, clear bottom.
20. Flow cytometer [e.g., MACSQuant™ VYB cytometer (Miltenyi Biotec, Germany), capable of detecting fluorescent compounds and particles with excitation and emission wavelength maxima of 493 nm and 636 nm (for propidium iodide and PI, respectively) and 490 nm and 520 nm (for the main component of the vitality and metabolic staining kit, respectively)]. The flow cytometer used in the determinations described herein is equipped with a diode-pumped solid-state (DPSS) laser, used for excitation at 488 nm. The RSG fluorescence signal is acquired with a 525/40 nm band-pass filter. The PI fluorescence signal is acquired with a 610 nm long-pass filter.
21. Software for analysis of FC data [e.g., Cyflogic™ 1.2.1 software (CyFlo Ltd., Turku, Finland) or FlowJo v. 9.6.2 software (FlowJo LLC, USA)].
22. *Bac*Light™ RedoxSensor™ Green (RSG) vitality and metabolic staining kit (ThermoFisher Scientific Ltd.). The reagent is a 1 mM solution of RSG in dimethyl sulfoxide (DMSO). Store this solution at −20 °C protected from light, and avoid many cycles of freezing and thawing as it could affect the RSG

reagent. Stored properly, the kit components should remain stable for at least 1 year.

23. 1 mg/mL PI (3,8-diamino-5-[3-(diethylmethylammonio) propyl]-6-phenylphenanthridinium diiodide) solution in DMSO. Store this solution at −20 °C protected from light, and avoid many cycles of freezing and thawing (a good practice is to work with small aliquots of the reagent that are discarded after use) (*see* **Note 2**).

3 Methods

3.1 Single-Cell Batch Cultures

1. Start a pre-inoculum culture of the strain to be tested in LB medium in capped polystyrene tubes (e.g., 2 mL of LB medium in a 12 × 75 mm tube) by dispersing a fresh single colony from an LB medium plate (*see* **Note 3**). In the case of *P. putida* KT2440, incubate the tubes with rotary agitation (e.g., 170 rpm) at 30 °C for 18 h.
2. Dilute 1:1000 the pre-inoculum bacterial culture in 10 mL of fresh LB medium placed in a 50 mL Erlenmeyer flask. Incubate as indicated in Subheading 3.1, **step 1**.
3. After 18 h, measure the OD_{600} of an appropriate dilution of this culture [in 0.9% (w/v) NaCl] in a spectrophotometer.
4. Centrifuge 5 mL of the bacterial suspension at room temperature (5 min at 8000 × *g* or 1 min at 14,000 × *g*) in a benchtop microcentrifuge.
5. Distribute the bacterial culture in several microcentrifuge tubes in this step (e.g., by placing 1 mL of bacterial suspension in several 2 mL microcentrifuge tubes), so that enough inoculum is available when (and if) needed.
6. Wash the cell suspension once with 1 mL of 0.9% (w/v) NaCl, and repeat the centrifugation step as described above.
7. Resuspend the biomass in each tube in 1 mL of 0.9% (w/v) NaCl. Adjust the OD_{600} of the suspension to 0.05 with an appropriate volume of the fresh culture medium to be used in the actual experiment (i.e., M9 minimal medium added with either glucose or glycerol). This suspension is the actual inoculum with which the single-cell batch cultures will be started.
8. Fill a 96-well microtiter plate by distributing M9 minimal medium containing glucose (160 μL per well) under sterile conditions. Use an eight-channel automatic pipette and a pipette reservoir to keep the culture medium.
9. Place the inoculum prepared in **step 7** in a different pipette reservoir, and add 40 μL of this suspension to the second column in the microtiter plate [i.e., the final volume will be

now 200 μL, and the initial OD_{600} will be 0.01, since the cell suspension used as inoculum has been diluted (1:5)]. Mix the contents of each well by pipetting the suspension up and down. Change the pipette tips and carefully transfer 40 μL of the cell suspension into the third column of the microtiter plate, so that the cell suspension is diluted (1:5) again (Fig. 1a).

10. Repeat the dilution procedure four times. Leave the first and twelfth columns filled with non-inoculated culture medium (i.e., the first and the last column in the microtiter plate) to serve as the blank for OD_{600} measurements.
11. Place the microtiter plates in an appropriate reader, and grow the cultures at 30 °C and rotary agitation (e.g., 15 s prior to each turbidimetric measurement) for as much as 72 h, taking OD_{600} measurements every 30 min.
12. Subtract the mean OD_{600} determined in the columns left as blanks from the OD_{600} in each well containing bacteria, and plot the growth curves as OD_{600} versus time (h). Results of turbidity measurements computed during exponential growth (log-linear regression of OD_{600} versus time) are used to calculate the specific growth rate, μ (h^{-1}), according to $\mu = [\ln(OD_{600} \text{ at } t) - \ln(OD_{600} \text{ at } t_0)]/(t - t_0)$.
13. Calculate the extension of the lag phase, λ (h), as $\lambda = t_{\Delta OD} - [\ln(OD_{600} \text{ at } t) - \ln(OD_{600} \text{ at } t_0)]/\mu$, where $t_{\Delta OD}$ is the time at which an increase of OD_{600} up to 0.05 is first noticed for any given well. The rationale behind these calculations has been explained in detail by Dalgaard and Koutsoumanis [42], and the reader is referred to this article for mathematical considerations on the calculations proposed herein.
14. Examine the growth curves and the corresponding λ values for each well, and select the dilution factor that results in $\lambda < 2$ h for glucose cultures ($D_{\lambda < 2\,h}$). With this information, set up a new experiment, in which exactly the same dilution of the inoculum culture ($D_{\lambda < 2\,h}$) is distributed in the entire microtiter plate (Fig. 1b). This experiment serves as the standard condition (i.e., a control experiment) to which the rest of the cultures on any given carbon source will be compared to. Under these conditions, the values of μ and λ should be similar in each well (with a typical standard error of ±10%).
15. Take aliquots of at least ten independent wells when OD_{600} = 0.1, 0.25, and 0.5 (for *P. putida* KT2440, the later OD_{600} value corresponds to the mid-exponential growth phase); dilute the bacterial suspensions in sterile 0.9% (w/v) NaCl in tenfold steps. Plate the resulting dilutions in triplicates onto LB medium plates (e.g., plate the 10^{-4}, 10^{-5}, 10^{-6}, and 10^{-7} dilutions). Incubate the plates upside down at 30 °C

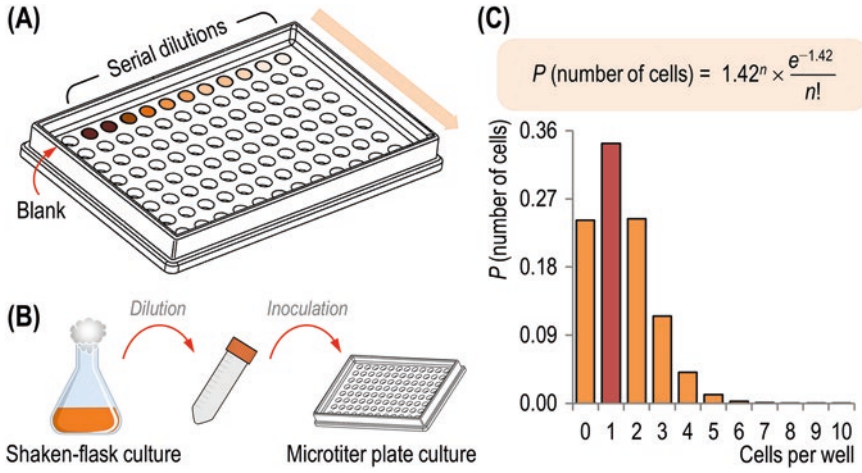

Fig. 1 General procedure for the implementation of single-cell batch cultures. (**a**) As a first step, the bacterial cell culture used as an inoculum (e.g., in LB medium) is serially diluted in fresh culture medium in 96-well microtiter plates in fivefold steps so that a wide range of initial cell densities are covered in the same plate. Bacterial growth in each well (estimated as the optical density measured at 600 nm, OD_{600}) is monitored over 72 h in a microtiter plate reader. Note that a column of wells is filled with fresh medium (i.e., no bacteria) and used as the blank for the rest of the OD_{600} measurements within the plate. (**b**) Once the right dilution of the inoculum needed to obtain single-cell cultures has been determined, a larger volume of an 18-h culture is diluted in fresh culture medium, and the cell suspension is now distributed in microtiter plates in order to monitor bacterial growth starting from a single cell in at least 500 independent wells. (**c**) Probability of inoculating a given number of cells in a particular well in the microtiter plate, as estimated by the *Poisson probability distribution*. After dilution of the cell suspension and its inoculation in independent wells, and due to stochastic variations (e.g., small differences in the volume transferred into each well), the actual number of cells per well (n) is not known. The probability P of inoculating zero, one, two, three, and up to ten cells per well is shown, indicating that the probability of inoculating a single cell is the most likely outcome. Also, note that P rapidly decreases down to zero beyond five cells per well. Adapted from Nikel et al. [30]

for at least 18 h, and count the number of colony-forming units (CFUs) in each plate afterward.

16. Determine the correlation factor (k) between CFUs and OD_{600} under the standard culture conditions. The value of k is determined by linear regression of CFUs versus OD_{600}, k being the regression coefficient in the equation $CFUs = k \times OD_{600} + b$. The parameter b is a constant. The k factor will be used in all the subsequent experiments to standardize the number of bacteria inoculated in each well (*see* **Note 4**).

17. Using k, estimate the dilution needed for any given inoculum to expect 1 CFU per well by measuring the OD_{600} of an appropriate dilution of the bacterial suspension. Considering that each well in the microtiter plate will be filled with 200 μL of culture medium, this would correspond to 5 CFUs/mL. Wash the cells with 0.9% (w/v) NaCl once, as indicated in Subheading 3.1, **step 6**, and dilute the bacterial suspension as needed in fresh M9 minimal medium containing either

glucose or glycerol. Distribute 200 μL of this suspension in each well in the microtiter plate, and incubate the cultures as indicated in Subheading 3.1, **step 11**. By following the procedure indicated in this section, it can be easily demonstrated that the maximal probability in a Poisson distribution of CFUs per well is that each well will receive 1 CFU (Fig. 1c).

18. Plot the OD_{600} values of individual well versus time (h) (Fig. 2a). In the case of glycerol cultures, it can be easily seen that there is a wide range of λ values in the plot. A new kinetic parameter is introduced here for the characterization of single-cell batch cultures, the so-called *time of metabolic response* (t_{MR}, h). This growth parameter is the time needed for any given culture to reach an OD_{600} of 60% of the maximum OD_{600} reached in stationary phase [i.e., OD_{600} (t_{MR})]. In the case of *P. putida* KT2440, the maximum OD_{600} observed in glycerol cultures is 0.5, and then t_{MR} is the time needed for a bacterial culture in any given well to reach OD_{600} = 0.3.
19. Record the characteristic t_{MR} value for each culture in at least 1000 independent wells. Plot the number of cultures that reached OD_{600} (t_{MR}) versus t_{MR} for each carbon source (Fig. 2b). The corresponding distribution of frequencies provides a first hint of the existence of potential phenotypic variation phenomena. In the case of *P. putida* KT2440, all the

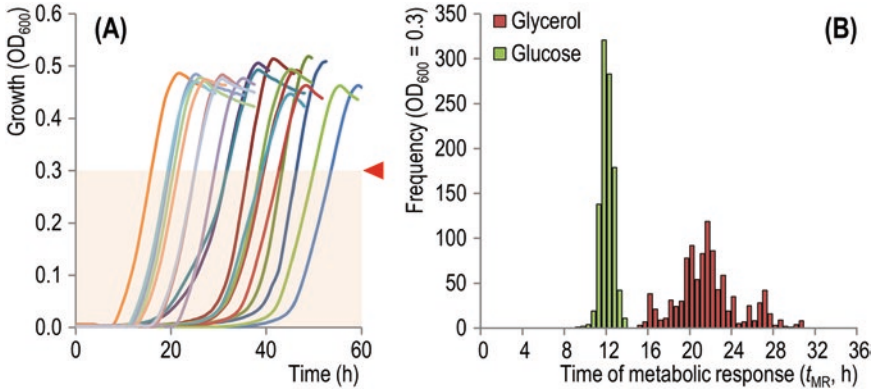

Fig. 2 Determination of growth parameters in single-cell batch cultures of *P. putida* KT2440 grown on different carbon sources. (**a**) Growth curves of *P. putida* KT2440 in glycerol single-cell batch cultures. Multi-well microtiter plates were inoculated with a highly diluted pre-culture in LB medium to start each culture from one cell per well. In this example, cells were grown at 30 °C in 200 μL of M9 minimal medium containing 40 mM glycerol. The time needed to reach an optical density measured at 600 nm (OD_{600}) = 0.3 (mid-exponential phase of growth) for 35 independent cultures is indicated by a red arrowhead to illustrate the delay in the growth takeoff among individual wells. This parameter, termed *time of metabolic response* (t_{MR}), is further used to quantify the response of single-cell batch cultures. (**b**) Frequency distribution of t_{MR} values in 1000 independent single-cell batch cultures of *P. putida* KT2440 carried out in microtiter plates with either glucose or glycerol as the carbon source. Each bar in the graph indicates the number of independent wells in which the cultures attained an OD_{600} = 0.3 at a given t_{MR} in glucose and glycerol cultures. Adapted from Nikel et al. [30]

cultures have a normal distribution of t_{MR} values when the cells are grown on glucose, while a less-defined distribution is observed for glycerol cultures (*see* **Note 5**).

20. The trajectories of residual carbon source in each culture should also be assessed in order to correlate growth and substrate consumption. Following the outline provided by the manufacturer's instructions, the enzymatic kits for substrate determinations are adapted to be used in microscale by reducing the volumes indicated in the original protocol. Typically, 10 μL aliquots of culture broth can be directly processed in a final reaction volume of 200 μL without affecting the dynamic detection range of the commercial kit. Correlate growth and substrate consumption in a linear plot to assess the overall growth yield on carbon source (*see* **Note 6**).

3.2 Flow Cytometry-Assisted Exploration of Metabolic Activity in Individual Cells

1. Allow the RSG and PI solutions to stand at room temperature for 20 min for gentle thawing.
2. Harvest the cells from glucose and glycerol cultures by centrifugation in a benchtop microcentrifuge as indicated in Subheading 3.1, **step 4**. After discarding the supernatant, resuspend the microorganisms with sodium phosphate buffer or PBS, and adjust the number of cells to 1×10^6 CFUs/mL using the *k* parameter calculated in Subheading 3.1, **step 16** in a final volume of 1 mL. Prepare two sets of tubes (e.g., in technical triplicates): one set of microbial samples will be stained with PI, and the other will be stained with the RSG reagent (*see* **Note 7**).
3. Add 1 μL of PI solution into the 1 mL of microbial cell suspension and vortex gently to mix. Incubate the microbial cells at room temperature for 5 min. Repeat the procedure in parallel but using 2 μL of RSG solution. In this case, incubate the cells after adding the RSG reagent at room temperature for 15 min (*see* **Note 8**).
4. Analyze the stained cells by flow cytometry (FC). Firstly, set the voltages on cytometer software to logarithmic amplification. Use forward or side scatter as the acquisition trigger parameter (we usually use the two parameters to create a gate for bacteria, Fig. 3). With an unstained sample of bacterial cells, set the amplification of the signals from forward and side scatter so that the bacteria are in the middle of the data space (gate A in Fig. 3). Stained bacteria can be assayed with a 488 nm DPSS laser. Fluorescence from samples stained with the RSG reagent may be collected using a 525 ± 40 nm bandpass filter. Fluorescence from PI-stained controls may be collected with a 610 nm long-pass filter. Create histogram plots for the RSG-treated bacterial samples, and set the negative controls using unstained *P. putida* cells (gray boxes in Fig. 3) (*see* **Note 9**).

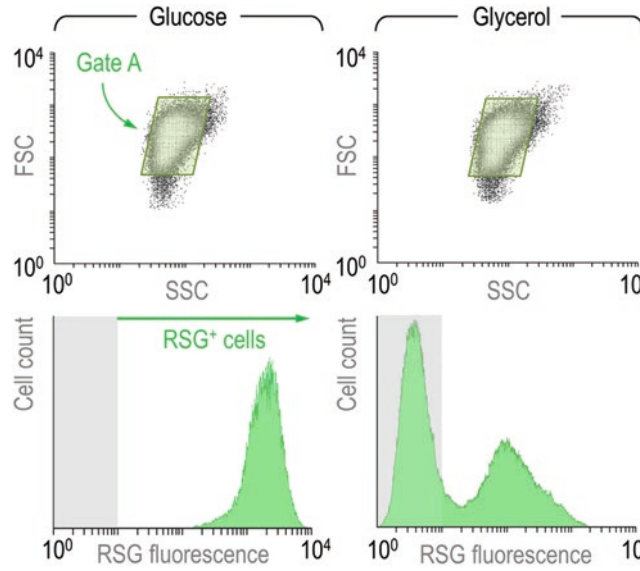

Fig. 3 Flow cytometry analysis of metabolically active subpopulations in *P. putida* cultures growing on different carbon sources. Cells were grown until the cultures reached the mid-exponential phase of growth, and bacteria were immediately treated with the *Bac*Light™ RedoxSensor™ Green (RSG) reagent as indicated in the protocol indicated in Subheading 3.2. The fluorescence intensity was quantified by flow cytometry. The gated population (gate A), in which the RSG signal was investigated, is indicated in the forward scatter (FSC) versus side scatter (SSC) plots (upper panel). The histograms in the lower panel show the distribution of RSG fluorescence in cells grown in glucose and glycerol cultures. The gray rectangle in each plot identifies the region considered negative for the RSG fluorescence signal (which was assessed with unstained cells from each culture condition). Adapted from Nikel et al. [30]

5. Using an adequate software for FC data analysis (e.g., the Cyflogic™ 1.2.1 software), analyze the percentage of RSG-positive and RSG-negative cells in each *P. putida* culture (make sure that the same number of bacterial cells is analyzed in each condition), and correlate the presence of microbial subpopulations to the growth parameters calculated in Subheading 3.1 (in particular λ) for each carbon source (*see* **Notes 10** and **11**).

4 Notes

1. All solutions used for experiments involving FC should be filter-sterilized (e.g., NaCl and sodium phosphate solutions, PBS, and PI solution). This suggestion also applies to culture media used to grow cells that will be analyzed by FC to reduce the background noise of non-bacterial particles in the suspension.

2. Since PI may be carcinogenic, please be careful in its handling and disposal.
3. In this context, the expression *single fresh colony* refers to isolated bacterial colonies obtained after streaking the cells (e.g., from a frozen glycerol stock) onto an LB medium plate and incubating at 30 °C for no longer than 18 h.
4. In principle, the *k* factor should be determined for every strain under test. However, we have found that *k* remains roughly constant for *P. putida* KT2440, and a number of single-knockout mutants provided that these are grown under the same culture conditions.
5. The frequency distribution of t_{MR} values is a very solid indicator of the existence of stochastic phenomena at the single-cell level that, in turn, could result in differences in macroscopic features (e.g., growth parameters). These plots can be analytically examined as indicated by Nikel et al. [30] to explore if there are noticeable microbial subpopulations within the bacterial culture.
6. Even when it is not the purpose of this protocol, it is recommended to execute an in-depth physiological characterization of the bacterial cultures for every carbon source to be analyzed. A detailed protocol for such physiological characterization has been recently published by Nikel and Chavarría [10].
7. Even when this procedure for the detection of microbial subpopulations differing in the level of metabolic activity is proposed for the single-cell batch cultures described in Subheading 3.1, the same principle can be applied to virtually any bacterial culture, provided that the cells are washed and stained as indicated in the protocol. We routinely harvest the cells during exponential growth (around OD_{600} = 0.3 in the culture system described herein), but other points along the growth curve could be considered as well. A time-lapse study is particularly important when different bacterial subpopulations are detected. Longer incubation times in the presence of either PI or RSG may be needed when studying bacterial species other than *P. putida* or *Escherichia coli*, and the bacterial suspension should be always kept protected from light as soon as the fluorescent compounds are added to the tubes until they are processed by FC.
8. The RSG reagent is a general indicator of bacterial reductase activity; this overall reductase activity is, in turn, a reliable marker for changes in both reductase function and electron transport chain function, and the RSG-associated fluorescence also serves as an indication of changes in vitality that occurs

following treatment with uncoupling reagents (e.g., antibiotics). We have found that 2 μL of the RSG reagent every 1×10^6 CFUs is enough to stably stain *P. putida* cells. Other concentrations of the RSG reagent could be used depending on the bacterial species under analysis, but DMSO may be detrimental to bacterial redox activity at concentrations above 1% (w/v), so this upper limit has to be observed. PI is an indicator of the overall membrane integrity. Bacteria with damaged cell membranes should represent a small population (typically <10% of the total population) during logarithmic growth. Excluding the PI-positive subpopulation by gating on the PI-negative population should not alter the distribution of RSG subpopulations.

9. Cells to be analyzed by FC have to be freshly harvested from the working cultures, and the whole procedure of manipulation should not last longer than 15 min. It is a good practice to have all the reagents and materials needed for these measurements already in place to work as quickly as possible.
10. The experiments described in this section should be independently repeated at least three times (in each case, with an adequate number of technical replicates) in order to apply the appropriate statistical tests to the data.
11. While the experimental setup described in this protocol deals with specific metabolic phenomena found in *P. putida*, the same methodologies and formalisms can be applied to any other case where the stochastic manifestation of a given phenotype in single cells gives individual bacteria a growth advantage with respect to the rest of the members in the population.

Acknowledgments

The authors are indebted to F. J. Romero-Campero (University of Seville, Seville, Spain) for his valuable help and suggestions in data analysis. The work described in this chapter was supported by the *CAMBIOS* Project of the Spanish Ministry of Economy and Competitiveness (RTC-2014-1777-3), *EVOPROG* (FP7-ICT-610730), *ARISYS* (ERC-2012-ADG-322797), and *EmPowerPutida* (EU-H2020-BIOTEC-2014-2015-6335536) Contracts of the European Union, and the *PROMPT* Project of the Autonomous Community of Madrid (CAM-S2010/BMD-2414) to V.D.L. P.I.N. gratefully acknowledges the support provided by the Novo Nordisk Foundation.

References

1. Danchin A (2012) Scaling up synthetic biology: do not forget the *chassis*. FEBS Lett 586:2129–2137. https://doi.org/10.1016/j.febslet.2011.12.024
2. Chubukov V, Mukhopadhyay A, Petzold CJ, Keasling JD, García-Martín H (2016) Synthetic and systems biology for microbial production of commodity chemicals. Syst Biol Appl 2:16009. https://doi.org/10.1038/npjsba.2016.9
3. Nielsen J, Keasling JD (2016) Engineering cellular metabolism. Cell 164:1185–1197. https://doi.org/10.1016/j.cell.2016.02.004
4. Godoy MS, Nikel PI, Cabrera Gomez JG, Pettinari MJ (2015) The CreC regulator of *Escherichia coli*, a new target for metabolic manipulations. Appl Environ Microbiol 82:244–254. https://doi.org/10.1128/AEM.02984-15
5. Kim J, Salvador M, Saunders E, González J, Avignone-Rossa C, Jiménez JI (2016) Properties of alternative microbial hosts used in synthetic biology: towards the design of a modular *chassis*. Essays Biochem 60:303–313. https://doi.org/10.1042/EBC20160015
6. Regenhardt D, Heuer H, Heim S, Fernández DU, Strömpl C, Moore ER, Timmis KN (2002) Pedigree and taxonomic credentials of *Pseudomonas putida* strain KT2440. Environ Microbiol 4:912–915. https://doi.org/10.1046/j.1462-2920.2002.00368.x
7. Poblete-Castro I, Borrero de Acuña JM, Nikel PI, Kohlstedt M, Wittmann C (2017) Host organism: *Pseudomonas putida*. In: Wittmann C, Liao JC (eds) Industrial biotechnology: microorganisms. Wiley-VCH Verlag GmbH & Co. KGaA, Weinheim, Germany. https://doi.org/10.1002/9783527807796.ch8
8. Nikel PI, Chavarría M, Fuhrer T, Sauer U, de Lorenzo V (2015) *Pseudomonas putida* KT2440 strain metabolizes glucose through a cycle formed by enzymes of the Entner-Doudoroff, Embden-Meyerhof-Parnas, and pentose phosphate pathways. J Biol Chem 290:25920–25932. https://doi.org/10.1074/jbc.M115.687749
9. Nikel PI, de Lorenzo V (2013) Implantation of unmarked regulatory and metabolic modules in gram-negative bacteria with specialised mini-transposon delivery vectors. J Biotechnol 163:143–154. https://doi.org/10.1016/j.jbiotec.2012.05.002
10. Nikel PI, Chavarría M (2016) Quantitative physiology approaches to understand and optimize reducing power availability in environmental bacteria. In: McGenity TJ, Timmis KN, Nogales-Fernández B (eds) Hydrocarbon and lipid microbiology protocols–synthetic and systems biology–tools. Humana Press, Heidelberg, Germany, pp 39–70. https://doi.org/10.1007/8623_2015_84
11. Blank LM, Ionidis G, Ebert BE, Bühler B, Schmid A (2008) Metabolic response of *Pseudomonas putida* during redox biocatalysis in the presence of a second octanol phase. FEBS J 275:5173–5190. https://doi.org/10.1111/j.1742-4658.2008.06648.x
12. Ebert BE, Kurth F, Grund M, Blank LM, Schmid A (2011) Response of *Pseudomonas putida* KT2440 to increased NADH and ATP demand. Appl Environ Microbiol 77:6597–6605. https://doi.org/10.1128/AEM.05588-11
13. Chavarría M, Nikel PI, Pérez-Pantoja D, de Lorenzo V (2013) The Entner-Doudoroff pathway empowers *Pseudomonas putida* KT2440 with a high tolerance to oxidative stress. Environ Microbiol 15:1772–1785. https://doi.org/10.1111/1462-2920.12069
14. Nikel PI (2012) A brief guide to Pseudomonas putida as a microbial cell factory. BioEssays, Available on line at: http://goo.gl/DXF1y
15. Nikel PI, Chavarría M, Danchin A, de Lorenzo V (2016) From dirt to industrial applications: *Pseudomonas putida* as a synthetic biology *chassis* for hosting harsh biochemical reactions. Curr Opin Chem Biol 34:20–29. https://doi.org/10.1016/j.cbpa.2016.05.011
16. Nikel PI, Martínez-García E, de Lorenzo V (2014) Biotechnological domestication of pseudomonads using synthetic biology. Nat Rev Microbiol 12:368–379. https://doi.org/10.1038/nrmicro3253
17. Benedetti I, de Lorenzo V, Nikel PI (2016) Genetic programming of catalytic *Pseudomonas putida* biofilms for boosting biodegradation of haloalkanes. Metab Eng 33:109–118. https://doi.org/10.1016/j.ymben.2015.11.004
18. Lieder S, Nikel PI, de Lorenzo V, Takors R (2015) Genome reduction boosts heterologous gene expression in *Pseudomonas putida*. Microb Cell Factories 14:23. https://doi.org/10.1186/s12934-015-0207-7
19. Martínez-García E, Nikel PI, Aparicio T, de Lorenzo V (2014) *Pseudomonas* 2.0: genetic upgrading of *P. putida* KT2440 as an enhanced host for heterologous gene expression. Microb Cell Factories 13:159. https://doi.org/10.1186/s12934-014-0159-3.
20. Martínez-García E, Nikel PI, Chavarría M, de Lorenzo V (2014) The metabolic cost of flagellar motion in *Pseudomonas putida* KT2440. Environ Microbiol 16:291–303. https://doi.org/10.1111/1462-2920.12309

21. Jiménez JI, Miñambres B, García JL, Díaz E (2002) Genomic analysis of the aromatic catabolic pathways from *Pseudomonas putida* KT2440. Environ Microbiol 4:824–841. https://doi.org/10.1046/j.1462-2920.2002.00370.x
22. Belda E, van Heck RGA, López-Sánchez MJ, Cruveiller S, Barbe V, Fraser C, Klenk HP, Petersen J, Morgat A, Nikel PI, Vallenet D, Rouy Z, Sekowska A, Martins dos Santos VAP, de Lorenzo V, Danchin A, Médigue C (2016) The revisited genome of *Pseudomonas putida* KT2440 enlightens its value as a robust metabolic *chassis*. Environ Microbiol 18:3403–3424. https://doi.org/10.1111/1462-2920.13230
23. Nelson KE, Weinel C, Paulsen IT, Dodson RJ, Hilbert H, Martins dos Santos VAP, Fouts DE, Gill SR, Pop M, Holmes M, Brinkac L, Beanan M, DeBoy RT, Daugherty S, Kolonay J, Madupu R, Nelson W, White O, Peterson J, Khouri H, Hance I, Chris Lee P, Holtzapple E, Scanlan D, Tran K, Moazzez A, Utterback T, Rizzo M, Lee K, Kosack D, Moestl D, Wedler H, Lauber J, Stjepandic D, Hoheisel J, Straetz M, Heim S, Kiewitz C, Eisen JA, Timmis KN, Düsterhöft A, Tümmler B, Fraser CM (2002) Complete genome sequence and comparative analysis of the metabolically versatile *Pseudomonas putida* KT2440. Environ Microbiol 4:799–808. https://doi.org/10.1046/j.1462-2920.2002.00366.x
24. Nikel PI, Giordano AM, de Almeida A, Godoy MS, Pettinari MJ (2010) Elimination of D-lactate synthesis increases poly(3-hydroxybutyrate) and ethanol synthesis from glycerol and affects cofactor distribution in recombinant *Escherichia coli*. Appl Environ Microbiol 76:7400–7406. https://doi.org/10.1128/AEM.02067-10
25. Nikel PI, Ramirez MC, Pettinari MJ, Méndez BS, Galvagno MA (2010) Ethanol synthesis from glycerol by *Escherichia coli* redox mutants expressing *adhE* from *Leuconostoc mesenteroides*. J Appl Microbiol 109:492–504. https://doi.org/10.1111/j.1365-2672.2010.04668.x.
26. Mattam AJ, Clomburg JM, González R, Yazdani SS (2013) Fermentation of glycerol and production of valuable chemical and biofuel molecules. Biotechnol Lett 35:831–842. https://doi.org/10.1007/s10529-013-1240-4
27. Yazdani SS, González R (2007) Anaerobic fermentation of glycerol: a path to economic viability for the biofuels industry. Curr Opin Biotechnol 18:213–219. https://doi.org/10.1016/j.copbio.2007.05.002
28. Kim J, Oliveros JC, Nikel PI, de Lorenzo V, Silva-Rocha R (2013) Transcriptomic fingerprinting of *Pseudomonas putida* under alternative physiological regimes. Environ Microbiol Rep 5:883–891. https://doi.org/10.1111/1758-2229.12090
29. Nikel PI, Kim J, de Lorenzo V (2014) Metabolic and regulatory rearrangements underlying glycerol metabolism in *Pseudomonas putida* KT2440. Environ Microbiol 16:239–254. https://doi.org/10.1111/1462-2920.12224
30. Nikel PI, Romero-Campero FJ, Zeidman JA, Goñi-Moreno A, de Lorenzo V (2015) The glycerol-dependent metabolic persistence of *Pseudomonas putida* KT2440 reflects the regulatory logic of the GlpR repressor. mBio 6:e00340-00315. https://doi.org/10.1128/mBio.00340-15
31. Casadesús J, Low DA (2013) Programmed heterogeneity: epigenetic mechanisms in bacteria. J Biol Chem 288:13929–13935. https://doi.org/10.1074/jbc.R113.472274
32. Dubnau D, Losick R (2006) Bistability in bacteria. Mol Microbiol 61:564–572. https://doi.org/10.1111/j.1365-2958.2006.05249.x
33. Brehm-Stecher BF, Johnson EA (2004) Single-cell microbiology: tools, technologies, and applications. Microbiol Mol Biol Rev 68:538–559. https://doi.org/10.1128/MMBR.68.3.538-559.2004
34. Czechowska K, Johnson DR, van der Meer JR (2008) Use of flow cytometric methods for single-cell analysis in environmental microbiology. Curr Opin Microbiol 11:205–212. https://doi.org/10.1016/j.mib.2008.04.006
35. Freed NE, Silander OK, Stecher B, Böhm A, Hardt WD, Ackermann M (2008) A simple screen to identify promoters conferring high levels of phenotypic noise. PLoS Genet 4:e1000307. https://doi.org/10.1371/journal.pgen.1000307.g003.
36. Mills E, Avraham R (2017) Breaking the population barrier by single cell analysis: one host against one pathogen. Curr Opin Microbiol 36:69–75. https://doi.org/10.1016/j.mib.2017.01.005
37. Ackermann M (2013) Microbial individuality in the natural environment. ISME J 7:465–467. https://doi.org/10.1038/ismej.2012.131
38. Nikel PI, Silva-Rocha R, Benedetti I, de Lorenzo V (2014) The private life of environmental bacteria: pollutant biodegradation at the single cell level. Environ Microbiol 16:628–642. https://doi.org/10.1111/1462-2920.12360
39. Veening JW, Smits WK, Kuipers OP (2008) Bistability, epigenetics, and bet-hedging in bacteria. Annu Rev Microbiol 62:193–210. https://doi.org/10.1146/annurev.micro.62.081307.163002

40. Arnoldini M, Vizcarra IA, Peña-Miller R, Stocker N, Diard M, Vogel V, Beardmore RE, Hardt WD, Ackermann M (2014) Bistable expression of virulence genes in *Salmonella* leads to the formation of an antibiotic-tolerant subpopulation. PLoS Biol 12:e1001928. https://doi.org/10.1371/journal.pbio.1001928
41. Balaban NQ, Merrin J, Chait R, Kowalik L, Leibler S (2004) Bacterial persistence as a phenotypic switch. Science 305:1622–1625. https://doi.org/10.1126/science.1099390
42. Dalgaard P, Koutsoumanis K (2001) Comparison of maximum specific growth rates and lag times estimated from absorbance and viable count data by different mathematical models. J Microbiol Methods 43:183–196. https://doi.org/10.1016/S0167-7012(00)00219-0

Part V

Chromatin and Cell Cycle Heterogeneity

Chapter 17

The Retinal Pigment Epithelial Cell Line (ARPE-19) Displays Mosaic Structural Chromosomal Aberrations

Elizaveta Fasler-Kan, Nijas Aliu, Kerstin Wunderlich, Sylvia Ketterer, Sabrina Ruggiero, Steffen Berger, and Peter Meyer

Abstract

The retinal pigment epithelial cell line ARPE-19 was established in 1996 and remains widely used today for biomedical and in particular ophthalmology research. We have analyzed the chromosomes of the ARPE-19 cell line and found cultured cells exist as a heterogeneous mixture having both normal karyotypes and chromosomal rearrangements. In ARPE-19 cells, we observed metaphases with a single translocation t(15;19) and metaphases with two translocations t(5;15) and t(15;19) and a derivative chromosome 9. Aneuploidies have also been detected (monosomy: −16; trisomy: +11, +18). Multiple attempts to isolate clones with a normal karyotype from those with aberrant karyotypes failed due to senescence of cells of normal karyotypes. We could, however, isolate clones with the translocation t(15;19) and clones with two translocations t(5;15) and t(15;19). In continued cell culture after second subcloning for 30 passages, all clones maintained their cytogenetic integrity.

We have further investigated the chromosomal profiles of the ARPE-19 cell line from another laboratory and observed cells with a normal karyotype as well as abnormalities in chromosomes 6p and 11q. The DNA profiles of the ARPE-19 cells from both labs were identical to the ATCC profiles, excluding contamination with other cell lines. Since chromosomal translocations in ARPE-19 cells differ from lab to lab and display a mosaicism for structural chromosomal aberrations, researchers dealing with ARPE-19 cells should screen their stocks for chromosomal aberrations and proceed with caution against misinterpretations during experimental manipulations with this cell line. This chapter describes in detail our laboratory methods for single cell cloning, karyotype analysis and fluorescence in situ hybridization (FISH), which we used for the identification and characterization of chromosomal translocations in the retinal pigment epithelial cell line ARPE-19.

Key words Retinal pigment cells, ARPE-19 cell line, Karyotype, Chromosomal translocations, Chromosomal aberrations, FISH, Single-cell cloning, Heterogeneity, Mosaicism

1 Introduction

Retinal pigment epithelial (RPE) cells play a major role in the blood-retinal barrier and are pivotal in the development of age-related macular degeneration (AMD). This degenerative macula disease leads to irreversible visual impairment and blindness.

Natasha S. Barteneva and Ivan A. Vorobjev (eds.), *Cellular Heterogeneity: Methods and Protocols*, Methods in Molecular Biology, vol. 1745, https://doi.org/10.1007/978-1-4939-7680-5_17,

Nearly 50 million people worldwide are suffering from AMD. Currently, AMD has no effective cure [1–5].

Clinically and histologically, AMD can be classified into two major subtypes: dry and wet. Dry AMD is characterized by macular changes consisting of abnormalities of the RPE, drusen and photoreceptor dysfunction and degeneration. Wet AMD is characterized by choroidal neovascularization and growth of new blood vessels behind the retina [6, 7].

The ARPE-19 cell line was established in 1996 and is widely used in ophthalmology research for in vitro studies of RPE. It has been shown that these cells form stable monolayers, which exhibit morphological and functional polarity [8, 9]. The cultures appeared to be rapidly growing RPE cells, which formed cobblestone monolayers and were pigmented after several months of culture. The authors have described this cell line as a normal diploid cell line with some cells showing a short interstitial deletion of the long arm of chromosome 8 as well as a small addition to the long arm of chromosome 19 [8].

We have investigated the chromosomes of ARPE-19 cell cultures and observed metaphases showing normal karyotypes, as well as several cell metaphases with two chromosomal translocations: t(5;15) and t(15;19) with a derivative chromosome 9 (Fig. 1). Moreover, we identified cell metaphases showing only one chromosomal translocation t(15;19) without a derivative chromosome 9 (Fig. 2). We have also observed several numerical aberrations (monosomy: −16; trisomy: +11, +18), possibly attributed as cultural artifacts. Therefore, the ARPE-19 cell line exists as a mixture of cells with normal and abnormal karyotypes.

We have in addition characterized karyotypes of ARPE-19 cells used by our colleagues in the Eye Clinic in Freiburg (Germany). These cells showed normal karyotypes and several metaphases with abnormalities in chromosomes 6p and 11q. DNA profiles (based on STRs: short tandem repeats) were identical between ARPE-19 cells from our laboratory, ARPE-19 cells from Freiburg and from the ATCC, thus excluding contamination with other cell lines.

We have subcloned ARPE-19 cells by limiting dilutions with the aim to separate cells with a normal karyotype from those with chromosomal translocations. All our attempts to clone and isolate ARPE-19 cells with normal karyotype failed. We were able to separate clones with a translocation t(15;19) and clones with two translocations t(15;19) and t(5;15). We confirmed these findings by fluorescence in situ hybridization (Figs. 3 and 4). After second subcloning, we analyzed every third passage for chromosomal aberrations (total 30 passages). These subcloned cells maintained their cytogenetic features. The subcloned ARPE-19 cells described here could be used to study the role of the translocation t(15;19) as well as two translocations t(15;19) and t(5;15) in ophthalmology research. Labs working with ARPE-19 cells are advised to be aware

Fig. 1 The ARPE-19 cells having both translocations (5;15) and (15;19) and derivative chromosome 9. 45,XY,t(5;15)(p?13;p?11.2),t(15;19)(q?11.2;q?13.4),?der(9)

that ARPE-19 cultures display mosaic structural chromosomal aberrations which may potentially directly or indirectly influence interpretation of experimental results.

It is known that extensive cell cultivation might alter karyotypes. It has been shown that the common HEK-293 cell line (human embryonic kidney cells) used widely in cell biology studies has a heterogeneous, unstable karyotype [10]. Total chromosome number counts and chromosomal aberrations differ between HEK-293 cells and derivatives, as well as between HEK-293 cells from different cell banks and labs. Those authors raised concern about the use of HEK-293 cells as a model for studying renal function or as "normal" human cells for transformation studies [10]. The tumorigenicity profile of HEK-293 cells alters with passage number, they are tumorigenic after passage 65, whereas low-passage (<52) HEK-293 cells showed that no tumors could be induced under identical conditions [11]. Another widely used cell line, the CHO (Chinese hamster ovarian cells), is the most broadly used cell line for the industrial production of recombinant biotherapeutics. It has been reported that the loss of a telomeric region of chromosome 8 correlates with higher recombinant productivity and increased production stabilities of CHO-K1a cells [12].

Fig. 2 The chromosomal analysis of ARPE-19 cell line. Cells having a translocation between chromosomes 15 and 19 are shown. 45,XY,t(15;19)(q?11.2;q?13.4)

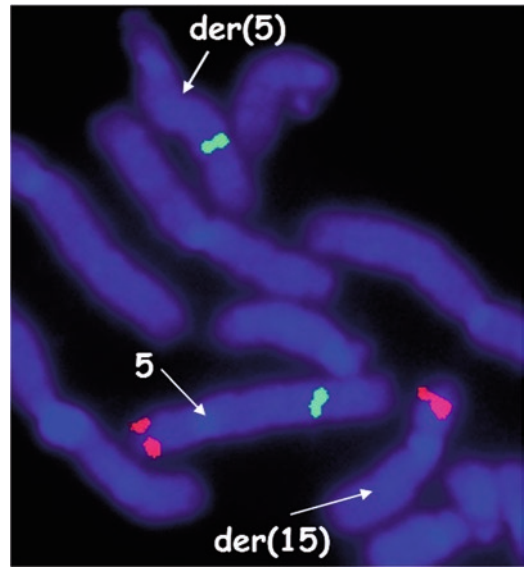

Fig. 3 FISH data confirmed translocation between chromosomes 5 and 15. LSI 5p15.2 (CTNND2) in *red* and LSI 5q31 (D5589) in *green*. The probes were from Kreatech (Leica Biosystems)

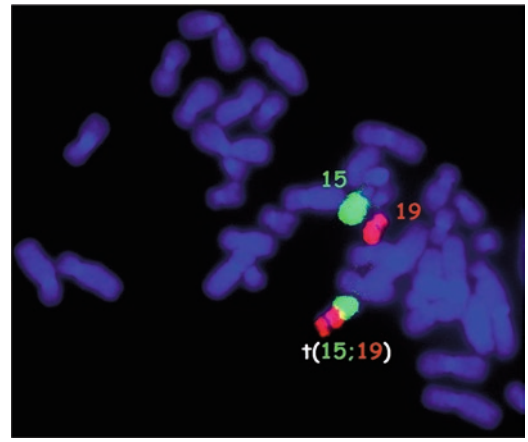

Fig. 4 FISH data confirmed translocation between chromosomes 15 and 19. The probes for whole chromosome painting (WC) WC 15 (*green*) and WC 19 (*red*) were from Kreatech (Leica Biosystems)

In addition stem cells in culture also display predisposition to genetic instability. Chromosomal aberrations accumulate with in vitro passages in conjunction with the loss of euploidy [13, 14]. It remains unclear what triggers these numerous and diverse chromosome abnormalities. These may be related to cell cultivation conditions. New culture conditions still need to be defined to decrease chromosomal alterations in long-term stem cell cultures [13]. Researchers are advised to perform routine cytogenetic studies to monitor chromosome aberrations of important or vital in vitro expanded cell cultures.

2 Materials

2.1 Lab Equipment

1. Microcentrifuge (Eppendorf) or similar.
2. Microscopes.
3. CO_2 incubator.
4. HYBrite (Vysis Hybrite Slide Stainers).
5. Laminar flow cabinet.
6. Water bath.
7. Heat plate.
8. Thermotron.
9. Vortex.
10. Hemocytometer (Neubauer chamber or similar).
11. Ventilated cell culture flasks.
12. Serological pipettes.
13. Centrifugation tubes for 15 and 50 ml.

14. 96-Well plate (low evaporation lid).
15. Cell freezing container ("Mister Frosty" or similar).
16. Multichannel pipetman.
17. Variable pipettes and tips.

2.2 Reagents and Solutions

1. ARPE-19 cells (ATCC collection).
2. DMEM/F12 medium.
3. Kanamycin.
4. Fetal calf serum.
5. Complete DMEM/F12 medium.
6. PBS.
7. DMSO.
8. Accutase (*see* **Note 1**).
9. 0.4% Trypan blue solution.
10. Fixative (3:1 ratio of methanol: glacial acetic acid).
11. FISH probes (Kreatech/Leica Biosystems, Abbott, Qbiogene, Cytocell, or other manufacturers).
12. 60 mM KCL (hypotonic solution).
13. Glass coverslip kits: Dish 35 mm and glass coverslip 22 × 22 mm (MatTek, USA).
14. 10 μg/ml colcemid (Gibco Life Technologies). To prepare a working solution of colcemid: mix 10 μl colcemid stock solution (10 μg/ml) with 90 μl HBSS (Hank's Balanced Salt Solution).
15. 10 mM BrdU (5-bromo-2-deoxyuridine) stock: dissolve 30 mg of BrdU in 10 ml of HBSS. If cells are 90–95% confluent on the day of experiment, then add only 25 μl of colcemid stock solution and incubate for 2 h at 37 °C with 5% CO_2.
16. 10% pepsin stock: 1 g of pepsin dissolve in 10 ml of sterile water.
17. Pepsin working solution: add 400 μl of 1 M HCl and 50 μl of 10% pepsin to 100 ml of sterile water.
18. Formaldehyde-$MgCl_2$ solution: dissolve 2.25 g $MgCl_2$ in 200 ml of PBS, add 12.5 ml of 37% formaldehyde, and bring final volume to 500 ml with PBS.
19. 20×SSC (saline-sodium citrate buffer) stock: 3 M NaCl, 0.3 M sodium citrate, pH 7.0.
20. 2×SSC with 0.2% Tween 20.
21. 0.5×SSC with 0.2% Tween 20.
22. 1.5 μg/ml DAPI.
23. 70%, 85% and 100% ethanol.

24. Neo-Mount (Merck).
25. Freezing medium: 90% FCS and 10% DMSO.

3 Methods

3.1 ARPE-19 Cell Line Propagation

1. Wash cells twice with PBS pH 7.4.
2. Add 1 ml prewarmed Accutase solution to a T-25 cm^2 flask.
3. Place the flask with cells in 37 °C incubator with 5% CO_2.
4. Check cells, if they have detached after 2–3 min.
5. Gently shake flask to further detach cells, if necessary.
6. Once all of the cells have detached, add 4 ml of complete medium.
7. Transfer cells into 15 ml tube and centrifuge cells to pellet at 300 × *g*, 5 min at room temperature (RT).
8. Resuspend cell pellet in fresh complete DMEM/F12 medium and distribute cells into new flasks.
9. Place flasks in an incubator with 5% CO_2 at 37 °C.

3.2 Karyotype Analysis

1. Detach ARPE-19 cells as described in Subheading 3.1 (**steps 1–6**).
2. Add 2 ml complete DMEM/F12 medium to dish with glass coverslip (glass coverslip kits).
3. Seed three drops (~150 µl) of ARPE-19 cell suspension on the top of the glass coverslip.
4. Incubate at 37 °C with 5% CO_2 until the required cell density is achieved (approx. 48 h).
5. Add 25 µl of BrdU and 25 µl of colcemid solution.
6. Incubate overnight (16–20 h) at 37 °C with 5% CO_2.
7. Remove all medium from dish.
8. Add 2 ml of prewarmed hypotonic solution and incubate for 8 min at 37 °C.
9. Add 100 µl of cold fresh fixative; incubate for 2 min at RT.
10. Add 300 µl of cold fresh fixative; incubate for 2 min at RT.
11. Add 600 µl of cold fresh fixative; incubate for 2 min at RT.
12. Add 1 ml of cold fresh fixative; incubate for 2 min at RT.
13. Remove all fluid from dish.
14. Add 3 ml of cold fresh fixative; incubate for 2 min at RT.
15. Transfer the dish to Thermotron (40% humidity and 25 °C).
16. Carefully remove the glass coverslip from the dish and allow to dry.

17. Mount it with the help of Neo-Mount in the middle of a glass slide, keeping the cell side up.
18. Check the chromosome spreading under the phase-contrast microscope.
19. Age slide for 1 h at 93 °C on a hot plate.
20. Stain the chromosomes with G-staining (GTG, *G*-bands by *T*rypsin using *G*iemsa) method (routinely used in cytogenetic labs).
21. Count and analyze at least 50 metaphases (using 100× objective) (*see* **Note 2**).
22. For image acquisition and chromosome analysis (karyotyping), use proprietary software (e.g., Genikon).

3.3 Single-Cell Cloning

1. Suspend the ARPE-19 cells to be subcloned by gently stirring the culture with a pipette tip. Perform a cell count (follow cell counting protocol) (*see* **Note 3**).
2. Place 1 ml of medium into tube A, 3 ml into tube B, and 2.7 ml into tube C.
3. Add 10 μl of the cell suspension (immediately before counting) to tube A (10^{-2} dilution), and shake to distribute the cells evenly.
4. Transfer 300 cells from tube A to tube B.
5. Disperse the cells in the tube using a 1 ml pipette and plate 0.1 ml into rows B and C of the 96-well plate.
6. Transfer 0.3 ml of the cell suspension to tube C (30 cells on 3 ml or 10 cells/ml), disperse the cells using 1 ml pipette, and plate 0.1 ml into rows D and E of the plate.
7. Using a new 1 ml pipette, add 1 ml of medium to tube C and again disperse the cells (now have five cells/ml or one cell/0.2 ml/well).
8. Plate the cell suspension into rows F and G of the plate.
9. Fill the perimeter wells with sterile water (200 μl/well) and incubate at 37 °C, 5% CO_2 for 7 days.
10. Add 0.1 ml of medium to each well on day 7.
11. Screen clones on days 10–14 as ready.
12. Expand desired clones first to one well of a 24-well plate, then to one well of a 6-well plate, then to a T-25 cm^2, and finally to a T-75 cm^2.
13. At this point, the cells can be frozen down (*see* **Note 4**).
14. Subcloning is required. All clones should be subcloned at least twice, i.e., cells selected from wells in rows containing at least 37% empty wells (*see* **Note 5**).

3.4 Fluorescence In Situ Hybridization (FISH) Analysis

1. Start with chromosome preparations or use the cells on slides left after chromosome analysis, *see* Subheading 3.2.
2. Incubate slides for 5 min in a cuvette with 50 ml prewarmed to 37 °C pepsin solution.
3. Incubate slides for 2 min in PBS at RT.
4. Incubate slides for 2 min at RT in a cuvette containing 50 ml formaldehyde-$MgCl_2$ solution.
5. Incubate slides for 2 min in PBS at RT.
6. Dehydrate slides in cuvette with 50 ml of 70% EtOH for 30 s.
7. Dehydrate slides in cuvette with 50 ml of 85% EtOH for 30 s.
8. Dehydrate slides in cuvette with 50 ml of 100% EtOH for 30 s.
9. Air-dry at RT.
10. Vortex the FISH probe briefly.
11. Place 10 μl FISH probe on each slide and cover with a coverslip.
12. Put the slide inside of HYBrite (denature slide at 75 °C for 2 min and then decrease temperature to 37 °C and hybridize overnight).
13. Wash slides in 0.5×SSC 0.02% Tween 20 at 75 °C for 2 min.
14. Wash slides in 2×SSC 0.02% Tween 20 for 2 min at RT.
15. Add 10 μl DAPI counterstain solution to slide and cover with a coverslip (*see* **Note 6**).
16. Observe slides under fluorescence microscope.

4 Notes

1. Accutase solution for cell detachment is kept frozen (−20 °C) or could be kept at +4 °C (not longer than 1 month**).**
2. At least 50 banded metaphases should be counted and examined for breaks, rearrangements, and other abnormal findings.
3. To obtain an accurate number, count at least 200 viable cells. For this purpose, mix 10 μl of cell suspension with 10 μl of trypan blue (dilution, 1:2). Transfer 10 μl of a mixture between the coverslip and the slide of the improved Neubauer chamber (or analog). The cell concentration is calculated using the following formula:

$$\frac{\text{total number of cells}}{\text{number of squares counted}} \times 2 \times 10^4 = \text{number of cells / ml}$$

4. Freeze down at least 1.0 × 10^6 cells in 0.5 ml of freezing medium in cryovials. First, cryovials are placed in Mister Frosty container overnight at −80 °C, and then they could be transferred to liquid nitrogen.

5. Subcloning a second time is necessary to increase the chances that the cells originated from a single cell.
6. Hybridized slides can be stored in the dark at 4 °C for several days without substantial loss of probe fluorescence.

Acknowledgments

The work was supported in part by Grant-in-Aid (University of Bern) and Batzebär grant. We are thankful to Friedel Wenzel (Cytogenetics Department, University of Basel) for his help. We are also grateful to Dr. Ron Tynes (University of Applied Sciences Northwestern Switzerland) for his help with the editing and preparation of the manuscript.

References

1. Pascolini D, Mariotti SP (2012) Global estimates of visual impairment:2010. Br J Ophthalmol 96(5):614–618. https://doi.org/10.1136/bjophthalmol-2011-300539.
2. Alfaro DV, Liggett PE, Mieler WF, Quiroz-Mercado H, Jager RD, Tano Y (eds) (2006) Age-related macular degeneration: a comprehensive textbook. Lippincott Williams & Wilkins, Philadelphia
3. Klein R, Klein BE, Linton KL (1992) Prevalence of age-related maculopathy. The Beaver Dam Eye Study. Ophthalmology 99(6):933–943
4. Ding X, Patel M, Chan CC (2009) Molecular pathology of age-related macular degeneration. Prog Retin Eye Res 28(1):1–18. https://doi.org/10.1016/j.preteyeres.2008.10.001
5. van Leewen R, Klaver CC, Vingerling JR, Hofman A, de Jong PT (2003) Epidemiology of age-related maculopathy: a review. Eur J Epidemiol 18(9):845–854
6. Hamdi HK, Kenney C (2003) Age-related macular degeneration: a new viewpoint. Front Biosci 8:e305–e314
7. Jager RD, Mieler WF, Miller JW (2008) Age-related macular degeneration. N Engl J Med 358:2606–2617. https://doi.org/10.1056/NEJMra0801537
8. Dunn KC, Aotaki-Keen AE, Putkey FR, Hjelmeland LM (1996) A human retinal pigment epithelial cell line with differentiated properties. Exp Eye Res 62:155–169
9. Dunn KC, Marmorstein AD, Bonilha VL, Rodriguez-Boulan E, Giordano F, Hjelmeland LM (1998) Use of the ARPE-19 cell line as a model of RPE polarity: basolateral secretion of FGF5. Invest Ophthalmol Vis Sci 39: 2744–2749
10. Stepanenko AA, Dmitrenko VV (2015) HEK-293 in cell biology and cancer research: phenotype,karyotype,tumorigenicity,andstress-induced genome-phenotype evolution. Gene 569:182–190. https://doi.org/10.1016/j.gene.2015.05.065
11. Shen C, Gu M, Song C, Miao L, Hu L, Liang D, Zheng C (2008) The tumorigenicity diversification in human embryonic kidney cell line cultured in vitro. Biologicals 36(4):263–268. https://doi.org/10.1016/j.biologicals.2008.02.002
12. Ritter A, Voedisch B, Wienberg J, Wilms B, Geisse S, Jostock T, Laux H (2016) Deletion of a telomeric region on chromosome 8 correlates with higher productivity and stability of CHO cell lines. Biotechnol Bioeng 113(5):1084–1093. https://doi.org/10.1002/bit.25876
13. Diaferia GR, Conti L, Redaelli S, Cattaneo M, Mutti C, DeBlasio P, Dalpra L, Cattaneo E, Biunno I (2011) Systematic chromosomal analysis of cultured mouse neural stem cell lines. Stem Cells Dev 20(8):1411–1423. https://doi.org/10.1089/scd.2010.0359
14. Harrison N (2012) Genetic instability in neural stem cells: an inconvenient truth? J Clin Invest 122(2):484–486. https://doi.org/10.1172/JCI62002

Chapter 18

FACS Isolation of Viable Cells in Different Cell Cycle Stages from Asynchronous Culture for RNA Sequencing

Daria M. Potashnikova, Sergey A. Golyshev, Alexey A. Penin, Maria D. Logacheva, Anna V. Klepikova, Anastasia A. Zharikova, Andrey A. Mironov, Eugene V. Sheval, and Ivan A. Vorobjev

Abstract

Recently developed high-throughput analytical techniques (e.g., protein mass spectrometry and nucleic acid sequencing) allow unprecedentedly sensitive, in-depth studies in molecular biology of cell proliferation, differentiation, aging, and death. However, the initial population of asynchronous cultured cells is highly heterogeneous by cell cycle stage, which complicates immediate analysis of some biological processes. Widely used cell synchronization protocols are time-consuming and can affect the finely tuned biochemical pathways leading to biased results. Besides, certain cell lines cannot be effectively synchronized. The current methodological challenge is thus to provide an effective tool for cell cycle phase-based population enrichment compatible with other required experimental procedures. Here, we describe an optimized approach to live cell FACS based on Hoechst 33342 cell-permeable DNA-binding fluorochrome staining. The proposed protocol is fast compared to traditional synchronization methods and yields reasonably pure fractions of viable cells for further experimental studies including high-throughput RNA-seq analysis.

Key words Cell cycle, Flow cytometry, FACS, Hoechst 33342, Population heterogeneity, RNA-seq

1 Introduction

Most cell cycle studies currently seek to identify key molecular determinants of DNA duplication, cell division, and its possible asymmetry thus providing new insights into the mechanisms of cell proliferation, differentiation, and malignization [1–4]. Monitoring the overall cell cycle progression-associated changes to identify putative cell-fate determinants brings high-throughput analysis techniques into research focus. Cycling cells' identification and profiling at various stages of cell cycle initially directed toward

Daria M. Potashnikova and Sergey A. Golyshev have contributed equally to this chapter.

Natasha S. Barteneva and Ivan A. Vorobjev (eds.), *Cellular Heterogeneity: Methods and Protocols*, Methods in Molecular Biology, vol. 1745, https://doi.org/10.1007/978-1-4939-7680-5_18, © Springer Science+Business Media, LLC 2018

proteomics [5, 6] nowadays address both protein and nucleic acid content [7]. A number of coding and noncoding RNAs have been shown to oscillate in a cell cycle-dependent manner [8, 9]. Due to the noncoding nature of some identified RNAs and their more transient lifetime compared to proteins [10, 11], RNA profiling constitutes a perspective area in cell cycle periodicity research. The oscillating RNAs have indisputable value for future studies as putative cell cycle drivers and as possible cell cycle hallmarks.

RNA analysis relies on a variety of techniques from qRT-PCR and microarrays to new generation sequencing that is essentially a label-free method with a potentially unlimited collected data space and the highest sensitivity. At this point, minimizing initial sample heterogeneity and accurate cycle phase determination is becoming vital for unbiased analysis [12]. Homogeneous cell samples at definite cell cycle stages can be obtained by various methods that have certain advantages and limitations and require thorough consideration during experiment planning.

While cell synchronization remains the prominent method in cell cycle studies [9, 12, 13], it does not always yield adequate results. Cell cycle synchronization is a collective name for a set of techniques that can be roughly split into biochemical and physiological. Biochemical approaches rely on cell cycle-disrupting agents, including spindle poisons [14–16], DNA replication inhibitors [16–18], other cell cycle checkpoint blockers [19], or their combinations. Physiology-based methods include nutrient starvation, growth factor deprivation, and mitotic shake-off method. While mitotic shake-off is only applicable to some adherent monolayer cell lines [15], serum starvation is mostly effective on primary non-transformed cell cultures [15] with but a few reports of its successful application to cancer-derived cell models [17]. Though accessible and simple to perform, all synchronization procedures are time-consuming as the average cell cycle duration of mammalian cell lines is 15–24 h [16, 17]. Moreover, prolonged cell cycle arrest uncouples nuclear and cytoplasmic events and may result in perturbed RNA and protein expression profiles [14, 18].

Recently developed microfluidics devices, which allow daughter cell separation from immobilized progenitors—so-called baby machines—constitute a perspective approach to obtaining synchronized populations of physiologically non-perturbed cells [20]. First developed for bacterial and yeast cells, this approach can in prospect be adapted for mammalian cell lines [21]; however, up to now it has not been broadly employed.

Cell size-based separation methods such as centrifugal elutriation present a fast and nonintrusive means of cell cycle subpopulation obtainment as cells increase their volume before division [14, 22]. This approach was successfully used to study cell cycle-associated changes in cellular proteome [23]. Unfortunately, this method requires specialized apparatus and is compromised when

dealing with cell populations highly heterogeneous by size (characteristic of many tumor cell lines and some primary specimens).

Fluorescence-activated cell sorting (FACS) has long been a well-acclaimed tool for cell cycle studies because of its statistical power, multi-parametric approach, and the possibility to physically separate suspended cells into subpopulations [24, 25]. Often used as an independent one-step procedure in the analysis mode to evaluate nucleic acid content throughout the cell cycle, FACS allows total DNA content measurements by DNA-intercalating dye staining, DNA and RNA synthesis evaluation [25, 26], and specific target detection by fluorescent hybridization techniques [27, 28]. Employed as a fast preparative method in sorting mode, FACS is compatible with many other detection techniques and is thus highly versatile. For cell cycle studies, fixed cells have been sorted for DNA analysis [29], and live cells have been sorted for high-throughput RNA screening [30]. To date, FACS allows the highest purity of resulting cell fractions which can diminish possible data variances in further analysis. Several proposed strategies for live cell cycle sorting are:

1. Sorting by DNA content after Hoechst 33342 staining [30, 31] that works well for cell models with little ploidy variance. This is the most convenient and versatile approach. However, the number of sorting gates has never exceeded three so far, which is not taking full advantage of the curve resolution.
2. Since Hoechst 33342 was shown to be cytotoxic at high concentrations [32], sorting by surface marker intensity staining was proposed [33]. This approach presents an advanced version of size-based purification (FACS normally accounts for particle size as forward light scatter parameter, FSC) as adding fluorescence of specific marker accounts for both cell activation status and size. However, this approach shares the limitations of size-based purification methods and is not universal as surface marker choice is model-dependent.
3. Finally, novel live sensor-based techniques (e.g., FUCCI cell cycle sensor) are earning popularity quite rapidly and have been utilized for sorting too [34, 35]. This is a promising approach; however, its applicability for RNA screening has to be verified as adding a viral construct to cells may affect their RNA expression profiles.

In this chapter we describe an optimized procedure for live cell isolation at specific cell cycle stages from a heterogeneous asynchronous population of K-562 cells by FACS, using Hoechst 33342 staining and optimized cell sorter settings. We introduce a more stringent gating strategy to separate four subpopulations and confirm the sorted fractions by molecular methods and microscopy.

2 Materials

2.1 Cells

K-562 (ATCC® CCL243™) human chronic myelogenous leukemia-derived cell line obtained from the American Type Culture Collection (ATCC). Maintained as suspended culture.

2.2 Cell Culture

1. Iscove's Modified Dulbecco's Medium (IMDM) with GlutaMax (Gibco, USA).
2. 10% fetal bovine serum (FBS).
3. Antibiotic-antimycotic mixture.
4. Ventilated T125 flasks.
5. Hemocytometer chamber.
6. Innova CO-170 CO_2 incubator.

2.3 Cell Fixation and Staining

1. Hoechst 33342 solution, 1 mg/ml, stored at +4 °C, protected from light.
2. Propidium iodide (PI), 1 mg/ml in double-deionized water, stored at +4 °C, protected from light.
3. RNase A, 5 mg/ml solution in double-deionized water, stored frozen at −20 °C.
4. Alexa488 and Alexa555 Click-iT EdU imaging kits (Thermo Fisher Scientific, USA).
5. Fixative solution for PI staining: ice-cold 70% ethanol in double-deionized water.
6. Formaldehyde (FA)—methanol-stabilized 37% aqueous formaldehyde solution, stored at +4 °C, diluted to a final concentration of 3% by PBS on the day of experiment.
7. Triton X-100—10% in double-deionized water, stored at +4 °C.
8. Bovine serum albumin (BSA), 10% water solution, stored frozen at −20 °C.
9. Tetramethylrhodamine, ethyl ester, perchlorate (TMRE) – 10 mM aliquots in DMSO stored frozen at −20 °C; thawed aliquot is diluted to 10 μM with PBS and stored at +4 °C.
10. Calcium- and magnesium-free phosphate-buffered saline (PBS), pH = 7.2–7.4.
11. Eppendorf MiniSpin plus centrifuge.
12. Centrifuge tubes 2 ml.

2.4 Flow Cytometry and Sorting

1. FACS sheath fluid.
2. CST beads for FACSAria instrument calibration (BD Biosciences, USA).

3. AccuDrop beads for drop delay calibration.
4. Sphero rainbow fluorescent particles (Cat# 556291, BD Biosciences, USA).
5. Polypropylene FACS tubes, 5 ml.
6. FACSAria SORP cell sorter equipped with 405 and/or 355, 488, 561, and 640 nm lasers (BD Biosciences, USA).
7. CytoFlex flow cytometer (Beckman-Coulter, USA) equipped with 488 nm laser.

2.5 Specimen Mounting for Microscopy and Cell Imaging

1. Mowiol (Calbiochem/Merck, Germany) mounting medium prepared as a working mix according to manufacturer's instruction with addition of 25 mg/ml 1,4-diazabicyclo[2.2.2] octane (DABCO) (Sigma-Aldrich, USA); stored frozen at −20 °C.
2. Glass slides.
3. Poly-L-lysine-coated coverslips prepared in-house by applying drops of 1 μg/ml poly-L-lysine solution on acid-washed dry quarters (12 × 12) of 24 × 24 mm coverslips for 1 h. Residual liquid is then removed by aspiration, and the coverslips are air-dried in dust-free environment.
4. Axiovert 200M inverted motorized fluorescent microscope (Carl Zeiss, Germany) equipped with filter cubes suitable for observing Hoechst 33342 (excitation BP 365/12 nm, Beamsplitter FT 395 nm, LP 397 nm), Alexa488 (BP 470/40, FT 495, BP 525/50), and propidium iodide (BP 545/25, FT 570, BP 605/70) and ORCA-II ERG2 digital camera (Hamamatsu Photonics, Japan) or equivalent.

2.6 RNA Manipulation and cDNA Preparation

1. RNALater (Qiagen, Netherlands).
2. RNEasy Mini RNA isolation kit (Qiagen, Netherlands).
3. Ribo-Zero rRNA Removal Kit (Human, Mouse, Rat) (Illumina, USA).
4. Agencourt RNAClean XP magnetic beads (Beckman Coulter, USA).
5. Agencourt AMPure XP magnetic beads (Beckman Coulter, USA).
6. Magnetic rack for 1.5 ml tubes.
7. Magnetic rack for 0.2 ml tubes.
8. RLT plus buffer (Qiagen, Netherlands).
9. 2-β-Mercaptoethanol.
10. DNase I. RNase-free (Qiagen, Netherlands).
11. TruSeq Stranded mRNA Library Prep Kit v2 (Illumina, USA).
12. MJ Mini PCR cycler (MJ Research, Canada).

13. Aria Mx real-time PCR cycler (Agilent, USA).
14. Bioanalyzer 2100 system (Agilent, USA).
15. RNA 6000 Pico kit (Agilent, USA).
16. High Sensitivity DNA kit (Agilent, USA).
17. 2.5× mix for real-time PCR with EvaGreen dye (Syntol, Russia).
18. Primers for I-qPCR-1.1
    - Forward:AATGATACGGCGACCACCGAGAT, I-qPCR-2.1
    - Reverse: CAAGCAGAAGACGGCATACGA
19. PhiX control library (Illumina, USA).
20. SuperScript II reverse transcriptase.
21. Qubit fluorometer (Thermo Fisher Scientific).

2.7 Sequencing

1. 0.1 M NaOH.
2. TruSeq SR Cluster Kit v3 (Illumina, USA).
3. TruSeq SBS Kit v3, 50 cycles (Illumina, USA).
4. HiSeq2000 sequencer (Illumina, USA).
5. cBot instrument (Illumina, USA).

2.8 Data Analysis Software

1. FACS Diva software (BD Biosciences, USA).
2. CytExpert software (Beckman-Coulter, USA).
3. CASAVA software (Illumina, USA).
4. CLC Genomics Workbench (Qiagen, Netherlands).
5. FastQC (free software, available for download at https://www.bioinformatics.babraham.ac.uk/projects/fastqc/).
6. HISAT2 2.0.5 release 11/4/2016 (free software, available for download at https://ccb.jhu.edu/software/hisat2/index.shtml).
7. Samtools (free software, available for download at http://samtools.sourceforge.net/).
8. HTSeq-0.7.2 (free software, available for download at http://www-huber.embl.de/HTSeq/doc/overview.html).
9. DESeq2 (free software, available for download at http://www.bioconductor.org/packages/release/bioc/html/DESeq2.html).
10. DAVID (online service located at https://david.ncifcrf.gov/).

3 Methods

3.1 Cell Culture

K-562 cells are maintained in suspension in IMDM, supplemented with antibiotic-antimycotic solution and 10% FBS, further referred to as growth medium. Cells are grown in ventilated T125 flasks in 5% CO_2 atmosphere at +37 °C. Cell culture density is routinely checked every 48 h using hemocytometer chamber, and the cell suspension is diluted to 0.2×10^6 cells/ml with fresh growth medium (*see* **Notes 1** and **2**). At this stage, quality control is performed by PI staining (*see* Subheading 3.2) to confirm normal cell cycle progression.

Cells are seeded at 0.4×10^6 cells/ml into 5 ml of growth medium and cultured for 24 h to obtain 0.8×10^6 cells/ml for subsequent experiments.

3.2 Propidium Iodide Staining

For cell culture control and as standard reference technique, cells should be stained with PI according to the following procedure. This also allows comparison of the results from different instruments (*see* Fig. 1 and **Note 3**).

1. Place cell suspension in 2 ml centrifuge tubes and spin down using MiniSpin centrifuge at 3000 × *g* for 3 min.
2. Remove supernatant by aspiration.
3. Add 2 ml of PBS and resuspend cell pellet thoroughly.
4. Spin cells down at 3000 × *g* for 3 min.
5. Overlay cell pellet with 1 ml of fixative solution (*see* **item 5** Subheading 2.3), and then resuspend by quick vortexing. Fix cells for at least 3 h at +4 °C.
6. Spin fixed cells down at 5000 × *g* for 5 min (*see* **Note 4**). Remove supernatant by aspiration.
7. Resuspend cells in 2 ml PBS, and disperse cell pellet thoroughly.
8. Spin cells down at 5000 × *g* for 5 min. Remove supernatant by aspiration.
9. Resuspend cells in 1 ml of PBS with 5 μg/ml RNase A and 30 μg/ml PI. Stain cells for 30 min at room temperature. Samples should be kept protected from light at this and the following stages.
10. Spin stained cells down at 5000 × *g* for 5 min. Remove supernatant by aspiration.
11. Resuspend cells in 2 ml PBS.
12. Spin cells down at 5000 × *g* for 5 min. Remove supernatant by aspiration.
13. Resuspend cells in PBS and proceed to Subheading 3.5 for flow cytometry analysis (also *see* **Notes 5** and **6**).

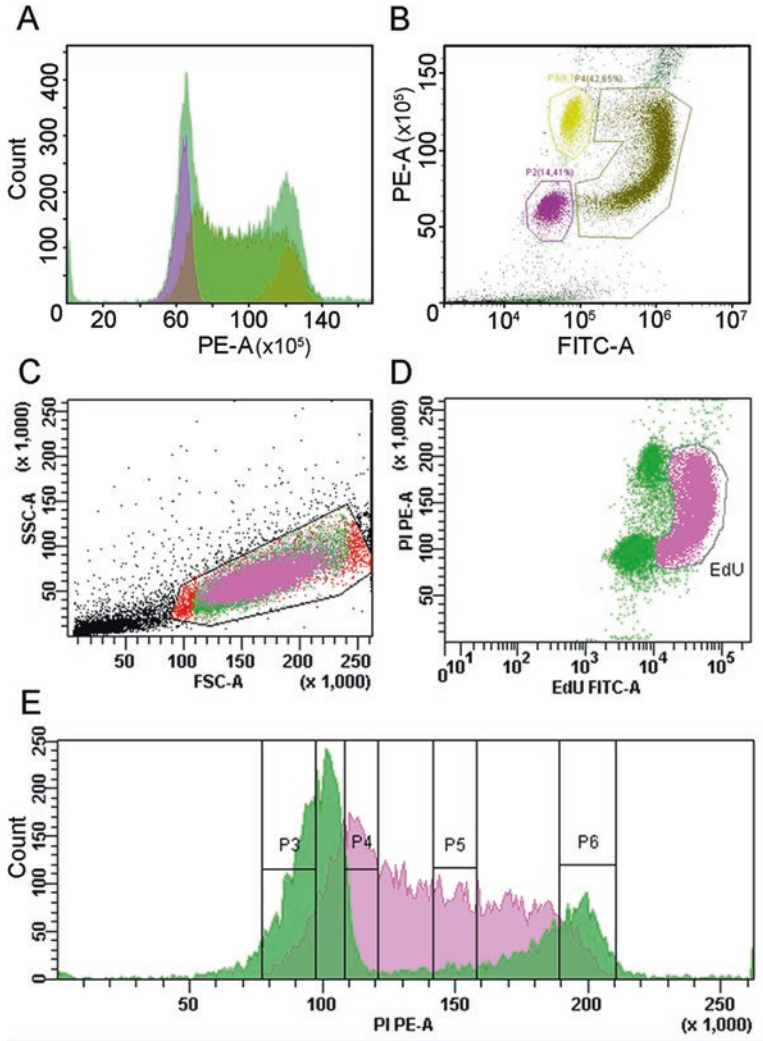

Population	%Parent	PI PE-A Mean	PI PE-A Median	PI PE-A %rCV
EdU	56.6	138,912	134,308	26.4
NO EdU	43.4	126,341	103,980	20.3
P3	14.9	90,174	91,162	6.2
P4	13.2	113,556	113,136	3.9
P5	8.9	149,502	149,524	4.1
P6	10.7	197,650	197,198	3.1

Fig. 1 Typical DNA content curves for exponentially growing K-562 cells; 24 h after dilution with fresh growth medium, cell density is 0.8×10^6 cells/ml. PI (PE channel) + EdU-Alexa488 (FITC channel). (**a**, **b**) Instrument, CytoFlex; excitation wavelength, 488 nm. (**a**) The histogram shows PI staining (G0/G1 vs G2/M peak resolution $k = 1.92$) with superimposed populations detected by EdU labeling of newly synthesized DNA. The populations are gated on the dot plot (**b**). (**c**–**e**) Instrument, FACSAria SORP; excitation wavelengths, 488 and 561 nm. (**c**) forward vs side light scatter; (**d**) EdU vs PI labeling; (**e**) PI staining histogram (G0/G1 vs G2/M peak resolution $k = 1.96$). Acquisition conditions are adjusted for maximum curve resolution prior to sorting. Populations P3, P4, P5, and P6 gated for sorting comprise 14.9%, 13.2%, 8.9%, and 10.7% of gated live single cells, respectively. P3 and P6 contain admixtures of DNA-synthesizing cells

3.3 EdU Labeling and DNA Replication Assessment by Flow Cytometry

To define the gating strategy, cells should be assayed for cell cycle phase. We use EdU labeling to determine G0/G1, early S, middle S, and G2/M subpopulations. Cells are labeled with 1 μM EdU to assess DNA synthesis. Total DNA can be labeled by PI for flow cytometry or by Hoechst 33342 for fluorescence microscopy (see Figs. 1 and 2, respectively).

For flow cytometry analysis of EdU incorporation:

1. Add EdU to the growth medium to the final concentration of 1 μM (*see* **Note 7**).
2. Incubate cells at +37 °C for 20 min.
3. Spin cells down and remove EdU-containing medium.
4. Perform **steps 1–8** described in Subheading 3.2.

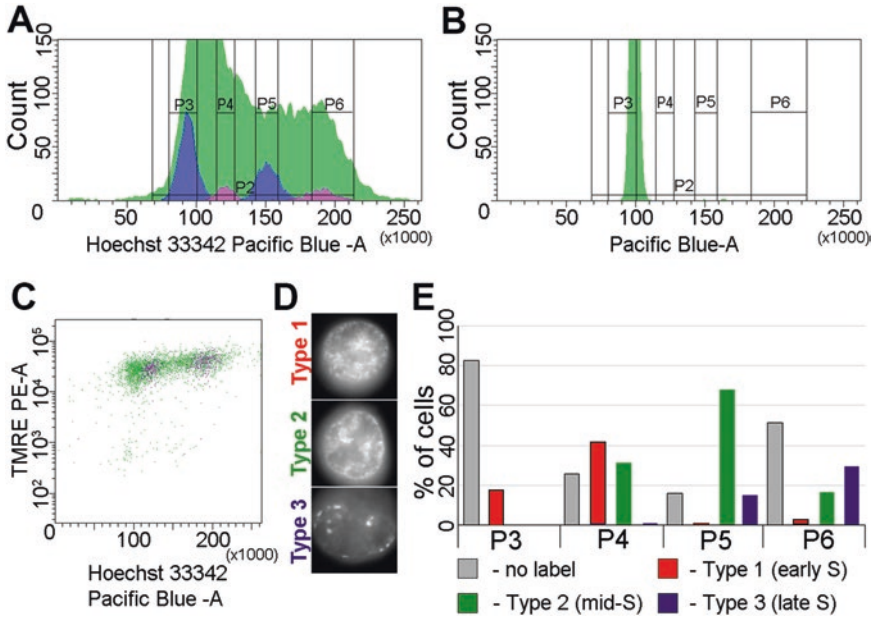

Fig. 2 Live K-562 cell sorting based on Hoechst 33342 DNA and TMRE viability staining. (**a**) The initial K-562 population is presented in green, G0/G1 vs G2/M peak resolution $k = 1.86$. Gates are set according to PI/EdU staining of fixed K-562 sample to contain similar cell percentages. Sorted populations (P3, P4, P5, P6) reanalyzed by flow cytometry are overlaid in blue and purple. Population variances are assessed as rCVs% and are rCV(P3) = 6.2%, rCV(P4) = 5.3%, rCV(P5) = 5.6%, rCV(P6) = 5.4%. (**b**) Sphero rainbow single peak particles from the same experiment are shown for comparison. Peak rCV% = 2.0%. (**c**) Sorted fractions stained for viability with TMRE. The initial K-562 population is presented in green. Overlaid in purple are P4 and P6 populations reanalyzed after a "recovery period" of 15–20 min post sorting; cells are shown to reconstitute mitochondrial membrane potential to pre-sorting values. (**d**) EdU-staining patterns typical for early (Type 1), middle (Type 2), and late (Type 3) S-phase. (**e**) Percentages of cells with particular labeling type calculated for each sorted fraction

5. Resuspend cells in 1 ml of 2% BSA in PBS, and incubate at room temperature for 30 min. At this step prepare EdU detection mix according to manufacturer's instructions (*see* **Note 8**).
6. Spin cells down at 5000 × *g* for 5 min.
7. Carefully remove supernatant by aspiration leaving as little residual liquid as possible. Resuspend cell pellet in 100 μl of detection mix.
8. Incubate samples in the dark at room temperature for 45 min. At the following steps, keep samples protected from light.
9. Spin cells down at 5000 × *g* for 5 min.
10. Remove supernatant by aspiration, resuspend cell pellet in 1 ml of 2% BSA in PBS, and incubate samples at room temperature for 10 min.
11. Spin cells down at 5000 × *g* for 5 min, and proceed to PI staining as described in **steps 9–12** of Subheading 3.2.
12. Resuspend cells in PBS, and proceed to Subheading 3.5 for flow cytometry analysis (also *see* **Note 9**).

3.4 Vital Dye (Hoechst 33342 and TMRE) Loading

Sorting for RNA content analysis requires live cells and thus vital dye usage. In this protocol, Hoechst 33342 alone or Hoechst 33342 and TMRE are used.

1. Hoechst 33342 is a live cell-permeable, DNA-binding dye. Prior to sorting, cell growth medium is supplemented with 1 μg/ml Hoechst 33342 (*see* **Notes 10** and **11**). Cells are allowed to equilibrate dye concentration for at least 45 min in complete culture medium (+37 °C, in the dark) before proceeding to analysis and sorting. FACS procedure is performed without washing steps (*see* **Note 12**).
2. TMRE is a cell-permeable potential-sensitive mitochondrial dye. It is similarly added to the growth medium to a final concentration of 30 nM. Cells are incubated at +37 °C in the dark for at least 45 min. No washing steps are required. The procedure is optional for cell cycle sorting experiments and is used to assess cell viability before and after the sort.

3.5 Cell Cycle FACS

1. Prior to analysis and sorting, make sure the routine instrument setup and calibration steps are performed. FACSAria performance is monitored using CST beads; drop delay for cell sorting is adjusted using AccuDrop beads both based on manufacturer's instructions. We propose to additionally analyze Sphero 1-peak Rainbow particles to account for instrumental variance. The intensity of particle peak closely resembles the intensity of the G0/G1 peak of Hoechst 33342-stained K-562 cells (*see* Fig. 2).

2. Cell cycle analysis and sorting are performed on a FACSAria SORP instrument using 100 μm nozzle with corresponding system pressure parameters. However, it is advisable to verify the staining quality on another flow cytometer with longer exposure time and thus better peak resolution (*see* **Note 13**).
3. PI is excited by 488 nm laser on CytoFlex flow cytometer and by 488 nm and 561 nm lasers on FACSAria SORP cell sorter. Optical filters for PI detection are as follows: FACSAria (488). 550 LP + 582/15 BP; FACSAria (561), 582/15 BP; and CytoFlex, 585/42 BP.
4. EdU-Alexa 488 is excited by 488 nm laser and detected using the following optical filters: 505 LP + 525/20 BP (FACSAria) and 525/40 BP on CytoFlex. Figure 1 shows a representative staining.
5. Hoechst 33342 can be excited by 355 nm or 405 nm lasers (see **Note 14**). Violet laser (405 nm) is used to minimize the negative effect of illumination on cell viability.
6. Hoechst 33342 fluorescence is detected using the optical filter 450/50 BP.
7. TMRE is excited by 561 nm laser, and fluorescence is detected using the optical filter 582/15 BP.
8. Four gates denoting G0/G1, early S, middle S, and late S/G2/M cell cycle stages are set in accordance with PI-/EdU-staining data (Fig. 1). Similar gates with the same cell percentages are used for sorting with Hoechst 33342 staining (Fig. 2).
9. Two-way sorting is performed in "Purity" mode into 5 ml polypropylene FACS tubes. P3 and P5 and then P4 and P6 populations are sorted simultaneously. If a total RNA control is required for subsequent experiments, it is recommended to sort the overall DNA-containing population setting the gate (P2) as shown in Fig. 2 (also *see* **Note 15**).
10. Sorting accuracy is verified by reanalyzing sorted samples (*see* Fig. 2a and **Notes 16** and **17**).
11. To assess cell viability, samples have to be Hoechst 33342 + TMRE-loaded prior to sorting. No noticeable drop of TMRE fluorescence intensity and therefore no depolarization of mitochondrial membranes have been observed after sorting (*see* Fig. 2c and **Note 18**).

3.6 Microscopic Verification of Fraction Enrichment

The best way to correlate newly developed or optimized synchronization/cell cycle-based separation protocol with established ones is to compare the so-called replication patterns in obtained cell populations. Replication patterns arise when cells are pulse-labeled with fluorescent or otherwise detectable DNA precursor such as EdU in different S-phase stages. Typically mammalian cells display

three easily discernible patterns corresponding to early, middle, and late S-phase (*see* Fig. 2d). To assess these patterns in sorted subpopulations by fluorescence microscopy:

1. Perform **steps 1–3** of Subheading 3.3 for EdU incorporation.
2. Perform **step 1** of Subheading 3.4 for Hoechst 33342 loading.
3. Proceed to FACS procedure as described in Subheading 3.5 and obtain required subpopulations.
4. Spin cells down at 3000 × *g* for 3 min. Remove supernatant by aspiration.
5. Resuspend cell pellet in 1 ml of 3% FA in PBS (*see* **Note 19**).
6. Fix cells for 20 min at room temperature.
7. Spin cells down at 3000 × *g* for 3 min. Remove supernatant by aspiration.
8. Resuspend cell pellet in 2 ml PBS and incubate for 5 min.
9. Spin cells down at 3000 × *g* for 3 min. Remove supernatant by aspiration.
10. Resuspend cell pellet in 1 ml of 0.1% Triton X-100 in PBS and incubate for 5 min.
11. Spin cells down at 3000 × *g* for 3 min. Remove supernatant by aspiration.
12. Resuspend cell pellet in 2 ml PBS and incubate for 5 min.
13. Repeat **steps 11** and **12** of Subheading 3.6.
14. Spin cells down at 3000 × *g* for 3 min. Remove supernatant by aspiration.
15. Resuspend cells in a small (~100 μl) volume of PBS.
16. Layer 100 μl of cell suspension in PBS over poly-L-lysine-coated coverslips. Allow cells to passively sediment on coverslips for 30–45 min.
17. Remove the excess liquid from coverslips by aspiration.
18. Additionally fix cells for 5 min by layering 3% FA in PBS over the coverslip.
19. Place the coverslips in an appropriate vessel, e.g., 30 mm Petri dish, and wash the coverslips twice in PBS for 5 min.
20. Incubate the coverslips in 2% BSA in PBS for 20 min.
21. While performing **step 20** of Subheading 3.6, prepare humidified chamber with clean parafilm-covered bottom.
22. Prepare Click-iT EdU detection mix according to manufacturer's instructions. Fluorochrome choice for EdU detection at this stage depends on available microscope configuration.

In this protocol Alexa488 was used for maximum compatibility of the samples with available instruments.

23. Place 30–50 μl droplets of detection mix on parafilm.
24. Place coverslips with cells facing down on the droplets of the detection mix. Incubate at room temperature protected from light for 45 min.
25. Reaction is stopped by placing the coverslips into 2% BSA in PBS and then in PBS.
26. Wash the coverslips once in PBS.
27. Mount the coverslips on microscope slides with Mowiol mounting medium supplemented with anti-bleaching agent, 1,4-diazabicyclo(2.2.2)octane (DABCO). No counterstaining for DNA is required, since the cells retain Hoechst 33342 staining throughout the procedure.
28. Allow Mowiol to dry overnight in the dark at room temperature.
29. Examine the specimens by fluorescence microscopy using high-numerical-aperture oil-immersion lens, and filter sets suitable for observing Hoechst 33342 and Alexa488/Alexa555. We use Axiovert 200M fluorescent microscope (Carl Zeiss) equipped with Plan Neofluar 100× NA 1.3 oil-immersion lens and ORCA2 ERG-II CCD camera (Hamamatsu Photonics). The scaling of resulting images is 67 nm per pixel, typical exposure for Alexa488 with given imaging setup is 400–500 ms.

We have employed "blind" counting of EdU incorporation patterns in sorted populations obtained through FACS procedure without strict pairing of patterns with S-phase stages (*see* **Notes 20** and **21**). Our results are shown in Fig. 2e.

3.7 RNA-Seq Analysis

Total RNA is obtained from sorted cell fractions (Subheading 3.5) preserved in 200 μl of RNALater.

1. Spin sorted cells down at 3000 × *g* for 3 min. Remove supernatant by aspiration.
2. Resuspend cell pellet in 200 μl of RNALater and transfer to microcentrifuge tubes.
3. Spin cells down in MiniSpin microcentrifuge (5 min, 6700 × *g*). Remove supernatant.
4. Add 450 μl of RLT Plus buffer and 10 μl of 2-mercaptoethanol per sample.
5. Extract RNA following Qiagen protocol, with the following modifications: (1) lysis time is increased up to 40 min; (2) on-column DNase I treatment is performed.

6. To assess RNA quantity and integrity use Qubit fluorometer (*see* **Note 22**).
7. To assess RNA length distribution use 2100 Bioanalyzer (*see* Fig. 3a and **Note 23**).
8. Deplete ribosomal RNA using Ribo-Zero rRNA Removal Kit following the manufacturer's protocol.
9. Concentrate resulting RNA using RNAClean magnetic beads. To do this 180 μl of magnetic beads is added to each RNA sample, resuspended, and incubated at room temperature for 15 min. After this, samples are placed on a magnetic rack and incubated for 5 min. Supernatant is then removed. Magnetic beads are washed twice with fresh 80% ethanol and dried out. RNA is resuspended in 11 μl of RNase-free water, incubated at room temperature for 2 min, and placed on magnetic rack for 5 min. 10 μl of supernatant containing rRNA-depleted RNA is used for cDNA synthesis.
10. Prepare cDNA libraries using the TruSeq Stranded mRNA Library Prep Kit v2 following the manufacturer's protocol.
11. Measure library concentration using Qubit fluorometer.
12. Assess length distribution using 2100 Bioanalyzer with High Sensitivity DNA kit (Fig. 3b). In case 120 bp fragments

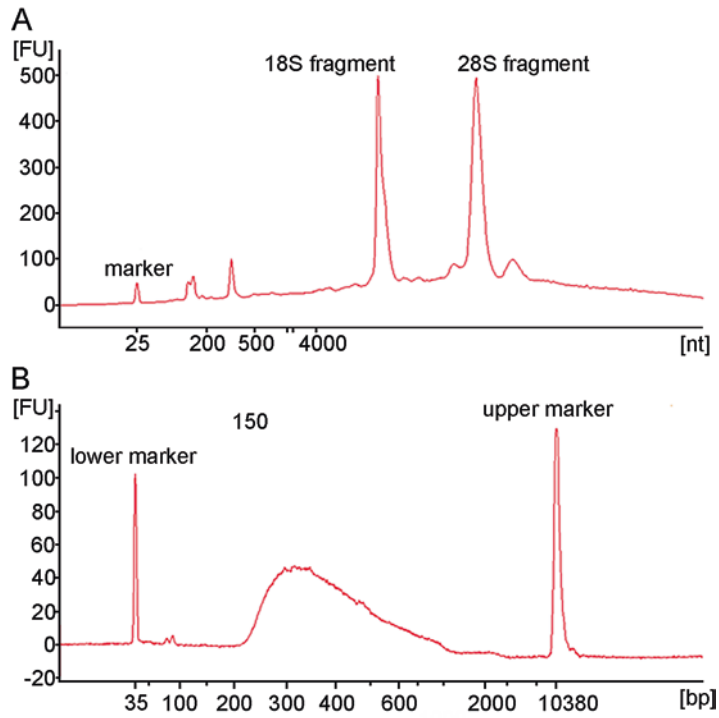

Fig. 3 (**a**) Total RNA length distribution (RIN 9.1). (**b**) Length distribution for DNA library

(adapter dimers) are present, an additional cleanup is performed using Ampure XP beads (according to manufacturer's protocol and with sample/bead ratio = 0.9).

13. Concentration of fragments that have adapters at both ends (effective concentration) is estimated using real-time qPCR with PhiX library used as a control. Libraries are diluted to 5 pM, and control library is diluted to 20, 10, 5, 2.5, and 1.25 pM (PCR program is as follows: 95 °C 5 min, then 25 cycles of 95 °C 15 s, 60 °C 1 min).
14. Cluster generation is performed using TruSeq SR cluster kit. Libraries are diluted with Milli-Q water to 2 nM, then 10 μl of 2 nM dilution is taken to a new tube, and 10 μl of 0.1 M NaOH is added. After a 5-min incubation at room temperature, 980 μl HT1 buffer (in the kit) is added, making 20 pM dilution. Then 550 μl of 20 pM dilution is transferred to a new tube, and 450 μl of HT1 buffer is added. The resulting 11 pM dilution is used for cluster generation on cBot instrument.
15. Sequencing is performed using HiSeq2000 instrument and TruSeq v.3 sequencing reagents with the following settings: first read 51 cycles, index read—7 cycles. Base-calling is performed using CASAVA v. 1.8.2.

3.8 Bioinformatics

1. Trimming (removal of adapters and low-quality nucleotides) is performed using CLC Genomics Workbench v. 8.5.1 with the following settings: quality scores, 0.005; trim ambiguous nucleotides, 2; remove 5′-terminal nucleotides, 1; remove 3′-terminal nucleotides, 1; and discard reads below length 25.
2. Perform quality analysis of reads with FastQC.
3. Map sequencing reads to the human genome (version hg19) using HISAT2. Human known splice sites for HISAT2 and list of genes for differential analysis can be obtained from GENCODE project (version 19).
4. Only uniquely mapped reads are saved using custom scripts.
5. Calculate reads associated with genes using HTSeq.
6. Remove genes that are not covered in any sample.
7. Differential expression between pairs of sorted samples (corresponding to different cell cycle stages) is analyzed using DESeq2. Figure 4 presents example data on cyclins E (*CCNE1*, *CCNE2*) and B (*CCNB1*, *CCNB2*) that are known to be transiently and inversely expressed during the cell cycle.
8. Analysis by GO terms: differentially expressed genes obtained in **steps 1**–7 of Subheading 3.8 can be analyzed using DAVID web service and thus clustered by function (Table 1) (padj $<10^{-10}$). In our case, the most significant terms are associated with cell cycle, cell division, mitosis, DNA damage, and repair.

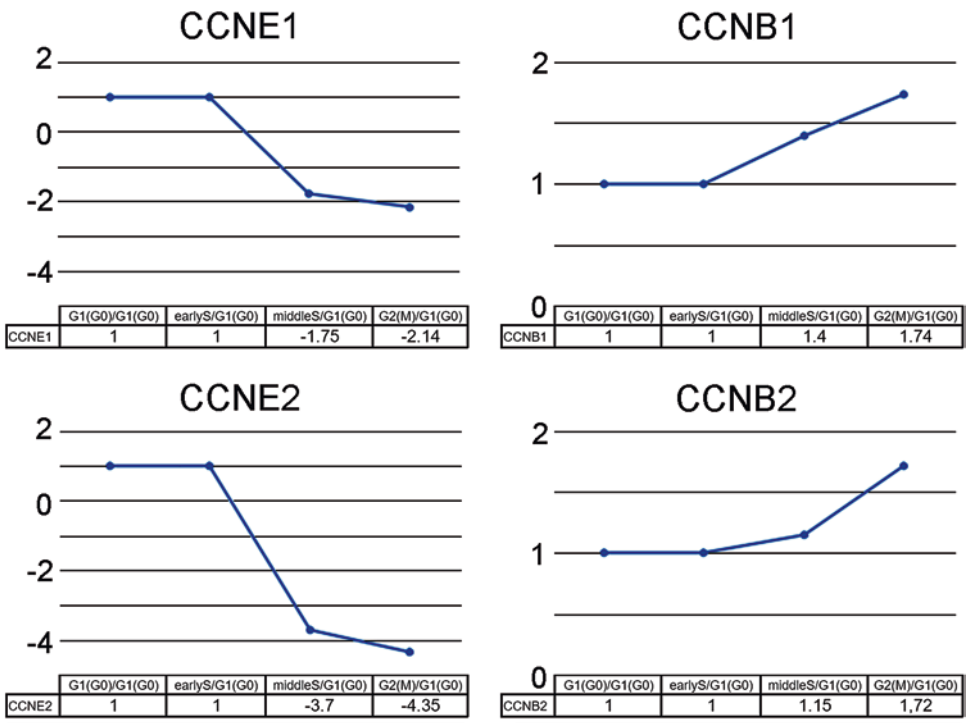

Fig. 4 Cell cycle subpopulations sorted as shown in Fig. 2a (termed G1(G0), early S, middle S, and G2(M) for further analysis) and subjected to RNA-seq analysis exhibit inverse expression patterns of E family and B family cyclins' mRNAs. The graphs present fold changes in gene expression levels compared to G1(G0) subpopulation (G1(G0)/G1(G0) = 1) for all genes; the differences between G1(G0) vs middle S and G1(G0) vs G2(M) cell cycle subpopulations are statistically significant for all genes—$p < 0.05$

Almost all stages have significantly overrepresented genes involved in cell cycle processes (Cell Cycle GO term). Predictably, major differences are observed between G2/M–G1/G0 and G2/M–early S subpopulations (over 100 differentially expressed mRNAs). However, closer subpopulations also demonstrate differential gene expression patterns.

4 Notes

1. K-562 cells are well-suited for the experiments described above. These cells are predominantly triploid and uniformly sized and show very low clumping in given growth and experimental conditions. Besides, 98% of K-562 cells are in the proliferative pool (*see* also **Note 9**).
2. It is essential to maintain cells in exponential growth phase and keep their concentration below 1×10^6 cells/ml. Higher cell densities result in DNA content curve distortions and complicate the gating procedure.

Table 1
GO analysis of differentially expressed genes between four sorted populations based on cell cycle stage

	G1/G0 vs early S UP	G1/G0 vs middle S UP	G1/G0 vs middle S DOWN	Early S vs middle S UP	Early S vs G2/M UP	G1/G0 vs G2/M UP	G1/G0 vs G2/M DOWN
Number of differential expressed genes	**86**	**112**	**17**	**8**	**125**	**508**	**150**
Acetylation	54.12%						
ATP-binding		18.92%		62.50%	20.16%		
Cell cycle		23.42%	43.75%	50.00%	37.90%	15.02%	7.48%
Cell division		21.62%	18.75%	50.00%	33.06%	12.85%	
Centromere		9.01%			12.90%	5.14%	
Chromosome	47.06%	13.51%			16.13%	7.11%	
Cytoskeleton		26.13%		62.50%	35.48%		
DNA damage			31.25%				10.88%
DNA repair			31.25%				8.16%
DNA replication							8.84%
DNA-binding	48.24%						
Helicase							4.08%
Kinetochore		6.31%			11.29%	4.35%	
Methylation	40.00%						
Microtubule		13.51%		37.50%	20.97%	8.70%	
Mitosis		18.02%		50.00%	28.23%	11.26%	
Motor protein		9.91%		37.50%	8.87%	3.75%	
Nucleosome core	35.29%						
Nucleotide-binding		20.72%		62.50%	23.39%		
Nucleus	70.59%		56.25%				

Cell populations sorted as shown in Fig. 2a (termed G1/G0, early S, middle S, and G2/M for further analysis) and subjected to RNA-seq analysis show differential expression of cell cycle-related mRNAs. Upregulated (UP) and downregulated (DOWN) mRNAs are shown separately for population pairs with differential mRNA expression. Second row (in bold) shows total number of differentially expressed genes between the corresponding populations. Further, percentages of genes present in the appropriate GO term from the total number of differentially expressed genes are given. In addition to the terms described in the table, there are other terms (associated with ubiquitination, metal binding, ribosome function, etc.), but since they have less significant padj (~0.001–0.005), they have not been included in the table

3. PI staining can be analyzed on virtually any flow cytometer as this fluorochrome is compatible with most optical configurations. In our protocol CytoFlex is used to verify the PI staining quality as it provides better peak resolution than FACSAria SORP sorter.
4. K-562 cells fixed with ethanol change their buoyancy and become harder to spin down. This should be kept in mind to avoid loss of material at this stage.
5. Note that DNA-binding dye staining is presented and analyzed on linear scale histograms. We routinely assess the peak resolution—*k*—as the ratio of G2/M to G0/G1 fluorescence intensity peaks on a cell cycle curve. It is also helpful to compare cell percentages in the gates set on the curve to monitor changes in cell culture and instrument variances.
6. Samples of PI-stained cells can be kept in PBS at +4 °C for at least 2 weeks without noticeable fluorescent signal deterioration.
7. EdU labeling prior to Hoechst 33342 loading results in higher staining intensity.
8. We have found that 100 μl of EdU detection mix is sufficient to stain up to 1×10^6 cells.
9. This staining procedure combined with cell cycle duration determination is described in [36]. Proliferative pool determination by prolonged EdU labeling provides cell cycle parameters of the given cell line avoiding tedious procedures. The overall cell cycle data obtained by EdU labeling for K-562 cells in given conditions are the following: with cell cycle duration around 19 h and 98% of proliferating cells (determined by microscopy), G1 phase lasts 4.2 h, S-phase lasts for 11.6 h, and G2 and mitosis cumulatively last 3.2 h.
10. As Hoechst 33342 is a live cell-permeable DNA-binding agent and potential carcinogenic/teratogenic substance, dye-containing solutions should be handled with care; wearing gloves and protective clothing is required.
11. Compared to the protocol originally described in [31], we decreased dye concentration (1 μg/ml vs 5 μg/ml).
12. G0/G1 vs G2/M peak resolution k is typically lower for vital Hoechst 33342 staining than for fixed PI staining. To minimize the difference and achieve better peak resolution, we compared a "no-wash" procedure and "dye efflux block" with the addition of verapamil to the culture medium. Since both methods yield very similar results, a "no-wash" approach has been favored as less invasive.
13. Since DNA-binding dyes are analyzed on a linear scale, they require a more stringent approach to data acquisition.

FACSAria is a high-throughput cell sorter with high flow speed, narrow laser intercept, and therefore short exposition period. To verify the sample staining quality, the use of another instrument is advisable (CytoFlex flow cytometer is a good option because of its high sensitivity, wide dynamic range, and especially low pressure and flow speed compared to FACSAria). Once the staining is verified, the sample is transferred to FACSAria to optimize sample acquisition parameters and makes DNA content curves comparable (*see* Fig. 1). To achieve maximal peak resolution on FACSAria instrument, sheath pressure and flow rate (pressure differential) have to be minimized (100 μm nozzle, flow rate = 1), and laser power has to be set to 60 mW (for 561, 488, and 405 nm lasers).

14. Hoechst 33342 is more efficiently excited by ultraviolet (355 nm) laser. However, it can also be excited by violet (405 nm) laser that is less efficient but also less phototoxic for live cells. In high-throughput FACS systems such as FACSAria, suboptimal excitation wavelength, and short exposition time are compensated for by high laser power density. To obtain similar resolution of DNA content peaks, 20 mW power of ultraviolet excitation and 60 mW power of violet excitation can be used.
15. Additionally, cells can be sorted onto glass slides in "single cell" mode for further microscopic examination.
16. Reanalyzing sorted fractions is a straightforward way to verify the sorting accuracy and can be performed before or after the primary cell sort. The instrument has to be thoroughly washed before and during reanalysis procedure.
17. Cells tend to lose their staining intensity when passed through a cell sorter; however, with vital dyes, the problem is solved by sorting cells into the medium containing same concentrations of vital dyes and providing a "recovery time" of at least 15 min at +37 °C for sorted cells. After that cells restore their staining intensities.
18. TMRE is often used as cell viability marker and restores its fluorescence intensity in sorted cells.
19. Both ethanol- and FA-based fixation protocols result in good EdU signal, but formaldehyde fixation better preserves the nuclear structure and is thus more suited for subsequent microscopy studies of isolated cell cycle subpopulations.
20. This was done as we were unable to reproduce the protocol for K-562 cell synchronization described in [17]. Our instance of this cell line didn't react on serum deprivation as described, transiting from proliferating state into apoptosis. Neither were we able to achieve reasonable synchronicity using double aphidicolin block method.

21. Three types of EdU incorporation patterns are discerned in K-562 cells; they were named Type 1, 2, and 3 (Fig. 2). The experiment was performed thrice yielding similar results. Representative images of EdU incorporation patterns and the enrichment diagram are shown in Fig. 2d, e, respectively.
22. Fluorescence-based Qubit RNA measurement is more preferable than standard UV-Vis spectrophotometry due to its specificity and sensitivity.
23. For each sorted sample, RNA integrity numbers (RIN) should be >8.5, indicating very low level of RNA degradation (see also Fig. 3a).

Acknowledgments

The work was supported by the Moscow State University Program of Development and by the Russian Science Foundation (grant #14-14-00088, sequencing and data analysis; grant #14-50-00029, optimization of RNA extraction and library preparation). Daria M. Potashnikova and Sergey A. Golyshev have contributed equally to this work.

References

1. Vermeulen K, Van Bockstaele DR, Berneman ZN (2003) The cell cycle: a review of regulation, deregulation and therapeutic targets in cancer. Cell Prolif 36(3):131–149. https://doi.org/10.1046/j.1365-2184.2003.00266.x
2. Zhong W (2008) Timing cell-fate determination during asymmetric cell divisions. Curr Opin Neurobiol 18(5):472–478. https://doi.org/10.1016/j.conb.2008.10.005
3. Wirtz-Peitz F, Nishimura T, Knoblich JA (2008) Linking cell cycle to asymmetric division: Aurora-A phosphorylates the Par complex to regulate Numb localization. Cell 135(1):161–173. https://doi.org/10.1016/j.cell.2008.07.049
4. Dey-Guha I, Wolfer A, Yeh AC, G Albeck J, Darp R, Leon E, Wulfkuhle J, Petricoin EF 3rd, Wittner BS, Ramaswamy S (2011) Asymmetric cancer cell division regulated by AKT. Proc Natl Acad Sci U S A 108(31):12845–12850. https://doi.org/10.1073/pnas.1109632108
5. Carpy A, Krug K, Graf S, Koch A, Popic S, Hauf S, Macek B (2014) Absolute proteome and phosphoproteome dynamics during the cell cycle of *Schizosaccharomyces pombe* (Fission Yeast). Mol Cell Proteomics 13(8):1925–1936. https://doi.org/10.1074/mcp.M113.035824
6. Hsieh SY, Zhuang FH, Wu YT, Chen JK, Lee YL (2008) Profiling the proteome dynamics during the cell cycle of human hepatoma cells. Proteomics 8(14):2872–2884. https://doi.org/10.1002/pmic.200800196
7. Marguerat S, Schmidt A, Codlin S, Chen W, Aebersold R, Bähler J (2012) Quantitative analysis of fission yeast transcriptomes and proteomes in proliferating and quiescent cells. Cell 151(3):671–683. https://doi.org/10.1016/j.cell.2012.09.019
8. Whitfield ML, Sherlock G, Saldanha AJ, Murray JI, Ball CA, Alexander KE, Matese JC, Perou CM, Hurt MM, Brown PO, Botstein D (2002) Identification of genes periodically expressed in the human cell cycle and their expression in tumors. Mol Biol Cell 13(6):1977–2000
9. Dominguez D, Tsai Y-H, Gomez N, Jha DK, Davis I, Wang Z (2016) A high-resolution transcriptome map of cell cycle reveals novel connections between periodic genes and cancer. Cell Res 26:946–962. https://doi.org/10.1038/cr.2016.84
10. Koval AP, Gogolevskaya IK, Tatosyan KA, Kramerov DA (2015) A 5′-3′ terminal stem in small non-coding RNAs extends their lifetime. Gene 555(2):464–468. https://doi.org/10.1016/j.gene.2014.10.061

11. Tatosyan KA, Kramerov DA (2016) Heat shock increases lifetime of a small RNA and induces its accumulation in cells. Gene 587(1):33–41. https://doi.org/10.1016/j.gene.2016.04.025
12. McDavid A, Finak G, Gottardo R (2016) The contribution of cell cycle to heterogeneity in single-cell RNA-seq data. Nat Biotechnol 34:591–593. https://doi.org/10.1038/nbt.3498
13. Velichko AK, Petrova NV, Razin SV, Kantidze OL (2017) Comparative analysis of the synchronization methods of normal and transformed human cells. Mol Biol 51:130–135. https://doi.org/10.1134/S0026893316060200
14. Sonoda E (2006) Synchronization of cells. Subcell Biochem 40:415–418
15. Schorl C, Sedivy JM (2007) Analysis of cell cycle phases and progression in cultured mammalian cells. Methods 41(2):143–150. https://doi.org/10.1016/j.ymeth.2006.07.022
16. Ma HT, Poon RY (2017) Synchronization of HeLa cells. Methods Mol Biol 1524:189–201. https://doi.org/10.1007/978-1-4939-6603-5_12
17. Wanda PE (1996) Immunochemical detection of cell cycle synchronization in a human erythroid cell line, K562. Methods Cell Sci 18:143–148. https://doi.org/10.1007/BF00122165
18. Urbani L, Sherwood SW, Schimke RT (1995) Dissociation of nuclear and cytoplasmic cell cycle progression by drugs employed in cell synchronization. Exp Cell Res 219(1):159–168. https://doi.org/10.1006/excr.1995.1216
19. Li CJ (2017) Flow cytometry analysis of cell cycle and specific cell synchronization with butyrate. Methods Mol Biol 1524:149–159. https://doi.org/10.1007/978-1-4939-6603-5_9
20. Helmstetter CE (2015) A ten-year search for synchronous cells: obstacles, solutions, and practical applications. Front Microbiol 6:238. https://doi.org/10.3389/fmicb.2015.00238
21. Shaw J, Payer K, Son S, Grover WH, Manalis SR (2012) A microfluidic "baby machine" for cell synchronization. Lab Chip 12(15):2656–2663. https://doi.org/10.1039/c2lc40277g
22. Banfalvi G (2017) Synchronization of mammalian cells and nuclei by centrifugal elutriation. Methods Mol Biol 1524:31–52. https://doi.org/10.1007/978-1-4939-6603-5_2
23. Ly T, Ahmad Y, Shlien A, Soroka D, Mills A, Emanuele MJ, Stratton MR, Lamond AI (2014) A proteomic chronology of gene expression through the cell cycle in human myeloid leukemia cells. eLife 3:e01630. https://doi.org/10.7554/eLife.01630
24. O'Donnell EA, Ernst DN, Hingorani R (2013) Multiparameter flow cytometry: advances in high resolution analysis. Immune Netw 13(2):43–54. https://doi.org/10.4110/in.2013.13.2.43
25. Darzynkiewicz Z, Crissman H, Jacobberger JW (2004) Cytometry of the cell cycle: cycling through history. Cytometry A 58(1):21–32. https://doi.org/10.1002/cyto.a.20003
26. Kim KH, Sederstrom JM (2015) Assaying cell cycle status using flow cytometry. Curr Protoc Mol Biol 111:28.6.1–28.6.11. https://doi.org/10.1002/0471142727.mb2806s111
27. Borisov VI, Korolkova OY, Kozhevnikov VS (2014) Application of flow-FISH for dynamic measurement of telomere length in cell division. Curr Protoc Cytom 69:8.14.1–8.14.10. https://doi.org/10.1002/0471142956.cy0814s69
28. Yu H, Ernst L, Wagner M, Waggoner A (1992) Sensitive detection of RNAs in single cells by flow cytometry. Nucleic Acids Res 20(1):83–88. https://doi.org/10.1093/nar/20.1.83
29. Yehuda Y, Blumenfeld B, Lehmann D, Simon I (2017) Genome-wide determination of mammalian replication timing by DNA content measurement. J Vis Exp (119):e55157. doi:https://doi.org/10.3791/55157.
30. Grolmusz VK, Tóth EA, Baghy K, Likó I, Darvasi O, Kovalszky I, Matkó J, Rácz K, Patócs A (2016) Fluorescence activated cell sorting followed by small RNA sequencing reveals stable microRNA expression during cell cycle progression. BMC Genomics 17:412. https://doi.org/10.1186/s12864-016-2747-6
31. Juan G, Hernando E, Cordon-Cardo C (2002) Separation of live cells in different phases of the cell cycle for gene expression analysis. Cytometry 49(4):170–175. https://doi.org/10.1002/cyto.10173
32. Siemann DW, Keng PC (1986) Cell cycle specific toxicity of the Hoechst 33342 stain in untreated or irradiated murine tumor cells. Cancer Res 46(7):3556–3559
33. Reno F, Luchetti F, Vitale M, Gregorini A, Valentini M, Papa S (1996) Sorting of cells from different cell cycle phases using surface antigen expression. Methods Cell Sci 18(2):93–98. https://doi.org/10.1007/BF00122159
34. Zielke N, Edgar BA (2015) FUCCI sensors: powerful new tools for analysis of cell proliferation. Wiley Interdiscip Rev Dev Biol 4:469–487. https://doi.org/10.1002/wdev.189
35. Wang D, Lu P, Liu Y, Chen L, Zhang R, Sui W, Dumitru AG, Chen X, Wen F, Ouyang HW, Ji J (2016) Isolation of live premature senescent cells using FUCCI technology. Sci Rep 6:30705. https://doi.org/10.1038/srep30705
36. Uzbekov RE (2004) Analysis of the cell cycle and a method employing synchronized cells for study of protein expression at various stages of the cell cycle. Biochem Mosc 69(5):485–496

Chapter 19

Measuring Nanoscale Chromatin Heterogeneity with Partial Wave Spectroscopic Microscopy

Scott Gladstein, Andrew Stawarz, Luay M. Almassalha, Lusik Cherkezyan, John E. Chandler, Xiang Zhou, Hariharan Subramanian, and Vadim Backman

Abstract

Despite extensive research in the area, current understanding of the structural organization of higher-order chromatin topology (between 20 and 200 nm) is limited due to a lack of proper imaging techniques at these length scales. The organization of chromatin at these scales defines the physical context (nanoenvironment) in which many important biological processes occur. Improving our understanding of the nanoenvironment is crucial because it has been shown to play a critical functional role in the regulation of chemical reactions. Recent progress in partial wave spectroscopic (PWS) microscopy enables real-time measurement of higher-order chromatin organization within label-free live cells. Specifically, PWS quantifies the nanoscale variations in mass density (heterogeneity) within the cell. These advancements have made it possible to study the functional role of chromatin topology, such as its regulation of the global transcriptional state of the cell and its role in the development of cancer. In this chapter, the importance of studying chromatin topology is explained, the theory and instrumentation of PWS are described, the measurements and analysis processes for PWS are laid out in detail, and common issues, troubleshooting steps, and validation techniques are provided.

Key words Partial wave spectroscopic microscopy, Chromatin structure, Chromatin topology, Nanoscale imaging, Fractal dimension, Cancer development, Heterogeneity, Live cell imaging, Transcriptional

1 Introduction

1.1 Chromatin Heterogeneity

Chromatin is a complex nuclear structure that comprises the genome including DNA, histones, RNA, and other nuclear proteins. Many of the most important cellular functions, such as DNA transcription, replication, and repair, occur within the chromatin

Electronic supplementary material: The online version of this chapter (https://doi.org/10.1007/978-1-4939-7680-5_19) contains supplementary material, which is available to authorized users.

Natasha S. Barteneva and Ivan A. Vorobjev (eds.), *Cellular Heterogeneity: Methods and Protocols*, Methods in Molecular Biology, vol. 1745, https://doi.org/10.1007/978-1-4939-7680-5_19,

structure. The organization of chromatin occurs across a range of length scales from a few nanometers up to the micron range. These changes are shown to have regulatory roles in these molecular functions. At the smallest length scales, the DNA molecule (1 nm) is wrapped around a core nucleosome particle (10 nm) whose regulatory role is mediated in part by posttranslational modification of the histone proteins. Above this length scale, chromatin is further compacted into a complex organization that is poorly understood (supranucleosomal structure). Studies utilizing chromatin conformation capture techniques have shown that between 100 and 300 nm, chromatin is organized into topologically associated domains, where genes within the same domain interact more frequently compared to adjacent regions [1]. At the largest length scales (>300 nm), chromatin is organized into chromatin territories, which can be resolved by visible-light diffraction-limited microscopy methods including confocal microscopy and wide-field fluorescence microscopy. Despite extensive research in this area, current understanding of chromatin organization in a range between 10 and 200 nm is still limited. Label-free visible-light optical microscopy techniques are optimal tools for studying cellular structures because they can image live cells in a noninvasive and nontoxic manner, but they are unable to resolve structures smaller than the diffraction limit (~200 nm). To probe these length scales, most methods to date rely on indirect measurements using chromatin conformation capture (3C, 4C, HiC, etc.) or direct measurements using electron microscopy, but these techniques involve intensive sample preparation and fixation, preventing temporal analysis of a cell in response to perturbation and potentially introducing artifacts. Therefore, noninvasive microscopic methods that are sensitive to structural alterations at these intermediate length scales are still lacking.

Notably, the organization of chromatin at these length scales (higher-order chromatin topology) defines the physical context (nanoenvironment) in which biological processes occur. In general, research into the aforementioned processes, such as DNA transcription or replication, has taken place in ex vivo dilute conditions, a context vastly different from what is found within cells. When the effects of the nanoenvironment are measured and taken into consideration, they demonstrate a critical functional role in the regulation of chemical reactions. For instance, multi-scale systems modeling using molecular dynamics simulations has shown that the physical environment, through macromolecular crowding, nonlinearly alters gene transcription by orders of magnitude [2]. Additionally, in vivo studies have shown that local nuclear density will slow the diffusion of macromolecules [3]. Finally, macromolecular crowding has been shown to affect protein binding stability and enzyme structure [4]. Thus, the capacity to measure and analyze the physical nanoenvironment modulated by higher-order

chromatin folding can increase our understanding of disease processes and molecular behaviors.

To study this physical nanoenvironment, we have developed a novel imaging technique, partial wave spectroscopic (PWS) microscopy, which allows real-time measurement of chromatin structure (chromatin folding) below the diffraction limit without introducing labels in live cells [5]. PWS microscopy allows one to measure variations in the interference spectrum of the backscattered light and to quantify heterogeneity in the structural organization within cells at the nanoscale level [6]. This capability derives from the interaction between light and intracellular mass. In particular, the wavelength-dependent variations in scattered light are determined by the density and distribution of molecules with sensitivity to macromolecular assemblies below the diffraction limit—i.e., higher-order chromatin in the nucleus. Analogously, while our eyes cannot resolve the micron-scale particles that compose clouds, we can obtain information on the size and distribution of particles when comparing the color of white clouds to the blue sky. When using PWS microscopy, the variations in mass density within a sample are quantified through $\sum$ (Fig. 1a, b) [5], which is a measure of intracellular nanoscale heterogeneity [6]. Chromatin heterogeneity refers to variations in structural density within the higher-order chromatin organization. Specifically, increases in heterogeneity result in an organization that is globally accessible paired with highly dense, local clumps of poorly accessible chromatin. As a visual example of what PWS microscopy measures, chromatin was simulated as a 10 nm "beads on a string" polymer with equivalent mass density, but different nanoscale organizations: differentially compacted (Fig. 2a) [5] and homogenously compacted (Fig. 2b) [5] chromatin fibers. The resulting diffraction-limited transmission microscopy images (Fig. 2c, d) [5] and $\sum$ images (Fig. 2e, f) [5] were calculated directly from the mass distribution of the simulations. The differences between these two configurations are nanoscale, so they cannot be resolved or sensed with the transmission microscope, but as a physical measure of heterogeneity at these length scales, PWS microscopy quantifies these differences with the heterogeneously organized chromatin producing a high-$\sum$ image compared to the homogenously organized chromatin.

1.2 Fractal Dimension

Intracellular nanoscale heterogeneity, measured using PWS, is directly correlated to the fractal dimension, D [6]. Fractal dimension defines the self-similarity of organization across a given range of length scales (the geometric relationship of a single nucleotide to a nucleosome to a fiber and so on) and is related to the space-filling capacity of a particular geometry. The organization of chromatin has been suggested to be fractal with dimension D using multiple techniques [7], such as small-angle neutron scattering [8],

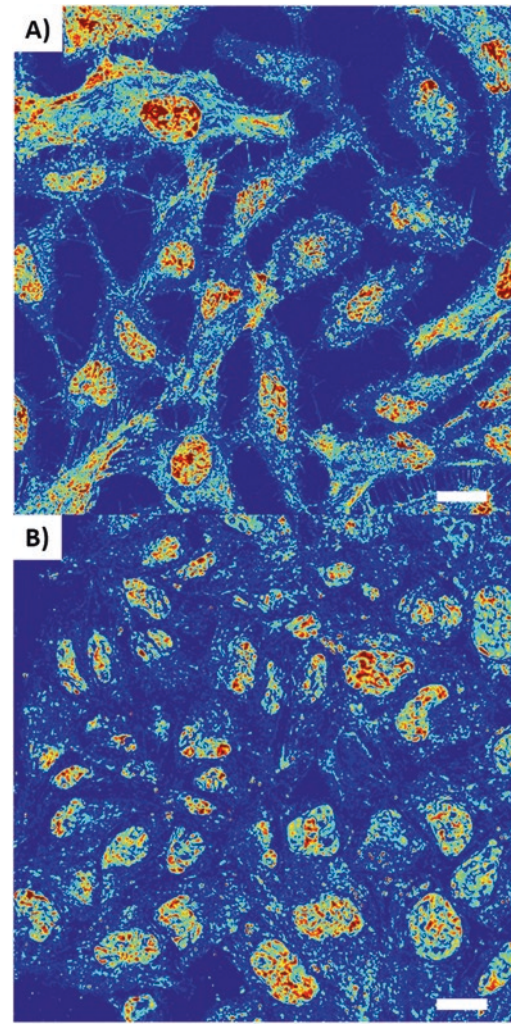

Fig. 1 Representative $\sum$ images of (**a**) HeLa cells and (**b**) Mes-SA cells quantify the heterogeneity of higher-order chromatin structure within label-free live cells. $\sum$ scaled to range between 0.01 and 0.05 in **a** and 0.01 and 0.065 in **b**. Scale bar: 20 μm. Figure originally published in [5]

fluorescence correlation spectroscopy [3], chromatin conformation capture [9], transmission electron microscopy [10, 11], and photon localization microscopy [12, 13]. It should be noted that the organization of chromatin as a fractal media is not synonymous with the fractal globule model. The fractal globule model is a specific case of a fractal structure with dimension $D = 3$ [14]; however, the power-law (fractal) scaling can be achieved by a random-loop polymer or a "fractal globule." Indeed, while the underlying scaling of chromatin organization can be explained by any of these models, all models converge on a self-similar geometry. Within chromatin, D is a measure of the structural heterogeneity. Increases

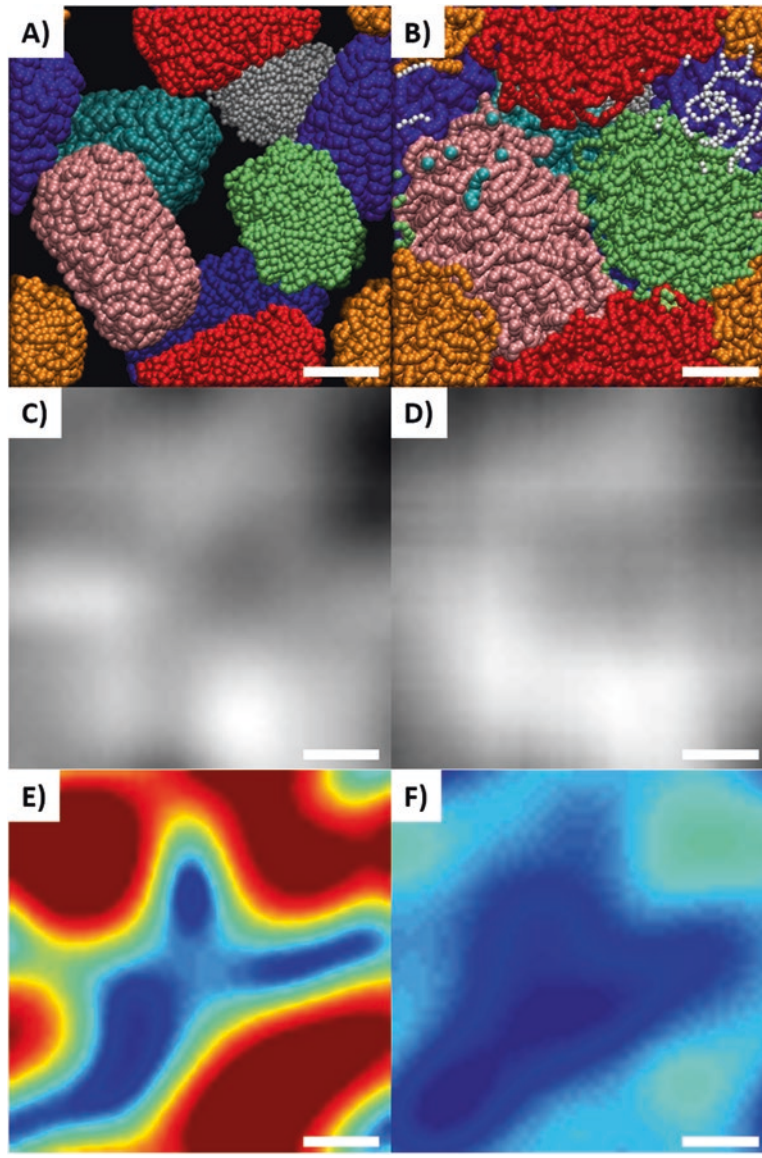

Fig. 2 Orthographic *z*-axis projection of molecular dynamics simulations of chromatin as a 10-nm-"beads-on-a-string" polymer with (**a**) differentially compacted (lc = 70 nm) and (**b**) homogenously compacted (lc = 20 nm) chromatin fibers. Diffraction-limited wide-field microscopy representation of the simulated (**c**) differentially compacted and (**d**) homogenously compacted chromatin fibers. These images were produced by calculating the average mass density at each pixel, and a Gaussian PSF of 250 nm was applied to simulate a conventional microscope. The grid size of the simulations was 10 nm. $\sum$ images calculated from the simulations of (**e**) differentially compacted and (**f**) homogenously compacted chromatin fibers. $\sum$ was calculated directly from the distribution of mass within configurations shown in A and B. $\sum$ scaled to range between 0.01 and 0.065. (Scale bar: 100 nm.) Figure originally published in [5]

in D will lead to an increase in chromatin surface area and variations in local density [15]. By increasing the chromatin surface area, DNA become more accessible to transcription factors. Conversely, increasing the heterogeneity of local density produces clumps of dense, inaccessible DNA. As these divergent responses are linked, it was theorized that a larger D leads to a divergence (or heterogeneity) in gene expression, where active genes become overexpressed, while repressed genes become further underexpressed [15]. We have demonstrated using PWS microscopy and microarray analysis that changes in $\sum$ result in global alterations in the pattern of gene expression, influencing critical cellular functions such as metabolism, proliferation, transcriptional regulation, signaling cascades, and cellular development [15]. As expected $\sum$ was correlated with the heterogeneity of gene expression, showing an overexpression of initially active genes, and an underexpression of initially repressed genes as $\sum$ increases [15]. Additionally, while the current consensus indicates that the spatial correlation function of chromatin density distribution follows power-law scaling, these results and our interpretations of PWS measurements are still valid under conditions where chromatin organization is non-fractal. Regardless of the nature of chromatin folding, the organization of chromatin can be described by a spatial correlation function of its density in the form of the Whittle-Matern family of functions [6]. In this approach, the scaling relation D remains proportional to the molecular correlation distance even for non-fractal media and quantifies the self-similarity of chromatin organization. As a result of the correlation between $\sum$ and D, PWS can be used to explore the relationship between higher-order chromatin structure and global changes in gene expression.

1.3 The Role of Chromatin Heterogeneity in Cancer

This divergence in gene expression in response to altered chromatin topology may play a role in the development of cancer. This would not be a surprise as the dysregulation of gene networks, in particular, the inhibition of tumor suppressors and the activation of pro-growth oncogenic pathways, is a hallmark of tumorigenesis. Histological (microscale) alterations in the nuclear structure, such as size, shape, chromatin texture, nuclear matrix, etc. have been a gold standard of tumor identification across multiple types of cancer [16, 17]. In addition to the typical histological markers, an increased microscale fractal dimension of chromatin has been detected across different cancer types and shows potential prognostic value [18–21]. Further, transmission electron microscopy (TEM) has identified increases in nanoscale chromatin fractal dimension at an early stage prior to any histologically detectable changes in colorectal cancer (CRC) animal models and human samples from patients with colorectal adenomas [11]. Fixed-cell PWS microscopy has detected these same structural changes, which extend to a variety of cancers: colorectal, lung, pancreas, ovarian,

esophagus, and prostate [22–27]. Furthermore, these alterations detected using TEM and PWS microscopy are observed throughout the entire organ, not just at the location of the lesion. This is due to field carcinogenesis which is the concept that diffuse molecular and structural alterations exist in healthy tissue prior to the development of a localized tumor. These results suggest that measuring chromatin topology in patient samples using PWS microscopy has promising potential as a tool for cancer screening.

These findings indicate that increased chromatin heterogeneity is an early and near-universal step in the development of cancer regardless of the underlying tissue or molecular pathway. Mechanistically, the role of a more heterogeneous chromatin topology in early carcinogenesis could be related to increasing the heterogeneity of gene expression, thereby enabling greater sampling of the genome—an advantageous survival response to repeated environmental stress conditions [15, 28]. Over time there will be an evolutionary selection for a population of cells with the greatest capacity to explore their genome, a higher tolerance to environmental stress, a broad distribution of initial cells states, and ability to delay commitment to apoptosis; these are features which may facilitate tumor formation [28].

1.4 PWS Microscopy Theory

The ability of PWS microscopy to probe intracellular nanoscale organization derives from the relationship between the distribution of mass density, refractive index, the scattering of light, and the interference of light. Mass density and refractive index are related by the Gladstone-Dale relationship $n = n_w + \alpha\rho$, where n_w is the refractive index of water, α is the specific refractive index increment (0.18 ml/g), and ρ is the cell density. Light incident upon cells will be weakly scattered due to variations in refractive index arising from the distribution of mass/macromolecular structures. Within our system, light interference is utilized to enhance the signal from this weakly scattered light.

Specifically, cells are illuminated from below, and the light reflects from two main sources: (1) the strong reflection at the glass-cell interface due to the large refractive index (RI) difference (referred to as the reference reflection) and (2) the weakly scattering light from within the cell due to RI variations (referred to as internal scattering) (Fig. 3). These two signals interfere, amplifying the scattering signal and resulting in spectral intensity variations, deriving from the distribution of RI with a sensitivity to length scales between 20 and 200 nm.

In more detail, if we assume an inhomogeneous sample with RI distribution $n_1[1 + n_\Delta(r)]$ as a function of location r (Fig. 3) is placed into the focal plane of our microscope, then for the spectral variance of the image intensity, $\sum^2(x, y)$, within the measured wavenumber range, Δk will be related to the organization of refractive index within the sample as

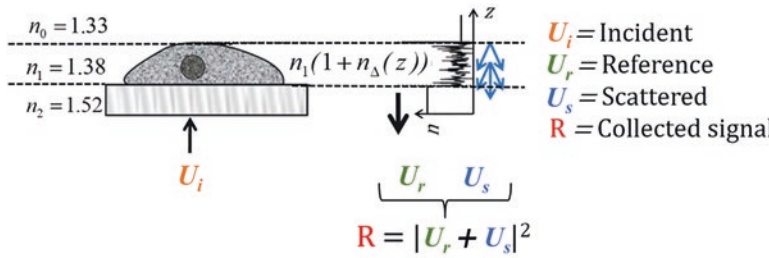

Fig. 3 Diagram of the live cell PWS sample geometry. PWS microscopy requires one strong reflection, referred to as the reference. In our live cell PWS setup, the reference originates from the refractive index difference between the glass and cell. The internal scattering signal comes from the refractive index variations within the cell due to the organization of mass. PWS quantifies the higher-order organization of chromatin by measuring the spectral variations due to the interference between the reference and the internal scattering

$$\frac{E\left[\Sigma^2\right]}{k_c L} = \frac{R k_c}{\Delta k} \int_{T_{3D}} \Phi_{n_\Delta}(k)\, d^3k \propto \sigma_{n_\Delta}^2 l_c$$

where $E[\sum^2]$ is the expected value of $\sum^2$, $\Phi_{n_\Delta} = \left|\mathcal{F}\left\{n_\Delta(r)/V\right\}\right|^2$ is the power spectral density of the sample RI variations n_Δ normalized by sample volume V, k_c is the central wavenumber of the illumination bandwidth evaluated inside the sample, L is the sample thickness, $R = R_{01}T_{01}T_{10}$ is an intensity normalization based on the Fresnel transmission (T_{01}, T_{10}) and reflection (R_{01}) intensities at the sample interfaces, T_{3D} includes spatial frequencies k with longitudinal coordinates k_z between $2k_1$ and $2k_2$ (k_1 and k_2 are the lower and upper wavenumbers of the instrument bandwidth) evaluated within the sample, $\sigma_{n\Delta}$ is the standard deviation of RI fluctuations, and l_c is the RI correlation length [6, 29].

In short, $\sum$ is a measure of the distribution of mass density within the sample. It is proportional to the variance of molecular density and the correlation length of the molecular density arrangement within the sample. The correlation length, l_c, describes the distribution of different length scales present in the sample. Furthermore, $\sigma_{n\Delta}$ and l_c are both proportional to the heterogeneity of the RI distribution.

1.5 PWS Instrument

A diagram of the live cell PWS instrument can be seen in Fig. 4 [5]. A broadband noncoherent white light (from X-Cite 120LED) is passed in through the episcopic port of a commercial microscope base (Leica DMIRB) with a low illumination NA. Then the light enters the filter cube, where a UV blocking filter is used to remove harmful wavelengths for live cell imaging, or alternative filters can be used for fluorescence colocalization. A high-magnification oil-immersion objective (63× Leica HCX PL APO, NA 0.6–1.4) focuses the light onto the sample. The backscattered light is collected and

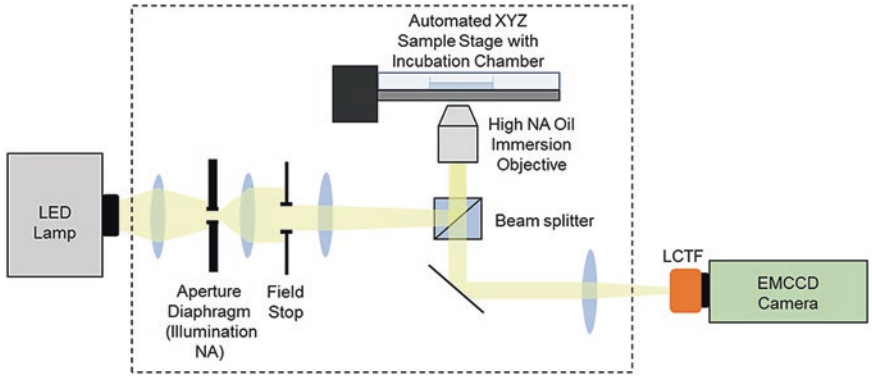

Fig. 4 Diagram of the PWS microscope. The system is built into an inverted commercial microscope base. The illumination is provided by a broadband white light source. The light scattered from within the cell is collected with an oil-immersion objective, spectrally filtered with a liquid crystal tunable filter and imaged on a CCD camera. Figure originally published in [5]

spectrally filtered (CRi VariSpec LCTF) across a range of wavelengths while imaging with a scientific camera (Hamamatsu Image-EM CCD) at each wavelength.

PWS instrumentation can be constructed in a variety of ways assuming the design criteria described above are met. Any nonspatially coherent broadband visible light source is viable if it has a relatively flat emission spectrum (without sharp peaks) in the visible range and low temporal variations. Spectral filtration can be performed on either the illumination or collection side of the system, although in a live cell instrument, filtration on the illumination side is preferred to minimize power at the sample. Another potential benefit of illumination side spectral filtration is that it can eliminate the need for additional filters to remove potentially damaging wavelengths (UV/IR) from the source spectrum before the sample. In addition to the location of the spectral filter, multiple methods of filtration can be used depending on the experimental goals of the system. On the illumination side an acousto-optic tunable filter (AOTF) or tunable monochromator works well, and on the collection side, a liquid crystal tunable filter (LCTF) or spectrometer can be used. These different filter methodologies provide options depending on the desired system complexity, speed, spectral resolution, and ability to perform experiments with other optical imaging modalities on the same hardware. Finally, any low-noise, high-sensitivity scientific camera such as an EMCCD or sCMOS designed for fluorescence microscopy should be suitable for image collection. The choice of camera and objective magnification should ideally provide a resolution of approximately two pixels per diffraction-limited spot for an accurate spatial sampling of the spectra.

1.6 Fluorescence Colocalization

As a multimodal system, the PWS microscope can also acquire fluorescence images for colocalization or other biological tests to combine

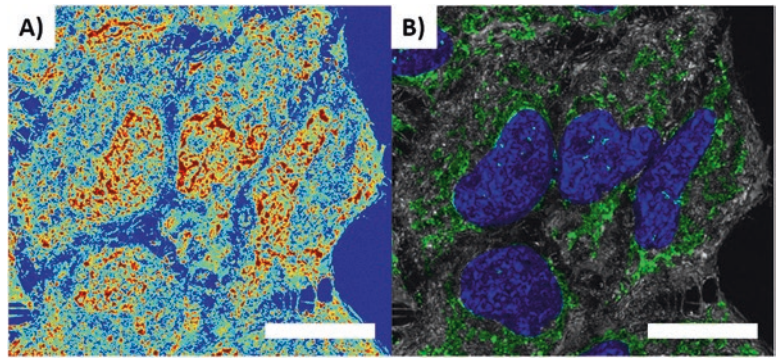

Fig. 5 The live cell PWS microscope is a multimodal instrument capable of colocalizing. (**a**) PWS $\sum$ images with (**b**) wide-field fluorescence microscopy showing mitochondria (green), nuclei (dark blue), and mitochondria-nucleus overlap (light blue). $\sum$ scaled to range between 0.0125 and 0.065. Scale bar: 20 μm. Figure originally published in [5]

molecular specificity with sensitivity to nanoscale structures. Not only does this enable easy segmentation of nuclear $\sum$ but allows for further segmentation to measure the macromolecular assemblies for a variety of cellular organelles and functional domains (Fig. 5) [5]. Additionally, colocalization with fluorescently labeled proteins (e.g., HER2: GFP) enhances the ability of PWS to explore the important relationship between cellular structure and molecular function in live cells. We have demonstrated the capability to integrate PWS microscopy with confocal [30] and wide-field fluorescence microscopy [5], and integration with super-resolution imaging methods such as PALM/STORM, SIM, or STED is achievable.

1.7 Experimentally Observed Chromatin Alterations

PWS microscopy is an ideal tool to study real-time alterations in chromatin structure because it (1) quantifies structural organization at length scales (20–200 nm) difficult to image with alternative techniques (2) using label-free contrast and low imaging power to preserve cellular integrity and function, with (3) high-throughput, real-time imaging speed, and (4) the ability to track individual cells over time. As an example of experimentally observed chromatin alterations, we have treated HeLa cells with 2 μM of daunorubicin for 15 min (Fig. 6). Daunorubicin is a chemotherapy drug that influences chromatin topology through multiple mechanisms, such as intercalation and nucleosomal eviction [31]. Through PWS imaging, we have observed that treatment with daunorubicin induces homogenization of the chromatin structure [33 ± 9% (mean ± SD) decrease in $\sum$, population measurements comparing treated with untreated, n = 18 experiments with ~30 cells in each group]. In the daunorubicin experiments, we have shown differences in chromatin topology between two population groups (treated vs. untreated).

As an example of using PWS to track chromatin alterations in individual cells, we have treated a triple-negative, mutant *TP53* breast cancer cell line, MDA-MB-231, with 5 μM of the zinc chelator

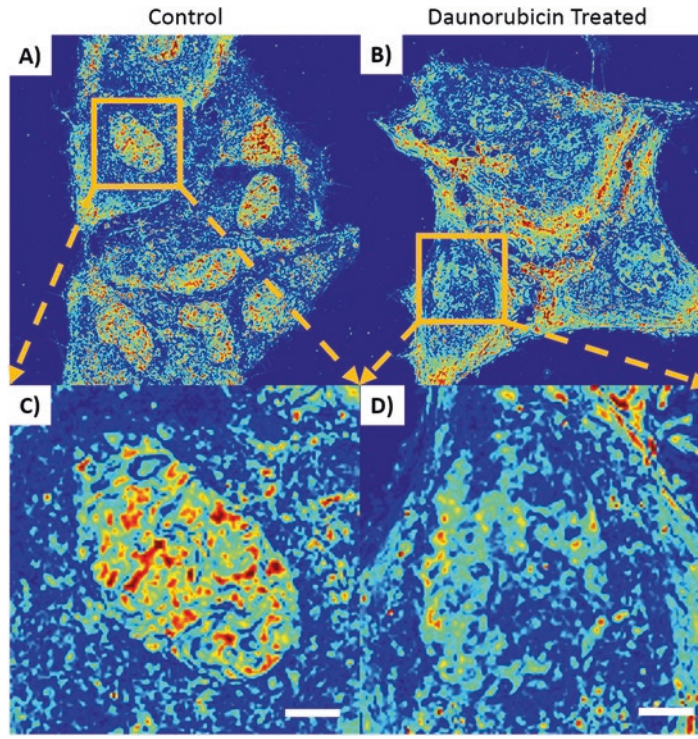

Fig. 6 Effects of daunorubicin on chromatin structure. (**a**) $\sum$ image of untreated HeLa cells. (**b**) $\sum$ image of HeLa cells treated with 2 μM of daunorubicin for 15 min. Daunorubicin treatment induces homogenization of chromatin organization. (**c**) Zoomed in $\sum$ image of untreated nuclei. (**d**) Zoomed in $\sum$ image of daunorubicin-treated nuclei. Scale bar: 5 μm

TPEN (Fig. 7). This treatment is expected to sequester intracellular labile zinc thus inducing a zinc-deficient state. Because of zinc's ubiquitous roles, the downstream effects of this treatment are likely multifold including a change in the concentration of ions in the nucleus, alteration of metalloprotein structure and activity, and disruption of key metabolic pathways. Under this treatment, there is an observed increase in the heterogeneity of chromatin within 30 min of treatment [8.2 ± 1.2% (mean ± SEM) decrease in $\sum$, individual cells tracked over 30 min, n = 24 cells]. Last, we show that PWS makes it possible to track individual cells over time by continuously imaging live MDA-MB-231 cells over the course of 30 min (Video 1).

2 Materials

2.1 Reagents

1. Immersion oil (Cargille Immersion Oil, Type 37 for imaging at 37 °C or LDH at room temperature).
2. Size 0, 1, or 1.5 sterile glass-bottom imaging dishes (can be purchased from MatTek, CellVis, or World Precision Instruments) (*see* **Note 1**).

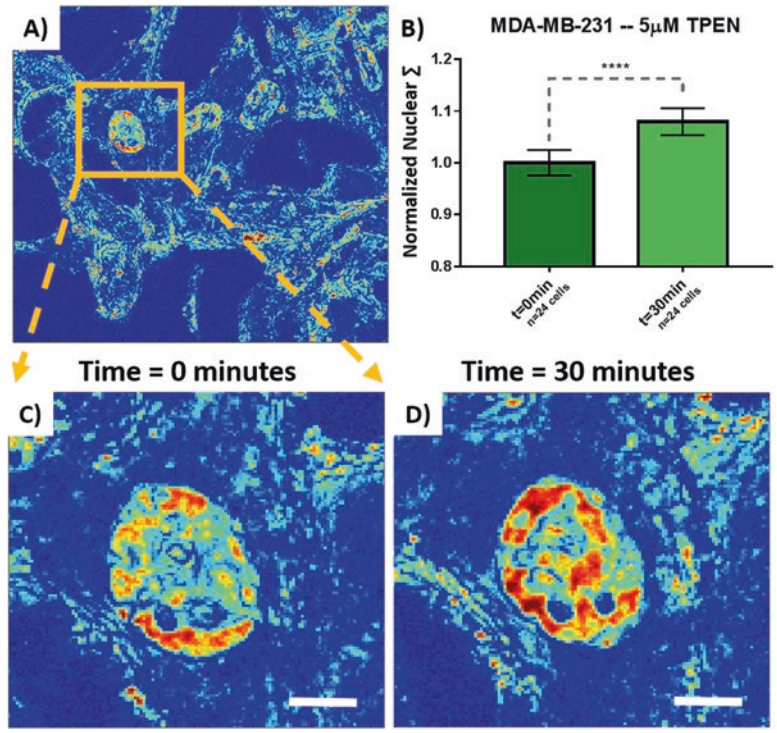

Fig. 7 Effects of the zinc chelator TPEN on chromatin structure. (**a**) $\sum$ image of the untreated MDA-MB-231 cell. (**b**) Quantification of average nuclear $\sum$ normalized to the initial state from the same cells before treatment and after 30 min of treatment with 5 μM TPEN. This TPEN treatment induces an increase in the heterogeneity of chromatin organization. (**c**) Zoomed in $\sum$ image of nuclei before treatment. (**d**) Zoomed in $\sum$ image of the same nuclei after 30 min of treatment. Scale bar: 5 μm. ****$p < 0.0001$ using paired student's *t*-test

3. Mixed balance (N_2, O_2, and CO_2) gas tanks to maintain atmospheric conditions and pH for continuous cell growth. Formulation of the mix depends on the cell line of interest.
4. Cell media is determined by the cell type of interest (RPMI 1640, McCoys 5A, DMEM, and many others are compatible with system measurements). Changes in phenol red absorption in pH-dependent experiments can alter the spectra.

2.2 Equipment

1. Commercial microscope base (preferably inverted) with an episcopic light path (e.g., Leica DMIRB).
2. Broadband nonspatially coherent white light source (X-Cite 120LED).

   It is ideal to select a source with a relatively flat output spectrum in the visible range (~400–700 nm) without any sharp peaks. It is also recommended that the instrument utilize a light source with minimal temporal variations.
3. High-magnification oil-immersion objective (63× Leica HCX PL APO, NA 0.6–1.4).

Objective and camera selected for imaging should result in a pixel size below the diffraction limit. (<250 nm), ideally yielding two pixels per diffraction-limited spot.

4. Spectral filter (CRi VariSpec LCTF).
   Many varieties are viable including AOTF, LCTF, tunable monochromator, or spectrometer. Can be placed in illumination or collection path depending on system design goals and filter type chosen.
5. Scientific camera such as an EMCCD or sCMOS (Hamamatsu Image-EM CCD).
   sCMOS is recommended for higher-speed imaging and a larger field of view unless other modalities being performed require the sensitivity of an EMCCD.
6. Automated stage.
   Allows for automatic collection of multiple fields of view.
7. Autofocus system is recommended for long-time series (>30 min) experiments.
8. Automated shutter.
   Can be used to automatically block light when not imaging to avoid damaging cells for multiple hour experiments (*see* Subheading 3.10).
9. Thin film phantoms (Filmetrics Inc.).
   Can be used for validation experiments (*see* Subheading 3.8).
10. Fluorescence filters.
11. UV filter. UV irradiation damages cells through multiple pathways, such as DNA damage [32], membrane permeabilization [33], and altered mitochondrial behavior [34]. It is advisable to block all UV light (100–400 nm) from illuminating the cells. If the tunable spectral filter is placed on the collection side of the instrument, then a UV filter must be added to the illumination side to prevent cell damage. If the tunable spectral filter is placed on the illumination side, then no extra filter is necessary, but you must avoid tuning the spectral filter to UV wavelengths during acquisition.
12. Live cell incubator.
13. Computer.

3 Methods

3.1 System Setup

1. Turn on the digital camera source and allow the requisite time for heating up before proceeding. Systems that require cooling should achieve a stable temperature before measurements begin. Then turn on light source and automated stage controller.

2. Set up the live cell incubated chamber if not already configured. Some cell lines require the use of a mixed balance, 21% O_2, 5% CO_2, and balance N_2. Prior to imaging, ensure a proper flow to the cells to produce a stable environment in the incubated chamber. Check to make sure the internal temperature of the chamber is stabilized at 37 °C unless the experiment requires an alternate temperature (*see* **Note 2**).
3. Set the microscope to episcopic/reflection mode.
4. Set the filter cube to UV blocking filter (if necessary) to protect the live cells from damage.

3.2 Preparing Samples

1. Using standard culture conditions and media requirements as applicable to the cell line of interest, grow cells on a glass-bottom petri dish until they are about 50–70% confluent. Cells can be observed using a separate transmission microscope to ensure proper density and morphology. Some cell lines require additional plating time to stabilize; in general we recommend at least 24 h after splitting to allow cells to adhere and acclimate before experimentation. These experimental protocols are designed to be used with adherent cell lines. Caution should be used with nonadherent cell lines, as changes in sample geometry (Fig. 3), cell motion, etc. can interfere with the PWS signal.
2. Switch to the oil-immersion objective of desired magnification. Place a drop of immersion oil on top of the objective, and then place the dish in the microscope incubation chamber. Course adjust the objective focus until oil contacts the glass bottom of the dish. Allow at least 15 min for the oil to reach thermal equilibrium in order to avoid focal drift during acquisition.
3. Tune the spectral filter to the central wavelength of the imaging range to focus on the cell imaging plane of interest (*see* **Note 3**).

3.3 Measuring Cellular Heterogeneity

1. Using either the microscope eyepieces or computer software with live feed camera display, fine adjust the objective focus until cells and/or substrate is in focus for a fixed wavelength. *See* **Note 4** if a clear focused image cannot be obtained.
2. Locate a region in the dish without any cells or debris for a normalization measurement. Normalization accounts for changes in the lamp, camera, and cell media prior to imaging. If a clear region cannot be located, a clean dish with identical cell media can be used for the normalization measurement.
3. Readjust focus as necessary.
4. Tune the spectral filter to scan the filtration wavelength through the chosen wavelength range, and sync the camera to collect an image at every wavelength. This configuration will

allow for a collection of interference spectra. *See* **Note 5** for details on setting up imaging parameters.

5. This interference spectra data should be saved as a 3-D image cube of dimensions x-pixel-range by y-pixel-range by wavelength range (x, y, λ). It is helpful to automatically save additional imaging parameters such as date, time, exposure time, lamp power, wavelength range and step size, stage position, etc.
6. Locate a field of view with desired cells to image and readjust focus if necessary.
7. Once located and focused, acquire the cellular interference spectra (3-D image cube). Make sure to record imaging location if you plan to reimage the same cells after treatment or later in the experiment.
8. It is best practice to analyze the first image cube to check for any artifacts before proceeding with the experiment (*see* **Note 6**).
9. Repeat **steps 6** and **7** as many times as needed to reach desired sample size.

3.4 Colocalization with Fluorescence (See Note 7)

1. Locate a field of view with desired cells to image and readjust focus if necessary.
2. Switch the filter cube to the appropriate filter for the fluorescence dye in use.
3. Tune the spectral filter to sweep the filtration wavelength based on the emission spectra of the fluorophore. Note, systems with multiple camera ports can utilize a second camera without a spectral filter for colocalization. Alignment between the two cameras can be made with a standard fiduciary marker.
4. Set the camera to capture an image at each wavelength, average those images together, and save the resulting fluorescence image.

3.5 Data Analysis

1. Subtract the dark counts of the digital camera from every point in the collected image cubes and normalization cube (*see* **Note 8**).
   $\text{image\_cube}(x, y, \lambda) = \text{image\_cube}(x, y, \lambda) - \text{dark counts}$
2. If exposure times varied, divide every point in the collected image cubes and normalization cube by the exposure time.
   $\text{image\_cube}(x, y, \lambda) = \text{image\_cube}(x, y, \lambda)/\text{exposure time}$
3. Divide the image cube of cell measurements by the normalization cube.
   $\text{image\_cube} = \text{image\_cube}/\text{normalization\_cube}$
4. Use a low-pass filter across the spectra at each x-y pixel in the normalized image cube to eliminate high-frequency noise.

- The cutoff frequency should be set to remove spectral frequencies that do not originate from the sample. First, there cannot be frequencies above the spectral resolution of the spectral filter being used. Also, the theoretical frequencies expected from the sample can be calculated from sample thickness and imaging parameters (*see* **Note 5**). Alternatively, this can be determined by checking the spectra (*see* Subheading 3.7).

5. To calculate Σ at each *x*-*y* pixel, take the standard deviation of the filtered, normalized image cube across the wavelength range. This will produce the 2-D matrix, Σ(*x*, *y*).
6. Perform region-of-interest analysis for each Σ image to capture average Σ of whole cells or cellular compartments (e.g., nuclei) (*see* **Note 9**). All operations may be performed in MATLAB.

3.6 Cleaning Up System

1. Remove the dish from the incubated chamber and properly dispose of.
2. Turn off the mixed balance tank and ensure flow stabilizes at 0 CCM.
3. Clean oil off the objective using lens paper with a few drops of methanol. Be very gentle to avoid damaging the objective.
4. Turn off the light source, manual stage controller, and digital camera source immediately.

3.7 Examining Spectra

Checking both the raw and normalized spectra is a good way to diagnose issues with the system or individual data.

3.7.1 Normalized Spectra

To examine the normalized spectra, perform the analysis procedure through the filtration **step** (#**4**). Then, plot the intensity as a function of wavelength at individual pixels to view the interference spectra (Fig. 8a, b).

Individual Pixel Spectra. Ideal spectra at individual pixels should vary from point to point and contain a variety of frequencies. If the spectra do not vary from point to point (in an inhomogeneous sample like a cell), then the instrument is not collecting the interference signal, or it is being dominated by an undesired signal. The spectra should contain all frequencies in *k*-space up to $n_1 \times L/\pi$, where n_1 is RI of the sample, and L is the sample thickness. Spectra from within the cell can be compared to background spectra to determine the frequencies that come from the sample versus noise. Noise should be filtered out in post-processing.

Averaging Spectra. Multiple individual spectra can be averaged over an area large enough to contain multiple diffraction-limited spots to observe the mean spectra. This averaging should remove the interference information. An ideal mean spectra should be relatively flat compared to the individual spectra. In regions without cells, the normalized intensity should be equal to one (image_cube

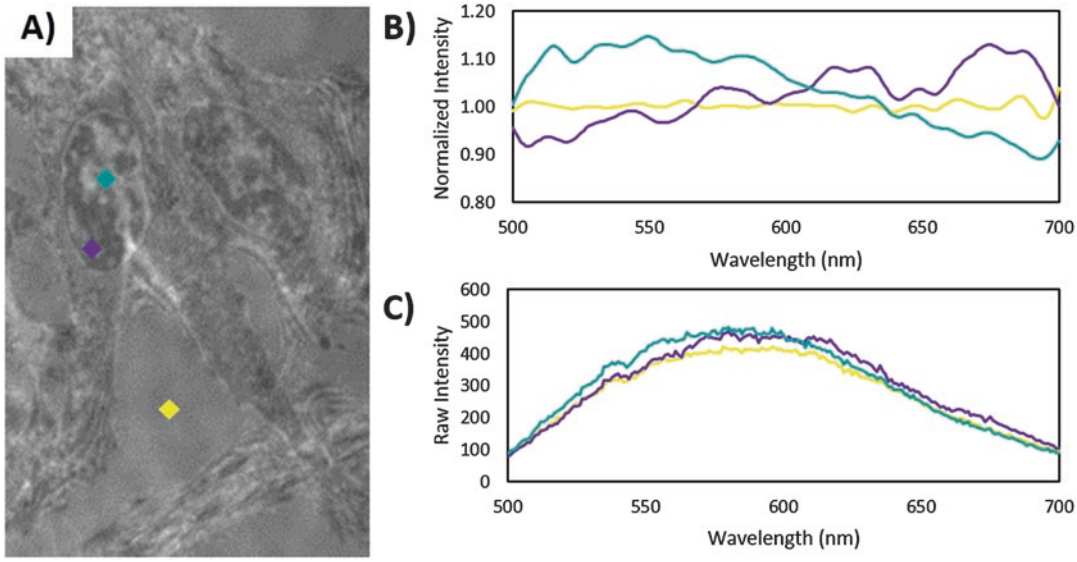

Fig. 8 Example spectra. (**a**) Reflection image of cells showing the location of the graphed spectra. (**b**) These normalized individual spectra from the nuclei (purple and turquoise) show a variety of frequencies and vary between locations. The spectrum from the background (yellow) is flat across the spectral range. (**c**) The raw spectra from the same locations are largely dominated by the lamp spectra

intensity equal to normalization_cube intensity). The standard deviation of the mean spectra can be compared to individual interference spectra to check how much of the signal is coming from interference versus other unwanted sources. Any spikes or consistent features of the mean spectra may be due to issues such as switching artifacts from the spectral filter, improper timing/delays of the spectral filter, and absorption or fluorescence from dyes.

Checking the spectra from phantoms (*see* Subheading 3.8) is a useful technique for validating your instrument. It should be noted that these phantoms are likely to be homogenous, so it is normal if the individual pixel and averaged spectra are identical.

3.7.2 Raw Spectra

No analysis is required to view the raw spectra. Just plot the intensity from your image_cube or normalization_cube as a function of wavelength at individual pixels (Fig. 8a, c). Raw spectra mostly provide information on the lamp profile, which is useful for determining the wavenumber range used for imaging. Avoid using regions in the lamp spectra with low signal. Raw spectra are also useful for identifying saturation regions of your spectra. These regions can be identified by looking for totally flat and maximized regions of the spectra. If the camera is saturating, the exposure time or lamp power must be reduced. Finally, raw spectra can be used to determine whether artifacts found in the normalized spectra are due to the image_cube or the normalization_cube or both as the spectra can be viewed individually.

3.8 System Validation: Phantoms

Phantoms can be used to provide a standard for system validation. The simplest phantoms are measurements taken from surface reflections with different theoretical reflection intensities, such as glass-air, glass-water, glass-glycerol, sapphire-air, silicon-air, etc. RI matching liquids (Cargille Laboratories) can be used to create a large variety of interfaces. The expected reflectances can be calculated with Fresnel equations. These tests can show extra reflections in the system, dirty lens/objectives, improper analysis normalization, and other issues. Care should be taken to match experimental and theoretical reflectance values in a wavelength-dependent manner since the wavelength-dependent precision of the instrument is crucial for PWS measurements.

Filmetrics, Inc. provides a variety of thin film thickness standards that produce a stable and well-characterized uniform interference signal. The measured spectral interference frequencies can be compared to theoretically calculated frequencies to validate your system. In addition to validation, these phantoms also provide a good standard to compare between different systems and to check your system's performance stability over time or after instrumentation changes.

3.9 System Validation: Live Cell Delta

One useful practice to ensure stability in the system and cell lines is to monitor a consistent structural alteration. The daunorubicin treatment (HeLa cells with 2 μM of daunorubicin for 15 min) previously discussed is a good experiment to use for this validation. While further work is needed to unravel the molecular basis of this alteration, it is stable and can be used to validate/monitor system sensitivity to chromatin structural alterations in many contexts: over time, after system changes, through cell line passages, after different cell preparation protocols, etc.

3.10 Cell Stability

Cell stability should be tested to ensure that the system, imaging parameters, and experimental design are not affecting your data. Acquire PWS images of the same cells without treatment over the duration of a typical experiment to check that $\sum$ is stable over time. It is normal for $\sum$ to fluctuate in time as chromatin structure is dynamic, but there should not be a directional change. If $\sum$ is not stable, it may be due to too bright illumination of the specimen or improper cell incubation/handling. There are a few solutions if lamp intensity is affecting the cells:

- Minimization of the light on cells can be achieved by employing spectral filtering at the illumination source instead of filtering at the collection side of the instrument.
- Reducing the duration of the experiment can help.
- Make sure proper UV filtering is being implemented.
- An automatic shutter can be used to block the light whenever measurements are not performed.

3.11 Using ImageJ to Create Movies

1. Acquire PWS data of the same field of view over desired period of time.
2. Analyze and output $\sum$ images into a folder with sequentially numbered file names.
3. Open ImageJ and select File-Import-Image Sequence.
4. Choose appropriate folder and change Sequence Option if desired.
5. Select File-Save As-AVI.
6. Set a number of frames per second and compression (if desired).
7. Save movie file.

4 Notes

1. **Sample Geometry and Substrates**

   To achieve the proper PWS interference signal, the sample geometry must contain one and only one strong reference reflection. For live cell PWS, this is produced by the cell-glass interface (RI mismatch: 1.52–1.38), while the cell-media interface (RI mismatch: 1.38–1.33) results in a weak reflection (Fig. 3). For fixed-cell PWS, the reference reflection is produced by the cell-air interface (RI mismatch: 1.0–1.53), while the cell-glass interface (RI mismatch: 1.53–1.53) produces almost no reflection. If the sample or substrates are changed, be sure this requirement is satisfied.

   In general, glass-bottom imaging dishes are used because they are affordable and compatible with our imaging parameters, but alternative substrates such as sapphire can be implemented to increase the strength of the reference, resulting in an increase in SNR. On the other hand, a weaker reference reflection will reduce the SNR of your system.

2. **Temperature Stabilization**

   It's preferable to have the temperature stabilize around 36–37 °C. If the temperature has stabilized below this range, then check that the set point temperature is properly set to 37 °C, ensure the incubator window is closed, and wait a few minutes. If the temperature has stabilized above this range, then check the configurations of the system. For experiments testing the influence of thermal stress (heat shock conditions), allow sufficient time for thermal expansion and stabilization of imaging oil.

3. **Scanning Wavelength**

   Searching for cells and adjusting focus with the spectral filter tuned to the central wavelength is ideal because it minimizes focal drift due to chromatic aberrations. If the maximum lamp

intensity occurs at a different wavelength, it is a good idea to check this wavelength to ensure the camera is not saturating with the current exposure time. Saturation of signal at any wavelength will result in improper measurements of the interference signal.

4. **Blurry Image, Focus Issues, etc.**

   If you are having trouble focusing/getting a clear image, there are a few easy-to-solve culprits:

   (a) Water or condensation on the bottom of the petri dish can cause artifacts like blurry images. Clean off the bottom of the imaging dish and objective with methanol before applying new oil to the objective and starting again.

   (b) Air bubbles in the immersion oil will cause large dark shapes in the field of view. These can be avoided simply by moving to a new area. If that doesn't solve the problem, clean off the bottom of the dish, clean the objective, add new oil to the objective, and start again.

   (c) If the glass on the bottom of your petri dish is thicker than the working distance of the objective, then you will need different dishes. Typically, size 0, 1, or 1.5 glass will work with most objectives. The working distance should be a specification provided when purchasing your objective.

5. **Imaging Parameters**

   Before taking measurements, imaging parameters must be set, which will vary based on your sample, system, and experimental design. There are four goals to consider when determining imaging parameters. First, you should capture all the spectral frequencies produced by your sample. The signal should contain all frequencies in k-space up to $n_1 \times L/\pi$, where n_1 is the RI of the sample, and L is the sample thickness. Second, the SNR of your signal should be maximized. Third, you want to avoid introducing artifacts into the measurement. Finally, the measurement time should be minimized to increase efficiency and reduce light exposure on the cells.

   Step Size: The chosen step size must be small enough to resolve the highest spectral frequency produced by your sample. The minimum requirement, based on the Nyquist criterion, says that the sampling rate must be greater than twice this frequency; therefore the step size in k-space should be smaller than $\pi/2 \times n_1 \times L$. Imaging close to this minimum rate will reduce the measurement SNR. We recommend a step size $\leq \pi/4 \times n_1 \times L$.

   Filtration Bandwidth: The bandwidth of the spectral filter will act as a low-pass filter. In order to avoid filtering out sample frequencies, the bandwidth should be narrower than

0.5 × step size. The bandwidth will also affect the SNR. While bandwidths larger than this limit will increase light intensity, it will actually reduce SNR by filtering out sample frequencies. Bandwidth smaller than this limit will reduce SNR by decreasing the collected intensity.

Wavenumber Range: In order to capture at least one full oscillation from our highest frequency, the wavenumber range, Δk, must be greater than $\pi/n_1 \times L$. This is a very minimal requirement. If the range is set to this exact limit, none of the lower frequency information will be captured, and SNR will be significantly reduced. Ideally, the largest range possible will produce the best SNR, but it will be at the expense of imaging time. Additionally, there will be limitations based on the intensity profile of your lamp and the efficiency profile of your spectral filter. You should avoid spectral regions with low output based on these equipment specifications. Finally, you will want to avoid irradiating your cells with spectra known to cause cell damage, in particular, UV light.

Exposure Time: An ideal exposure time is a tradeoff between SNR and measurement time. The most important requirement for exposure time is to avoid saturating the camera at any wavenumbers (*see* Subheading 3.7).

Lamp Power: Lamp power can also be increased to improve SNR but should not be so strong as to damage the cells or saturate the camera (*see* Subheadings 3.7 and 3.10).

Spectral Filter Delays: Proper delays must be set between each image when tuning the spectral filter to ensure the filter is stabilized at each wavelength. Improper delays will introduce spectral artifacts.

6. **First image cube check**

   It is best practice to analyze the first image cube to check for any artifacts before proceeding with the experiment. Unexpected lamp fluctuations, system vibrations, floating debris, and other various issues can interfere with proper measurements and experimental findings. If there is an issue with the normalization measurement, the artifact will propagate through all your data. It is best to catch these errors early so that the measurements can be retaken.

7. **Colocalization with Fluorescence**

   For optimal colocalization, each fluorescent image should be acquired directly after each PWS measurement before moving the stage. This may not always be possible depending on your staining protocol (e.g. immunofluorescence). A second camera can be used, or the spectral filter can be removed to achieve higher-quality fluorescence images. If fluorescence images cannot be taken directly after PWS measurements or a secondary camera is used, image alignment will need to be per-

formed using a fiduciary marker if accurate colocalization is required.

Caution should be used when designing experiments and choosing fluorophores. In general, most fluorophore absorption/emission is negligible relative to the backscattered intensity that it will not interfere with PWS signal, but this should be confirmed for each experimental design. Another concern is structural and functional alteration due to staining prior to the acquisition of PWS data. We have shown that Hoechst 33342, a commonly used live cell DNA binding dye, will cause DNA fragmentation within seconds of excitation [5]. Acquiring PWS data prior to cell staining will preserve the integrity of the PWS data, but structural and functional alteration due to preparation procedures (e.g., cell fixation) can still interfere with the interpretation of colocalization data.

8. **Dark counts**

   Camera dark count should be reported in the camera literature. Additionally, this can be measured by recording counts with the camera turned on and all light sources turned off.

9. **Region-of-interest analysis**

   Region-of-interest (ROI) analysis can be performed on a single-wavelength image from each cube. If nuclei are not clearly visible, it can be helpful to acquire colocalized phase, transmission, or fluorescence images to create ROIs. Fluorescence colocalization is particularly useful as heterogeneity in structures other than the nucleus can be obtained. While performing region-of-interest analysis, users may find it helpful to refer to the corresponding bright-field image to more accurately locate the boundaries of cell membranes and cell nuclei.

References

1. Sexton T, Yaffe E, Kenigsberg E, Bantignies F, Leblanc B, Hoichman M, Parrinello H, Tanay A, Cavalli G (2012) Three-dimensional folding and functional organization principles of the drosophila genome. Cell 148(3):458–472. https://doi.org/10.1016/j.cell.2012.01.010
2. Matsuda H, Putzel GG, Backman V, Szleifer I (2014) Macromolecular crowding as a regulator of gene transcription. Biophys J 106(8):1801–1810. https://doi.org/10.1016/j.bpj.2014.02.019
3. Bancaud A, Huet S, Daigle N, Mozziconacci J, Beaudouin J, Ellenberg J (2009) Molecular crowding affects diffusion and binding of nuclear proteins in heterochromatin and reveals the fractal organization of chromatin. EMBO J 28(24):3785–3798. https://doi.org/10.1038/emboj.2009.340
4. Batra J, Xu K, Qin S, Zhou HX (2009) Effect of macromolecular crowding on protein binding stability: modest stabilization and significant biological consequences. Biophys J 97(3):906–911. https://doi.org/10.1016/j.bpj.2009.05.032
5. Almassalha LM, Bauer GM, Chandler JE, Gladstein S, Cherkezyan L, Stypula-Cyrus Y, Weinberg S, Zhang D, Thusgaard Ruhoff P, Roy HK, Subramanian H, Chandel NS, Szleifer I, Backman V (2016) Label-free imaging of the native, living cellular nanoarchitecture using

partial-wave spectroscopic microscopy. Proc Natl Acad Sci U S A 113(42):E6372–E6381. https://doi.org/10.1073/pnas.1608198113

6. Cherkezyan L, Zhang D, Subramanian H, Capoglu I, Taflove A, Backman V (2017) Review of interferometric spectroscopy of scattered light for the quantification of subdiffractional structure of biomaterials. J Biomed Opt 22(3):030901–030901. https://doi.org/10.1117/1.JBO.22.3.030901
7. Bancaud A, Lavelle C, Huet S, Ellenberg J (2012) A fractal model for nuclear organization: current evidence and biological implications. Nucleic Acids Res 40(18):8783–8792. https://doi.org/10.1093/nar/gks586
8. Lebedev DV, Filatov MV, Kuklin AI, Islamov AK, Kentzinger E, Pantina R, Toperverg BP, Isaev-Ivanov VV (2005) Fractal nature of chromatin organization in interphase chicken erythrocyte nuclei: DNA structure exhibits biphasic fractal properties. FEBS Lett 579(6):1465–1468. https://doi.org/10.1016/j.febslet.2005.01.052
9. Lieberman-Aiden E, van Berkum NL, Williams L, Imakaev M, Ragoczy T, Telling A, Amit I, Lajoie BR, Sabo PJ, Dorschner MO, Sandstrom R, Bernstein B, Bender MA, Groudine M, Gnirke A, Stamatoyannopoulos J, Mirny LA, Lander ES, Dekker J (2009) Comprehensive mapping of long-range interactions reveals folding principles of the human genome. Science 326(5950):289–293. https://doi.org/10.1126/science.1181369
10. Wu W, Radosevich AJ, Eshein A, Nguyen T-Q, Yi J, Cherkezyan L, Roy HK, Szleifer I, Backman V (2016) Using electron microscopy to calculate optical properties of biological samples. Biomed Opt Express 7(11):4749–4762. https://doi.org/10.1364/BOE.7.004749
11. Cherkezyan L, Stypula-Cyrus Y, Subramanian H, White C, Dela Cruz M, Wali R, Goldberg M, Bianchi L, Roy H, Backman V (2014) Nanoscale changes in chromatin organization represent the initial steps of tumorigenesis: a transmission electron microscopy study. BMC Cancer 14(1):189
12. Dong B, Almassalha LM, Stypula-Cyrus Y, Urban BE, Chandler JE, Nguyen T-Q, Sun C, Zhang HF, Backman V (2016) Superresolution intrinsic fluorescence imaging of chromatin utilizing native, unmodified nucleic acids for contrast. Proc Natl Acad Sci U S A 113(35):9716–9721. https://doi.org/10.1073/pnas.1602202113
13. Boettiger AN, Bintu B, Moffitt JR, Wang S, Beliveau BJ, Fudenberg G, Imakaev M, Mirny LA, Wu C-t, Zhuang X (2016) Super-resolution imaging reveals distinct chromatin folding for different epigenetic states. Nature 529(7586):418–422. https://doi.org/10.1038/nature16496. http://www.nature.com/nature/journal/v529/n7586/abs/nature16496.html#supplementary-information
14. Mirny LA (2011) The fractal globule as a model of chromatin architecture in the cell. Chromosom Res 19(1):37–51. https://doi.org/10.1007/s10577-010-9177-0
15. Almassalha LM, Tiwari A, Ruhoff PT, Stypula-Cyrus Y, Cherkezyan L, Matsuda H, Dela Cruz MA, Chandler JE, White C, Maneval C, Subramanian H, Szleifer I, Roy HK, Backman V (2017) The global relationship between chromatin physical topology, fractal structure, and gene expression. Sci Rep 7:41061. https://doi.org/10.1038/srep41061
16. Zink D, Fischer AH, Nickerson JA (2004) Nuclear structure in cancer cells. Nat Rev Cancer 4(9):677–687
17. Robbins SL, Kumar V, Cotran RS (2010) Robbins and Cotran pathologic basis of disease. Saunders/Elsevier, Philadelphia, PA
18. Bedin V, Adam RL, de Sa BC, Landman G, Metze K (2010) Fractal dimension of chromatin is an independent prognostic factor for survival in melanoma. BMC Cancer 10:260. https://doi.org/10.1186/1471-2407-10-260
19. Tambasco M, Costello BM, Kouznetsov A, Yau A, Magliocco AM (2009) Quantifying the architectural complexity of microscopic images of histology specimens. Micron (Oxford) 40(4):486–494. https://doi.org/10.1016/j.micron.2008.12.004
20. Tambasco M, Magliocco AM (2008) Relationship between tumor grade and computed architectural complexity in breast cancer specimens. Hum Pathol 39(5):740–746. https://doi.org/10.1016/j.humpath.2007.10.001
21. Metze K (2013) Fractal dimension of chromatin: potential molecular diagnostic applications for cancer prognosis. Expert Rev Mol Diagn 13(7):719–735. https://doi.org/10.1586/14737159.2013.828889
22. Subramanian H, Roy HK, Pradhan P, Goldberg MJ, Muldoon J, Brand RE, Sturgis C, Hensing T, Ray D, Bogojevic A, Mohammed J, Chang JS, Backman V (2009) Nanoscale cellular changes in field carcinogenesis detected by partial wave

spectroscopy. Cancer Res 69(13):5357–5363. https://doi.org/10.1158/0008-5472.can-08-3895

23. Damania D, Roy HK, Subramanian H, Weinberg DS, Rex DK, Goldberg MJ, Muldoon J, Cherkezyan L, Zhu Y, Bianchi LK, Shah D, Pradhan P, Borkar M, Lynch H, Backman V (2012) Nanocytology of rectal colonocytes to assess risk of colon cancer based on field cancerization. Cancer Res 72:2720–2727. https://doi.org/10.1158/0008-5472.CAN-11-3807
24. Konda VJ, Cherkezyan L, Subramanian L, Becker V, Goldberg MJ, Chennat JS, Karl LR, Waxman I, Roy LK, Backman V (2011) Nanoscale differences assessed by partial wave spectroscopy in the field of esophageal cancer and Barrett's esophagus. Gastroenterology 140(5):S752–S752
25. Roy HK, Brendler CB, Subramanian H, Zhang D, Maneval C, Chandler J, Bowen L, Kaul KL, Helfand BT, Wang CH, Quinn M, Petkewicz J, Paterakos M, Backman V (2015) Nanocytological field carcinogenesis detection to mitigate overdiagnosis of prostate cancer: a proof of concept study. PLoS One 10(2):e0115999. https://doi.org/10.1371/journal.pone.0115999
26. Damania D, Roy HK, Kunte D, Hurteau JA, Subramanian H, Cherkezyan L, Krosnjar N, Shah M, Backman V (2013) Insights into the field carcinogenesis of ovarian cancer based on the nanocytology of endocervical and endometrial epithelial cells. Int J Cancer 133(5):1143–1152. https://doi.org/10.1002/ijc.28122
27. Subramanian H, Pradhan P, Liu Y, Capoglu IR, Rogers JD, Roy HK, Brand RE, Backman V (2009) Partial-wave microscopic spectroscopy detects subwavelength refractive index fluctuations: an application to cancer diagnosis. Opt Lett 34(4):518–520. https://doi.org/10.1364/OL.34.000518
28. Almassalha LM, Bauer GM, Chandler JE, Gladstein S, Szleifer I, Roy HK, Backman V (2016) The greater genomic landscape: the heterogeneous evolution of cancer. Cancer Res 76:5605–5609. https://doi.org/10.1158/0008-5472.can-16-0585
29. Cherkezyan L, Capoglu I, Subramanian H, Rogers JD, Damania D, Taflove A, Backman V (2013) Interferometric spectroscopy of scattered light can quantify the statistics of subdiffractional refractive-index fluctuations. Phys Rev Lett 111(3):033903
30. Chandler JE, Stypula-Cyrus Y, Almassalha L, Bauer G, Bowen L, Subramanian H, Szleifer I, Backman V (2016) Colocalization of cellular nanostructure using confocal fluorescence and partial wave spectroscopy. J Biophotonics 10:377–384. https://doi.org/10.1002/jbio.201500298
31. Yang F, Teves SS, Kemp CJ, Henikoff S (2014) Doxorubicin, DNA torsion, and chromatin dynamics. Biochim Biophys Acta 1845(1):84–89. https://doi.org/10.1016/j.bbcan.2013.12.002
32. Roos WP, Thomas AD, Kaina B (2016) DNA damage and the balance between survival and death in cancer biology. Nat Rev Cancer 16(1):20–33. https://doi.org/10.1038/nrc.2015.2
33. Schwarz T (1998) UV light affects cell membrane and cytoplasmic targets. J Photochem Photobiol B 44(2):91–96. https://doi.org/10.1016/S1011-1344(98)00126-2
34. Gniadecki R, Thorn T, Vicanova J, Petersen A, Wulf HC (2000) Role of mitochondria in ultraviolet-induced oxidative stress. J Cell Biochem 80(2):216–222

INDEX

Natasha S. Barteneva and Ivan A. Vorobjev (eds.), *Cellular Heterogeneity: Methods and Protocols*, Methods in Molecular Biology, vol. 1745, https://doi.org/10.1007/978-1-4939-7680-5, © Springer Science+Business Media, LLC 2018

I

L

M

N

O

P

R

S

T

V

X